

ABSTRACT

REUTHER JR., JAMES FREDRICK. Synthesis, Characterization, and Applications of Helical Polycarbodiimide Homopolymers and Copolymers. (Under the direction of Bruce M. Novak).

Polycarbodiimides are a young class of helical polymers formed using transition-metal mediated polymerization techniques that display a blend of favorable properties. In order to identify necessary structure-property relationships, it is imperative to first unambiguously determine the correct polymer microstructures/ macrostructures formed upon polymerization of carbodiimide monomers. The presence of two pendant groups per repeat unit results in the possibility of two regioisomers formed during propagation. Using ^{15}N -isotope labeling and subsequent ^{15}N NMR spectroscopy, we demonstrate that the polymers formed using both Ti(IV) and Ni(II) initiators are fully regioregular when employing carbodiimide monomers with sterically inequivalent pendant groups. The bulkier pendant groups (i.e., 2° carbons attached to the backbone nitrogen) were shown to be relegated, in all cases studied, to the imine nitrogen whereas the less bulky pendant groups were bound exclusively to the amine nitrogen.

Furthermore, ^{15}N NMR spectroscopy was applied to study the highly unique chiroptical switching property exhibited by poly(*N*-1-naphthyl-*N*-octadecylcarbodiimide) (PNOC). The ^{15}N NMR spectra of the isotope-enriched PNOC reveals two peaks associated with the backbone imine nitrogen that change in population as a function of temperature and solvent. This result suggests that the chiroptical switching is the consequence of a dynamic equilibrium between two specific polymer conformations (denoted state A and B).

Using variable-temperature ^{15}N NMR to measure the proportions of each conformation as a function of temperature, the van't Hoff enthalpies and entropies of the chiroptical switching process were calculated revealing that the process is endothermic in all solvent studied. The VCD spectra of PNOC in $\text{DCM-}d_2$ (state A) and CDCl_3 (state B) display distinct characteristics corresponding to each specific conformation which was then matched up with two DFT-optimized 7mer models with oppositely oriented naphthyl groups. These models produce theoretical VCD spectra that match up nicely with the experimental VCD of state A and B.

A significant helical contraction was also noted going from the more expanded 5/1 helix in model A to a more contracted 7/2 helix in model B. This helical contraction was shown to cause hierarchical changes in the self-assembly behaviors of PNOC which is evident by AFM and POM. The lyotropic liquid crystalline properties of PNOC were shown to go through specific mesophase transitions as a function of temperature and solvent with highly unique blue phase mesophases adopted at higher temperature in concentrated benzene, CHCl_3 , and THF solutions. The thin-film morphologies of PNOC were also shown to be affected by the conformational switching, with the polymer adopting larger helical aggregates when spin-coated from toluene (state A) and smaller nanofiber aggregates when spin-coated from benzene (state B). Additionally, the thin-films spin-coated from and annealed in toluene caused interesting, unique surface reorganization when small droplets of propanediol and ethylene glycol were applied.

We also report the new controlled living polymerization of carbodiimides with bis(triphenylphosphino)aryl nickel(II) bromide initiators. Two functional initiators were also synthesized with protected alkyne and aliphatic alkene moieties appended to the 4-position of

the aryl transfer ligand. Upon polymerization with these initiators, the reactive functionalities are covalently appended to the end of the polymer chains.

Finally, the alkyne end-functionalized poly(*N*-1-phenethyl-*N*'-methylcarbodiimide) (PPEMC) was successfully coupled with mono- and bis(azide) terminated poly(ethylene glycol) (PEG) via “click” reaction. In THF/ H₂O solvent mixtures, these new RCPs aggregate into simple spherical micelles and vesicles. The PPEMC-*b*-PEG copolymers, however, adopt non-spherical, maggot-like and worm-like micelles in THF/ MeOH solutions. Blending the RCPs with PPEMC homopolymer triggers the formation of long, interconnected nanofibers in THF/ MeOH solutions with the hydrophobic homopolymer encapsulated within.

Synthesis, Characterization, and Applications of Helical Polycarbodiimide Homopolymers
and Copolymers

by
James Fredrick Reuther Jr.

A dissertation submitted to the Graduate Faculty of
North Carolina State University
in partial fulfillment of the
requirements for the degree of
Doctor of Philosophy

Chemistry

Raleigh, North Carolina

2014

APPROVED BY:

Bruce M. Novak
Committee Co-Chair

Elon A. Ison
Committee Co-Chair

Christian C. Melander

Alan E. Tonelli

DEDICATION

I dedicate this manuscript to my parents, Jim and Paula Reuther, who have taught me throughout my childhood that anything is possible if you put your mind to it. Into my adult life, they allowed me to create my own path and encouraged me to simply follow my heart in all of my life decisions which has never steered me wrong. I owe everything to them since, without their undying love and support; I would not be where I am today.

BIOGRAPHY

James Fredrick Reuther Jr. was born in July of 1988 in Washington D.C. He grew up, however, in Montgomery County, Maryland where his parents still currently reside. He first realized his love for the sciences, and chemistry in particular, when enrolled in Sherwood HS where he excelled in AP chemistry and calculus courses. Entering his freshman year at Virginia Tech, he began his studies with a focus major in chemistry and minor in mathematics in which he remained throughout his 4 years. He worked in Dr. Harry Gibson's research group as an undergraduate researcher where he first realized his true passion for synthetic organic and polymer chemistry. He graduated from Virginia Tech in May, 2010 with a B.S. Degree in chemistry and minor in mathematics and decided to immediately take the next step to graduate school. He joined the Ph. D program at North Carolina State University in August, 2010 where he immediately recognized the professor he wanted to work under. Dr. Bruce M. Novak accepted him into his group where he quickly asserted himself as a leader. In his 2nd year, Dr. Novak accepted a job at the University of Texas at Dallas to be the Dean of the Natural Sciences and Mathematics College. James followed his principle investigator to Dallas to complete his graduate studies. He became an active member in the ACS Polymer and Organic Divisions and, in 2014, was recognized for outstanding graduate research in the field of polymer chemistry at the Excellence in Polymer Graduate Research symposium at the 2014 Spring ACS National Meeting in Dallas, TX.

ACKNOWLEDGEMENTS

Graduate school is an extremely stressful, emotionally taxing process that I could not have accomplished without the love and support of my family and friends. I first want to show my eternal gratitude to my loving parents, Jim and Paula Reuther, whom I dedicate this dissertation to. They pushed me throughout my life to be the best person I can be in every aspect of life. From an early age, they emphasized the importance of excelling in school which I carried with me all the way through grade school and college. I would not be where I am today without the love and support they provided and I cannot say enough to begin to describe the level of appreciation I have for the way they raised me and my sister. To my sister, Jenni Reuther, thank you for being a wonderful sister and friend. You helped me in ways that you probably aren't even aware of and I truly appreciate you always being there when I need to talk to someone. I also want to thank the rest of my family, including all of my cousins, aunts, and uncles, whom I am very close with and love very much.

To my good friends Jimmy Price and Nirav Shah that have always helped distract me from all of the stress that comes with graduate school, thanks for all of the fun times. Without them, I don't think I would have been able to retain my sanity. I have also established several great and lasting friendships during my time at both NCSU and UTD. Entering graduate school at NCSU, I was not sure what to expect. But meeting people like James Hemphill, Alex Prokup, Lance Wilson, Dan Frasco, Angelito Nepomuceno, Kalyn Brown, and Conni Bond, who are just like me entering in the same situation, made the early times in graduate school much easier. When I was surprised by the prospect of moving to Dallas, I was supported by my friends and family to follow my heart and do what I thought was best.

Special thanks go to fellow Novakians Dr. Joseph DeSousa, Dr. Justin Kennemur, and Dr. Januka Budhathoki-Uprety who were in the group when I joined. Their guidance in teaching me the ins and outs of polycarbodiimide chemistry and what graduate school was all about helped tremendously to make the transition from the undergraduate level. To the current Novakians at UTD, thanks so much for your help in thesis preparation and all of our projects. Thanks to Raymond Campos and Ben Batchelor, in particular, for not only their help in research but also the fun times we shared at Jack Mac's talking science over beers. I would also like to thank my girlfriend, Nimmy Mammootil, whom I met while at UTD. Your continued love and support has made me happier than you could ever know.

Thank you to my committee members Dr. Christian Melander, Dr. Elon Ison, and Dr. Alan Tonelli, all of whom I had the pleasure of having as teachers, for agreeing to be on my committee. Thank you for all your combined support and for all you have taught me. Finally, I am truly indebted to Dr. Bruce M. Novak, my research advisor, for accepting me into his research group and giving me the freedom to pursue my own research projects and ideas. Thank you so much for your guidance through the past four years and your continued encouragement. I could not ask for a better P.I. to work under and I am proud to be considered a Novakian for the rest of my chemistry career.

TABLE OF CONTENTS

LIST OF TABLES.....	xi
LIST OF SCHEMES.....	xii
LIST OF FIGURES.....	xv
LIST OF ABBREVIATIONS.....	xxxvi
CHAPTER 1: INTRODUCTION TO POLYCARBODIIMIDES.....	1
1.1. History and Background.....	1
1.2. Proposed Mechanism of Polymerization.....	4
1.3. Polycarbodiimides as Static and Dynamic Helices.....	8
1.4. Properties of Polycarbodiimides.....	13
1.5. References.....	21
CHAPTER 2: USING ¹⁵ N NMR SPECTROSCOPY TO DIRECTLY PROBE THE REGIOREGULARITY OF POLYCARBODIIMIDES.....	25
2.1 Origin of Regioregularity in Polycarbodiimides.....	25
2.2 Difficulties in Determining Regioregularity.....	27
2.3 Initial ¹⁵ N NMR Experiments to Directly Probe the Regioregularity.....	33
2.4 Probing the Effect of Altered Electronics in the Phenyl Side Group.....	38
2.5 Steric Influences of Pendant Groups on Regioregularity.....	43

2.6	Identification of Regioregularity in Specific, Unusual Cases.....	48
2.7	Effect of Different Transition Metal Catalysts on the Regioregularity.....	52
2.8	Conclusions.....	54
2.9	Experimental Section.....	55
2.10	References.....	111
CHAPTER 3: DEFINITELY IDENTIFYING THE MECHANISM OF CHIROPTICAL SWITCHING BY ¹⁵ N NMR AND VCD SPECTROSCOPY.....		114
3.1	Background of Chiroptical Switches.....	114
3.2	The Discovery and Advancement of Chiroptical Switching Polycarbodiimides.....	120
3.3	Effect of Solvent on the ¹⁵ N NMR, IR, and ECD Spectra.....	130
3.4	¹⁵ N NMR studies in Mixed Solvent Systems.....	137
3.5	Effect of the Switching Process on the Amine Nitrogen.....	139
3.6	Variable Temperature ¹⁵ N NMR of Poly-29 and Poly-31	144
3.7	Using Van't Hoff Analysis to Calculate the Thermodynamic Parameters of Switching.....	151
3.8	Identifying the Specific Conformations of State A and B Using VCD spectroscopy.....	156
3.9	Comparing VCD Spectra of Poly-6 and Poly-14	162
3.10	Attempted Synthesis of New, Chiroptical Switching Polycarbodiimides.....	165

3.11 Conclusions.....	170
3.12 Experimental Section.....	173
3.13 References.....	214
CHAPTER 4: POTENTIAL APPLICATIONS FOR PNOC AND RELATED POLYCARBODIIMIDES.....	218
4.1 Introduction to Microscopy.....	218
4.1.1 Electron Microscopy.....	219
4.1.2 Contact-Mode AFM.....	220
4.1.3 Tapping-Mode AFM.....	222
4.1.4 Analyzing Liquid Crystals with Polarizing Optical Microscopy.....	224
4.2 Dynamic Lyotropic Liquid Crystallinity of PNOC.....	226
4.3 Comparison of LC Behaviors Exhibited by PNOC and PPOC.....	238
4.4 Tunable Surface Morphology of PNOC.....	242
4.5 Unique Droplet Movement Induced by Surface Reorganization of Thin PNOC and PPOC Films.....	249
4.6 Conclusions.....	257
4.7 Experimental Section.....	259
4.8 References.....	270
CHAPTER 5: CONTROLLED “LIVING” POLYMERIZATION OF CARBODIIMIDES USING VERSATILE NICKEL(II) INITIATORS.....	274

5.1	Introduction to Living Polymerizations.....	274
5.2	End Functionalization of Macromolecules Using Functional Initiators.....	278
5.3	Controlled “Living” Ni(II) Mediated Polymerization of Carbodiimides.....	286
5.4	Grafting PPEMC from Poly(4-bromostyrene).....	297
5.5	End-Functionalization of PPEMC with Functional Ni(II) Initiators.....	302
5.6	Attempted Copolymerization of Polycarbodiimides with Poly(3-hexylthiophene) Using Nickel(II) Complexes.....	315
5.7	Conclusions.....	319
5.8	Experimental Section.....	321
5.9	References.....	359
CHAPTER 6: SYNTHESIS AND SELF-ASSEMBLY OF NOVEL ROD-COIL		
BLOCK COPOLYMERS WITH CHIRAL POLYCARBODIIMIDE SEGMENTS.....		
		363
6.1	Background on Rod-Coil Block Copolymers.....	363
6.2	Synthesis of Amphiphilic PPEMC- <i>b</i> -PEG RCPs.....	368
6.3	Surface Morphologies of PPEMC- <i>b</i> -PEG RCPs.....	375
6.4	Self-Assembly of PPEMC-PEG Copolymers Cast from THF/H ₂ O.....	386
6.5	Self-Assembly of PPEMC-PEG Copolymers Cast from THF/MeOH.....	400
6.6	Self-Assembly of PPEMC-PEG Copolymer/ PPEMC Homopolymer Blends.....	411
6.7	Attempted Synthesis of PPEMC- <i>b</i> -PDMS- <i>b</i> -PPEMC via Hydrosilation.....	422
6.8	Conclusions.....	425

6.9	Experimental Section.....	426
6.10	References.....	452

LIST OF TABLES

Table 3.1	Empirically calculated van't Hoff enthalpies and entropies of the reversible, chiroptical switching process using the relative integration the nitrogen-15 NMR peaks corresponding to the imine nitrogen to measure the populations of each polymer conformation.....	154
Table 6.1	Summarized MW data for Poly-44 and resulting copolymers synthesized via successful alkyne-azide “click” coupling of end groups.....	372
Table 6.2	Advancing and receding water contact angles of PPEMC-PEG block copolymer thin-films prepared via the same protocol used for AFM sample preparation.....	386

LIST OF SCHEMES

- Scheme 1.1 The proposed mechanism of polymerization for polycarbodiimides carried out with transition metal initiators. The carbodiimide monomer is initiated upon ligand transfer creating a metal-amidinate complex that allows for sequential insertion of additional monomers..... 4
- Scheme 1.2 The proposed propagation mechanisms for asymmetric polycarbodiimides can produce two different regioisomers along the backbone. Depending on the particular bias of monomer insertion (or lack thereof), the polymerization will form a regioregular polymer with an excess of a single regioisomer or a regioirregular polymer with mixed populations of both..... 7
- Scheme 1.3 Synthesis of select polycarbodiimides designed specifically to have high energies of racemization. The large anthracene pendant group provides the necessary steric bulk to restrict helical inversion..... 13
- Scheme 2.1 The proposed mechanism of polymerization of carbodiimide monomers with titanium(IV) catalysts. The monomer can insert into the initiated titanium-amidinate complex through two possible pathways giving way to the possible formation of two regioisomers..... 26

Scheme 2.2	Proposed thermal degradation pathway for polycarbodiimides at elevated temperatures of 150 – 200 °C. Depending on the degree of regioregularity, different populations of three monomers can be formed upon unzipping of the polymer backbone.....	29
Scheme 2.3	General synthesis of ¹⁵ N-labeled polycarbodiimides.....	34
Scheme 2.4	Synthesis scheme for Poly-29 using the ¹⁵ N-enriched sodium nitrate...	51
Scheme 3.1	Some examples of small molecule chiroptical switches including overcrowded alkenes, diarylethene switches, and azobenzene derivatives.....	116
Scheme 3.2	Examples of macromolecular chiroptical switches that are affected by a variety of stimuli including irradiation, redox chemistry, temperature change, and solvent change.....	118
Scheme 3.3	Synthesis scheme of Poly-31 using the ¹⁵ N-enriched reagents Na ¹⁵ NO ₃ and ¹⁵ N-potassium phthalimide.....	141
Scheme 3.4	Synthesis scheme for potential di-aryl chiroptical switching polycarbodiimides.....	168
Scheme 3.5	Synthesis scheme for the possible water soluble polycarbodiimide.....	170
Scheme 5.1	Synthesis of amphiphilic, tadpole-shaped POSS-PAA hybrid polymer using T ₈ -isobutyl POSS functionalized RAFT agents.....	282

- Scheme 5.2 Synthesis of nickel (II) initiators **Ni-1** and **Ni-2** and applied polymerizations of various carbodiimide monomers forming high MW liquid crystalline macromolecules..... 287
- Scheme 5.3 Synthesis of (*S*)-PPEMC-*g*-PBrS rod-coil graft copolymer by forming the active Ni(II) macroinitiator appended to ~22 % of the aryl bromide pendant groups of PBrS..... 298
- Scheme 5.4 Synthesis of protected alkyne and alkene functionalized bis(triphenylphosphino)aryl nickel(II) bromide initiators and subsequent polymerization of **Mono-1R** forming end-functionalized polycarbodiimides..... 304
- Scheme 5.5 Proposed synthesis of P3HT-*b*-(*R*)-PPEMC using dppe ligated **Ni-1** via one-pot tandem Kumada polycondensation/controlled “living” nickel(II) mediated polymerization of carbodiimides..... 317
- Scheme 6.1 Synthesis of amphiphilic (*R*)-PPEMC-*b*-PEG and (*S*)-PPEMC-*b*-PEG-*b*-(*S*)-PPEMC di- and tri- RCPs (n denotes number of polycarbodiimide repeat units and m denotes number of PEG repeat units) via CuAAC “click” reaction of functional end-groups..... 369
- Scheme 6.2 Hydrosilation reaction of **Poly-45** with bis(silane) terminated PDMS forming a new class of RCP with highly flexible PDMS and highly rigid polycarbodiimide segments..... 386

LIST OF FIGURES

Figure 1.1	The two opposite handed helices are enantiomers of one another. The <i>P</i> -helix proceeds away from the viewer in a clockwise rotational motion and vice versa for the <i>M</i> -helix.....	2
Figure 1.2	The linear plot of monomer: initiator (catalyst) ratio vs. the number average molecular weight indicates the lack of chain transfer in the polymerization of Mono-1R	5
Figure 1.3	The racemic mixture of <i>M</i> and <i>P</i> helices for Poly-2 is biased to an induced helical sense upon chiral perturbation with the molecular chaperone CSA.....	9
Figure 1.4	Specific optical rotation changes of Poly-3 and Poly-4 upon annealing as a function of time. This shows the evolution from the kinetically controlled conformation to the energetically favored thermodynamically controlled conformation.....	10
Figure 1.5	Representation of most common liquid crystalline mesophases.....	14
Figure 1.6	Representation of the liquid crystalline layering of Poly-2 and poly(<i>n</i> -hexyl isocyanate). The increased density of the hexyl side groups on Poly-2 forms a barrier between adjacent chains resulting lyotropic smectic A mesophase seen in the polarizing optical microscope (POM) image.....	15

- Figure 1.7 Series of polymers showing varying cases of liquid crystallinity with polymers wielding identical side chains adopting more ordered smectic mesophases and ones with different side chains adopting a nematic mesophase. The chiral **Poly-1R** adopts a helical chiral nematic mesophase..... 17
- Figure 1.8 POM images of lyotropic liquid crystalline **Poly-1(rac)** in toluene, **Poly-1R** in CHCl₃, and **Poly-9** in 1,1,2,2-tetrachloroethane at 65 °C.... 17
- Figure 1.9 POM images of thermotropic liquid crystalline **Poly-11** at 118 °C and **Poly-8** at 130 °C displaying smectic mesophases..... 19
- Figure 1.10 Mechanism of depolymerization of polycarbodiimides occurs via homolytic cleavage of the C-N backbone bond followed by unzipping of the rest of the backbone..... 19
- Figure 2.1 ¹³C NMR chemical shifts for the *sp*³ α-carbons of the aliphatic side groups and the C=N imine stretches of IR spectra for the series of polycarbodiimides synthesized to determine possible microstructures... 30
- Figure 2.2 FTIR spectra of **Poly-14**, **Poly-15**, and variable temperature FTIR spectrum of **Poly-14** in CHCl₃. The two peaks present in the imine region for **Poly-14** change in intensity as a function of time whereas the peaks for **Poly-15** do not..... 32

Figure 2.3	^{15}N NMR chemical shifts of nitrogen-15 enriched amidine compounds used for comparison to the polycarbodiimide repeat unit to aid in peak assignment of both backbone nitrogens in the ^{15}N NMR spectra of isotope-enriched polycarbodiimides.....	35
Figure 2.4	^{15}N NMR spectra of Poly-16 , Poly-17 , and Poly-18 supporting regioregular placement throughout the entire polymer backbone.....	37
Figure 2.5	Series of polycarbodiimides synthesized to probe the effect of pendant group electronics on monomer insertion.....	39
Figure 2.6	^{15}N NMR spectra of Poly-19 and Poly-20 in CDCl_3 . Both polymers display only one peak (i.e. regioregular) with the aromatic pendant group bonded to the imine position in all cases.....	40
Figure 2.7	Comparison of C=N imine stretch in the FTIR spectra of Poly-20 , Poly-21 , and the unlabeled poly(<i>N</i> -4-methylphenyl- <i>N'</i> -hexylcarbodiimide).....	41
Figure 2.8	FTIR spectra zoomed in on the C=N imine region for Poly-22 and Poly-23 as well as the unlabeled versions of the polymers. The absence of a ^{15}N -isotope shift in both cases is evidence of regioregular placement along the backbone.....	43
Figure 2.9	Series of ^{15}N -labeled polycarbodiimides synthesized to probe the effect of altered sterics in the side groups.....	44

Figure 2.10	^{15}N -NMR spectra of Poly-24 and Poly-25 support the idea that the primary bias for monomer insertion is governed by sterics.....	46
Figure 2.11	^{15}N NMR spectra of Poly-26 and Poly-27 showing the loss of regioisomer selectivity as the sterically bulky aryl group moves farther away from the polymer backbone.....	48
Figure 2.12	FTIR imine stretch of the unlabeled Poly-14 and Poly-15 and the ^{15}N -enriched Poly-28 and Poly-29	50
Figure 2.13	^{15}N NMR spectra of Poly-28 and Poly-29 used to help elucidate the reason for multiple peaks in imine region of the IR spectra.....	52
Figure 2.14	^{15}N NMR spectrum of Poly-17(Ni) polymerized from Cat-5	54
Figure 3.1	Mono-6 polymerized with the enantiopure Cat-6 exhibited chiroptical switching properties capable of drastic alterations to both the SOR and CD Cotton effect simply upon small changes to the temperature or solvent.....	122
Figure 3.2	Three possible molecular motions capable of exhibiting the large SOR changes seen for Poly-6 include helical inversion (φ), imine inversion (ω), and rotation of the N-C _{anthracene} bond (θ).....	123
Figure 3.3	The model compound was used to compute the theoretical VCD spectra to fit with experimental VCD spectra of Poly-6 in toluene and chloroform. The IR spectra is shown as well.....	124

Figure 3.4	Proposed two states of switching in Poly-6 optimized at both the semiempirical (AM1) level and molecular-mechanics (MMFF94) level.....	125
Figure 3.5	VT-polarimetry in CHCl ₃ , THF, and toluene and VT-ECD in THF of Poly-14 showing drastic chiroptical switching as a function of temperature and solvent.....	127
Figure 3.6	VT- ¹ H NMR spectra of Poly-14 in THF from 0 – 40 °C display new chemical shifts arising at higher temperatures.....	128
Figure 3.7	VT-polarimetry on Poly-14 dissolved in benzene and various alkyl substituted aromatic solvents.....	129
Figure 3.8	VT-polarimetry of Poly-29 in CHCl ₃ , THF, and toluene showing the ability to change ~620° simply by altering the solvent or temperature...	131
Figure 3.9	The two FTIR C=N imine stretches for Poly-29 change in intensity as the solvent is changed from benzene to CHCl ₃ to THF to DCM suggesting that the chiroptical switching is consequence of varying populations of two states.....	132
Figure 3.10	¹⁵ N NMR of Poly-29 in CDCl ₃ , THF-d ₈ , and toluene-d ₈ displays two peaks correlating to specific conformations of the polymer found in solution.....	133

- Figure 3.11 ^{15}N NMR spectra of **Poly-29** in benzene- d_6 and DCM- d_2 displaying only one peak in each meaning the all of the polymer chains are predominantly in one conformation. The ^{15}N NMR of **Poly-30** also displayed one peak confirming that the two conformations present in **Poly-29** are consequence of the switching process..... 135
- Figure 3.12 ECD spectra of **Poly-29** in DCM, THF, and cyclohexane show the switching CD Cotton effect as a function of solvent. The UV-Vis spectrum is also shown..... 137
- Figure 3.13 ^{15}N NMR spectra of **Poly-29** dissolved in varying concentrations of mixed chloroform-toluene systems to selectively tune the populations of the two polymeric conformations..... 139
- Figure 3.14 VT-polarimetry of **Poly-31** THF, toluene, and chloroform displays a SOR change $\sim 150^\circ$ simply by varying the temperature and/or the solvent..... 141
- Figure 3.15 ^{15}N NMR spectra of **Poly-31** in CDCl_3 , THF- d_8 , toluene- d_8 showing the effect of the chiroptical switching phenomenon on the amine nitrogen..... 143
- Figure 3.16 VT- ^{15}N NMR spectra of **Poly-29** in toluene- d_8 at 35 - 55 $^\circ\text{C}$ showing the conformational shift upon heating the polymer solution..... 146
- Figure 3.17 VT- ^{15}N NMR spectra of **Poly-31** in toluene- d_8 at 35 - 55 $^\circ\text{C}$ showing the conformational shift upon heating the polymer solution..... 147

- Figure 3.18 VT-¹⁵N NMR of **Poly-29** in THF-*d*₈ at 20 - 40 °C displaying a more drastic population shift compared to that of toluene polymer solutions.. 148
- Figure 3.19 VT-¹⁵N NMR of **Poly-31** in THF-*d*₈ at 20 - 40 °C displaying a more drastic population shift compared to that of toluene polymer solutions.. 149
- Figure 3.20 VT-¹⁵N NMR spectra of **Poly-29** in CDCl₃ at 10 - 20 °C showing the most pronounced population change over a smaller temperature range.. 150
- Figure 3.21 VT-¹⁵N NMR spectra of **Poly-31** in CDCl₃ at 10 - 20 °C showing the most pronounced population change over a smaller temperature range.. 151
- Figure 3.22 Van't Hoff Plots of **Poly-29** and **Poly-31** in toluene-*d*₈, THF-*d*₈, and CDCl₃ used to determine the thermodynamics of the chiroptical switching process..... 153
- Figure 3.23 VCD and IR spectra of **Poly-14** in DCM-*d*₂, THF-*d*₈, CDCl₃ showing different spectra corresponding to the two different states of chiroptical switching..... 158
- Figure 3.24 Simplistic representation of the DFT optimized model of **Poly-14** with atom labels..... 159
- Figure 3.25 Two simplified 7mer model structures of **Poly-14** optimized using DFT calculations with right-handed helicity (*P*-helix) and oppositely oriented naphthyl pendant groups shown in the side view and the view down the helix..... 160

Figure 3.26	Experimental VCD and IR spectra of Poly-14 in DCM- d_2 and $CDCl_3$ showing different spectra corresponding to the two distinct side group conformations along with DFT calculated VCD and IR spectra of two optimized 7mer models.....	162
Figure 3.27	The effect of the helix pitch on the calculated VCD spectra highlighted by comparison of the optimized models A (5/1 helix, $C_3-N_4-C_5-C_6 = 135^\circ$) and B (7/2 helix, $C_3-N_4-C_5-C_6 = -125^\circ$) with the A' (5/1 helix, $C_3-N_4-C_5-C_6 = -120^\circ$) and B' (7/2 helix, $C_3-N_4-C_5-C_6 = +140^\circ$).....	164
Figure 3.28	A new library of polycarbodiimides synthesized to determine the electronic, steric, and pendant group attachment effects on the switching process.....	166
Figure 4.1	Representation of the optical sensing systems used for contact-mode AFM with labels of each working component.....	221
Figure 4.2	Depiction of the oscillating probe used for TMAFM and the sinusoidal resonant frequency displayed for free oscillation as well as the response felt when oscillating on the sample surface.....	224
Figure 4.3	Schematic representation of the working components of POM with labels and the path of light that travels through cross-polarizers and the birefringent LC sample.....	225
Figure 4.4	X/Y Representation of simple-twist and frustrated double-twist structures and the assembled double-twist cylinder in blue-phase LCs..	228

Figure 4.5	Representation of the three-dimensional cubic arrays of BP I (body-centered cubic) and BP II (simple cubic) mesophases and the defect line that result.....	229
Figure 4.6	POM images of 15 w% solutions of Poly-14 in benzene, CHCl ₃ , and THF at 25 and 40 °C displaying the clear mesophase transition to the lyotropic BP I mesophase at higher temperatures.....	231
Figure 4.7	POM images of thin-films cast from 15 w% LC solutions of Poly-14 in benzene, CHCl ₃ , and THF.....	233
Figure 4.8	POM images of 25 w% LC solutions of Poly-14 dissolved in benzene, CHCl ₃ , and THF at 25 and 40 °C showing the proposed N*→ BP I mesophase transition.....	235
Figure 4.9	POM images of 25 w% toluene solutions of Poly-14 at 25, 50, and 80 °C as well as the image after cooling back to 25 °C.....	237
Figure 4.10	POM images of Poly-14 thin-films cast from 25 w% LC solutions in benzene, CHCl ₃ , THF, and toluene.....	238
Figure 4.11	POM images of 25 w% Poly-41 LC solutions in benzene, CHCl ₃ , THF, and toluene at 25 and 40 °C.....	240
Figure 4.12	POM images of Poly-41 thin-films cast from 25 w% LC solutions in benzene, CHCl ₃ , THF, and toluene.....	241

- Figure 4.13 Extended 35mer models of **Poly-14** with added octadecyl pendant groups used to better visualize the subtle conformational changes associated with switching from state A to B..... 243
- Figure 4.14 Height and phase AFM micrographs of **Poly-14** thin-films spin-coated from toluene and annealed in toluene vapor for 48 hours. Also shown are two zoomed height images used to measure the dimensions of the helical bundles..... 245
- Figure 4.15 Height and phase AFM micrographs of **Poly-14** spin-coated from benzene and annealed under benzene vapor for 48 hours prior to imaging..... 247
- Figure 4.16 Two proposed interdigitation pathways of state A which, in turn, cause the formation of the large, helical aggregates observed by AFM..... 247
- Figure 4.17 Height and phase AFM micrographs of **Poly-41** spin-coated from and annealed in toluene and benzene showing nanofibular morphologies similar to **Poly-14** cast from benzene in both cases..... 249
- Figure 4.18 Contact angle measurements of propanediol dropped on (*R*)-PNOC (**Poly-14**) thin-films prepared by spin-coating from toluene and benzene and annealed under solvent vapor for 48 hours. Also shown are the images of the drops at specific times showing the droplet movement after surface reorganization on the toluene-cast film..... 251

- Figure 4.19 Contact angle measurements of propanediol dropped on (*S*)-PPOC (**Poly-41**) thin-films prepared by spin-coating from toluene and benzene and annealed under solvent vapor for 48 hours. Also shown are the images of the drops at specific times showing the droplet movement after surface reorganization on the toluene-cast film..... 254
- Figure 4.20 Picture of the moving propanediol droplets on **Poly-14** and **Poly-41** thin films prepared by spin-coating from and annealing in toluene..... 256
- Figure 5.1 Examples of functional initiators (or chain transfer agent for RAFT) used in ATRP, RAFT polymerizations, NMP, and Kumada polycondensation where FG is a generic functional group..... 279
- Figure 5.2 Synthesis of dendritic, multi-arm star copolymer and AFM image of resulting amphiphilic star polymer..... 280
- Figure 5.3 TEM image cast from water; Cryo-TEM image in water of POSS-PAA micelle at pH = 8.5 and plot of hydrodynamic radius vs. pH showing a decrease in radius at low pH due to the collapsed protonated PAA polymer chains..... 282
- Figure 5.4 Synthesis of patterned photopolymer film, schematic of proposed surface polymerization, and photopolymer composition with 10 wt% ATRP or NMP initiator methacrylate moiety..... 284

- Figure 5.5 AFM images of patterned photopolymer film before and after surface graft polymerization showing an increase in diameter of the nanopillar arrays from 60 nm to 75 nm..... 284
- Figure 5.6 ^1H NMR and ^{15}N NMR spectra of ^{15}N -labeled **Poly-18(Ni)** clearly showing the phenyl end group and the formation of a single regioisomer upon polymerization with **Ni-1**..... 288
- Figure 5.7 VCD and IR spectra of **Poly-1R** and **Poly-1S** in CDCl_3 showing the formation of opposite handed helices through mirror-image VCD spectra..... 290
- Figure 5.8 The polymerization kinetics of **Mono-1** with **Ni-1** and **Ni-2** shown in two plots: time vs. $\ln([M_0]/[M])$ and percent conversion vs. M_n . The linear relationship in both plots provides further evidence of “living” character..... 292
- Figure 5.9 MALDI-TOF mass spec of **Poly-1R** showing a high degree of phenyl end group incorporation via polymerizations initiated by **Cat-1**. The second end group was also confirmed to be a hydrogen due to abstraction of a proton from methanol solvent molecule upon work up. 294
- Figure 5.10 ^{19}F NMR of **Poly-3** polymerized using **Cat-2** allowing for quantification of the average number of repeat units by relative integration of the chemical shift of the end group versus the chemical shift of the pendant group..... 295

Figure 5.11	Plot of M_n vs. [Mono-42]/[Ni-2] portraying the high degree of control over MW simply by altering the monomer-to-catalyst ratio. The M_n values were calculated using the relative integration between the ^{19}F chemical shifts of the end group with respect to the pendant group chemical shifts.....	296
Figure 5.12	^1H NMR of PBrS; Ni(II) activated PBrS macroinitiator, and ^{31}P NMR of macroinitiator complex.....	298
Figure 5.13	GPC chromatogram of parent PBrS (blue) and (<i>S</i>)-PPEMC- <i>g</i> -PBrS (red) showing distinct shift in retention time indicative of significant increases of MW upon graft copolymerization.....	300
Figure 5.14	DSC and TGA thermograms of (<i>S</i>)-PPEMC- <i>g</i> -PBrS.....	300
Figure 5.15	Height and Phase TMAFM micrographs of (<i>S</i>)-PPEMC- <i>g</i> -PBrS spin coat from CHCl_3 and annealed in saturated CHCl_3 vapor for 24 hrs.....	302
Figure 5.16	^1H NMR and ^{31}P NMR spectra of Ni-3	305
Figure 5.17	^1H NMR and ^{31}P NMR spectra of Ni-4	306
Figure 5.18	^1H NMR spectra of the protected alkyne terminated Poly-43 and deprotected Poly-44 showing the clear loss of the TIPS protons upon reaction with TBAF.....	307
Figure 5.19	^{13}C DEPTQ135 NMR spectra of Poly-43 with peak assignments.....	308
Figure 5.20	MALDI-TOF MS of TIPS protected alkyne end-functionalized Poly-43 showing the major mass distribution corresponding to the desired two end groups plus H^+	311

Figure 5.21	MALDI-TOF MS of deprotected alkyne end-functionalized Poly-44 after deprotection with TBAF showing the major mass distribution corresponding to the desired two end groups plus H ⁺	311
Figure 5.22	¹ H NMR spectrum of alkene end-functionalized Poly-45 with peak assignments.....	312
Figure 5.23	¹³ CDEPTQ135 NMR spectra of Poly-45 with peak assignments.....	313
Figure 5.24	MALDI-TOF MS of Poly-45 showing the clear mass distribution corresponding to the alkene end functionalized PPEMC.....	315
Figure 5.25	¹ H NMR spectrum of P3HT- <i>b</i> -(<i>R</i>)-PPEMC.....	318
Figure 5.26	Examples of GPC chromatograms for two attempted copolymerizations of P3HT and (<i>R</i>)-PPEMC showing the multimodal distributions corresponding to multiple MW distributions.....	319
Figure 6.1	POM and Fluorescence micrographs of different shaped supramolecular assemblies of PS- <i>b</i> -PPQ including spheres, cylinders, and vesicles used for the encapsulation of C ₆₀ and C ₇₀ fullerenes. Also shown are the fluorescence and SEM micrographs of the highly ordered, microporous thin-film resulting from the slow evaporation of the vesicle aggregates.....	365

- Figure 6.2 CuAAC “click” reaction of alkyne terminated P3HT and azide terminated PEG forming a novel, π -conjugated RCP. Also shown are TEM images of resulting nanofiber aggregates of copolymer cast from water, bundled nanofibers of RCP and P3HT homopolymer blends cast from methanol, and highly branched superstructures of 480:1 molar ratio RCP: P3HT homopolymer cast from water/ methanol mixtures.... 366
- Figure 6.3 Structure of PBLG-*b*-PEG; TEM and height AFM micrographs of spherical micelles adopted by PBLG-*b*-PEG in THF/DMF-water solutions and helical ribbon/ ring aggregates of RCP blended with high MW PBLG homopolymer. Also shown, with the AFM image, is the height step-function across the length of the helical aggregate showing the relative periodicity of the helical rotation, i.e., the helical pitch..... 368
- Figure 6.4 ^1H NMR spectra of **CoPoly-1**, **2**, and **3** with zoomed regions of **CoPoly-1**..... 373
- Figure 6.5 DSC thermograms of **CoPoly-1**, **2**, and **3**..... 375
- Figure 6.6 Height and phase AFM micrographs of **CoPoly-1** and **CoPoly-2** showing ordered nanofibular morphologies with distinct phase separation..... 377

- Figure 6.7 Cartoon representations of **CoPoly-1** and **2** with estimated chain dimensions are shown with the zoomed AFM phase image and step function across the dotted-black line showing the distinct phases. Statistical analysis of the diameter for each phase results in the predicted morphology depicted above..... 379
- Figure 6.8 Height and phase AFM micrograph of **CoPoly-3** spin-coated from THF solution and annealed at 65 °C displaying the macroporous morphology. The porous morphology is also observed in the SEM micrograph bulk polymer precipitated from THF and annealed at 65 °C..... 381
- Figure 6.9 POM images of **CoPoly-3** in concentrated 30 wt% and 40 wt% THF solutions showing the large vesicle-like aggregates. Also depicted is the hypothesized ordering of the vesicles upon solvent evaporation and melting of the aggregates forming the large, sub-micron diameter craters observed in AFM..... 383
- Figure 6.10 POM images of **CoPoly-1, 2, and 3** in concentrated toluene solutions displaying the ordered, chiral nematic mesophase in portions of the solution..... 384
- Figure 6.11 AFM height image of **CoPoly-1, 2, and 3** spin-coated from toluene and annealed at 65 °C for 24 hour..... 385

- Figure 6.12 DLS plots of hydrodynamic radius (R_h) vs. scattering intensity for **CoPoly-1, 2, and 3** in THF/ 10v% water and Water/ 10v% THF showing the change in aggregation size and behavior as a function of water content..... 389
- Figure 6.13 2D Height and phase AFM micrographs and 3D height plot of **CoPoly-1** spin-coated from H₂O/ 10 v% THF displaying micellular aggregation behaviors with the structure depicted. Statistical analysis of the AFM image provides average diameter of the micelles and the standard deviation..... 390
- Figure 6.14 2D Height and phase AFM micrographs and 3D height plot of **CoPoly-1** spin-coat from THF/ 10 v% H₂O displaying vesicles aggregation behaviors with the structure depicted. Statistical analysis of the AFM image provides average diameter of the vesicles; the bilayer and their standard deviations..... 392
- Figure 6.15 2D Height and phase AFM micrographs and 3D height plot of **CoPoly-2** spin-coat from H₂O / 10 v% THF displaying micelle aggregation. The height step function shown was used for statistical analysis providing an average diameter of the micelles and their standard deviations..... 394

- Figure 6.16 2D Height and phase AFM micrographs and 3D height plot of **CoPoly-2** spin-coat from THF/ 10 v% H₂O displaying vesicles aggregation behaviors. The phase step function shows the phase difference associated with the edge and the hollow interior of the vesicle. Statistical analysis of the AFM image provides average diameter of the vesicles; the bilayer and their standard deviations..... 395
- Figure 6.17 2D Height and phase AFM micrographs and 3D height plot of **CoPoly-3** spin-coat from H₂O / 10 v% THF displaying micelle aggregation. The height step function shown was used for statistical analysis providing an average diameter of the micelles and their standard deviations..... 397
- Figure 6.18 Cryo-TEM images of **CoPoly-3** vitrified in H₂O/ 10 v% THF solutions and embedded in a carbon grid showing the presence of both micelles and vesicles in solution..... 398
- Figure 6.19 2D Height and phase AFM micrographs and 3D Height plot of **CoPoly-3** spin-coat from THF/ 10 v% H₂O displaying vesicles aggregation behaviors. Statistical analysis of the AFM image provides average diameter of the vesicles; the bilayer and their standard deviations with larger than expected diameter values associated with the bilayer leading to the hypothesized structure shown..... 400

- Figure 6.20 DLS plots of **CoPoly-1, 2, and 3** in THF/ 10 v% MeOH and MeOH/ 10 v% THF showing the change in aggregation behavior as a function of solvent combinations..... 401
- Figure 6.21 2D Height and phase AFM micrograph and 3D height plot of **CoPoly-1** spin-coat from THF/ 10 v% MeOH displaying maggot-like micelle aggregation behaviors. The height step function shown was used for statistical analysis providing an average width and length of the micelles and their standard deviations..... 403
- Figure 6.22 2D Height and phase AFM micrographs of **CoPoly-1** spin-coat from MeOH/ 10 v% THF showing mixtures of spherical and worm-like micelle assemblies..... 405
- Figure 6.23 2D Height and phase AFM micrograph and 3D Height plot of **CoPoly-2** spin-coat from THF/ 10 v% MeOH displaying spherical micelle aggregation behaviors. The height step function shown was used for statistical analysis providing an average diameters of the micelles and their standard deviations..... 406
- Figure 6.24 2D Height and phase AFM micrograph and 3D Height plot of **CoPoly-2** spin-coat from MeOH/ 10 v% THF displaying worm-like micelle aggregation behaviors. The formation of these assemblies is believed to be consequence of the bundling of spherical micelles as evident by the undulation displayed in the height step function across the length of the worm..... 408

- Figure 6.25 2D Height and phase AFM micrograph and 3D Height plot of **CoPoly-3** spin-coat from THF/ 10 v% MeOH displaying both spherical and worm-like micelle aggregation behaviors. The step function shows the height and phase across the worm-like aggregate shown in the zoomed AFM image..... 409
- Figure 6.26 2D Height and phase AFM micrograph of **CoPoly-3** spin-coat from MeOH/ 10 v% THF showing the presence of worm-like micelles that, in more concentrated areas, aggregate together forming large bundled networks of worm-like micelles..... 411
- Figure 6.27 SEM micrograph of **CoPoly-1** spin-coat from dilute THF/ 10 v% H₂O solutions with 15 wt% PPEMC₇₇₄ homopolymer blended showing micelle/ vesicle assemblies with the homopolymer chains encapsulated within..... 412
- Figure 6.28 2D Height and phase AFM micrograph of **CoPoly-1** blended with 25 wt% high MW PPEMC₇₇₄ spin-coated from THF/ 25 v% MeOH displaying long, interconnected nanofibers with the hypothesized structure depicted..... 414
- Figure 6.29 2D Height and phase AFM micrograph; 3D height plot of **CoPoly-2** blended with 25 wt% high MW PPEMC₇₇₄ spin-coated from THF/ 25 v% MeOH displaying long, interconnected nanofibers with the hypothesized structure depicted..... 415

- Figure 6.30 2D Height and phase AFM micrograph; 3D height Plot of **CoPoly-3** blended with 25 wt% high MW PPEMC₇₇₄ spin-coated from THF/ 25 v% MeOH. The height step function shown was used for statistical analysis providing an average width of the nanofibers and their standard deviations..... 417
- Figure 6.31 2D Height and phase AFM micrograph; Zoomed 2D height micrograph; 3D height Plot of **CoPoly-1** blended with 50 wt% high MW PPEMC₇₇₄ spin-coated from THF/ 25 v% MeOH displaying long, interconnected nanofibers and small, looped nanofibers..... 418
- Figure 6.32 2D Height and phase AFM micrograph of **CoPoly-2** blended with 50 wt% high MW PPEMC₇₇₄ spin-coated from THF/ 25 v% MeOH displaying long, interconnected nanofibers with specific parallel, perpendicular, and helically twisted bundling visualized..... 420
- Figure 6.33 2D Height and phase AFM micrograph of **CoPoly-2** blended with 50 wt% high MW PPEMC₇₇₄ spin-coated from THF/ 25 v% MeOH displaying long, parallel bundled nanofiber with several branching points interconnecting the nanofiber network..... 421
- Figure 6.34 ¹H NMR spectrum of attempted hydrosilation reaction between **Poly-45** and bis(silane) terminated PDMS carried out at 50 °C for 6 days showing distinct chemical shifts associated with both polymers..... 423

LIST OF ABBREVIATIONS

List of Monomers- The polymers discussed in this document are derived from the carbodiimides of the same number. **Poly-43, 44, 45** are the polymers of **Mono-1** with specific protected alkyne, deprotected alkyne, and alkene end-groups, respectively.

Mono-1	<i>N</i> -1-phenethyl- <i>N'</i> -methylcarbodiimide (PEMC)
Mono-2	<i>N,N'</i> -di- <i>n</i> -hexylcarbodiimide
Mono-3	<i>N</i> -(<i>R</i>)-2,6-dimethylheptyl- <i>N'</i> -hexylcarbodiimide
Mono-4	<i>N</i> -(<i>R</i>)-2,6-dimethylheptyl- <i>N'</i> -phenylcarbodiimide
Mono-5	<i>N</i> -methyl- <i>N'</i> -2-methyl-6-isopropylphenylcarbodiimide
Mono-6	<i>N</i> -1-anthryl- <i>N</i> -octadecylcarbodiimide
Mono-7	<i>N</i> -(<i>R</i> or <i>S</i>)-2,6-dimethylheptyl- <i>N'</i> -1-anthrylcarbodiimide
Mono-8	<i>N</i> -12-(4'-Methoxybiphenyl-4-oxy)dodecyl- <i>N'</i> -dodecylcarbodiimide
Mono-9	<i>N</i> -6-(4-(4-Methoxyphenylazo)phenyloxy)hexyl- <i>N'</i> -hexylcarbodiimide
Mono-10	<i>N</i> -6-(4'-Methoxybiphenyl-4-oxy)hexyl- <i>N'</i> -hexylcarbodiimide
Mono-11	<i>N,N'</i> -di- <i>n</i> -dodecylcarbodiimide
Mono-12	<i>N,N'</i> -di-4-butylphenylcarbodiimide
Mono-13	<i>N</i> -phenyl- <i>N'</i> -hexylcarbodiimide (PHC)
Mono-14	<i>N</i> -1-naphthyl- <i>N'</i> -octadecylcarbodiimide (NOC)
Mono-15	<i>N,N'</i> -dibenzylcarbodiimide
Mono-16	¹⁵ <i>N</i> -phenyl- ¹⁵ <i>N'</i> -hexylcarbodiimide
Mono-17	¹⁵ <i>N</i> -phenyl- <i>N</i> -hexylcarbodiimide
Mono-18	<i>N</i> -phenyl- ¹⁵ <i>N</i> -hexylcarbodiimide

Mono-19	<i>N</i> -4-methoxyphenyl- ¹⁵ <i>N</i> -hexylcarbodiimide
Mono-20	¹⁵ <i>N</i> -4-methylphenyl- <i>N</i> -hexylcarbodiimide
Mono-21	<i>N</i> -4-methylphenyl- ¹⁵ <i>N</i> -hexylcarbodiimide
Mono-22	<i>N</i> -4-chlorophenyl- ¹⁵ <i>N</i> -hexylcarbodiimide
Mono-23	<i>N</i> -4-nitrophenyl- ¹⁵ <i>N</i> -hexylcarbodiimide
Mono-24	<i>N</i> -cyclohexyl- ¹⁵ <i>N</i> -hexylcarbodiimide
Mono-25	<i>N</i> -propyl- ¹⁵ <i>N</i> -hexylcarbodiimide
Mono-26	<i>N</i> -benzyl- ¹⁵ <i>N</i> -hexylcarbodiimide
Mono-27	<i>N</i> -2-phenethyl- ¹⁵ <i>N</i> -hexylcarbodiimide
Mono-28	¹⁵ <i>N,N</i> -dibenzylcarbodiimide
Mono-29	¹⁵ <i>N</i> -1-naphthyl- <i>N</i> -octadecylcarbodiimide
Mono-30	¹⁵ <i>N</i> -2-naphthyl- <i>N</i> -octadecylcarbodiimide
Mono-31	¹⁵ <i>N</i> -1-naphthyl- ¹⁵ <i>N'</i> -octadecylcarbodiimide
Mono-32	<i>N</i> -(4-methoxy-1-naphthyl)- <i>N'</i> -dodecylcarbodiimide
Mono-33	<i>N</i> -(4-methyl-1-naphthyl)- <i>N'</i> -dodecylcarbodiimide
Mono-34	<i>N</i> -(4-bromo-1-naphthyl)- <i>N'</i> -dodecylcarbodiimide
Mono-35	<i>N</i> -(4-chloro-1-naphthyl)- <i>N'</i> -dodecylcarbodiimide
Mono-36	<i>N</i> -1-pyrenyl- <i>N'</i> -octadecylcarbodiimide
Mono-37	<i>N</i> -1-quinoline- <i>N'</i> -dodecylcarbodiimide
Mono-38	<i>N</i> -1-indane- <i>N'</i> -dodecylcarbodiimide
Mono-39	<i>N</i> -1-naphthylmethyl- <i>N'</i> -dodecylcarbodiimide
Mono-40	<i>N</i> -1-naphthyl- <i>N'</i> -(tetraethylene glycol)carbodiimide

- Mono-41** *N*-phenyl-*N'*-octadecylcarbodiimide
- Mono-42** *N*-4-fluorophenyl-*N'*-dodecylcarbodiimide

List of Catalysts/ Initiators-

- Cat-1** η^5 -cyclopentadienyl-dichlorotitanium(IV) isopropoxide
- Cat-2** (*R*) or (*S*)-BINOL- titanium(IV) diisopropoxide
- Cat-3** Trichlorotitanium(IV) 2,2,2-trifluoroethoxide
- Cat-4** η^5 -cyclopentadienyl-dichlorotitanium(IV) (2,4-dinitrophenylthio)ethoxide
- Cat-5** η^1 -phenyl(triphenylphosphino) nickel(II) [2,6-bis(1-methylethyl)-*N*-(1-*H*-pyrrol-2-ylmethylene)-benzenamine]
- Ni-1** Bis(triphenylphosphino)phenyl nickel(II) bromide
- Ni-2** Bis(triphenylphosphino)(4-trifluoromethylphenyl) nickel(II) bromide
- Ni-3** Bis(triphenylphosphino)(4-triisopropylsilylethynyl-2-methylphenyl) nickel(II) bromide
- Ni-4** Bis(triphenylphosphino)(2-methyl-4-(pent-4-en-1-yloxy)phenyl) nickel(II) bromide

Other Abbreviations Used-

- GPC** Gel permeation chromatography
- MW** Molecular weight
- NMR** Nuclear magnetic resonance
- P*** Persistence length

CSA	Camphorsulfonic acid
KCC	Kinetically controlled conformation
TCC	Thermodynamically controlled conformation
SA-XRD	Small-angle X-ray diffraction
PHIC	Poly(<i>n</i> -hexyl isocyanate)
LC	Liquid crystal
N	Nematic
SmA-C	Smectic A-C
N*	Chiral nematic (cholesteric)
POM	Polarizing optical microscope(y)
TGA	Thermogravametric analysis
ECD	Electronic circular dichroism
ADMET	Acyclic diene metathesis
GC	Gas chromatography
FTIR	Fourier transform infrared
LUMO	Lowest unoccupied molecular orbital
VT	Variable temperature
TEA	Triethylamine
MS	Mass spectrometry
NBS	<i>N</i> -bromosuccinimide
DBU	1,8-diazabicyclo[5.4.0]undec-7-ene
VCD	Vibrational circular dichroism

de	Diastereomeric excess
OR	Optical rotation
SOR	Specific optical rotation
CPL	Circularly polarized light
PNOC	Poly(<i>N</i> -1-naphthyl- <i>N'</i> -octadecylcarbodiimide) (Poly-14)
UV-Vis	Ultraviolet-visible
DFT	Density functional theory
ROA	Raman optical activity
OM	Optical microscopy
EM	Electron microscopy
SPM	Scanning probe microscopy
TEM	Transmission electron microscope(y)
SEM	Scanning electron microscope(y)
(TM)AFM	(Tapping-mode) Atomic force microscope(y)
STM	Scanning tunneling microscope(y)
RMS	Root-mean square
BP I-III	Blue phase I-III
PPOC	Poly(<i>N</i> -phenyl- <i>N'</i> -octadecylcarbodiimide) (Poly-41)
PPEMC	Poly(<i>N</i> -1-phenethyl- <i>N'</i> -methylcarbodiimide) (Poly-1)
PPHC	Poly(<i>N</i> -phenyl- <i>N'</i> -hexylcarbodiimide) (Poly-13)
PDI	Polydispersity index
ATRP	Atom transfer radical polymerization
RAFT	Reversible addition-fragmentation chain transfer

NMP	Nitroxide-mediated polymerization
ITP	Iodine transfer polymerization
OFET	Organic field-effect transistor
POSS	Polyhedral oligomeric silsesquioxane
PAA	Poly(acrylic acid)
COD	1,5-cyclooctadiene
MALDI-TOF	Matrix-assisted laser desorption ionization- time of flight
PBrS	Poly(4-bromostyrene)
P3HT	Poly(3-hexylthiophene)
DSC	Differential scanning calorimetry
M_L	Mass-per-length
TIPS	Triisopropylsilyl
CuAAC	Copper-catalyzed azide-alkyne [3+2] cycloaddition
TBAF	Tetrabutylammonium fluoride
dppe	1,2-Bis(diphenylphosphino)ethane
DBHT	2,5-dibromo-3-hexylthiophene
AIBN	Azobisisobutyronitrile
PTFE	Poly(tetrafluoroethylene)
RCP	Rod-coil block copolymer
CCP	Coil-coil block copolymer
PS	Polystyrene
PPQ	Poly(<i>p</i> -phenyl quinolone)
PEG	Poly(ethylene glycol)

PBLG	Poly(γ -benzyl-L-glutamate)
RI	Refractive index
S/N	Signal-to-noise
DLS	Dynamic light scattering
R_h	Hydrodynamic radius
D_h	Hydrodynamic diameter
PDMS	Poly(dimethylsiloxane)

CHAPTER 1: Introduction to Polycarbodiimides

1.1 History and Background-

Chiral, helical macromolecules, both synthetic and naturally occurring, have become one of the most researched sub-classes of polymers since the discovery of the α -helical nature of peptides and DNA in the early 1950s. Shortly after, in 1955, Natta and co-workers reported the first synthetic polymer to adopt a helical conformation in the solid state.¹ Their catalyst system successfully polymerized propylene monomers in a stereoregular fashion to form highly isotactic polypropylene. The 1,3-dimethyl steric interactions present in the low energy anti-conformations force the backbone C-C bond to rotate slightly giving the polymer its helical structure. Today, synthetic helical macromolecules polymerized by various helix-sense selective polymerization techniques have become an intense area of interest and include oligio-² and poly(*m*-phenylene ethynylene),³ poly(phenyl acetylenes),^{4,5} polysilanes,⁶ polyisocyanates,⁷⁻¹⁰ polyisocyanides,¹¹⁻¹⁴ poly(quinoxaline-2,3-diyl)s,^{15,16} poly(cis-acetylenes),^{17,18} polythiophenes,¹⁹ and polycarbodiimides,²⁰ to name a few. These polymer systems possess a wide array of potential applications including molecular data storage, asymmetric catalyst supports, macromolecular chiroptical switches, liquid crystalline displays, polymer semiconductors, mimics of biological macromolecules, stationary phases in chiral chromatography, and chiral sensing.²¹⁻²⁶ The chirality of helical polymers prepared from achiral monomers is drawn directly from the secondary structure of the polymeric backbone. The polymer can exist in either helical conformational sense, i.e., the plus (*P*)

enantiomer or minus (*M*) enantiomer shown in Figure 1.1, or as a racemic mixture of both. Biasing the helical sense of the polymers can be achieved multiple ways including use of chiral catalysts, addition of a small amount of chiral monomer into the polymer synthesis (the sergeants and soldiers effect), and use of molecular chaperones.

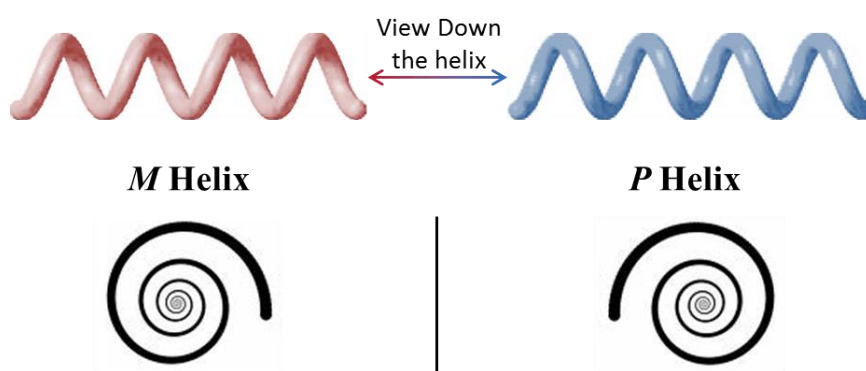


Figure 1.1- The two opposite handed helices are enantiomers of one another. The *P*-helix proceeds away from the viewer in a clockwise rotational motion and vice versa for the *M*-helix.

Helical polymers are typically divided into two specific classes known as static helices and dynamic helices. Static helical polymers, like polyisocyanides, have a relatively high helical inversion barrier meaning the polymer cannot interconvert between *M* and *P* helices readily at low temperatures. Deming and Novak reported a helical inversion barrier of >27 kcal/mol for poly(*t*-butylisocyanide).²⁷ Dynamic helices, like polyisocyanates, can readily racemize at low temperatures due to their low helical inversion barrier. Green and co-workers previously reported the calculated energy of racemization of 12 kcal/mol for poly(*n*-hexyl isocyanate).²⁸

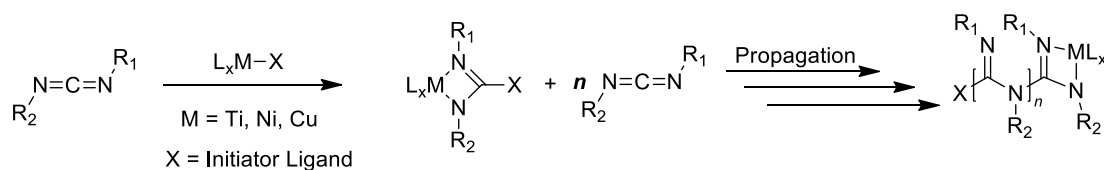
Persistence length, another term used commonly in polymer chemistry, is described by Wiggins and Nelson as the length scale in which the polymer maintains its tangent orientation.²⁹ In other words, persistence length is the physical measure of chain stiffness in the polymer backbone. If the persistence length (P) in a polymer is long, then the polymer backbone acts as a rigid rod and, on average, continues along a single axis for the length P . If the persistence length is relatively short, then the polymer chain adopts a more random coil geometry which removes some access to the functionality in the polymer, i.e. the interior pendent groups. Polyisocyanides typically have very short persistence lengths (ca. 32 Å for poly(α -phenylethylisocyanide)¹⁴ as reported by Green and co-workers. In contrast, the helical backbone of polyisocyanates can behave as a rigid-rod due to the partial conjugation of the amide functionality in the repeat unit with $P = \sim 600$ Å in some cases.⁷

The polymerization of carbodiimides was first reported in 1964 by Robinson and co-workers via anionic polymerization albeit with very little control.³⁰ The polymers synthesized were of low molecular weight and displayed less than admirable properties. Future research in the subject ceased until 1994 when Novak and co-workers successfully polymerized carbodiimide monomers in a living fashion using organotitanium(IV) catalysts.²⁰ Since this discovery, a variety of transition metal catalysts have proven to polymerize carbodiimide monomers including copper,^{31,32} zirconium,³³ and nickel. Structurally, polycarbodiimides are a blend between polyisocyanides (which contain one sp^2 nitrogen per repeat unit that bears the functionality of the polymer) and polyisocyanates (which contain a backbone sp^3-n amide nitrogen where n = the degree of distortion toward planarity). Additionally, these polymers possess a fusion of favorable properties from both polyisocyanides and polyisocyanates.

Polycarbodiimides, like polyisocyanates, act as rigid-rod helical polymers and have been reported to have persistence lengths of $\sim 400 \text{ \AA}$.³⁴ These polymer systems also can act as either dynamic or static helical polymers depending on the pendent groups attached.

1.2 Proposed Mechanism of Polymerization

Previously, the Novak research group developed a series of organotitanium(IV) catalysts that successfully promoted the living polymerization of isocyanates by covalently bonding the anionic amide propagating end group.¹⁰ This minimizes potential side reactions thereby allowing for controlled propagation to occur. Because carbodiimides are isoelectronic with isocyanates, the idea occurred to attempt to polymerize carbodiimides with the same living control using similar titanium(IV) catalysts. The polymerization is hypothesized to be initiated by the insertion of one of the imine- π -bonds into the Ti-X bond. Upon initiation, the titanium center donates an initiator ligand (X in Figure 1.3, typically either an alkoxide or amine ligand) to the center carbon of the carbodiimide creating a titanium(IV) amidinate complex. Sequential insertion of additional monomers into this complex propagates the polymer in a living chain growth manner.



Scheme 1.1- The proposed mechanism of polymerization for polycarbodiimides carried out with transition metal initiators. The carbodiimide monomer is initiated upon ligand transfer creating a metal-amidinate complex that allows for sequential insertion of additional monomers.

The living nature of the polymerization was demonstrated by Goodwin and Novak and prompted a series of experiments to determine the mechanism of polymerization.⁹ Two of the necessary attributes for a polymerization to be considered living is the absence of both termination and chain transfer steps. The polymerization of *N*-methyl-*N'*-(*R*)-1-phenylethylcarbodiimide (**Mono-1R**) lacking a chain transfer was verified by plotting the molecular weight of a series of polymers versus their corresponding monomer: catalyst ratios (Figure 1.2). The linear nature of the plot indicates that each titanium catalyst center initiates only one polymer chain and remains bound to the chain throughout the polymerization process.

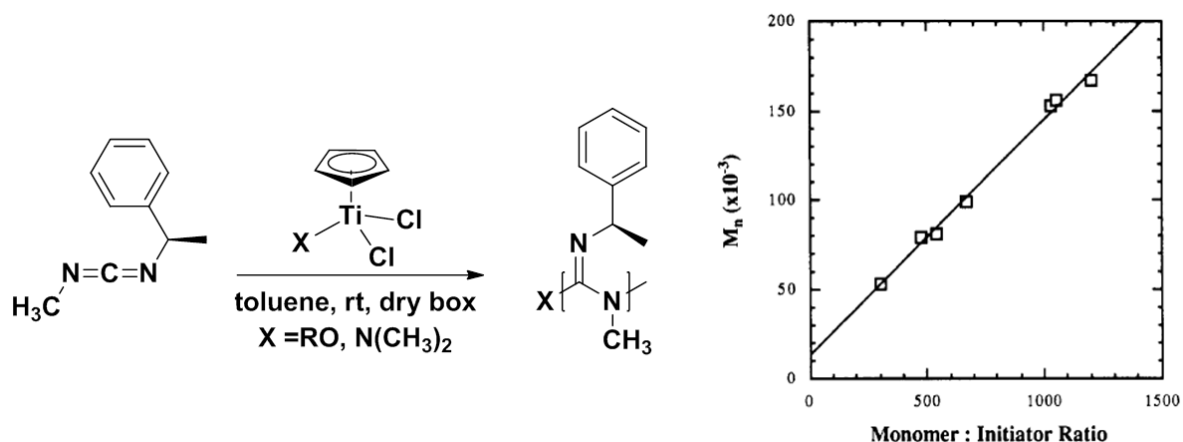


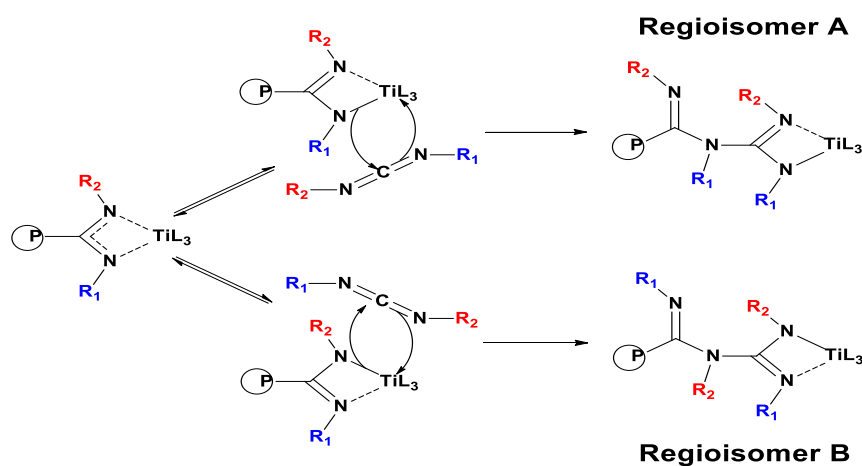
Figure 1.2- The linear plot of monomer: initiator (catalyst) ratio vs. the number average molecular weight (right) indicates the lack of chain transfer in the polymerization of **Mono-1R** (left). (Copyright 1994 American Chemical Society, reprinted with permission)⁹

The living nature of the polymerization is further substantiated by kinetic analysis of the process. This polymerization is considered an equilibrium polymerization with repeated,

reversible coordination to the titanium(IV) center. In addition, the absence of a termination step was proven simply by addition of another viable monomer succeeding the consumption of the initial monomer. This, in turn, formed a block copolymer with the incorporation of both monomers into the backbone in consecutive order. The polymer samples can then be isolated by precipitation upon addition to methanol in good yields of ~70-95%. Living polymerizations will be discussed in detail in Chapter 5.

Analysis of the molecular weight of these polymer systems by gel permeation chromatography (GPC) has been significantly challenging. Erroneous data with broad elution patterns indicates that the polymers formed are very polydisperse, i.e. the separate polymer chains have a wide range of molecular weights (MW). However, light scattering measurements showed a very narrow range of molecular weights eluting over the unusually large volume. This can be attributed to the polymer's nitrogen rich backbone having a high affinity to the crosslinked polystyrene, GPC stationary phase in certain solvents. In addition, GPC requires the use of a polystyrene standard to provide accurate molecular weight determination so the data received is only relative to that standard. The random coil nature of the polystyrene standard is very different than the rigid rod nature of polycarbodiimides so it is expected that the polymers would proceed through the GPC stationary phase in a dissimilar manner. Further analysis of the molecular weight distributions of these polymer systems by tandem GPC/ Light Scattering for various monomer: catalyst ratios consistently gave results seen in monodisperse samples ($M_w/M_n \leq 1.2$).⁹ This is even more evidence for the polymerization occurring under living control.

Due to the di-functional nature of carbodiimides, the issue of regioirregularity becomes a factor when incorporating asymmetric monomers. The two sites available for each pendant group include the sp^2 nitrogen typically referred to as the imine nitrogen and the sp^3 -n nitrogen in the backbone referred to as the amine nitrogen. Depending on how the monomer insertion pathway is biased by these particular pendant groups, either a regioregular polymer with all of the substituents on specific nitrogens throughout the entire polymer chain or a regioirregular polymer with mixed proportions of both isomers will ensue (Scheme 1.2). Biases can include steric effects or differences in electronics (i.e., conjugation). Many experiments to determine the regioirregularity of polycarbodiimides have produced mixed and inconclusive results prior to ^{15}N isotope labeling of the backbone nitrogens and subsequent ^{15}N NMR analysis. These experiments and more will be discussed further in Chapter 2.



Scheme 1.2- The proposed propagation mechanisms for asymmetric polycarbodiimides can produce two different regioisomers along the backbone. Depending on the particular bias of monomer insertion (or lack thereof), the polymerization will form a regioregular polymer with an excess of a single regioisomer or a regioirregular polymer with mixed populations of both.

1.3 Polycarbodiimides as Static and Dynamic Helices-

Schlitzer and Novak first reported polycarbodiimides as a dynamic helical polymer in 1998 when they biased the helical nature of a racemic poly(*N,N'*-di-*n*-hexylcarbodiimide) (**Poly-2**) using a chiral molecular chaperone under acidic conditions.³⁵ This was achieved via addition of a small amount of chiral camphorsulfonic acid (CSA) which protonated the backbone nitrogen. The chiral perturbator creates an ion pair with the protonated backbone that can form different diastereomers depending on the helical sense of the backbone. The backbone protonation resulted in a slight decrease in the helical inversion barrier causing the polymer to adopt a single helical sense after annealing. When the concentration of either (*R*)- or (*S*)-CSA is increased, the helical nature of the racemic polymer is biased producing an induced helical sense and was monitored by polarimetry. Upon chiral perturbation, the specific optical rotation of **Poly-2** increases slowly to $\sim 250^\circ$ (either positive or negative depending on the enantiomer of CSA used) as the concentration of CSA increases. This process is illustrated in Figure 1.3.

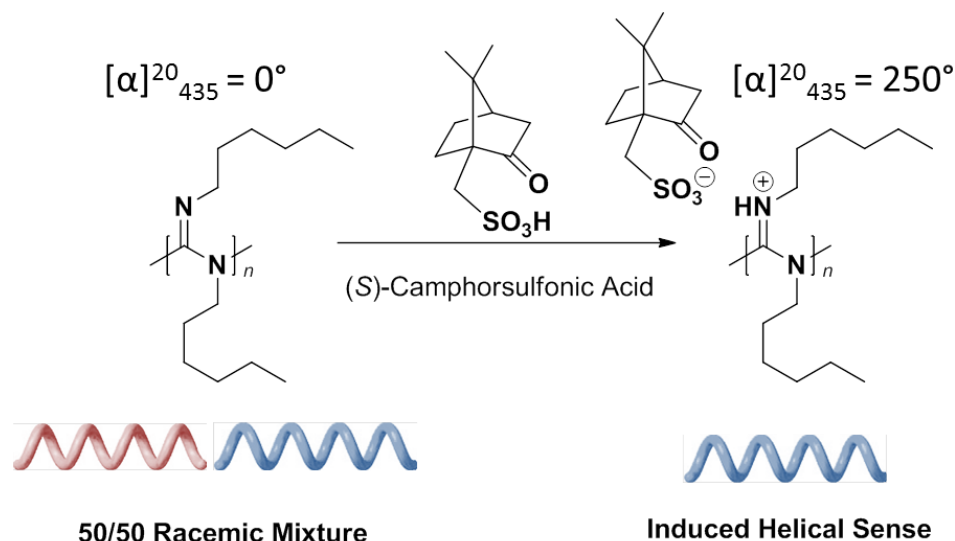


Figure 1.3- The racemic mixture of *M* and *P* helices for **Poly-2** is biased to an induced helical sense upon chiral perturbation with the molecular chaperone CSA.³⁵

In addition to these findings, Schlitzer reported the polymerization of the chiral *N*-(*R*)-2,6-dimethylheptyl-*N'*-*n*-hexylcarbodiimide (**Mono-3**) with η^5 -cyclopentadienyl-dichloro-titanium(IV) isopropoxide (**Cat-1**).³⁵ Typically, the formation of helical polymers from chiral monomers will result in a drastic enhancement of the specific optical rotation upon polymerization. However, the polymerization of **Mono-3** to **Poly-3** showed no amplification of specific optical rotations ($[\alpha]_{365} = +7.6^\circ$ for **Mono-3** to $[\alpha]_{365} = +7.5^\circ$ for **Poly-3** at room temperature). Upon annealing the polymer in dilute solution at elevated temperature (ca. 75 - 85 °C) for extended periods of time (ca. 5 - 9 hrs.), the specific optical rotation magnitude increased to $[\alpha]_{365} = -157.5^\circ$ while passing through 0° in the process and eventually reaching a plateau. This type of chiral amplification is very unusual and can be ascribed to the polymer sample's irreversible evolution from the kinetically controlled conformation (KCC) to the thermodynamically controlled conformation (TCC). In other

words, the polymer backbone readjusts specific helical inversions to adopt a more energetically favorable conformation. The helical inversion barrier for this process was calculated by Tian and co-workers to be 21.6 kcal/mol.³⁶ Tian also reported an even larger enhancement of optical rotation upon annealing the more sterically crowded poly(*N*-(*R*)-2,6-dimethylheptyl-*N'*-phenylcarbodiimide) (**Poly-4**). This polymer showed a change in magnitude of 464° from $[\alpha]_{435} = -209^\circ$ to $+255^\circ$ after annealing at 75 °C for 60 hours and the calculated helical inversion barrier was found to be 29.6 kcal/mol. The data for **Poly-3** and **Poly-4** is shown in Figure 1.4.

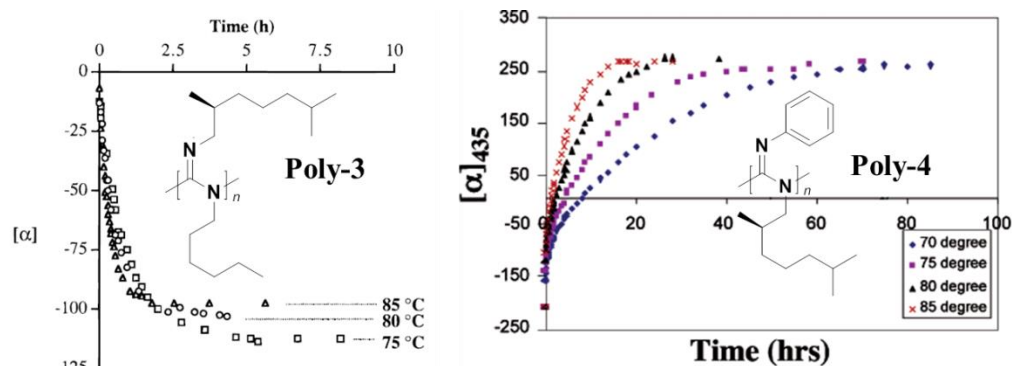


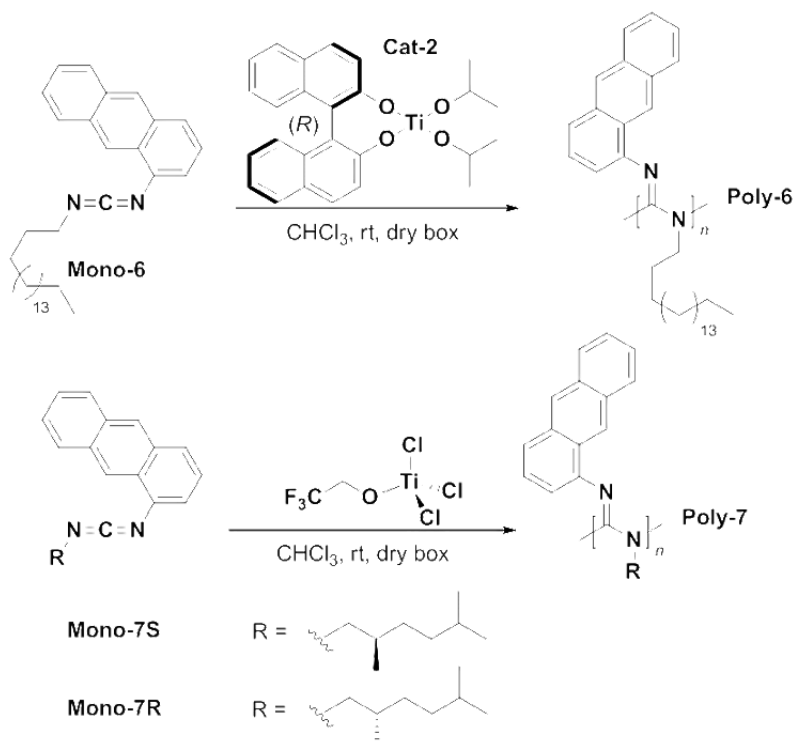
Figure 1.4- Specific optical rotation changes of **Poly-3** (left) and **Poly-4** (right) upon annealing as a function of time. This shows the evolution from the kinetically controlled conformation to the energetically favored thermodynamically controlled conformation. (Copyright 1998 American Chemical Society, reprinted with permission)^{35,36}

Stable helices with an excess helical sense of one enantiomer that cannot interconvert between opposite handed helices readily, i.e., possess a high helical inversion barrier, are necessary in certain real world applications. Polymerization with chiral monomers for the

formation of single-screw sense polymers is limited by both the relatively minute amount of viable monomers and cost. For this reason, it is important to design alternative ways to develop chiral macromolecules with a specific helical bias without the use of optically active monomers. One of the most common techniques employed is the use of chiral catalysts to bias the polymerization to an excess single-handed enantiomer. The use of chiral catalysts for the polymerization of carbodiimide monomers was first reported in 1998 but only yielded modest results.¹² In 2004, Tian and Lu showed that the chiral (*S*)-BINOL titanium(IV) diisopropoxide (**Cat-2S**) could successfully polymerize a series of achiral monomers at good yields and with an excess helical sense. Initial observations of these polymers indicated that as the steric bulk of the pendant groups increases, as does the energy of racemization (i.e., helical inversion barrier). To further increase the energy of racemization and build permanently optically active polycarbodiimides, increasing the sterics of the pendant groups with 2,6 substituted aryl substituents was employed. The most viable monomer of this class for polymerization was proven to be *N*-methyl-*N'*-2-methyl-6-isopropylphenylcarbodiimide (**Mono-5**) and was successfully polymerized with **Cat-2S**.³⁶ This polymer proved to be very interesting not only because of the high specific optical rotations ($[\alpha]_{435} = -867^\circ$ in toluene and $[\alpha]_{435} = -1034^\circ$ in chloroform) but also due to the fact that upon annealing at 50 °C for extended periods of time, the specific optical rotation, however, does not ever reach 0°, i.e., the polymer would not completely racemize. The values plateaued instead at $[\alpha]_{435} = -360^\circ$ in chloroform and were indefinitely stable (ca. 70 hours). The energy of racemization for the initial process was calculated via Arrhenius analysis to be 23 kcal/mol. This was attributed to a high level of asymmetry that is inherently and permanently built into the backbone. This

was believed to be attributed to tight packing of the adjacent aryl pendant groups which prohibited concerted rotation to occur with the necessary level of cooperation to obtain full racemization.

Also in 2004, Tang and coworkers published the synthesis of a series of polycarbodiimides that possessed the highest helical inversion barrier to date. Poly(*N*-1-anthryl-*N*-octadecylcarbodiimide) (**Poly-6**) exhibited a helical inversion barrier of 36 kcal/mol in toluene but was able to be racemized after extended annealing at 80 °C.³⁷ **Poly-6** also was the first polycarbodiimides to show reversible thermo- and solvo- controlled chiroptical switching.³⁸ The specifics into the switching phenomenon will be further expanded on in Chapter 3. **Poly-7S** and **7R** polymerized with trichlorotitanium(IV) 2,2,2-trifluoroethoxide complex (**Cat-3**) displayed a significant increase in specific optical rotation, $[\alpha]_{577}^{25} = -778^{\circ}$ and $[\alpha]_{577}^{25} = +791^{\circ}$, respectively, compared to their corresponding monomers indicating the formation of stable excess one-handed helices. In addition, upon extended annealing for more than 34 hours, no significant decrease in optical rotation was observed. To date, these polymer systems remain the most stable helical polycarbodiimides and additional research in the field of static polycarbodiimides is necessary for additional applications to be developed.



Scheme 1.3- Synthesis of select polycarbodiimides designed specifically to have high energies of racemization. The large anthracene pendant group provides the necessary steric bulk to restrict helical inversion.³⁷

1.4- Properties of Polycarbodiimides

As previously stated, the chirality and rod-like character of helical polycarbodiimides allows for a broad spectrum of interesting applications including liquid crystal displays, macromolecular chiroptical switches, biological mimics, and asymmetric catalyst supports to name a few. Liquid crystals (LC), in particular, have been a huge area of interest for synthetic, rigid-rod like, helical macromolecules.³⁹⁻⁴³ LCs are a unique phase of matter (mesophase) that lie between crystalline solids and normal, isotropic liquids. Polyisocyanates, due to their large persistence lengths, were found to possess lyotropic LC

properties in various solvents. *Lyotropic* is a term typically used for liquid crystalline materials in which the long-range orientational order is induced by the addition of solvent above specific concentrations. In other words, upon solvation at a critical concentration, all of the polymer chains will order themselves in a specific fashion. The most common mesophases in liquid crystalline materials include nematic, chiral nematic (or cholesteric), smectic-A, B, and C (see Figure 1.5). Nematic LC materials tend to align directionally but have no positional order. Smectic mesophases possess both positional and directional order with three typical subsets observed. Smectic-A LCs align in layers parallel with one another whereas smectic B align in layers perpendicular to one another. The smectic-C mesophase aligns in diagonally arranged layers. More details on the application and design of novel liquid crystalline materials will be further discussed in Chapter 4.

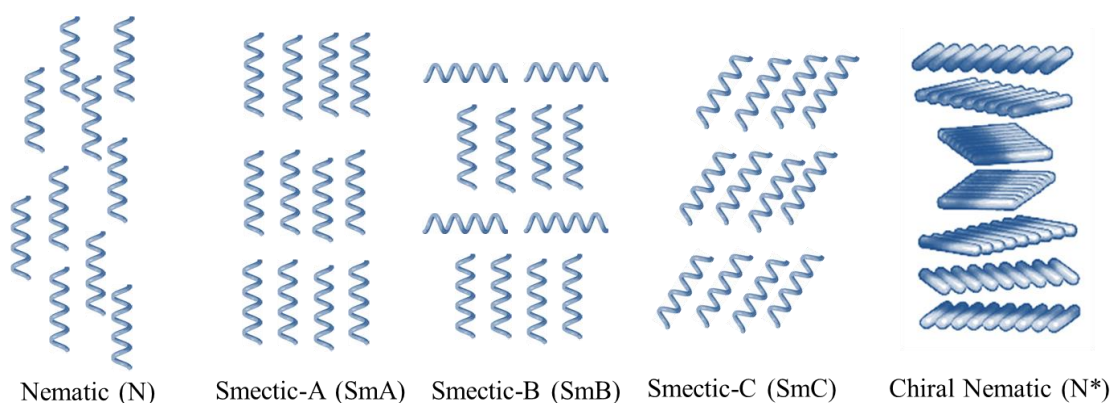


Figure 1.5- Representation of most common liquid crystalline mesophases (helices = generic mesogen).

Poly(*n*-hexyl isocyanate) (PHIC) forms a nematic mesophase in solution meaning the polymers distribute themselves with orientational order.⁴⁴ Due to the rod-like conformations of polycarbodiimides in solution, as demonstrated by Nieh et al., these polymers were also hypothesized to possess liquid crystalline behaviors. Kim et al. reported polarizing microscope and small-angle X-ray diffraction (SA-XRD) studies of **Poly-2** in 2004 to first mimic the previously studied PHIC.⁴⁵ He found that **Poly-2** adopts an ordered, layered smectic mesophase with positional order in addition to orientational order seen in nematic phases of PHIC. This additional order can be attributed to the increased density of aliphatic side chains forming a more uniform and impenetrable barrier between adjacent polymer chains. The difference between both polymers is illustrated further in Figure 1.6.

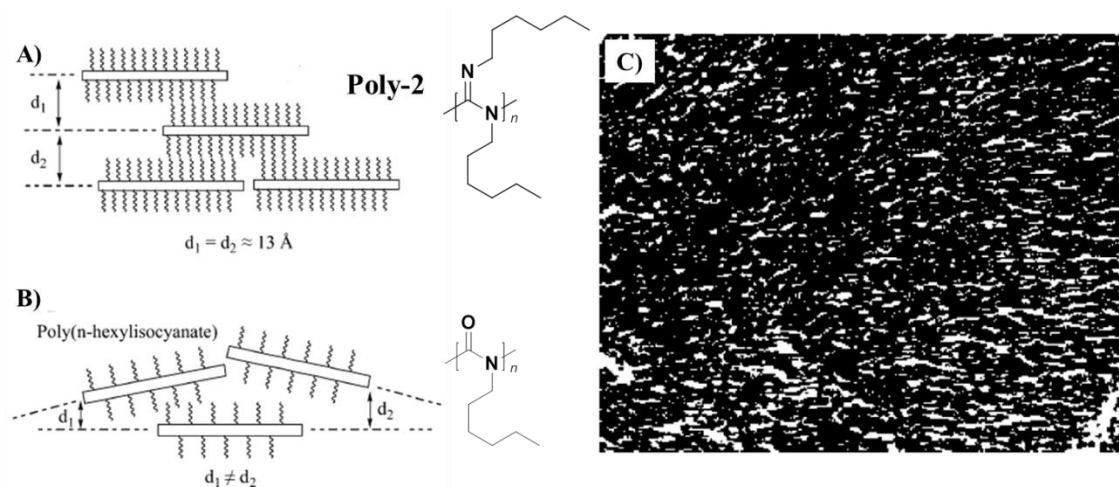


Figure 1.6- Representation of the liquid crystalline layering of **Poly-2** (A) and poly(*n*-hexyl isocyanate) (B).⁴⁵ The increased density of the hexyl side groups on **Poly-2** forms a barrier between adjacent chains resulting lyotropic smectic A mesophase seen in the polarizing optical microscope (POM) image (C). (Copyright 2004 American Chemical Society, reprinted with permission)⁴⁵

The discovery of the liquid crystalline properties of **Poly-2** was the onset to a series of polymers synthesized to tailor specific LC behavior. The polymers (**Poly-1**, **Poly-2**, and **Poly-8** to **Poly-11**) reported by Kim and Novak in 2004 are shown in Figure 1.7.⁴⁶ Each polymer was subject to SA-XRD experiments and viewed under polarizing optical microscope (POM) to determine the liquid crystalline mesophase. All of the polymers formed lyotropic liquid crystals with varying degrees of order. **Poly-1(rac)** and **Poly-9** displayed nematic mesophases which were observed using POM. The (*R*)-configuration on the chiral pendant group of **Poly-1R** causes the polymer to adopt a single-handed helical sense. This, in turn, influences the higher-order packing of the rod-like mesogens in solution causing **Poly-1R** to adopt a chiral nematic mesophase in concentrated CHCl₃ solutions (ca. 12.5 w%). The POM images of these polycarbodiimide LCs can be found in Figure 1.8. The packing of the rigid backbones occurs itself in a helical fashion with each polymer chain rotating slightly as the crystal packing continues perpendicular to the extended chain direction.

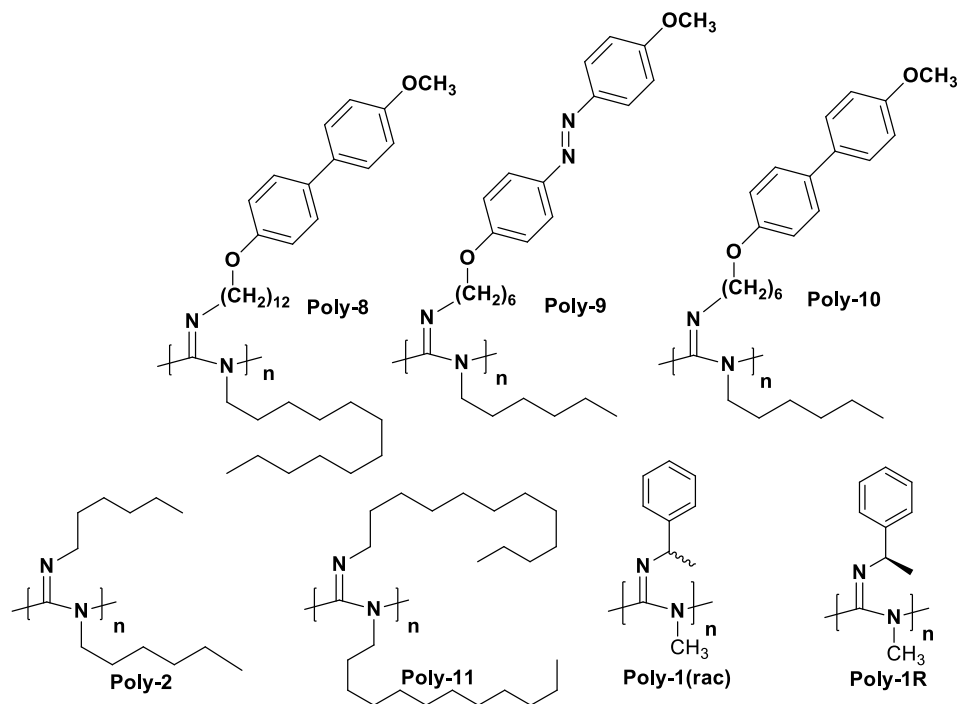


Figure 1.7- Series of polymers showing varying cases of liquid crystallinity with polymers wielding identical side chains adopting more ordered smectic mesophases and ones with different side chains adopting a nematic mesophase. The chiral **Poly-1R** adopts a helical chiral nematic mesophase.⁴⁶

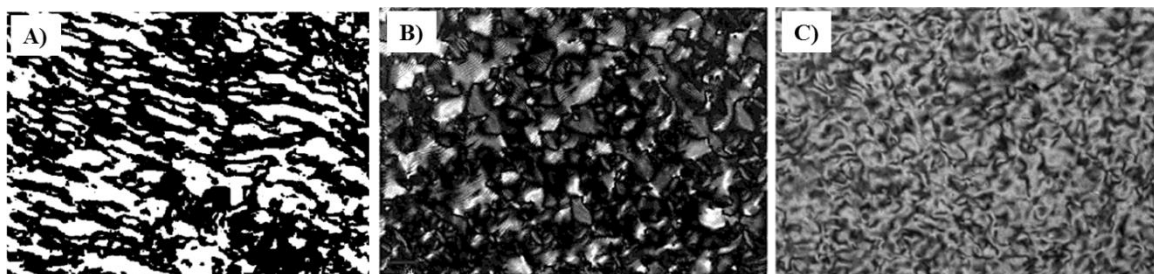


Figure 1.8- POM images of lyotropic liquid crystalline **Poly-1(rac)** in toluene (A; 35 wt%; nematic), **Poly-1R** in CHCl_3 (B; 12 wt%; chiral nematic), and **Poly-9** in 1,1,2,2-tetrachloroethane at 65 °C (C; 21 wt%; nematic). (Copyright 2004 American Chemical Society, reprinted with permission)⁴⁶

Poly-11, like **Poly-2**, has two identical side chains allowing for a more ordered, layered smectic structure in both solution and the melt (Figure 1.9). The large aliphatic corona surrounding the polycarbodiimide backbone causes the degradation temperature to increase enough to observe specific melting behaviors. In the melt, the rigid rod polymer side chains undergo thermotropic phase transitions which order and align the rigid backbones within the molten paraffin. This is observed by differential scanning calorimetry. **Poly-8** also displays thermotropic mesophase formation at temperatures greater than 119 °C. Analysis of the X-ray diffraction data of this polymer at 130 °C provides evidence for a smectic mesophase maintained at high temperatures. Thermotropic mesophase formation is not a common feature seen in polycarbodiimides due to the fact that they decompose back to the starting monomer around 150-200 °C followed by vaporization of the monomer. For this reason, nearly all of these polymers depolymerize before any phase transitions can be observed. The depolymerization of the polymer is a quantitative process and is thought to occur via homolytic cleavage of the backbone C-N bond followed by sequential unzipping of the polymer backbone. This is illustrated in Figure 1.10. This property makes polycarbodiimides an important area of interest in the field of green/recyclable polymers.

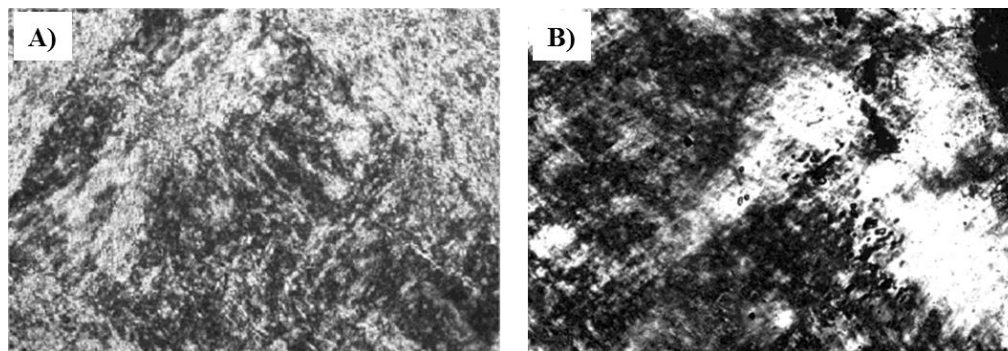


Figure 1.9- POM images of thermotropic liquid crystalline **Poly-11** at 118 °C (A) and **Poly-8** at 130 °C (B) displaying smectic mesophases. (Copyright 2004 American Chemical Society, reprinted with permission)⁴⁶

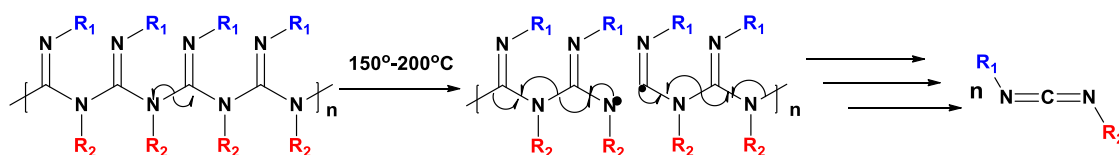


Figure 1.10- Mechanism of depolymerization of polycarbodiimides occurs via homolytic cleavage of the C-N backbone bond followed by unzipping of the rest of the backbone.

Due to the ligand transfer process of the initiation mechanism of polycarbodiimides, creating specifically functionalized catalysts allows for end group functionalization of our polymers with a high degree of flexibility. In 2005, Yujie Lu successfully polymerized **Mono-2** with a new bischloro- η^5 -cyclopentadienyl-(2,4-dinitrophenylthio)ethoxy titanium(IV) complex (**Cat-4**).⁴⁷ The 2,4-dinitrophenylthioethoxy transfer ligand bears a protected thiol group that is easily deprotected upon addition of 2-mercaptoethanol. This, in turn, provides a free thiol terminated **Poly-2** that can be subsequently attached to thin gold films creating helical polymer brushes. More research in the area of end group functionalization is necessary to explore the vast options of possibilities present. The end

functionalization of polycarbodiimides will be demonstrated and discussed further in Chapter 5.

Recently, many researchers have shown a great deal of interest in developing polymers that can act as solid supports for catalysts/ reagents. Upon immobilization, the reagents are typically stabilized and ease the work up of the reaction. Typically, the reagent attached to the solid polymer support can be simply removed by filtration leaving only the product/ leftover starting material. In 2010, Budhatoki-Uprety and Novak published a series of pyridine functionalized polycarbodiimides capable of immobilizing borane (BH_3) for sequential reductions of carbonyl compounds to the corresponding alcohol.⁴⁸ Borane coordination is evident by both the altered thermogram (data from TGA) of the coordinated polymer and the appearance of the strong IR absorbance at 2368 cm^{-1} signifying the B-H bond. To ensure that the borane was not coordinating with the basic backbone of polycarbodiimides, control experiments were carried out to determine if borane would complex with either poly(*N*-phenyl-*N'*-hexylcarbodiimide) or poly(*N,N'*-di-*n*-hexylcarbodiimide) (**Poly-2**). Resulting thermograms of both polymers showed no difference before and after addition of borane meaning neither complexation nor reduction of the imine nitrogen occurred. Using predominantly single handed helical supports, no chiral induction of the resulting products was seen and, in most cases, products developed were 50/50 racemic mixtures of both enantiomers. Further optimization of the process may yield substantial enantiomeric excess but further studies are pending.

One of the most interesting and studied properties of polycarbodiimides is the chiroptical switching phenomenon that was first observed in poly(*N*-1-anthryl-*N'*-

octadecylcarbodiimide) (**Poly-6**). The switching process is controlled by both the solvent used and temperature.⁴⁹ Throughout the process, the specific optical rotation of the polymer and the electronic circular dichroism (ECD) switch from positive in sign to negative (or vice versa) merely by solvent and temperature change. This process will be explained thoroughly in Chapter 3 and 4.

1.5 References-

- (1) Natta, G.; Pino, P.; Corradini, P.; Danusso, F.; Mantica, E.; Mazzanti, G.; Moraglio, G. *J. Am. Chem. Soc.* **1955**, *77*, 1708-1710.
- (2) Prest, P.-J.; Prince, R. B.; Moore, J. S. *J. Am. Chem. Soc.* **1999**, *121*, 5933-5939.
- (3) Banno, M.; Yamaguchi, T.; Nagai, K.; Kaiser, C.; Hecht, S.; Yashima, E. *J. Am. Chem. Soc.* **2012**, *134*, 8718-8728.
- (4) Aoki, T.; Kaneko, T.; Maruyama, N.; Sumi, A.; Takahashi, M.; Sato, T.; Teraguchi, M. *J. Am. Chem. Soc.* **2003**, *125*, 6346-6347.
- (5) Kwak, G.; Masuda, T. *J. Poly. Sci. Part A: Poly. Chem.* **2001**, *39*, 71-77.
- (6) Fujiki, M. *J. Am. Chem. Soc.* **1994**, *116*, 11976-11981.
- (7) Green, M. M.; Gross, R. A.; Crosby, C., III; Schilling, F. C. *Macromolecules* **1987**, *20*, 992-999.
- (8) Green, M. M.; Gross, R. A.; Crosby, C., III; Schilling, F. C. *Macromolecules* **1987**, *20*, 992-999.
- (9) Lifson, S.; Green, M. M.; Andreola, C.; Peterson, N. C. *J. Am. Chem. Soc.* **1989**, *111*, 8850-8858.
- (10) Patten, T. E.; Novak, B. M. *Macromolecules* **1993**, *26*, 436-439.
- (11) Nolte, R. J. M.; Van, B. A. J. M.; Drenth, W. *J. Am. Chem. Soc.* **1974**, *96*, 5932-5933.

- (12) Takei, F.; Yanai, K.; Onitsuka, K.; Takahashi, S. *Angew. Chem., Int. Ed.* **1996**, *35*, 1554-1556.
- (13) Van, B. A. J. M.; Nolte, R. J. M.; Naaktgeboren, A. J.; Zwikker, J. W.; Drenth, W.; Hezemans, A. M. F. *Macromolecules* **1983**, *16*, 1679-1689.
- (14) Green, M. M.; Gross, R. A.; Schilling, F. C.; Zero, K.; Crosby, C., III *Macromolecules* **1988**, *21*, 1839-1846.
- (15) Ito, Y.; Ihara, E.; Murakami, M. *Angew. Chem., Int. Ed.* **1992**, *31*, 1509-1510.
- (16) Ito, Y.; Ihara, E.; Murakami, M.; Sisido, M. *Macromolecules* **1992**, *25*, 6810-6813.
- (17) Hasegawa, T.; Morino, K.; Tanaka, Y.; Katagiri, H.; Furusho, Y.; Yashima, E. *Macromolecules* **2006**, *39*, 482-488.
- (18) Lam, J. W. Y.; Tang, B. Z. *Acc. Chem. Res.* **2005**, *38*, 745-754.
- (19) Richter, T. V.; Braun, C. H.; Link, S.; Scheuble, M.; Crossland, E. J. W.; Stelzl, F.; Wuerfel, U.; Ludwigs, S. *Macromolecules Ahead of Print*.
- (20) Goodwin, A.; Novak, B. M. *Macromolecules* **1994**, *27*, 5520-5522.
- (21) Yashima, E.; Maeda, K.; Iida, H.; Furusho, Y.; Nagai, K. *Chem. Rev.* **2009**, *109*, 6102-6211.
- (22) Gellman, S. H. *Acc. Chem. Res.* **1998**, *31*, 173-180.
- (23) Green, M. M.; Peterson, N. C.; Sato, T.; Teramoto, A.; Cook, R.; Lifson, S. *Science* **1995**, *268*, 1860-1866.
- (24) Nakano, T.; Okamoto, Y. *Chem. Rev.* **2001**, *101*, 4013-4038.
- (25) Schwartz, E.; Koepf, M.; Kitto, H. J.; Nolte, R. J. M.; Rowan, A. E. *Polym. Chem.* **2011**, *2*, 33-47.
- (26) Yashima, E.; Maeda, K. *Macromolecules* **2008**, *41*, 3-12.
- (27) Deming, T. J.; Novak, B. M. *J. Am. Chem. Soc.* **1992**, *114*, 7926-7927.
- (28) Green, M. M.; Peterson, N. C.; Sato, T.; Teramoto, A.; Cook, R.; Lifson, S. *Science* **1995**, *268*, 1860-1866.

- (29) Wiggins, P. A.; Nelson, P. C. *Phys. Rev. E: Stat., Nonlinear, Soft Matter Phys.* **2006**, *73*, 31901-31906.
- (30) Robinson, G. C. *J. Polym. Sci.* **1964**, *Pt. A 2*, 3901-3908.
- (31) Heintz, A. M.; Novak, B. M. *Polym. Prepr.* **1998**, *39*, 429-430.
- (32) Shibayama, K.; Seidel, S. W.; Novak, B. M. *Macromolecules* **1997**, *30*, 3159-3163.
- (33) Lee, H.-S.; Novak, B. M. *Polym. Prepr.* **2005**, *46*, 839-840.
- (34) Nieh, M.-P.; Goodwin, A. A.; Stewart, J. R.; Novak, B. M.; Hoagland, D. A. *Macromolecules* **1998**, *31*, 3151-3154.
- (35) Schlitzer, D. S.; Novak, B. M. *J. Am. Chem. Soc.* **1998**, *120*, 2196-2197.
- (36) Tian, G.; Lu, Y.; Novak, B. M. *J. Am. Chem. Soc.* **2004**, *126*, 4082-4083.
- (37) Tang, H.-Z.; Lu, Y.; Tian, G.; Capracotta, M. D.; Novak, B. M. *J. Am. Chem. Soc.* **2004**, *126*, 3722-3723.
- (38) Tang, H.-Z.; Novak, B. M.; He, J.; Polavarapu, P. L. *Angew. Chem., Int. Ed.* **2005**, *44*, 7298-7301.
- (39) Akagi, K.; Wiley-VCH Verlag GmbH & Co. KGaA: 2010, p 289-301.
- (40) Inomata, K.; Iguchi, Y.; Mizutani, K.; Sugimoto, H.; Nakanishi, E. *ACS Macro Lett.* **2012**, *1*, 807-810.
- (41) Kajitani, T.; Onouchi, H.; Sakurai, S.-i.; Nagai, K.; Okoshi, K.; Onitsuka, K.; Yashima, E. *J. Am. Chem. Soc.* **2011**, *133*, 9156-9159.
- (42) Ryabchun, A.; Bobrovsky, A.; Sobolewska, A.; Shibaev, V.; Stumpe, J. *J. Mater. Chem.* **2012**, *22*, 6245-6250.
- (43) Suda, K.; Akagi, K. *Macromolecules* **2011**, *44*, 9473-9488.
- (44) Aharoni, S. M.; Walsh, E. K. *Macromolecules* **1979**, *12*, 271-276.
- (45) Kim, J.; Novak, B. M.; Waddon, A. J. *Macromolecules* **2004**, *37*, 1660-1662.
- (46) Kim, J.; Novak, B. M.; Waddon, A. J. *Macromolecules* **2004**, *37*, 8286-8292.

- (47) Lu, Y.; Tang, H.-Z.; Novak, B. M. *Polym. Prepr.* **2005**, *46*, 397-398.
- (48) Budhathoki-Uprety, J.; Novak, B. M. *Polymer* **2010**, *51*, 2140-2146.
- (49) Tang, H.-Z.; Boyle, P. D.; Novak, B. M. *J. Am. Chem. Soc.* **2005**, *127*, 2136-2142.

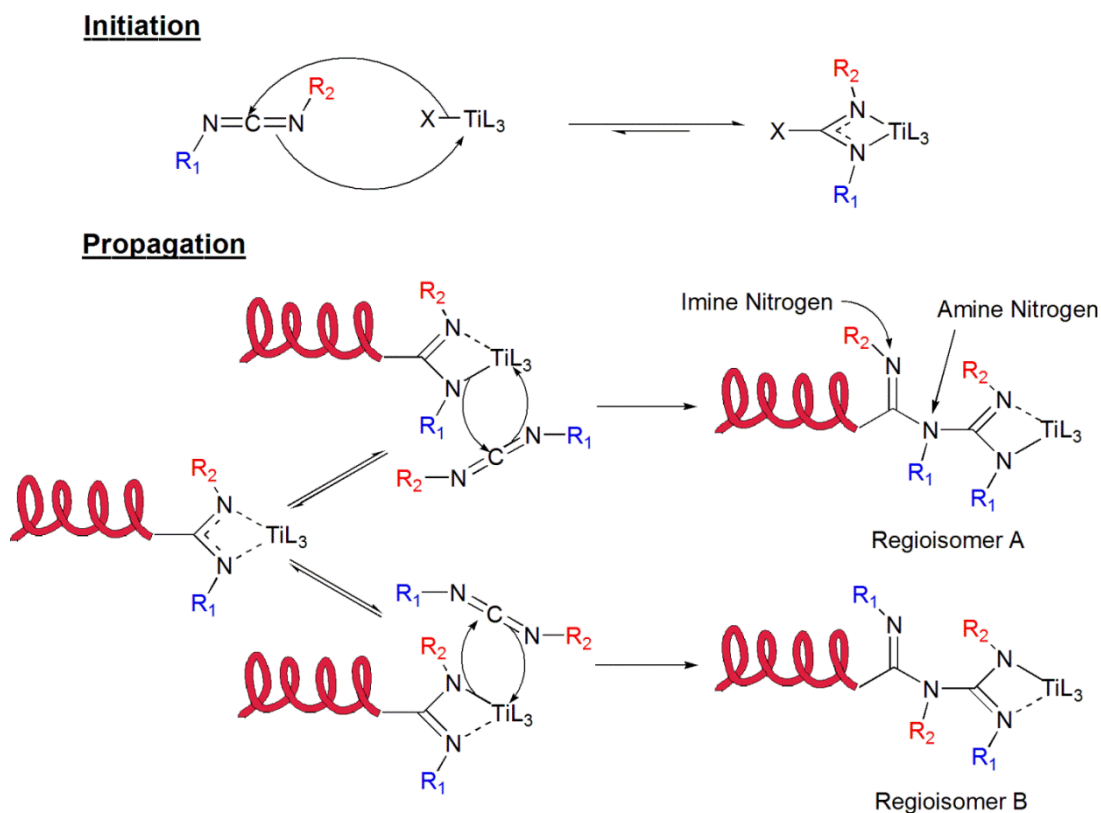
CHAPTER 2: Using ^{15}N NMR Spectroscopy to Directly Probe the Regioregularity of Polycarbodiimides

2.1 Origin of Regioregularity in Polycarbodiimides-

The connectivity of polymer systems (i.e. the regioregularity) can play a large role in specific polymer properties. For this reason, the absolute determination of polymer microstructures is of significant importance. For example, the electronic and photovoltaic properties of various polythiophenes are greatly affected by the extent of regioregularity along the polymer backbone.¹⁻⁶ Altering the degree of regioregularity in certain polyesters displayed significant changes in the thermotropic liquid crystalline order of the polymer.⁷ The formation of highly regioregular, fluorene-based polyolefins by acyclic diene metathesis (ADMET) allowed for the precise tuning of the polymer microstructure in order to amplify electroactive properties.^{8,9} Extensive research has been carried out on the formation of catalyst systems capable of polymerizing various olefins with high regio- and stereoregularity.¹⁰⁻¹³

As previously discussed, the presence of two functional nitrogens in carbodiimides allows for the incorporation of two possible regioisomers upon polymerization of asymmetric monomer units. Each pendant group of the monomer can be relegated to either the imine nitrogen or the amine nitrogen to form a regioregular polymer or can vary in populations of each site randomly throughout the polymer backbone. The formation of the preferred regioisomer stems directly from the proposed mechanism of propagation seen in Scheme 2.1.

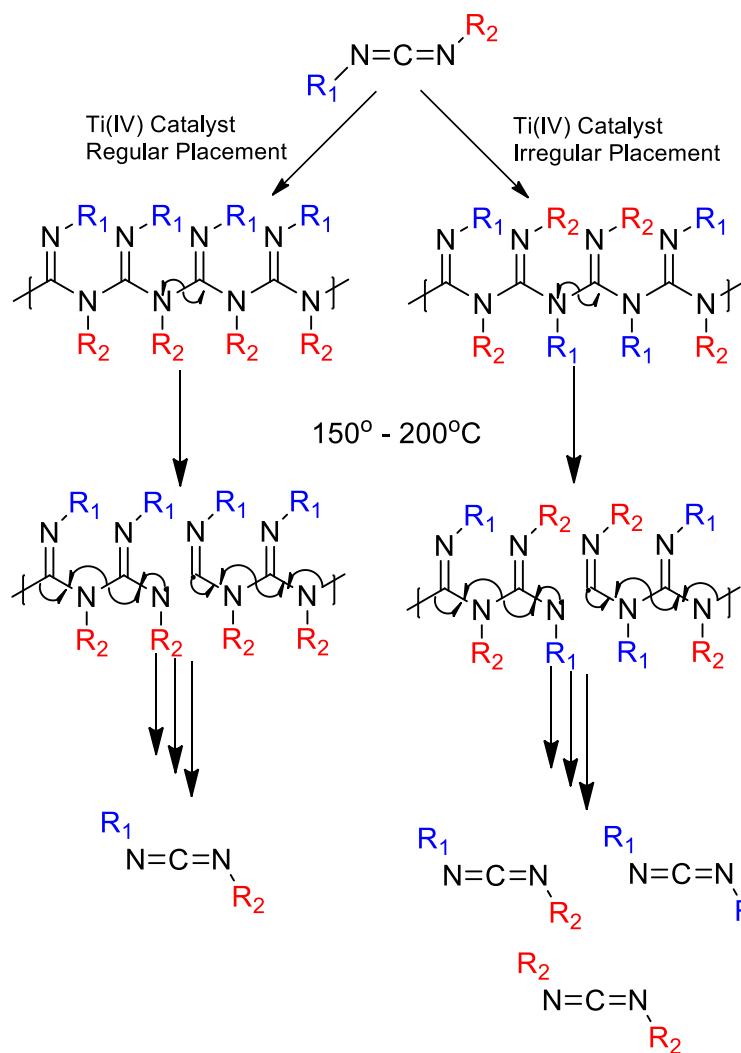
If the monomer insertion is biased to form one preferred regioisomer, a regioregular polymer will ensue. If no such bias exists, the polymer formed will be regioirregular with a 50/50 mixture of both regioisomers incorporated randomly along the backbone.



Scheme 2.1- The proposed mechanism of polymerization of carbodiimide monomers with titanium(IV) catalysts. The monomer can insert into the initiated titanium-amidinate complex through two possible pathways giving way to the possible formation of two regioisomers.

2.2 Difficulties in Determining Regioregularity-

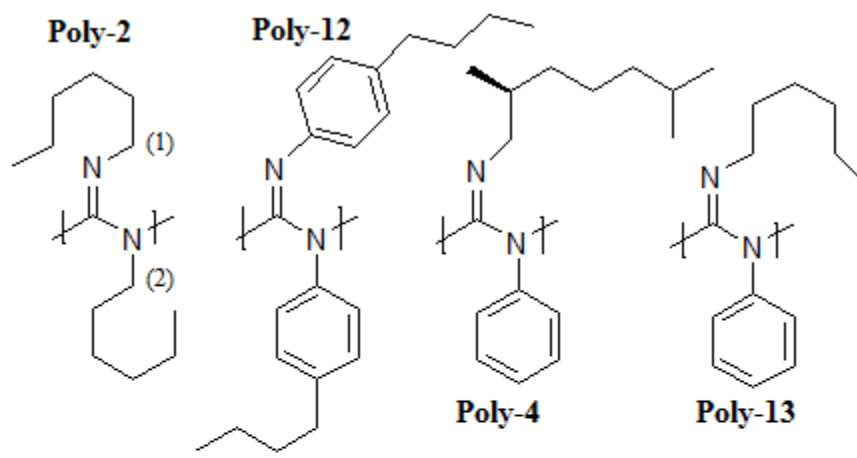
The absolute identification of the preferred regioisomer formed upon polymerization of carbodiimides with titanium(IV) catalysts has proved difficult. Initial attempts to probe the regioregularity of polycarbodiimides took advantage of the previously discussed thermal degradation of the polymer at temperatures above 150 - 200 °C. Using gas chromatography (GC) to characterize the monomers formed upon depolymerization, Goodwin studied the degradation of a series of polycarbodiimides synthesized from various titanium(IV) catalysts.¹⁴ If the depolymerization occurred via an intramolecular process only, then only one thermal degradation product will be formed for a regioregular polymer whereas a regioirregular polymer will result in up to three degradation products upon unzipping of the backbone. The three products possible include the original monomer and the metathesis products consequent of irregular placement (Scheme 2.2). The outcome of this experiment provided mixed results with no apparent trend present. Kennemur also attempted this experiment with various symmetric di-alkyl and di-aryl polycarbodiimides as well as asymmetric alkyl-aryl polycarbodiimides and revealed the same issues in his experiment.¹⁵ This experiment was deemed particularly inaccurate for classification of the polymer microstructure due to many side reactions possible at such elevated temperature including the dimerization (and possibly trimerization) of the carbodiimide monomer. The dimer (or trimer) can then revert back to either the original monomer or the two metathesis products skewing the results dramatically.



Scheme 2.2- Proposed thermal degradation pathway for polycarbodiimides at elevated temperatures of 150 – 200 °C. Depending on the degree of regioregularity, different populations of three monomers can be formed upon unzipping of the polymer backbone.

^{13}C NMR is a widely used spectroscopic technique for assigning polymer microstructures in multiple systems including poly(2,5-thienylene vinylene)s¹⁶, polythiophenes¹⁷, poly(p-alkoxyphenylenes)¹⁸, and simple polyolefins.¹⁹⁻²¹ Using ^{13}C NMR analysis, Yujie Lu attempted to assign regioisomers for a series of polycarbodiimides by

building trends between the chemical shifts of di-aryl polycarbodiimides, di-alkyl polycarbodiimides, and asymmetric alkyl/aryl polycarbodiimides.²² The polymers tested include the symmetric poly(*N,N'*-di-*n*-hexylcarbodiimide) (**Poly-2**), poly(*N,N'*-di-4-butylphenylcarbodiimide) (**Poly-12**), the asymmetric poly(*N*-(*R*)-2,6-dimethylheptyl-*N'*-phenylcarbodiimide) (**Poly-4**), and poly(*N*-phenyl-*N'*-hexylcarbodiimide) (**Poly-13**). Examination of the ¹³C NMR spectrum of **Poly-2** reveals a distinct peak for the *sp*³ carbons directly attached to both the imine and amine position. The corresponding chemical shifts of each are 48.7 ppm and 32.3 ppm, respectively; with the carbon connected to the amine nitrogen believed to be located farther upfield. In comparison to the ¹³C NMR of **Poly-13**, which displays the α -carbon peak of the hexyl side chain at 47.3 ppm, with **Poly-2**, the determination was made that the hexyl side chain is directed to the imine position due to the downfield nature of the peak. This was also the conclusion for **Poly-4** which contains the ¹³C NMR chemical shift corresponding to the α -carbon of the (*R*)-2,6-dimethylheptyl pendant group at 52.6 ppm. Coupling these trends with FTIR spectroscopy, Lu also built trends between the C=N imine stretch of the corresponding polymers and their regioisomers. **Poly-2**, **Poly-4**, and **Poly-13** show strong stretching frequencies at 1636, 1641, and 1624 cm⁻¹, respectively. **Poly-12**, however, displays the imine stretch at 1665 cm⁻¹ which is significantly greater than the other three polymers. This was hypothesized to be attributed to the *N*- π conjugation between the phenyl lowest unoccupied molecular orbital (LUMO) and the lone pair on the imine nitrogen which increases the C=N stretching force constant. The data reported by Lu is displayed in Figure 2.1 below.



	^{13}C NMR (ppm)	IR (cm^{-1}) C=N stretching mode
Poly-2	(1) 48.7, (2) 32.3	1644
Poly-12	-	1665
Poly-4	52.6	1637
Poly-13	47.3	1624

Figure 2.1- ^{13}C NMR chemical shifts for the sp^3 α -carbons of the aliphatic side groups and the C=N imine stretches of IR spectra for the series of polycarbodiimides synthesized to determine possible microstructures.

The trends observed in Lu's experiments acted as a qualitative way to assign regioisomers in Novak group for years to come. Examination of the C=N imine stretch through FTIR spectroscopy became the primary probe to determine if the polymer in question was regio(ir)regular. The presence of one peak in the region, $1670 - 1610 \text{ cm}^{-1}$, was believed to be evidence of regioregular placement throughout the polymer backbone while the presence of two (or in some cases more) peaks was evidence of regioirregularity. Tang and co-workers attributed the appearance of two IR stretches at 1641 cm^{-1} and 1620 cm^{-1} for

poly(*N*-1-anthryl-*N'*-octadecylcarbodiimide) (**Poly-6**) to be evidence of regioirregularity while the appearance of only one peak at 1622 cm⁻¹ for poly(*N*-1-anthryl-*N'*-(*R*)-3,7-dimethyloctylcarbodiimide) (**Poly-7R**) was considered evidence of the polymer being uniformly regioregular.²³ Kennemur also observed two imine stretches in the IR spectra of poly(*N*-1-naphthyl-*N'*-octadecylcarbodiimide) (**Poly-14**), an interesting polymer with amplified chiroptical switching properties capable of specific optical rotation changes of ~1700° simply by changing the solvent and/or temperature.²⁴ Initially, the multiple IR stretches were attributed to irregular placement of two regioisomers along the backbone, but subsequent variable-temperature FTIR spectroscopy disproved that conclusion.²⁵ The analysis showed intensity changes of both peaks as a function of temperature and was later determined to be a consequence of the chiroptical switching process. The VT-FTIR spectrum is shown in Figure 2.2. Examination of the imine region of the symmetric poly(*N,N'*-dibenzylcarbodiimide) (**Poly-15**) (Figure 2.2) also reveals two stretches even though a regioirregular polymer is not possible. The two peaks do not, however, change in intensity as a function of temperature like **Poly-14**. These findings, among others, have cast doubt on the utilization of the imine stretch for the absolute determination of regioregularity. It is clear, however, that the imine stretch yields a wealth of information about this polymer system and further investigations are necessary for additional clarification.

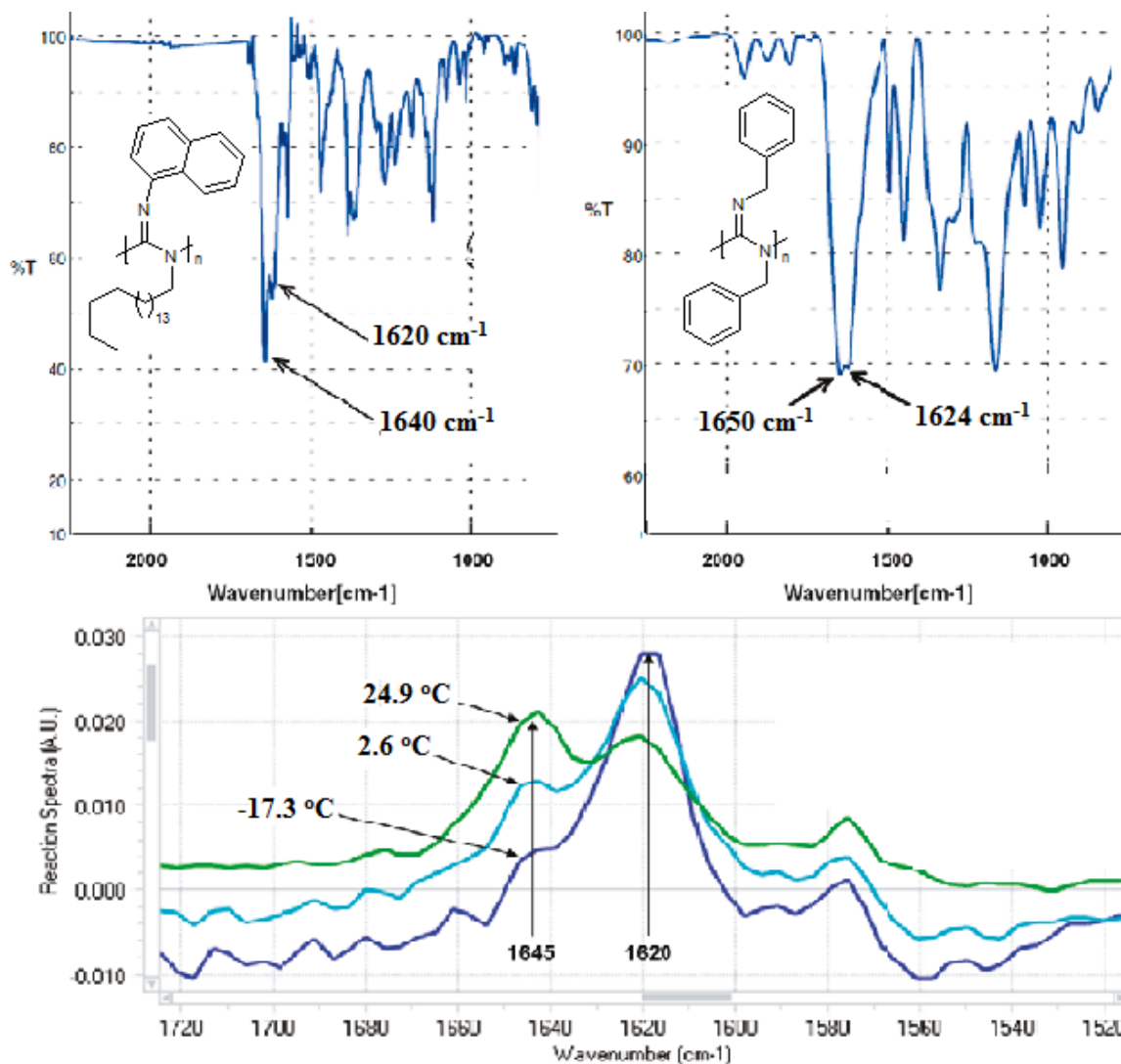
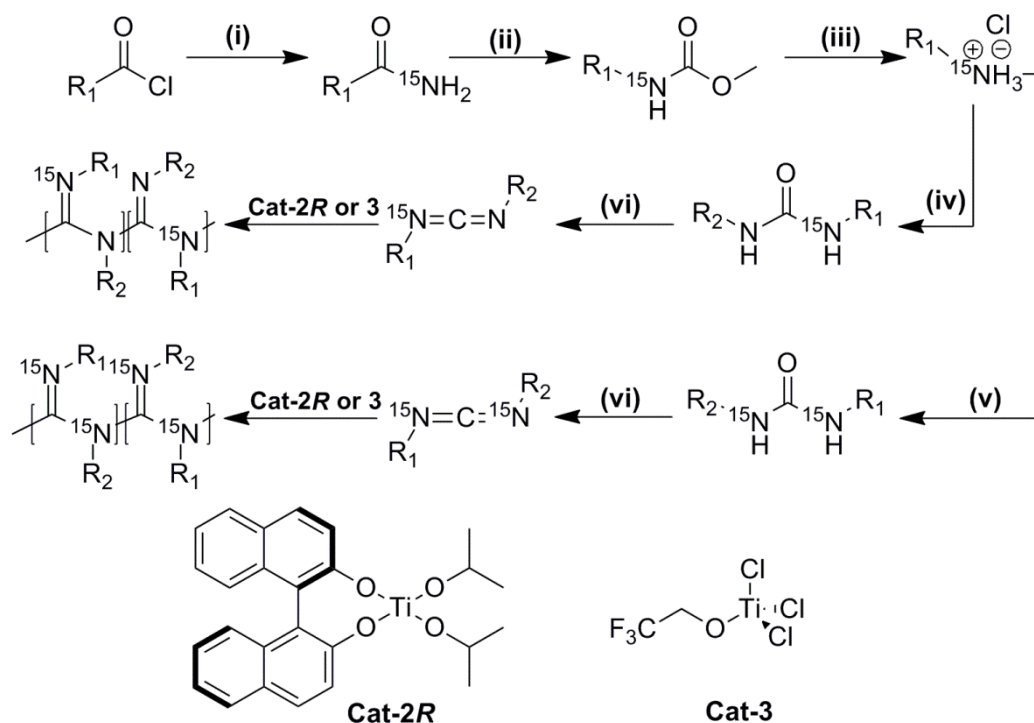


Figure 2.2- FTIR spectra of **Poly-14** (top left), **Poly-15** (top right), and variable temperature FTIR spectrum of **Poly-14** in CHCl₃ (bottom). The two peaks present in the imine region for **Poly-14** change in intensity as a function of time whereas the peaks for **Poly-15** do not.²⁵

2.3 Initial ^{15}N NMR Experiments to Directly Probe the Regioregularity-

Due to difficulties aforementioned with more indirect methods such as thermal degradation, ^{13}C NMR, and IR spectroscopy, a more direct method was developed to determine the connectivity of polycarbodiimides by DeSousa and Novak involving nitrogen-15 isotopic enrichment of the polymer backbone.²⁶ Nitrogen-15 NMR spectroscopy was then employed for ^{15}N -labeled polymers to unambiguously determine the regioisomer(s) present. The labeling synthesis scheme (Scheme 2.3) involved formation of the ^{15}N -enriched amide by reacting the corresponding acid chloride with 99% ^{15}N -enriched ammonium chloride ($^{15}\text{NH}_4\text{Cl}$). Subsequent Hofmann rearrangement of the amide in methanol formed the labeled methyl carbamates which were then deprotected by acidolysis in concentrated HCl to form the corresponding nitrogen-15 enriched amine HCl salt. The labeled amine was then used to form mono-labeled ureas and thioureas upon coupling with different isocyanates and isothiocyanates. To form di-labeled thioureas, the ^{15}N -labeled isothiocyanate was synthesized in situ by reacting the labeled amine with thiophosgene. A second ^{15}N -enriched amine can then be added to the reaction mixture to produce the di-labeled thiourea. Dehydration of ureas (or protodesulfurization of thioureas) with dibromotriphenylphosphorane (PPh_3Br_2) and triethylamine (TEA) resulted in the formation of the labeled carbodiimide monomers. The monomers were then polymerized with **Cat-2R** and **Cat-3** to form labeled polycarbodiimides. The first polymers subject to ^{15}N -enrichment included the simple poly(*N*-phenyl-*N'*-hexylcarbodiimide) labeled at both nitrogens (**Poly-16**), the aromatic nitrogen only (**Poly-17**), and the aliphatic nitrogen only (**Poly-18**). These pendant groups were applied first

to provide different sterics and electronics between pendant groups in order to produce a system with a significant bias for the monomer insertion pathway.



Scheme 2.3. General synthesis of ^{15}N -labeled polycarbodiimides. The reagents and conditions for each step are as follows: (i) $^{15}\text{NH}_4\text{Cl}$, KOH, H_2O /Diethyl Ether, $0\text{ }^\circ\text{C}$ to r.t.; (ii) NBS, DBU, MeOH, reflux; (iii) 12M HCl, reflux; (iv) XCN- R_2 (X= O, S), TEA, CHCl_3 , r.t. (for alkyl amines) or reflux (for aryl amines); (v) 1) thiophosgene, NaOH, DIPEA, DCM, $0\text{ }^\circ\text{C}$ to r.t.; 2) $\text{R}_2\text{-}^{15}\text{NH}_2\cdot\text{HCl}$, DIPEA, DCM, r.t.; (vi) PPh_3Br_2 , TEA, DCM, $0\text{ }^\circ\text{C}$ to r.t.; the polymerizations were all conducted at r.t. in an inert N_2 atmosphere dry box in distilled chloroform or without solvent.

The presence of two peaks in the ^{15}N NMR spectra of the doubly labeled poly(^{15}N -phenyl- $^{15}\text{N}'$ -hexylcarbodiimide) (**Poly-16**) would be evidence of regioregularity in the system

but absolute determination of the specific regioisomer present can only be verified upon analysis of either the mono-labeled **Poly-17** or **Poly-18**. If four peaks are present in the spectra of the di-labeled polymer, or two in the mono-labeled sample, then the polymer in question would be regioirregular. In order to acquire ^{15}N NMR spectra with good resolution in a timely fashion, the common NMR relaxation reagent gadolinium(III) acetylacetonate, $\text{Gd}(\text{acac})_3$, was introduced into the NMR samples of the polymers. Model ^{15}N -labeled amidine compounds bearing variations of aryl and alkyl substituents were used to gauge the presence of peaks in the ^{15}N NMR of the polycarbodiimides due to the similarities between the amidine structure and the polycarbodiimide repeat unit²⁷ (Figure 2.3). All the spectra (for the polycarbodiimides and the amidine model compounds) were referenced externally to ^{15}N -benzamide set $\delta = 0.00$ ppm.

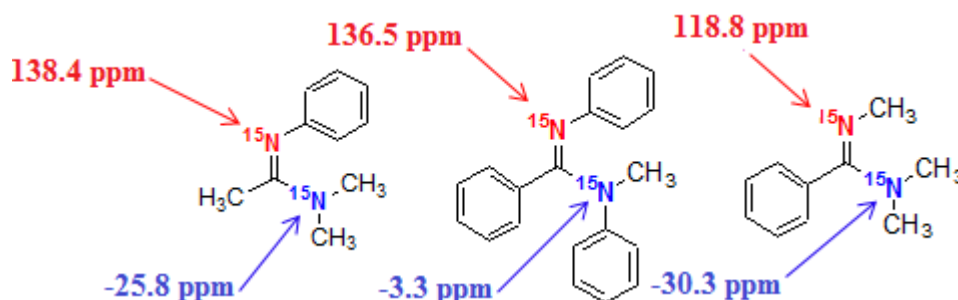


Figure 2.3- ^{15}N NMR chemical shifts of nitrogen-15 enriched amidine compounds used for comparison to the polycarbodiimide repeat unit to aid in peak assignment of both backbone nitrogens in the ^{15}N NMR spectra of isotope-enriched polycarbodiimides.

^{15}N NMR analysis of **Poly-16** derived from **Mono-16** using **Cat-3** revealed two peaks with the peak at $\delta = 136$ ppm correlating to the imine nitrogen and the peak at $\delta = 15.5$ ppm associated with the amine nitrogen. This confirms that the polymer is indeed regioregular but the exact, predominant regioisomer is still in question. ^{15}N NMR analysis of **Poly-17** confirms that the regioisomer formed upon polymerization contains the more bulky aromatic phenyl group exclusively on the imine nitrogen. This is evident by the presence of the labeled aromatic nitrogen only present at $\delta = 136$ ppm in the imine region of the spectra. Spectra acquisition of **Poly-18** further supports these findings with the nitrogen-15-labeled *n*-hexyl side group relegated to the amine nitrogen only. The ^{15}N NMR spectra of these three polymers are shown in Figure 2.4. In addition, it is noteworthy that **Poly-18**, synthesized using different Ti(IV) catalyst than **Poly-16** and **Poly-17**, also formed the same regioisomer. This supports the fact that different auxiliary ligands attached to the metal center do not alter the preferred insertion pathway.

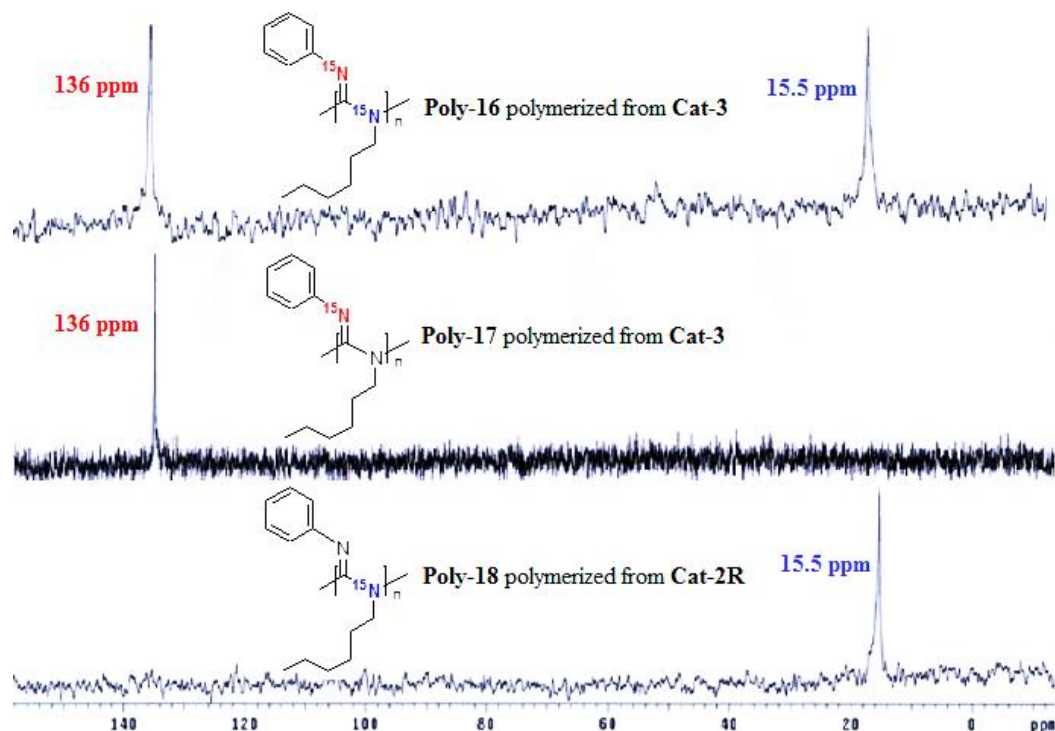


Figure 2.4- ^{15}N NMR spectra of **Poly-16**, **Poly-17**, and **Poly-18** supporting regioregular placement throughout the entire polymer backbone. (Copyright 2012 American Chemical Society, reprinted with permission)²⁶

Although examination of the imine IR stretch has typically been misleading, comparing the imine stretch of ^{15}N -labeled polymers with the unlabeled versions of the same polymers offers another source of evidence for regioregularity. This is due to the significant isotope shift observed in the IR spectra when the ^{15}N -labeled nitrogen is present on the imine position. This shift is based on both the mass difference of the isotope which affects the electronic mass of the compound and the volume difference which changes the charge distribution of the atom. For the vibrational frequency of a diatomic group, equation (1) can

be used to approximate the change when introducing different isotopes where μ is the reduced mass of the atoms in question (i.e., $\mu=(m_1m_2/m_1 + m_2)$).²⁸

$$(1) \quad v(\text{isotopic}) = v(\text{normal}) \sqrt{\frac{\mu(\text{normal})}{\mu(\text{isotopic})}}$$

For polycarbodiimides, the imine C=N stretch of the unlabeled polymers can be compared to the imine stretch of the labeled polymers and, if an isotope shift is not present, the ¹⁵N-labeled group must be segregated to the amine position. Here in, we report the synthesis of multiple isotopically labeled polymers to further probe the influence of pendant groups on the regioregularity of polycarbodiimides.

2.4 Probing the Effect of Altered Electronics in the Phenyl Side Group-

Initial ¹⁵N-NMR analysis of **Poly-16**, **17**, and **18** displayed regioregular placement of repeat units along the entire polymer backbone with the more sterically bulky phenyl group confined to the imine nitrogen only. The particular bias of this system is not fully understood so new ¹⁵N-isotopically enriched polycarbodiimides were synthesized to selectively investigate possible biases for monomer insertion. A series of polycarbodiimides was synthesized for the purpose of directly probing the effect of changing the electronics of the phenyl ring on the regioregularity. This was accomplished via attachment of a variety of substituents with various electronics to the 4-position of the ring. The substituents chosen include the strongly electron donating methoxy- group (**Poly-19**), mildly electron donating methyl- group (**Poly-20** and **Poly-21**), mildly electron withdrawing chloro- group (**Poly-22**), and strongly electron withdrawing nitro- group (**Poly-23**) (Figure 2.5).

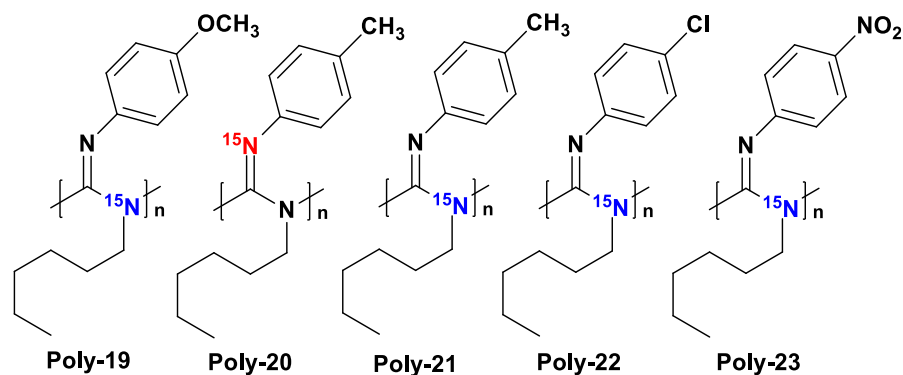


Figure 2.5- Series of polycarbodiimides synthesized to probe the effect of pendant group electronics on monomer insertion.

Poly-19 was synthesized using both **Cat-2R** and **Cat-3** to further study the influence of auxiliary ligands in the titanium(IV) catalyst on the regioregularity of the polymer. The ¹⁵N NMR spectra presented in Figure 2.6 agrees with the previous assessment that the ligands attached to the titanium(IV) catalyst do not affect the regiochemical outcome. The resulting polymers were regioregular with the labeled alkyl nitrogen uniformly segregated to the amine position. **Poly-20** was synthesized using **Cat-2R** as well and resulted in the same regioisomer with, in this case, the labeled aryl nitrogen forced to the imine position only. The decrease in signal-to-noise and peak resolution for the ¹⁵N NMR spectra of **Poly-20** is a consequence of the poor solubility of the polymer in chloroform (the solvent used to collect the NMR data).

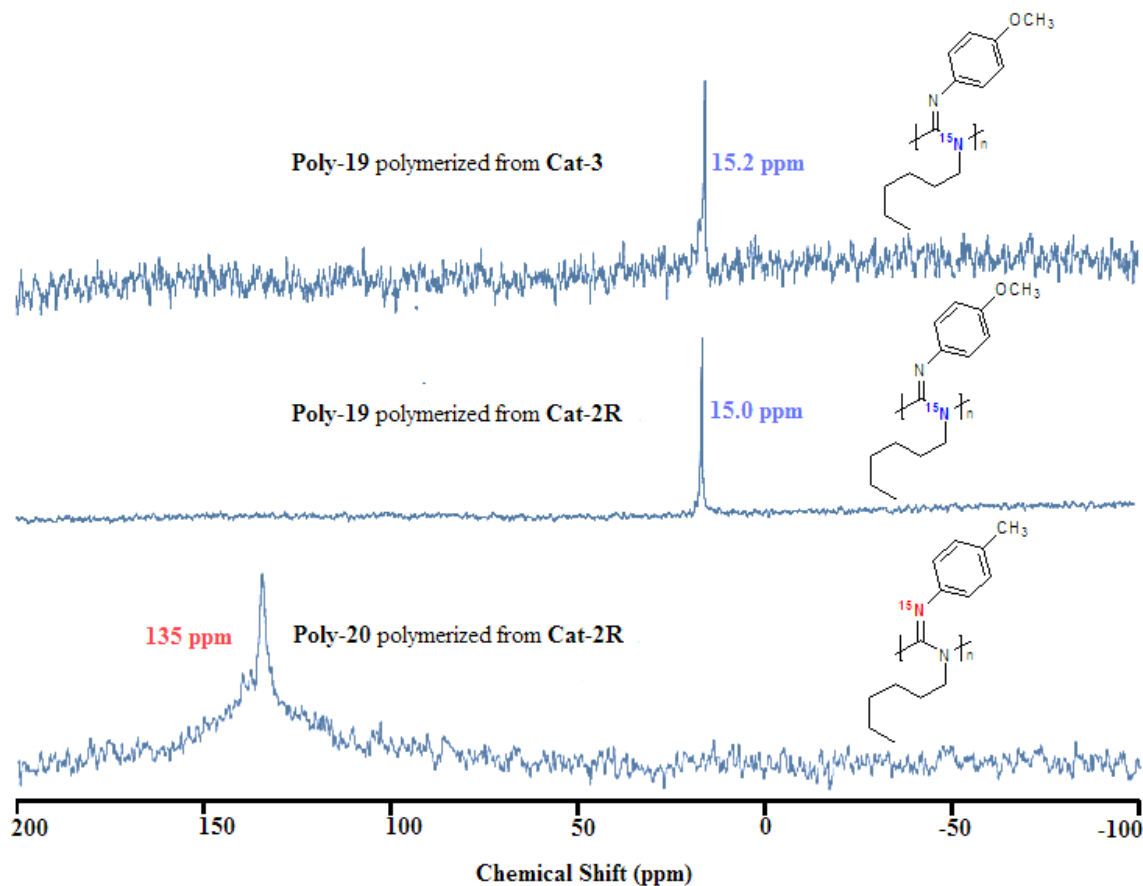


Figure 2.6- ^{15}N NMR spectra of **Poly-19** and **Poly-20** in CDCl_3 . Both polymers display only one peak (i.e. regioregular) with the aromatic pendant group bonded to the imine position in all cases.

Comparison of the IR spectra for the unlabeled poly(*N*-4-methylphenyl-*N'*-hexylcarbodiimide) with the labeled **Poly-20** and **Poly-21** provides further evidence of regioregularity. The C=N imine stretch of the unlabeled polymer at 1628 cm^{-1} matches that of **Poly-21** meaning that the imine nitrogen does not experience any isotopic shift. This shift, however, is apparent upon examination of the IR spectra of **Poly-21** where the imine stretch

is shifted to 1619 cm^{-1} . The IR spectra zoomed in on the imine region for these three polymers are displayed in Figure 2.7.

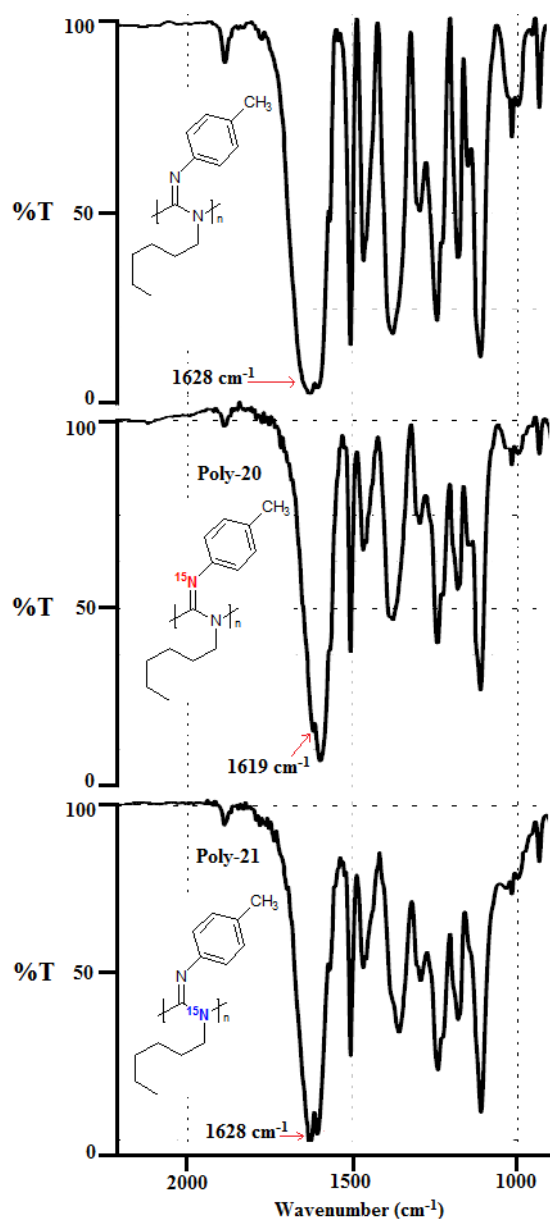


Figure 2.7- Comparison of C=N imine stretch in the FTIR spectra of **Poly-20**, **Poly-21**, and the unlabeled poly(*N*-4-methylphenyl-*N'*-hexylcarbodiimide).

Poly-22 and **Poly-23** were successfully derived from their respective monomers using the achiral **Cat-3**. The resulting polymers, however, proved to be difficult to characterize by solution-based ^{15}N NMR spectroscopy due to their insolubility in all conventional solvents. For this reason, the solution ^{15}N NMR for these polymers was not collected. Both the polymers, however, were characterized by FTIR spectroscopy in the solid state and compared to the spectra of the unlabeled versions of the polymers to identify the regioisomer present in the system. **Poly-22** displayed an imine stretch at 1628 cm^{-1} which matches perfectly with the imine stretch of the unlabeled poly(*N*-4-chlorophenyl-*N'*-hexylcarbodiimide). The lack of an isotope shift corresponds to the labeled alkyl nitrogen being located exclusively at the amine position. **Poly-23** also displayed no isotope shift in the imine region of the IR spectra. The strong imine stretch at 1633 cm^{-1} for the labeled **Poly-23** matched up nearly perfectly with the imine stretch of the unlabeled poly(*N*-4-nitrophenyl-*N'*-hexylcarbodiimide) at 1634 cm^{-1} . This suggests that the asymmetric polycarbodiimides with an aliphatic and aromatic pendant group discussed thus far are uniformly regioregular with the aryl substituents of varying electronics all segregated to the imine nitrogen only. The IR spectra of **Poly-22** and **Poly-23** as well as the unlabeled versions of the polymers are shown in Figure 2.8.

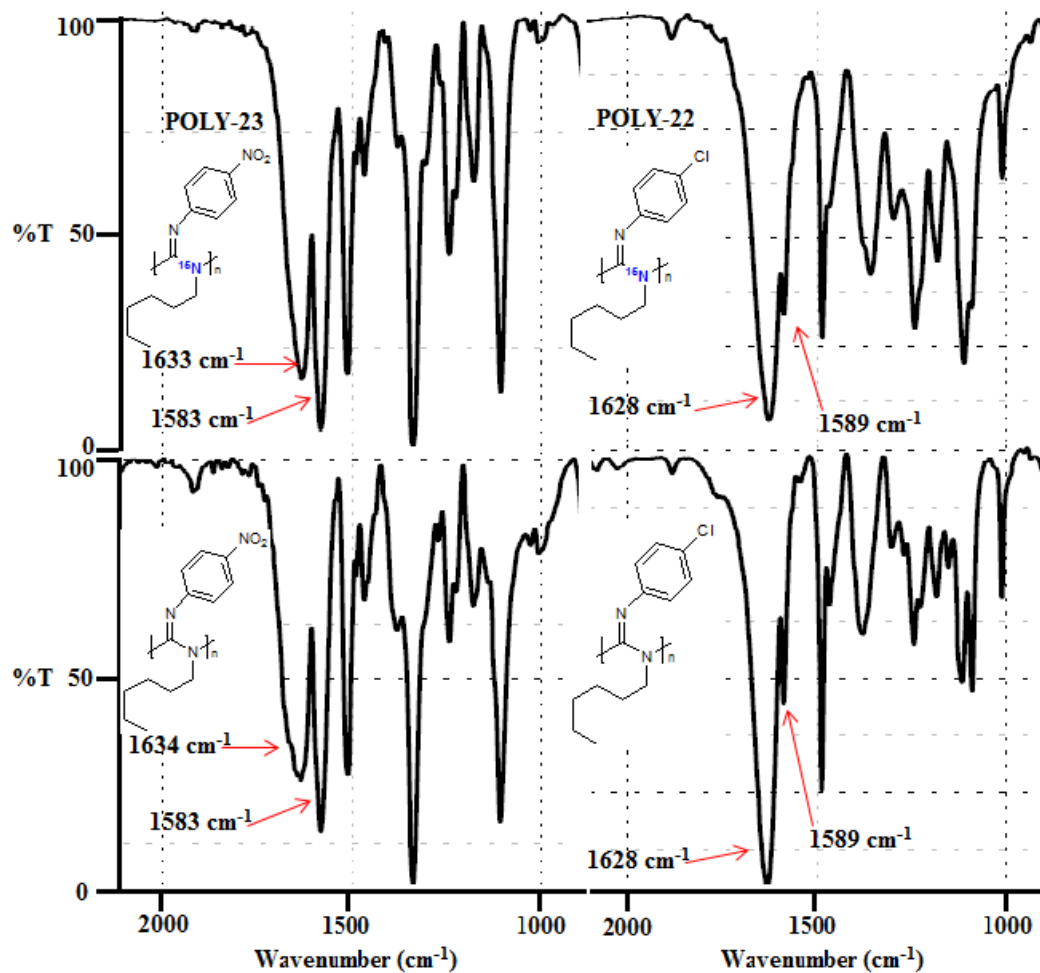


Figure 2.8- FTIR spectra zoomed in on the C=N imine region for **Poly-22** and **Poly-23** as well as the unlabeled versions of the polymers. The absence of a ^{15}N -isotope shift in both cases is evidence of regioregular placement along the backbone.

2.5 Steric Influence of Pendant Groups on Regioregularity-

It has been determined, in all cases tested, that the more sterically bulky aryl pendant groups are bonded to the imine nitrogen. However, it is still uncertain whether sterics is actually the main bias of monomer insertion or if a directly attached aromatic system is necessary in a pendant group to allow for regioregular placement. To further illuminate the

steric influence of pendant groups, **Poly-24** – **27** were synthesized and subject to ^{15}N NMR spectroscopy. (Figure 2.9) **Poly-24** and **Poly-25** were synthesized to determine if sterics are the main source of bias for monomer insertion. **Poly-26** and **Poly-27** were formed in hopes to determine the exact point in which the steric bias is lost.

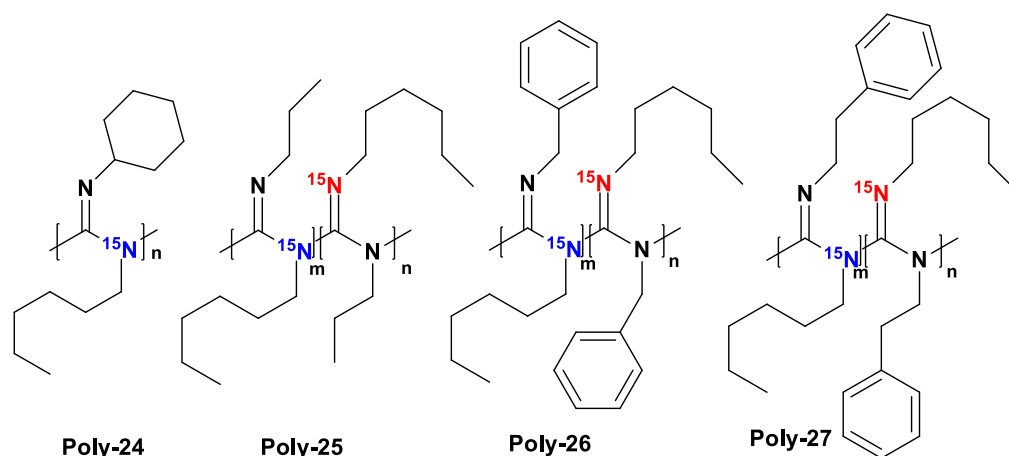


Figure 2.9- Series of ^{15}N -labeled polycarbodiimides synthesized to probe the effect of altered sterics in the side groups.

Poly-24 allows for a substituent with comparable steric A-value (kJ/mol) to the phenyl pendant group ($A = 2.15$ for cyclohexyl substituents and $A = 3.00$ for phenyl substituents as reported by Gordon and Ford)²⁹ but removes the aromaticity. Labeled hexylamine salt was synthesized and coupled with cyclohexyl isocyanate followed by dehydration of the resulting urea to the carbodiimide monomer. Polymerization of *N*-cyclohexyl, ^{15}N -hexylcarbodiimide with **Cat-3** afforded **Poly-24**. ^{15}N NMR spectroscopy of the polymer displays only one peak at $\delta = 1.20$ ppm meaning that the resulting polymer is

indeed regioregular. This supports the idea that the steric hindrance of the pendant group is the primary bias for monomer insertion (Figure 2.10).

When introducing two pendant groups sterically equivalent up to the γ -carbon, such as **Poly-25**, the bias is expected to be significantly diminished. The urea was synthesized by coupling the ^{15}N -labeled hexylamine salt with *n*-propyl isocyanate followed by subsequent dehydration to the corresponding monomer. The polymerization was then conducted with **Cat-3** to produce **Poly-25**. The ^{15}N -NMR spectrum of the polymer is displayed in Figure 2.10. The isotopically labeled nitrogen is distributed between two regioisomers showing incorporation of the ^{15}N -labeled hexyl side chain in both the amine and imine positions randomly throughout the polymer backbone. The relative integration of the imine peak at $\delta = 133$ ppm and the amine peak at $\delta = 1.68$ ppm shows a 1:1 mixture of both regioisomers. This supports the belief that incorporating two aliphatic pendant groups with sterically equivalent structures up to the γ -carbon eliminates the bias for monomer insertion.

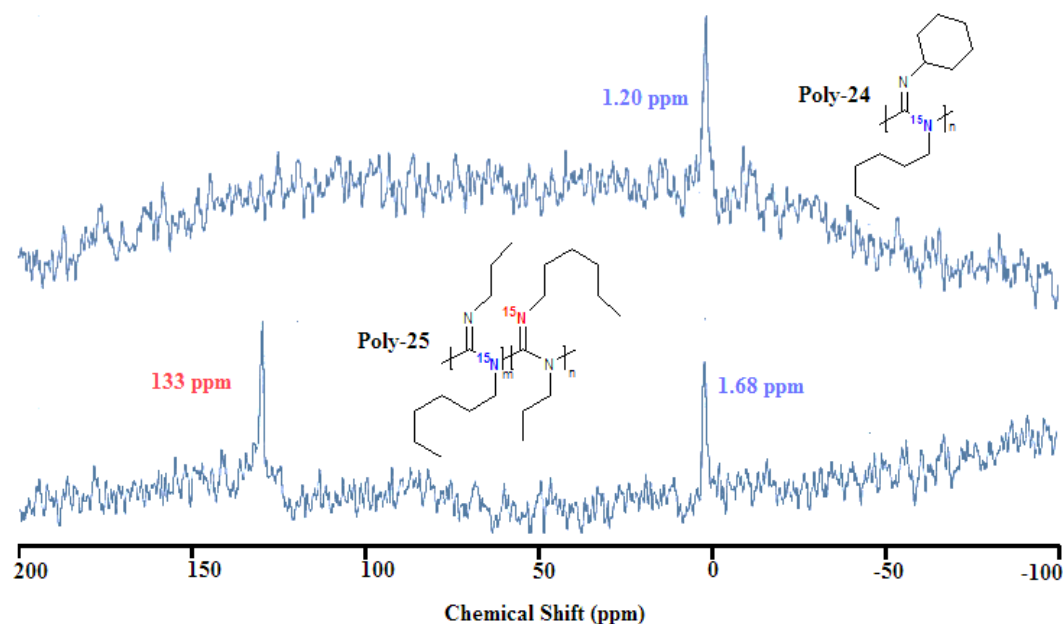


Figure 2.10- ^{15}N -NMR spectra of **Poly-24** and **Poly-25** support the idea that the primary bias for monomer insertion is governed by sterics.

Now that the two extremes of the sterically controlled bias for monomer insertion have been determined, new pendant groups can be implemented to find the exact point where the bias begins to be eliminated. Pendant groups with secondary α -carbons, i.e., carbons directly attached to one of the backbone nitrogen atoms, have been shown to be relegated to the imine nitrogen upon polymerization in all cases with primary α -carbons as the second substituent. **Poly-26** was synthesized to determine if additional sterics on the β -carbon, i.e. one carbon away from the backbone nitrogens, will result in regioregular or regioirregular placement of the pendant groups along the backbone. The corresponding monomer labeled at the *n*-hexyl side group was polymerized with **Cat-3** to afford **Poly-26**. The ensuing ^{15}N NMR spectrum, seen in Figure 2.11, supports the fact that the mode for monomer insertion is still

biased to a particular extent. The resulting polymer is regioirregular but only slightly with a small amount of the ^{15}N -labeled hexyl group present on the imine nitrogen. Relative integration of the two peaks in the ^{15}N NMR spectrum revealed about an 8:1 ratio of the two regioisomers with the majority of the sterically demanding benzyl group located on the imine nitrogen. With these results, it is now important to determine whether steric unbalance on the γ -carbon, i.e., two carbons away from the backbone nitrogen, will also provide some sort of bias for monomer insertion. The ^{15}N -enriched hexylamine salt was coupled with 2-phenethyl isocyanate to obtain the corresponding urea derivative followed by subsequent dehydration to the corresponding monomer. The polymerization was performed with the **Cat-3** to afford **Poly-27**. Examination of the ^{15}N NMR spectra, seen in Figure 2.11, shows a loss of selectivity for insertion with a ~1:1 mixture of the two possible regioisomers present in the polymer.

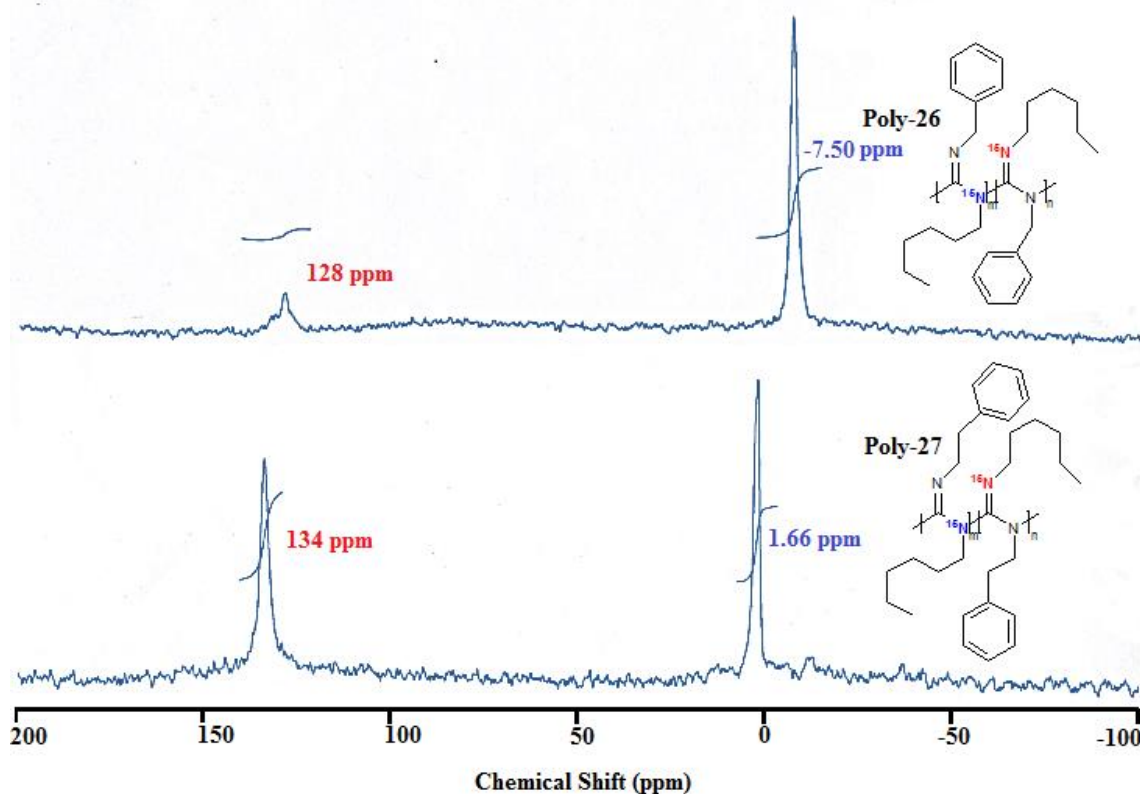


Figure 2.11- ^{15}N NMR spectra of **Poly-26** and **Poly-27** showing the loss of regioisomer selectivity as the sterically bulky aryl group moves farther away from the polymer backbone.

2.6 Identification of Regioregularity in Specific, Unusual Systems-

As previously discussed, certain polycarbodiimides have been shown to possess a variety of interesting properties including liquid crystallinity^{30,31} and chiroptical switching.^{24,32,33} The imine C=N stretch in the IR spectra was previously believed to be a sufficient probe for determining regioregularity in polycarbodiimides. The presence of multiple imine stretches, like in the chiroptical switching **Poly-14**, was initially thought to be evidence of regioirregularity. This was later disproved upon variable-temperature IR analysis of the polymer.²⁵ Also, the IR spectra of the symmetric **Poly-15** displayed two peaks in the

imine C=N region even though the presence of two regioisomers is not possible. For this reason, both polymers were subject to ^{15}N -isotope enrichment and subsequent ^{15}N NMR analysis.

The ^{15}N -labeled benzylamine salt was neutralized and allowed to react with benzyl isocyanate to form the mono-labeled $^{15}\text{N},\text{N}$ -dibenzylurea. Following subsequent dehydration, the monomer was then polymerized with **Cat-3** to afford **Poly-28**. Comparison of the IR spectra of **Poly-28** with the unlabeled version of the polymer (Figure 2.12) offers some insight into the possible classification of each peak. The imine stretch at 1650 cm^{-1} for **Poly-15** experiences an isotopic shift upon ^{15}N -labeling and overlaps with the second peak in the region at 1625 cm^{-1} . This means the peak at 1650 cm^{-1} is the only stretch that actually corresponds to the imine C=N whereas the peak at 1625 cm^{-1} most likely correlates with a C=C aryl stretching mode. Sequential ^{15}N NMR analysis of **Poly-28** shows the expected spectra with the peak for the imine nitrogen at $\delta = 137\text{ ppm}$ and the peak for the amine nitrogen at $\delta = 3.00\text{ ppm}$ integrating to a 1:1 ratio (Figure 2.13).

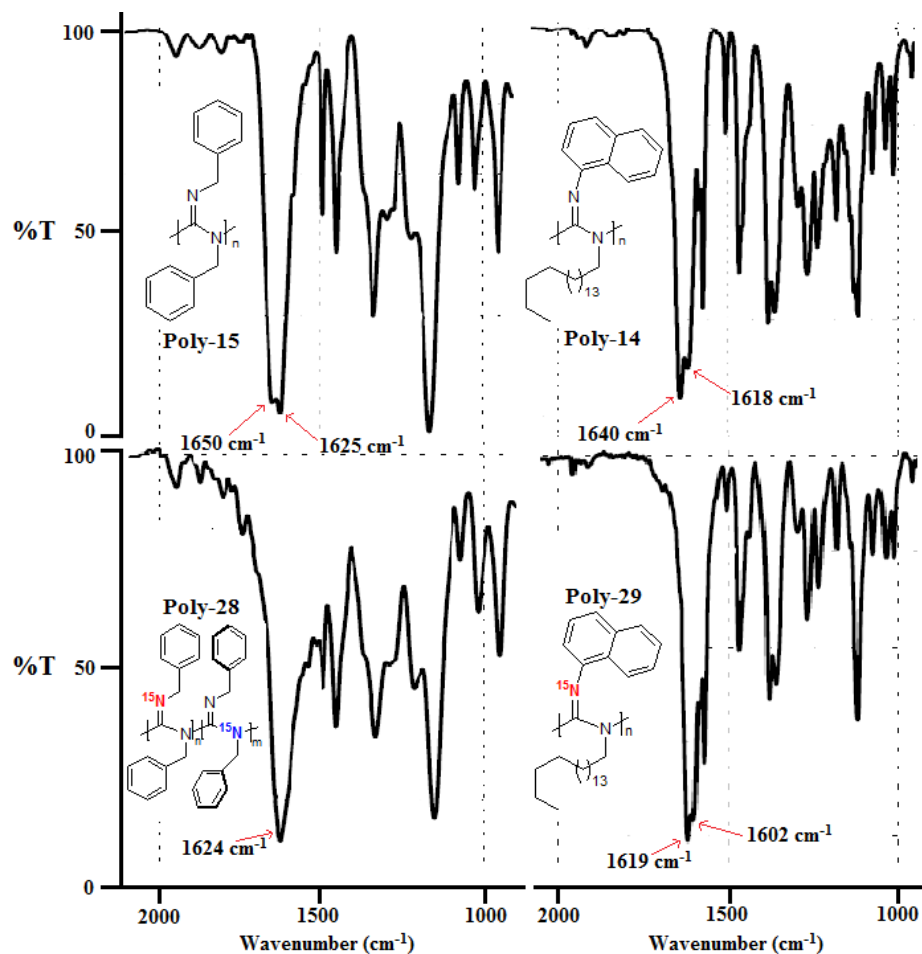
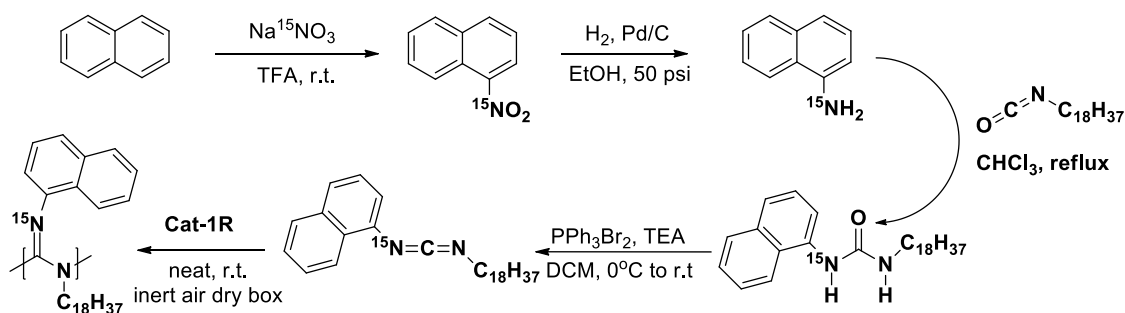


Figure 2.12- FTIR imine stretch of the unlabeled **Poly-14** and **Poly-15** and the ¹⁵N-enriched **Poly-28** and **Poly-29**.

Synthesis of the ¹⁵N-labeled 1-naphthylamine was performed utilizing an alternate procedure including nitration of naphthalene with Na¹⁵NO₃ followed by reduction of the nitro group via hydrogenolysis (Scheme 2.4). The amine was then reacted with n-octadecyl isocyanate to form the mono-labeled urea followed by successive dehydration to the carbodiimide monomer. The monomer was then polymerized with **Cat-2R** to form the

optically active **Poly-29** with an excess helical sense. The chiroptical switching properties of the polymer are further studied in Chapter 3.



Scheme 2.4- Synthesis scheme for **Poly-29** using the ^{15}N -enriched sodium nitrate.

Initially, the multiple imine stretches in the IR spectra of **Poly-14** were believed to support regioirregular placement but VT-FTIR showed that these two peaks undergo intensity changes as a function of temperature.²⁵ This property is not a consequence of regioregularity, since bond breaking must occur for the population change of regioisomers to occur, and is believed to be a direct result of the chiroptical switching process. These two stretches at 1640 cm^{-1} and 1618 cm^{-1} in the IR spectra of **Poly-14** both undergo an isotope shift upon ^{15}N -labeling which is evidence of both peaks coinciding with the imine $\text{C}=\text{N}$ (Figure 2.12). The ^{15}N NMR spectrum of **Poly-29** in toluene- d_8 (Figure 2.13) displayed one peak at $\delta = 139\text{ ppm}$ indicating that the polymer is indeed regioregular despite the presence of two imine stretches in the IR spectrum. The study of the effect of solvent and temperature on the ^{15}N NMR spectrum of **Poly-29** is explained in Chapter 3.

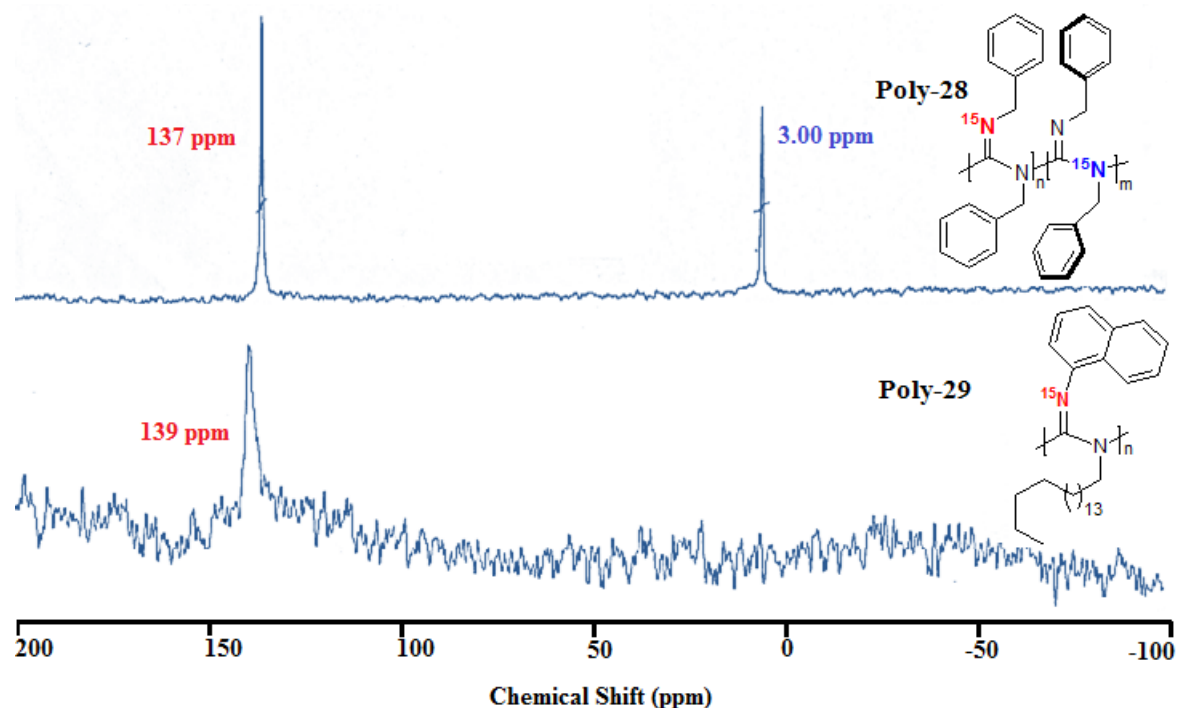


Figure 2.13- ^{15}N NMR spectra of **Poly-28** and **Poly-29** used to help elucidate the reason for multiple peaks in imine region of the IR spectra.

2.7 Effect of Different Transition Metal Catalysts on the Regioregularity-

Carbodiimide monomers have been shown to polymerize with a variety of different transition metal catalysts including titanium, zirconium, copper, and nickel. To study the effect of using different transition metal catalysts on the regioregularity of polycarbodiimides, ^{15}N NMR analysis was performed with the ^{15}N -isotopically labeled **Poly-17** polymerized from η^1 -phenyl(triphenylphosphino) nickel(II) [2,6-bis(1-methylethyl)-*N*-(1-*H*-pyrrol-2-ylmethylene)-benzenamine] (**Cat-5**). This d^8 nickel catalyst allows for the use of a more electron rich metal center compared to the electron deficient Ti(IV) d^0 species

typically used in the synthesis of polycarbodiimides, as discussed earlier. The insertion pathway may be altered due to the catalyst center being significantly less electrophilic. The nickel catalyst used for this polymerization was previously synthesized by Gonglu Tian and stored in a desiccator. The nickel complexes are appreciably more stable than their titanium(IV) counterparts which need to be stored in an inert N₂ atmosphere to prevent degradation. The mono-labeled ¹⁵N-phenyl-*N*-hexylcarbodiimide (**Mono-17**) was synthesized using the same protocol as previously discussed and polymerized with the Ni(II) catalyst (**Cat-5**). Following dehydration of the urea to the corresponding carbodiimide, the monomer was polymerized with **Cat-5** to form **Poly-17(Ni)**. ¹⁵N NMR analysis reveals that the polymer is indeed regioregular and produces the same regioisomer formed by titanium(IV) catalysts. The peak present at $\delta = 136$ ppm matches exactly with **Poly-17** polymerized from **Cat-3**. Small peaks present around the base of the predominant peak as well as ~21 ppm may be evidence of small defects in the polymer chain. This would, in turn, mean that the polymerization with the nickel catalyst is slightly less controlled than the polymerization with titanium complexes. The spectrum for **Poly-17(Ni)** can be found in Figure 2.14.

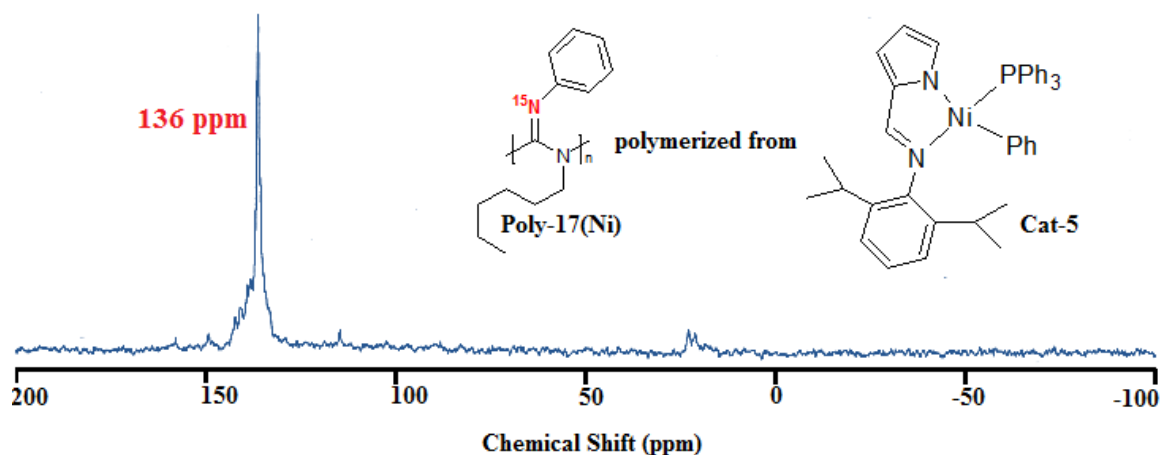


Figure 2.14- ^{15}N NMR spectrum of Poly-17(Ni) polymerized from Cat-5.

2.8 Conclusions-

It has been determined that the sterics of the pendant groups attached to the propagating species bias the monomer insertion pathway. In all cases, the more sterically bulky substituents, i.e. aryl pendant groups or groups with 2° carbons directly attached to the carbodiimide nitrogen, are relegated to the imine position upon polymerization when the other substituent is a simple, unbranched alkyl chain. When incorporating sterically equivalent pendant groups up to the γ -position, the bias is lost and the resulting polymer is regioirregular with random placement of the two regioisomers along the polymer backbone. Introducing sterics on the β -carbon of one the substituents biases the monomer insertion to a certain degree but not fully. The bias is, however, lost when the sterically bulky aryl group is moved to the γ -carbon.

Poly(*N*-1-naphthyl-*N*-octadecylcarbodiimide) is indeed regioregular with one peak in the imine region of the ^{15}N NMR spectrum in toluene- d_8 despite the presence of two peaks in the imine region of the IR spectrum. This suggests that simply examining the C=N imine stretch in the IR spectra of unlabeled polycarbodiimides can be misleading and is not a proper handle for determining the overall connectivity in these polymer systems. The use of different transition metal catalysts also produces a regioregular polymer from a given non-symmetric monomer with the same predominant regioisomer present along the backbone. Now that the primary bias for monomer insertion has been determined, it is possible to tailor polymers with specific properties and allows for the ability to fine tune these properties by altering the microstructure of the polymer backbone.

2.9 Experimental Section-

Materials- The ^{15}N -labeled starting materials- ammonium chloride ($^{15}\text{NH}_4\text{Cl}$), ^{15}N -potassium phthalimide, and sodium nitrate ($\text{Na}^{15}\text{NO}_3$) were received from Cambridge Isotope Laboratories (Cambridge, MA) as 99% ^{15}N -isotope enriched and used as received. All other reagents were used as received unless otherwise stated. All solvents were purchased commercial vendors such as Fischer Scientific (Hampton, NH) and Sigma Aldrich (Milwaukee, MI). The majority of NMR spectra were collected in deuterated chloroform or deuterated dimethyl sulfoxide (DMSO) purchased from Sigma Aldrich (Milwaukee, MI). The deuterated toluene, THF, DCM, and benzene NMR solvents were purchased from Cambridge Isotope Laboratories (Cambridge, MA) and used as received.

Instrumentation- ^1H NMR spectra were collected on both a Varian Mercury 400 MHz and 300 MHz NMR spectrometer with an Oxford Narrow Bore superconducting magnet. All ^{15}N NMR and ^{13}C NMR spectra were conducted on the Varian Mercury 400 MHz Spectrometer. IR spectra were collected on a Jasco Model 410 FTIR spectrometer either cast onto a KBr salt plate or pressed into a KBr pellet in the solid state. Mass spectrometry data was collected by the NCSU Department of Chemistry Mass Spectrometry Facility on the Agilent Technologies 6210 LC-TOF Mass Spectrometer.

^{15}N NMR Collection of Precursor Compounds and Polymers-

A small amount of each ^{15}N -enriched precursor compound (5 mg - 15 mg) was dissolved in ~0.6 mL of deuterated chloroform and pipetted into the NMR sample tube. The amount of polymer added for each NMR sample varied depending on both solubility of the polymer and viscosity of the NMR solution. To collect ^{15}N -NMR data of the polymers in a timely fashion, a common relaxation agent, gadolinium(III) acetylacetonate, $\text{Gd}(\text{acac})_3$, was used. ~10 mg of the reagent was added directly into the premade NMR sample. No relaxation reagent was necessary for the NMR collection of the small molecule precursors. The ^{15}N NMR spectra were collected with 128 scans at 2.00 second delay times for the small molecules. For the polymer samples, the NMR was collected with a delay time of 8.00 seconds for varying times of 6-10 hours. All spectra were referenced to ^{15}N -enriched benzamide set at $\delta = 0.00$ ppm. The ^{15}N NMR spectrum for each monomer was not collected due to 90 second delay times.

Synthesis of ^{15}N -labeled Precursor Compounds-

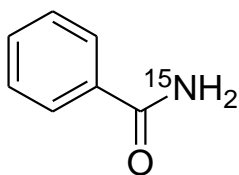
The synthesis of nitrogen-15 enriched amides was done using a modified procedure by Zhang et al.³⁴ The subsequent Hofmann Rearrangement was conducted using a modified procedure outlined by Huang et al.³⁵ The synthesis of nitrogen-15 enriched 1-nitronaphthalene was modified from the reaction reported by Spitzer et al.³⁶ The general procedures for each step are outlined before providing all the specified amounts of reagents, yields, ^1H NMR data, ^{13}C NMR data, ^{15}N NMR data, FTIR data, and MS data collected for the ^{15}N -enriched amides, methyl carbamates, amine HCl salts, 1-nitronaphthalene, and 1-naphthylamine. All J-coupling values are reported in hertz and the FTIR labels are as follows: s = strong intensity, m = moderate intensity, and w = weak intensity. ^1H NMR peak splitting labels are as follows: s = singlet, d = doublet, t = triplet, q = quartet, m = multiplet (greater than quartet), dd = doublet of doublets, td = triplet of doublets, etc. All ^1H NMR spectra is referenced to TMS set at $\delta = 0.00$ ppm.

(i) *Synthesis of ^{15}N -enriched amides-*

The ^{15}N -enriched ammonium chloride ($^{15}\text{NH}_4\text{Cl}$, 1.0 eq.) was added to a round bottom flask along with 50 mL of deionized water and a stir bar. The reaction flask was cooled to 0 °C in an ice bath and 80 mL of diethyl ether was added to the unperturbed system. The corresponding acid chloride (1.5-2.0 eq.) was then added directly into the ether layer. The potassium hydroxide (KOH, 6.0 eq.) was dissolved in 30 mL of deionized water in a separate beaker and pipetted directly into the bottom of the aqueous layer. Upon addition, the reaction mixture was left unperturbed for 10 minutes followed by mild agitation for 10

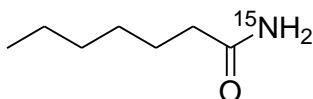
minutes. The ice bath was then removed and the mixture was vigorously stirred for an additional 35 minutes. The ether layer was collected in a separate flask and the remaining product was extracted from the aqueous layer with additional diethyl ether (4 x 50 mL). The ether extracts were combined and dried over anhydrous sodium sulfate. The solution was decanted into a clean flask and the solvent was removed via rotatory evaporation. The product was collected and dried under high vacuum without further purification or purified by was recrystallized and filtered.

¹⁵N-Benzamide-



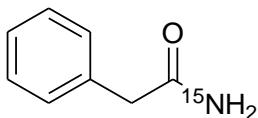
Following the procedure from above for nitrogen-15 enriched amides: 1.81 g (33.9 mmol, 1.0 eq.) of 99% ¹⁵N-enriched ammonium chloride, 5.90 mL (50.9 mmol, 1.5 eq.) of heptanoyl chloride, 11.4 g (203 mmol, 6.0 eq.) of potassium hydroxide (KOH).

Yield 3.19 g (26.1 mmol) white crystals, 77 %. FTIR (KBr pellet, cm⁻¹): 3356 (s, ¹⁵N-H str), 3188 (s, ¹⁵N-H str), 2956 (m, C-H alkyl), 2937 (m, C-H alkyl), 2870 (m, C-H alkyl), 1653 (s, C=O), 1633 (w, ¹⁵N-H bend). ¹H-NMR (400 MHz, CDCl₃): δ (ppm) 7.82 (Ar-H, *J* = 14.0 Hz, 2H, dt), 7.57 – 7.43 (Ar-H, 2H, m). 6.18 (¹⁵N-H, *J* = 72 Hz, 2H, d), 5.89 (¹⁵N-H, *J* = 72 Hz, 2H, d). ¹³C-NMR (100 MHz, CDCl₃): 169.9, 133.6, 132.2, 128.8, 127.5 ¹⁵N-NMR (40.5 MHz, CDCl₃): δ (ppm) 0.00. HRMS-ESI: *M*_{theoretical} = 123.0571, *M*_{sample} = 123.0569, Δ*M* = -0.2 mmass units (-1.6 ppm), C₇H₇¹⁵NO.

¹⁵N-Heptamide-

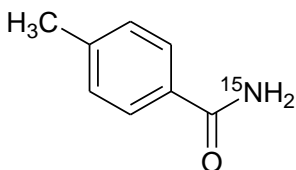
Following the outlined procedure from above for nitrogen-15 enriched amides: 2.92 g (54.7 mmol, 1.0 eq.) of 99% ¹⁵N-enriched ammonium chloride, 12.7 mL (82.0 mmol, 1.5 eq.) of heptanoyl chloride, 18.5 g (329 mmol, 6.0 eq.) of potassium hydroxide (KOH).

Yield: 5.94 g (45.9 mmol) white crystals, 84 %. FTIR (KBr pellet, cm⁻¹): 3356 (s, ¹⁵N-H str), 3188 (s, ¹⁵N-H str), 2956 (m, C-H alkyl), 2937 (m, C-H alkyl), 2870 (m, C-H alkyl), 1653 (s, C=O), 1633 (w, ¹⁵N-H bend). ¹H-NMR (400 MHz, CDCl₃): δ (ppm) 5.57 (¹⁵N-H, *J*_{15N-1H} = 88 Hz, 1H, d), 5.46 (¹⁵N-H, *J*_{15N-1H} = 88 Hz, 1H, d), 2.22 (-CH₂CH₂(CH₂)₃CH₃, *J* = 8.0 Hz, 2H, t), 1.64 (-CH₂CH₂(CH₂)₃CH₃, *J* = 7.2 Hz, 2H, p), 1.38 – 1.30 (-CH₂CH₂(CH₂)₃CH₃, 6H, m), 0.89 (-CH₂CH₂(CH₂)₃CH₃, *J* = 7.2 Hz, 3H, t). ¹³C-NMR (100 MHz, CDCl₃): δ (ppm) 176.0 (*J*_{13C-15N} = 12.9 Hz), 36.1 (*J*_{13C-15N} = 33.0 Hz), 31.7, 29.1, 25.7, 22.7, 14.2. ¹⁵N-NMR (40.5 MHz, CDCl₃): δ (ppm) 6.38. HRMS-ESI: *M*_{theoretical} = 131.1197, *M*_{sample} = 131.1198, Δ*M* = 0.1 mmass units (0.7 ppm), C₇H₁₅¹⁵NO.

¹⁵N-2-Phenylacetamide-

Following the outlined procedure from above for nitrogen-15 enriched amides: 1.44 g (26.5 mmol, 1.0 eq.) of 99% ¹⁵N-enriched ammonium chloride, 7.00 mL (52.9 mmol, 2.0 eq.) of 2-phenylacetyl chloride, 8.90 g (159 mmol, 6.0 eq.) of KOH.

Yield: 3.51 g (25.8 mmol) white crystals, 97.5 %. FTIR (KBr pellet, cm⁻¹): 3348 (s, ¹⁵N-H), 3172 (s, ¹⁵N-H), 3060 (w, aryl-H), 2918 (w, alkyl-H), 1705 (s, C=O). 1496 (w, C=C). ¹H NMR (400 MHz, CDCl₃): δ (ppm) 7.38 – 7.26 (Ar-H, 5H, m), 6.08 (¹⁵N-H, *J*_{15N-1H} = 89.2 Hz, *J*_{1H-1H} = 3.2 Hz, 1H, dd), 5.43 (¹⁵N-H, *J*_{15N-1H} = 89.2 Hz, *J*_{1H-1H} = 2.8 Hz, 1H, dd), 3.58 (benzyl-H, 2H, s). ¹³C NMR (100 MHz, CDCl₃): δ (ppm) 174.2 (*J*_{15N-13C} = 15.2 Hz), 134.9, 129.6, 129.3, 128.7, 127.7, 43.4 (*J*_{13C-15N} = 8.4 Hz). ¹⁵N NMR (40.5 MHz, CDCl₃): δ (ppm) 8.55. HRMS-ESI: *M*_{theoretical} = 137.0733, *M*_{sample} = 137.0731, Δ*M* = -0.2 mmass units (- 1.4 ppm), C₈H₉¹⁵NO.

¹⁵N-p-Toluamide-

Following the outlined procedure from above for nitrogen-15 enriched amides: 2.07 g (38.7 mmol, 1.0 eq.) of 99% ¹⁵N-enriched ammonium chloride, 7.50 mL (56.7 mmol, 1.5

eq.) of *p*-toluoyl chloride, 12.7g (226 mmol, 6.0 eq.) of KOH. The product was recrystallized from ethanol for further purification. The product was then filtered and dried under high vacuum.

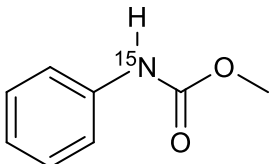
Yield: 4.46 g (33.0 mmol) white crystals, 85%. FTIR (KBr pellet, cm^{-1}): 3336 (s, $^{15}\text{N-H}$) 3156 (s, $^{15}\text{N-H}$), 3058 (w, Ar-H), 1668 (s, C=O) 1569 (m, C=C aryl). ^1H NMR (400 MHz, DMSO-d_6): δ (ppm) 7.91 ($^{15}\text{N-H}$, $J_{^{15}\text{N-}^1\text{H}} = 88$ Hz, 1H, d) 7.77 (Ar-H, $J_{^1\text{H-}^1\text{H}} = 8.0$ Hz, 2H, d), 7.30 ($^{15}\text{N-H}$, $J_{^{15}\text{N-}^1\text{H}} = 88$ Hz, 1H, d), 7.23 (Ar-H, $J_{^1\text{H-}^1\text{H}} = 8.0$ Hz), 2.31 (- CH_3 , s, 3H). ^{13}C NMR (100 MHz, DMSO-d_6): δ (ppm) 167.8 ($J_{^{15}\text{N-}^{13}\text{C}} = 15.9$ Hz), 141.1, 131.5 ($J_{^{13}\text{C-}^{15}\text{N}} = 7.6$ Hz), 128.8, 127.6, 20.9. ^{15}N NMR (40.5 MHz, CDCl_3): δ (ppm) -0.84. HRMS-ESI: $M_{\text{theoretical}} = 137.0727$, $M_{\text{sample}} = 137.0730$, $\Delta M = -0.30$ (-2.18 ppm), $\text{C}_8\text{H}_9^{15}\text{NO}$.

(ii) *Synthesis of ^{15}N -enriched methyl carbamates-*

The ^{15}N -labeled amide (1.0 eq.), first addition of *N*-bromosuccinimide (NBS, 1.0 eq.), and 1,8-diazabicyclo[5.4.0]undec-7-ene (DBU, 2.0 eq.) were added to a round bottom flask along with ~300 mL of methanol. The mixture was heated to reflux and allowed to stir for 15 minutes. A second addition of NBS (1.0 eq.) was then added to the boiling mixture slowly and the reflux was continued for an additional 35 minutes. Upon cooling to room temperature, the solvent was removed under reduced pressure. The product was redissolved in ethyl acetate and washed with 6M HCl (2 x 100 mL), 1M NaOH (2 x 100 mL), and Brine solution (1 x 100 mL). The organic layer was then collected and dried over anhydrous sodium sulfate. The solution was decanted into a clean flask and the solvent was again removed under reduced pressure. The product was further purified via column

chromatography (Specific mobile phase is shown below for each step). The product was collected and dried under high vacuum.

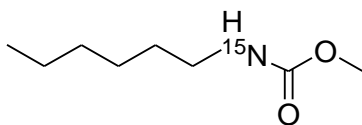
Methyl ¹⁵N-phenylcarbamate



Following the outlined procedure from above for the modified Hofmann Rearrangement of the nitrogen-15 labeled amides: 500 ml of methanol, 2.57 g (21.0 mmol, 1 eq) benzamide, 3.75 g (21.0 mmol, 1 eq.) N-bromosuccinimide (NBS), 7.14 ml (7.27 g, 47.8 mmol, 2.27 eq), 1,8-diazabicyclo[5.4.0]undec-7-ene (DBU), 3.75 g (21.0 mmol, 1 eq) NBS (2nd addition). The crude product was purified by column chromatography with a 1:1 hexane : ethyl acetate as the mobile phase.

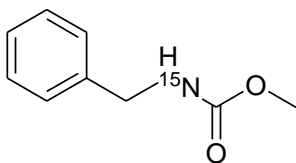
Yield: 2.12 g (14.0 mmol) of a white crystals, 78 %. FTIR (KBr pellet, cm⁻¹): 3296 (s, ¹⁵N-H), 3126 (w, aryl-H), 3061 (m, aryl-H), 2952 (m, alkyl-H), 1709 (s, C=O), 1599 (m, C=C). ¹H NMR (400 MHz, DMSO-d₆): δ (ppm) 9.64 (¹⁵N-H, $J_{15\text{N}-1\text{H}} = 91.2$ Hz, 1H, d), 7.45 (Ar-H, $J = 8.0$ Hz, 2H, d), 7.27 (Ar-H, $J = 7.6$ Hz, 2H, t), 6.98 (Ar-H, $J = 7.2$ Hz, 2H, t), 3.66 (-CH₃, 3H, s). ¹³C NMR (100 MHz, DMSO-d₆): δ (ppm) 153.9 ($J_{15\text{N}-13\text{C}} = 26.5$ Hz), 139.1 ($J_{15\text{N}-13\text{C}} = 15.2$ Hz), 128.8, 122.4, 118.1, 51.6. ¹⁵N NMR (40.5 MHz, CDCl₃): δ (ppm) 7.1. HRMS-ESI: $M_{\text{theoretical}} = 153.0676$, $M_{\text{sample}} = 153.0698$, $\Delta M = 2.2$ mmass units (14.4 ppm), C₈H₉¹⁵NO₂.

Methyl ¹⁵N-(n-hexyl)carbamate



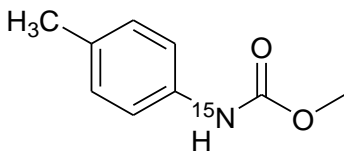
Following the outlined procedure from above for the modified Hofmann Rearrangement of the nitrogen-15 labeled amides: 300 mL of methanol, 4.61 g (35.7 mmol, 1.0 eq.) of ¹⁵N-labeled heptamide, 11.8 mL (78.6 mmol, 2.0 eq) of 1,8-diazabicyclo[5.4.0]undec-7-ene (DBU), 6.46 g (35.8 mmol, 1.0 eq.) for 1st addition of *N*-bromosuccinimide (NBS), and 6.46 g (35.8 mmol, 1.0 eq.) for 2nd addition of *N*-bromosuccinimide (NBS). The crude product was purified by column chromatography with a 1:1 hexane : ethyl acetate as the mobile phase.

Yield: 4.39 g (27.6 mmol) of pale-yellow liquid, 77%. FTIR (KBr pellet, cm⁻¹): 3333 (m, ¹⁵N-H), 2929 (m, Alkyl-H), 2860 (m, Alkyl-H), 1701 (s, C=O). ¹H-NMR (400 MHz, DMSO_{d6}): δ (ppm) 7.08 (¹⁵N-H, $J_{15\text{N}-1\text{H}} = 92.0$ Hz, $J_{\text{H}-\text{H}} = 5.6$ Hz, 1H, dt), 3.50 (-CH₃, 3H, s), 2.95 (-CH₂(CH₂)₄CH₃, $J = 6.4$ Hz, 2H, pentet), 1.39 – 1.23 (-CH₂(CH₂)₄CH₃, 8H, m), 0.86 (-CH₂(CH₂)₄CH₃, $J = 7.2$ Hz, 3H, t). ¹³C-NMR (100 MHz, CDCl₃): δ (ppm) 156.6 ($J_{15\text{N}-13\text{C}} = 26.5$ Hz), 51.0, 40.2 ($J_{15\text{N}-13\text{C}} = 10.6$ Hz), 31.0, 29.4, 25.9, 22.1, 13.9. ¹⁵N-NMR (40.5 MHz, CDCl₃): δ (ppm) – 13.2. $M_{\text{theoretical}} = 161.1302$, $M_{\text{sample}} = 161.1298$, $\Delta M = -0.4$ mmass units (-2.48 ppm), C₈H₁₇¹⁵NO₂.

Methyl ¹⁵N-benzylcarbamate

Following the outlined procedure from above for the modified Hofmann Rearrangement of the nitrogen-15 labeled amides: 300 mL of methanol, 3.37 g (24.8 mmol, 1.0 eq.) of ¹⁵N-2-phenylacetamide, 8.40 mL (56.2 mmol, 2.0 eq) of 1,8-diazabicyclo[5.4.0]undec-7-ene (DBU), 2.41 g (24.8 mmol, 1.0 eq.) for 1st addition of *N*-bromosuccinimide (NBS), and 2.41 g (24.8 mmol, 1.0 eq.) for 2nd addition of *N*-bromosuccinimide (NBS). The crude product was purified by column chromatography with a 1:1 hexane : ethyl acetate as the mobile phase.

Yield: 3.34 g (20.1 mmol) of clear oil, 81 %. FTIR (KBr Plate, cm⁻¹): 3365 (s, ¹⁵N-H), 3086 (w, aryl-H), 3062 (w, aryl-H), 3030 (m, aryl-H), 2952 (m, alkyl-H), 1705 (s, C=O), 1454 (m, C=C aryl). ¹H NMR (400 MHz, DMSO_{d6}): δ (ppm) 7.69 (¹⁵N-H, *J*_{15N-1H} = 92.8 Hz, *J*_{1H-1H} = 6.4 Hz, 2H, d), 7.31 (Ar-H, *J* = 7.6 Hz, 2H, td), 7.23 (Ar-H, *J* = 7.6 Hz, 2H, t), 4.17 (benzyl-H, *J* = 6.4 Hz, 2H, d), 3.54 (-CH₃, 3H, s). ¹³C NMR (100 MHz, CDCl₃): δ (ppm) 156.9 (*J*_{15N-13C} = 12.2 Hz), 139.8, 128.3, 127.0, 126.8, 51.4, 43.8 (*J*_{15N-13C} = 12.2 Hz). ¹⁵N NMR (40.5 MHz, CDCl₃): δ (ppm) -11.65. HRMS-ESI: *M*_{theoretical} = 167.0833, *M*_{sample} = 167.0832, Δ*M* = -0.1 mmass units (-0.6 ppm), C₉H₁₁¹⁵NO₂.

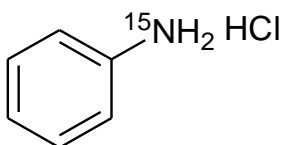
Methyl ¹⁵N-p-tolyl carbamate-

Following the outlined procedure from above for the modified Hofmann Rearrangement of the nitrogen-15 labeled amides: 300 mL of methanol, 4.06 g (30.0 mmol, 1.0 eq.) of ¹⁵N-*p*-toluamide, 10.0 mL (66.9 mmol, 2.0 eq) of 1,8-diazabicyclo[5.4.0]undec-7-ene (DBU), 5.54 g (30.7 mmol, ~1.0 eq.) for 1st addition of *N*-bromosuccinimide (NBS), and 5.35 g (29.8 mmol, ~1.0 eq.) for 2nd addition of *N*-bromosuccinimide (NBS). The crude product was purified by column chromatography with a 1:1 hexane : ethyl acetate as the mobile phase.

Yield: 3.95 g (23.9 mmol) white crystals, 80 %. FTIR (KBr Pellet, cm⁻¹): 3326 (s, ¹⁵N-H str), 3112 (m, Ar-H), 3027 (m, Ar-H), 2952 (w, -CH₃), 1741 (s, C=O), 1598 (m, C=C aryl). ¹H NMR (400 MHz, CDCl₃): δ (ppm) 7.28 (Ar-H, broad, 2H), 7.07 (Ar-H, *J*_{1H-1H} = 4 Hz, d, 2H), 7.05 (¹⁵N-H, *J*_{15N-1H} = 90.8 Hz, d, 1H), 3.05 (O-CH₃, s, 3H), 2.28 (Ar-CH₃, s, 3H). ¹³C NMR (100 MHz, CDCl₃): δ (ppm) 155.1 (*J*_{15N-13C} = 26 Hz), 135.6 (*J*_{15N-13C} = 15.1 Hz), 133.2, 129.7, 129.6, 119.2, 52.5, 21.0. ¹⁵N NMR (40.5 MHz, CDCl₃): δ (ppm) 5.09. HRMS-ESI: *M*_{theoretical} = 167.0833, *M*_{sample} = 167.0830, Δ*M* = 0.25 mmass units (1.49 ppm), C₉H₁₁¹⁵NO₂.

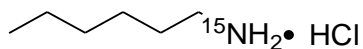
(iii) *Deprotection to ¹⁵N-labeled Amine Salt*

The labeled carbamate was added to a 250 mL round bottom flask along with ~50 mL of 12M HCl and a stir bar. The mixture was allowed to reflux while stirring for 16 hrs. Upon completion, the mixture was cooled to 0 °C in an ice bath and was neutralized to ~pH = 5 with 1M NaOH solution. The aqueous layer was washed with ethyl acetate (3 x 100 mL) and the solvent from the aqueous layer was removed under reduced pressure. 100 mL of ethanol was added to the flask and the mixture was allowed to stir for 15 min. The remaining solids were filtered off and the filtrate was collected. The solvent was removed and the resulting solid was further dried under high vacuum to afford pure product.

¹⁵N-Aniline HCl-

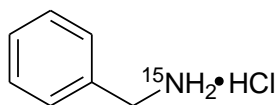
Following the procedure outlined above for acidolysis of methyl carbamates: 1.64 g (10.78 mmol) of methyl *15*N-hexylcarbamate, 50 mL of 12 M HCl.

Yield 0.58 g (4.44 mmol) of a yellow solid, 41.0 %. ¹H-NMR (400 MHz, DMSO-d₆): δ (ppm) 10.43 (¹⁵N-H, 3H, b), 7.48 (Ar-H, *J* = 7.6 Hz, 2H, td), 7.41 – 7.38 (Ar-H, 3H, m). ¹³C NMR (100 MHz, DMSO-d₆): δ (ppm) 132.1 (*J*_{15N-13C} = 8.4 Hz), 129.7 (*J*_{15N-13C} = 1.5 Hz), 127.8, 123.2. HRMS-ESI: *M*_{theoretical} = 95.0622, *M*_{sample} = 95.0625, Δ*M* = 0.3 mmass units (3.1 ppm), C₆H₇ ¹⁵N.

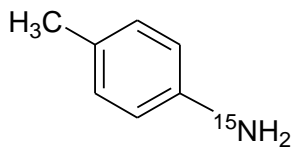
¹⁵N-Hexylamine HCl Salt-

Following the outlined above for acidolysis of methyl carbamates: 50 mL of 12 M HCl, 2.87 g (18.0 mmol, 1.0 eq.) of ¹⁵N-labeled methyl carbamate.

2.01 g (14.5 mmol) of off-white solid, 81 %. ¹H-NMR (400 MHz, CDCl₃): δ (ppm) 8.19 (¹⁵N-H, $J_{15\text{N}-1\text{H}} = 73$ Hz, 3H, d), 5.46 (¹⁵N-H, $J_{15\text{N}-1\text{H}} = 88$ Hz, 1H, d), 2.22 (-CH₂CH₂(CH₂)₃CH₃, $J = 8.0$ Hz, 2H, t), 1.64 (-CH₂CH₂(CH₂)₃CH₃, $J = 7.2$ Hz, 2H, p), 1.38 – 1.30 (-CH₂CH₂(CH₂)₃CH₃, 6H, m), 0.89 (-CH₂CH₂(CH₂)₃CH₃, $J = 7.2$ Hz, 3H, t). ¹³C-NMR (100 MHz, CDCl₃): 40.1 ($J_{15\text{N}-13\text{C}} = 4.6$ Hz), 31.3, 27.7, 26.4, 22.6, 14.1. ¹⁵N-NMR (40.5 MHz, CDCl₃): δ (ppm) – 50.1. HRMS-ESI: $M_{\text{theoretical}} = 103.1258$, $M_{\text{sample}} = 103.1242$, $\Delta M = 0.4$ mmass units (3.8 ppm), C₆H₁₅¹⁵N.

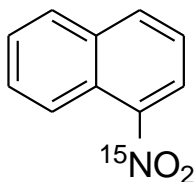
¹⁵N-Benzylamine HCl Salt-

Following the outlined procedure from above of the main text for the acidolysis of the labeled carbamates. Due to difficulties purifying as a result of some side reaction taking place, the yield, IR data, NMR data, and MS data were not collected for this compound. The crude material was used directly after the deprotection to form the di-labeled ¹⁵N, ¹⁵N'-dibenzylurea.

¹⁵N-p-Toluidine -

Following the outlined procedure from above for the carbamate acidolysis: 50 mL of 12 M HCl, 3.19 g (19.3 mmol, 1.0 eq.) of ¹⁵N-labeled methyl p-tolylcarbamate. The product was collected and characterized as the free-amine upon neutralizing with NaOH and subsequent extraction with diethyl ether.

Yield: 1.87 g (13.0 mmol) off white powder, 67 %. FTIR (KBr pellet, cm⁻¹): 3453 (s, ¹⁵N-H), 3365 (s, ¹⁵N-H), 3029 (m, Ar-H), 3017(w, Ar-H), 2923 (m, -CH₃), 1519 (s, C=C aryl). ¹H NMR (400 MHz, CDCl₃): δ (ppm) 6.96 (Ar-H, *J*_{1H-1H} = 8.4 Hz, d, 2H), 6.61 (Ar-H, *J*_{1H-1H} = 12.8 Hz, *J*_{15N-1H} = 2.4 Hz, dq, 2H), 3.44 (¹⁵NH₂, s, 2H), 2.22 (Ar-CH₃, s, 3H). ¹³C NMR (100 MHz, CDCl₃): δ (ppm) 143.9 (*J*_{15N-13C} = 10.6 Hz), 129.9, 128.0, 115.4 (*J*_{15N-13C} = 2.3 Hz), 20.6. ¹⁵N NMR (40.5 MHz, CDCl₃): δ (ppm) -43.35.

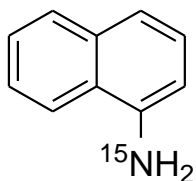
(iv) Synthesis of 1-Nitronaphthalene-

1.72 g (20.2 mmol, 1.0 eq) of ¹⁵N-sodium nitrate (Na¹⁵NO₃, 99% ¹⁵N-enriched) was added to a 250 mL round bottom flask along with ~40 mL of trifluoroacetic acid (TFA) and a stir bar. The nitrate was allowed to dissolve prior to addition of 2.59 g (20.2 mmol, 1.0 eq.)

of naphthalene to the stirring mixture. The solution was then allowed to stir for 5 hours at room temperature. The reaction flask was then cooled to 0 °C in an ice bath and the TFA was basified with 50-60 mL of 6M NaOH. The product was then extracted with diethyl ether (4 x 75 mL) and the ether extracts were dried over anhydrous sodium sulfate. The solution was then decanted into a clean flask and the solvent was removed under reduced pressure. The product was collected as a yellow solid and dried under high vacuum without further purification.

Yield: 3.39 g (19.5 mmol) of yellow solid, 96 %. FTIR (KBr pellet, cm^{-1}): 3072 (Ar-H, w), 1598 (C=C aryl, w), 1488 ($^{15}\text{N-O}_{\text{nitro}}$ str, s), 1315 ($^{15}\text{N-O}_{\text{nitro}}$ str, s). ^1H NMR (400 MHz, CDCl_3): δ (ppm) 8.54 (Ar-H, $J_{1\text{H}-1\text{H}} = 8.8$ Hz, d, 1H), 8.21 (Ar-H, m, 1H), 8.10 (Ar-H, $J_{1\text{H}-1\text{H}} = 8.0$ Hz, d, 1H), 7.94 (Ar-H, $J_{1\text{H}-1\text{H}} = 8.0$ Hz, d, 2H), 7.70 (Ar-H, $J_{1\text{H}-1\text{H}} = 7.2$ Hz, $J_{1\text{H}-1\text{H}} = 1.2$ Hz, td, 1H), 7.62 (Ar-H, $J_{1\text{H}-1\text{H}} = 7.2$ Hz, $J_{1\text{H}-1\text{H}} = 3.6$ Hz, td, 2H), 7.53 (Ar-H, $J_{1\text{H}-1\text{H}} = 8.0$ Hz, $J_{1\text{H}-1\text{H}} = 4.0$ Hz, td, 2H). ^{13}C NMR (100 MHz, CDCl_3): δ (ppm) 146.9 ($J_{15\text{N}-13\text{C}} = 12.4$ Hz), 135.0, 129.7, 128.9, 127.6, 124.4, 124.3, 124.3, 124.2, 123.3. ^{15}N NMR (40.5 MHz, CDCl_3): δ (ppm) -277.7.

(v) *Hydrogenolysis of ^{15}N -labeled 1-Nitronaphthalene-*



2.03 g (11.7 mmol, 1.0 eq.) of ^{15}N -labeled 1-nitronaphthalene and 0.1268 g (~5 wt% with respect to 1-nitronaphthalene) of palladium on carbon (10 wt%) catalyst were added to a

50 mL Erlenmeyer flask along with ~30 mL of ethanol and a stir bar. The reaction vessel was then placed in a high pressure Parr reactor under H₂ atmosphere at 50 psi. The mixture was allowed to stir under these conditions for 14 hours. The reaction flask was then removed from the reactor and filtered through Celite™ to remove the Pd/C catalyst. The filtrate was then collected and the solvent was removed under reduced pressure to afford pure ¹⁵N-labeled 1-naphthylamine as a brown solid. The product was collected and dried under high vacuum.

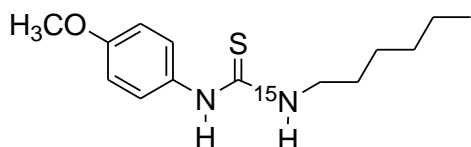
Yield: 1.50 g (10.4 mmol) brown solid, 89 %. FTIR (KBr pellet, cm⁻¹): 3442 (s, ¹⁵N-H str), 3361 (s, ¹⁵N-H), 3048 (m, Ar-H), 1619 (s, ¹⁵N-H bend), 1553 (m, C=C aryl). ¹H NMR (400 MHz, CDCl₃): δ (ppm) 7.80 (Ar-H, overlapped m, 2H), 7.45 (Ar-H, overlapped m, 2H), 7.31 (Ar-H, overlapped m, 1H), 6.77 (Ar-H, $J_{1H-1H} = 8.8$ Hz, $J_{1H-1H} = 2.4$, dt, 1H), 4.13 (¹⁵NH₂, $J_{15N-1H} = 104$ Hz, d, 2H). ¹³C NMR (100 MHz, CDCl₃): δ (ppm) 142.4 ($J_{15N-13C} = 10.0$ Hz), 134.7, 128.8, 126.7, 126.2, 126.2, 125.2, 123.9, 121.1, 110.0 ($J_{15N-13C} = 2.3$ Hz). ¹⁵N NMR (40.5 MHz, CDCl₃): δ (ppm) -43.95.

Synthesis of ¹⁵N-labeled Ureas/Thioureas-

The labeled amine HCl salt (1.0 eq.) was added to a round bottom flask along with triethylamine (2.0 eq.), a stir bar, and 70 mL of CHCl₃. The mixture was allowed to stir for 15 minutes prior to addition of the corresponding isocyanate/ isothiocyanate (1.2 eq.) The reaction mixture was then allowed to stir at room temperature when employing alkyl amines or allowed to reflux when employing aryl amines. In both cases, the reaction was carried out for 10-15 hours. Upon completion, the solvent was removed under reduced pressure and the

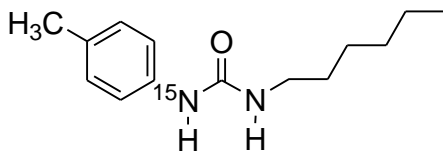
crude product was recrystallized from ethanol. The product, typically a white powder, was filtered and washed with ice-cold ethanol repeatedly. The solid was then collected and dried under high vacuum. This reaction with 1-naphthylamine, 2-naphthylamine, and *p*-toluidine was carried out using the same procedure without triethylamine.

¹⁵N-Hexyl, N-(4-methoxyphenyl)thiourea-



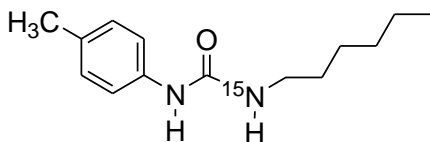
Following the outlined procedure above for asymmetric ureas/ thioureas: 50 mL of CHCl_3 , 0.68 g (4.90 mmol, 1.0 eq) of ^{15}N -hexylamine HCl, 0.81 mL (5.88 mmol, 1.2 eq.) of 4-methoxyphenyl isothiocyanate, and 1.30 mL (9.79 mmol, 2.0 eq.) of triethylamine.

Yield: 0.50 g (1.88 mmol) white crystals, 38 %. FTIR (KBr pellet, cm^{-1}): 3257 (s, $^{15}\text{N-H}$), 3176 (s, N-H), 3055 (s, Ar-H), 2958 (m, alkyl-H) 1608 (m, C=C aryl), 1543 (m, C=S). ^1H NMR (400 MHz, CDCl_3): δ (ppm) 7.47 (N-H, s, 1H), 7.13 (Ar-H, $J_{\text{H-H}} = 6.4$ Hz, dd, 2H), 6.96 (Ar-H, $J_{\text{H-H}} = 5.6$ Hz, dd, 2H), 6.77 ($^{15}\text{N-H}$, $J_{^{15}\text{N-H}} = 89.6$ Hz, d, 1H), 3.84 (-OCH₃, s, 3H), 3.59 (-CH₂CH₂(CH₂)₃CH₃, m, 2H), 1.59 (CH₂CH₂CH₂(CH₂)₂CH₃, m, 4H), 1.26 (CH₂CH₂CH₂(CH₂)₂CH₃, m, 4H), 0.86 (CH₂CH₂CH₂(CH₂)₂CH₃, $J_{\text{H-H}} = 6.8$ Hz, t, 3H). ^{15}N NMR (40.5 MHz, CDCl_3): δ (ppm) 18.5. HRMS-ESI: $M_{\text{theoretical}} = 268.1496$, $M_{\text{sample}} = 268.1494$, $\Delta M = -0.2$ mmass units (-0.75 ppm), $\text{C}_{14}\text{H}_{22}^{15}\text{NNSO}$.

N-Hexyl, ¹⁵N-(4-methylphenyl)urea

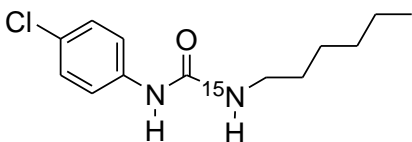
Following the outlined procedure for asymmetric ureas/ thioureas: 100 mL of CHCl₃, 1.35 g (13.0 mmol, 1.0 eq) of ¹⁵N-toluidine, 2.30 mL (15.9 mmol, 1.2 eq.) of *n*-hexyl isocyanate.

Yield: 1.79 g (4.15 mmol) white crystals, 60 %. FTIR (KBr pellet, cm⁻¹): 3348 (s, N-H), 3011 (s, Ar-H), 2956 (m, alkyl-H), 2929 (m, alkyl-H), 1632 (s, C=O), 1597 (m, C=C aryl). ¹H NMR (400 MHz, CDCl₃): δ (ppm) 7.37 (¹⁵N-H, overlapped d, 1H), 7.14 (Ar-H, overlapped m, 2H), 7.04 (Ar-H, *J*_{1H-1H} = 8.4 Hz, d, 2H), 5.50 (N-H, s, 1H), 3.13 (-CH₂CH₂(CH₂)₃CH₃, *J*_{1H-1H} = 6.8 Hz, q, 2H), 2.27 (Ar-CH₃, s, 3H), 1.41 (CH₂CH₂CH₂(CH₂)₂CH₃, m, 2H), 1.25 (CH₂CH₂CH₂(CH₂)₂CH₃, m, 6H), 0.86 (CH₂CH₂CH₂(CH₂)₂CH₃, *J*_{1H-1H} = 6.4 Hz, t, 3H). ¹³C NMR (100 MHz, DMSO-d₆): δ (ppm) 157.0 (*J*_{15N-13C} = 20.5 Hz), 136.5 (*J*_{15N-13C} = 15.2 Hz), 133.2, 129.8, 121.3, 40.5, 31.8, 30.4, 26.9, 22.8, 21.0, 14.3. ¹⁵N NMR (40.5 MHz, CDCl₃): δ (ppm) 5.60. HRMS-ESI: *M*_{theoretical} = 236.1775, *M*_{sample} = 236.1776, Δ*M* = -0.1 mmass units (-0.42 ppm), C₁₄H₂₂¹⁵NNO.

¹⁵N-hexyl, N-(4-methylphenyl)urea-

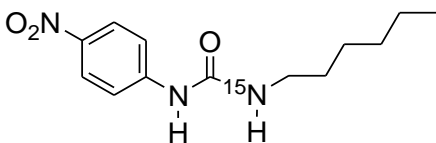
Following the outlined procedure for asymmetric ureas/ thioureas: 50 mL of CHCl_3 , 0.68 g (4.90 mmol, 1.0 eq) of ^{15}N -hexylamine HCl, 0.75 mL (5.88 mmol, 1.2 eq.) of 4-methylphenyl isocyanate, and 1.30 mL (9.79 mmol, 2.0 eq.) of triethylamine.

Yield: 0.95 g (4.15 mmol) white crystals, 85 %. FTIR (KBr pellet, cm^{-1}): 3332 (s, N-H), 3033 (s, Ar-H), 2956 (m, alkyl-H), 2929 (m, alkyl-H), 1633 (s, C=O), 1597 (m, C=C aryl). ^1H NMR (400 MHz, DMSO-d_6): δ (ppm) 8.27 (N-H, s, 1H), 7.23 (Ar-H, $J_{\text{1H-1H}} = 8.4$ Hz, d, 2H), 7.00 (Ar-H, $J_{\text{1H-1H}} = 6.8$ Hz, td, 2H), 6.06 (^{15}N -H, $J_{\text{15N-1H}} = 88.8$ Hz, $J_{\text{1H-1H}} = 5.6$, dt, 1H), 3.05 ($-\text{CH}_2\text{CH}_2(\text{CH}_2)_3\text{CH}_3$, m, 2H), 2.22 (Ar- CH_3 , s, 3H), 1.40 ($\text{CH}_2\text{CH}_2\text{CH}_2(\text{CH}_2)_2\text{CH}_3$, m, 2H), 1.27 ($\text{CH}_2\text{CH}_2\text{CH}_2(\text{CH}_2)_2\text{CH}_3$, m, 6H), 0.86 ($\text{CH}_2\text{CH}_2\text{CH}_2(\text{CH}_2)_2\text{CH}_3$, $J_{\text{1H-1H}} = 6.4$ Hz, t, 3H). ^{13}C NMR (100 MHz, DMSO-d_6): δ (ppm) 155.1 ($J_{\text{15N-13C}} = 20.4$ Hz), 140.6, 128.6, 120.9, 117.5, 93.9, 31.0, 29.7, 26.1, 22.1. ^{15}N NMR (40.5 MHz, CDCl_3): δ (ppm) -9.93. HRMS-ESI: $M_{\text{theoretical}} = 236.1775$, $M_{\text{sample}} = 236.1776$, $\Delta M = -0.1$ mmass units (-0.42 ppm), $\text{C}_{14}\text{H}_{22}^{15}\text{NNO}$.

¹⁵N-Hexyl, N-(4-chlorophenyl)urea-

Following the outlined procedure for asymmetric ureas/ thioureas: 50 mL of CHCl_3 , 0.68 g (4.90 mmol, 1.0 eq) of ^{15}N -hexylamine HCl, 0.90 g (5.88 mmol, 1.2 eq.) of 4-methylphenyl isocyanate, and 1.30 mL (9.79 mmol, 2.0 eq.) of triethylamine.

Yield: 0.73 g (2.86 mmol) white powder, 59 %. FTIR (KBr pellet, cm^{-1}): 3327 (s, N-H str), 3087 (w, Ar-H), 2954 (m, alkyl-H), 2931 (m, alkyl-H), 2860 (m, alkyl-H), 1631 (s, C=O), 1591 (m, C=C aryl). ^1H NMR (400 MHz, DMSO-d_6): δ (ppm) 8.52 (N-H, s, 1H), 7.40 (Ar-H, $J_{\text{H-H}} = 8.0$ Hz, dd, 2H), 7.25 (Ar-H, $J_{\text{H-H}} = 8.0$ Hz, dd, 2H), 6.14 (^{15}N -H, $J_{^{15}\text{N-H}} = 89.6$ Hz, $J_{\text{H-H}} = 5.6$, dt, 1H), 3.06 ($-\text{CH}_2\text{CH}_2(\text{CH}_2)_3\text{CH}_3$, m, 2H), 1.41 ($-\text{CH}_2\text{CH}_2\text{CH}_2(\text{CH}_2)_2\text{CH}_3$, broad, 2H), 1.27 ($\text{CH}_2\text{CH}_2\text{CH}_2(\text{CH}_2)_2\text{CH}_3$, m, 6H), 0.87 ($\text{CH}_2\text{CH}_2\text{CH}_2(\text{CH}_2)_2\text{CH}_3$, $J_{\text{H-H}} = 5.2$ Hz, t, 3H). ^{15}N NMR (40.5 MHz, CDCl_3): δ (ppm) -8.76. HRMS-ESI: $M_{\text{theoretical}} = 256.1229$, $M_{\text{sample}} = 256.1227$, $\Delta M = -0.2$ mmass units (-0.78 ppm), $\text{C}_{13}\text{H}_{19}^{15}\text{NNOCl}$.

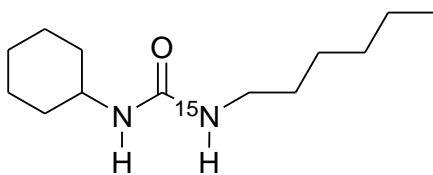
¹⁵N-hexyl, N-(4-nitrophenyl)urea

Following the outlined procedure for asymmetric ureas/ thioureas: 50 mL of CHCl_3 ,

0.68 g (4.90 mmol, 1.0 eq) of ^{15}N -hexylamine HCl, 0.97 mL (5.91 mmol, 1.2 eq.) of 4-nitrophenyl isocyanate, and 0.82 mL (5.90 mmol, 1.2 eq.) of triethylamine.

Yield: 0.68 g (2.58 mmol) yellow powder, 53 %. FTIR (KBr pellet, cm^{-1}): 3376 (s, N-H), 3307 (s, N-H), 2958 (w, alkyl-H), 2929 (m, alkyl-H), 2863 (w, alkyl-H), 1664 (s, C=O), 1614 (m, C=C aryl). ^1H NMR (400 MHz, DMSO- d_6): δ (ppm) 9.22 (N-H, s, 1H), 8.12 (Ar-H, $J_{\text{H-H}} = 6.8$ Hz, $J_{\text{H-}^{15}\text{N}} = 2.0$ Hz, dt, 2H), 7.61 (Ar-H, $J_{\text{H-H}} = 6.8$ Hz, $J_{\text{H-}^{15}\text{N}} = 3.2$ Hz, dt, 2H), 6.43 (^{15}N -H, $J_{\text{N-H}} = 89.6$ Hz, $J_{^{15}\text{N-H}} = 36.4$ Hz, dt, 1H), 3.09 (- $\text{CH}_2\text{CH}_2(\text{CH}_2)_3\text{CH}_3$, $J_{\text{H-H}} = 6.8$ Hz, q, 2H), 1.43 (- $\text{CH}_2\text{CH}_2\text{CH}_2(\text{CH}_2)_2\text{CH}_3$, m, 2H), 1.27 (- $\text{CH}_2\text{CH}_2\text{CH}_2(\text{CH}_2)_2\text{CH}_3$, m, 6H), 0.87 (- $\text{CH}_2\text{CH}_2\text{CH}_2(\text{CH}_2)_2\text{CH}_3$, $J_{\text{H-H}} = 6.4$ Hz, t, 3H). ^{13}C NMR (100 MHz, DMSO- d_6): δ (ppm) 155.4 ($J_{^{15}\text{N-}^{13}\text{C}} = 39.5$ Hz), 141.0, 125.8, 118.7, 117.4, 31.7, 30.2, 26.7, 22.8, 14.6.

^{15}N -hexyl, N-cyclohexylurea-

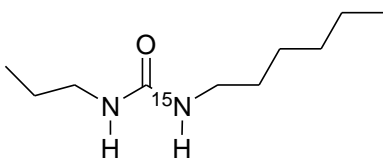


Following the outlined procedure for asymmetric ureas/ thioureas: 75 mL of CHCl_3 , 0.84 g (6.04 mmol, 1.0 eq) of ^{15}N -hexylamine HCl, 0.85 mL (6.69 mmol, 1.2 eq.) of 4-methylphenyl isocyanate, and 1.20 mL (8.66 mmol, 1.5 eq.) of triethylamine.

Yield: 1.16 g (5.12 mmol) white crystals, 85 %. FTIR (KBr pellet, cm^{-1}): ^1H NMR (400 MHz, CDCl_3): δ (ppm) 4.97 (^{15}N -H, overlapped d, 1H), 4.74 (CH -N, m, 1H), 3.49 (N-

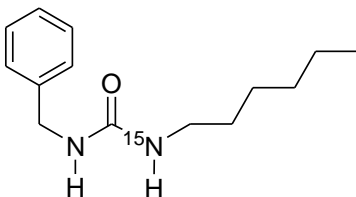
H, s, 1H), 3.11 (N-CH₂-, $J_{1H-1H} = 6.0$ Hz, q, 2H), 1.90 (-CH₂-, $J_{1H-1H} = 12.4$ Hz, $J_{1H-1H} = 3.6$ Hz, dt, 2H), 1.67 (-CH₂-, $J_{1H-1H} = 13.6$, $J_{1H-1H} = 4.0$ Hz, dt, 2H), 1.44 (-CH₂-, m, 2H), 1.24 (overlapped m, 8H), 1.10 (overlapped m, 4H), 0.86 (-CH₃, $J_{1H-1H} = 6.8$ Hz, t, 3H). ¹³C NMR (100 MHz, CDCl₃): δ (ppm) 158.2 ($J_{15N-13C} = 20.5$ Hz), 49.1, 40.7 ($J_{15N-13C} = 10.6$ Hz), 34.2, 31.8, 30.5, 26.7, 25.9, 25.2, 22.8, 14.3. ¹⁵N NMR (40.5 MHz, CDCl₃): δ (ppm) -13.3.

¹⁵N-hexyl, N-propylurea-



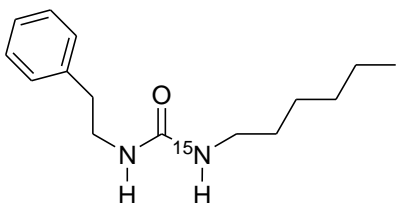
Following the outlined procedure for asymmetric ureas/ thioureas: 50 mL of CHCl₃, 0.50 g (3.60 mmol, 1.0 eq) of ¹⁵N-hexylamine HCl, 0.41 mL (4.33 mmol, 1.2 eq.) of 4-methylphenyl isocyanate, and 1.30 mL (9.79 mmol, ~2.5 eq.) of triethylamine.

Yield: 0.50 g (2.65 mmol) white crystals, 74 %. FTIR (KBr pellet, cm⁻¹): 3329 (s, N-H), 2960 (m, alkyl-H), 2931 (m, alkyl-H), 2860 (m, alkyl-H), 1622 (s, C=O). ¹H NMR (400 MHz, DMSO-d₆): δ (ppm) 5.74 (N-H, s, 1H), 5.74 (¹⁵N-H, $J_{15N-1H} = 88.4$ Hz, $J_{1H-1H} = 4.8$, dt, 1H), 2.92 (N-CH₂-, m, 4H), 1.38 – 1.23 (-CH₂-, overlapped m, 10H), 0.87 - 0.79 (-CH₃, overlapped m, 6H). ¹³C NMR (100 MHz, DMSO-d₆): δ (ppm) 158.0 ($J_{15N-13C} = 18.9$ Hz), 41.1, 31.1, 26.1, 23.3, 22.1, 13.9, 11.4. ¹⁵N NMR (40.5 MHz, CDCl₃): δ (ppm) -12.6. HRMS-ESI: $M_{\text{theoretical}} = 188.1775$, $M_{\text{sample}} = 188.1776$, $\Delta M = -0.1$ mmass units (-0.53 ppm), C₁₀H₂₂¹⁵NNO.

¹⁵N-hexyl, N-benzylurea-

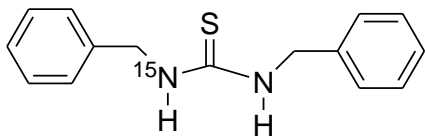
Following the outlined procedure for asymmetric ureas/ thioureas: 50 mL of CHCl_3 , 0.70 g (5.06 mmol, 1.0 eq) of ^{15}N -hexylamine HCl, 0.69 mL (5.63 mmol, 1.2 eq.) of benzyl isocyanate, and 0.78 mL (5.63 mmol, 1.2 eq.) of triethylamine.

Yield: 1.16 g (4.95 mmol) white crystals, 97 %. FTIR (KBr pellet, cm^{-1}): 3332 (s, $^{15}\text{N-H}$), 3085 (m, Ar-H), 3062 (m, Ar-H), 2953 (s, alkyl-H), 2921 (s, alkyl-H), 2856 (s, alkyl-H), 1623 (s, C=O). ^1H NMR (400 MHz, CDCl_3): δ (ppm) 7.29 (Ar-H, m, 5H), 4.68 ($^{15}\text{N-H}$, $J_{^{15}\text{N-1H}} = 88.0$ Hz, $J_{\text{1H-1H}} = 5.2$, dq, 1H), 4.33 (benzyl-H, $J_{\text{1H-1H}} = 5.6$ Hz, d, 2H), 4.24 (overlapped N-H, dq, 1H), 3.12 ($-\text{CH}_2\text{CH}_2(\text{CH}_2)_3\text{CH}_3$, $J_{\text{1H-1H}} = 6.4$ Hz, q, 2H), 1.42 ($\text{CH}_2\text{CH}_2\text{CH}_2(\text{CH}_2)_2\text{CH}_3$, m, 2H), 1.27 ($\text{CH}_2\text{CH}_2\text{CH}_2(\text{CH}_2)_2\text{CH}_3$, m, 6H), 0.87 ($\text{CH}_2\text{CH}_2\text{CH}_2(\text{CH}_2)_2\text{CH}_3$, $J_{\text{1H-1H}} = 6.4$ Hz, t, 3H). ^{13}C NMR (100 MHz, CDCl_3): δ (ppm) 158.6 ($J_{^{15}\text{N-}^{13}\text{C}} = 21.2$ Hz), 139.6, 128.8, 128.7, 128.6, 127.5, 44.7, 40.8 ($J_{^{15}\text{N-}^{13}\text{C}} = 10.6$), 31.8, 30.4, 26.8, 22.8, 14.3. ^{15}N NMR (40.5 MHz, CDCl_3): δ (ppm) -12.73.

¹⁵N-hexyl, N-(2-phenethyl)urea-

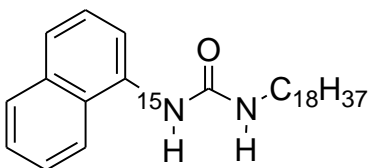
Following the outlined procedure for asymmetric ureas/ thioureas: 40 mL of CHCl_3 , 0.63 g (4.55 mmol, 1.0 eq) of ^{15}N -hexylamine HCl, 0.70 mL (5.06 mmol, 1.2 eq.) of phenethyl isocyanate, and 0.71 mL (5.12 mmol, 1.2 eq.) of triethylamine.

Yield: 0.51 g (2.05 mmol) white crystals, 45 %. FTIR (KBr pellet, cm^{-1}): 3336 (s, N-H), 3322 (s, N-H), 3058 (w, Ar-H), 3023 (w, Ar-H), 2952 (s, alkyl-H), 2929 (s, alkyl-H), 2857 (s, alkyl-H), 1614 (s, C=O), 1569 (s, C=C aryl). ^1H NMR (400 MHz, CDCl_3): δ (ppm) 7.25 (Ar-H, m, 5H), 4.43 (N-H, s, 1H), 4.38 (^{15}N -H, $J_{^{15}\text{N}-^1\text{H}} = 87.2$ Hz, $J_{^1\text{H}-^1\text{H}} = 5.0$, dt, 1H), 3.43 (N- CH_2 -, $J_{^1\text{H}-^1\text{H}} = 6.4$ Hz, q, 2H), 3.09 (Ar- CH_2 -, $J_{^1\text{H}-^1\text{H}} = 6.4$ Hz, q, 2H), 2.80 (^{15}N - $\text{CH}_2\text{CH}_2(\text{CH}_2)_3\text{CH}_3$, $J_{^1\text{H}-^1\text{H}} = 6.4$ Hz, t, 2H), 1.44 ($\text{CH}_2\text{CH}_2\text{CH}_2(\text{CH}_2)_2\text{CH}_3$, m, 2H), 1.28 ($\text{CH}_2\text{CH}_2\text{CH}_2(\text{CH}_2)_2\text{CH}_3$, m, 6H), 0.88 ($\text{CH}_2\text{CH}_2\text{CH}_2(\text{CH}_2)_2\text{CH}_3$, $J_{^1\text{H}-^1\text{H}} = 6.8$ Hz, t, 3H). ^{13}C NMR (100 MHz, DMSO_d6): δ (ppm) 158.4 ($J_{^{15}\text{N}-^{13}\text{C}} = 20.5$ Hz), 139.5, 129.1, 128.8, 126.6, 41.8, 40.8 ($J_{^{15}\text{N}-^{13}\text{C}} = 9.8$ Hz), 36.7, 31.8, 30.4, 26.8, 22.8, 14.3. ^{15}N NMR (40.5 MHz, CDCl_3): δ (ppm) -10.19.

¹⁵N,N-Dibenzylthiourea-

Following the procedure outlined in the experimental section of the text formation of asymmetric urea/ thioureas: 0.42 g (3.86 mmol, 1.0 eq) of ¹⁵N-benzylamine, 0.62 mL (4.67 mmol, 1.2 eq) of benzyl isothiocyanate.

Yield: 0.70 g (2.72 mmol) white crystals, 71 %. FTIR (KBr pellet, cm⁻¹): 3311 (s, N-H), 3086 (s, Ar-H), 3062 (s, Ar-H), 2922 (m, alkyl-H), 2875 (m, alkyl-H), 1624 (s, C=O), 1562 (m, C=C aryl). ¹H NMR (300 MHz, DMSO_{d6}): δ (ppm) 7.33-7.22 (Ar-H, overlapped m, 10H), 6.45 (¹⁵N-H, *J*_{15N-1H} = 89.4 Hz, *J*_{1H-1H} = 15.0, dt, 1H), 4.23 (benzyl-H, *J*_{1H-1H} = 6.0, d, 2H). ¹³C NMR (100 MHz, DMSO_{d6}): δ (ppm) 158.1 (*J*_{15N-13C} = 19.1 Hz), 140.9, 128.2, 127.0, 126.6, 43.0. ¹⁵N NMR (40.5 MHz, CDCl₃): δ (ppm) -10.9. HRMS-ESI: *M*_{theoretical} = 243.1306, *M*_{sample} = 243.1297, Δ*M* = -0.9 mmass units (-3.72 ppm), C₁₅H₁₆¹⁵NNO.

¹⁵N-(1-naphthyl), N-(n-octadecyl)urea-

Following the outlined procedure for asymmetric ureas/ thioureas: 40 mL of CHCl₃, 1.45 g (10.0 mmol, 1.0 eq) of ¹⁵N-1-naphthylamine, and 4.20 mL (12.0 mmol, 1.2 eq.) of *n*-octadecyl isocyanate.

Yield: 3.56 g (8.11 mmol) white powder, 81 %. FTIR (KBr pellet, cm^{-1}): 3336 (s, N-H) 3282 (s, N-H), 2917 (s, alkyl-H), 2848 (m, alkyl-H), 1619 (s, C=O), 1563 (m, C=C aryl). ^1H NMR (400 MHz, CDCl_3): δ (ppm) 8.07 (Ar-H, $J_{1\text{H}-1\text{H}} = 4.4$ Hz, t, 1H), 7.89 (Ar-H, m, 1H), 7.78 (Ar-H, $J_{1\text{H}-1\text{H}} = 8.4$ Hz, d, 1H), 7.53 (Ar-H, m, 4H), 6.52 (^{15}N -H, $J_{15\text{N}-1\text{H}} = 88.4$ Hz, d, 1H), 4.68 (N-H, s, 1H), 3.20 ($-\text{CH}_2\text{CH}_2(\text{CH}_2)_{15}\text{CH}_3$, $J_{1\text{H}-1\text{H}} = 6.8$ Hz, t, 2H), 1.41 ($\text{CH}_2\text{CH}_2\text{CH}_2(\text{CH}_2)_{14}\text{CH}_3$, unresolved m, 2H), 1.23 ($\text{CH}_2\text{CH}_2\text{CH}_2(\text{CH}_2)_{14}\text{CH}_3$, m, 30H), 0.88 ($\text{CH}_2\text{CH}_2\text{CH}_2(\text{CH}_2)_2\text{CH}_3$, $J_{1\text{H}-1\text{H}} = 6.4$ Hz, t, 3H). ^{15}N NMR (40.5 MHz, CDCl_3): δ (ppm) -1.96. HRMS-ESI: $M_{\text{theoretical}} = 440.3653$, $M_{\text{sample}} = 440.3649$, $\Delta M = 0.45$ mmass units (1.03 ppm), $\text{C}_{29}\text{H}_{46}^{15}\text{NNO}$.

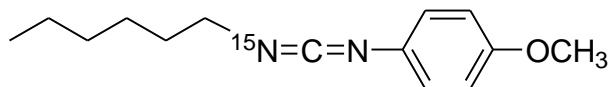
Synthesis of ^{15}N -labeled Carbodiimide Monomers

The specific amounts of reagents, yields, NMR data, MS data, and FTIR data are reported below for each monomer. The ^{15}N NMR data was not collected on any of the carbodiimide monomers due to greater than 90 second delay times.

The dibromotriphenylphosphorane salt (PPh_3Br_2 , 1.2 eq.) was added to a round bottom flask along with ~5 mL of DCM. The reaction flask was then placed under N_2 atmosphere and cooled to 0 °C in an ice bath. The TEA (2.5 eq.) was then added to the stirring mixture and the resulting vapors were allowed to dissipate. The ^{15}N -labeled urea/thiourea (1.0 eq.) was then added to the mixture and the solution was allowed to stir until completion (ca. 1-10 hours) with the reaction progress monitored by IR spectroscopy. Upon completion, the reaction was quenched with ~300 mL of pentane and the resulting precipitate was filtered and washed with additional pentane. The filtrate was collected and the solvent was removed

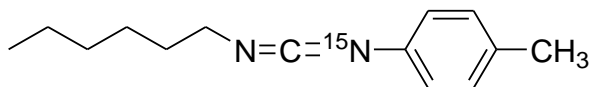
via rotatory evaporation. This quenching process was repeated twice more to remove most of the byproducts from the system. The product was further purified by column chromatography (DCM as mobile phase) and was collected. The solvent was removed and the product was dried under high vacuum to afford pure product.

¹⁵N-hexyl, N-(4-methoxyphenyl)carbodiimide-



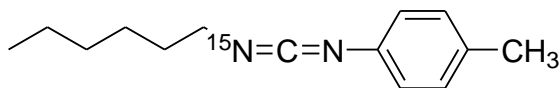
Following the procedure for the dehydration of ureas/ thioureas: 10 mL of DCM, 2.10 g (4.95 mmol, 1.2 eq.) of dibromotriphenylphosphorane, 1.32 mL (1.00 g, 9.91 mmol, 2.5 eq.) of triethylamine, and 1.02 g (3.82 mmol, 1.0 eq.) of *¹⁵N-hexyl-N'-(4-methoxyphenyl)thiourea*.

Yield: 0.31 g (1.33 mmol) of clear liquid, 35 %. FTIR (KBr thinfilm, cm⁻¹): 3033 (w, aryl-H), 2951 (m, alkyl-H), 2931 (m, alkyl-H), 2858 (m, alkyl-H), 2110 (s, ¹⁵N=C=N), 1581 (w, C=C). ¹H NMR (400 MHz, CDCl₃): δ (ppm) 7.01 (Ar-H, *J* = 4.8 Hz, 2H, dd), 6.82 (Ar-H, *J* = 5.1 Hz, 2H, dd), 3.78 (-OCH₃, 3H, s), 3.38 (-CH₂CH₂(CH₂)₃CH₃, *J* = 5.1 Hz 2H, m), 1.66 (-CH₂CH₂(CH₂)₃CH₃, 2H, m) 1.30 (-CH₂CH₂(CH₂)₃CH₃, 6H, m), 0.89 (-CH₂CH₂(CH₂)₃CH₃, *J* = 5.1 Hz, 3H, t). ¹³C NMR (100 MHz, CDCl₃): 156.9, 137.2 (*J*_{15N-13C} = 29.6Hz), 133.3, 124.5, 114.8, 55.7, 47.2, 31.6, 26.7, 22.8, 14.2. HRMS-ESI: *M*_{theoretical} = 234.1619, *M*_{sample} = 234.1613, Δ*M* = 0.57 mmass units (2.43 ppm), C₁₄H₂₀¹⁵NNO.

¹⁵N-(4-methylphenyl), N-hexylcarbodiimide-

Following the procedure for the dehydration of ureas/ thioureas: 6 mL of DCM, 3.92 g (9.29 mmol, 1.2 eq.) of dibromotriphenylphosphorane, 2.70 mL (19.4 mmol, 2.5 eq.) of triethylamine, and 1.77 g (7.67 mmol, 1.0 eq.) of *N*-hexyl-¹⁵*N*-(4-methylphenyl)urea.

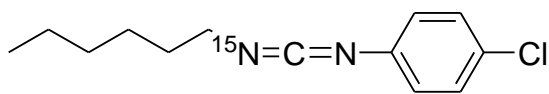
Yield: 1.02 g (4.70 mmol) of pale yellow liquid, 61 %. FTIR (KBr thinfilm, cm⁻¹): 3026 (w, aryl-H), 2947 (s, alkyl-H), 2927 (s, alkyl-H), 2857 (m, alkyl-H), 2123 (s, ¹⁵N=C=N), 1608 (w, C=C_{aryl}), 1573 (w, C=C_{aryl}). ¹H NMR (400 MHz, CDCl₃): δ (ppm) 7.09 (Ar-H, *J* = 8.4 Hz, 2H, d), 6.98 (Ar- H, *J*_{1H-1H} = 8.4 Hz, *J*_{1H-1H} = 2.0 Hz, 2H, dd), 3.39 (-CH₂CH₂(CH₂)₃CH₃, *J*_{1H-1H} = 6.4 Hz, 2H, t), 2.31 (Ar-CH₃, 3H, s), 1.67 (-CH₂CH₂(CH₂)₃CH₃, 2H, m) 1.41 (-CH₂CH₂ CH₂ (CH₂)₂CH₃, 2H, m), 1.31 (-CH₂CH₂ CH₂ (CH₂)₂CH₃, 4H, m), 0.89 (-CH₂CH₂(CH₂)₃CH₃, *J* = 6.8 Hz, 3H, t). ¹³C NMR (100 MHz, CDCl₃): 138.7, 137.1, 134.5, 130.2 (*J*_{15N-13C} = 2.3 Hz), 123.5 (*J*_{15N-13C} = 3.8 Hz), 47.2, 31.6, 26.7, 22.8, 21.2, 14.3. HRMS-ESI: *M*_{theoretical} = 218.1670, *M*_{sample} = 218.1665, Δ*M* = 0.45 mmass units (2.05 ppm), C₁₄H₂₀¹⁵NN.

¹⁵N-hexyl, N-(4-methylphenyl)carbodiimide-

Following the procedure for the dehydration of ureas/ thioureas: 10 mL of DCM, 1.08 g (2.54 mmol, 1.2 eq.) of dibromotriphenylphosphorane, 0.71 mL (5.31 mmol, 2.5 eq.) of triethylamine, and 0.50 g (2.12 mmol, 1.0 eq.) of ¹⁵*N*-hexyl-*N*-(4-methylphenyl)urea.

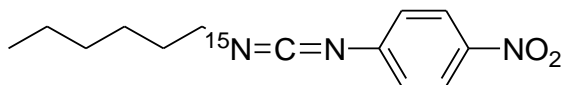
Yield: 1.02 g (4.70 mmol) of pale yellow liquid, 61 %. FTIR (KBr thinfilm, cm^{-1}): 3062 (w, Ar-H), 2957 (s, alkyl-H), 2927 (s, alkyl-H), 2857 (m, alkyl-H), 2109 (s, $^{15}\text{N}=\text{C}=\text{N}$), 1608 (w, $\text{C}=\text{C}_{\text{aryl}}$), 1576 (w, $\text{C}=\text{C}_{\text{aryl}}$). ^1H NMR (300 MHz, CDCl_3): δ (ppm) 7.08 (Ar-H, 2H, m), 6.98 (Ar-H, $J_{\text{H-H}} = 4.8$ Hz, $J_{\text{H-}^{15}\text{N}} = 2.0$ Hz, 2H, dd), 3.38 ($-\text{CH}_2\text{CH}_2(\text{CH}_2)_3\text{CH}_3$, $J_{\text{H-H}} = 5.1$ Hz, 2H, t), 2.31 (Ar- CH_3 , 3H, s), 1.67 ($-\text{CH}_2\text{CH}_2(\text{CH}_2)_3\text{CH}_3$, 2H, m) 1.42 ($-\text{CH}_2\text{CH}_2(\text{CH}_2)_3\text{CH}_3$, 6H, m), 0.89 ($-\text{CH}_2\text{CH}_2(\text{CH}_2)_3\text{CH}_3$, $J = 5.1$ Hz, 3H, t). ^{13}C NMR (100 MHz, CDCl_3): 138.7, 137.1, 134.5, 130.2, 123.5, 47.2, 31.6, 26.7, 22.8, 21.2, 14.2. HRMS-ESI: $M_{\text{theoretical}} = 218.1670$, $M_{\text{sample}} = 218.1666$, $\Delta M = 0.39$ mmass units (1.77 ppm), $\text{C}_{14}\text{H}_{20}^{15}\text{NN}$.

^{15}N -hexyl, N -(4-chlorophenyl)carbodiimide-



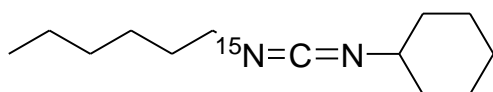
Following the procedure for the dehydration of ureas/ thioureas: 10 mL of DCM, 1.39 g (3.28 mmol, 1.2 eq.) dibromotriphenylphosphorane, 0.91 mL (0.69 g, 6.84 mmol, 2.5 eq.) triethylamine, and 0.70 g (2.73 mmol, 1.0 eq.) ^{15}N -hexyl- N' -(4-chlorophenyl)urea.

Yield: 0.21 g (0.98 mmol) of clear liquid, 42 %. FTIR (KBr thinfilm, cm^{-1}): 3025 (w, Ar-H), 2929 (m, alkyl-H), 2858 (m, alkyl-H), 2127 (s, $\text{N}=\text{C}=\text{N}$), 1591 (m, $\text{C}=\text{C}$). ^1H NMR (300 MHz, CDCl_3): δ (ppm) 7.24 (Ar-H, 2H, m), 7.01 (Ar-H, $J = 4.5$ Hz, 2H, dd), 3.41 ($-\text{CH}_2\text{CH}_2(\text{CH}_2)_3\text{CH}_3$, $J = 6.9$ Hz, 2H, t), 1.66 ($-\text{CH}_2\text{CH}_2(\text{CH}_2)_3\text{CH}_3$, 2H, m), 1.32 ($-\text{CH}_2\text{CH}_2(\text{CH}_2)_3\text{CH}_3$, 6H, m), 0.88 ($-\text{CH}_2\text{CH}_2(\text{CH}_2)_3\text{CH}_3$, $J = 6.6$ Hz, 3H, t). ^{13}C NMR (100 MHz, CDCl_3): δ (ppm) 134.3 ($J_{^{15}\text{N}-^{13}\text{C}} = 52.4$ Hz), 129.9, 129.6, 124.9, 47.0 ($J_{^{15}\text{N}-^{13}\text{C}} = 3.0$ Hz), 31.5, 26.7, 26.6, 22.8, 14.2. HRMS-ESI: $M_{\text{theoretical}} = 238.1123$, $M_{\text{sample}} = 238.1120$, $\Delta M = 0.31$ mmass units (1.30 ppm), $\text{C}_{13}\text{H}_{17}^{15}\text{NNCl}$.

¹⁵N-hexyl, N-(4-nitrophenyl)carbodiimide-

Following the procedure for the dehydration of ureas/ thioureas: 10 mL of DCM, 1.32 g (3.12 mmol, 1.2 eq.) of dibromotriphenylphosphorane, 0.90 mL (6.50 mmol, 2.5 eq.) of triethylamine, and 0.68 g (2.56 mmol, 1.0 eq.) of ¹⁵N-hexyl-N-(4-nitrophenyl)urea.

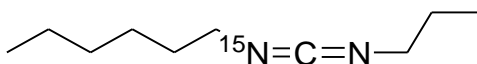
Yield: 0.10 g (0.421 mmol) of yellow liquid, 16 %. FTIR (KBr thinfilm, cm⁻¹): 3110 (w, Ar-H), 3079 (w, Ar-H), 2952 (s, alkyl-H), 2927 (s, alkyl-H), 2857 (m, alkyl-H), 2132 (s, ¹⁵N=C=N), 1614 (w, C=C_{aryl}), 1569 (w, C=C_{aryl}). ¹H NMR (400 MHz, CDCl₃): δ (ppm) 8.16 (Ar-H, *J*_{1H-1H} = 6.8 Hz, *J*_{1H-1H} = 2.0 Hz, 2H, dt), 7.14 (Ar- H, *J*_{1H-1H} = 7.2 Hz, *J*_{1H-1H} = 2.4 Hz, 2H, dt), 3.51 (-CH₂CH₂(CH₂)₃CH₃, *J*_{1H-1H} = 6.8 Hz, 2H, t), 1.72 (-CH₂CH₂(CH₂)₃CH₃, 2H, m) 1.43 (-CH₂CH₂ CH₂ (CH₂)₂CH₃, 2H, m), 1.32 (-CH₂CH₂ CH₂ (CH₂)₂CH₃, 4H, m) 0.90 (-CH₂CH₂(CH₂)₃CH₃, *J* = 6.8 Hz, 3H, t). ¹³C NMR (100 MHz, CDCl₃): 152.5, 135.1, 134.6 (*J*_{15N-13C} = 29.6 Hz), 125.4, 123.9, 46.8, 31.4, 26.6, 22.7, 14.2. HRMS-ESI: *M*_{theoretical} = 249.1364, *M*_{sample} = 249.1354, Δ*M* = 0.97 mmass units (3.90 ppm), C₁₃H₁₇¹⁵NNO₂.

¹⁵N-hexyl, N-cyclohexylcarbodiimide-

Following the procedure for the dehydration of ureas/ thioureas: 10 mL of DCM, 2.57 g (6.09 mmol, 1.2 eq.) of dibromotriphenylphosphorane, 1.75 mL (12.6 mmol, 2.5 eq.) of triethylamine, and 1.14 g (5.02 mmol, 1.0 eq.) of ¹⁵N-hexyl-N-cyclohexylurea.

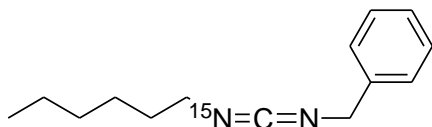
Yield: 0.39 g (1.76 mmol) of yellow liquid, 35 %. FTIR (KBr thinfilm, cm^{-1}): 2929 (s, alkyl-H), 2856 (m, alkyl-H), 2113 (s, $^{15}\text{N}=\text{C}=\text{N}$). ^1H NMR (400 MHz, CDCl_3): δ (ppm) 3.20 (overlapped N-CH- and N-CH₂-, $J_{1\text{H}-1\text{H}} = 6.8$ Hz, 3H, t), 1.90 ($(\text{CH}_2)_{\text{Cy}}$, 2H, m), 1.75 ($(\text{CH}_2)_{\text{Cy}}$, 2H, m), 1.57 (overlapped, 4H, m), 1.32 (overlapped, 12H, m) 0.89 (-CH₂CH₂(CH₂)₃CH₃, $J = 7.2$ Hz, 3H, t). ^{13}C NMR (100 MHz, CDCl_3): 141.6, 55.9, 47.1, 35.1, 31.6 ($J_{^{15}\text{N}-^{13}\text{C}} = 6.8$ Hz), 26.8, 25.7, 24.9, 22.8, 14.3. HRMS-ESI: $M_{\text{theoretical}} = 210.1983$, $M_{\text{sample}} = 210.1976$, $\Delta M = 0.62$ mmass units (2.98 ppm), $\text{C}_{13}\text{H}_{24}^{15}\text{NN}$.

¹⁵N-hexyl, N-propylcarbodiimide-



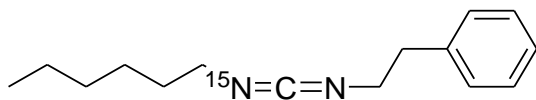
Following the procedure for the dehydration of ureas/ thioureas: 10 mL of DCM, 1.24 g (2.95 mmol, 1.2 eq.) dibromotriphenylphosphorane, 0.82 mL (0.62 g, 6.14 mmol, 2.5 eq.) triethylamine, and 0.46 g (2.46 mmol, 1.0 eq.) *¹⁵N-hexyl-N'-propylurea*.

Yield: 0.21 g (0.98 mmol) of clear liquid, 42 %. FTIR (KBr thinfilm, cm^{-1}): 2954 (m, alkyl-H), 2931 (m, alkyl-H), 2862 (m, alkyl-H), 2119 (s, $\text{N}=\text{C}=\text{N}$). ^1H NMR (400 MHz, CDCl_3): δ (ppm) 3.18 (overlapped, 4H, m), 1.58 (overlapped, 4H, m) 1.34 (overlapped, 6H, m), 0.96 (-CH₂CH₂CH₃, $J_{1\text{H}-1\text{H}} = 7.6$ Hz, 3H, t) 0.89 (-CH₂CH₂(CH₂)₃CH₃, $J = 6.8$ Hz, 3H, t). ^{13}C NMR (100 MHz, CDCl_3): 131.1, 48.8, 47.0, 31.6, 31.5, 26.7, 28.4, 22.8, 14.3, 11.7. HRMS-ESI: $M_{\text{theoretical}} = 170.1670$, $M_{\text{sample}} = 170.1666$, $\Delta M = 0.34$ mmass units (1.98 ppm), $\text{C}_{10}\text{H}_{20}^{15}\text{NN}$

¹⁵N-hexyl, N-benzylcarbodiimide-

Following the procedure for the dehydration of ureas/ thioureas: 10 mL of DCM, 2.36 g (5.59 mmol, 1.2 eq.) of dibromotriphenylphosphorane, 1.70 mL (12.2 mmol, 2.5 eq.) of triethylamine, and 1.15 g (4.90 mmol, 1.0 eq.) of ¹⁵N-hexyl-N-benzylurea.

Yield: 0.30 g (1.38 mmol) of pale yellow liquid, 28 %. FTIR (KBr thinfilm, cm⁻¹): 3087 (w, Ar-H), 2957 (s, alkyl-H), 2927 (s, alkyl-H), 2857 (m, alkyl-H), 2114 (s, ¹⁵N=C=N), 1601 (w, C=C_{aryl}), 1585 (w, C=C_{aryl}). ¹H NMR (300 MHz, CDCl₃): δ (ppm) 7.33 (Ar-H, 5H, m), 3.14 (-CH₂CH₂(CH₂)₃CH₃, J_{1H-1H} = 9.2 Hz, 2H, t), 1.45 (-CH₂CH₂(CH₂)₃CH₃, 2H, m), 1.25 (-CH₂CH₂(CH₂)₃CH₃, 6H, m), 0.89 (-CH₂CH₂(CH₂)₃CH₃, J = 9.6 Hz, 3H, t). ¹³C NMR (100 MHz, CDCl₃): 138.9, 128.8, 127.7, 50.8, 46.8 (J_{15N-13C} = 2.2 Hz), 31.6, 26.6, 22.7, 14.2. HRMS-ESI: M_{theoretical} = 218.1670, M_{sample} = 218.1672, ΔM = -0.25 mmass units (-1.15 ppm), C₁₄H₂₀¹⁵NN.

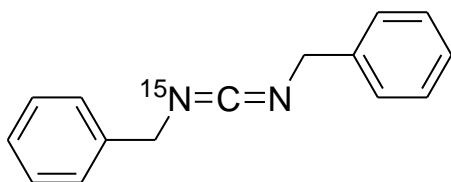
¹⁵N-hexyl, N-(2-phenethyl)carbodiimide

Following the procedure for the dehydration of ureas/ thioureas: 10 mL of DCM, 1.03 g (2.45 mmol, 1.2 eq.) of dibromotriphenylphosphorane, 0.70 mL (5.03 mmol, 2.5 eq.) of triethylamine, and 0.50 g (2.01 mmol, 1.0 eq.) of ¹⁵N-hexyl-N-(2-phenethyl)urea.

Yield: 0.28 g (1.19 mmol) of clear liquid, 59 %. FTIR (KBr thinfilm, cm⁻¹): 3079 (w, Ar-H), 3060 (w, Ar-H), 3025 (m, Ar-H), 2933 (s, alkyl-H), 2857 (s, alkyl-H), 2117 (s,

$^{15}\text{N}=\text{C}=\text{N}$), 1614 (w, $\text{C}=\text{C}_{\text{aryl}}$), 1569 (w, $\text{C}=\text{C}_{\text{aryl}}$). ^1H NMR (300 MHz, CDCl_3): δ (ppm) 7.31 (Ar-H, 5H, m), 3.47 (N- CH_2 - CH_2 -Ar, $J_{1\text{H}-1\text{H}} = 7.2$ Hz, 2H, t), 3.02 (^{15}N - $\text{CH}_2\text{CH}_2(\text{CH}_2)_3\text{CH}_3$, $J_{1\text{H}-1\text{H}} = 6.6$ Hz, 2H, t), 2.90 (N- CH_2 - CH_2 -Ar, $J_{1\text{H}-1\text{H}} = 6.9$ Hz, 2H, t), 1.43 (- $\text{CH}_2\text{CH}_2(\text{CH}_2)_3\text{CH}_3$, 2H, m) 1.27 (- $\text{CH}_2\text{CH}_2(\text{CH}_2)_3\text{CH}_3$, 6H, m), 0.89 (- $\text{CH}_2\text{CH}_2(\text{CH}_2)_3\text{CH}_3$, $J = 6.6$ Hz, 3H, t). ^{13}C NMR (100 MHz, CDCl_3): 140.8, 139.1, 129.1, 128.7, 126.7, 48.1 ($J_{15\text{N}-13\text{C}} = 1.5$ Hz), 46.8 ($J_{15\text{N}-13\text{C}} = 2.6$ Hz), 37.9, 31.6, 31.3, 26.7, 22.8, 14.3. HRMS-ESI: $M_{\text{theoretical}} = 232.1826$, $M_{\text{sample}} = 232.1819$, $\Delta M = 0.67$ mmass units (2.89 ppm), $\text{C}_{15}\text{H}_{22}^{15}\text{NN}$.

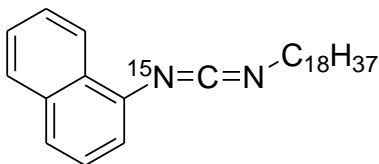
^{15}N , *N*-dibenzylcarbodiimide-



Following the procedure outlined in the experimental section for the dehydration of ureas/ thioureas: 10 mL of DCM, 1.32 g (3.14 mmol, 1.2 eq.) of dibromotriphenylphosphorane, 0.91 mL (6.54 mmol, 2.5 eq), and 0.65 g (2.54 mmol) of ^{15}N ,*N*-dibenzylurea.

Yield: 0.39 g (1.74 mmol) of clear oil, 68 %. FTIR (KBr thinfilm, cm^{-1}): 3086 (w, aryl-H), 3062 (w, aryl-H), 3030 (w, aryl-H), 2918 (m, alkyl-H), 2850 (m, alkyl-H), 2102 (s, $\text{N}=\text{C}=\text{N}$), 1605 (m, $\text{C}=\text{C}$). ^1H NMR (400 MHz, CDCl_3): δ (ppm) 7.29 (overlapped, 10H, m), 4.30 (benzyl-H, 4H, s). ^{13}C NMR (100 MHz, CDCl_3): 137.5, 135.8, 134.6, 129.0, 128.0, 126.6, 126.1, 126.0, 124.7, 123.8, 119.8, 47.2, 32.2, 31.7, 30.0, 29.9, 29.8, 29.7, 29.6, 29.4, 27.1, 23.0, 14.4. HRMS-ESI: $M_{\text{theoretical}} = 224.1200$, $M_{\text{sample}} = 224.1197$, $\Delta M = 0.35$ mmass units (1.57 ppm), $\text{C}_{15}\text{H}_{14}^{15}\text{NN}$.

¹⁵N-(1-naphthyl), N-octadecylcarbodiimide-



Following the procedure for the dehydration of ureas/ thioureas: 10 mL of DCM, 4.12 g (9.81 mmol, 1.2 eq.) of dibromotriphenylphosphorane e, 2.80 mL (20.2 mmol, 2.5 eq.) of triethylamine, and 3.55 g (8.10 mmol, 1.0 eq.) of ¹⁵N-(1-naphthyl), N-octadecylurea.

Yield: 2.12 g (5.04 mmol) of pale yellow liquid, 62 %. FTIR (KBr thin film, cm⁻¹): 3050 (w, Ar-H), 2921 (s, alkyl-H), 2854 (m, alkyl-H), 2133 (s, ¹⁵N=C=N), 1573 (w, C=C_{aryl}). ¹H NMR (400 MHz, CDCl₃): δ (ppm) 8.28 (Ar-H, 1H, m), 7.81 (Ar-H, 1H, m), 7.61 (Ar-H, *J*_{1H-1H} = 8.0 Hz, 1H, d), 7.50 (Ar-H, 2H, m), 7.40 (Ar-H, *J*_{1H-1H} = 7.2 Hz, 1H, t), 7.29 (Ar-H, 1H, m), 3.47 (-CH₂CH₂(CH₂)₁₅CH₃, *J*_{1H-1H} = 6.8 Hz, 2H, t), 1.72 (-CH₂CH₂(CH₂)₁₅CH₃, 2H, m) 1.44 (-CH₂CH₂CH₂(CH₂)₁₄CH₃, 2H, m), 1.25 (-CH₂CH₂CH₂(CH₂)₁₄CH₃, 28H, m) 0.88 (-CH₂CH₂(CH₂)₁₅CH₃, *J* = 6.8 Hz, 3H, t). ¹³C NMR (100 MHz, CDCl₃): 137.5, 135.8, 134.6, 129.0, 128.0, 126.6, 126.1, 126.0, 124.7, 123.8, 119.8, 47.2, 32.2, 31.7, 30.0, 29.9, 29.8, 29.7, 29.6, 29.4, 27.1, 23.0, 14.4. HRMS-ESI: *M*_{theoretical} = 422.3548, *M*_{sample} = 422.3549, Δ*M* = -0.15 (-0.37 ppm), C₂₉H₄₄¹⁵NN.

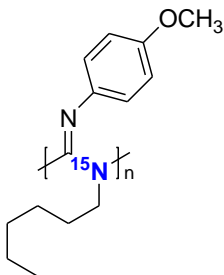
Polymerization of ¹⁵N-labeled Carbodiimides-

All polymerizations were conducted in the inert N₂ atmosphere dry box. The monomers were placed in a clean vial equipped with a stir bar and added to the dry box. A catalyst

solution was made in the clean vial in dry chloroform followed by injection of a specified amount into the vial containing the monomer. The polymerization times vary greatly depending on the nature of the monomer used. The pre-weighed amount of catalyst was added directly into the monomer vial for solvent-free polymerizations. See below for specific monomer: catalyst ratios, solvent choice, and polymerization time. The majority of the polymerizations were conducted with **Cat-2** due to its higher activity. To form optically active polymers with a helical bias, **Cat-1R** was utilized for chiral induction upon polymerization. All polymers were worked up by re-dissolving them in the minimal amount of chloroform and precipitating the product upon addition to methanol, a typical anti-solvent. The resulting precipitate was then collected and dried under high vacuum.

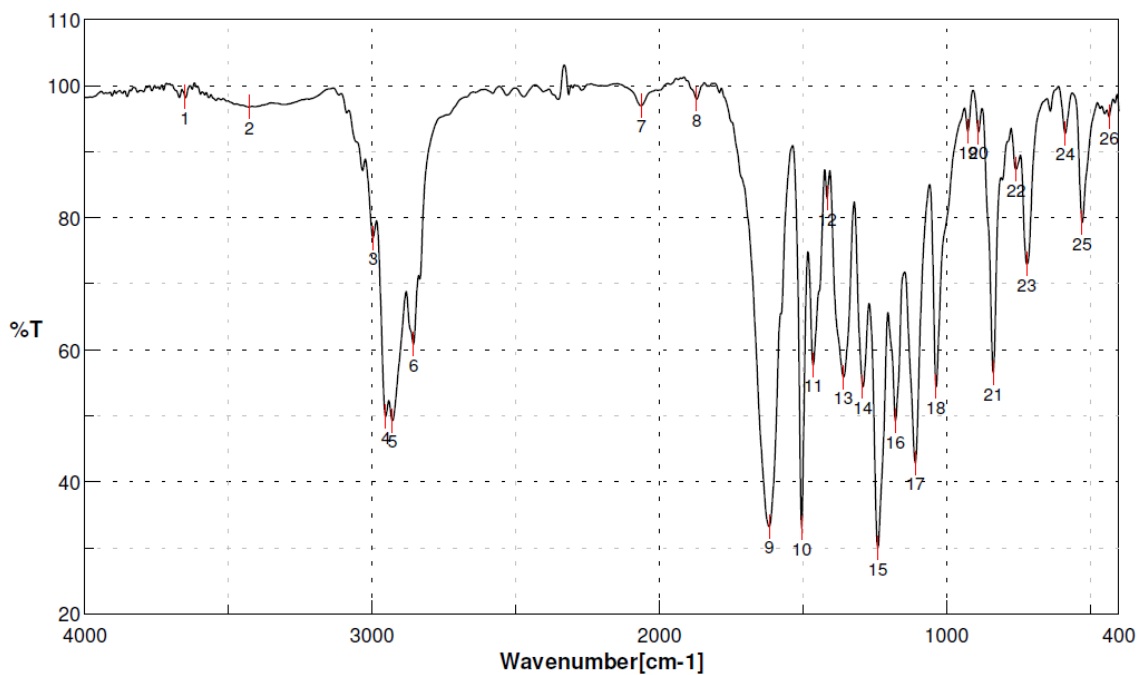
The monomer-to-catalyst ratio, yield, ^1H NMR, IR, and ^{15}N NMR data of each polymer is reported below as well as scans of the IR spectra. NMR data for **Poly-22** and **Poly-23** was not collected due to insolubility of the polymer in all conventional solvents. All characterization of **Poly-16** through **Poly-18** was previously reported by DeSousa and Novak.²⁶ The unlabeled poly(*N*-1-naphthyl-*N*-octadecylcarbodiimide) and poly(*N,N'*-dibenzylcarbodiimide) were previously reported.^{24,25}

Poly(¹⁵N-hexyl-N'-4-methoxyphenylcarbodiimide) (Poly-19)-



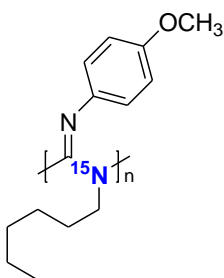
Following the outlined procedure for the polymerization of carbodiimide monomers: 0.15 g (0.63 mmol, 119 eq.) ¹⁵N-hexyl-N'-(4-methoxyphenyl)carbodiimide, 1.33 mg (0.0053 mmol 1.0 eq.) **Cat-3**, and 0.49 mL dry CHCl₃.

Yield: 16 mg (0.067 mmol) off-white solid, 10 %. FTIR (KBr pellet, cm⁻¹): 3039 (w, aryl-H), 2929 (m, alkyl-H), 2856 (m, alkyl-H), 1617 (s, C=N), 1576 (m, C=C). ¹H-NMR (400 MHz, CDCl₃): δ (ppm) 6.60 (Ar-H, 4H, very broad doublet), 3.64 (Ar-O-CH₃, 3H, broad singlet), 1.58 – 0.40 (Alkyl-H, 13H, very broad). ¹⁵N-NMR (40.5 MHz, CDCl₃): δ (ppm) 15.2 (¹⁵N-C).



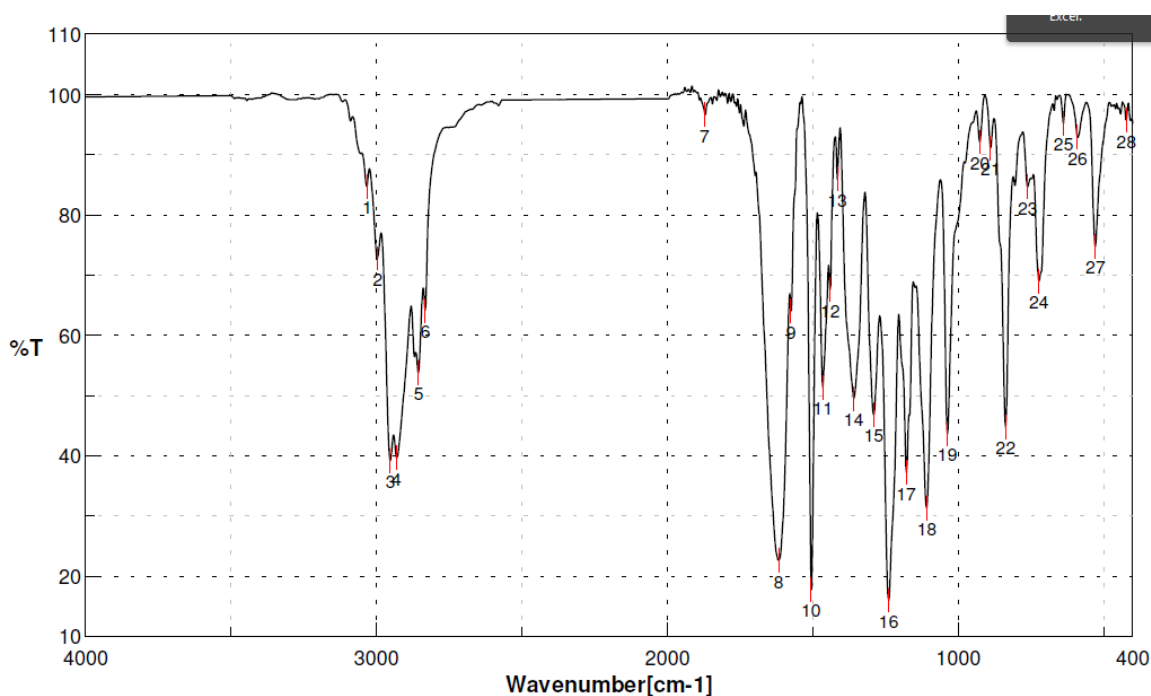
No.	cm-1	%T	No.	cm-1	%T	No.	cm-1	%T
1	3652.52	98.351	2	3428.81	96.8007	3	2996.84	76.992
4	2952.48	49.9119	5	2929.34	49.2524	6	2856.06	60.8795
7	2063.46	97.0144	8	1870.61	98.01	9	1617.98	33.2419
10	1504.2	32.9886	11	1463.71	57.7435	12	1415.49	82.9554
13	1359.57	55.9048	14	1292.07	54.42	15	1240	29.9919
16	1178.29	49.2104	17	1108.87	42.8428	18	1037.52	54.4371
19	925.664	93.1086	20	889.023	93.0284	21	836.955	56.5009
22	757.888	87.348	23	721.247	72.979	24	586.254	92.8247
25	528.4	79.2756	26	433.905	95.3086			

(R)-Poly(¹⁵N-hexyl-N'-4-methoxyphenylcarbodiimide) (**Poly-19R**)-



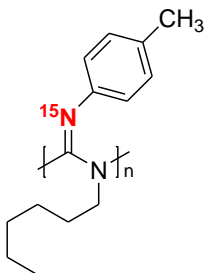
Following the outlined procedure for the polymerization of carbodiimide monomers:
 0.16 g (0.70 mmol, 121 eq.) ¹⁵N-hexyl-N'-(4-methoxyphenyl)carbodiimide, 2.64 mg (0.0058 mmol 1.0 eq.) **Cat-2R**, and 0.69 mL dry CDCl₃.

Yield: 57 mg (0.242 mmol) off-white solid, 35 %. FTIR (KBr pellet, cm^{-1}): 3030 (w, aryl-H), 2952 (m, alkyl-H), 2931 (m, alkyl-H), 2856 (m, alkyl-H), 1618 (s, C=N), 1576 (m, C=C). $^1\text{H-NMR}$ (400 MHz, CDCl_3): δ (ppm) 6.60 (Ar-H, 4H, very broad doublet), 3.64 (Ar-O-CH₃, 3H, broad singlet), 1.58 – 0.40 (Alkyl-H, 13H, very broad). $^{15}\text{N-NMR}$ (40.5 MHz, CDCl_3): δ (ppm) 15.0 ($^{15}\text{N-C}$).



No.	cm-1	%T	No.	cm-1	%T	No.	cm-1	%T
1	3033.48	84.7481	2	2996.84	72.8152	3	2952.48	39.1691
4	2931.27	39.6763	5	2856.06	53.7959	6	2832.92	64.1657
7	1870.61	96.611	8	1617.98	22.6236	9	1575.56	64.0538
10	1506.13	17.7444	11	1465.63	51.3685	12	1440.56	67.6353
13	1415.49	85.9385	14	1359.57	49.5352	15	1290.14	46.8381
16	1240	15.9642	17	1178.29	37.2615	18	1108.87	31.3342
19	1037.52	43.6222	20	925.664	92.11	21	889.023	91.1448
22	836.955	44.8065	23	761.744	84.6706	24	723.175	69.0152
25	638.323	95.2775	26	590.111	92.8863	27	528.4	74.8096
28	422.334	95.7326						

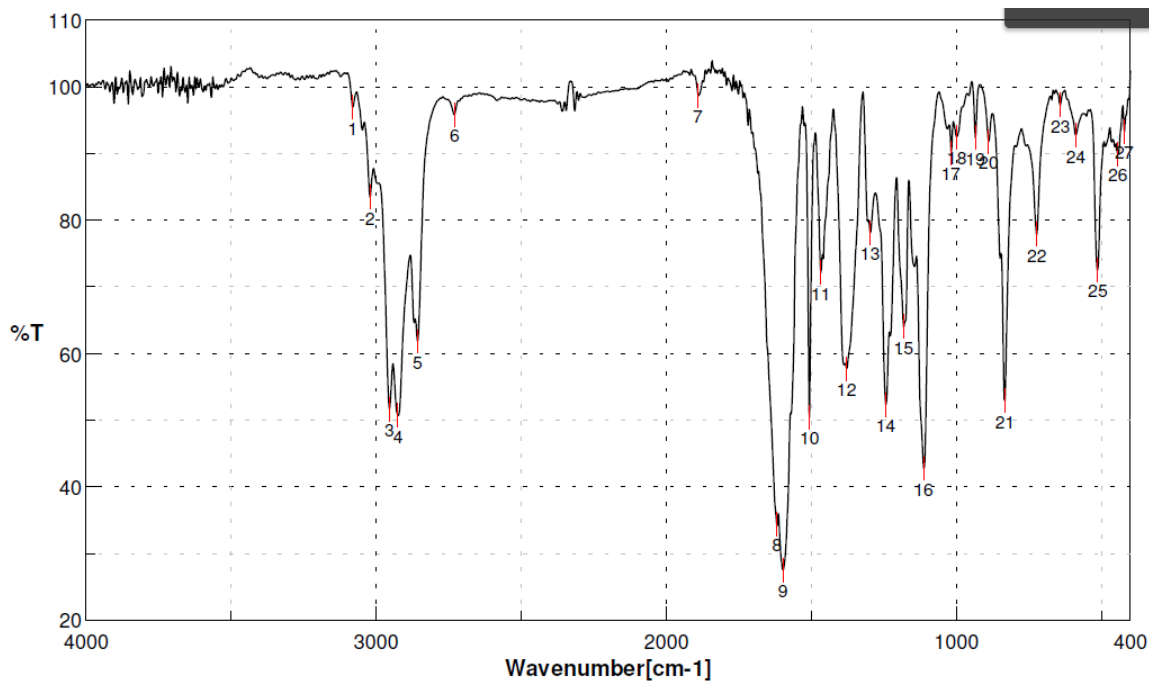
Poly(¹⁵N-4-methylphenyl-N-hexylcarbodiimide) (Poly-20)-



Following the outlined procedure for the polymerization of carbodiimide monomers: 1.00 g (4.70 mmol, 125 eq.) of ¹⁵N-4-methylphenyl-N-hexylcarbodiimide, 16.9 mg (37.5 μmol, 1.0 eq.) of **Cat-2R**, 0.40 mL of dry CHCl₃.

Yield: 0.92 g (4.32 mmol) orange solid, 92 %. FTIR (KBr pellet, cm⁻¹): 3021 (w, aryl-H), 2954 (s, alkyl-H), 2925 (s, alkyl-H), 2857 (m, alkyl-H), 1619 (s, C=N). ¹H-NMR (400 MHz, CDCl₃): δ (ppm) 6.72 (Ar-H, 4H, very broad doublet), 2.15 (Ar-CH₃, 3H, broad singlet), 1.57 – 0.40 (Alkyl-H, 13H, very broad). ¹⁵N-NMR (40.5 MHz, CDCl₃): δ (ppm) 135.0 (¹⁵N=C).

No.	cm-1	%T	No.	cm-1	%T	No.	cm-1	%T
1	3081.69	97.0124	2	3021.91	83.4858	3	2954.41	51.6646
4	2925.48	50.7059	5	2857.99	61.8256	6	2730.71	95.8764
7	1889.9	98.7004	8	1619.91	34.3983	9	1598.7	27.5412
10	1506.13	50.4493	11	1467.56	72.1579	12	1378.85	57.7481
13	1297.86	78.1438	14	1243.86	52.369	15	1182.15	64.0265
16	1112.73	42.744	17	1018.23	90.1589	18	998.946	92.5255
19	935.306	92.4448	20	889.023	91.8542	21	833.098	52.8999
22	723.175	77.868	23	642.179	97.3171	24	588.182	92.7962
25	512.972	72.6241	26	443.547	89.9776	27	420.406	93.3484

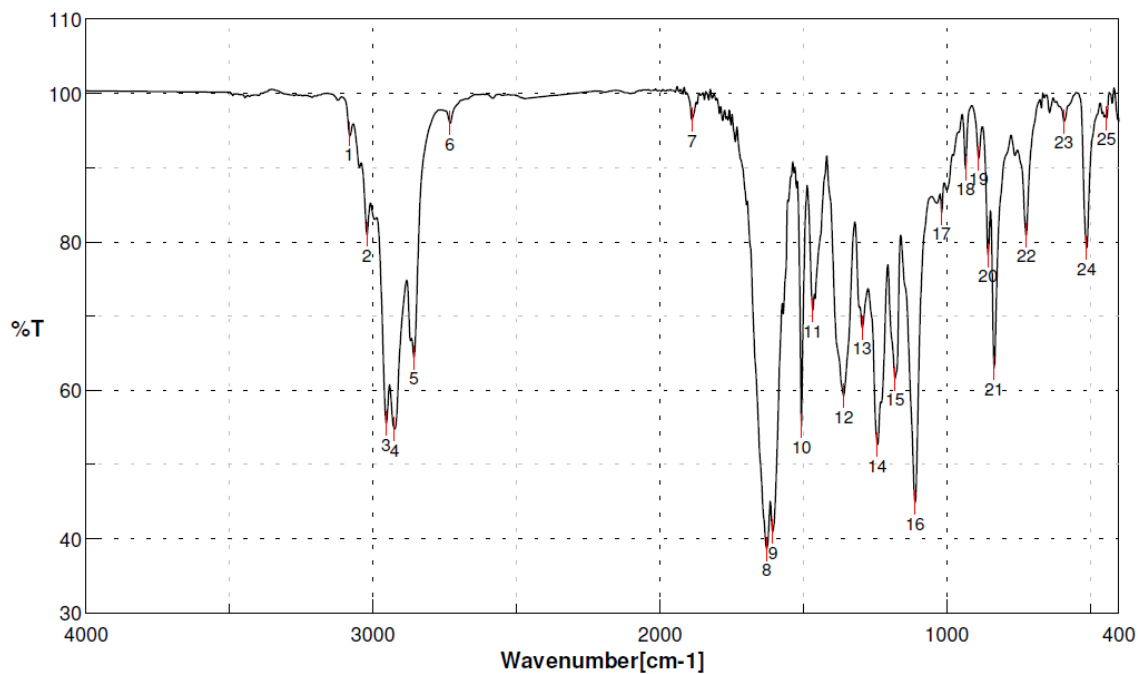


Poly(¹⁵N-hexyl-N-4-methylphenylcarbodiimide) (Poly-21)-



Following the outlined procedure for the polymerization of carbodiimide monomers: 0.45 g (2.07 mmol, 120 eq.) of *N*-4-methylphenyl-¹⁵N-hexylcarbodiimide, 7.8 mg (17.3 μmol, 1.0 eq.) of **Cat-2R**, w/o solvent.

Yield: 0.41 g (1.87 mmol) orange solid, 90 %. FTIR (KBr pellet, cm⁻¹): 3022 (w, aryl-H), 2954 (s, alkyl-H), 2925 (s, alkyl-H), 2857 (m, alkyl-H), 1627 (s, C=N). ¹H-NMR (400 MHz, CDCl₃): δ (ppm) 6.72 (Ar-H, 4H, very broad doublet), 2.16 (Ar-CH₃, 3H, broad singlet), 1.57 – 0.40 (Alkyl-H, 13H, very broad).



No.	cm-1	%T	No.	cm-1	%T	No.	cm-1	%T
1	3083.62	94.63	2	3021.91	81.0375	3	2954.41	55.5661
4	2925.48	54.7826	5	2857.99	64.4598	6	2732.64	96.0315
7	1887.97	96.4784	8	1627.63	38.6183	9	1606.41	40.9605
10	1506.13	55.2007	11	1467.56	70.7851	12	1359.57	59.2881
13	1295.93	68.4835	14	1241.93	52.6608	15	1180.22	61.5849
16	1110.8	44.8748	17	1018.23	83.9679	18	935.306	89.9124
19	889.023	91.2822	20	856.239	78.2696	21	835.026	63.0082
22	723.175	80.9276	23	592.039	96.2173	24	512.972	79.1985
25	443.547	96.6854						

Poly(N-4-methylphenyl-N-hexylcarbodiimide)-



Following the outlined procedure for the polymerization of carbodiimide monomers: 0.36 g (2.07 mmol, 150 eq.) of *N*-4-methylphenyl-*N*-hexylcarbodiimide, 5.0 mg (11.1 μ mol, 1.0 eq.) of **Cat-2R**, 0.25 mL of dry CHCl_3 .

Yield: 0.13 g (0.61 mmol) white solid, 37 %. FTIR (KBr pellet, cm^{-1}): 3022 (w, aryl-H), 2954 (s, alkyl-H), 2925 (s, alkyl-H), 2857 (m, alkyl-H), 1627 (s, C=N). $^1\text{H-NMR}$ (400 MHz, CDCl_3): δ (ppm) 6.87 (Ar-H, 4H, very broad peak), 2.21 (Ar- CH_3 , 3H, broad singlet), 1.61 – 0.40 (Alkyl-H, 13H, very broad).

*Poly(^{15}N -*N*-hexyl-*N*-4-chlorophenylcarbodiimide) (Poly-22)*

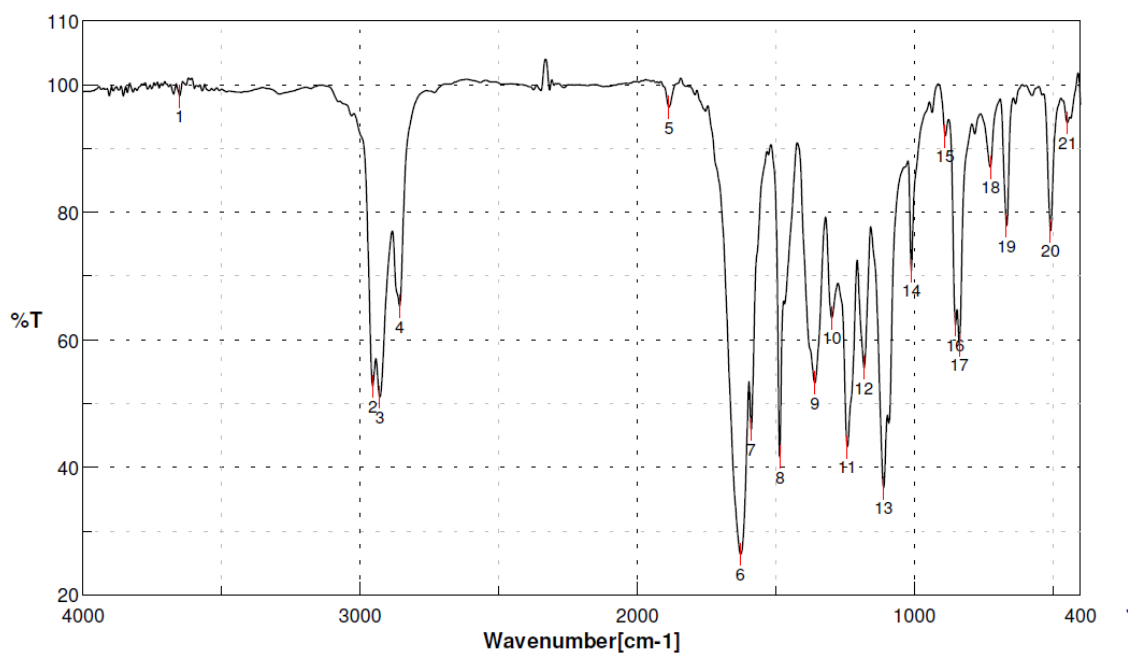


Following the outlined procedure for the polymerization of carbodiimide monomers: 0.29 g (1.22 mmol, 131 eq.) of *N*-4-chlorophenyl- ^{15}N -hexylcarbodiimide, 2.4 mg (9.32 μ mol, 1.0 eq.) of **Cat-3**, w/o solvent.

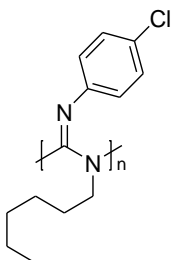
Yield: 0.073 g (0.31 mmol) off white solid, 25 %. FTIR (KBr pellet, cm^{-1}): 2954 (s, alkyl-H), 2929 (s, alkyl-H), 2858 (m, alkyl-H), 1628 (s, C=N), 1589 (s, C=C_{aryl}). $^1\text{H-NMR}$

(400 MHz, CDCl_3): δ (ppm) 6.88 (Ar-H, 4H, very broad doublet), 3.44 - 2.61 (N- CH_2 -, 2H, very broad), 1.30 - 0.40 (Alkyl-H, 11H, very broad).

No.	cm-1	%T	No.	cm-1	%T	No.	cm-1	%T
1	3652.52	98.2256	2	2954.41	52.7185	3	2929.34	51.0328
4	2857.99	65.2733	5	1886.04	96.5174	6	1627.63	26.4012
7	1589.06	45.9536	8	1484.92	41.6002	9	1359.57	53.2345
10	1297.86	63.4807	11	1241.93	43.2054	12	1182.15	55.6309
13	1110.8	36.8196	14	1010.52	70.8478	15	889.023	92.0245
16	852.382	62.3687	17	836.955	59.2782	18	725.104	87.1132
19	667.25	77.9084	20	509.115	77.1089	21	447.404	94.0755



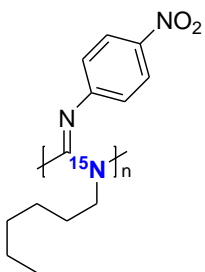
Poly(N-4-chlorophenyl-N'-hexylcarbodiimide)-



Following the outlined procedure for the polymerization of carbodiimide monomers: 0.27 g (1.12 mmol, 120 eq.) of *N*-4-chlorophenyl-*N'*-hexylcarbodiimide, 4.2 mg (9.35 μ mol, 1.0 eq.) of **Cat-2R**, 0.2 mL of dry CHCl_3 .

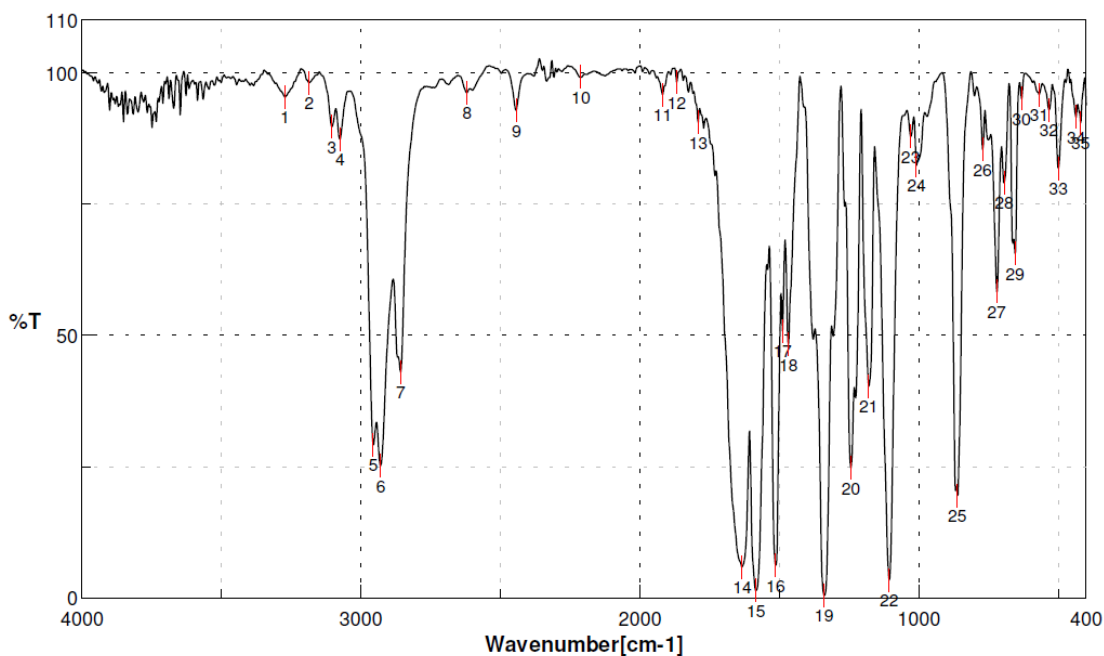
Yield: 0.064 g (0.27 mmol) off white solid, 24 %. FTIR (KBr pellet, cm^{-1}): 2954 (s, alkyl-H), 2929 (s, alkyl-H), 2858 (m, alkyl-H), 1628 (s, C=N), 1589 (s, C=C_{aryl}). ^1H NMR (400 MHz, CDCl_3): δ (ppm) 6.89 (Ar-H, 4H, very broad doublet), 3.47 - 2.60 (N- CH_2 -, 2H, very broad), 1.30 - 0.40 (Alkyl-H, 11H, very broad).

*Poly(^{15}N -hexyl-*N*-4-nitrophenylcarbodiimide) (**Poly-23**)-*

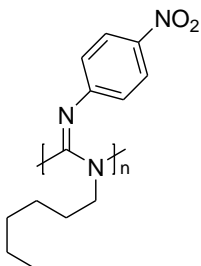


Following the procedure outlined for the polymerization of carbodiimides: 0.10 g (0.404 mmol, 106 eq.) of *N*-4-nitrophenyl- ^{15}N -hexylcarbodiimide, 0.96 mg (3.79 μ mol, 1.0 eq.) of **Cat-3**, w/o solvent.

Yield: 0.074 g (0.30 mmol) yellow powder, 74 %. FTIR (KBr pellet, cm^{-1}): 3104 (w, Ar-H), 3087 (w, Ar-H), 2956 (s, alkyl-H), 2929 (s, alkyl-H), 2858 (m, alkyl-H), 1633 (s, C=N), 1583 (s, C=C_{aryl}). NMR data was not collected due to insolubility of the resulting polymer.



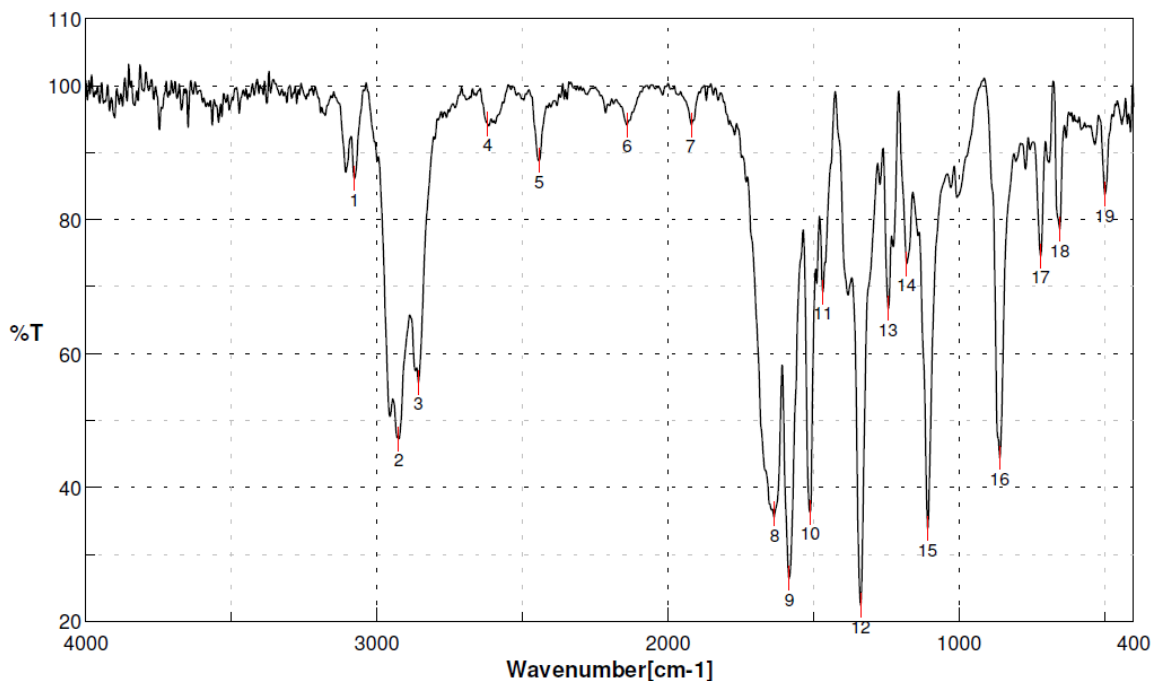
No.	cm-1	%T	No.	cm-1	%T	No.	cm-1	%T
1	3272.61	95.3837	2	3185.83	98.1236	3	3104.83	89.754
4	3075.9	87.3629	5	2956.34	29.2094	6	2929.34	25.2058
7	2857.99	43.0046	8	2620.79	96.229	9	2443.37	92.8901
10	2211.95	99.1874	11	1918.82	95.8534	12	1868.68	98.2285
13	1791.55	90.6026	14	1633.41	5.9365	15	1583.27	1.43608
16	1513.85	6.22669	17	1488.78	50.8699	18	1467.56	48.3153
19	1340.28	0.510756	20	1243.86	24.7595	21	1180.22	40.3492
22	1106.94	3.45141	23	1029.8	87.8928	24	1008.59	82.3948
25	862.025	19.5117	26	771.387	85.4284	27	721.247	58.3736
28	694.248	79.067	29	655.679	65.6297	30	632.537	95.1239
31	568.898	95.8535	32	534.185	92.9827	33	499.473	81.841
34	435.834	91.6011	35	420.406	90.4794			

Poly(N-hexyl-N-4-nitrophenylcarbodiimide)-

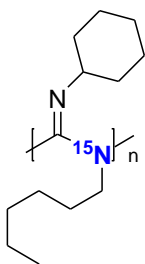
Following the procedure outlined for the polymerization of carbodiimides: 1.95 g (7.90 mmol, 106 eq.) of *N*-4-nitrophenyl-*N*-hexylcarbodiimide, 13.1 mg (51.7 μ mol, 1.0 eq.) of **Cat-3**, w/o solvent.

Yield: 1.41 g (5.68 mmol) yellow powder, 72 %. FTIR (KBr pellet, cm^{-1}): 3077 (w, Ar-H), 2956 (s, alkyl-H), 2929 (s, alkyl-H), 2858 (m, alkyl-H), 1633 (s, C=N), 1583 (s, C=C_{aryl}). NMR data was not collected due to insolubility of the resulting polymer.

No.	cm-1	%T	No.	cm-1	%T	No.	cm-1	%T
1	3077.83	86.1655	2	2925.48	47.3006	3	2857.99	55.6994
4	2620.79	94.3903	5	2443.37	88.8509	6	2140.6	94.1897
7	1920.75	94.2437	8	1633.41	36.0662	9	1583.27	26.414
10	1511.92	36.3497	11	1467.56	69.2092	12	1338.36	22.386
13	1243.86	66.7805	14	1180.22	73.45	15	1108.87	33.8972
16	860.096	44.4525	17	719.318	74.6113	18	653.75	78.6214
19	499.473	83.8202						



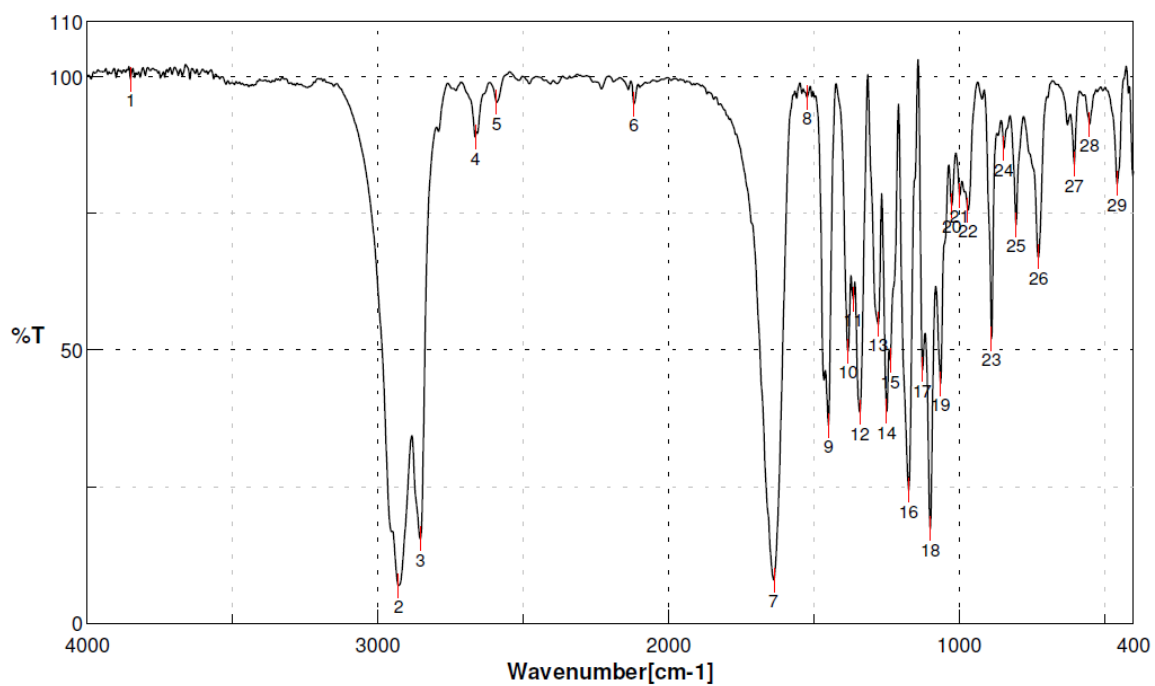
Poly(¹⁵N-hexyl-N-cyclohexylcarbodiimide) (Poly-24)-



Following the procedure for the polymerization of carbodiimides: 0.37 g (1.70 mmol, 185 eq.) of *N*-cyclohexyl-¹⁵*N*-hexylcarbodiimide, 2.32 mg (9.19 μmol, 1.0 eq.) of **Cat-3**, w/o solvent.

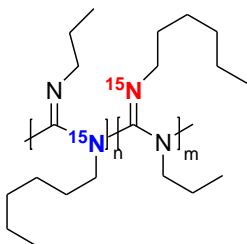
Yield: 0.20 g (0.90 mmol) yellow powder, 52 %. FTIR (KBr pellet, cm⁻¹): 2929 (s, alkyl-H), 2854 (m, alkyl-H), 1637 (s, C=N), 1523 (s, N-C bend). ¹H NMR (400 MHz, CDCl₃): δ (ppm) 2.18 (cy-H, broad singlet, 2H), 1.59 (overlapped, broad, 6H), 1.27

(overlapped, broad doublet, 9H), 0.89 (-CH₃, broad peak, 3H). ¹⁵N NMR (40.5 MHz, CDCl₃): δ (ppm) 1.20.



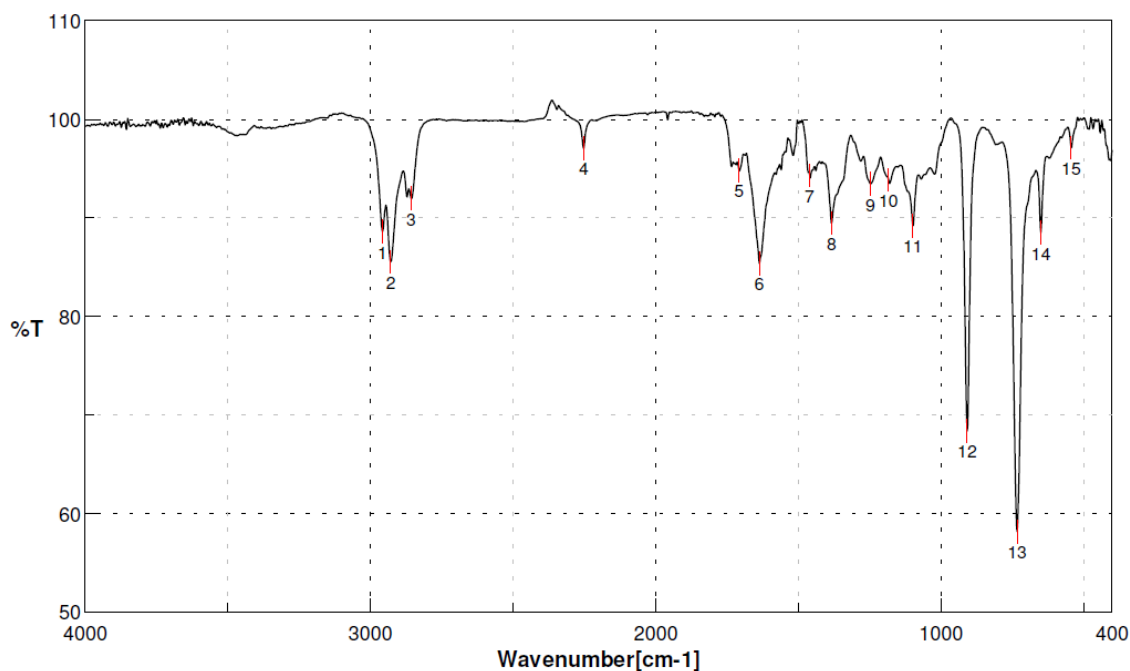
No.	cm-1	%T	No.	cm-1	%T	No.	cm-1	%T
1	3851.15	99.5438	2	2929.34	6.92394	3	2854.13	15.4655
4	2665.14	88.9649	5	2591.86	95.3425	6	2119.39	95.0511
7	1637.27	7.94909	8	1523.49	96.2252	9	1450.21	36.2587
10	1382.71	49.8043	11	1365.35	59.2963	12	1342.21	38.5886
13	1278.57	54.7542	14	1249.65	38.7692	15	1238.08	48.1119
16	1174.44	24.3348	17	1126.22	46.4302	18	1099.23	17.3784
19	1064.51	43.8549	20	1025.94	76.4891	21	998.946	78.2752
22	970.019	75.6262	23	889.023	52.0823	24	846.597	86.9064
25	804.171	72.897	26	727.032	67.0123	27	603.61	83.982
28	551.542	91.3312	29	457.047	80.471			

Poly(¹⁵N-hexyl-N-propylcarboiimide) (Poly-25)-



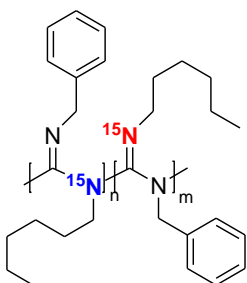
Following the procedure outlined the polymerization of carbodiimides: 19.2 mg (0.113 mmol, 120 eq.) ¹⁵N-hexyl-N-propylcarbodiimide, 0.2 mg (0.0001 mmol 1.0 eq.) of **Cat-3**, and 0.10 mL dry CHCl₃.

Yield: 10 mg (0.05 mmol) white solid, 53 %. FTIR (KBr pellet, cm⁻¹): 2958 (m, alkyl-H), 2929 (m, alkyl-H), 2858 (m, alkyl-H), 1637 (s, C=N). ¹H NMR (400 MHz, CDCl₃): δ (ppm) 3.14 (4H, broad), 1.30 (10H, very broad doublet) 0.89 (16H, broad singlet). ¹⁵N NMR (40.5 MHz, CDCl₃): δ (ppm) 133.5 (¹⁵N=C, 1N), 2.0 (¹⁵N-C, 1N).



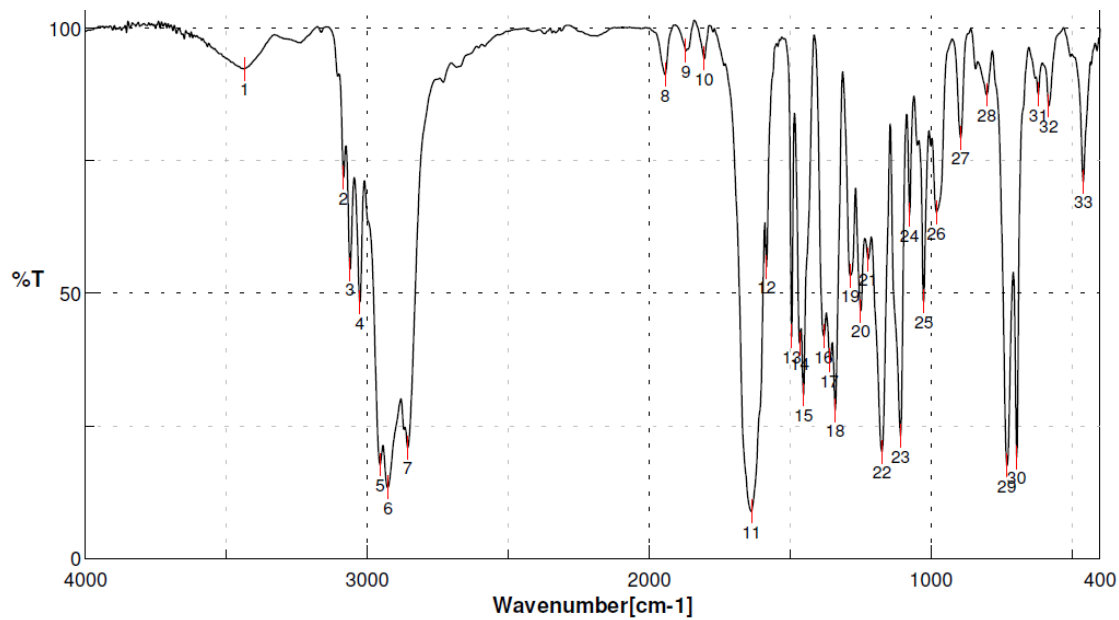
No.	cm-1	%T	No.	cm-1	%T	No.	cm-1	%T
1	2958.27	88.6283	2	2929.34	85.5443	3	2857.99	91.9545
4	2252.45	97.0731	5	1708.62	94.8639	6	1637.27	85.3985
7	1459.85	94.3302	8	1384.64	89.4696	9	1247.72	93.4532
10	1184.08	93.8624	11	1099.23	89.2062	12	908.308	68.3784
13	732.817	58.1493	14	649.893	88.5107	15	543.828	97.1188

Poly(¹⁵N-hexyl-N-benzylcarbodiimide) (Poly-26)-



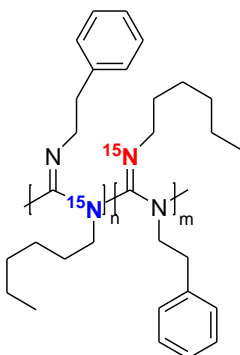
Following the procedure outlined for the polymerization of carbodiimides: 0.29 g (1.35 mmol, 132 eq.) ¹⁵N-hexyl-N-benzylcarbodiimide, 2.58 mg (10.2 μmol 1.0 eq.) of **Cat-3**, and 0.20 mL dry CHCl₃.

Yield: 0.15 g (0.682 mmol) white solid, 51 %. FTIR (KBr pellet, cm⁻¹): 3062 (m, Ar-H), 3027 (m, Ar-H), 2954 (s, alkyl-H), 2927 (s, alkyl-H), 2858 (s, alkyl-H), 1637 (s, C=N). ¹H NMR (400 MHz, CDCl₃): δ (ppm) 7.10 (Ar-H, very broad, 5H) 4.42 (benzyl-H, 2H, broad), 3.08 (N-CH₂-, 2H, broad singlet), 1.25 - 0.63 (11H, broad singlet). ¹⁵N NMR (40.5 MHz, CDCl₃): δ (ppm) 128.4 (¹⁵N=C, 1N), -7.50 (¹⁵N-C, 1N).



No.	cm-1	%T	No.	cm-1	%T	No.	cm-1	%T
1	3436.53	92.3291	2	3085.55	71.8405	3	3062.41	54.6148
4	3027.69	48.3123	5	2954.41	17.7192	6	2927.41	13.3815
7	2857.99	20.9659	8	1943.89	91.2271	9	1870.61	95.7366
10	1805.05	94.2413	11	1637.27	8.85957	12	1583.27	55.0085
13	1494.56	41.8837	14	1465.63	40.5043	15	1452.14	30.9235
16	1380.78	41.9211	17	1359.57	37.3392	18	1340.28	27.9469
19	1286.29	53.3296	20	1249.65	46.6846	21	1222.65	56.4232
22	1174.44	20.1857	23	1108.87	23.091	24	1076.08	64.8185
25	1025.94	48.4663	26	981.59	65.2762	27	894.809	79.3374
28	802.242	87.4251	29	730.889	17.5248	30	696.177	19.131
31	619.038	87.5277	32	582.397	85.376	33	458.975	71.0681

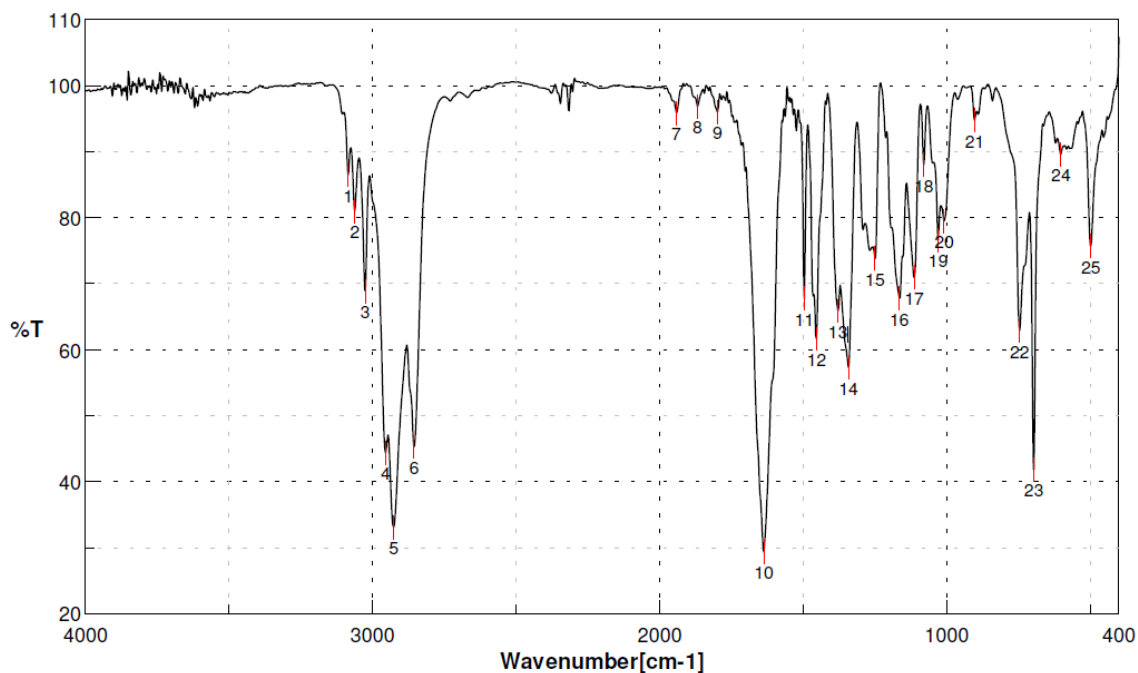
Poly(¹⁵N-hexyl-N-2-phenethylcarbodiimide) (Poly-27)-



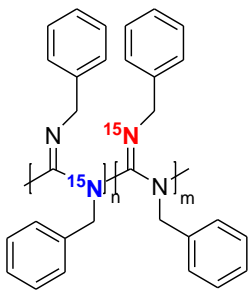
Following the procedure outlined for the polymerization of carbodiimides: 0.25 g (1.09 mmol, 124 eq.) ¹⁵N-hexyl-N-phenethylcarbodiimide, 2.22 mg (10.2 μmol 1.0 eq.) of **Cat-3**, and 0.20 mL dry CHCl₃.

Yield: 0.12 mg (0.505 mmol) white solid, 50 %. FTIR (KBr pellet, cm⁻¹): 3062 (m, Ar-H), 3026 (m, Ar-H), 2954 (s, alkyl-H), 2927 (s, alkyl-H), 2856 (s, alkyl-H), 1637 (s, C=N). ¹H NMR (400 MHz, CDCl₃): δ (ppm) 7.30 - 6.83 (Ar-H, very broad, 5H) 3.45 - 2.77 (overlapped, 4H, broad), 2.18 – 0.86 (13H, overlapped broad peaks). ¹⁵N NMR (40.5 MHz, CDCl₃): δ (ppm) 133.8 (¹⁵N=C, 1N), 1.66 (¹⁵N-C, 1N).

No.	cm-1	%T	No.	cm-1	%T	No.	cm-1	%T
1	3085.55	86.4902	2	3062.41	81.0082	3	3025.76	68.9006
4	2954.41	44.389	5	2927.41	33.1363	6	2856.06	45.289
7	1941.97	95.9075	8	1868.68	96.9331	9	1799.26	96.0628
10	1637.27	29.3358	11	1496.49	67.7974	12	1454.06	61.6653
13	1378.85	65.8954	14	1342.21	57.2742	15	1249.65	73.8235
16	1164.79	67.8154	17	1112.73	70.9685	18	1079.94	88.0423
19	1029.8	76.6603	20	1008.59	79.5439	21	902.523	94.7901
22	746.317	62.9074	23	696.177	41.8448	24	601.682	89.6432
25	497.544	75.7012						



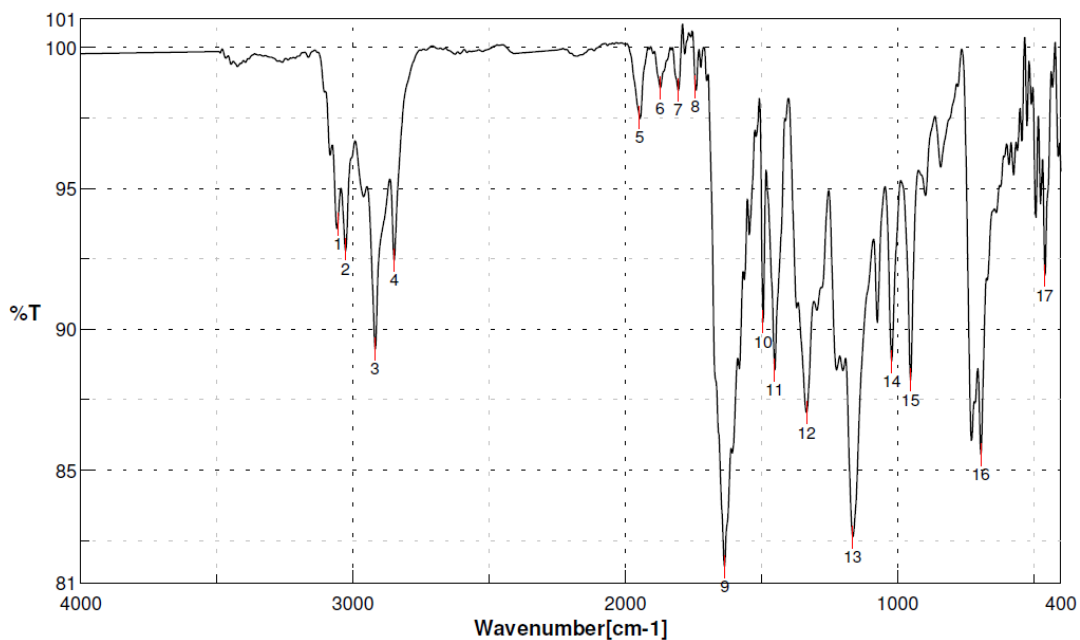
Poly(¹⁵N,N-dibenzylcarbodiimide) (Poly-28)-



Following the procedure outlined for the polymerization of carbodiimides: 0.288 g (1.29 mmol, 150 eq.) ¹⁵N,N'-dibenzylcarbodiimide, 0.00218 g (0.0085 mmol, 1.0 eq.) of **Cat3**, and 0.80 mL dry CHCl₃.

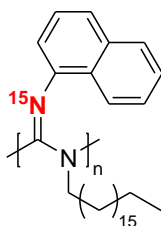
Yield: 0.155 g (0.69 mmol) off-white solid, 54 %. FTIR (KBr pellet, cm⁻¹): 3060 (m, aryl-H), 3028 (m, aryl-H), 2958 (m, alkyl-H), 2920 (m, alkyl-H), 2848 (m, alkyl-H), 1635 (s, C=N). ¹H NMR (400 MHz, CDCl₃): δ (ppm) 7.05 – 6.49 (Ar-H, 10H, very broad triplet),

5.41 (benzyl-H, 1H, broad singlet), 4.45 (benzyl-H, 1H, broad singlet), 4.00 (benzyl-H, $J = 14.8$, 1H, broad doublet), 3.57 (benzyl-H, $J = 14.8$, 1H, broad doublet). ^{15}N NMR (40.5 MHz, CDCl_3): δ (ppm) 137.4 ($^{15}\text{N}=\text{C}$, 1N), 3.1 ($^{15}\text{N}-\text{C}$, 1N).



No.	cm-1	%T	No.	cm-1	%T	No.	cm-1	%T
1	3056.62	93.7321	2	3029.62	92.8451	3	2919.7	89.3047
4	2848.35	92.4552	5	1947.75	97.5176	6	1872.54	98.5644
7	1806.97	98.503	8	1743.33	98.6146	9	1635.34	81.5851
10	1494.56	90.2705	11	1452.14	88.565	12	1334.5	87.0506
13	1164.79	82.6395	14	1022.09	88.8665	15	952.663	88.2023
16	694.248	85.5661	17	458.975	91.9129			

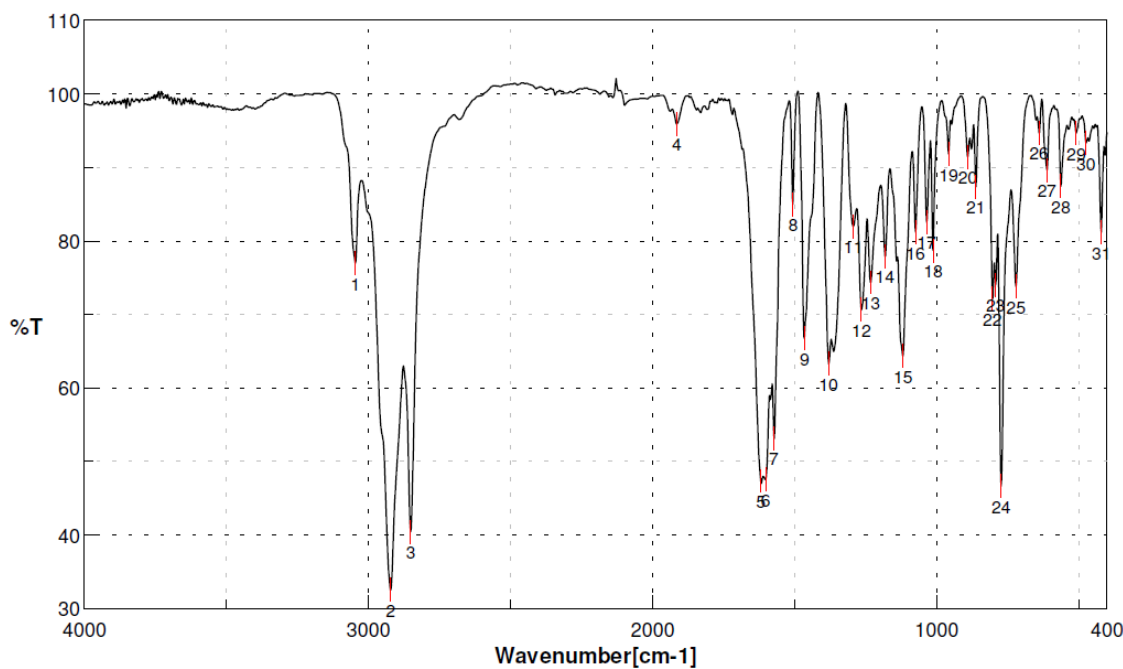
Poly(^{15}N -1-naphthyl-*N*-octadecylcarbodiimide) (**Poly-29**)-



Following the procedure outlined for the polymerization of carbodiimides: 2.13 g (5.07 mmol, 200 eq.) ^{15}N -1-naphthyl-*N*-octadecylcarbodiimide, 11.7 mg (26.0 μmol 1.0 eq.)

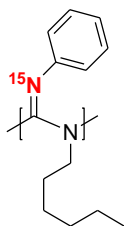
of **Cat-2R**, and 0.40 mL dry CHCl_3 .

Yield: 1.96 g (4.67 mmol) off-white solid, 92 %. FTIR (KBr pellet, cm^{-1}): 3047 (m, aryl-H), 2924 (m, alkyl-H), 2852 (m, alkyl-H), 1619 (s, $^{15}\text{N}=\text{C}$), 1602 (s, $^{15}\text{N}=\text{C}$). ^1H NMR (400 MHz, CDCl_3): δ (ppm) 7.90 – 7.03 (Ar-H, 5H, very broad), 6.62 (Ar-H, 1H, broad doublet), 1.27 (octadecyl-H, 34H, broad singlet), 0.88 (- CH_3 , 3H, singlet). ^{15}N NMR (40.5 MHz, toluene- d_8): δ (ppm) 139.4 ($^{15}\text{N}=\text{C}$, 1N).



No.	cm-1	%T	No.	cm-1	%T	No.	cm-1	%T
1	3046.98	76.9937	2	2923.56	32.5264	3	2852.2	40.4425
4	1914.97	95.9269	5	1619.91	47.3745	6	1602.56	47.5579
7	1571.7	53.1676	8	1506.13	85.0074	9	1465.63	66.7654
10	1380.78	63.3047	11	1294	82.0009	12	1265.07	70.6488
13	1232.29	74.4059	14	1182.15	77.9184	15	1118.51	64.4108
16	1074.16	81.2029	17	1035.59	82.5737	18	1012.45	78.7207
19	958.448	91.8442	20	890.952	91.443	21	862.025	87.3883
22	804.171	72.1457	23	792.6	74.0178	24	773.315	46.6538
25	721.247	73.8302	26	640.251	94.725	27	611.324	89.6559
28	563.112	87.4543	29	509.115	94.6784	30	474.403	93.3486
31	420.406	81.1972						

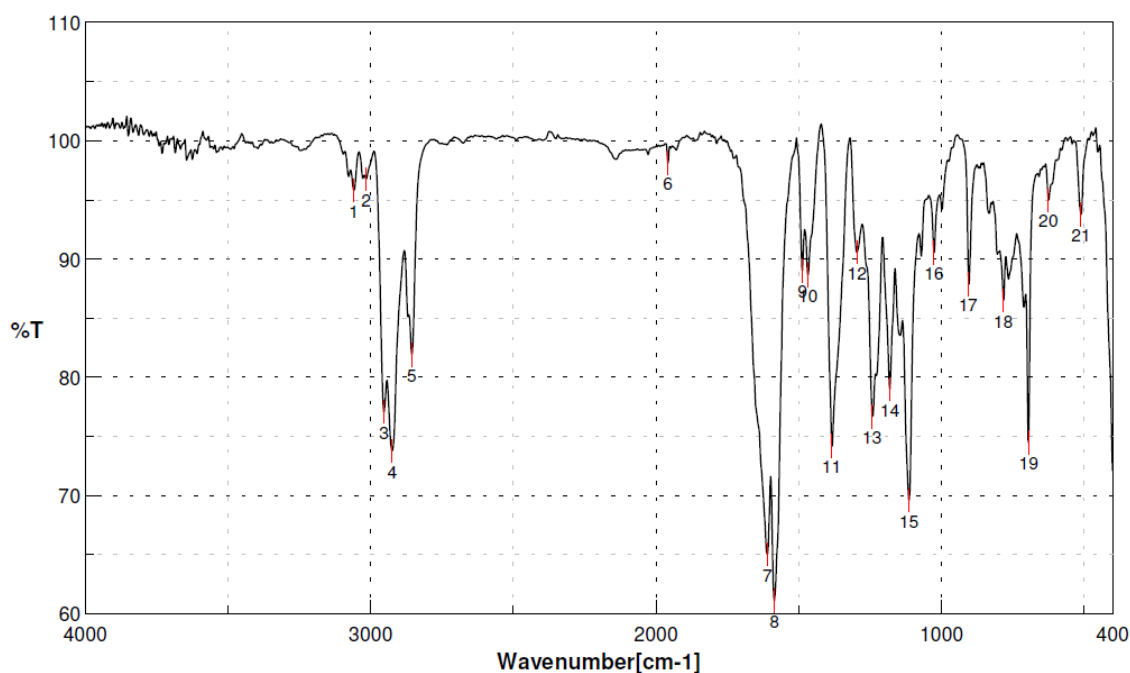
Poly(¹⁵N-phenyl-N-hexylcarbodiimide) from Nickel catalyst (Poly-17Ni)-



Following the procedure outlined for the polymerization of carbodiimides: 0.368 g (1.35 mmol, 51 eq.) ¹⁵N-phenyl-N-hexylcarbodiimide, 23.6 mg (35.4 μmol 1.0 eq.) of **Cat-5**, w/o solvent.

Yield: 0.309 g (1.52 mmol) white solid, 84 %. FTIR (KBr pellet, cm⁻¹): 3058 (m, Ar-H), 3016 (m, Ar-H), 2952 (s, alkyl-H), 2925 (s, alkyl-H), 2856 (s, alkyl-H), 1610 (s, C=N), 1585 (s, C=C_{aryl}). ¹H NMR (400 MHz, CDCl₃): δ (ppm) 7.01 - 6.76 (Ar-H, very broad, 5H) 3.56 (N-CH₂, broad, 1H), 2.80 – 2.15 (N-CH₂, broad s, 1H), 1.59 – 0.40 (overlapped broad peaks, 11H). ¹⁵N NMR (40.5 MHz, CDCl₃): δ (ppm) 136.0 (¹⁵N=C), 21.5 (very small peak, ¹⁵N-C).

No.	cm-1	%T	No.	cm-1	%T	No.	cm-1	%T
1	3058.55	95.7927	2	3016.12	96.762	3	2952.48	77.0803
4	2925.48	73.7631	5	2856.06	81.9025	6	1959.32	98.1297
7	1610.27	65.0141	8	1585.2	61.0654	9	1486.85	89.041
10	1467.56	88.6345	11	1384.64	74.1812	12	1295.93	90.5692
13	1241.93	76.6772	14	1180.22	79.0065	15	1112.73	69.5795
16	1025.94	90.531	17	904.451	87.8724	18	782.958	86.4863
19	694.248	74.4555	20	624.823	94.9931	21	511.044	93.7551



2.10 References-

- (1) Higashihara, T.; Goto, E.; Ueda, M. *ACS Macro Lett.* **2012**, *1*, 167-170.
- (2) Kohn, P.; Huettner, S.; Komber, H.; Senkovskyy, V.; Tkachov, R.; Kiriy, A.; Friend, R. H.; Steiner, U.; Huck, W. T. S.; Sommer, J.-U.; Sommer, M. *J. Am. Chem. Soc.* **2012**, *134*, 4790-4805.
- (3) McMahon, D. P.; Cheung, D. L.; Goris, L.; Dacuna, J.; Salleo, A.; Troisi, A. *J. Phys. Chem. C* **2011**, *115*, 19386-19393.
- (4) Zhai, T.; Xie, L.; Peng, M.; Zhou, X.; Xia, H.; Fei, G. *Huagong Xinxing Cailiao* **2011**, *39*, 84-87.
- (5) Zhou, C. Y.; Yan, L. T.; Zhang, L. N.; Ai, X. D.; Li, T. X. *Adv. Mater. Res.* **2011**, *306-307*, 1649-1652.
- (6) Zhou, C. Y.; Yan, L. T.; Zhang, L. N.; Ai, X. D.; Li, T. X.; Dai, C. A. *J. Macromol. Sci., Part A: Pure Appl. Chem.* **2012**, *49*, 293-297.

- (7) Jin, J.-I. L. *Mol. Cryst. Liq. Cryst. Sci. Technol., Sect. A* **1994**, 254, 197-207.
- (8) Aitkin, B. S.; Mei, J.; Graham, K. R.; Reynolds, J. R.; Wagener, K. B. *Polym. Prepr. (Am. Chem. Soc., Div. Polym. Chem.)* **2011**, 52, No pp. given.
- (9) Mei, J.; Aitken, B. S.; Graham, K. R.; Wagener, K. B.; Reynolds, J. R. *Macromolecules* **2010**, 43, 5909-5913.
- (10) Leatherman, M. D.; Brookhart, M. *Macromolecules* **2001**, 34, 2748-2750.
- (11) Fujita, M.; Seki, Y.; Miyatake, T. *J. Polym. Sci., Part A: Polym. Chem.* **2004**, 42, 1107-1111.
- (12) Busico, V.; Cipullo, R. *J. Organomet. Chem.* **1995**, 497, 113-118.
- (13) Coates, G. W.; Cherian, A.; Rose, J. M.; Cornell Research Foundation, Inc., USA . 2010, p 5pp.; Chemical Indexing Equivalent to 147:73179 (WO).
- (14) Goodwin, A. A., North Carolina State University, Thesis, 1996.
- (15) Kennemur, J. G., North Carolina State University, Thesis, 2010.
- (16) Dilien, H.; Chambon, S.; Cleij, T. J.; Lutsen, L.; Vanderzande, D.; Adriaensens, P. J. *Macromolecules* **2011**, 44, 4711-4720.
- (17) Roviello, A.; Buono, A.; Carella, A.; Roviello, G.; Cassinese, A.; Barra, M.; Biasucci, M. *J. Polym. Sci., Part A: Polym. Chem.* **2007**, 45, 1758-1770.
- (18) Bai, W. B.; Zhan, C. M. *Chem. Lett.* **2005**, 34, 924-925.
- (19) Cheng, H. N.; Cambridge Univ. Press: 1988, p 599-623.
- (20) Grassi, A.; Zambelli, A.; Resconi, L.; Albizzati, E.; Mazzocchi, R. *Macromolecules* **1988**, 21, 617-622.
- (21) Sessa, I.; Ferro, D. R.; Grisi, F.; Liguori, D.; Milano, G.; Zambelli, A. *Macromol. Chem. Phys.* **2002**, 203, 2604-2615.
- (22) Lu, Y., North Carolina State University, Thesis 2005.
- (23) Tang, H.-Z.; Lu, Y.; Tian, G.; Capracotta, M. D.; Novak, B. M. *J. Am. Chem. Soc.* **2004**, 126, 3722-3723.

- (24) Kennemur, J. G.; Clark, J. B.; Tian, G.; Novak, B. M. *Macromolecules* **2010**, *43*, 1867-1873.
- (25) Kennemur, J. G.; DeSousa, J. D.; Martin, J. D.; Novak, B. M. *Macromolecules* **2011**, *44*, 5064-5067.
- (26) DeSousa, J. D.; Novak, B. M. *ACS Macro Lett.*, **2012**, *1*, 672-675.
- (27) Oszczapowicz, J.; Wawer, I.; Dargatz, M.; Kleinpeter, E. *J. Chem. Soc., Perkin Trans. 2* **1995**, 1127-1131.
- (28) Lambert, J. B.; Shurvell, H. F.; Lightner, D. A.; Cooks, R. G. *Organic Structural Spectroscopy*; Prentice Hall, 1998.
- (29) A. Ford, A. J. G. a. R. *The Chemist's Companion: A Handbook of Practical Data, Techniques, and References*; John Wiley and Sons Inc.: New York, 1972.
- (30) Kim, J.; Novak, B. M.; Waddon, A. J. *Macromolecules* **2004**, *37*, 8286-8292.
- (31) Kim, J.; Novak, B. M.; Waddon, A. J. *Macromolecules* **2004**, *37*, 1660-1662.
- (32) Tang, H.-Z.; Novak, B. M.; He, J.; Polavarapu, P. L. *Angew. Chem., Int. Ed.* **2005**, *44*, 7298-7301.
- (33) Tang, H.-Z.; Boyle, P. D.; Novak, B. M. *J. Am. Chem. Soc.* **2005**, *127*, 2136-2142.
- (34) Zhang, Y.; Lin, C.; Li, Z.; Qin, L.; Wen, H. *J. Labelled Compd. Radiopharm.* **2010**, *53*, 183-185.
- (35) Huang, X.; Seid, M.; Keillor, J. W. *J. Org. Chem.* **1997**, *62*, 7495-7496.
- (36) Spitzer, U. A.; Stewart, R. *J. Org. Chem.* **1974**, *39*, 3936.

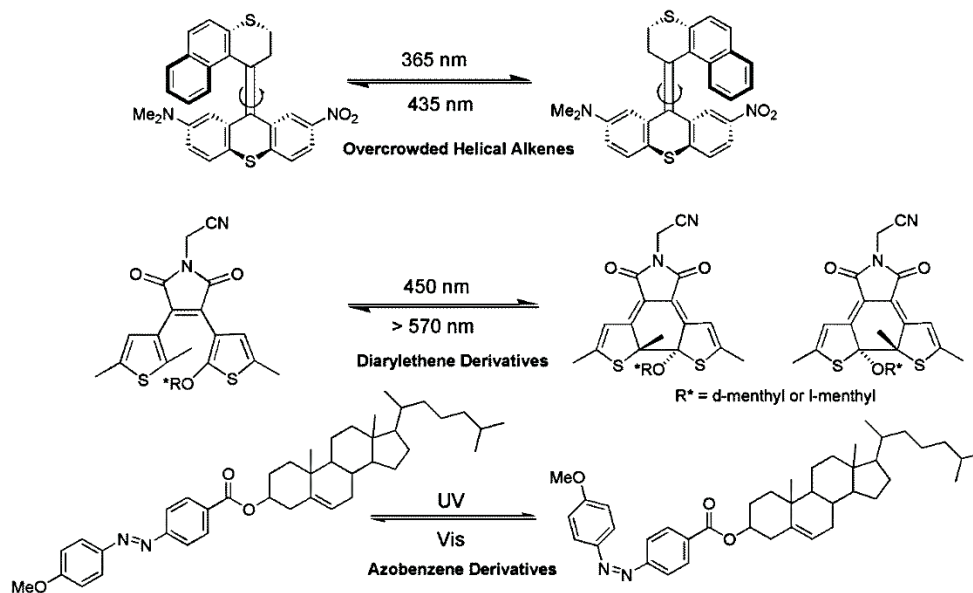
CHAPTER 3: Definitively Identifying the Mechanism of Chiroptical Switching by ^{15}N NMR and VCD Spectroscopy.

3.1 Background of Chiroptical Switches-

Synthesis and control of molecular switches presents important, significant challenges in designing of nanomachines capable of minute changes to the overall primary or secondary structure at the molecular level. Bistability, i.e., the presence of two specific molecular structures that can interconvert between one another upon influence from external stimuli, is a necessary attribute in all molecular switches. Various external stimuli have been shown to cause this phenomenon including alterations of photochemical irradiation,¹ solvent,² heat,³ pressure,⁴ magnetic/ electronic fields,⁵ or pH change,⁶ with irradiation and heat being the predominant stimuli studied. Chiroptical switches undergo molecular modifications that precisely alter the chirality of the compound in question. The effect on the molecular structure of the switch can vary from helical inversion to cis-trans isomerization to cyclization.⁷ Chiroptical changes are typically monitored by polarimetry, electronic circular dichroism (ECD), vibrational circular dichroism (VCD), and RAMAN spectroscopy.⁷

The two bistable structures of photochromic chiroptical switches are accessible through irradiation of the molecule with varying wavelengths of UV, visible, or infrared light. Some of the first chiroptical switches focused on the steric interactions of overcrowded alkenes and the ability to isomerize the double bond using various wavelengths of UV light.⁸

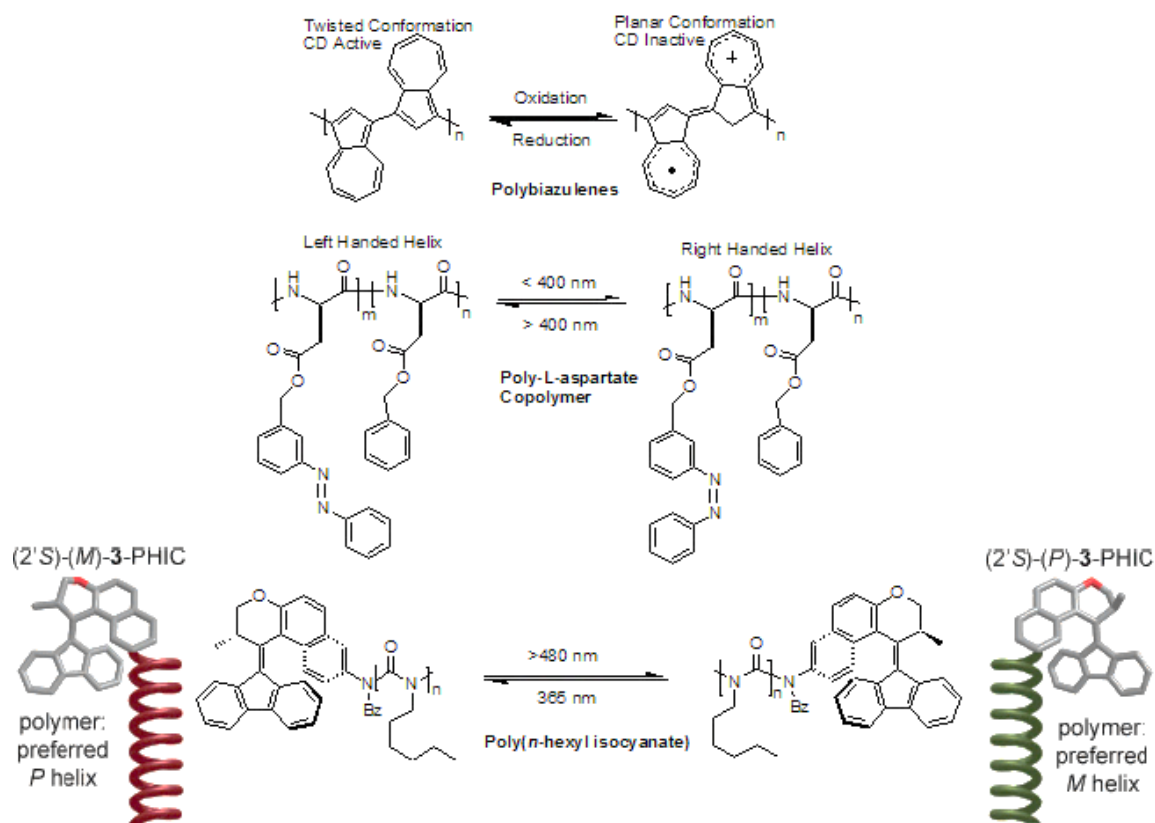
Due to the overcrowded nature of the compound, it adopts a helical conformation which can interconvert between both helical arrays (*M* or *P* helices) upon irradiation. Multiple diarylethenes, most notably di(thiophene)ethenes, have been shown to undergo a reversible, photo-induced cyclization reaction upon irradiation creating two distinct molecular structures that are easily interconverted. The resulting cyclization reaction is diastereoselective upon introduction of *d* or *l*-menthyl substituents at the 2-position of the thiophene rings in dithiophene maleimide conjugates forming the cyclized product with an 86.6 % diastereomeric excess (de).⁹ The solvent polarity was also shown to play a significant role in the process with the switching occurring in THF and toluene but not in the nonpolar hexanes solution. Azobenzenes have also proven to be effective light and heat activated chiroptical switches with bistable conformations corresponding to the cis-trans isomerization of the azo N=N bond.¹⁰ Shinkai et al. reported photo- and thermal- reversibility of gel formation in cholesterol functionalized azobenzene moieties.¹¹ Examples of these small molecule conjugates are displayed in Scheme 3.1.



Scheme 3.1- Some examples of small molecule chiroptical switches including overcrowded alkenes (top), diarylethene switches (middle), and azobenzene derivatives (bottom).^{8,9,11}

Specific molecular switch functional groups have also been incorporated into several macromolecular systems including polymethacrylates,¹² polypeptides,¹³ DNA,¹⁴ and polyisocyanates¹⁵ to name a few. These systems offer a vast number of potential applications in the field of material science. Chiral polyazulenes and polybiazulenes have been reported to possess redox activated switching of two bistable conformations in the polymer backbone.¹⁶ The nonplanar configuration of the neutral form is distorted to planarity upon oxidation of the backbone. This conversion is shown by the loss of chirality evident by the disappearance of the CD band. Subsequent reduction of the backbone displays a reemergence of the CD absorption proving that the process is indeed reversible. Helical poly(*L*-aspartate) copolymers bearing β -*m*-benzyl and β -*m*-benzylazo substituents showed complete helical

inversion upon irradiation of the backbone and successive cis-trans isomerization of the -N=N- azo functional group.¹³ When the benzylazo side group adopts the all trans conformation, the polymer backbone prefers to adopt a left handed helix with 86 % excess. Photoisomerization of the azo bond resulted in a reversal of configuration and led to exclusively right handed helices. Only a small amount of the benzylazo containing sub-unit was necessary to greatly affect the overall secondary structure of the helix with only 9.7 % incorporation leading to 70 % of the polymer chains adopting a right handed helix. Pijper et al. reported end group functionalized poly(*n*-hexylisocyanate) (PHIC) bearing the overcrowded alkene molecular motor covalently tethered to the chain end of the polymer.¹⁵ This functionalized polymer showed the ability to switch the helical conformation of the polymer backbone and reorder the cholesteric, liquid crystalline mesophase when the end group molecular motor was influenced by photo- and thermal- stimuli. These examples can be found in Scheme 3.2 below.



Scheme 3.2- Examples of macromolecular chiroptical switches that are affected by a variety of stimuli including irradiation, redox chemistry, temperature change, and solvent change.^{13,15,16}

Before we review the chiroptical switching behaviors of various polycarbodiimides, it is first necessary to discuss the characterization tools used to study chiral molecules and macromolecules. Optical rotation (OR; α) is measured by passing plane polarized light at a specific wavelength through a chiral analyte and recording the angle of rotation of the exiting light with a polarimeter. This value is typically normalized and reported as specific optical rotation (SOR; $[\alpha]$) which can be easily converted from OR using equation (1) below where c

is the concentration of the analyte in grams per milliliters and l is the pathlength in decimeters.

$$(1) \quad [\alpha]_{\lambda}^T = \frac{100\alpha}{cl}$$

This calculated value is always reported with the temperature (T) in Celsius, wavelength (λ) in nanometers, and solvent used; since these factors play a large role in the values observed. SOR measurements are typically carried out in dilute solutions to limit intermolecular aggregation of chiral species.

Circular dichroism (CD) is a widely expanding technique for identification of chiral systems. CD measures the unbalanced absorption of left and right circularly polarized light (CPL) at a variety of wavelengths. Electronic CD (ECD) essentially couples UV-Vis spectroscopy with polarimetry by exposing a solution containing a chiral chromophore to circularly polarized UV-Vis radiation. The chromophore present in the molecule can then preferentially absorb one hand of light over another converting the CPL to elliptically polarized light. The angle of ellipticity (θ) measured is typically a small number and is reported in milidegrees. This value, like OR, is usually reported as the normalized value called molar ellipticity. This conversion is simple and is shown in equation (2) below where M is the molarity in moles per liter and l is the path length in centimeters.

$$(2) \quad [\theta]_{\lambda}^T = \frac{100\theta}{Ml}$$

The molar ellipticity of a sample is reported in units of $M^{-1}m^{-1}$. For macromolecular systems, the molecular weight of the repeat unit is used to calculate the molarity of the solution studied. CD data is also reported as molar circular dichroism ($\Delta\epsilon$) which is the difference between extinction coefficients in the left and right direction. Molar ellipticity and molar circular dichroism have the same units and can be interconverted using equation (3) below.

$$(3) \quad [\theta]_{\lambda}^T = 3300(\Delta\epsilon)$$

Vibrational circular dichroism (VCD) has only recently become a powerful tool for absolute identification of chiral species due to the difficulties in resolving the overall CD spectrum. VCD couples the functions of infrared spectroscopy with polarimetry and employs the same theory as ECD except the preferential absorption of right or left CPL is measured through the vibrational modes of the influenced bonds. These spectra can then be fit with theoretical DFT calculations to determine the absolute handedness of the chiral analyte in question.

3.2 The Discovery and Advancements of Chiroptical Switching Polycarbodiimides-

In 2004, Tang and co-workers reported the first polycarbodiimide to display thermo- and solvo- driven chiroptical switching in toluene. Poly(*N*-1-anthryl-*N'*-octadecylcarbodiimide), **Poly-6**, showed the ability to selectively tune the SOR and ECD Cotton effect reversibly from positive to negative values simply upon heating over 38.5 °C or by doping the toluene solution with ~10% THF¹⁷ (Figure 3.1). This same polymer is shown

to have the highest helical inversion barrier of any polycarbodiimide synthesized thus far.¹⁸ **Poly-6** dissolved in chloroform and THF exhibited strong negative SOR and ECD Cotton effects but did not switch as a function of temperature. The polymerization of **Poly-6** was conducted with two variations of enantiopure, BINOL ligated titanium(IV) catalysts. The [(*R*)-3,3'-Dibromo-2,2'-binaphthoxy] titanium(IV) di-*t*-butoxide (**Cat-6**) was found to be the more effective and controlled catalyst for the polymerization of carbodiimides as evident by the polydispersity (M_n/M_w) and annealing behaviors of the samples. **Poly-6** polymerized from **Cat-6** was found to have a relatively narrow polydispersity of 2.7 and required more than 100 hours to racemize at 80 °C, which is 6 times longer than **Poly-6** synthesized from **Cat-2**. It is important to note that the batch of **Cat-2** used in this experiment may have contained some impurities which is evident in the ¹H NMR spectra in the supplemental section of the article. This may cause the polymerization to occur with diminished control and would explain the broad range of molecular weights and poor thermal properties of **Poly-6** from **Cat-2**.

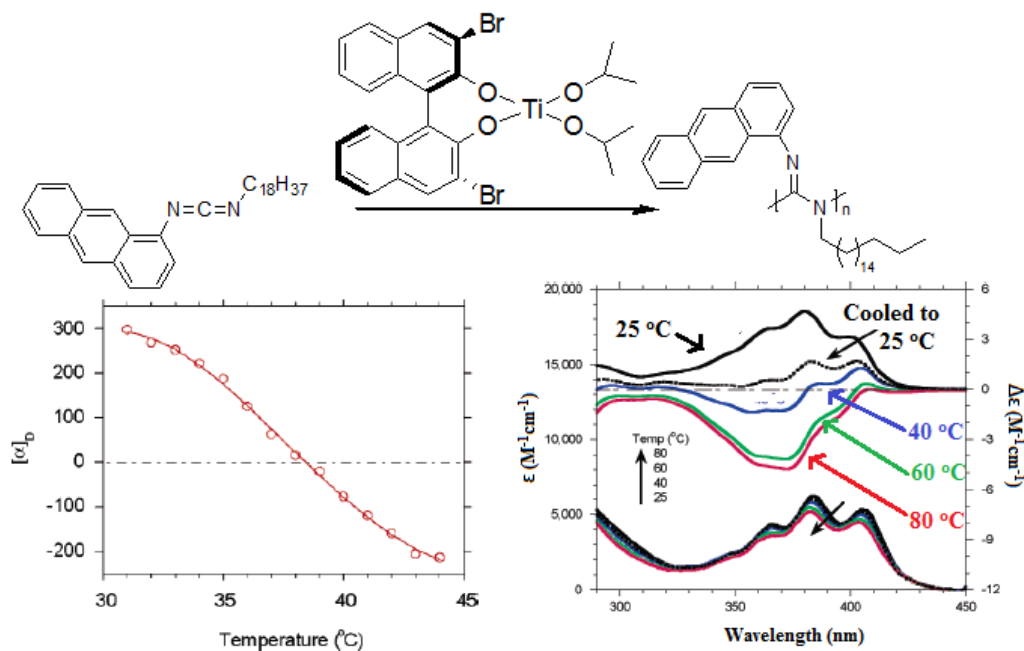


Figure 3.1- Mono-6 polymerized with the enantiopure **Cat-6** exhibited chiroptical switching properties capable of drastic alterations to both the SOR and CD Cotton effect simply upon small changes to the temperature or solvent. (Copyright 2005 American Chemical Society, reprinted with permission)¹⁷

Three molecular motions were suggested as the possible source of this chiroptical switching including helical inversion (φ), imine inversion (ω), and/or rotation of the N- $C_{anthracene}$ bond (θ) (Figure 3.2). The stable helical nature of **Poly-6** rules out helical inversion as a viable explanation due to the relatively low temperature changes required for the drastic specific OR alterations to occur. Imine inversion, however, is harder to rule out for macromolecular systems. Even so, small molecule analogues reveal imine inversion barriers of 20-26 kcal/mol (correlating to ~50 - 180 $^{\circ}C$) which is significantly larger than the energy required for the chiroptical switching.¹⁹ This leaves the N- C_{aryl} bond rotation as the only molecular motion possible at the low temperatures in which the process occurs. VCD

analysis of **Poly-6** in toluene and chloroform was employed to couple with the data collected thus far in order to clarify the specific mechanism of action.²⁰ The experimental data was fit with the model compound, shown in Figure 3.3, initially optimized with molecular mechanics MMFF94 and further optimized to the *P* helix using DFT at the B3LYP/6-31(d) level.

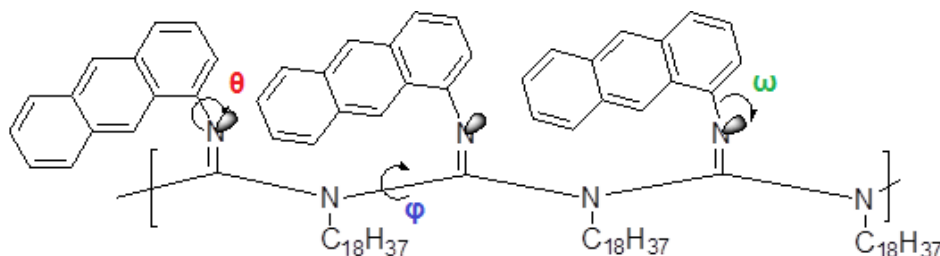


Figure 3.2- Three possible molecular motions capable of exhibiting the large SOR changes seen for **Poly-6** include helical inversion (φ), imine inversion (ω), and rotation of the N-C_{anthracene} bond (θ).

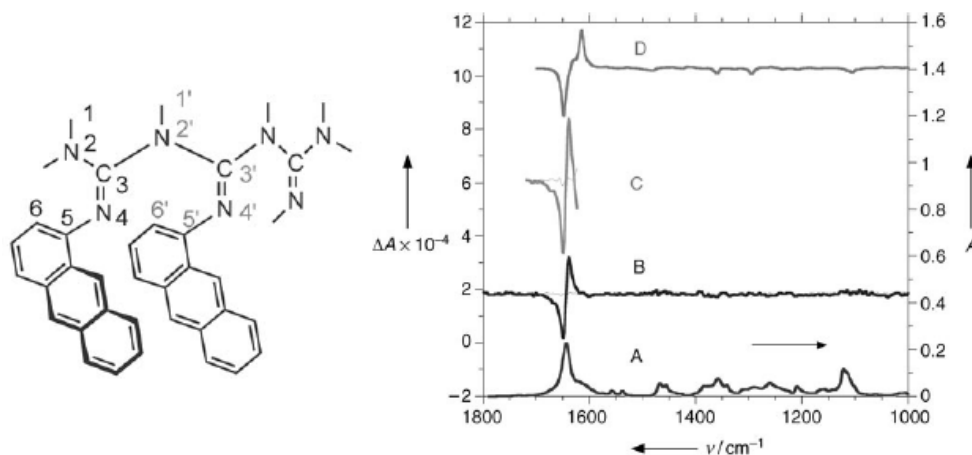


Figure 3.3- The model compound (left) was used to compute the theoretical VCD spectra (D on right) to fit with experimental VCD spectra of **Poly-6** in toluene (C) and chloroform (B). The IR spectra is shown as well (A). (Copyright 2005 John Wiley & Sons Inc., reprinted with permission)²⁰

The experimental VCD spectra matched very well with the theoretical spectrum meaning the polymer does adopt an excess *P* helix when polymerized from **Cat-6R**. Strangely, the spectra in chloroform correlated very closely with the spectra in toluene despite being opposite in sign in both SOR and ECD signal. This result suggests that simultaneous wagging of the anthracene units in a shutter like motion relative to the lone pair on the nitrogen changes the lone-pair/ π -electron interactions without affecting the overall chirality of the backbone, i.e., helical inversions are not involved in the process. Computational modeling of the system was also carried out using semiempirical AM1 calculations to test two proposed conformations possibly present in the system. In this model exists a low-energy state (I in Figure 3.4) composed of the polymer with the anthracene side groups aligned against the helical director (dipole moment $\mu = 6.9$ debyes) and the higher

energy state (II in Figure 3.4) with the anthracene groups pointed with the helical director ($\mu = 7.7$ debyes).²⁰ This was first believed to be the mechanism of action in the switching process with the more polar solvents such as CHCl_3 and THF stabilizing the higher energy state. Variable temperature (VT) ^1H and ^{13}C NMR analysis was attempted on this polymer as well to help elucidate some of these findings but was inconclusive due to the significant signal broadening seen in high-polymer systems.

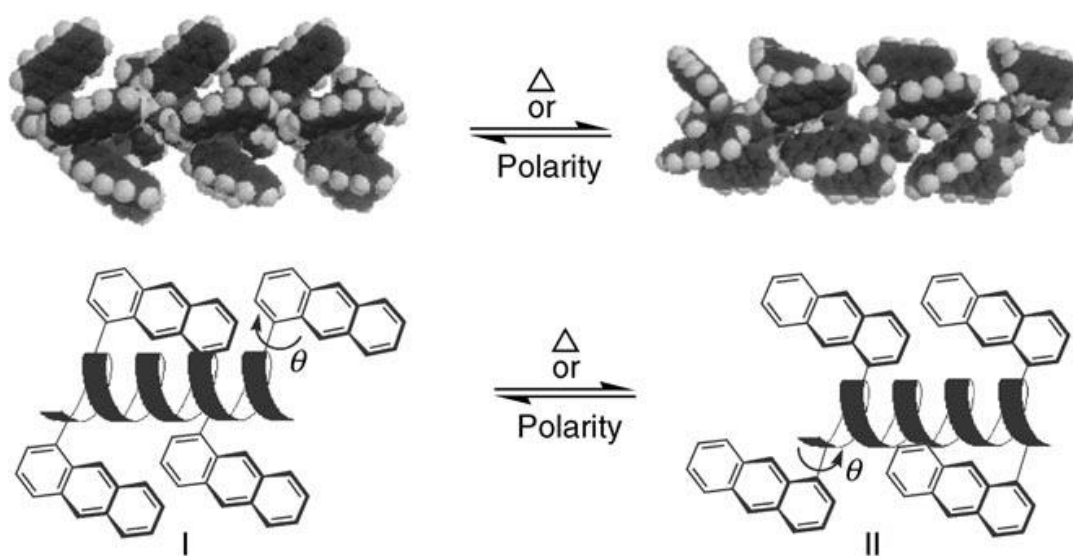


Figure 3.4- Proposed two states of switching in **Poly-6** optimized at both the semiempirical (AM1) level and molecular-mechanics (MMFF94) level. (Copyright 2005 John Wiley & Sons Inc., reprinted with permission)²⁰

This discovery launched a series of experiments in an attempt to amplify and optimize the switching process by altering the pendant groups slightly. In a first attempt, Kennemur et al. synthesized a series of polycarbodiimides bearing phenyl side groups substituted at the meta position of the ring with respect to the imine connection.²¹ These

polymers, however, did not display any of the observed behavior seen in **Poly-6** and further tuning was required to determine what was necessary for the SOR switch to occur. It wasn't until 2010 when Kennemur discovered a new, highly versatile polycarbodiimide capable of high SOR changes.²² Poly(*N*-1-naphthyl-*N'*-octadecylcarbodiimide) (PNOC; **Poly-14**) contains the 1-naphthyl moiety capable of acting as the rotating flap similar to the 1-anthryl pendant group in **Poly-6**. This polymer greatly expanded the functionality of the switch and showed the ability to alter the SOR in a variety of solvents including chloroform, THF, toluene, ethylbenzene, chlorobenzene, xylenes, 1,2-dichlorobenzene, and cumene. Chloroform, THF, and toluene were found to have the greatest versatility of all solvents with very large chiroptical switching profiles in each solvent (Figure 3.5). **Poly-14** displays low negative SOR values at room temperature in chloroform and switches into the positive OR regime at ~ 0.5 °C. In THF, the switching temperature is increased to 19.5 °C and both the maximum and minimum rotation values are increased 300 - 400°. When **Poly-14** is dissolved in toluene, the switching temperature is shifted further to 36 °C with the specific rotations remaining positive for the majority of temperatures studied. VT-ECD of **Poly-14** in THF displays complete inversion of the observed Cotton effects when the temperature is increased from 9 °C to 40 °C (Figure 3.5). The net observed SOR change is $\sim 1700^\circ$ which is still by far the greatest of any polycarbodiimide to date. It has also been shown to switch, i.e., pass from positive OR to negative, in eight different solvents, also a record in terms of polycarbodiimides.

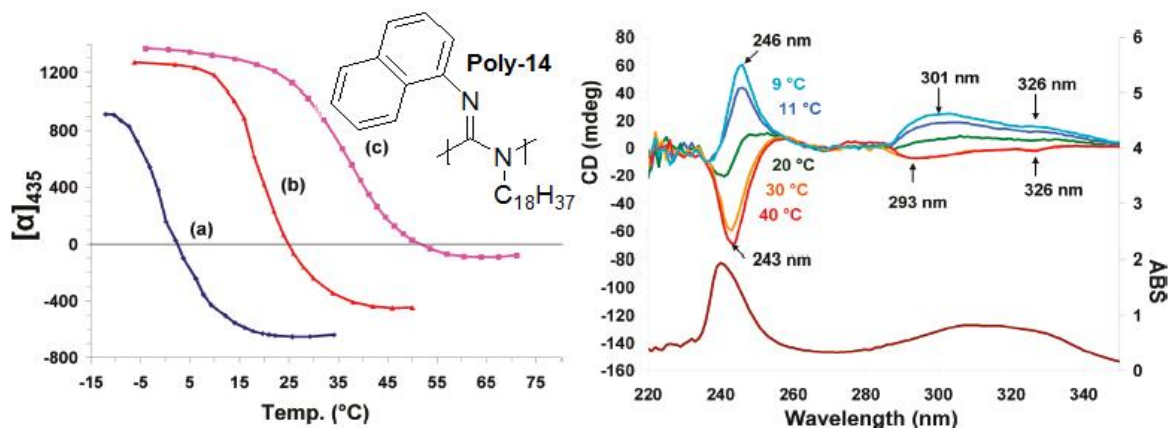


Figure 3.5- VT-polarimetry (left) in CHCl_3 (a), THF (b), and toluene (c) and the VT-ECD in THF of **Poly-14** showing drastic chiroptical switching as a function of temperature and solvent. (Copyright 2010 American Chemical Society, reprinted with permission)²²

Poly-14 offers further evidence that the switching process does not involve helical inversions or imine inversions with the chiroptical switching property occurring at very low temperatures in chloroform. Intermolecular aggregation, however, is achievable at these low temperatures due to the possible π - π interactions between the pendant groups of adjacent polymer chains in solution. Significant conformational changes in chiral polythiophenes caused by interchain, supramolecular aggregation has been observed via ECD analysis.²³ We are confident that this process is not a function of aggregation due to the lack of change in chiroptical switching as a function of concentration. Also, the large *n*-octadecyl side chain acts as an aliphatic chain-spacer to improve solubility and dampen interchain interactions. The chiroptical properties were also shown to be completely reversible upon multiple heat-cool cycles without significant racemization of the polymer backbone (especially in CHCl_3 and THF where the switching occurs at lower temperatures). Rapid heating of the polymer solution in THF by preheating the circulation bath showed that the conformation change is

almost instantaneous and that the SOR can be held constant with temperature for multiple hours.²² VT-¹H NMR spectra presented in Figure 3.6 supports the proposed mechanism of rotation about the N-C_{naphthyl} bond with new peaks arising at ~6.5 ppm upon heating in THF revealing that the naphthyl protons do indeed experience a change in environment as a function of the switching process. (Figure 3.6)

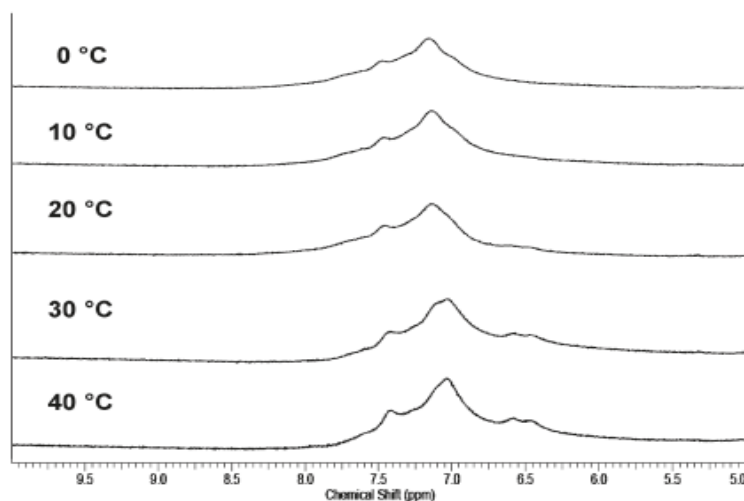


Figure 3.6- VT-¹H NMR spectra of **Poly-14** in THF from 0 – 40 °C display new chemical shifts arising at higher temperatures. (Copyright 2010 American Chemical Society, reprinted with permission)²²

At first examination of **Poly-6**, one would think that the solvent effects on the chiroptical switching most likely correlate to the polarity of the solvent, but when studying the solvent effects on the properties of **Poly-14**, which are much more pronounced, no such trend exists. An example is comparing the SOR data of the polymer in chloroform with the polymer in dichloromethane. **Poly-14** shows no chiroptical switching in DCM but have the

highest positive rotation values among all solvents. The volatility of the solvent does not allow for high temperatures to be studied and low temperatures cause the polymer to precipitate from the solution. In chloroform, however, the SOR values of **Poly-14** at room temperature are in the very low negative regime (see Figure 3.5) and show immense variability as a function of temperature. Even more interesting is the chiroptical switching profiles of **Poly-14** dissolved in benzene compared to various alkyl substituted benzenes (i.e., toluene, ethylbenzene, propylbenzene, etc.) (Figure 3.7).

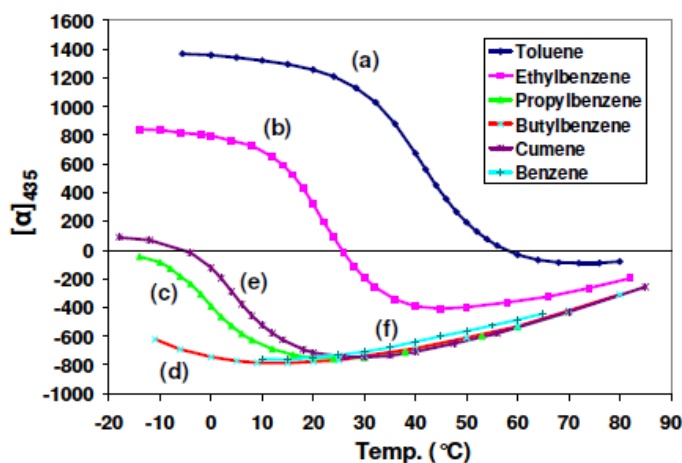


Figure 3.7- VT-polarimetry on **Poly-14** dissolved in benzene and various alkyl substituted aromatic solvents.(Reprinted from Justin Kennemur's thesis)²¹

In benzene, the polymer shows no chiroptical switching but, along with cyclohexane, does provide one of the lowest OR values of any other solvent. Simply adding a methyl group onto the benzene solvent molecules (i.e., dissolving in toluene) causes the SOR to spring into the high positive range at room temperature and the switching profile to become

pronounced. Increasing the substituent chain length on the solvent molecules one carbon (ethylbenzene) shifts the switching profile and the switching temperature ~ 16 °C lower, and, furthermore, increasing the length an additional carbon (propylbenzene) shifts the profile exclusively below 0 °C. Finally, butylbenzene causes the polymer to act as it does in benzene with the SOR values lining up nearly perfectly at all temperatures studied. This observation remains a mystery but it is believed that the balance between aliphatic and aromatic interactions allows the solvent molecule to penetrate the aliphatic corona surrounding the nitrogen rich backbone.

It is obvious that additional characterization techniques must be employed to better understand the overall chiroptical switching process. Here in, we report the use of ^{15}N -isotope labeling and subsequent ^{15}N NMR analysis to help elucidate the true cause of this phenomenon.

3.3 Effect of Solvent on the ^{15}N NMR, IR, and ECD Spectra-

Tian and co-workers first reported the synthesis of a polycarbodiimide bearing the 1-naphthyl pendant group in 2004 when he noticed the polymers extreme, SOR dependence on the solvent used.²⁴ This polymer displayed an optical rotation varying from -256° in heptane to $+302^\circ$ in dichloromethane as well as a birefringent, cholesteric mesophase. The switching of the polymer was not, however, discovered at this time. Formation of a thin film upon solvent evaporation forms a highly opalescent film due to frozen cholesteric domains in the solid state. As previously discussed, **Poly-14** (which also possesses a 1-naphthyl pendant group) was discovered to be the most versatile of a family of polycarbodiimides with

chiroptical switching properties.²² To better examine the switching process (and determine the regioregularity) of **Poly-14**, ¹⁵N-enrichment of the polymer was commenced. The synthesis used is explained in further detail in section 2.6. The polymerization of the labeled ¹⁵N-1-naphthyl-N-octadecylcarbodiimide was performed with the chiral **Cat-2R** to produce **Poly-29** with an excess helical sense. Successive variable-temperature (VT) polarimetry of the polymer, presented in Figure 3.8, displays the same pattern of SOR dependence on temperature and solvent as reported by Kennemur et al. but with diminished amplitude. The decreased amplitude of chiroptical switching in **Poly-29** is believed to be a consequence of both the molecular weight of the polymer and the purity/age of the catalyst used to polymerize **Mono-29**.

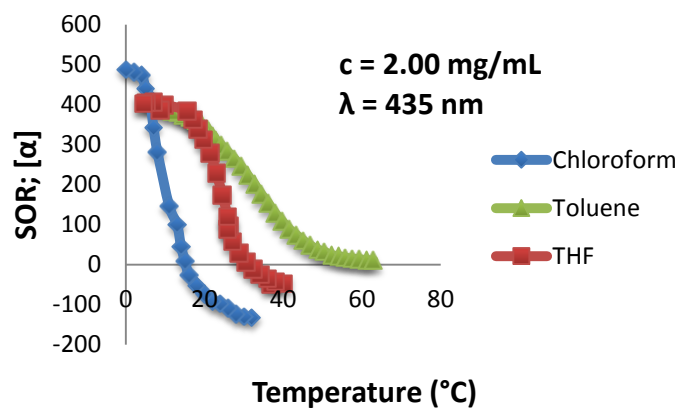


Figure 3.8- VT-polarimetry of **Poly-29** in CHCl₃ (blue), THF (green), and toluene (red) showing the ability to change ~620° simply by altering the solvent or temperature.

Examination of the IR imine stretch of **Poly-29** dissolved in different solvents reveals an interesting result. The peak at 1619 cm^{-1} is predominant when the polymer was dissolved in CHCl_3 but the intensities switch when the polymer was dissolved in THF where the peak at 1602 cm^{-1} becomes larger. When dissolved in toluene and cast onto the salt plate, the peak at 1619 cm^{-1} completely disappears leaving only one peak in the region at 1601 cm^{-1} . These findings are displayed in Figure 3.9.

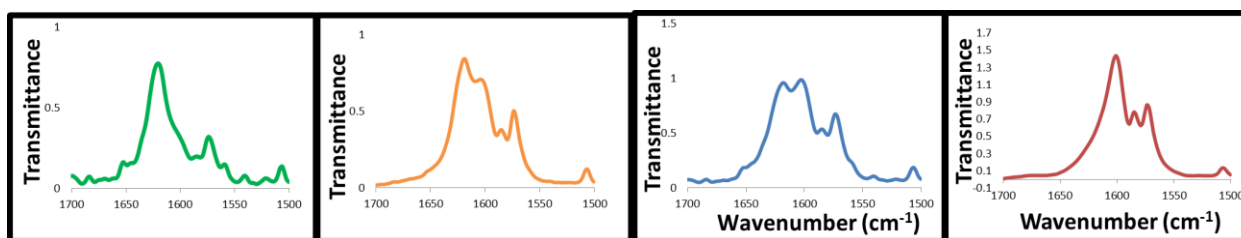


Figure 3.9- The two FTIR C=N imine stretches for **Poly-29** change in intensity as the solvent is changed from benzene to CHCl_3 to THF to DCM (left to right respectively) suggesting that the chiroptical switching is consequence of varying populations of two states.

This peak intensity change occurs in a similar fashion as the IR stretches that reversibly switch in intensities as a function of temperature in chloroform (Figure 2.2). ^{15}N NMR analysis of the labeled **Poly-29** in different solvents may provide more interesting information about the switching process. The ^{15}N NMR spectra for this polymer dissolved in CDCl_3 (top), THF-d_8 (middle), and toluene- d_8 (bottom) are shown in Figure 3.10.

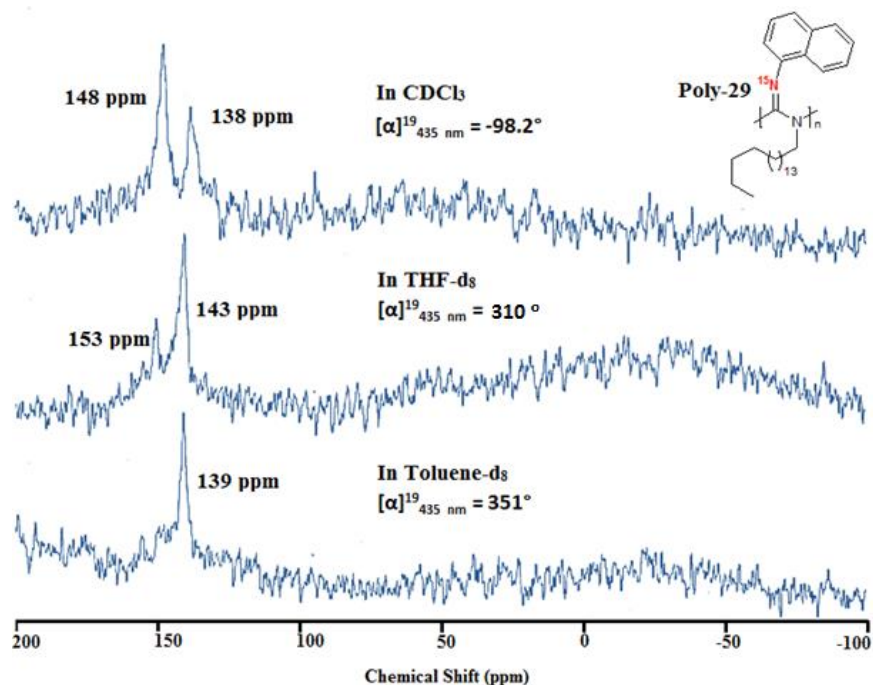


Figure 3.10- ^{15}N NMR of **Poly-29** in CDCl_3 , THF-d_8 , and toluene-d_8 displays two peaks correlating to specific conformations of the polymer found in solution.

The same trend seen in the IR spectra of the polymer in each solvent is observed in the ^{15}N NMR spectra. In CDCl_3 , two peaks are present with the peak at $\delta = 148$ ppm being the predominant chemical shift in the spectrum and the relative integration of each peak equals $\sim 2:1$. In THF-d_8 , both peaks are shifted slightly farther downfield and switch in intensities with the relative integration of the peaks at $\delta = 153$ ppm and $\delta = 143$ ppm equal to about $1:2$, respectively. In toluene-d_8 , the downfield peak is nearly completely diminished with one peak at $\delta = 139$ ppm in the imine region. The polymer is still regioregular since both ^{15}N NMR peaks correspond to the imine nitrogen. The IR and ^{15}N NMR peaks corresponding to the imine nitrogen/bond appear to be directly correlated with the SOR of the polymer.

High positive optical rotation values seem to correlate to the upfield peak in the ^{15}N NMR and the peak at 1602 cm^{-1} in the IR (state A) whereas the downfield peak and the peak at 1619 cm^{-1} seem to correlate to the lower negative values (state B). This data suggests that the switching process may occur in a concerted fashion with the OR changes observed consequence of fluctuating populations of two distinct conformations.

Chloroform, THF, and toluene were found to be the most versatile solvents for the chiroptical switching process in this polymer system so they were the natural choice for inaugural NMR studies. In an attempt to establish the extremes of the system, multiple solvents were studied to determine which solvents reach the maximum positive values and minimum negative values of SOR. Dichloromethane (DCM) was found to provide the highest SOR, $[\alpha]_{435\text{nm}}^{22} = 625^\circ$, at room temperature while benzene posted the lowest value, $[\alpha]_{435\text{nm}}^{22} = -152^\circ$, of any other solvent. The SOR of **Poly-29** in DCM and benzene, however, do not vary greatly as a function of temperature and never pass through 0° . The ^{15}N NMR spectra of the polymer in DCM- d_2 displays one peak corresponding to the imine nitrogen at $\delta = 139$ ppm which agrees with the trend of the upfield chemical shift correlating with the higher positive values of SOR. Also, in concurrence with the trend, the spectra in benzene- d_6 displays one downfield peak at $\delta = 148$ ppm matching up with the predominant peak in the spectra of **Poly-29** in CDCl_3 . This suggests that the vast majority of the naphthyl pendant groups attached to the imine nitrogen are in a single conformation in both DCM and benzene, albeit opposite from one another. This makes them an important subject for further study to determine what causes the polymer conformation to be increasingly stable in these solvents so that the switching process becomes less favored.

The chiroptical switching properties of the polymer are completely removed upon changing the connectivity of the naphthyl pendant group as evident by switching the imine connection from the 1-position to the 2-position of the ring.²² For this reason, poly(¹⁵N-2-naphthyl-*N*-octadecylcarbodiimide) (**Poly-30**) was synthesized using the original protocol designed by DeSousa et al.²⁵ The ¹⁵N NMR spectra of **Poly-30** in CDCl₃ displayed only one peak in the imine region unlike the very similar **Poly-29**. This proves that the presence of two conformations is site specific to the attachment of the naphthyl ring just like the optical rotation dependence on solvent and temperature. The ¹⁵N NMR spectra of **Poly-30** and **Poly-29** in DCM-d₂ and benzene-d₆ are shown in Figure 3.11.

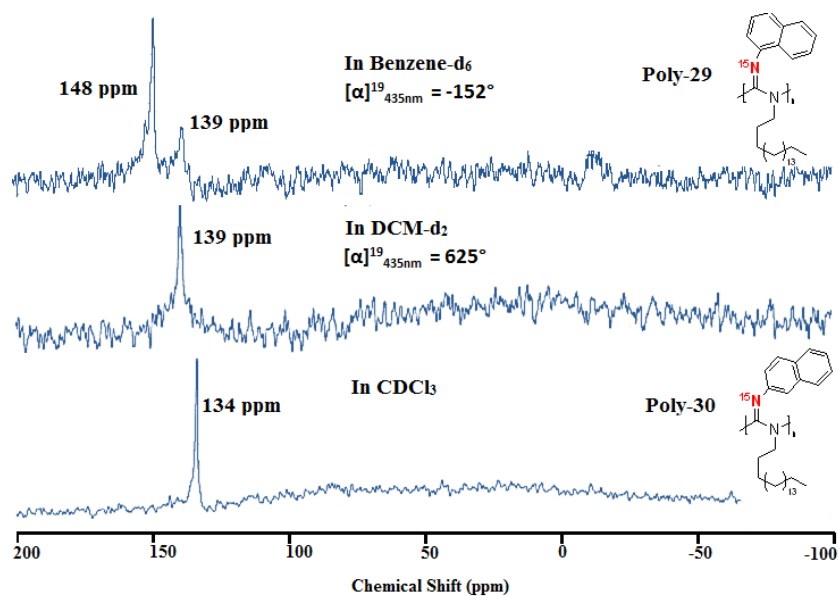


Figure 3.11- ¹⁵N NMR spectra of **Poly-29** in benzene-d₆ and DCM-d₂ displaying only one peak in each meaning the all of the polymer chains are predominantly in one conformation. The ¹⁵N NMR of **Poly-30** also displayed one peak confirming that the two conformations present in **Poly-29** are consequence of the switching process.

ECD analysis of the switching process is somewhat limited due to the UV cut offs in solvents of interest such as benzene, chloroform, and toluene. For this reason, ECD was carried out in DCM, THF and cyclohexane to provide solvents which cause a wide breadth of SOR when solvating **Poly-29**. (Figure 3.12) The high positive rotation values of **Poly-29** dissolved in DCM correlate well with the strong positive CD band at 244 nm. The strong negative CD Cotton effect exhibited by the polymer dissolved in cyclohexane (Cy) also correlates with the low negative SOR values also observed in Cy. **Poly-14** in THF is somewhat puzzling, however, due to significant negative CD band at room temperature despite having a positive SOR. This is most likely due to the overlapped Cotton effect of the backbone imine chromophore influencing the chirality opposite to the effect produced by the pendant group. This same effect explains the increased intensity of the CD band in cyclohexane compared to in DCM; since when the polymer backbone and naphthyl group exhibits a negative Cotton effect, the CD effect is additive. The blue shift of the λ_{\max} observed in both CD bands matches the shift reported by Kennenmur and co-workers and is most likely due to the auxochromic effect felt by the backbone upon reorientation of the side groups.²²

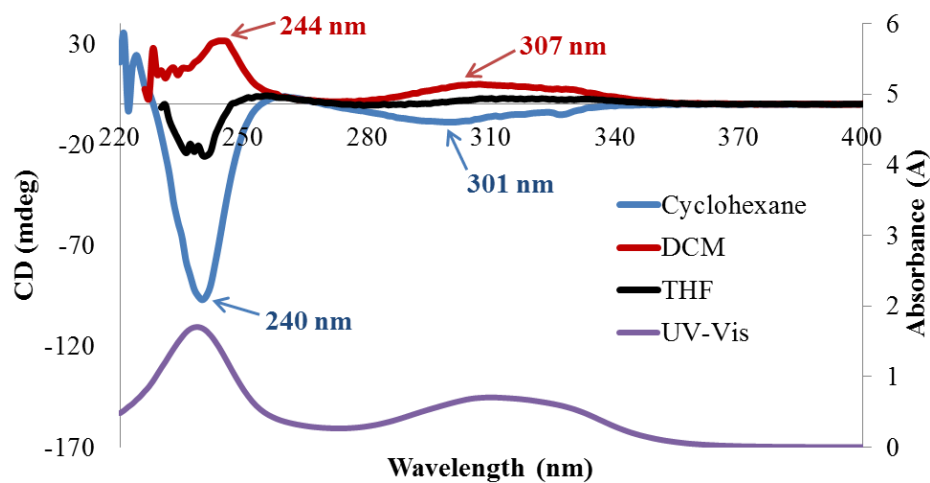


Figure 3.12- ECD spectra of **Poly-29** in DCM (red), THF (green), and cyclohexane (blue) show the switching CD Cotton effect as a function of solvent. The UV-Vis spectrum (purple) is also shown.

3.4 ^{15}N NMR studies in Mixed Solvent Systems-

The precise tuning of the specific rotation is possible in two different ways. One is by changing the temperature of the sample which is not practical for certain applications needing constant temperature. The other is by changing the composition of the solvent in the sample. **Poly-14** was shown to incrementally shift its chiroptical switching curves in chloroform simply upon addition of specific amounts of toluene to the system.²¹ The switching temperatures rise from about $-2\text{ }^{\circ}\text{C}$ to $9\text{ }^{\circ}\text{C}$ simply by adding 20 % (v/v) toluene into the system. The switching temperature was shifted all the way to $36\text{ }^{\circ}\text{C}$ when the solvent composition is primarily toluene (70 %). ^{15}N NMR analysis of **Poly-29** in various concentrations of mixed chloroform-toluene polymer solutions were launched to determine if

the conformational populations continue to vary in the same pattern seen before (Figure 3.12). As the concentration of toluene is increased, the downfield peak at $\delta = 148$ ppm begins to diminish and the peak at $\delta = 137$ ppm becomes more prominent. The relative integrations of the two peaks exhibit equal populations of the two conformations when the solvent mixture is 70 % chloroform. The polymer in this solvent composition (i.e., addition of the 30% of toluene into the system) shifts the SOR to -107° from -130° in pure CHCl_3 at 24°C . When the concentration of toluene is increased to 50 %, the upfield peak at $\delta = 137$ ppm begins to predominate with relative integrations of the two peaks equal to 3:2. The SOR reaches -39° in the 50-50 mixture of toluene-chloroform and passes through zero to 140° when increasing the concentration to 70 % toluene in chloroform (v/v). The downfield peak in the spectrum of **Poly-29** dissolved in a 70-30 mixture of toluene and CHCl_3 , respectively, is nearly completely diminished meaning that the polymer in this mixture of solvents behaves very similarly to how the polymer behaves in pure toluene.

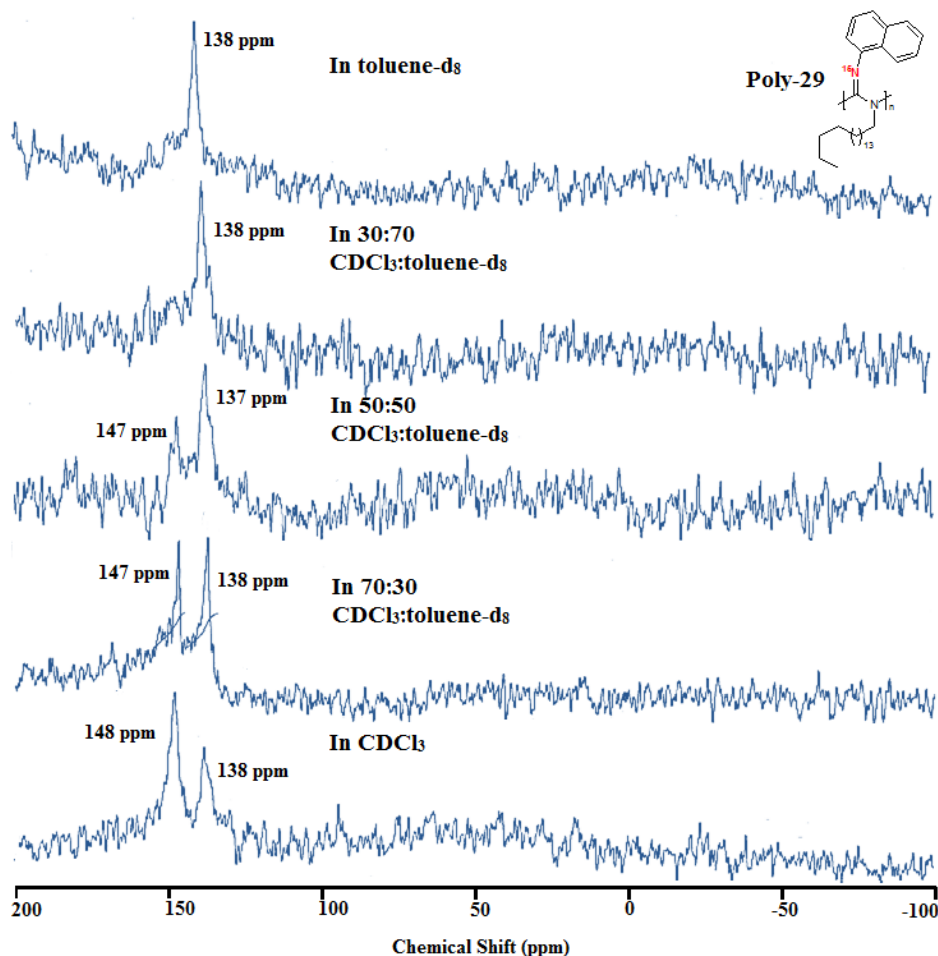
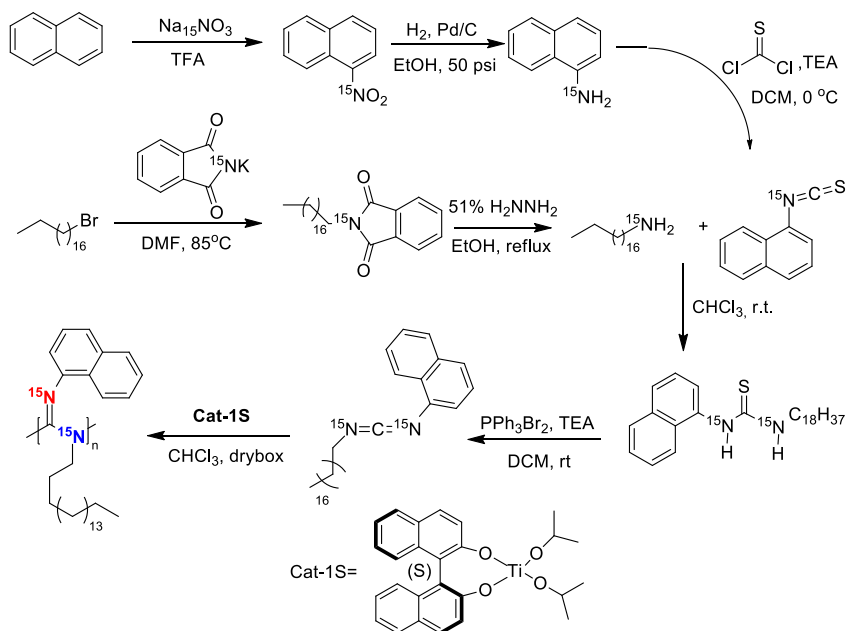


Figure 3.13- ^{15}N NMR spectra of **Poly-29** dissolved in varying concentrations of mixed chloroform-toluene systems to selectively tune the populations of the two polymeric conformations.

3.5 Effect of the Switching Process on the Amine Nitrogen-

The chiroptical switching process is known to have a great deal of effect on the imine nitrogen and its environment as evident by FTIR spectroscopy. It is still unclear, however, whether the amine nitrogen plays a role or is even affected in the overall process. To probe

the effect of the process on the amine nitrogen, a new synthesis scheme was created to produce the di-labeled poly[^{15}N -(1-naphthyl), ^{15}N -octadecylcarbodiimide] (**Poly-31**). To form the labeled *n*-octadecylamine, 1-bromooctadecane was reacted with 98% ^{15}N -enriched potassium phthalimide followed by deprotection of the phthalimide group with hydrazine. ^{15}N -1-naphthylamine was synthesized using the same procedure as before and subsequently reacted with thiophosgene and TEA to form the ^{15}N -labeled 1-naphthyl isothiocyanate. The ^{15}N -enriched *n*-octadecylamine was then coupled with the labeled 1-naphthyl isothiocyanate to form the di-labeled ^{15}N -1-naphthyl- $^{15}\text{N}'$ -octadecylthiourea which was then protodesulfurated to the corresponding carbodiimide. The monomer was then polymerized with **Cat-2S** to form **Poly-31**. The enantiomer of the catalyst used for the polymerization of **Poly-29** was employed to see if the opposite handed helix of **Poly-31** formed upon polymerization would affect the presence of the peaks in the imine region of the ^{15}N NMR spectra. The SOR profiles have been shown to reverse (positive values become negative values) which is typical when observing mirror images via polarimetry. The synthesis of **Poly-31** is shown in Scheme 3.3. The chiroptical switching profile of the polymer displays significantly diminished amplitude which is again most likely attributed to the difference in molecular weight and/or the purity of the catalyst used (Figure 3.14).



Scheme 3.3- Synthesis of **Poly-31** using the ^{15}N -enriched reagents $\text{Na}^{15}\text{NO}_3$ and ^{15}N -potassium phthalimide.

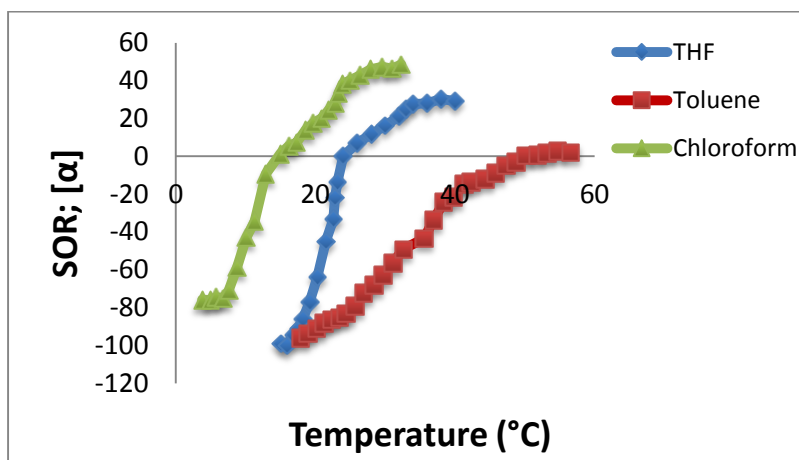


Figure 3.14- VT-polarimetry of **Poly-31** THF, toluene, and chloroform displays a SOR change $\sim 150^\circ$ simply by varying the temperature and/or the solvent.

The lower molecular weight of **Poly-31** does provide an advantage for ^{15}N NMR collection. Due to the high viscosity of the NMR solution of **Poly-29** (a result of increased amounts of chain entanglements in higher MW polymer samples), only about 20 mg of the polymer was able to be utilized while still maintaining a free flowing solution. This, as well as the fact that this polymer has the highest molecular weight per repeat unit of any other polymer tested, resulted in the lower resolution of the ^{15}N NMR spectra. The NMR samples of **Poly-31**, however, contained about 40 mg of the polymer and, in turn, resulted in a significant increase of the signal-to-noise ratio in the spectra collected. The initial ^{15}N NMR spectra were collected in the same solvents as in the studies of **Poly-29** (CDCl_3 , THF-d_8 , and toluene- d_8 in Figure 2.19). The resulting peaks corresponding to the imine nitrogen of **Poly-31** mimicked the peaks seen in the spectra of **Poly-29** with the same pattern observed in all three solvents. The amine nitrogen also displayed two peaks in a mirror image of the imine nitrogen chemical shifts. In CDCl_3 , the peak at $\delta = 148$ ppm for imine nitrogen and the peak at $\delta = 11.5$ ppm corresponding to the amine nitrogen predominate in the spectra, whereas the peaks at $\delta = 138$ ppm and $\delta = 19.9$ ppm correlate with the minority population of polymer chains. The spectrum in THF-d_8 continues the trend with the intensities of both sets of peaks switching. Another interesting observation is the shift downfield of all four peaks. This was also observed in the spectrum of **Poly-29** where both chemical shifts corresponding to the imine nitrogen migrate downfield a total of 5 ppm. This can most likely be attributed to some specific solvent-backbone interaction that adds to the magnetic shielding of the backbone nitrogens. In toluene- d_8 , the peaks are also shifted slightly downfield. This observation differs from the peak identified in the imine region of **Poly-29** in toluene- d_8 in which the peak

corresponding to the imine nitrogen is located at $\delta = 139$ ppm. This purpose of this outcome is still unknown and is under further investigation. The populations of polymer conformations, however, correlate perfectly with the expected trend seen with **Poly-29**. The peaks $\delta = 151$ ppm and $\delta = 14.7$ ppm are nearly completely diminished with only one peak in both the imine and amine regions. These spectra can be found in Figure 3.16.

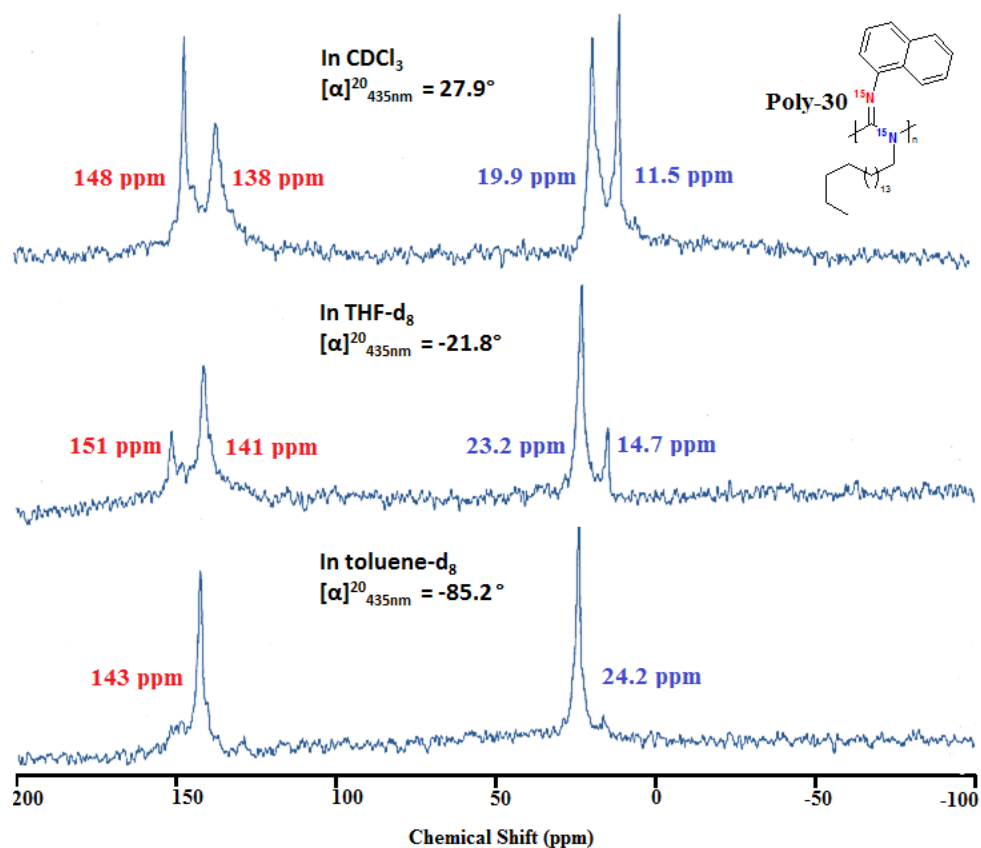


Figure 3.15- ^{15}N NMR spectra of **Poly-31** in CDCl_3 , THF-d_8 , toluene-d_8 showing the effect of the chiroptical switching phenomenon on the amine nitrogen.

As previously stated, the SOR of polymers derived from the same achiral monomers reverse when employing the enantiomer of the polymerization catalyst. The two possible helical orientations are chiral, mirror images of one another (see Figure 1.1). As a result of the opposite handed helical conformation of **Poly-31** compared to **Poly-29**, the chiroptical switching profile of **Poly-31** is the mirror image, albeit with diminished amplitude, of **Poly-29** (see Figures 3.8 and 3.15). The populations of the two secondary conformations remains constant between the two polymer samples, however, supporting the fact that the populations of the secondary polymer structures in the polymer sample are independent of the chirality of the helix.

3.6 Variable Temperature ^{15}N NMR of Poly-29 and Poly-31-

In addition to changing the solvent composition of dilute polymer solutions, altering the temperature in solutions of **Poly-29** and **Poly-31** causes the SOR and CD to vary drastically in a reversible fashion. As expected, variable temperature ^{15}N NMR provided further insight into how the population of each specific polymer conformation is modulated as a function of temperature. Both **Poly-29** and **Poly-31** have very similar if not identical integration values corresponding to the two states of the imine nitrogen so, for simplicity, the integrations will be discussed for **Poly-29** only. The ^{15}N NMR spectra of **Poly-29** and **Poly-31** at 35, 40, 45, 50, and 55 °C in toluene- d_8 are displayed in Figure 3.16 and Figure 3.17, respectively. When the temperature is increased and the SOR of the polymer sample decreases, and the intensity of the peak at $\delta = 152$ ppm slowly increases suggesting that the

population of the secondary conformation corresponding to the downfield chemical shift is also increasing. At 45 °C, the relative integration of the downfield peak and the peak at $\delta = 142$ ppm reveals ~1:2 ratio, respectively, which mimics the polymers behaviors in THF at room temperature. At 55 °C, the trend continues the conformation population analogous to the downfield peak grows in intensity integrating relative to the upfield chemical shift to 1:1.5, respectively. In all solvents, state B is populated with increasing abundance as temperatures increase evident by the ^{15}N chemical shift at ca. 150 ppm and the negative SOR values.

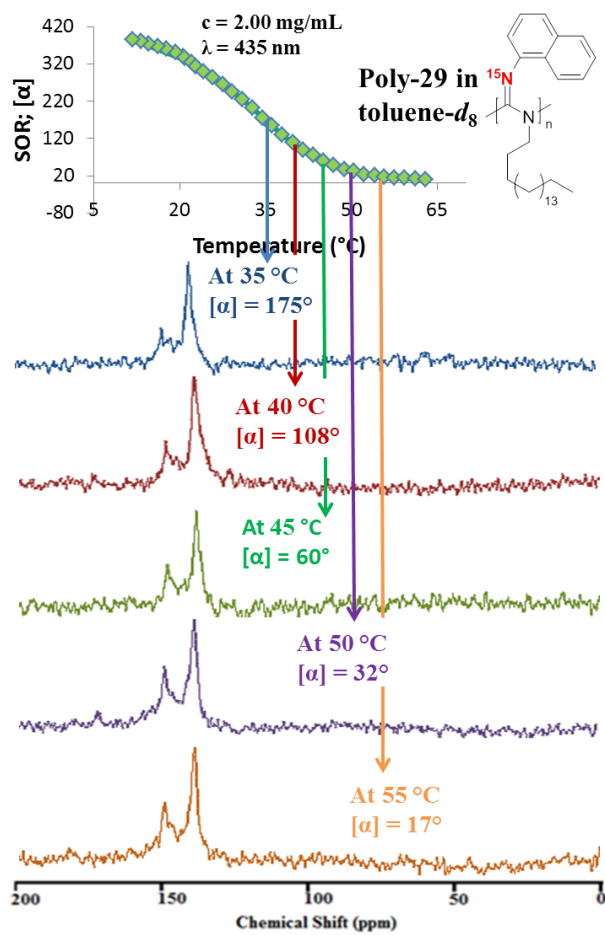


Figure 3.16- VT- ^{15}N NMR spectra of **Poly-29** in $\text{toluene-}d_8$ at 35 - 55 °C showing the conformational shift upon heating the polymer solution.

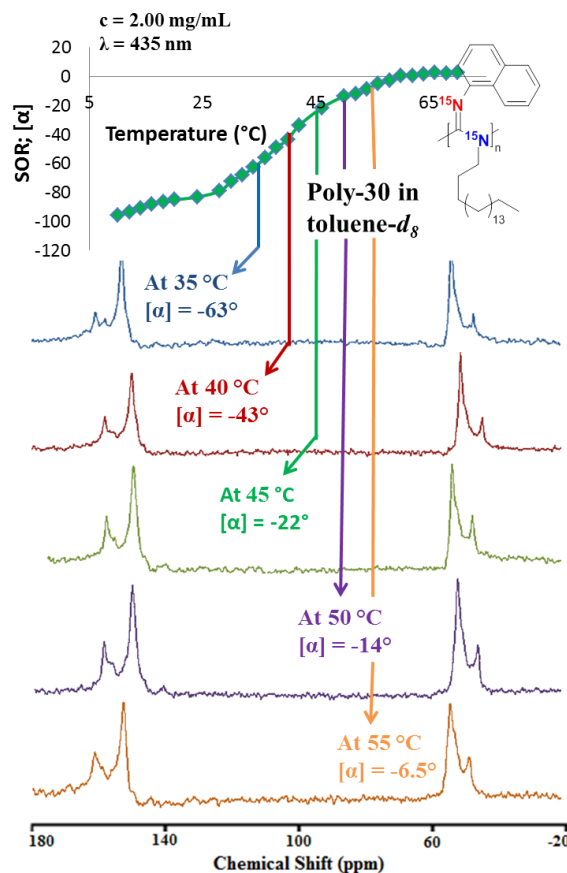


Figure 3.17- VT- ^{15}N NMR spectra of **Poly-31** in toluene- d_8 at 35 - 55 °C showing the conformational shift upon heating the polymer solution.

The VT- ^{15}N NMR spectra of **Poly-29** and **Poly-31** in THF- d_8 are significantly different with the populations of each conformation altering much more drastically than in toluene- d_8 (Figure 3.18 and 3.19, respectively). To observe the most significant alterations of the polymer conformation in THF, temperatures of 20, 25, 30, 35, and 40 °C were chosen for variable temperature studies. At 20 °C, the upfield chemical shift in the ^{15}N NMR spectrum of **Poly-3** predominates significantly with the relative integration of the downfield peak with respect to the upfield peak equal to about 1:2.2. Increasing the temperature of the NMR

solution to 30 °C results in an increase in the relative population of the downfield chemical shift at 151 ppm and a decrease in the specific OR from $[\alpha]_{435}^{25} = 313^\circ$ to $[\alpha]_{435}^{30} = 7.1^\circ$. Further heating the solution to 40 °C causes the specific OR to reach the minimum value in THF of $[\alpha]_{435}^{40} = -55^\circ$ and the relative ratio of the downfield peak to the upfield peak equal to about 1:1.1, respectively. Interestingly, the populations of each **Poly-3** conformation never favors the state corresponding to the downfield shift in THF similar to when dissolved in toluene- d_8 , however, the population change is slightly more significant.

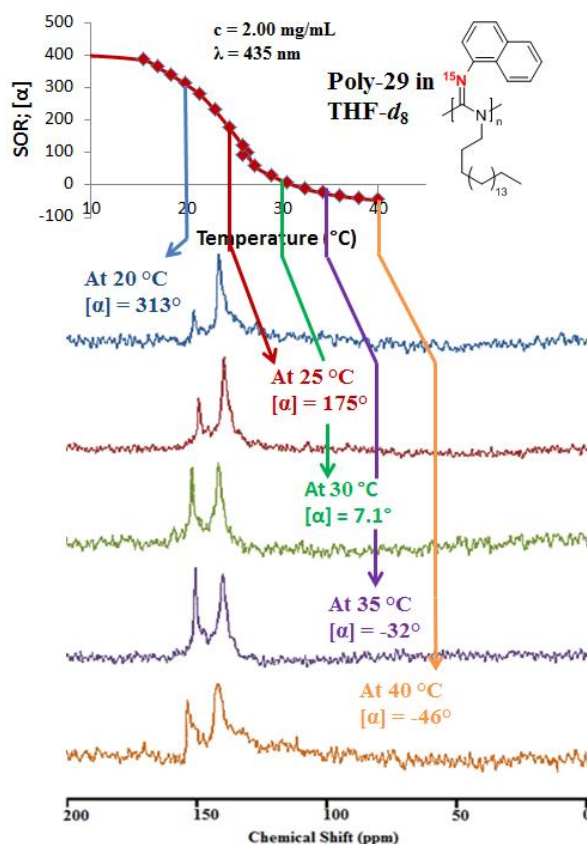


Figure 3.18- VT- ^{15}N NMR of **Poly-29** in THF- d_8 at 20 - 40 °C displaying a more drastic population shift compared to that of toluene polymer solutions.

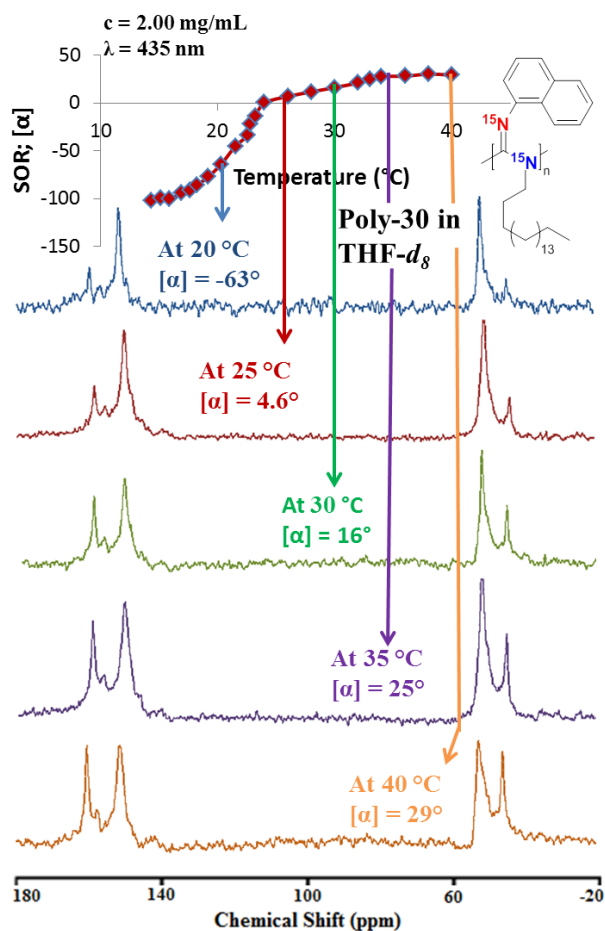


Figure 3.19- VT-¹⁵N NMR of **Poly-31** in THF-*d*₈ at 20 - 40 °C displaying a more drastic population shift compared to that of toluene polymer solutions.

In CDCl₃, the VT-¹⁵N NMR spectra of **Poly-29** and **Poly-31** display a considerably more pronounced population change over a smaller range of temperatures when compared to toluene-*d*₈ and THF-*d*₈ (Figure 3.20 and 3.21, respectively). At 0 °C, the specific OR of **Poly-29** is at the maximum value (ca. $[\alpha]^{19}_{435} = 418^\circ$) in this particular solvent. ¹⁵N NMR analysis at this temperature reveals a single peak in the spectra matching nicely with the trend seen in previous spectra (see experimental section). The population of state B grows significantly in population with respect to the upfield peak upon heating the polymer solution

to 10 °C with relative integrations of the two peaks equal to about 1:2. The downfield conformation becomes even more prominent when the temperature is increased to 15 °C. An equal amount of polymer chains adopt both states upon further heating to 17.5 °C. At 20 °C, the equilibrium shifts in favor of state B corresponding with the downfield shift, with the relative integrations of the two peaks equal to ~1.2:1. The VT-¹⁵N NMR spectra of **Poly-29** and **Poly-31** are shown in Figure 3.20 and 3.21, respectively. This data continues to match nicely with the observed trend between the chiroptical changes and the population change of two distinct conformations.

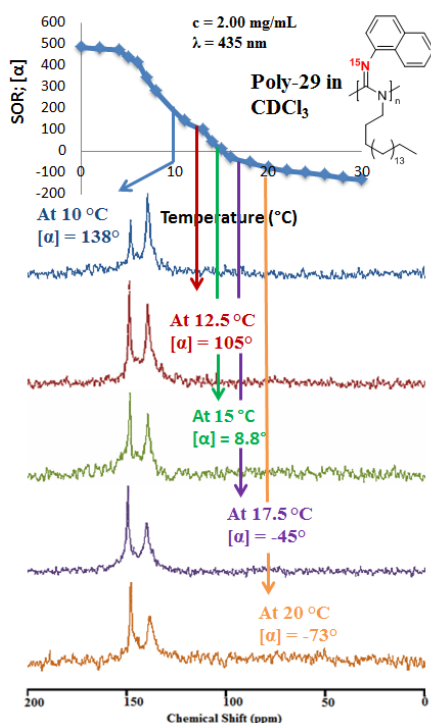


Figure 3.20- VT-¹⁵N NMR spectra of **Poly-29** in CDCl₃ at 10 - 20 °C showing the most pronounced population change over a smaller temperature range.

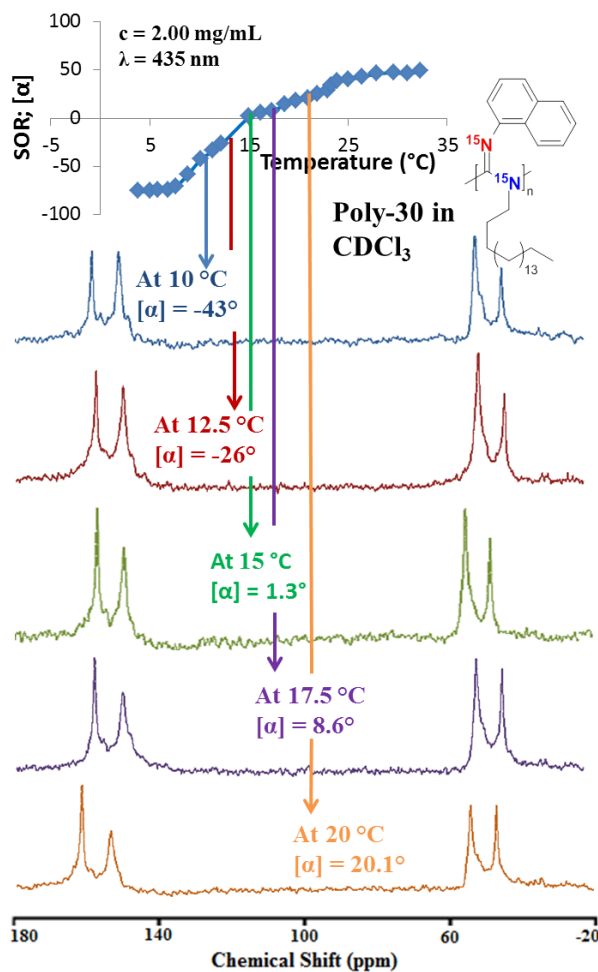


Figure 3.21- VT-¹⁵N NMR spectra of **Poly-31** in CDCl₃ at 10 - 20 °C showing the most pronounced population change over a smaller temperature range.

3.7 Using Van't Hoff Analysis to Calculate the Thermodynamic Parameters of Switching-

Since we can now quantify the specific proportions of each polymer conformation in solution at different temperatures, it is now possible to calculate empirically the change in

enthalpy and entropy during the equilibrium process. This can be accomplished using the van't Hoff relationship shown below in equation (1) where K_{eq} is the equilibrium constant, R is the gas constant (1.989 cal/(mol•K)), and T is the temperature in Kelvin. This method is used extensively to study biological macromolecular systems in order to examine specific functions and dynamic behavior in DNA and peptides.^{26,27}

$$(1) \ln(K_{eq}) = -\frac{\Delta H_{switching}}{RT} + \frac{\Delta S_{switching}}{R}$$

For our system where the equilibrium consists of the interconversions of two specific states, the relative integrations of the peaks in the ^{15}N NMR spectra at various temperatures allows for a qualitative measure of the specific proportions of each conformation in solution. With these proportions, one can now calculate K_{eq} simply by dividing the relative concentration of state B by the relative concentration of state A (i.e., $K_{eq} = [\text{B}]/[\text{A}]$). Plotting the values of $\ln(K_{eq})$ vs. $1/T$ should result in a linear plot with the slope equal to $-\Delta H_{eq}/R$ and the y-intercept equal to $\Delta S_{eq}/R$. The results of this analysis are shown in Figure 3.22.

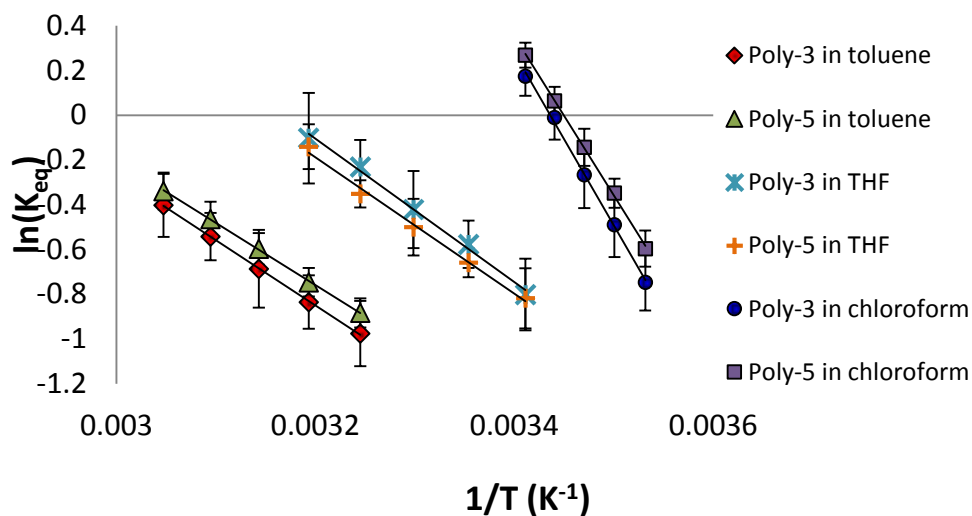


Figure 3.22- Van't Hoff Plots of **Poly-29** and **Poly-31** in toluene- d_8 , THF- d_8 , and $CDCl_3$ used to determine the thermodynamics of the chiroptical switching process.

This analysis provides consistent results between different batches of identical polymers. The results of the van't Hoff analysis and the errors associated to the error of integration for both **Poly-29** and **Poly-31** are outlined in Table 1. The van't Hoff Plots for **Poly-31** match up very well with the plots of **Poly-29** providing similar energy values further substantiating the validity of this analysis.

Table 3.1- Empirically calculated van't Hoff enthalpies and entropies of the reversible, chiroptical switching process using the relative integration the nitrogen-15 NMR peaks corresponding to the imine nitrogen to measure the populations of each polymer conformation.

<i>Solvent</i>	<i>Poly-3</i>			<i>Poly-5</i>		
	<i>Toluene</i>	<i>THF</i>	<i>Chloroform</i>	<i>Toluene</i>	<i>THF</i>	<i>Chloroform</i>
<i>Specific OR changes</i> ^a	15°–375°	-50°–406°	-132°–488°	-76°–46°	-99°–30°	-99°–3°
$\Delta H_{switching}$ (kcal/mol)	5.8 (± 2.9)	6.4 (± 3.3)	15 (± 3.4)	5.5 (± 1.4)	6.1 (± 2.2)	14 (± 2.4)
$\Delta S_{switching}$ (cal•mol ⁻¹ •K ⁻¹)	17 (± 9.0)	20 (± 11)	53 (± 12)	16 (± 4.5)	19 (± 7.5)	49 (± 8.3)
$\Delta G_{switching}$ @ 25 °C (kcal/mol) ^b	+0.77	+0.36	-0.37	+0.71	+0.40	-0.39

^a All specific OR measurements recorded for 2.00 mg/mL in dilute, polymer solutions at 435 nm.

^b Free energy of switching estimated using the van't Hoff enthalpies and entropies

These polymers display positive enthalpy changes in all solvents indicating that we are populating a higher energy state as the conformations are shifted from state A to state B. Interestingly, both **Poly-29** and **Poly-31** have the highest observed $\Delta H_{switching}$ when dissolved in CHCl₃ despite the entire switching process occurring below room temperature. This is due to the larger quantity of polymer chains occupying the higher energy state B compared to the switching process in toluene. The driving force behind this phenomenon is the very large entropy change associated with the switching in CHCl₃. The increase in the enthalpies and entropies of switching for both polymers when the solvent is changed from toluene to THF to

chloroform implies that the change in disorder of the system (polymer and solvent) is substantially larger when the polymer is dissolved in CHCl_3 . If we assume that the entropy change associated with the specific molecular motion of the polymer will be the same in all solvents, then the large difference in $\Delta S_{\text{switching}}$ could be attributed to increased disorder in the chloroform solvent molecules as the polymer undergoes the switching process. This assumption is reasonable since both conformations present in solution are the same or very similar in all three solvents as evident by the comparable chemical shift values. This is most likely due to ordered solvent-polymer interactions between the chloroform solvent molecules and the polymer chains adopting state A.

As switching from state A to state B occurs, the solvent-polymer ordering becomes less, thus increasing the entropy of the system. An even stronger solvent-polymer ordered interaction in toluene cause the switching process to become less favorable and, in turn, inhibits the polymer chains from predominantly adopting the higher energy state B. We propose that the toluene solvent molecules may associate with the polymer chains more favorably with respect to CHCl_3 through ordered π - π stacking between the solvent and the naphthyl pendant groups. Due to this increasingly ordered interaction, the switching phenomenon from state A to state B is much less favorable in toluene due to the diminished propensity of the toluene molecules to dissociate upon switching. This hypothesis supports the higher observed switching temperatures of **Poly-29** and **Poly-31** in toluene as well as the limited number of polymer chains adopting state B in toluene.

The free energy of the switching process was then estimated using the van't Hoff energies measured for **Poly-29** and **Poly-31** (Table 1). The positive free energy values for both polymers in toluene and THF matches well with the higher switching temperatures of the polymers in both solvents and the fact that the equilibrium never shifts in favor of the state B at any temperature observed. Additionally, the estimated free energy of switching for **Poly-29** and **Poly-31** in chloroform reveals negative $\Delta G_{\text{switching}}$ which is also in concurrence with the observed trend due to the entire switching process occurring below room temperature and the equilibrium shifting in favor of the downfield conformation at temperatures greater than 18 °C. This new data offers new insight in what has proven to be an intensely interesting polymer behavior, but is limited in the determination of the specific structures associated with each state. For this, VCD spectroscopy coupled with density functional theory (DFT) calculations was employed to definitively identify the mechanism of switching.

3.8 Identifying the Specific Conformations of State A and B Using VCD spectroscopy-

Vibrational circular dichroism (VCD) has only recently emerged as one of the most powerful characterization tool for assigning absolute configurations in chiral small molecules,²⁸⁻³¹ metal complexes,³²⁻³⁴ and nanoparticles.^{35,36} In addition, VCD spectroscopy has been used extensively to study the folding and conformational behavior of biological macromolecules such as DNA,³⁷ RNA,³⁸ and peptides.^{39,40} Coupled with density functional theory (DFT) modeling, VCD has also opened up new opportunities in the absolute

identification of the specific single-handed helical sense in chiral polymers. Merten et al. previously performed VCD spectroscopy and Raman Optical Activity (ROA) coupled with density functional theory (DFT) calculations to assign a *P* helical conformation to poly(trityl methacrylate) polymerized via anionic polymerization initiated by *n*-butyl lithium and (–)-sparteine.^{41,42} Additional reports identifying the specific helical handedness in chiral polyisocyanides,⁴³ polythiophenes,⁴⁴ and polycarbodiimides⁴⁵ have also been recently published further substantiating the usefulness of this characterization tool.

To better understand the two specific conformational states associated with the chiroptical switching process, VCD spectroscopy was performed on the unlabeled **Poly-14** (formed using **Cat-2R**) in different solvents to observe the subtle changes in the chiroptical response through specific vibrational modes of the polymer (most notably the C=N imine stretch). For this analysis, DCM-*d*₂ (state A), THF-*d*₈ (2:1 state A:state B), and CDCl₃ (1:2 state A:state B) were chosen as the solvents to provide a wide breadth of conformational populations. The deuterated forms of the solvents were employed in order to shift any overlapping solvent vibrational modes out of the area of interest. Because of the significant overlap in the VCD and IR spectra of toluene and benzene with **Poly-14**, these solvents were not used for this technique. These initial VCD and IR results can be found in Figure 3.23.

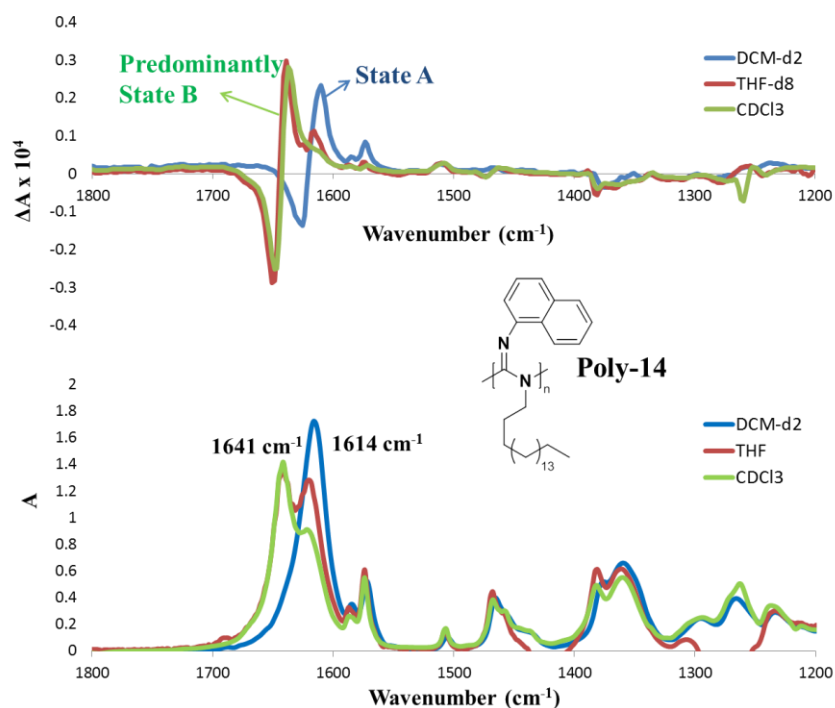


Figure 3.23- VCD and IR spectra of **Poly-14** in DCM- d_2 (blue), THF- d_8 (red), CDCl_3 (green) showing different spectra corresponding to the two different states of chiroptical switching.

The IR and VCD spectra of **Poly-14** in the various solvents display distinct differences in the characteristic bands corresponding to the C=N imine stretching mode and the C=C naphthyl ring breathing mode. In DCM- d_2 , the imine stretching vibration appears at 1614 cm^{-1} with a -/+ bisignate VCD couplet and the naphthyl breathing mode shows a positive VCD band at 1572 cm^{-1} . When **Poly-14** is predominantly adopting state B, as it is in CDCl_3 , the imine VCD bisignate experiences a blueshift to 1641 cm^{-1} and appears as two peaks in the IR spectra (1641 cm^{-1} and 1614 cm^{-1} , respectively). Additionally, the positive VCD band correlating with the C=C aromatic breathing mode becomes VCD inactive upon

population of state B. In THF-*d*₈, both conformations are visible in the VCD spectra further substantiating the presence of both conformations as observed in the ¹⁵N NMR spectra of **Poly-29** and **Poly-31**. These findings confirm that the switching process can be monitored by VCD spectroscopy unlike **Poly-6** which showed no significant changes in the VCD upon switching. All other IR bands below 1500 cm⁻¹ show only weak and negligible VCD activity.

In order to accurately correlate the observed experimental spectra with specific polymer conformations, high-level DFT calculations are necessary to model both states and provide theoretical spectra for comparison. For this reason, two model conformations of **Poly-14** were constructed consisting of seven repeating units oriented to form a right-handed *P*-helix with the octadecyl side group shortened to a methyl for simplicity. The simplistic representation of the model with atom labels is shown in Figure 3.24 and the actual optimized 3-D model structure is shown in Figure 3.25.

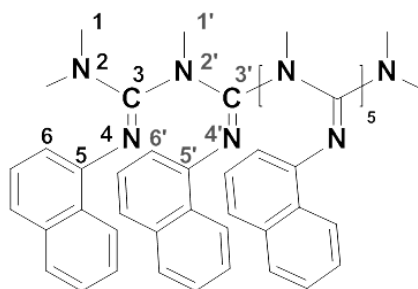


Figure 3.24- Simplistic representation of the DFT optimized model of **Poly-14** with atom labels.

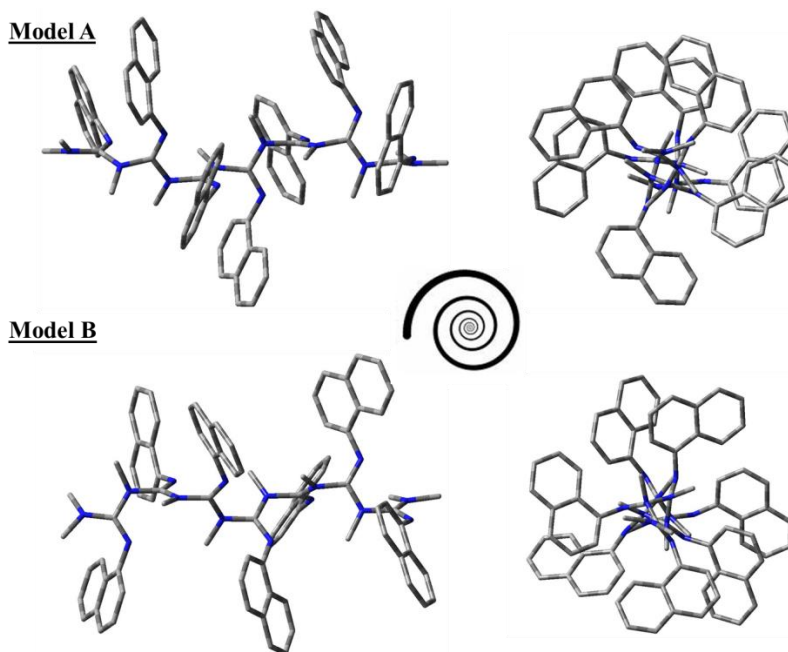


Figure 3.25- Two simplified 7mer model structures of **Poly-14** optimized using DFT calculations with right-handed helicity (*P*-helix) and oppositely oriented naphthyl pendant groups shown in the side view (left) and the view down the helix (right).

The two constructed geometries were optimized at the B3LYP/6-31G(2d,p) level of theory with the implicit solvation IEFPCM(chloroform) model without any geometry constraints. The final conformational geometries showed the $C_3-N_4-C_5-C_6$ naphthyl bridge angle is on average 135° in model A and is reoriented to -124° in model B (see Figure 3.24 for atom labels). The theoretical spectra associated with both models show an astounding level of agreement with the experimental VCD spectra of **Poly-14**. The calculated VCD and IR spectra of model A displays a near exact match to observed spectra of **Poly-14** in $DCM-d_2$ (state A). In addition, the VCD and IR spectra of **Poly-14** in $CDCl_3$ (predominantly state B) correlate very nicely with the theoretical VCD spectra model B. Especially noteworthy is the

fact that not only the shift of the C=N stretching vibration is predicted by the calculation, but also the silencing of the naphthyl breathing modes in model B. The calculations also give a predicted value for the optical rotation which nicely matches the experimentally observed trend of a large positive optical rotation for model/state A (calculated $[\alpha]_D = +1880^\circ$) and a negative value for model/state B (calc. $[\alpha]_D = -1060^\circ$). Interestingly, although both starting geometries featured the same helical backbone angles, the final backbone C₁-N₂-C₃-N₄ dihedral angles obtained for models A and B were (on average) -70° and -103° , respectively. Therefore, the reorientation of the naphthyl side groups lead to an alteration of the helical pitch from 5/1 to a more contracted 7/2 pitch. Hence, after many years of ambiguity, VCD has finally provided the necessary capabilities to definitively assign and confirm the specific conformational reorientation responsible for this intensely interesting polymer property. These results can be found in Figure 3.26.

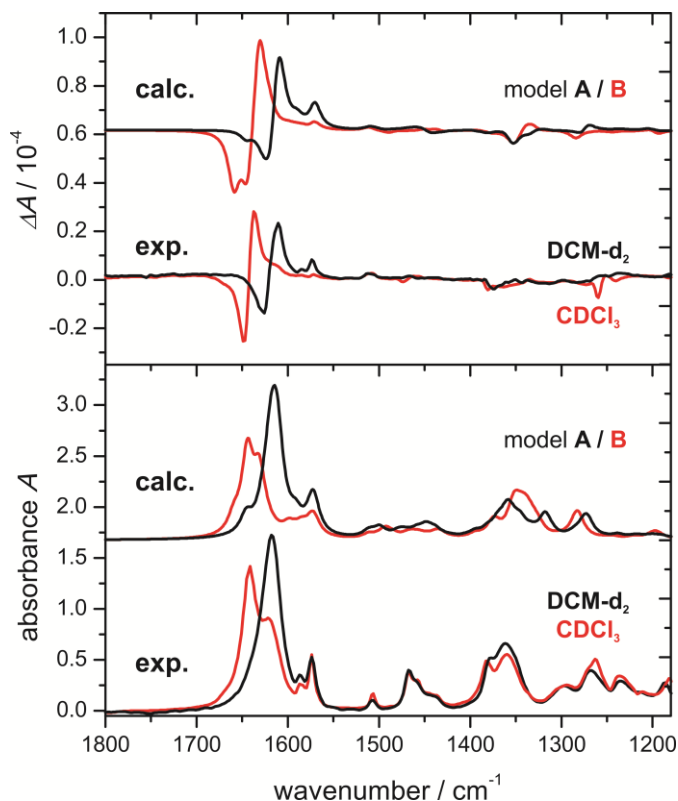


Figure 3.26- Experimental VCD and IR spectra of **Poly-14** in DCM- d_2 and $CDCl_3$ showing different spectra corresponding to the two distinct side group conformations along with DFT calculated VCD and IR spectra of two optimized 7mer models.

3.9 Comparing VCD Spectra of Poly-6 and Poly-14-

In the previous study by Tang et al., **Poly-6** was studied using VCD spectroscopy.²⁰ **Poly-6** shows a positive SOR in toluene, and negative values in chloroform similar to that of **Poly-14**. However, there was no significant difference between the VCD spectra measured in the two different solvents. Interestingly, the VCD couplet of the C=N stretching vibrations of **Poly-6** was observed as a strong bisignate couplet at 1641 cm^{-1} which is the same wavenumber and VCD pattern found for the C=N vibrations of **Poly-14** in chloroform. This

correlation implies further similarities between the helical structures of the polymers. The key to a deeper understanding of these structural similarities are the calculated structures and the corresponding VCD spectra. As the reorientation of the side groups has been identified as the main cause of the large changes in SOR and ECD spectra of both polymers, the change of the VCD spectra of **Poly-14** is likely linked to an additional effect.

After the optimization of the two 7mer-structures, a change in the helical pitch was noted. Going from model A to model B (or from DCM to chloroform), the helical backbone was found to contract from a 5/1 to a 7/2 pitch. In order to evaluate whether this contraction results in the change of the VCD spectra, two additional models A' and B' were generated which are supposed to reflect the effect of the helix pitch. Model A' featured the optimized 5/1-backbone of model A with the naphthyl group orientation of model B (angle $C_3-N_4-C_5-C_6 = -120^\circ$), while B' consisted of the 7/2 backbone of model B with the side groups oriented like in model A (angle $C_3-N_4-C_5-C_6 = +140^\circ$).

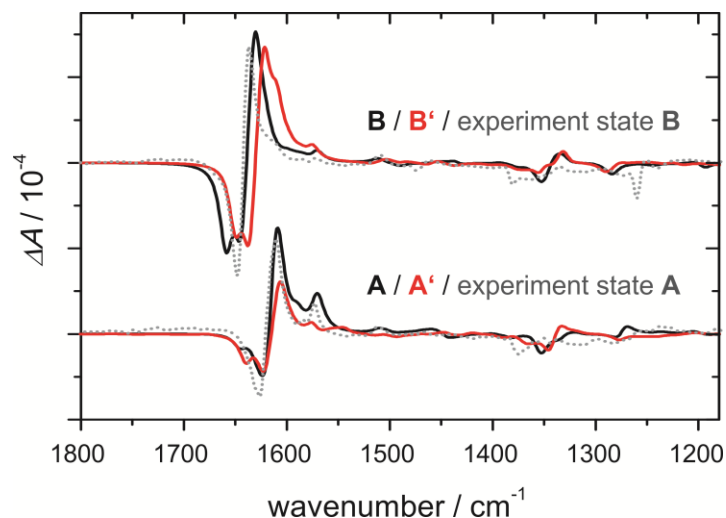


Figure 3.27- The effect of the helix pitch on the calculated VCD spectra highlighted by comparison of the optimized models A (5/1 helix, $C_3-N_4-C_5-C_6 = 135^\circ$) and B (7/2 helix, $C_3-N_4-C_5-C_6 = -125^\circ$) with the A' (5/1 helix, $C_3-N_4-C_5-C_6 = -120^\circ$) and B' (7/2 helix, $C_3-N_4-C_5-C_6 = +140^\circ$)

VCD spectra were calculated for both models without prior optimization in order to keep the helical structure identical with the corresponding models A and B. From the obtained spectra shown in Figure 3.27, it can clearly be concluded that the change of VCD spectra when going from state A to B originated from the helix contraction. In fact, the effect of the naphthyl side group orientation is rather small compared to the change in the position and intensity of the bisignate VCD couplet of the C=N stretching mode. Therefore, it can be concluded that the change in OR and ECD is caused by the reorientation of the side groups while the change in the VCD arises from the change of the helical pitch. This helical contraction could also explain the large entropy gain upon switching from state A to B. This entropy gain is believed to be associated with the solvent molecules around the polymer chain. In state A, the helix is slightly more expanded allowing for solvent molecules to

penetrate the more accessible aliphatic sheath surrounding the helical backbone. Upon switching to state B, the helix contracts forcing the penetrated solvent molecules out of the aliphatic corona resulting in a large increase in entropy.

3.10 Attempted Synthesis of New, Chiroptical Switching Polycarbodiimides-

In addition to determining the mechanism of the switching process, another goal of my research was to further tune the attached pendant groups in order to optimize the system. This, coupled with the further insight provided by new data collected thus far and in the future, will potentially unleash a wealth of knowledge into the dynamic chiroptical properties of these polymers. Kennemur attempted to skew these properties when he synthesized a new series of chiroptical switching polycarbodiimides with varying electronic influences.⁴⁶ This was accomplished via attachment of an assortment of substituents at the 4-position of the naphthyl ring ranging from the mildly electron withdrawing chloro and bromo groups to the strongly electron donating methoxy group. (Figure 3.28) The electronics of these polymers showed a major influence on the switching profiles and eliminated the temperature dependent chiroptical properties in certain solvents for some of the polymers. For example, **Poly-32** showed versatile chiroptical properties with SOR changes reaching $\sim 1900^\circ$ in THF but the switching temperatures for the polymer dissolved in chloroform and toluene were altered greatly.

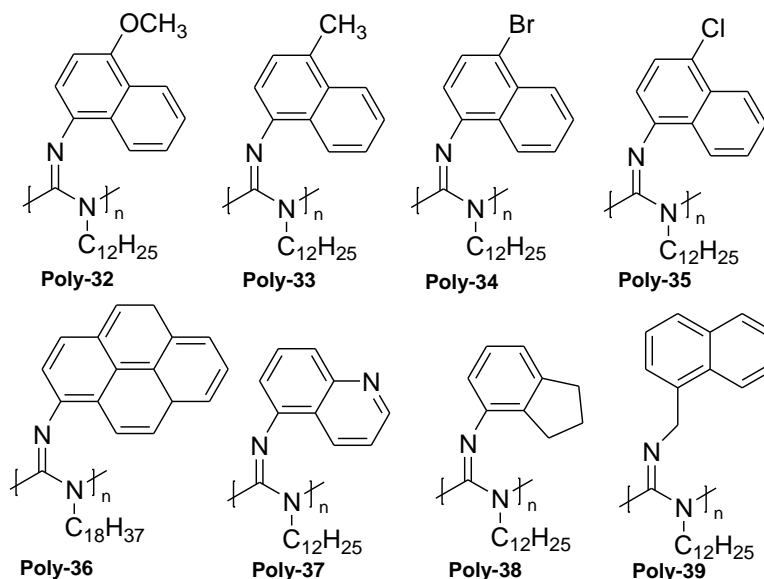


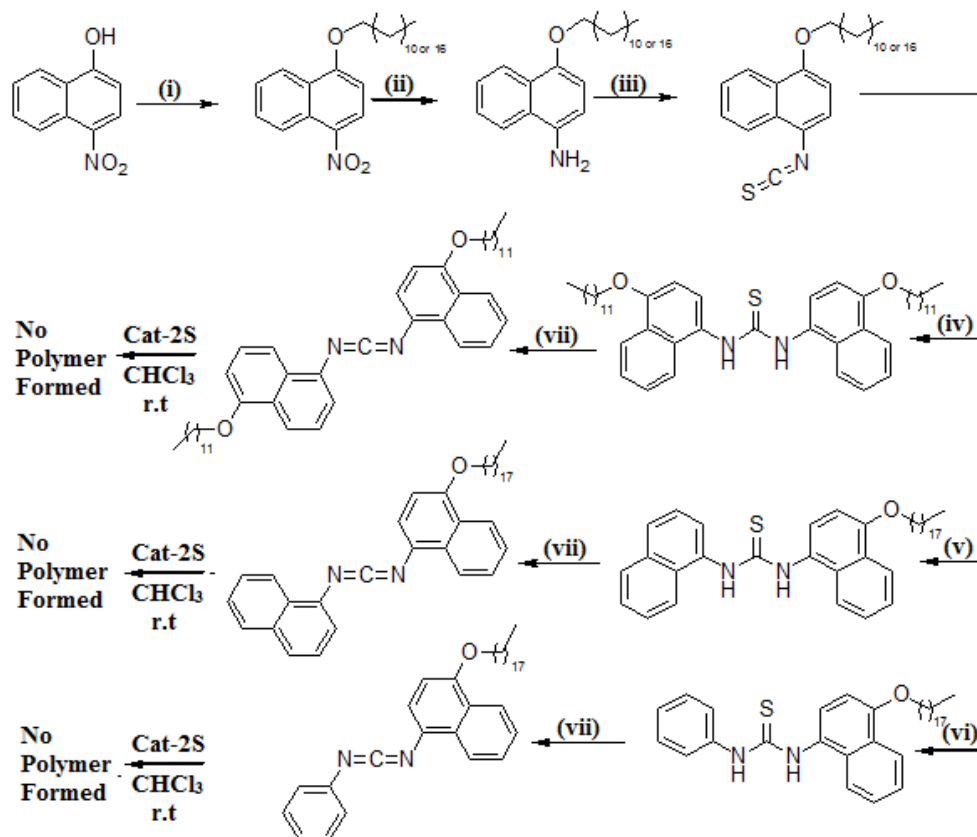
Figure 3.28- A new library of polycarbodiimides synthesized to determine the electronic, steric, and pendant group attachment effects on the switching process.

The switching temperature in toluene is shifted all the way to ~ 10 °C and remains in the negative regime for the majority of the process. In chloroform, the polymer never reaches negative values and the energy required for the conformational change to occur is much greater. Adding a simple methyl group onto the 4-position, as in **Poly-33**, causes the switching to be completely lost in all solvents tested. The more bulky **Poly-36** requires significantly greater energy for the conformational change to occur as anticipated due to the increased steric repulsion.²²

Kennemur also showed the ability to incorporate the 5-quinolyl pendant group (**Poly-37**) although the polymerization proceeded very slowly and took more than a month to complete. This is due to the reversible coordination of the nitrogen containing, heterocyclic

side group to the titanium(IV) center which competes with the coordination and insertion of the monomer into the amidinate propagating species. This polymer only showed the chiroptical switching properties in chloroform and with diminished amplitude when compared to **Poly-14**. This polymer is the first chiroptical switching polycarbodiimide with a heterocyclic, aromatic side group and could be used similarly to the pyridine containing polycarbodiimides as a chiral catalyst support. Combining the molecular switching properties with the chiral supporting properties may provide a polymer support capable of asymmetric induction. **Poly-37** did not show the ability for this to occur but, with further optimization, may still be possible. **Poly-38** and **Poly-39** showed no chiroptical switching under experimental conditions suggesting that a directly attached, fully aromatic pendant group with significant steric influences is necessary for the chiroptical switching to occur.

Research is currently ongoing to synthesize a switcher with directly attached aromatic systems occupying both the amine and imine nitrogen. Kennemur first attempted this when he synthesized *N,N'*-dinaphthylcarbodiimide and attempted to polymerize it with **Cat-2R**. The resulting polymer (or oligomer) precipitated from solution and was completely insoluble in all conventional solvents. This was not an unexpected outcome due to the need for long aliphatic chain spacers to solubilize **Poly-14** so the project was abandoned. Recently, the project was reinitiated with a new idea to directly attach the long aliphatic chain onto the 4-position of one or both of the aromatic rings. In addition to the di-naphthyl system, the naphthyl-phenyl substituted polycarbodiimide has never been synthesized and could greatly affect the switching process due to the altered pendant groups. The synthesis of these monomers is shown in Scheme 3.4.



Scheme 3.4- Synthesis scheme for potential di-aryl chiroptical switching polycarbodiimides. The reaction conditions for each step are as follows: (i) 1-bromododecane/1-bromooctadecane, K₂CO₃, DMF, 85 – 90 °C; (ii) H₂, Pd/C, MeOH, 50 psi; (iii) thiophosgene, TEA, DCM, 0 °C; (iv) 2nd eq. of amine, CHCl₃, Reflux; (v) 1-naphthylamine, CHCl₃, Reflux; (vi) aniline, CHCl₃, Reflux, (vii) PPh₃Br₂, TEA, DCM, 0 °C to r.t.

The 4-nitro-1-naphthol was alkylated using potassium carbonate and select alkyl bromides followed by reduction of the nitro-group by hydrogenolysis. The 1-naphthylamine derivatives were then reacted with thiophosgene and TEA to form the isothiocyanate and further reacted with various amines to form thioureas. Each thiourea was subject to protodesulfurization to form the corresponding carbodiimide monomer. Unfortunately, all

three monomers resisted polymerization at room temperature with **Cat-2S** due to the increased sterics of the pendant groups. Another reason for the decreased activity is the fact that all of the monomers synthesized were solid carbodiimides. This requires the use of solvent to dissolve the monomer which has been shown to slow the process significantly when compared to polymerizations in the bulk. For these reasons, the formation of even oligomers of the carbodiimides shown was not observed by FTIR spectroscopy (the main spectroscopic technique used to monitor these polymerizations).

The thermal decomposition of polycarbodiimide systems back to starting monomers limits the use of heat during polymerizations due to the potential cleavage of the backbone competing with polymer formation. In addition, elevated temperatures may cause the reversible dimerization (and trimerization) to occur creating the possibility of incorporating metathesis products in the polymerization. For these reasons, polycarbodiimides have almost exclusively been synthesized at room temperature. However, increasing the temperature over the melting point of the monomers will allow for solvent-free polymerizations. Polymerizations were attempted at 30, 50, and 70 °C but decomposition of the monomer was observed before any polymer was formed.

To continue to expand the versatility of the chiroptical switching polycarbodiimides, more polar side chains at the amine nitrogen should allow for the dissolution of the polymer in high polarity solvents such as dimethylformamide (DMF), dimethylsulfoxide (DMSO), acetonitrile and possibly even water. Water solubility in polycarbodiimide systems has been accomplished by attachment of various polar substituents and/or cationic side groups.⁴⁷ The

completely insoluble in high polarity solvents such as methanol, ethanol, DMF, DMSO, and water. Interestingly, **Poly-40** did not show any chiroptical switching in CHCl_3 and toluene. This is somewhat of a peculiar result considering the only difference between **Poly-40** and **Poly-14** is the solubilizing group attached to the amine nitrogen. It is clear that the increased polarity on the solubilizing pendant group greatly affects the overall switching process. One possible explanation that goes along with the hypothesized mechanism of switching is that the more polar side group allows for dissolution of the polymer. This could cause the dihedral angle of the polymer backbone to be slightly altered allowing the naphthyl pendant groups the necessary space to orient into state B shown in Scheme 3.4 and disfavoring state A. Due to the small amount of sample collected, no other solvents investigated. Increasing the chain length of the polar glycol subunit may promote water solubility. Another option is to directly tether a tertiary amine capable of methylation in post-polymerization. This would, in turn, form a quaternary, cationic amine salt which may introduce water solubility in the resulting polycarbodiimides.

3.11 Conclusions-

The synthesis of ^{15}N -labeled poly(^{15}N -1-naphthyl-*N*-octadecylcarbodiimide) (**Poly-29**) and poly(^{15}N -1-naphthyl- $^{15}\text{N}'$ -octadecylcarbodiimide) (**Poly-31**) has helped elucidate more insights on the chiroptical switching process. We have discovered that the process occurs in a concerted manner with the changes in specific OR being caused by varying populations of two specific polymer conformations. These populations were found to possess

extremely potent temperature and solvent dependence in all cases studied. Using VT-¹⁵N NMR, the thermodynamics parameters of the chiroptical switching process were empirically calculated through van't Hoff analysis. This analysis revealed that the switching process is endothermic (positive $\Delta H_{\text{switching}}$) in all solvents studied (toluene-*d*₈, THF-*d*₈, CDCl₃) indicating that the polymer is adopting a higher energy state upon switching from state A to B. The driving force behind this unique molecular switch is the large increase in entropy which is believed to be a result of increased disorder in the solvation sphere upon switching from state A to B.

Interestingly, CDCl₃ resulted in the highest enthalpy of the three solvents despite the entire chiroptical switching process occurring below room temperature. The compensating factor is the larger entropy change (ca. $\Delta S_{\text{switching}} = 53 \text{ cal}\cdot\text{mol}^{-1}\cdot\text{K}^{-1}$) associated with switching from state A to B in CDCl₃ when compared to that of toluene-*d*₈. The added order of the toluene solvent molecule is believed to be consequence of ordering of the local solvent molecules in some specific manner around the polymer chains (most likely π - π interactions between the solvent and the naphthyl pendant group). These interactions are believed to hinder the switching process causing the process to occur at higher temperatures and only a limited number of polymer chains to adopt state B. Additionally, the free energies of switching ($\Delta G_{\text{switching}}$) were also calculated at 25 °C with the van't Hoff enthalpies and entropies of **Poly-29** and **Poly-31** in all solvents. In concurrence with the observed trend, this analysis provided a negative $\Delta G_{\text{switching}}$ in CDCl₃ and a positive $\Delta G_{\text{switching}}$ in toluene-*d*₈ matching with the observed switching temperatures in both solvents.

To determine the specific conformational structure associated with both states of **Poly-14**, VCD spectroscopy was employed coupled with DFT calculations. The experimental IR and VCD spectra of each state were collected by dissolving **Poly-14** in DCM- d_2 (state A) and CDCl₃ (predominantly state B). These spectra were then correlated with DFT calculated VCD spectra constructed using two simplified 7mer models with oppositely oriented naphthyl pendant groups. The constructed theoretical and observed experimental spectra show an astounding level of agreement providing, for the first time, definitive evidence for the proposed mechanism of switching. In this mechanism, the naphthyl group is directed opposing the helical rotation (when polymerized with the **Cat-2R**) at low temperatures (state A) and, upon heating in switchable solvents, the pendants reorient to align with the backbone helicity. Additionally, this reorientation causes a significant contraction of the backbone helical pitch (ca. 5/1 to 7/2 pitch) which has been proven to be the true cause of the change in VCD whereas the pendant reorientation causes the change in ECD and SOR. After several years of ambiguity, the true cause of the chiroptical switching process observed in **Poly-14** and the thermodynamic parameters accompanying the process in the three most versatile solvents have now been definitively identified through ¹⁵N NMR and VCD spectroscopy.

3.12 Experimental Section-

Materials- The ¹⁵N-labeled starting materials- ammonium chloride (¹⁵NH₄Cl), ¹⁵N-potassium phthalimide, and sodium nitrate (Na¹⁵NO₃) were received from Cambridge Isotope

Laboratories (Cambridge, MA) as 99% ^{15}N -isotope enriched and used as received. All other reagents were used as received unless otherwise stated. All solvents were purchased commercial vendors such as Fischer Scientific (Hampton, NH) and Sigma Aldrich (Milwaukee, MI). The majority of NMR spectra were collected in deuterated chloroform or deuterated dimethyl sulfoxide (DMSO) purchased from Sigma Aldrich (Milwaukee, MI). The deuterated toluene, THF, DCM, and benzene NMR solvents were purchased from Cambridge Isotope Laboratories (Cambridge, MA) and used as received.

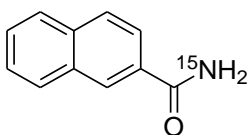
Instrumentation- ^1H NMR spectra were collected on both a Varian Mercury 400 MHz and 300 MHz NMR spectrometer with an Oxford Narrow Bore superconducting magnet. The majority of ^{15}N NMR and ^{13}C NMR spectra were conducted on the Varian Mercury 400 MHz Spectrometer. The variable temperature ^{15}N NMR spectra for van't Hoff analysis were collected on a new Bruker AVANCE IIITM 500 MHz NMR spectrometer for better resolution. IR spectra were collected on a Jasco Model 410 FTIR spectrometer either cast onto a KBr salt plate or pressed into a KBr pellet in the solid state. Mass spectrometry data was collected by the NCSU Department of Chemistry Mass Spectrometry Facility on the Agilent Technologies 6210 LC-TOF Mass Spectrometer. Molecular weight determination was performed using a Shimadzu Prominence Modular HPLC/GPC system connected to a refractive index (RI) detector relative to a polystyrene standard. A two-column system was employed consisting of an Agilent Mixed-E and Mixed-C column. The polymer samples were dissolved in HPLC grade chloroform (ca. 1.8 mg/mL) with 0.5% (v/v) *N,N*-dimethylethylenediamine added to the sample. The samples were passed through 0.45 μm PTFE filter prior to injection. The flow rate for all samples was 1.0 mL/min and the injection

volume was 50 μ L. Experimental IR and VCD spectra of (*R*)-PNOC were collected on a BioTools ChiralIR-2XTM VCD spectrometer for CDCl₃ and DCM-*d*₂ polymer solutions (*c* = 25.0 mg/mL, 50 μ m pathlength).

Synthesis of ¹⁵N-labeled Precursors-

The synthesis of nitrogen-15 enriched amides was done using a modified procedure by Zhang et al.⁴⁸ The subsequent Hofmann Rearrangement was conducted using a modified procedure outlined by Huang et al.⁴⁹ The synthesis of nitrogen-15 enriched 1-nitronaphthalene was modified from the reaction reported by Spitzer et al.⁵⁰ The general procedures for each step are outlined before providing all the specified amounts of reagents, yields, ¹H NMR data, ¹³C NMR data, ¹⁵N NMR data, FTIR data, and MS data collected for the ¹⁵N-enriched amides, methyl carbamates, amine HCl salts, 1-naphthyl isothiocyanate, ¹⁵N-octadecyl phthalimide, and *n*-octadecylamine. All J-coupling values are reported in hertz and the FTIR labels are as follows: s = strong intensity, m = moderate intensity, and w = weak intensity. ¹H NMR peak splitting labels are as follows: s = singlet, d = doublet, t = triplet, q = quartet, m = multiplet (greater than quartet), dd = doublet of doublets, td = triplet of doublets, etc.

¹⁵N-2-Naphthamide-

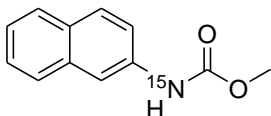


Following the outlined procedure from above for nitrogen-15 enriched amides in Chapter 2: 1.02 g (19.2 mmol, 1.0 eq.) of 99% ¹⁵N-enriched ammonium chloride, 4.42 g

(23.2 mmol, 1.5 eq.) of 2-naphthoyl chloride, and 6.48 g (116 mmol, 6.0 eq.) of KOH. The product was also recrystallized from ethanol for further purification. The product was then filtered and dried under high vacuum.

Yield: 3.10 g (17.9 mmol) of white crystals, 94 %. FTIR (KBr Pellet, cm^{-1}): 3367 ($^{15}\text{N-H}$ str, s), 3191 ($^{15}\text{N-H}$ str, s), 3052 (Ar-H, s), 1648 (C=O, s), 1608 ($^{15}\text{N-H}$ bend, s), 1569 (C=C aryl, m). ^1H NMR (400 MHz, DMSO-d_6): δ (ppm) 8.51 (Ar-H, s, 1H), 8.20 ($^{15}\text{N-H}$, $J_{^{15}\text{N-H}} = 88.8$ Hz, d, 1H), 7.98 (Ar-H, overlapped, 4H), 7.59 (Ar-H, overlapped, 2H), 7.52 ($^{15}\text{N-H}$, $J_{^{15}\text{N-H}} = 87.6$ Hz). ^{13}C NMR (100 MHz, DMSO-d_6): δ (ppm) 168.0 ($J_{^{15}\text{N-}^{13}\text{C}} = 16.0$ Hz), 134.2, 132.2, 131.7 ($J_{^{15}\text{N-}^{13}\text{C}} = 8.3$ Hz), 128.9, 127.9, 127.8, 127.6, 126.7, 124.4. ^{15}N NMR (40.5 MHz, CDCl_3): δ (ppm) 0.482. HRMS-ESI: $M_{\text{theoretical}} = 195.0547$, $M_{\text{sample}} = 195.0546$, $\Delta M = 0.11$ mmass units (0.64 ppm), $\text{C}_{11}\text{H}_9^{15}\text{NO}$.

Methyl ^{15}N -2-Naphthycarbamate-

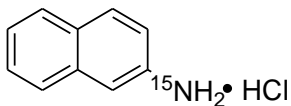


Following the outlined procedure for the modified Hofmann Rearrangement of the nitrogen-15 labeled amides in Chapter 2: 300 mL of methanol, 1.19 g (6.90 mmol, 1.0 eq.) of ^{15}N -2-naphthamide, 2.10 mL (14.0 mmol, 2.0 eq) of 1,8-diazabicyclo[5.4.0]undec-7-ene (DBU), 1.53 g (8.46 mmol, ~1.2 eq.) for of *N*-bromosuccinimide (NBS). The second addition of NBS was omitted due to a side reaction that takes place where the NBS brominates the

aromatic ring at the 1-position. Column chromatography was performed with a 3:1 hexane : ethyl acetate as the mobile phase.

Yield: 0.6112 g (3.02 mmol) off white crystals, 44 %. FTIR (KBr Pellet, cm^{-1}): 3267 (s, $^{15}\text{N-H}$ str), 3052 (w, Ar-H), 2929 (m, $-\text{CH}_3$), 1699 (s, C=O), 1608 ($^{15}\text{N-H}$ bend, w), 1579 (m, C=C aryl). ^1H NMR (400 MHz, CDCl_3): δ (ppm) 7.98 (Ar-H, s, 1H), 7.76 (Ar-H, $J_{1\text{H}-1\text{H}} = 8.4$ Hz, d, 3H), 7.46 (Ar-H, $J_{1\text{H}-1\text{H}} = 7.2$ Hz, $J_{1\text{H}-1\text{H}} = 1.6$ Hz, td, 1H), 7.35 (Ar-H, overlapped, 2H), 6.83 ($^{15}\text{N-H}$, $J_{15\text{N}-1\text{H}} = 90.4$ Hz, d, 1H), 3.81 (O- CH_3 , s, 3H). ^{13}C NMR (100 MHz, CDCl_3): δ (ppm) 154.4 ($J_{15\text{N}-13\text{C}} = 22.4$ Hz), 135.4 ($J_{15\text{N}-13\text{C}} = 15.9$ Hz), 134.1, 130.4, 129.1, 128.34, 128.0, 127.75, 126.7, 125.5, 124.9, 52.6. ^{15}N NMR (40.5 MHz, CDCl_3): δ (ppm) 6.38. HRMS-ESI: $M_{\text{theoretical}} = 203.0833$, $M_{\text{sample}} = 203.0836$, $\Delta M = -0.29$ mmass units (-1.46 ppm), $\text{C}_{12}\text{H}_{11}^{15}\text{NO}_2$.

^{15}N -2-naphthylamine HCl salt

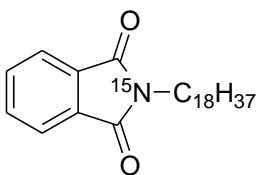


Following the outlined procedure for the carbamate acidolysis: 50 mL of 12 M HCl, 0.6005 g (2.97 mmol, 1.0 eq.) of methyl ^{15}N -2-naphthylcarbamate. The product was collected and characterized as the free-amine upon neutralizing with NaOH and subsequent extraction with diethyl ether.

Yield: 0.4021 g (2.79 mmol) off orange-brown solid, 94 %. FTIR (KBr pellet, cm^{-1}): 3386 (s, $^{15}\text{N-H}$ str), 3311 (s, $^{15}\text{N-H}$ str), 3068 (m, Ar-H), 3017(w, Ar-H), 1629 (s, $^{15}\text{N-H}$

bend), 1598 (m, C=C aryl). ^1H NMR (400 MHz, CDCl_3): δ (ppm) 7.66 (Ar-H, $J_{1\text{H}-1\text{H}} = 8.0$ Hz, q, 2H), 7.59 (Ar-H, $J_{1\text{H}-1\text{H}} = 8.0$ Hz, d, 1H), 7.36 (Ar-H, $J_{1\text{H}-1\text{H}} = 6.8$ Hz, t, 1H), 7.22 (Ar-H, $J_{1\text{H}-1\text{H}} = 7.6$ Hz, t, 1H), 6.95 (Ar-H, overlapped, 2H), 3.86 ($^{15}\text{NH}_2$, s, 2H). ^{13}C NMR (100 MHz, CDCl_3): δ (ppm) 144.3 ($J_{15\text{N}-13\text{C}} = 11.4$ Hz), 135.1, 129.5, 128.2, 127.9, 126.6, 122.7, 118.5, 118.4, 108.8 ($J_{15\text{N}-13\text{C}} = 2.2$). ^{15}N NMR (40.5 MHz, CDCl_3): δ (ppm) -40.31.

^{15}N -Octadecyl phthalimide-

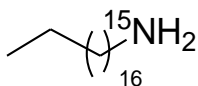


1.03 g of 98% ^{15}N -enriched potassium phthalimide (1.0 eq.) and 1.86 g of 1-bromooctadecane (1.0 eq.) were added to a 250 mL round bottom flask along with ~25 mL of DMF. The mixture was heated to 95 °C and allowed to stir for 21 hrs. The flask was then allowed to cool to room temperature and the reaction mixture was diluted with 100 mL of D.I. water. The product was then extracted with diethyl ether (4 x 50 mL) and the ether extracts were collected. The extracts were dried over anhydrous sodium sulfate (Na_2SO_4) and decanted into a clean flask. The solvent was then removed and the product was recrystallized from ethanol. The product was filtered with suction as a white crystalline solid and dried under high vacuum for 8 hrs.

Yield: 2.00 g (5.01 mmol) white crystalline solid, 90 %. FTIR (KBr pellet, cm^{-1}): 3110 (w, Ar-H), 3056 (w, Ar-H), 3031 (w, Ar-H), 2915 (s, alkyl-H), 2848 (s, alkyl-H), 1708 (m, C=O_{imide}), 1698 (s, C=O_{imide}). ^1H NMR (400 MHz, CDCl_3): δ (ppm) 7.84 (Ar-H, $J_{1\text{H}-1\text{H}} =$

4.4 Hz, q, 2H), 7.70 (Ar-H, $J_{1H-1H} = 4.4$ Hz, q, 2H), 3.67 ($^{15}\text{N-CH}_2$ -, $J_{1H-1H} = 10.4$ Hz, t, 2H), 1.68 ($^{15}\text{N-CH}_2\text{-CH}_2$ -, m, 2H), 1.27 ($-\text{CH}_2\text{-CH}_2\text{-(CH}_2\text{)}_{15}\text{-CH}_3$, m, 30H), 0.88 ($-\text{CH}_3$, $J_{1H-1H} = 8.8$ Hz, t, 3H). ^{13}C NMR (100 MHz, CDCl_3): δ (ppm) 168.7 ($J_{15\text{N}-13\text{C}} = 13.6$ Hz), 134.1, 132.5, 132.4, 123.4, 38.3 ($J_{15\text{N}-13\text{C}} = 8.3$ Hz), 32.2, 29.9, 29.8, 29.7, 29.6, 29.4, 28.9, 27.1, 22.9, 14.4. ^{15}N NMR (40.5 MHz, CDCl_3): δ (ppm) 67.2.

Deprotection of Phthalimide Group with Hydrazine-

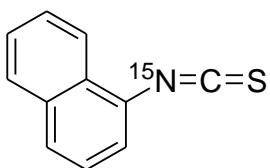


1.84 g (4.61 mmol, 1.0 eq.) of ^{15}N -octadecyl phthalimide and 0.71 mL of 51 % hydrazine hydrate (11.5 mmol, 2.5 eq.) were added to a 250 mL round bottom flask along with 75 mL of ethanol. The mixture was heated to reflux and allowed to stir for 5 hrs. Upon cooling to room temperature, the resulting precipitate was filtered off and washed repeatedly with DCM. The solvent was removed and the product was redissolved in DCM. The solution was then washed with 6M NaOH (2 x 100 mL) and brine (1 x 100 mL). The organic layer was then collected, dried over anhydrous Na_2SO_4 , and decanted into a clean flask. The solvent was removed again via rotatory evaporation and the solid was collected and dried under high vacuum to afford pure product.

Yield: 1.05 g (3.89 mmol) white crystalline solid, 84 %. FTIR (KBr pellet, cm^{-1}): 3324 (w, $^{15}\text{N-H}$ str.), 3251 (w, $^{15}\text{N-H}$ str.), 3160 (w, $^{15}\text{N-H}$), 2917 (s, alkyl-H), 2848 (s, alkyl-H), 1602 (m, $^{15}\text{N-H}$ bend), 1562 (m, $^{15}\text{N-H}$ bend). ^1H NMR (400 MHz, CDCl_3): δ (ppm) 2.67 ($^{15}\text{N-CH}_2$ -, $J_{1H-1H} = 6.8$ Hz, t, 2H), 1.43 ($^{15}\text{N-CH}_2\text{-CH}_2$ -, m, 2H), 1.25 ($-\text{CH}_2\text{-CH}_2\text{-(CH}_2\text{)}_{15}\text{-CH}_3$, m, 30H), 0.88 ($-\text{CH}_3$, t, 3H).

CH₃, m, 30H), 1.14 (¹⁵NH₂, s, 2H), 0.88 (-CH₃, $J_{1H-1H} = 8.8$ Hz, t, 3H). ¹³C NMR (100 MHz, CDCl₃): δ (ppm) 42.5 ($J_{15N-13C} = 3.8$ Hz), 34.1, 32.1, 29.9, 29.8, 29.7, 29.6, 27.1, 22.9, 14.3. ¹⁵N NMR (40.5 MHz, CDCl₃): δ (ppm) -73.1.

Synthesis of ¹⁵N-labeled 1-naphthylisothiocyanate-



0.64 mL (6.35 mmol, 1.2 eq.) of thiophosgene was added to a 250 mL round bottom flask along with 25 mL of DCM. The mixture was cooled to 0 °C in an ice bath and 1.01 g (6.99 mmol, 1.0 eq.) of ¹⁵N-enriched 1-naphthylamine and 3.86 mL (27.9 mmol, 4.0 eq.) of triethylamine (TEA) were dissolved in 15 mL of DCM in an addition funnel. The amine solution was then added dropwise into the cold, stirring solution of thiophosgene. When the amine solution was completely added, the ice bath was removed and the solution was allowed to stir at room temperature for an additional 2.5 hrs. The solution was then washed with brine (2 x 50 mL) and dried over anhydrous sodium sulfate. The mixture was decanted into a clean flask and the solvent was removed via rotatory evaporation. The product was then further purified by column chromatography (DCM as mobile phase) and collected as a yellow solid. The product was collected and dried under high vacuum for 4 hrs.

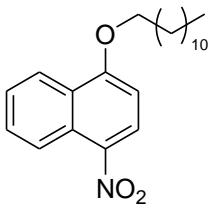
Yield: 0.98 g (5.26 mmol) yellow solid, 75 %. FTIR (KBr pellet, cm⁻¹): 3058 (w, Ar-H), 2951 (w, Ar-H), 2069 (s, S=C=¹⁵N), 1508 (m, C=C aryl). ¹H NMR (400 MHz, CDCl₃): δ (ppm) 8.12 (Ar-H, $J_{1H-1H} = 8.4$ Hz, $J_{1H-1H} = 0.8$ Hz, dd, 1H), 7.88 (Ar-H, $J_{1H-1H} = 8.0$ Hz, d,

1H), 7.79 (Ar-H, overlapped m, 1H), 7.59 (Ar-H, m, 2H), 7.43 (Ar-H, m, 2H). ^{13}C NMR (100 MHz, CDCl_3): δ (ppm) 136.5, 134.2, 129.5, 128.7, 127.9, 127.6, 127.4, 125.6 ($J_{15\text{N}-13\text{C}} = 3.0$ Hz), 123.7 ($J_{15\text{N}-13\text{C}} = 2.3$ Hz), 123.0 ($J_{15\text{N}-13\text{C}} = 1.5$ Hz). ^{15}N NMR (40.5 MHz, CDCl_3): δ (ppm) 65.2.

Synthesis of Unlabeled Precursor Compounds-

The synthesis and characterization of the tosylated tetraethylene glycol monomethyl ether was previously reported by Gentilini et al.⁵¹ The synthesis and characterization of the azide functionalized tetraethylene glycol monomethyl ether was previously reported by Kitto et al.⁵²

4-Dodecoxy-1-nitronaphthalene-

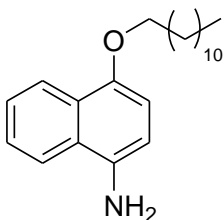


0.623 g (3.29 mmol, ~1.0 eq) of 4-nitro-1-naphthol, 0.780 mL (3.25 mmol, 1.0 eq.) of 1-bromododecane, and 0.969 g (7.01 mmol, 2.15 eq.) of potassium carbonate (K_2CO_3) were added to a 250 mL round bottom flask along with 25 mL of DMF. The mixture was heated to 85 – 90 °C in an oil bath and allowed to stir for 24 hours. Upon cooling to room temperature, the mixture was diluted with 100 mL of D.I. water and the product was extracted with diethyl ether (4 x 50 mL). The ether extracts were combined and washed with 1M NaOH (2 x 50 mL), brine solution (2 x 50 mL), and D.I. water (1 x 50 mL) and dried over anhydrous

sodium sulfate. The solution was then decanted into a clean flask and the solvent was removed by rotatory evaporation. The product was then recrystallized from ethanol, filtered with suction, and washed repeatedly with ice-cold ethanol. The product was then collected and dried under high vacuum.

Yield: 0.897 g (2.52 mmol) yellow solid, 78 %. FTIR (KBr pellet, cm^{-1}): 3141 (w, Ar-H), 3085 (w, Ar-H), 3050 (w, Ar-H), 2946 (m, alkyl-H), 2925 (s, alkyl-H), 2848 (s, alkyl-H), 1571 (s, $\text{C}=\text{C}_{\text{aryl}}$). ^1H NMR (400 MHz, CDCl_3): δ (ppm) 8.79 (Ar-H, $J_{1\text{H}-1\text{H}} = 8.8$ Hz, d, 1H), 8.39 (Ar-H, $J_{1\text{H}-1\text{H}} = 8.8$ Hz, d, 2H), 7.72 (Ar-H, m, 1H), 7.58 (Ar-H, m, 1H), 6.78 (Ar-H, $J_{1\text{H}-1\text{H}} = 8.8$ Hz, d, 1H), 4.22 (O-CH₂-, $J_{1\text{H}-1\text{H}} = 6.4$ Hz, t, 2H), 1.96 (-CH₂CH₂CH₂(CH₂)₈CH₃, m, 2H), 1.57 (-CH₂CH₂CH₂(CH₂)₈CH₃, m, 2H), 1.32 (-CH₂CH₂CH₂(CH₂)₈CH₃, m, 16H), 0.88 (-CH₂CH₂CH₂(CH₂)₈CH₃, $J_{1\text{H}-1\text{H}} = 7.2$ Hz, t, 3H). ^{13}C NMR (100 MHz, CDCl_3): δ (ppm) 160.4, 139.1, 130.2, 127.6, 127.2, 126.7, 125.9, 123.7, 123.1, 102.7, 69.4, 32.2, 29.9, 29.8, 29.6, 29.2, 26.4, 22.9, 14.4.

4-Dodecoxy-1-naphthylamine-

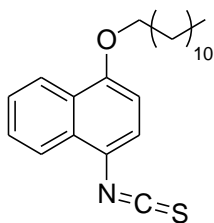


0.759 g (2.13 mmol, 1.0 eq.) of 4-dodecoxy-1-nitronaphthalene and 0.0461 g (5 w% with respect to the reagent) of Pd/C (10 wt%) was added to a 50 mL Erlenmeyer flask along with 20 mL of methanol and a stir bar. The reaction flask was then added to a Parr reactor

and purged with H₂ gas 3 times. The reaction vessel was then placed under H₂ atmosphere at 50 psi and the solution was left stirring for 24 hours. Upon completion, the reaction flask was removed from the reactor and the solution was filtered through Celite to remove the Pd/C catalyst. The filtrate was then collected, the solvent was removed, and the product was dried under high vacuum without further purification.

Yield: 0.627 g (1.93 mmol) purple solid, 90 %. FTIR (KBr pellet, cm⁻¹): 3401 (m, N-H), 3336 (w, N-H), 3056 (w, Ar-H), 3018 (w, Ar-H), 2952 (m, alkyl-H), 2917 (s, alkyl-H), 2850 (s, alkyl-H), 1589 (m, C=C_{aryl}). ¹H NMR (400 MHz, CDCl₃): δ (ppm) 8.28 (Ar-H, m, 1H), 7.81 (Ar-H, m, 1H), 7.48 (Ar-H, m, 2H), 6.68 (Ar-H, *J*_{1H-1H} = 8.0 Hz, q, 2H), 4.06 (O-CH₂-, *J*_{1H-1H} = 6.4 Hz, t, 2H), 3.81 (N-H, s, 2H), 1.89 (-CH₂CH₂CH₂(CH₂)₈CH₃, m, 2H), 1.54 (-CH₂CH₂CH₂(CH₂)₈CH₃, m, 2H), 1.33 (-CH₂CH₂CH₂(CH₂)₈CH₃, m, 16H), 0.88 (-CH₂CH₂CH₂(CH₂)₈CH₃, *J*_{1H-1H} = 6.8 Hz, t, 3H). ¹³C NMR (100 MHz, CDCl₃): δ (ppm) 148.9, 135.2, 126.6, 125.8, 125.4, 122.9, 121.2, 110.0, 105.7, 68.8, 32.2, 29.9, 29.7, 29.6, 26.5, 22.9, 14.4.

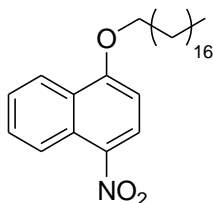
4-Dodecoxy-1-naphthylisothiocyanate-



0.140 mL (1.83 mmol, 1.0 eq.) of thiophosgene was added to a 250 mL round bottom flask along with about 25 mL of DCM. The flask was cooled to 0 °C in an ice bath. 0.597 g

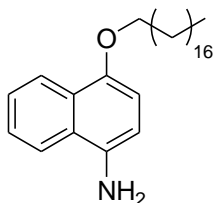
(1.83 mmol, 1.0 eq.) of 4-dodecoxy-1-naphthylamine and 0.760 mL (5.49 mmol, 3.0 eq.) of TEA were dissolved in 25 mL of DCM and placed into an addition funnel. The amine solution was then dripped into the stirring reaction mixture over the course of 15 minutes. The reaction was then allowed to stir for 4 hours and was monitored by FTIR spectroscopy. The solution was then washed with Brine (2 x 50 mL) and dried over anhydrous sodium sulfate. The product was decanted into a clean flask and the solvent was removed via rotatory evaporation. The crude product was further purified by column chromatography (1:1 ethyl acetate : hexanes as mobile phase). The product was then collected, concentrated, and dried under high vacuum.

Yield: 0.420 g (1.14 mmol) off-white solid, 62 %. FTIR (KBr pellet, cm^{-1}): 3068 (w, Ar-H), 2923 (s, alkyl-H), 2852 (s, alkyl-H), 2107 (s, S=C=N), 1583 (s, Ar-H). ^1H NMR (400 MHz, CDCl_3): δ (ppm) 8.28 (Ar-H, m, 1H), 7.81 (Ar-H, m, 1H), 7.48 (Ar-H, m, 2H), 6.68 (Ar-H, $J_{\text{H-H}} = 8.0$ Hz, q, 2H), 4.06 (O-CH₂-, $J_{\text{H-H}} = 6.4$ Hz, t, 2H), 1.89 (-CH₂CH₂CH₂(CH₂)₈CH₃, m, 2H), 1.54 (-CH₂CH₂CH₂(CH₂)₈CH₃, m, 2H), 1.33 (-CH₂CH₂CH₂(CH₂)₈CH₃, m, 16H), 0.88 (-CH₂CH₂CH₂(CH₂)₈CH₃, $J_{\text{H-H}} = 6.8$ Hz, t, 3H). ^{13}C NMR (100 MHz, CDCl_3): δ (ppm) 148.9, 135.2, 126.6, 125.8, 125.4, 122.9, 121.2, 110.0, 105.7, 68.8, 32.2, 29.9, 29.7, 29.6, 26.5, 22.9, 14.4.

4-Octadecyloxy-1-nitronaphthalene-

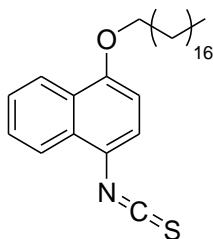
Following the same procedure outlined for the synthesis of 4-dodecoxy-1-nitronaphthalene except replacing 1-bromododecane with 1-bromooctadecane: 0.607 g (3.21 mmol, 1.0 eq.) of 4-nitro-1-naphthol, 1.29 g (3.88 mmol, 1.2 eq.) of 1-bromooctadecane, 1.14 g (8.27 mmol, 2.5 eq.) of potassium carbonate.

Yield: 1.13 g (2.56 mmol) yellow crystals, 80 %. FTIR (KBr pellet, cm^{-1}): 3141 (w, Ar-H), 3085 (w, Ar-H), 3050 (w, Ar-H), 2946 (m, alkyl-H), 2925 (s, alkyl-H), 2848 (s, alkyl-H), 1571 (s, $\text{C}=\text{C}_{\text{aryl}}$). ^1H NMR (400 MHz, CDCl_3): δ (ppm) 8.80 (Ar-H, $J_{\text{H-H}} = 8.8$ Hz, d, 1H), 8.40 (Ar-H, $J_{\text{H-H}} = 8.8$ Hz, d, 2H), 7.74 (Ar-H, m, 1H), 7.58 (Ar-H, m, 1H), 6.78 (Ar-H, $J_{\text{H-H}} = 8.8$ Hz, d, 1H), 4.24 (O- CH_2 -, $J_{\text{H-H}} = 6.4$ Hz, t, 2H), 1.97 (- $\text{CH}_2\text{CH}_2\text{CH}_2(\text{CH}_2)_{14}\text{CH}_3$, m, 2H), 1.57 (- $\text{CH}_2\text{CH}_2\text{CH}_2(\text{CH}_2)_{14}\text{CH}_3$, m, 2H), 1.32 (- $\text{CH}_2\text{CH}_2\text{CH}_2(\text{CH}_2)_{14}\text{CH}_3$, m, 28H), 0.88 (- $\text{CH}_2\text{CH}_2\text{CH}_2(\text{CH}_2)_8\text{CH}_3$, $J_{\text{H-H}} = 6.4$ Hz, t, 3H). ^{13}C NMR (100 MHz, CDCl_3): δ (ppm) 160.4, 130.3, 127.6, 127.2, 126.7, 125.9, 123.7, 123.1, 102.7, 69.4, 32.2, 29.9, 29.8, 29.6, 29.2, 26.4, 22.9, 14.4.

4-Octadecyloxy-1-naphthylamine-

Following the same procedure outlined for the synthesis of 4-dodecoxy-1-naphthylamine: 1.06 g (2.41 mmol, 1.0 eq.) of 4-octadecyloxy-1-nitronaphthalene and 0.0563 g (10 wt% with respect to the reagent) Pd/C.

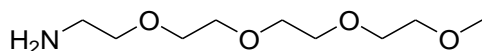
Yield: 0.937 g (2.28 mmol) beige solid, 71 %. FTIR (KBr pellet, cm^{-1}): 3401 (m, N-H), 3336 (w, N-H), 3056 (w, Ar-H), 3018 (w, Ar-H), 2952 (m, alkyl-H), 2917 (s, alkyl-H), 2850 (s, alkyl-H), 1589 (m, $\text{C}=\text{C}_{\text{aryl}}$). ^1H NMR (400 MHz, CDCl_3): δ (ppm) 8.28 (Ar-H, m, 1H), 7.81 (Ar-H, m, 1H), 7.48 (Ar-H, m, 2H), 6.68 (Ar-H, $J_{\text{1H-1H}} = 8.0$ Hz, q, 2H), 4.06 (O-**CH**₂-, $J_{\text{1H-1H}} = 6.8$ Hz, t, 2H), 3.83 (N-H, s, 2H), 1.89 (-**CH**₂**CH**₂**CH**₂(**CH**₂)₁₄**CH**₃, m, 2H), 1.54 (-**CH**₂**CH**₂**CH**₂(**CH**₂)₁₄**CH**₃, m, 2H), 1.33 (-**CH**₂**CH**₂**CH**₂(**CH**₂)₁₄**CH**₃, m, 28H), 0.88 (-**CH**₂**CH**₂**CH**₂(**CH**₂)₈**CH**₃, $J_{\text{1H-1H}} = 6.8$ Hz, t, 3H). ^{13}C NMR (100 MHz, CDCl_3): δ (ppm) 148.9, 135.3, 126.6, 125.8, 125.4, 122.9, 121.2, 110.0, 105.7, 68.9, 32.2, 29.9, 29.7, 29.6, 26.5, 22.9, 14.4.

4-Octadecyloxy-1-naphthylisothiocyanate-

Following the same procedure for the synthesis of 4-dodecoxy-1-naphthylisothiocyanate except DCM was used as the mobile phase in column chromatography: 0.717 g (1.74 mmol, 1.0 eq.), 0.160 mL (2.09 mmol, 1.2 eq.) of thiophosgene, 0.720 mL (5.19 mmol, 3.0 eq.) of TEA.

Yield: 0.557 g (1.23 mmol) purple solid, 62 %. FTIR (KBr pellet, cm^{-1}): 3068 (w, Ar-H), 2923 (s, alkyl-H), 2852 (s, alkyl-H), 2106 (s, S=C=N), 1583 (s, Ar-H). ^1H NMR (400 MHz, CDCl_3): δ (ppm) 8.28 (Ar-H, $J_{\text{H-H}} = 8.4$ Hz, d, 1H), 8.04 (Ar-H, $J_{\text{H-H}} = 8.4$ Hz, d, 1H), 7.63 (Ar-H, m, 1H) 7.55 (Ar-H, m, 1H), 7.35 (Ar-H, $J_{\text{H-H}} = 8.4$ Hz, d, 1H), 6.71 (Ar-H, $J_{\text{H-H}} = 8.4$ Hz, m, 1H), 4.13 (O-CH₂-, $J_{\text{H-H}} = 6.0$ Hz, t, 2H), 1.93 (-CH₂CH₂CH₂(CH₂)₁₄CH₃, m, 2H), 1.55 (-CH₂CH₂CH₂(CH₂)₁₄CH₃, m, 2H), 1.34 (-CH₂CH₂CH₂(CH₂)₁₄CH₃, m, 28H), 0.88 (-CH₂CH₂CH₂(CH₂)₈CH₃, $J_{\text{H-H}} = 6.4$ Hz, t, 3H). ^{13}C NMR (100 MHz, CDCl_3): δ (ppm) 162.4, 128.1, 126.5, 124.2, 123.1, 122.7, 104.1, 68.8, 32.2, 29.9, 29.8, 29.6, 26.4, 22.9, 14.4.

2-(2-(2-(2-methoxyethoxy)ethoxy)ethoxy)ethanamine



0.597 g (2.56 mmol, 1.0 eq.) of 1-azido-2-(2-(2-(2-methoxyethoxy)ethoxy)ethoxy)ethane was added to a 50 mL Erlenmeyer flask along with 0.0360 g (~5 w%) of Pd/C, 25 mL of MeOH, and a stir bar. The reaction flask was then placed in a Parr reactor under H₂ atmosphere at 50 psi and allowed to stir for 24 hours. The flask was then removed from the reactor and the solution was filtered through Celite™ to remove the Pd/C catalyst. The solvent was then removed via rotatory evaporation and the oil was collected and dried under high vacuum to afford pure product.

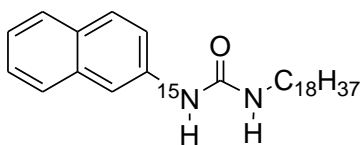
Yield: 0.500 g (2.41 mmol) of yellowish-brown liquid, 94 %. FTIR (KBr pellet, cm⁻¹): 3437 (s, NH₂), 2913 (s, alkyl-H), 2877 (s, alkyl-H), 1101 (s, C-O). ¹H NMR (400 MHz, CDCl₃): δ (ppm) 3.64 (-OCH₂CH₂O-, overlapped m, 12H), 3.56 (H₂NCH₂CH₂O-, overlapped, 2H), 3.38 (-OCH₃, s, 3H), 2.86 (H₂NCH₂CH₂O-, *J*_{1H-1H} = 7.2 Hz, t, 2H), 1.53 (NH₂, broad s, 2H). ¹³C NMR (100 MHz, CDCl₃): δ (ppm) 73.7, 72.1, 70.8, 70.7, 70.5, 59.2, 42.0. HRMS-ESI: *M*_{theoretical} = 208.1543, *M*_{sample} = 208.1551, Δ*M* = -0.76 mmass units (-3.68 ppm), C₉H₂₁O₄N.

Synthesis of Asymmetric Ureas/ Thioureas-

The amine (1.0 - 1.2 eq.) was added to a 250 mL round bottom flask along a stir bar and 70 mL of CHCl₃. The mixture was allowed to stir for 15 minutes prior to addition of the corresponding isocyanate/ isothiocyanate (1.0 - 1.2 eq.) The reaction mixture was then

allowed to stir at room temperature when employing alkyl amines or heated to reflux when employing aryl amines. In both cases, the solution was allowed to stir for 10-15 hours. Upon completion, the solvent was removed under reduced pressure and the crude product was recrystallized from ethanol. The product, typically a white powder, was filtered and washed with ice-cold ethanol repeatedly. The solid was then collected and dried under high vacuum.

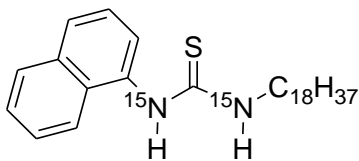
¹⁵N-(2-naphthyl), N-(n-octadecyl)urea-



Following the outlined procedure for asymmetric ureas/ thioureas: 75 mL of CHCl₃, 0.40 g (2.74 mmol, 1.0 eq) of ¹⁵N-2-naphthylamine, and 1.05 mL (3.01 mmol, 1.2 eq.) of *n*-octadecyl isocyanate. Due to insolubility in all conventional NMR solvents (e.g., CDCl₃, CD₂Cl₂, benzene-d₆, toluene-d₈, THF-d₈, 1,2-dichloroethane-d₄, methanol-d₄, acetone-d₆, DMSO-d₆), NMR data were collected. The FTIR spectrum was taken in the solid state and HRMS-ESI is reported below.

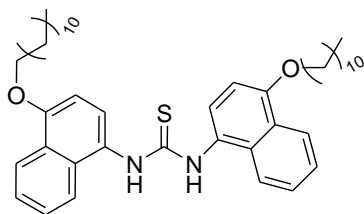
Yield: 0.88 g (2.01 mmol) white powder, 73 %. FTIR (KBr pellet, cm⁻¹): 3338 (s, N-H str), 2952 (s, alkyl-H), 2917 (s, alkyl-H), 2848 (m, alkyl-H), 1618 (s, C=O), 1570 (m, C=C aryl). HRMS-ESI: M_{theoretical} = 440.3653, M_{sample} = 440.3662, ΔM = -0.85 mmass units (-1.94 ppm), C₂₉H₄₆¹⁵NNO.

¹⁵N-(1-naphthyl), ¹⁵N-octadecylthiourea-



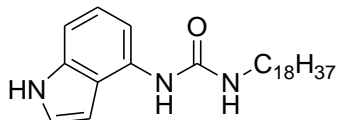
0.9729 g (5.22 mmol, 1.0 eq.) of ¹⁵N-labeled 1-naphthyl isothiocyanate and 1.44 g (5.34 mmol, 1.05 eq.) of ¹⁵N-labeled octadecylamine were added to a 250 mL round bottom flask along with 75 mL of DCM. The mixture was allowed to stir at room temperature until the disappearance of the isothiocyanate peak in the IR spectra (ca. 14 hours). The solvent was then removed under reduced pressure and the product was recrystallized from ethanol. The product was filtered and washed with ice-cold ethanol. The product was collected as white crystals and dried under high vacuum.

Yield: 2.14g (4.70 mmol) white crystalline powder, 90 %. FTIR (KBr pellet, cm⁻¹): 3378 (s, ¹⁵N-H str) 3251 (s, ¹⁵N-H str), 3050 (w, Ar-H), 2921 (s, alkyl-H), 2852 (s, alkyl-H), 1523 (s, C=S), 1465 (m, ¹⁵N-H bend). ¹H NMR (400 MHz, CDCl₃): δ (ppm) 8.01 (Ar-H, m, 1H), 7.92 (Ar-H, m, 2H), 7.65 (¹⁵N-H, overlapped, 1H), 7.57 (Ar-H, overlapped m, 2H), 7.44 (Ar-H, *J*_{1H-1H} = 7.2 Hz, d, 1H), 5.65 (¹⁵N-H, *J*_{15N-1H} = 87.2 Hz, d, 1H), 3.56 (-CH₂CH₂(CH₂)₁₅CH₃, *J*_{1H-1H} = 6.0 Hz, q, 2H), 1.44 (CH₂CH₂CH₂(CH₂)₁₄CH₃, unresolved m, 2H), 1.23 (CH₂CH₂CH₂(CH₂)₁₄CH₃, m, 30H), 0.88 (CH₂CH₂CH₂(CH₂)₂CH₃, *J*_{1H-1H} = 6.4 Hz, t, 3H). ¹³C NMR (100 MHz, CDCl₃): δ (ppm) 180.7, 134.9, 130.2, 129.3, 128.8, 127.8, 127.4, 126.0 (*J*_{15N-13C} = 2.3 Hz), 125.5, 122.8, 45.8 (*J*_{15N-13C} = 11.4 Hz), 32.2, 29.9, 29.8, 29.7, 29.6, 29.4, 29.2, 26.9, 22.9, 14.4. ¹⁵N NMR (40.5 MHz, CDCl₃): δ (ppm) -2.02, -10.6.

N,N'-di(4-dodecoxy-1-naphthyl)thiourea

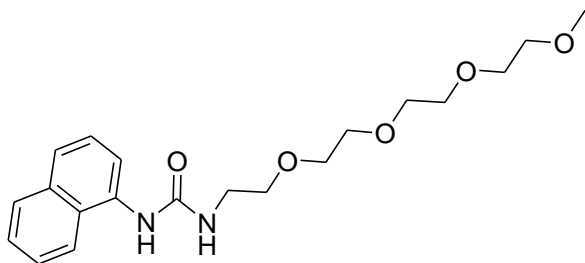
Following the outlined procedure for the formation of asymmetric ureas/ thioureas: 0.420 g (1.14 mmol, 1.0 eq.) of 4-dodecoxy-1-naphthylisothiocyanate and 0.372 g (1.15 mmol, 1.0 eq.) of 4-dodecoxy-1-naphthylamine, 50 mL of CHCl_3 .

Yield: 0.359g (0.518 mmol) purplish-grey powder, 45 %. FTIR (KBr pellet, cm^{-1}): 3353 (m, N-H) 3163 (s, N-H), 3070 (w, Ar-H), 2923 (s, alkyl-H), 2854 (s, alkyl-H), 1583 (s, C=C_{aryl}), 1508 (s, C=S). ^1H NMR (400 MHz, CDCl_3): δ (ppm) 8.29 (Ar-H, broad s, 2H), 7.48 (Ar-H, broad s, 6H), 6.77 (Ar-H, broad s, 2H), 4.12 (-**CH**₂CH₂CH₂(CH₂)₈CH₃, broad s, 2H), 1.91 (CH₂**CH**₂CH₂(CH₂)₈CH₃, broad m, 2H), 1.55 (CH₂CH₂**CH**₂(CH₂)₈CH₃, m, 2H), 1.35 (CH₂CH₂CH₂(**CH**₂)₈CH₃, m, 16H), 0.88 (CH₂CH₂CH₂(CH₂)₂**CH**₃, $J_{1\text{H}-1\text{H}} = 6.4$ Hz, t, 3H). ^{13}C NMR (100 MHz, CDCl_3): δ (ppm) 183.9, 131.4, 130.2, 126.9, 123.1, 122.4, 104.1, 68.6, 32.2, 29.9, 29.8, 29.6, 29.4, 26.5, 22.9, 14.4. HRMS-ESI: $M_{\text{theoretical}} = 697.4689$, $M_{\text{sample}} = 697.4773$, $\Delta M = -0.22$ ppm, $\text{C}_{45}\text{H}_{64}\text{N}_2\text{O}_2\text{S}$.

N-indole-*N'*-octadecylurea

Following the outlined procedure for the formation of ureas/ thioureas: 0.505 g (3.82 mmol, 1.0 eq.) of 1H-indol-4-amine, 1.73 mL (4.92 mmol, 1.3 eq.) of *n*-octadecyl isocyanate, 50 mL of CHCl₃

Yield: 0.979 g (2.29 mmol) of light purple solid, 60 %. ¹H NMR (400 MHz, CDCl₃): δ (ppm) 8.73 (N-H_{cyclic}, s, 1H), 7.25 (Ar-H, m, 1H), 7.18 (Ar-H, overlapped m, 3H), 6.69 (N-H, s, 1H), 6.56 (Ar-H, *J*_{1H-1H} = 2.0 Hz, t, 1H), 3.23 (-CH₂CH₂CH₂(CH₂)₁₄CH₃, *J*_{1H-1H} = 7.2 Hz, q, 2H), 1.47 (CH₂CH₂CH₂(CH₂)₁₄CH₃, m, 2H), 1.26 (CH₂CH₂(CH₂)₁₅CH₃, m, 2H), 0.88 (CH₂CH₂CH₂(CH₂)₂CH₃, *J*_{1H-1H} = 6.4 Hz, t, 3H). ¹³C NMR (100 MHz, CDCl₃): δ (ppm) 157.0, 137.3, 130.4, 124.6, 122.8, 114.4, 108.8, 99.9, 58.7, 40.6, 32.1, 30.4, 29.9, 29.8, 29.6, 29.4, 27.1, 22.9, 18.6, 14.4.

1-(2-(2-(2-(2-methoxyethoxy)ethoxy)ethoxy)ethyl)-3-(naphthalen-1-yl)urea

1.21 g (5.84 mmol, 1.0 eq.) of 2-(2-(2-(2-methoxyethoxy)ethoxy)ethoxy)ethanamine was added to a 250 mL round bottom flask along with 40 mL of CHCl₃ and a stir bar. 0.880 mL (6.13 mmol, 1.2 eq.) of the 1-naphthyl isocyanate was then added to the stirring mixture and the reaction was allowed to proceed for 32 hours at room temperature. The solution was

then washed with 1M HCl (2 x 25 mL) and brine solution (1 x 50 mL). The reaction mixture was dried over anhydrous sodium sulfate and decanted into a clean flask. The solvent was removed via rotatory evaporation and the product was further purified by column chromatography (ethyl acetate as mobile phase). The product was then collected and dried under high vacuum.

Yield: 0.800 g (2.12 mmol) light brown solid, 36 %. FTIR (KBr pellet, cm^{-1}): 3290 (m, N-H) 3070 (m, Ar-H), 2879 (s, alkyl-H), 1653 (s, C=O), 1558 (s, C=C_{aryl}). ^1H NMR (400 MHz, CDCl_3): δ (ppm) 8.03 (Ar-H, $J_{\text{1H-1H}} = 9.2$ Hz, d, 1H), 7.80 (Ar-H, overlapped m, 2H), 7.61 (Ar-H, $J_{\text{1H-1H}} = 10.8$ Hz, d, 1H), 7.55 (N-H, s, 1H), 7.42 (Ar-H, overlapped m, 3H), 5.93 (N-H, s, 1H), 3.51 (($\text{CH}_2\text{CH}_2\text{O}$)₄, overlapped m, 16H), 3.26 (OCH_3 , s, 3H). ^{13}C NMR (100 MHz, CDCl_3): δ (ppm) 157.2, 134.5, 134.3, 128.7, 128.4, 126.2, 126.1, 125.1, 122.0, 120.9, 72.0, 70.8, 70.7, 70.6, 70.5, 70.3, 59.1, 40.5. HRMS-ESI: $M_{\text{theoretical}} = 377.2071$, $M_{\text{sample}} = 377.2069$, $\Delta M = 0.17$ mmass units (0.45 ppm), $\text{C}_{20}\text{H}_{28}\text{N}_2\text{O}_5$.

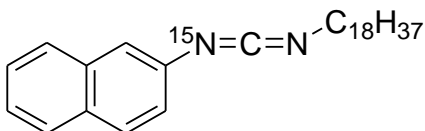
Synthesis of Carbodiimide Monomers-

The specific amounts of reagents, yields, NMR data, MS data, and FTIR data are reported below for each monomer. The ^{15}N NMR data was not collected on any of the carbodiimide monomers due to greater than 90 second delay times.

The dibromotriphenylphosphorane salt (PPh_3Br_2 , 1.2 eq.) was added to a round bottom flask along with ~5 mL of DCM. The reaction flask was then placed under N_2 atmosphere and cooled to 0 °C in an ice bath. The TEA (2.5 eq.) was then added to the stirring mixture

and the resulting vapors were allowed to dissipate. The ^{15}N -labeled urea/thiourea (1.0 eq.) was then added to the mixture and the solution was allowed to stir until completion (ca. 1-10 hours) with the reaction progress monitored by IR spectroscopy. Upon completion, the reaction was quenched with ~300 mL of pentane and the resulting precipitate was filtered and washed with additional pentane. The filtrate was collected and the solvent was removed via rotatory evaporation. This quenching process was repeated twice more to remove most of the byproducts from the system. The product was further purified by column chromatography (DCM as mobile phase) and was collected. The solvent was removed and the monomer was dried under high vacuum to afford pure product.

^{15}N -(2-naphthyl), N -octadecylcarbodiimide-

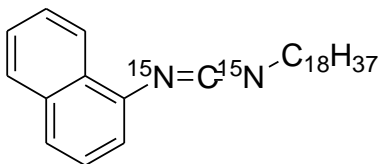


Following the procedure for the synthesis of carbodiimides from ureas/ thioureas: 10 mL of DCM, 1.89 g (4.47 mmol, 1.2 eq.) of dibromotriphenylphosphorane, 1.26 mL (9.11 mmol, 2.5 eq.) of triethylamine, and 1.60 g (3.64 mmol, 1.0 eq.) of ^{15}N -(2-naphthyl), N -octadecylurea.

Yield: 1.09 g (2.59 mmol) of white solid, 71 %. FTIR (KBr thinfilm, cm^{-1}): 3050 (w, Ar-H), 2920 (s, alkyl-H), 2852 (m, alkyl-H), 2130 (s, $^{15}\text{N}=\text{C}=\text{N}$), 1562 (w, $\text{C}=\text{C}_{\text{aryl}}$). ^1H NMR (400 MHz, CDCl_3): δ (ppm) 7.76 (Ar-H, overlapped m, 3H), 7.38 (Ar-H, overlapped m, 3H), 7.24 (Ar-H, $J_{\text{1H-1H}} = 8.4$ Hz, $J_{\text{1H-1H}} = 2.0$ Hz 1H, dt), 3.46 ($-\text{CH}_2\text{CH}_2(\text{CH}_2)_{15}\text{CH}_3$, $J_{\text{1H-1H}} = 6.8$ Hz, 2H, t), 1.72 ($-\text{CH}_2\text{CH}_2(\text{CH}_2)_{15}\text{CH}_3$, 2H, m) 1.44 ($-\text{CH}_2\text{CH}_2\text{CH}_2(\text{CH}_2)_{14}\text{CH}_3$, 2H, m),

1.25 (-CH₂CH₂CH₂(CH₂)₁₄CH₃, 28H, m) 0.88 (-CH₂CH₂(CH₂)₁₅CH₃, $J = 6.8$ Hz, 3H, t). ¹³C NMR (100 MHz, CDCl₃): 138.4, 136.3, 134.3, 131.1, 129.4, ($J_{15\text{N}-13\text{C}} = 1.5$ Hz), 127.9, 127.3, 126.7, 125.3, 123.4 ($J_{15\text{N}-13\text{C}} = 3.0$ Hz), 120.5, 47.2, 32.2, 31.7, 30.0, 29.9, 29.8, 29.7, 29.6, 29.4, 27.1, 23.0, 14.4. HRMS-ESI: $M_{\text{theoretical}} = 422.3548$, $M_{\text{sample}} = 422.3549$, $\Delta M = -0.09$ (-0.22 ppm), C₂₉H₄₄¹⁵NN.

¹⁵N-(1-naphthyl), N-octadecylcarbodiimide-

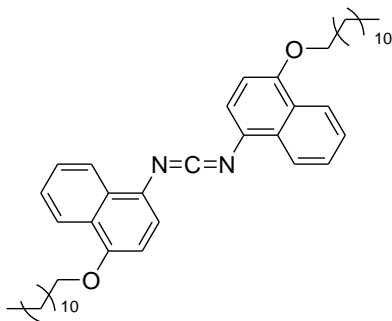


Following the procedure for the synthesis of carbodiimides from ureas/ thioureas: 10 mL of DCM, 1.72 g (4.08 mmol, 1.2 eq.) of dibromotriphenylphosphorane, 1.18 mL (8.51 mmol, 2.5 eq.) of triethylamine, and 1.53 g (3.36 mmol, 1.0 eq.) of ¹⁵N-(1-naphthyl), ¹⁵N-octadecyl thiourea.

Yield: 0.97 g (2.29 mmol) of pale yellow liquid, 68 %. FTIR (KBr thinfilm, cm⁻¹): 3048 (m, Ar-H), 2923 (s, alkyl-H), 2852 (m, alkyl-H), 2379 (s, ¹⁵N=C=N), 1573 (w, C=C_{aryl}). ¹H NMR (400 MHz, CDCl₃): δ (ppm) 8.28 (Ar-H, 1H, m), 7.81 (Ar-H, 1H, m), 7.61 (Ar-H, $J_{1\text{H}-1\text{H}} = 8.0$ Hz, 1H, d), 7.50 (Ar-H, 2H, m), 7.40 (Ar-H, $J_{1\text{H}-1\text{H}} = 7.2$ Hz, 1H, t), 7.29 (Ar-H, 1H, m), 3.47 (-CH₂CH₂(CH₂)₁₅CH₃, $J_{1\text{H}-1\text{H}} = 6.8$ Hz, 2H, t), 1.72 (-CH₂CH₂(CH₂)₁₅CH₃, 2H, m) 1.44 (-CH₂CH₂CH₂(CH₂)₁₄CH₃, 2H, m), 1.25 (-CH₂CH₂CH₂(CH₂)₁₄CH₃, 28H, m) 0.88 (-CH₂CH₂(CH₂)₁₅CH₃, $J = 6.8$ Hz, 3H, t). ¹³C NMR (100 MHz, CDCl₃): 137.5, 135.8, 134.6, 129.0, 128.0, 126.6, 126.1, 126.0, 124.7, 123.8, 119.8, 47.2, 32.2, 31.7, 30.0, 29.9, 29.8, 29.7,

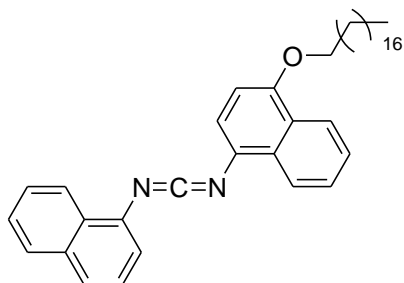
29.6, 29.4, 27.1, 23.0, 14.4. HRMS-ESI: $M_{\text{theoretical}} = 423.3482$, $M_{\text{sample}} = 423.3502$, $\Delta M = -1.98$ mmass units (-4.69 ppm), $C_{29}H_{44}^{15}N_2$.

N,N'-di(4-dodecoxy-1-naphthyl)carbodiimide-



Following the outlined procedure for the synthesis of carbodiimides from ureas/thioureas to carbodiimide monomers: 0.359 g (0.515 mmol, 1.0 eq.) of *N,N'*-di(4-dodecoxy-1-naphthyl)thiourea, 0.284 g (0.672 mmol, 1.2 eq.) of PPh_3Br_2 , 0.200 mL (1.44 mmol, 2.5 eq.) of TEA.

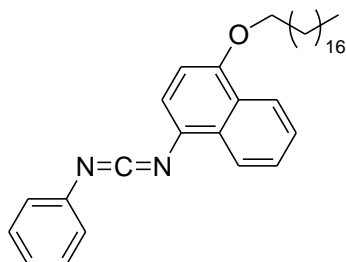
Yield: 0.0982 g (0.148 mmol) of white solid, 29 %. FTIR (KBr thinfilm, cm^{-1}): 3046 (w, Ar-H), 2917 (s, alkyl-H), 2848 (m, alkyl-H), 2129 (s, N=C=N), 1587 (m, C=C_{aryl}). 1H NMR (400 MHz, $CDCl_3$): δ (ppm) 8.30 (Ar-H, m, 2H), 7.54 (Ar-H, m, 2H), 7.33 (Ar-H, 2H, m), 6.75 (Ar-H, $J_{1H-1H} = 8.4$ Hz, 1H, d), 4.12 (O-**CH**₂CH₂(CH₂)₉CH₃, $J_{1H-1H} = 6.0$ Hz, 2H, t), 1.92 (-CH₂**CH**₂(CH₂)₉CH₃, 2H, m) 1.56 (-CH₂CH₂**CH**₂(CH₂)₈CH₃, 2H, m), 1.32 (-CH₂CH₂CH₂(**CH**₂)₈CH₃, 16H, m) 0.88 (-CH₂CH₂(CH₂)₉**CH**₃, $J = 6.8$ Hz, 3H, t). ^{13}C NMR (100 MHz, $CDCl_3$): 153.1, 135.7, 130.6, 129.0, 127.6, 127.0, 125.9, 123.4, 122.5, 121.0, 104.8, 68.7, 32.2, 31.7, 30.0, 29.9, 29.7, 29.6, 29.5, 26.5, 23.0, 14.4.

N-(4-octadecyloxy-1-naphthyl)-*N'*-1-naphthylcarbodiimide-

Following the outlined procedure for the dehydration/ protodesulfurization of ureas/ thioureas to carbodiimide monomers: 0.559 g (0.962 mmol, 1.0 eq.) of *N*-(4-octadecyloxy-1-naphthyl)-*N'*-1-naphthylurea, 0.490 g (1.15 mmol, 1.2 eq.), 0.330 mL (2.39 mmol, 2.5 eq.) of TEA.

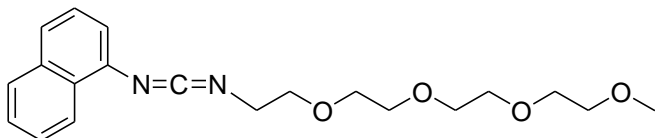
Yield: 0.165 g (0.293 mmol) of off-white solid, 30 %. FTIR (KBr thinfilm, cm^{-1}): 3048 (w, Ar-H), 2915 (s, alkyl-H), 2850 (m, alkyl-H), 2146 (s, N=C=N), 1589 (m, C=C_{aryl}). ^1H NMR (400 MHz, CDCl_3): δ (ppm) 8.40 (Ar-H, m, 2H), 8.30 (Ar-H, m, 2H), 7.68 (Ar-H, $J_{\text{1H-1H}} = 6.0$ Hz, $J_{\text{1H-1H}} = 3.6$ Hz, dd, 1H), 7.56 (Ar-H, m, 4H), 7.46 (Ar-H, 2H, m), 7.35 (Ar-H, $J_{\text{1H-1H}} = 8.0$ Hz, d, 1H), 6.76 (Ar-H, $J_{\text{1H-1H}} = 8.0$ Hz, 1H, d), 4.14 (O-CH₂CH₂(CH₂)₁₅CH₃, $J_{\text{1H-1H}} = 6.0$ Hz, 2H, t), 1.93 (-CH₂CH₂(CH₂)₁₅CH₃, 2H, m) 1.57 (-CH₂CH₂CH₂(CH₂)₁₄CH₃, 2H, m), 1.30 (-CH₂CH₂CH₂(CH₂)₁₄CH₃, 28H, m) 0.88 (-CH₂CH₂(CH₂)₁₅CH₃, $J = 6.8$ Hz, 3H, t). ^{13}C NMR (100 MHz, CDCl_3): 153.3, 135.9, 134.7, 129.8, 129.1, 128.1, 127.6, 127.2, 126.7, 126.5, 126.1, 126.0, 125.5, 123.8, 123.3, 122.6, 121.4, 120.9, 104.7, 68.7, 32.2, 29.9, 29.7, 29.6, 29.5, 26.5, 22.9, 14.4.

N-(4-octadecyloxy-1-naphthyl)-*N'*-phenylcarbodiimide-



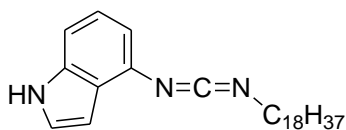
Following the outlined procedure for the dehydration/ protodesulfurization of ureas/ thioureas to carbodiimide monomers: 0.880 g (1.61 mmol, 1.0 eq.) of thiourea, 0.8208 g (1.94 mmol, 1.2 eq.) of PPh₃Br₂, 0.560 mL (4.04 mmol, 2.5 eq.) of TEA.

Yield: 0.605 g (1.18 mmol) of white solid, 73 %. FTIR (KBr thinfilm, cm⁻¹): 3049 (w, Ar-H), 2925 (s, alkyl-H), 2858 (m, alkyl-H), 2123 (s, N=C=N), 1588 (m, C=C_{aryl}). ¹H NMR (400 MHz, CDCl₃): δ (ppm) 8.27 (Ar-H, overlapped m, 2H), 7.54 (Ar- H, overlapped m, 2H), 7.27 (Ar-H, overlapped m, 6H), 6.73 (Ar-H, *J*_{1H-1H} = 8.0 Hz, d, 1H), 4.12 (O-**CH**₂CH₂(CH₂)₁₅CH₃, *J*_{1H-1H} = 6.0 Hz, 2H, t), 1.92 (-CH₂**CH**₂(CH₂)₁₄CH₃, 2H, m) 1.55 (-CH₂CH₂**CH**₂(CH₂)₁₄CH₃, 2H, m), 1.30 (-CH₂CH₂CH₂(**CH**₂)₁₄CH₃, m, 28H), 0.88 (-CH₂CH₂(CH₂)₁₅**CH**₃, *J* = 6.0 Hz, t, 3H). ¹³C NMR (100 MHz, CDCl₃): 153.4, 135.3, 129.7, 127.2, 126.5, 126.4, 126.0, 125.4, 124.3, 123.3, 122.6, 121.4, 104.7, 68.7, 32.2, 29.9, 29.8, 29.7, 29.6, 29.5, 26.5, 22.9, 14.4.

N-(1-naphthyl)-*N'*-(2-(2-(2-(2-methoxyethoxy)ethoxy)ethoxy)ethyl)carbodiimide-

Following the outlined procedure for the dehydration/ desulfurization of ureas/ thioureas to carbodiimide monomers except for using ethyl acetate as the mobile phase in column chromatography: 1.01 g (2.69 mmol, 1.0 eq.) of urea, 1.37 g (3.25 mmol, 1.2 eq.) of PPh_3Br_2 , 0.930 mL (6.72 mmol, 2.5 eq.) of TEA.

Yield: 0.693 g (1.93 mmol) of white solid, 73 %. FTIR (KBr thinfilm, cm^{-1}): 3050 (w, Ar-H), 2927 (s, alkyl-H), 2873 (s, alkyl-H), 2130 (s, N=C=N), 1573 (m, C=C_{aryl}). ^1H NMR (400 MHz, CDCl_3): δ (ppm) 8.28 (Ar-H, m, 1H), 7.80 (Ar-H, m, 1H), 7.61 (Ar-H, $J_{\text{1H-1H}} = 7.6$ Hz, d, 1H), 7.49 (Ar-H, overlapped m, 2H), 7.38 (Ar-H, overlapped m, 2H), 3.75 (glycol-H, $J_{\text{1H-1H}} = 4.8$ Hz, t, 2H), 3.64 (glycol-H, overlapped m, 4H) 3.53 (glycol-H, overlapped m, 10H), 3.36 (OCH_3 , s, 3H). ^{13}C NMR (100 MHz, CDCl_3): 138.6, 134.3, 127.7, 126.3, 125.8, 125.7, 124.6, 123.6, 120.2, 71.9, 70.7, 70.6, 70.5, 70.4, 59.0, 46.7.

N-indole-*N'*-octadecylcarbodiimide-

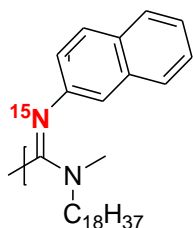
Following the outlined procedure for the dehydration/ desulfurization of ureas/ thioureas to carbodiimide monomers: 0.979 g (2.28 mmol, 1.0 eq.) of *N*-indole-*N*-octadecyl urea, 1.16 g (2.75 mmol, 1.2 eq.) of PPh_3Br_2 , 0.793 mL (5.72 mmol, 2.5 eq.) of TEA.

Yield: 0.300 g (0.731 mmol) of white solid, 32 %. ^1H NMR (400 MHz, CDCl_3): δ (ppm) 8.21 (N- H_{cyclic} , s, 1H), 7.20 (Ar- H, $J_{1\text{H}-1\text{H}} = 3.2$ Hz, t, 1H), 7.17 (Ar-H, s, 1H), 7.10 (Ar-H, $J_{1\text{H}-1\text{H}} = 7.6$ Hz, t, 1H), 6.84 (Ar-H, $J_{1\text{H}-1\text{H}} = 7.2$ Hz, s, 1H), 7.60 (Ar-H, $J_{1\text{H}-1\text{H}} = 2.4$ Hz, t, 1H), 3.45 (N- $\text{CH}_2\text{CH}_2(\text{CH}_2)_{15}\text{CH}_3$, $J_{1\text{H}-1\text{H}} = 7.2$ Hz, 2H, t), 1.71 ($-\text{CH}_2\text{CH}_2(\text{CH}_2)_{14}\text{CH}_3$, 2H, m) 1.43 ($-\text{CH}_2\text{CH}_2\text{CH}_2(\text{CH}_2)_{14}\text{CH}_3$, 2H, m), 1.25 ($-\text{CH}_2\text{CH}_2\text{CH}_2(\text{CH}_2)_{14}\text{CH}_3$, 28H, m), 0.88 ($-\text{CH}_2\text{CH}_2(\text{CH}_2)_{15}\text{CH}_3$, $J = 6.8$ Hz, 3H, t). ^{13}C NMR (100 MHz, CDCl_3): 123.9, 122.8, 114.5, 108.1, 100.5, 94.6, 47.3, 32.2, 31.5, 29.9, 29.8, 29.7, 29.6, 29.4, 27.1, 22.9, 14.3.

The Polymerization of Carbodiimide Monomers-

All polymerizations were conducted in the inert N_2 atmosphere dry box. The monomers were placed in a clean vial equipped with a stir bar and added to the dry box. A catalyst solution was made in the clean vial in dry chloroform followed by injection of a specified amount into the vial containing the monomer. The polymerization times vary greatly depending on the nature of the monomer used. The pre-weighed amount of catalyst was added directly into the monomer vial for solvent-free polymerizations. To form optically active polymers with a helical bias, **Cat-2R** was utilized for chiral induction upon polymerization of all polymers in this chapter. All polymers were worked up by re-dissolving them in the minimal amount of chloroform and precipitating the product upon addition to methanol, a typical anti-solvent. The polymer product was then filtered, collected and dried under high vacuum. The monomer-to-catalyst ratio, yield, ^1H NMR, IR, and ^{15}N NMR data (for labeled polymers) of each polymer is reported below as well as scans of the IR spectra.

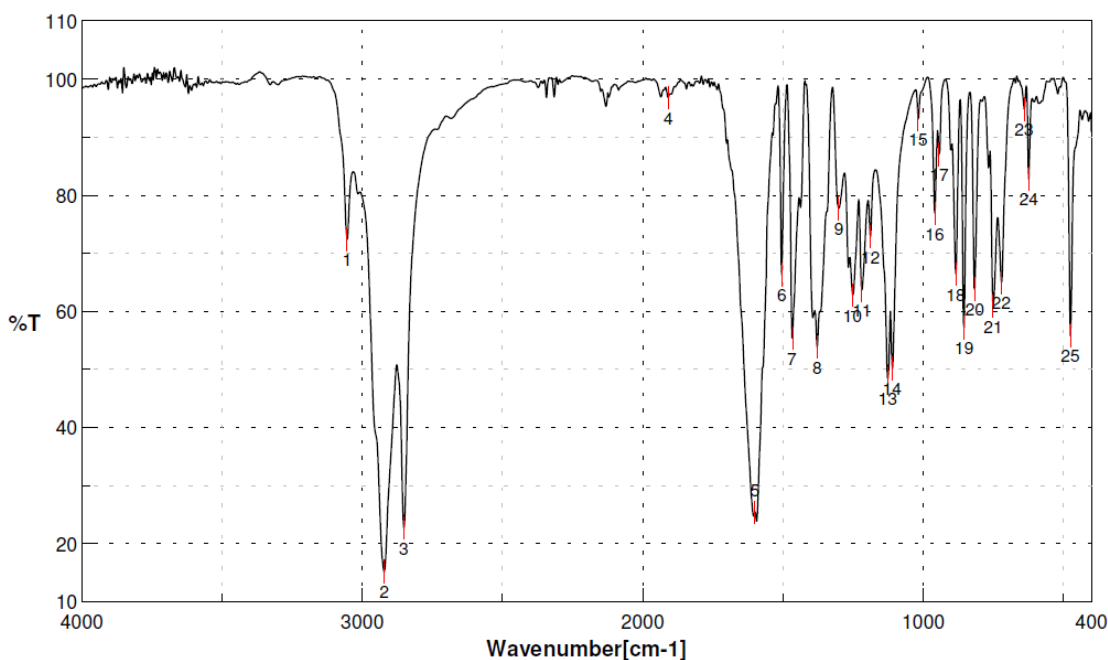
Poly(¹⁵N-2-naphthyl-N-octadecylcarbodiimide) (Poly-30)-



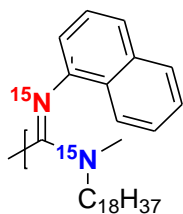
Following the outlined procedure for the polymerization of carbodiimide monomers with titanium(IV) catalysts: 1.08 g (2.56 mmol, 200 eq) of ¹⁵N-2-naphthyl-N-octadecylcarbodiimide, 5.76 mg (12.8 μmol, 1.0 eq), of **Cat-2R**, 0.40 mL of dry CHCl₃.

Yield: 0.904 g (2.15 mmol) of orangish-white solid, 84 %. FTIR (KBr pellet, cm⁻¹): 3054 (m, Ar-H), 2922 (s, alkyl-H), 2852 (s, alkyl-H), 1600 (s, ¹⁵N=C), 1504 (m, C=C_{aryl}). ¹H NMR (400 MHz, CDCl₃): δ (ppm) 8.01 - 6.92 (Ar-H, broad overlapped), 1.27 (octadecyl-H, broad s), 0.88 (-CH₃, broad s). ¹⁵N NMR (40.5 MHz, CDCl₃): δ (ppm) 133.6.

No.	cm-1	%T	No.	cm-1	%T	No.	cm-1	%T
1	3054.69	72.3423	2	2921.63	15.1653	3	2852.2	22.6958
4	1909.18	96.8523	5	1600.63	25.4	6	1504.2	66.3504
7	1465.63	55.3878	8	1378.85	53.8403	9	1301.72	77.7586
10	1251.58	62.8196	11	1218.79	63.6852	12	1187.94	72.8859
13	1126.22	48.3964	14	1110.8	50.1234	15	1018.23	93.1258
16	958.448	76.8794	17	943.02	87.0236	18	883.238	66.4209
19	854.311	57.2446	20	815.742	63.7747	21	750.174	60.893
22	721.247	65.0531	23	640.251	94.8303	24	622.895	82.773
25	474.403	55.8184						



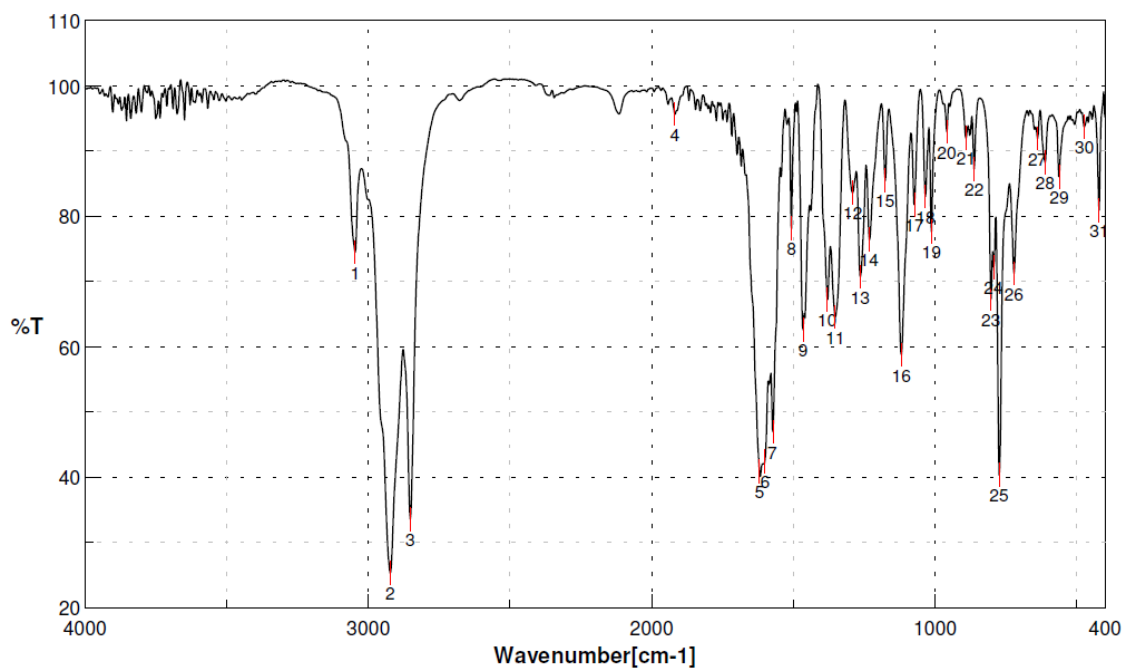
Poly(¹⁵N-1-naphthyl-¹⁵N-octadecylcarbodiimide) (Poly-31)-



Following the outlined procedure for the polymerization of carbodiimide monomers with titanium(IV) catalysts: 0.944 g (2.24 mmol, 198 eq) of ¹⁵N-1-naphthyl-¹⁵N-octadecylcarbodiimide, 5.10 mg (11.3 μmol, 1.0 eq), of **Cat-2S**, w/o solvent.

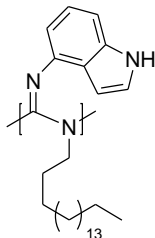
Yield: 0.880 g (2.09 mmol) of orangish-brown solid, 93 %. FTIR (KBr pellet, cm⁻¹): 3046 (m, Ar-H), 2924 (s, alkyl-H), 2852 (s, alkyl-H), 1619 (s, ¹⁵N=C), 1601 (s, ¹⁵N=C), 1571 (m, C=C_{aryl}). ¹H NMR (400 MHz, CDCl₃): δ (ppm) 8.01 - 6.32 (Ar-H, broad overlapped), 1.90 - 1.27 (octadecyl-H, broad s), 0.88 (-CH₃, broad s). ¹⁵N NMR (40.5 MHz,

CDCl₃: δ (ppm) 147.7 (¹⁵N=C), 137.8 (¹⁵N=C), 19.9 (¹⁵N-C), 11.5 (¹⁵N-C).



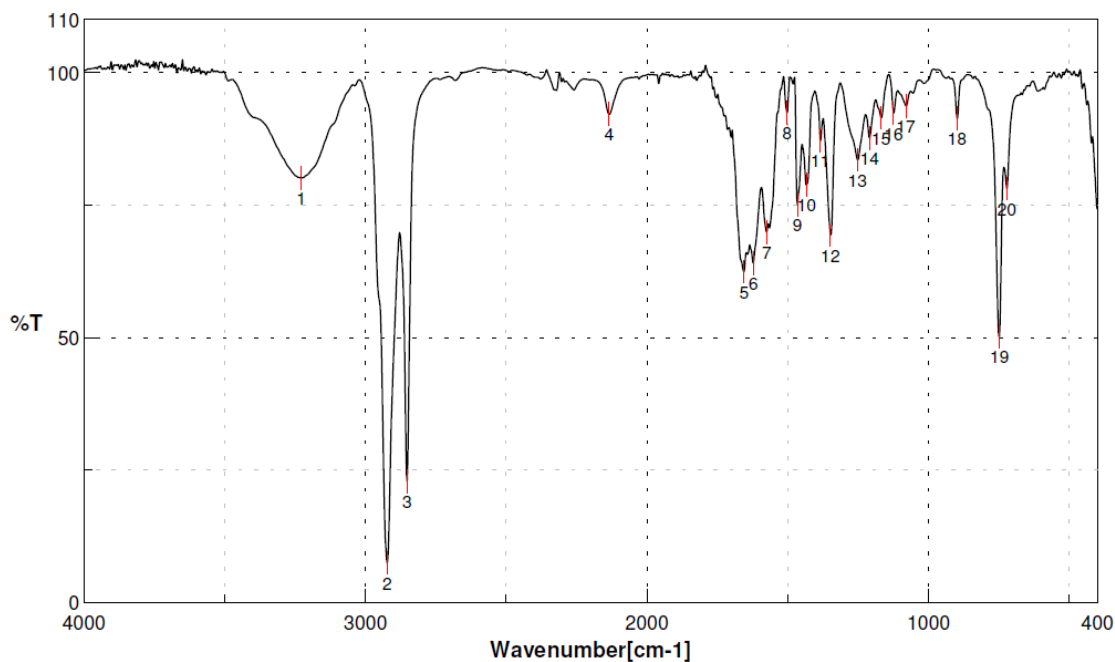
No.	cm-1	%T	No.	cm-1	%T	No.	cm-1	%T
1	3046.98	74.5289	2	2923.56	25.3335	3	2852.2	33.6238
4	1918.82	95.7059	5	1619.91	40.9686	6	1600.63	42.4883
7	1571.7	46.9899	8	1506.13	78.168	9	1465.63	62.6326
10	1380.78	67.2492	11	1351.86	64.6091	12	1290.14	83.6521
13	1263.15	70.7965	14	1232.29	76.4491	15	1176.36	85.5172
16	1118.51	58.8067	17	1072.23	81.818	18	1033.66	83.0662
19	1012.45	77.7033	20	958.448	92.9863	21	890.952	92.0063
22	862.025	87.2934	23	802.242	67.3473	24	792.6	72.2194
25	773.315	40.3542	26	721.247	71.2989	27	638.323	91.9582
28	611.324	88.2695	29	561.184	86.1133	30	472.474	93.7338
31	420.406	80.9864						

Poly(N-indole-N'-octadecylcarbodiimide) (Poly-41)-



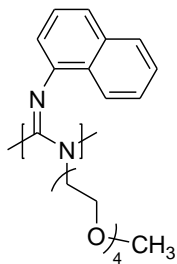
Following the outlined procedure for the polymerization of carbodiimide monomers with titanium(IV) catalysts: 0.300 g (0.732 mmol, 206 eq) of *N*-indole-*N*'-octadecylcarbodiimide, 1.65 mg (3.55 μ mol, 1.0 eq), of **Cat-2S**, w/o solvent.

Yield: 0.115 g (0.281 mmol) of yellow powder, 38 %. FTIR (KBr pellet, cm^{-1}): 3228 (s broad, N-H_{cyclic}), 2924 (s, alkyl-H), 2852 (s, alkyl-H), 1655 (s, N=C), 1622 (s, N=C), 1576 (m, C=C_{aryl}). ¹H NMR (400 MHz, CDCl₃): δ (ppm) 8.56 (N-H, broad s), 7.13 – 6.62 (Ar-H, broad overlapped), 3.20 (N-CH₂, broad s), 1.63 - 1.25 (octadecyl-H, broad s), 0.88 (-CH₃, broad s). $[\alpha]_{435}^{20} = -7.25^\circ$ ($l = 10.0$ cm, CHCl₃)



No.	cm-1	%T	No.	cm-1	%T	No.	cm-1	%T
1	3228.25	80.1226	2	2923.56	7.47067	3	2852.2	22.8617
4	2134.81	92.1695	5	1654.62	62.4368	6	1621.84	64.0702
7	1575.56	69.9255	8	1502.28	92.43	9	1465.63	75.1494
10	1432.85	78.832	11	1384.64	87.1826	12	1348	69.3627
13	1251.58	83.5448	14	1209.15	87.6816	15	1168.65	91.5574
16	1124.3	92.4013	17	1079.94	93.751	18	898.666	91.3365
19	748.245	50.2019	20	721.247	78.1284			

Poly(N-1-naphthyl-N'-(2-(2-(2-(2-methoxyethoxy)ethoxy)ethoxy)ethyl)carbodiimide)

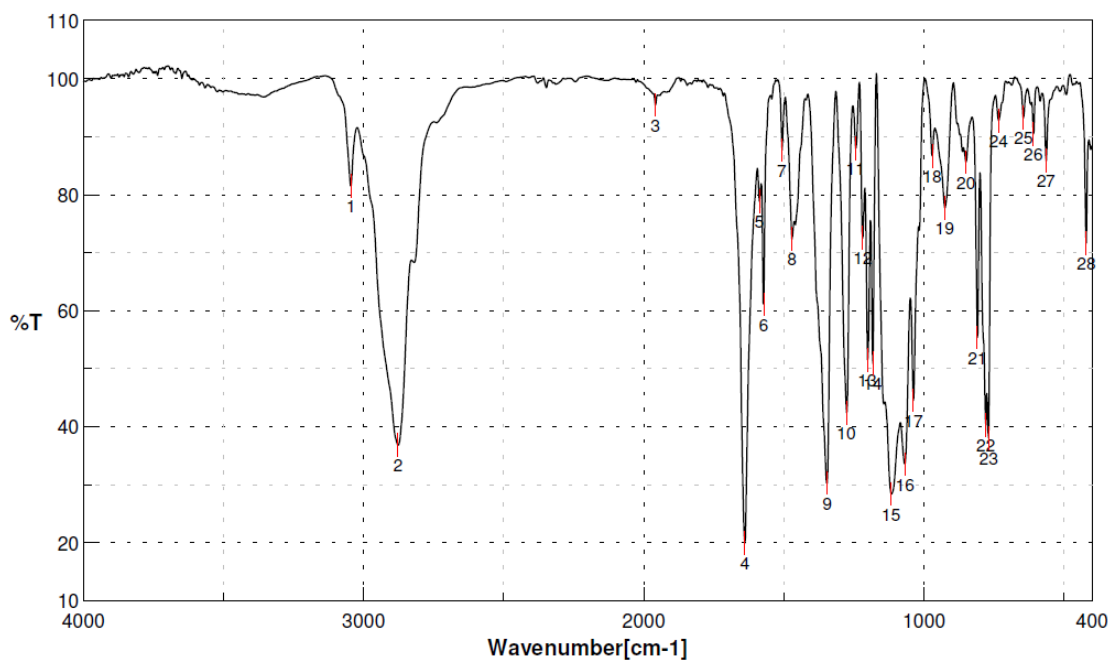


Following the outlined procedure for the polymerization of carbodiimide monomers with titanium(IV) catalysts: 0.680 g (1.89 mmol, 200 eq) of N-1-naphthyl-N'-(2-(2-(2-(2-methoxyethoxy)ethoxy)ethoxy)ethyl)carbodiimide, 4.25 mg (9.43 μ mol, 1.0 eq), of **Cat-2S**,

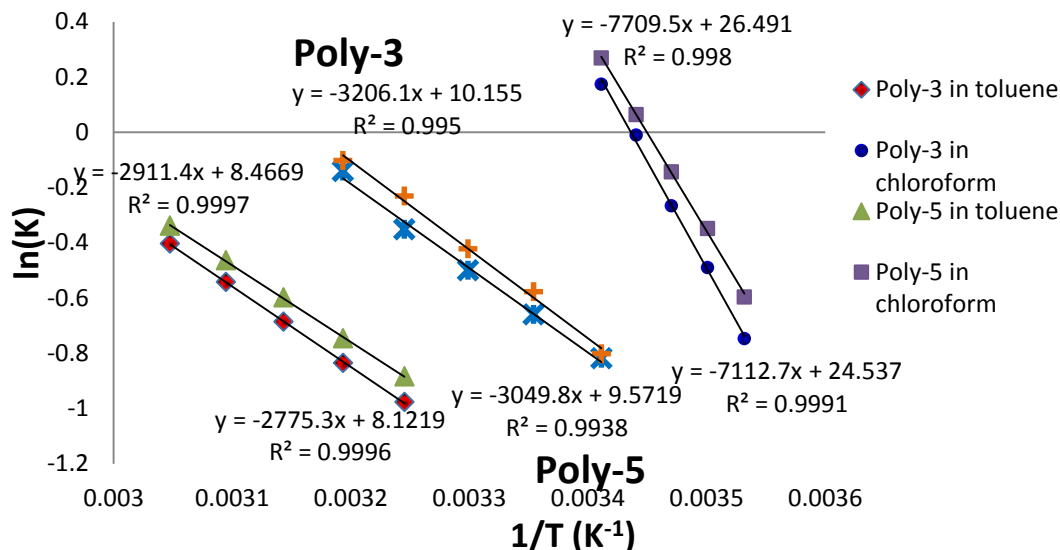
0.20 mL of dry CHCl_3 .

Yield: 0.094 g (0.262 mmol) of yellow solid, 14 %. FTIR (KBr pellet, cm^{-1}): 3045 (m, Ar-H), 2877 (s, alkyl-H), 1655 (s, N=C), 1639 (s, N=C), 1587 (w, C=C_{aryl}), 1571 (m C=C_{aryl}), 1117 (s, C-O). ^1H NMR (400 MHz, CDCl_3): δ (ppm) 7.36 – 6.98 (Ar-H, broad overlapped), 6.45 (Ar-H, broad d), 4.17 (glycol-H, broad s), 3.49 – 3.30 (glycol-H, overlapped broad), 2.87 – 2.70 (glycol-H, overlapped broad), 2.34 (OCH₃, broad s). $[\alpha]_{435}^{20} = -29.85^\circ$ ($l = 10.00$ cm, CHCl_3 , toluene)

No.	cm-1	%T	No.	cm-1	%T	No.	cm-1	%T
1	3045.05	81.5078	2	2877.27	36.8085	3	1959.32	95.5027
4	1639.2	19.9347	5	1587.13	78.8847	6	1571.7	61.0928
7	1506.13	87.7053	8	1471.42	72.3761	9	1346.07	30.282
10	1276.65	42.4158	11	1243.86	88.0323	12	1218.79	72.5259
13	1201.43	51.5426	14	1182.15	50.9093	15	1116.58	28.411
16	1068.37	33.543	17	1037.52	44.5841	18	970.019	86.6877
19	925.664	77.7494	20	850.454	85.6163	21	809.956	55.3679
22	779.101	40.2869	23	769.458	38.0604	24	732.817	92.778
25	644.108	93.2697	26	609.396	90.4568	27	563.112	85.8085
28	420.406	71.6751						



Raw van't Hoff data with R^2 Values and Equations-



Estimated error values- Maximum Errors associated with each data point were calculated using the errors of integration estimated using the relationship between errors and NMR signal-to-noise in the equation reported by Malz et al.⁵³ These error values were then extrapolated to the energies values reported in the discussion. These errors are believed to be a good estimation of the maximum deviations for each van't Hoff energy value calculated.

Cartesian Coordinates for DFT-optimized Models-

The geometry optimizations as well as the IR and VCD spectra calculations were performed with the Gaussian 09 D.01 software package at the B3LYP/6-31G(d,p) level of theory. Implicit solvation was taken into account by the integral equation formalism variant of the polarizable continuum model (IEFPCM) for chloroform. For better visual comparison, the calculated frequencies were scaled by a factor of 0.975 and line broadening was simulated by assigning a Lorentzian band

shape of 8 cm^{-1} half-width at half-height to the calculated dipole and rotational strength. The Cartesian coordinates for the two models are as follows:

Model A

C	5.60457500	4.54588800	-28.43461400
C	5.69634400	6.68628500	-27.24150100
C	6.97943600	2.50942200	-28.31798400
N	6.93705900	1.13518600	-28.48333700
N	5.72684800	3.12234800	-28.31715600
N	5.79672100	5.26095000	-27.26996600
N	6.64673700	7.38338600	-27.94776900
N	4.85453800	7.32476200	-26.50906800
N	5.22428200	5.14193800	-29.49925200
N	8.00774400	3.25791600	-28.09463900
C	4.49145100	2.42289700	-27.94956000
H	3.88090400	3.07246200	-27.31663300
H	3.89437800	2.14698900	-28.82409700
H	4.74195500	1.52348600	-27.38617100
C	6.00682700	4.59328100	-25.97941200
H	5.11047600	4.07145200	-25.63348200
H	6.84696700	3.90355500	-26.06419900
H	6.25363900	5.35728500	-25.24357200
C	7.84429900	6.77776700	-28.54064000
H	8.73484200	7.29819600	-28.18443100
H	7.91498100	5.73120300	-28.25136600
H	7.79689700	6.84836900	-29.63176000
C	6.57645000	8.81369600	-28.02932200
C	6.19192400	0.52740600	-29.58068700
H	6.88777600	0.06399100	-30.29182100
H	5.50440800	-0.24584300	-29.21637700
H	5.62208700	1.28401200	-30.11900900
C	7.93906600	0.27522000	-27.87427900
H	7.45294800	-0.65606000	-27.56023800
H	8.75528700	0.02508600	-28.56300700
H	8.36270500	0.75736100	-26.99430100
N	7.46636400	9.60733100	-27.55256500
C	9.34884300	2.88806800	-28.27567700
C	9.88418200	2.41184700	-29.52330400
C	10.21700400	3.09504600	-27.21498900
C	9.09416800	2.24836900	-30.69050800
C	11.28385800	2.10599900	-29.60581800
C	11.58914700	2.79380800	-27.30866200
H	9.81014700	3.49109800	-26.29067200
C	9.63788900	1.78177700	-31.86492500
H	8.04760900	2.51876300	-30.66157000
C	11.80936100	1.62033500	-30.83246200
C	12.11677100	2.29787200	-28.47564300
H	12.22677500	2.95768700	-26.44563500
C	11.01018300	1.45491200	-31.93672400
H	9.00890200	1.67107500	-32.74264900
H	12.86904600	1.38659800	-30.88078100
H	13.17301400	2.06062700	-28.55453300
H	11.43071800	1.08431200	-32.86603500
C	5.14047700	4.49891000	-30.74871300
C	3.86630500	4.11646300	-31.28164100

C	6.27288600	4.35451700	-31.52842500
C	2.65927700	4.26780400	-30.55214700
C	3.80508900	3.56484600	-32.60269900
C	6.20062300	3.81320700	-32.83010500
H	7.22593600	4.68416200	-31.13179000
C	1.45191300	3.88781500	-31.08966300
H	2.70449500	4.69443500	-29.55799300
C	2.54228700	3.17967400	-33.12339000
C	4.99603700	3.42078400	-33.35901600
H	7.11290600	3.71829100	-33.41046500
C	1.39196400	3.33487700	-32.38852700
H	0.53879200	4.01831500	-30.51779900
H	2.50284200	2.75994500	-34.12429800
H	4.93551000	3.00743600	-34.36092400
H	0.43446800	3.03801400	-32.80423000
C	3.72024500	6.71618500	-25.95479800
C	3.44995900	6.90225800	-24.55834200
C	2.80523600	6.02707400	-26.73395900
C	4.31889600	7.63565000	-23.71121800
C	2.26512400	6.32696200	-23.99683800
C	1.63479900	5.47489200	-26.17237500
H	2.98626800	5.94857600	-27.79971500
C	4.04045900	7.78876900	-22.37313700
H	5.19975800	8.09287700	-24.14442100
C	2.01367800	6.49862600	-22.61071200
C	1.37093700	5.60855500	-24.83101300
H	0.93800200	4.94630200	-26.81590100
C	2.87917800	7.20935300	-21.81475300
H	4.71319200	8.36058500	-21.74206400
H	1.11431100	6.05852100	-22.18985200
H	0.47211500	5.18370200	-24.39522900
H	2.66984200	7.33403200	-20.75717400
C	8.42360800	9.23751800	-26.60281800
C	9.77067000	9.70735600	-26.77759000
C	8.10227100	8.52746700	-25.45648600
C	10.16756100	10.46532900	-27.90839400
C	10.75056900	9.39948200	-25.78011100
C	9.07463200	8.23897600	-24.47720900
H	7.07624200	8.21368600	-25.30844700
C	11.46580000	10.89582300	-28.05369800
H	9.42269200	10.71294500	-28.65387200
C	12.08174100	9.85477100	-25.96546000
C	10.37355200	8.65637500	-24.63261000
H	8.78187100	7.68505000	-23.59040500
C	12.43526300	10.58407900	-27.07481800
H	11.74798800	11.47998500	-28.92372100
H	12.81983500	9.61647100	-25.20508000
H	11.12373800	8.43574300	-23.87955500
H	13.45756000	10.92671400	-27.19946900
C	5.41714300	10.76237500	-28.89188200
C	4.68765300	12.84368300	-27.87592100
C	5.70300900	15.04780700	-27.73255500
C	4.61717300	8.55363100	-29.58984000
H	4.60851200	8.94294200	-30.61042600
H	4.92776100	7.51140300	-29.61870000
H	3.60672000	8.61505700	-29.17280600
C	4.41011700	10.78147600	-26.58470900
H	3.34036000	10.97674400	-26.47033500
H	4.56880500	9.70663300	-26.63188400

H	4.93971400	11.18083600	-25.71450800
C	7.10466200	13.04754300	-27.33377500
H	7.07957100	12.69052400	-26.30073900
H	7.38756400	12.22566300	-27.98827400
H	7.85492900	13.83444800	-27.40396300
N	5.63553600	11.41481100	-29.97746500
C	6.27397700	10.88779300	-31.10546500
C	5.71374800	11.19419600	-32.39393200
C	7.46160100	10.17580800	-31.04239300
C	4.52271800	11.95021200	-32.53970700
C	6.37385600	10.72102100	-33.57311600
C	8.10834300	9.72599500	-32.21232600
H	7.90814200	9.98338600	-30.07527000
C	4.00081700	12.21920600	-33.78373300
H	4.03688200	12.32513500	-31.64788400
C	5.80410800	11.01254000	-34.83980900
C	7.57752100	9.98075000	-33.45269800
H	9.03961200	9.17554600	-32.11967800
C	4.64458300	11.74168800	-34.94688000
H	3.08973700	12.80227000	-33.87346600
H	6.30887500	10.64650900	-35.72933200
H	8.07278200	9.63179900	-34.35353500
H	4.22328300	11.95640400	-35.92395400
N	3.53206700	13.39216200	-27.92897000
N	6.01512200	15.77413400	-26.71475800
N	5.54743300	9.33681300	-28.77379200
N	4.90965800	11.42242900	-27.80254700
N	5.81848500	13.61799300	-27.75204300
N	5.32078600	15.63469700	-28.89785400
C	5.30529300	14.97353600	-30.18897800
H	4.28942500	14.96766100	-30.60227400
H	5.95689000	15.51002400	-30.89097000
H	5.65067100	13.94547400	-30.10579500
C	5.02095800	17.05457300	-28.90558800
H	5.89813800	17.65320200	-29.18702700
H	4.22292000	17.24549100	-29.63048200
H	4.70115500	17.36518900	-27.91223100
C	2.33399200	12.71907100	-28.17266300
C	1.19341100	13.09613200	-27.38173500
C	2.16870300	11.78744600	-29.18650400
C	1.27440200	14.08590200	-26.36996700
C	-0.06480200	12.45717400	-27.61949900
C	0.91761700	11.18038700	-29.42395600
H	3.01136900	11.54149200	-29.81962200
C	0.17397000	14.41748200	-25.61431700
H	2.21964700	14.59289600	-26.22114000
C	-1.17703300	12.81748200	-26.81496400
C	-0.17514000	11.49193700	-28.65298100
H	0.82853600	10.45876600	-30.23050900
C	-1.06324000	13.77098300	-25.83226800
H	0.25426000	15.18191400	-24.84790400
H	-2.12777300	12.32421600	-26.99661100
H	-1.13608500	11.01881100	-28.83094200
H	-1.92460700	14.03596200	-25.22710400
C	6.15648200	15.28146800	-25.41930400
C	7.30015900	15.70895600	-24.66040600
C	5.20478200	14.48311500	-24.80076000
C	8.29639800	16.54482100	-25.22366500
C	7.44638200	15.27750700	-23.30417300

C	5.35617400	14.07041200	-23.46005600
H	4.32248600	14.18926100	-25.35726700
C	9.39216100	16.93440600	-24.48927100
H	8.16235100	16.87682300	-26.24637000
C	8.59089000	15.69616600	-22.57655100
C	6.45237900	14.44896900	-22.72330100
H	4.58642800	13.44924700	-23.01137400
C	9.54312200	16.50276800	-23.15213600
H	10.14436000	17.57777600	-24.93497100
H	8.69989700	15.36450300	-21.54766700
H	6.56844000	14.13030600	-21.69189600
H	10.41191000	16.81341200	-22.57996600

Model B

C	-5.39322500	4.24936200	-17.05904600
C	-5.80844600	6.44616200	-16.17411800
C	-4.27854500	2.13268700	-16.75976600
N	-4.41423000	0.77240300	-16.94974300
N	-5.47393600	2.84884700	-16.80451200
N	-5.56784700	5.05756600	-15.95318000
N	-4.72635400	7.26499600	-15.93973300
N	-6.91809300	6.94550700	-16.56937800
N	-5.18327300	4.77974600	-18.20450600
N	-3.20386300	2.78334900	-16.44687500
C	-6.74466000	2.29181800	-16.33859300
H	-7.36826600	3.10280100	-15.95794200
H	-7.29706000	1.80207100	-17.14795700
H	-6.57164400	1.56548400	-15.54091200
C	-5.31011300	4.58978800	-14.58918800
H	-6.17247700	4.04783600	-14.18599500
H	-4.42706000	3.94935700	-14.57265100
H	-5.13774600	5.45908100	-13.95218400
C	-3.34659400	6.77648600	-15.87043300
H	-3.05776700	6.55469200	-14.83741800
H	-3.22811100	5.87756300	-16.47500400
H	-2.67826100	7.55411200	-16.24603100
C	-4.96171100	8.67313200	-15.87754100
C	-5.20304300	0.22747300	-18.04655800
H	-4.54417900	-0.29136600	-18.75631100
H	-5.94732600	-0.49286800	-17.68419800
H	-5.70638900	1.02782200	-18.58723100
C	-3.48311200	-0.16053400	-16.33846900
H	-4.03354000	-1.06445700	-16.05290200
H	-2.66731000	-0.44491500	-17.01473000
H	-3.04849200	0.28071900	-15.44176400
N	-5.47260600	9.28640700	-14.87878400
C	-1.92101800	2.34172600	-16.78503400
C	-0.88053800	2.43069700	-15.79818100
C	-1.59435000	1.92027200	-18.06563200
C	-1.13873100	2.85906700	-14.47201200
C	0.45759200	2.06815700	-16.15445300
C	-0.27144100	1.56798500	-18.40571000
H	-2.36694000	1.89584200	-18.82595600
C	-0.13041000	2.93116300	-13.53887800
H	-2.15358400	3.13330800	-14.21040400
C	1.47328200	2.15316900	-15.16694200

C	0.73709900	1.63421000	-17.47572100
H	-0.05769200	1.24993300	-19.42155100
C	1.19063000	2.57367300	-13.88951800
H	-0.34752200	3.26474700	-12.52900700
H	2.48701300	1.87703100	-15.44306600
H	1.75581300	1.36508600	-17.73745700
H	1.98068600	2.63300600	-13.14749100
C	-5.27761600	4.05908100	-19.40006300
C	-4.16504900	4.07156200	-20.30487100
C	-6.45657200	3.44054900	-19.78611800
C	-2.94427000	4.71823300	-19.98602500
C	-4.28675400	3.41035500	-21.56886300
C	-6.56793300	2.80052600	-21.03925100
H	-7.31946100	3.49443300	-19.13179200
C	-1.88953700	4.71199000	-20.86846900
H	-2.86177700	5.22017800	-19.02999900
C	-3.17550400	3.41794700	-22.45161100
C	-5.50728100	2.77372700	-21.91145100
H	-7.51036600	2.33444700	-21.30997300
C	-2.00430300	4.05201100	-22.11268000
H	-0.96248000	5.21265200	-20.60853600
H	-3.27128800	2.91263600	-23.40847600
H	-5.59180000	2.28222000	-22.87584500
H	-1.16483300	4.05035500	-22.80087900
C	-8.10215900	6.19992300	-16.61547900
C	-8.80718100	6.10115400	-17.86069700
C	-8.66483800	5.65218400	-15.47368000
C	-8.29841200	6.66283400	-19.05868300
C	-10.06042800	5.41023000	-17.89998200
C	-9.90438900	4.97805100	-15.52364700
H	-8.16297800	5.78643700	-14.52226400
C	-8.99041100	6.55155400	-20.24160400
H	-7.34985600	7.18329700	-19.02026000
C	-10.74476200	5.30982500	-19.13976700
C	-10.58760600	4.84943300	-16.70829000
H	-10.31775000	4.56800800	-14.60727000
C	-10.22562800	5.86636800	-20.28380000
H	-8.58578200	6.98723100	-21.14938500
H	-11.69530400	4.78451700	-19.16505100
H	-11.54169400	4.33269200	-16.74725900
H	-10.76313600	5.78227300	-21.22310400
C	-5.66101400	8.66564300	-13.63682000
C	-6.98897700	8.56753000	-13.10451900
C	-4.58856000	8.24944600	-12.86510200
C	-8.12541200	8.99688500	-13.83538900
C	-7.17630200	8.01199500	-11.79832900
C	-4.78559700	7.70726400	-11.57631000
H	-3.58226500	8.38765600	-13.24355700
C	-9.38941400	8.88618900	-13.30539500
H	-7.97434900	9.41038400	-14.82459100
C	-8.49569700	7.90901900	-11.28491500
C	-6.04870200	7.58263500	-11.05184700
H	-3.92029300	7.39676000	-10.99878800
C	-9.57741500	8.33510800	-12.01757800
H	-10.24874600	9.21790300	-13.87905400
H	-8.63358500	7.48675100	-10.29361200
H	-6.20131500	7.16840600	-10.05987700
H	-10.57960500	8.25042600	-11.60910400
C	-4.56296200	10.79228900	-16.93008000

C	-5.53572600	12.84972500	-17.69716300
C	-6.37324300	15.00255800	-16.99748600
C	-4.38856400	8.72491300	-18.31129500
H	-3.33500500	8.46042600	-18.45201900
H	-4.99703400	7.82538300	-18.40136900
H	-4.66632200	9.42811000	-19.09901800
C	-6.89837500	10.76901000	-17.82958200
H	-6.92795200	10.45395800	-18.87825400
H	-7.04480800	9.89901400	-17.18988800
H	-7.71571500	11.47525900	-17.66700700
C	-6.62484800	13.06636500	-15.45761200
H	-7.69552400	12.83357500	-15.45755300
H	-6.06654500	12.16495800	-15.20881400
H	-6.43722900	13.81967400	-14.68859000
N	-3.63887500	11.46671900	-16.35580300
C	-2.44067300	10.87779300	-15.93068600
C	-2.07783200	10.96960800	-14.54592700
C	-1.55134600	10.30720900	-16.82671500
C	-2.93060500	11.56559400	-13.58278300
C	-0.81965200	10.43674200	-14.11847900
C	-0.31151000	9.78879500	-16.39389400
H	-1.79686400	10.30256100	-17.88241800
C	-2.56190700	11.63805200	-12.25994800
H	-3.88303000	11.96012300	-13.91365500
C	-0.47483800	10.52289600	-12.74404000
C	0.04864900	9.84211100	-15.06968300
H	0.36046900	9.35196400	-17.12606400
C	-1.32200700	11.10950500	-11.83497900
H	-3.22712300	12.09753100	-11.53598300
H	0.48037000	10.11634300	-12.42390800
H	1.00184000	9.44406800	-14.73557200
H	-1.04133400	11.16907500	-10.78796600
N	-4.89526200	13.41772600	-18.64477500
N	-7.26395000	15.48998000	-17.77746800
N	-4.60331200	9.36614300	-17.01124800
N	-5.63037800	11.43170000	-17.51414900
N	-6.19829100	13.59683600	-16.75261100
N	-5.55465500	15.82113600	-16.26461000
C	-4.20486100	15.42205500	-15.88593400
H	-3.46561500	15.82059300	-16.59434700
H	-3.97251800	15.81572200	-14.89077900
H	-4.10763700	14.33787900	-15.86850500
C	-5.77019400	17.25536200	-16.36826700
H	-5.29824700	17.74364300	-15.51064400
H	-5.34059000	17.66788500	-17.29157400
H	-6.83930300	17.46588700	-16.37146800
C	-4.37859200	12.69741300	-19.72965600
C	-2.96059300	12.68382400	-19.94148100
C	-5.20855900	12.09262800	-20.65886900
C	-2.06210000	13.30882400	-19.04048700
C	-2.43411400	12.01484300	-21.09238600
C	-4.67800600	11.43911600	-21.79265000
H	-6.28246200	12.16431400	-20.52924200
C	-0.70504500	13.27726000	-19.26104200
H	-2.47238000	13.80751000	-18.17137300
C	-1.02771300	11.99760200	-21.28497900
C	-3.32195600	11.39140200	-22.00646400
H	-5.35939100	10.97845100	-22.50119400
C	-0.18181900	12.61308700	-20.39363100

H	-0.03054500	13.76024600	-18.56136100
H	-0.63111900	11.48752300	-22.15834600
H	-2.91318100	10.88967200	-22.87822500
H	0.89112700	12.59173000	-20.55756400
C	-8.26733600	14.71008600	-18.36103100
C	-8.31495300	14.60973500	-19.79166600
C	-9.27700500	14.12884900	-17.61163900
C	-7.32585700	15.20574800	-20.61399100
C	-9.38471700	13.88495900	-20.40681100
C	-10.33130500	13.42004600	-18.22872000
H	-9.27203900	14.25610400	-16.53439500
C	-7.38642600	15.09231600	-21.98305100
H	-6.52036300	15.74793100	-20.13468400
C	-9.41212300	13.78424700	-21.82254600
C	-10.38556700	13.29088400	-19.59494000
H	-11.10521300	12.97934900	-17.60761100
C	-8.43871500	14.37296500	-22.59378800
H	-6.62114000	15.55288800	-22.59936100
H	-10.22431000	13.23206400	-22.28687700
H	-11.19482900	12.74552300	-20.07064400
H	-8.47589700	14.28797700	-23.67540700

3.12 References-

- (1) Agati, G.; McDonagh, A. F. *J. Am. Chem. Soc.* **1995**, *117*, 4425-4426.
- (2) Suk, J.-m.; Naidu, V. R.; Liu, X.; Lah, M. S.; Jeong, K.-S. *J. Am. Chem. Soc.* **2011**, *133*, 13938-13941.
- (3) Zou, G.; Jiang, H.; Zhang, Q.; Kohn, H.; Manaka, T.; Iwamoto, M. *J. Mater. Chem.* **2010**, *20*, 285-291.
- (4) Lindoy, L. F.; Jolliffe, K. A.; Clegg, J. K.; Meehan, G. V.; Parsons, S.; Tasker, P. A.; Turner, P.; White, F. J.; American Chemical Society: 2010, p INOR-10.
- (5) Li, D.; Wang, Z. Y.; Ma, D. *Chem. Comm.* **2009**, 1529-1531.
- (6) Zhang, G.; Liu, M. *J. Mater. Chem.* **2009**, *19*, 1471-1476.
- (7) Feringa, B. L.; van, D. R. A.; Koumura, N.; Geertsema, E. M. *Chem. Rev.* **2000**, *100*, 1789-1816.
- (8) Feringa, B. L.; Huck, N. P. M.; Schoevaars, A. M. *Adv. Mater.* **1996**, *8*, 681-684.
- (9) Yamaguchi, T.; Uchida, K.; Irie, M. *J. Am. Chem. Soc.* **1997**, *119*, 6066-6071.
- (10) Peng, X.; Wu, J.; Zhang, L.; Yan, W.; Yin, H.; Chen, S. *Jishou Daxue Xuebao, Ziran Kexueban* **2010**, *31*, 82-85.

- (11) Murata, K.; Aoki, M.; Nishi, T.; Ikeda, A.; Shinkai, S. *Chem. Comm.* **1991**, 1715-1718.
- (12) Oosterling, M. L. C. M.; Schoevaars, A. M.; Haitjema, K. J.; Feringa, B. L. *Isr. J. Chem.* **1997**, *36*, 341-348.
- (13) Ueno, A.; Takahashi, K.; Anzai, J.; Osa, T. *J. Am. Chem. Soc.* **1981**, *103*, 6410-6415.
- (14) Mammana, A.; Carroll, G. T.; Areephong, J.; Feringa, B. L. *J. Phys. Chem. B* **2011**, *115*, 11581-11587.
- (15) Pijper, D.; Jongejan, M. G. M.; Meetsma, A.; Feringa, B. L. *J. Am. Chem. Soc.* **2008**, *130*, 4541-4552.
- (16) Porsch, M.; Sigl-Seifert, G.; Daub, J. *Adv. Mater.* **1997**, *9*, 635-639.
- (17) Tang, H.-Z.; Boyle, P. D.; Novak, B. M. *J. Am. Chem. Soc.* **2005**, *127*, 2136-2142.
- (18) Tang, H.-Z.; Lu, Y.; Tian, G.; Capracotta, M. D.; Novak, B. M. *J. Am. Chem. Soc.* **2004**, *126*, 3722-3723.
- (19) Jennings, W. B.; Boyd, D. R. *J. Am. Chem. Soc.* **1972**, *94*, 7187-7188.
- (20) Tang, H.-Z.; Novak, B. M.; He, J.; Polavarapu, P. L. *Angew. Chem., Int. Ed.* **2005**, *44*, 7298-7301.
- (21) Kennemur, J. G., North Carolina State University, Thesis, 2010.
- (22) Kennemur, J. G.; Clark, J. B.; Tian, G.; Novak, B. M. *Macromolecules* **2010**, *43*, 1867-1873.
- (23) Goto, H.; Yashima, E.; Okamoto, Y. *Chirality* **2000**, *12*, 396-399.
- (24) Tian, G.; Lu, Y.; Novak, B. M. *J. Am. Chem. Soc.* **2004**, *126*, 4082-4083.
- (25) DeSousa, J. D.; Novak, B. M. *ACS Macro Lett.*, **2012**, *1*, 672-675.
- (26) Ambrosone, L.; Ragone, R. *Int. J. Biol. Macromol.* **2000**, *27*, 241-244.
- (27) Lavelle, L.; Fresco, J. R. *Nucleic Acids Res.* **1995**, *23*, 2692-2705.
- (28) Burgueño-Tapia, E.; García-Rojas, C. M. C.; Joseph-Nathan, P. *Phytochemistry* **2012**, *74*, 190-195.

- (29) Felipe, L. G.; Batista Jr, J. M.; Baldoqui, D. C.; Nascimento, I. R.; Kato, M. J.; He, Y.; Nafie, L. A.; Furlan, M. *Org. Biomol. Chem.* **2012**, *10*, 4208-4214.
- (30) García-Rojas, C. M. C.; Catalán, C. A. N.; Muro, A. C.; Joseph-Nathan, P. *J. Nat. Prod.* **2008**, *71*, 967-971.
- (31) Gussem, E. D.; Bultinck, P.; Feledziak, M.; Marchand-Brynaert, J.; Stevens, C. V.; Herrebout, W. *Phys. Chem. Chem. Phys.* **2012**, *14*, 8562-8571.
- (32) Chamayou, A.-C.; Lüdeke, S.; Brecht, V.; Freedman, T. B.; Nafie, L. A.; Janiak, C. *Inorg. Chem.* **2011**, *50*, 11363-11374.
- (33) Merten, C.; Amkreutz, M.; Hartwig, A. *Phys. Chem. Chem. Phys.* **2010**, *12*, 11635-11641.
- (34) Sato, H.; Mori, Y.; Fukuda, Y.; Yamagishi, A. *Inorg. Chem.* **2009**, *48*, 4354-4361.
- (35) Gautier, C.; Bürgi, T. *Chem. Comm.* **2005**, *43*, 5393-5395.
- (36) Gautier, C.; Bürgi, T. *J. Phys. Chem. C* **2010**, *114*, 15897-15902.
- (37) Yang, L.; Keiderling, T. A. *Biopolymers* **1993**, *33*, 315-327.
- (38) Gulotta, M.; Goss, D. J.; Diem, M. *Biopolymers* **1989**, *28*, 2047-2058.
- (39) Dukor, R. K.; Keiderling, T. A. *Biopolymers* **1991**, *31*, 1747-1761.
- (40) Yoder, G.; Polese, A.; Silva, R. A. G. D.; Formaggio, F.; Crisma, M.; Broxterman, Q. B.; Kamphuis, J.; Toniolo, C.; Keiderling, T. A. *J. Am. Chem. Soc.* **1997**, *119*, 10278-10285.
- (41) Merten, C.; Barron, L. D.; Hecht, L.; Johannessen, C. *Angew. Chem. Int. Ed.* **2011**, *50*, 9973-9976.
- (42) Merten, C.; Hartwig, A. *Macromolecules* **2010**, *43*, 8373-8378.
- (43) Schwartz, E.; Domingos, S. r. R.; Vdovin, A.; Koepf, M.; Buma, W. J.; Cornelissen, J. J. L. M.; Rowan, A. E.; Nolte, R. J. M.; Woutersen, S. *Macromolecules* **2010**, *43*, 7931-7935.
- (44) Wang, F.; Polavarapu, P. L.; Lebon, F.; Longhi, G.; Abbate, S.; Catellani, M. *J. Phys. Chem. A* **2002**, *106*, 5918-5923.

- (45) Tang, H.-Z.; Garland, E. R.; Novak, B. M.; He, J.; Polavarapu, P. L.; Sun, F. C.; Sheiko, S. S. *Macromolecules* **2007**, *40*, 3575-3580.
- (46) Kennemur, J. G.; Kilgore, C. A.; Novak, B. M. *J. Polym. Sci. Part A: Polym. Chem.* **2011**, *49*, 719-728.
- (47) Kreutzer, G.; Ternat, C.; Nguyen, T. Q.; Plummer, C. J. G.; Mnson, J.-A. E.; Castelletto, V.; Hamley, I. W.; Sun, F.; Sheiko, S. S.; Herrmann, A.; Ouali, L.; Sommer, H.; Fieber, W.; Velazco, M. I.; Klok, H.-A. *Macromolecules* **2006**, *39*, 4507-4516.
- (48) Zhang, Y.; Lin, C.; Li, Z.; Qin, L.; Wen, H. *J. Labelled Compd. Radiopharm.* **2010**, *53*, 183-185.
- (49) Huang, X.; Seid, M.; Keillor, J. W. *J. Org. Chem.* **1997**, *62*, 7495-7496.
- (50) Spitzer, U. A.; Stewart, R. *J. Org. Chem.* **1974**, *39*, 3936.
- (51) Gentilini, C.; Boccalon, M.; Pasquato, L. *Eur. J. Org. Chem.* **2008**, 3308-3313.
- (52) Kitto, H. J.; Schwartz, E.; Nijemeisland, M.; Koepf, M.; Cornelissen, J. J. L. M.; Rowan, A. E.; Nolte, R. J. M. *J. Mater. Chem.* **2008**, *18*, 5615-5624.
- (53) Malz, F.; Jancke, H. *J. Pharm. Biomed. Anal.* **2005**, *38*, 813-823.

CHAPTER 4: Potential Applications for PNOC and Related Polycarbodiimides

4.1 Introduction to Microscopy-

Throughout the remainder of this document, several different microscopy techniques will be employed in the imaging and characterization of polycarbodiimide homopolymers and copolymers such as optical microscopy (OM), scanning probe microscopy (SPM), and electron microscopy (EM). For this reason, it is imperative to briefly discuss the history and unique advantages of each of these techniques in the examination of polymer microstructures and morphologies. The characterization of structure and morphology of polymers is of the utmost importance and has been under investigation for more than 60 years. The necessity for new advanced imaging techniques such as SPM and EM first became apparent at the turn of the nineteenth century when the pioneering studies of Abbe, Zeiss, and Schott yielded the true physical resolution limits of OM ($\sim 0.2 \mu\text{m}$ which is half of the wavelength of visible light).¹ The first EM was developed in the 1930s providing substantially enhanced resolution compared to the best optical microscope available due to the substantially smaller wavelength ($\sim 100,000\times$ smaller) of electrons compared to visible light photons. The utilization of these techniques, including both transmission electron microscopy (TEM) and scanning electron microscopy (SEM), to investigate polymer morphologies ignited in the 1960s and 1970s when researchers began studying complex polymer structures such as the lamellar crystallization of polyethylene, phase separation of polymer blends/ block copolymers, fracturing of polymer surfaces, etc.²

4.1.1 Electron Microscopy-

The resolving power of SEM lies between that of OM and TEM, but the real advantage of SEM is the substantial depth of focus allowing for the surface imaging of bulk samples from ~200 nm to millimeter size scales. SEM produces images by scanning focused, high-voltage electron beams across a bulk sample resulting in several different energy dissipation mechanisms including through heat, emission of electrons, light emission, or X-Ray emission. The relative intensity changes of these energy conversions across the area of the sample are recorded and displayed in the image providing differences in contrast as a function of topography and composition changes throughout the bulk material. The imaging in TEM, however, is accomplished by passing high-voltage electron beams *through* thin, partially-transparent specimens. Only portions of the electron beam pass through the sample reaching the objective lens with several portions of the beams being scattering out of plane. These intensity variations per unit area create the difference in intensity of the transmitted electron beam which is then converted to the 2D contrast image typically reported.

Today, advancements in instrumentation and processing have increased the resolution power of electron microscopes to angstrom levels (~0.1 nm or 1 Å) for inorganic crystal structures. This resolution, however, is impossible for polymer systems due to their high electron irradiation sensitivity and low contrast.¹ SPM, including atomic force microscopy (AFM) and scanning tunneling microscopy (STM), provided the next significant improvement in the field with the first ever atomically-resolved three-dimensional imaging of surfaces. In general, SPM and EM can be easily differentiated into two categories of

detection with SPM involving the “feeling” of surfaces with small, extremely sharp probes and EM involving illumination of solid samples with electron beams. With the ever-growing development of EM /SPM techniques and the vast improvements in spatial resolution (e.g. the minimum distance distinguishable between two adjacent objects), we now have the capabilities to determine specific relationships between bulk properties and micron/nanometer scale structural features.

4.1.2 Contact-Mode AFM-

Herein, by far, the microscopy technique utilized the most for the morphological studies of polycarbodiimides is AFM, a specific class of SPM. For insulating materials such as polymers, AFM is generally applicable for the 3D topological imaging of very small features with lateral length scales ranging from $\sim 100 \mu\text{m}$ to $\sim 1 \text{ nm}$. AFM uses extremely sharp cantilever probes that gently move across the surface with various modes of contact (tapping-mode being the most employed method and the specific method used herein) with a constant force (typically 10^{-11} to 10^{-6} N) measuring the deflection of the cantilever and the interatomic van der Waals forces relative to the surface according to Hooke's Law.³ Different materials provide different cantilever responses depending on the structural and mechanical properties of the sample allowing for the high-resolution mapping of heterogeneous systems such as block copolymers and blends.

In Figure 4.1, components of the optical sensing system for contact-mode AFM are outlined.⁴ The cantilever probe is constantly adjusted so that the force between the tip and sample remains constant as it moves across the surface. This mechanism is necessary to

avoid catastrophic collisions with the topological features of the surface and is accomplished using a XYZ piezoelectric transistor that constantly measures the impact forces as the tip makes contact with the surface. The vertical displacement of the cantilever is recorded by the laser diode that is angled directly on top of the cantilever probe where the tip meets the sample surface. The laser is then reflected back to the photodiode array providing the $z(x, y)$ topography map of the sample.

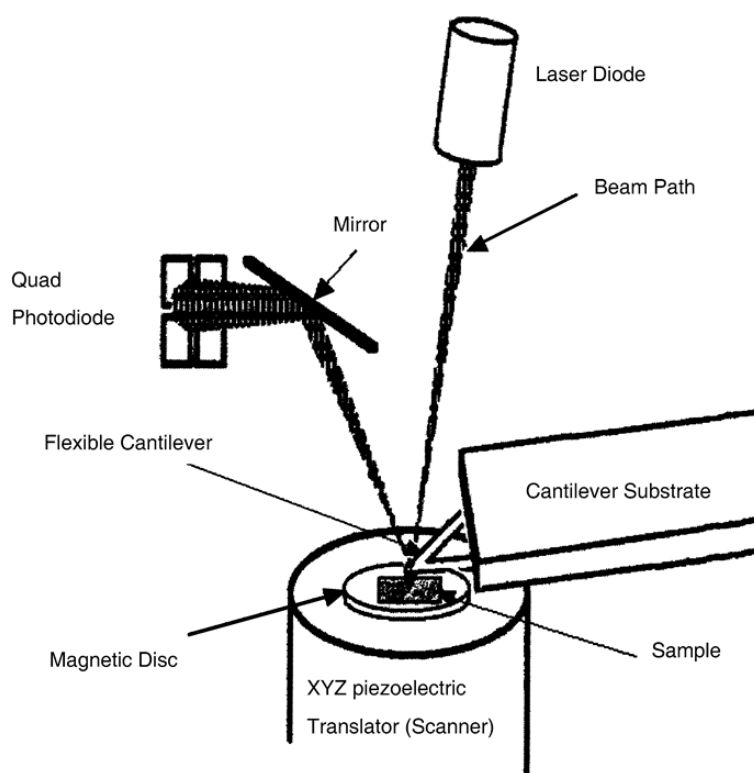


Figure 4.1- Representation of the optical sensing systems used for contact-mode AFM with labels of each working component. (Copyright 2008 Springer-Verlag, reprinted with permission)⁴

In contact-mode AFM, the tip of the probe lightly drags across the sample surface with a constant force. The tip height is constantly adjusted to keep the force between the probe and the surface fixed allowing for lateral resolutions of ~ 1.5 nm and vertical resolutions of ~ 0.05 nm. This method provides information about the physical properties of the sample such as elasticity, adhesion, hardness, and morphological features. The main disadvantage of contact-mode AFM is the substantial damage inflicted on samples and the tip often causing artifacts in the micrograph images. The solution of this significant detriment came in the development of a new, less stressful scanning method known as tapping-mode AFM (TMAFM).

4.1.3 Tapping-Mode AFM-

Tapping-mode, also known as intermittent contact or dynamic force mode, scans the sample surface via rapid oscillation of stiff cantilever probe in order to reduce the potential surface/probe damage observed in contact-mode. This method was first introduced by Zhong et al. in 1993 and shows dramatically improved lateral resolution for soft samples.⁵ The cantilever oscillates at a specific frequency, called the resonant frequency, which is initiated when the piezoelectric crystal excites the cantilever vertically, causing it vibrate up and down (Figure 4.2a). The laser source is again angled directly at the cantilever probe and deflected in a regular, sinusoidal pattern back to the photodiode array. This electronic signal is converted a root mean square (RMS, R_q) amplitude value which is directly correlated to the roughness of the sample using equation (1). In this equation, the root mean square of the

vertical height Z is calculated where Z_{avg} is the average of the Z values, Z_i is the current value, and N is the number of points per unit area.

$$(1) R_q = \sqrt{\frac{\sum(Z_i - Z_{avg})^2}{N}}$$

The deflection of the cantilever probe by the surface features and topography of the sample are measured by the relative alterations to the resonant frequency amplitude (shown in Figure 4.2b) revealing information on the vertical height and sample characteristics such as hardness. The differences in surface properties are typically shown in the phase contrast image that complements the topography height map. This image displays the change or “delay” in resonant frequency oscillation of the cantilever which varies as the adhesion, elasticity, and/or friction of the sample changes. This phase imaging is especially useful for quantification of the phase separated domains in block copolymers (typically with nanometer-size domains) and heterogeneous polymer blends (typically with micrometer-size domains).⁶ This difference in response, measured in degrees, is consequence of the slight penetration of the tip into softer samples causing a small delay in the oscillation (also shown in Figure 4.2b).

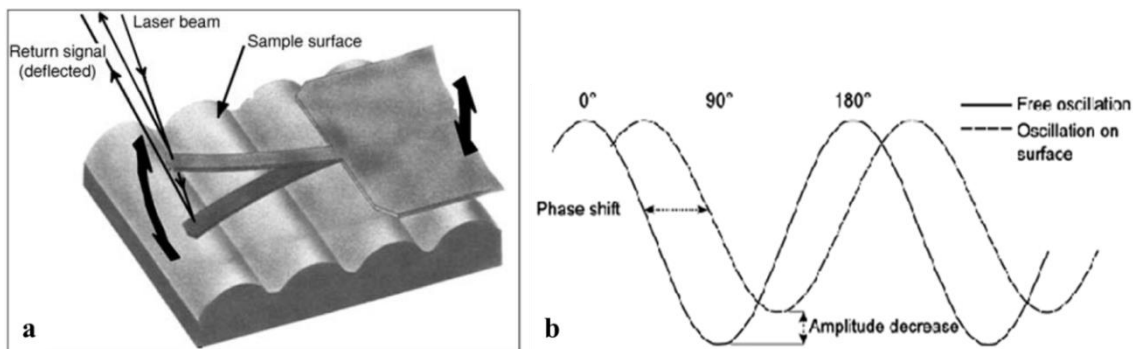


Figure 4.2- Depiction of the oscillating probe used for TMAFM (a)⁴ and the sinusoidal resonant frequency displayed (b)⁶ for free oscillation as well as the response felt when oscillating on the sample surface. (Copyright 2008 Springer-Verlag, reprinted with permission)

4.1.4 Analyzing Liquid Crystals with Polarizing Optical Microscopy (POM)-

Liquid Crystals (LC) are a unique phase of matter (mesophase) lying between crystalline solids and normal, isotropic liquids. As previously mentioned in Chapter 1, lyotropic liquid crystals, the class discussed throughout this document, are solvent induced and occur at specific concentration and temperatures in concentrated mesogen solutions. Imaging of specific, ordered LC phases is most typically accomplished using polarizing optical microscopy (POM) which makes use of plane-polarized visible light to illuminate birefringent samples such as anisotropic crystals or LCs. Polarizers are directional light filters that only allow light oriented in a specific direction to pass through. Two polarizers are typically employed in POM with the first located directly above the incident light beam and the second above the objective lens of the microscope (Figure 4.3).

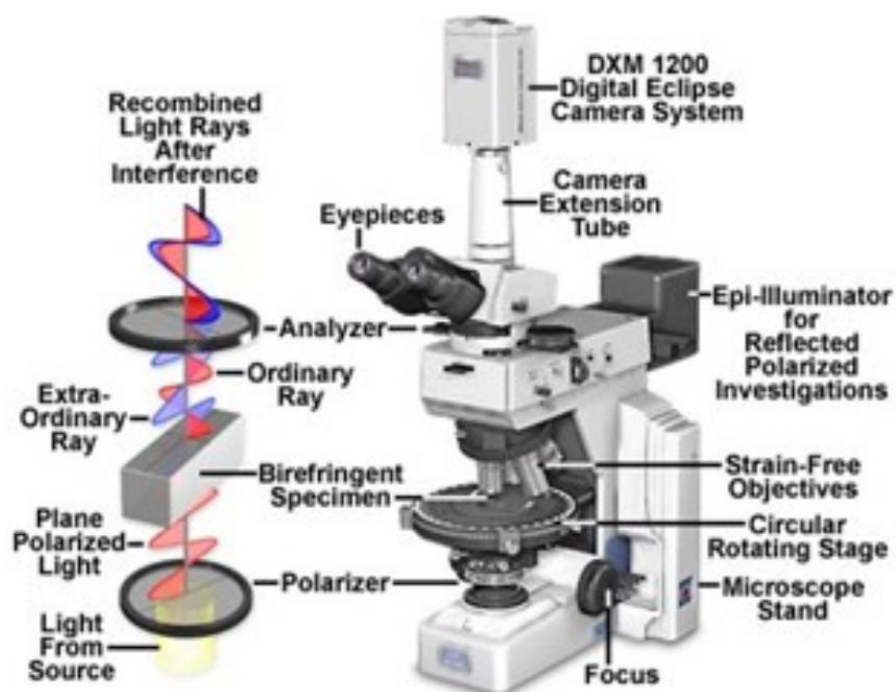


Figure 4.3- Schematic representation of the working components of POM with labels and the path of light that travels through cross-polarizers and the birefringent LC sample.⁷

The two polarizers are oriented perpendicular to one another which is termed cross-polarization. The function of the cross-polarizers is also illustrated in Figure 4.3. As the plane polarized light passes through birefringent samples, the beam of light is split into two rays termed the ordinary ray (same orientation as incident plane polarized light) and extraordinary ray (the newly formed ray). These rays are then recombined by the second polarizer by both constructive and destructive interference. The combined waves reflected from the birefringent sample are now either circularly or elliptically polarized providing distinct domains specific to the specimen. If the sample shows no birefringence (i.e., isotropic liquid), the light remains unaltered when passing through the sample and the second polarizer filters the remaining light causing the image to appear black and featureless.

4.2 Dynamic Lyotropic Liquid Crystallinity of PNOC-

Liquid crystals have been widely studied over the past several decades due to their unique ability to manipulate light. For this reason, they are of particular interest in the fabrication of liquid crystal displays (LCDs), photonic crystals, and nonlinear optical devices.⁸ In particular, the cholesteric (or chiral nematic; N*) mesophase has been the most widely applicable due to the selective Bragg reflections of visible light causing it to exhibit brilliant colors with the wavelength (λ) of reflected light dependent on the helical pitch (p) of the cholesteric phase ($\lambda = np$).⁹ Other materials that exhibit selective Bragg reflections do so by periodically modulating refractive indices throughout the material which creates a “forbidden gap” that excludes specific wavelength modes of visible light, i.e., the photonic band-gap. These materials, known as photonic crystals, are required to have periodic structures with length scales ranging from approximately 400/2 nm (blue) to 700/2 nm (red), i.e., half of the wavelength of visible light.¹⁰ Photonic crystals have been of significant interest to researchers in the past two decades due to their extensive applications as reflective coatings for lens, optical waveguides, reflective mirrors for lasers, color pigments in inks and paints, to name a few.¹⁰⁻¹³

Research in the field of photonic crystals has progressed greatly through the years moving away from more expensive/difficult “bottom-up” fabrication techniques such as electrochemical etching¹⁴ and holographic lithography.¹⁵ Recent advances focus on the self-assembly of monodisperse colloidal nanoparticles, such as silica or polystyrene microspheres,¹⁶ and well-defined block copolymers¹⁷ that assemble into ordered arrays with these forbidden photonic band-gaps. The need for tunable photonic structures with distinct

Bragg reflection behaviors modulated by external stimuli has grown tremendously in recent years attracting many top researchers in the field. Examples of external stimuli reported include light,^{18,19} heat,^{9,20} pH,²¹ electrical,²² humidity,²³ solvent swelling,¹⁷ magnetic,²⁴ and mechanical force.¹²

Another LC mesophase that has yet to be discussed is the blue phase LC mesophase which typically is only stable within a very small temperature ranges (0.5 – 2 °C).²⁵ Classically, blue phases were only formed a small temperature window upon cooling from isotropic to cholesteric mesophases. Recently, however, new examples of thermodynamically stable blue phase LCs have been reported offering exciting new opportunities in the field of tunable photonics.^{20,25-27} Blue phase LCs are a subset of cholesteric LCs and can be observed in three different variations denoted BP I, BP II, and BP III. BP III is largely amorphous, in that it lacks long range translational order, and it appears as isotropic under POM. The structures of BP I and II are complex and three-dimensional consisting of helically-aligned mesogen units within frustrated “double-twist” cylinders (Figure 4.4b).²⁸ This specific packing, compared to the simple twist of the chiral nematic phase which can fluidly pack in three-dimensions, is significantly higher in energy due to the inevitability for defects to occur (Figure 4.4a) when the mesogens are twisted on both the x- and y-axis. The double-twist cylinders themselves align in a 3D-hierarchical fashion with BP I and BP II adopting body-centered cubic and simple-cubic symmetry, respectively (Figure 4.5). The double-twist cylinders stack like logs on top of one another with right angles between all meeting points resulting in specific defect lines (highlighted in Figure 4.5b and d). The lattice periods within

the blue phase are on the order of the visible light spectrum and, because of the fluidity of the blue phase, these periods can be easily modulated by external electric fields to induce specific lattice parameters capable of reflecting the entire visible light spectrum selectively making them one of the only examples of 3D photonic crystals observed experimentally.²⁵ For this reason, stable blue phases have been widely sought after for many years owing to their vast applicability.

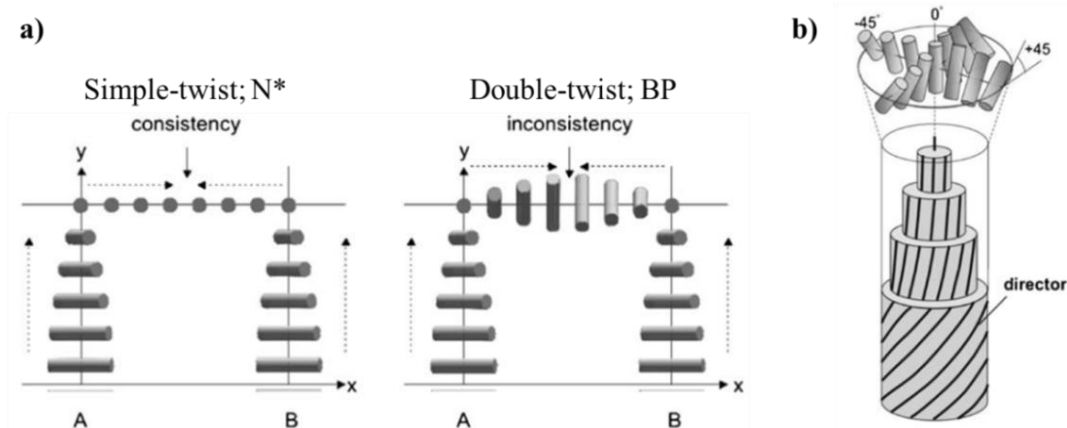


Figure 4.4- X/Y Representation of simple-twist and frustrated double-twist structures (a) and the assembled double-twist cylinder in blue-phase LCs (b). (Copyright 2008 Springer-Verlag, reprinted with permission)²⁸

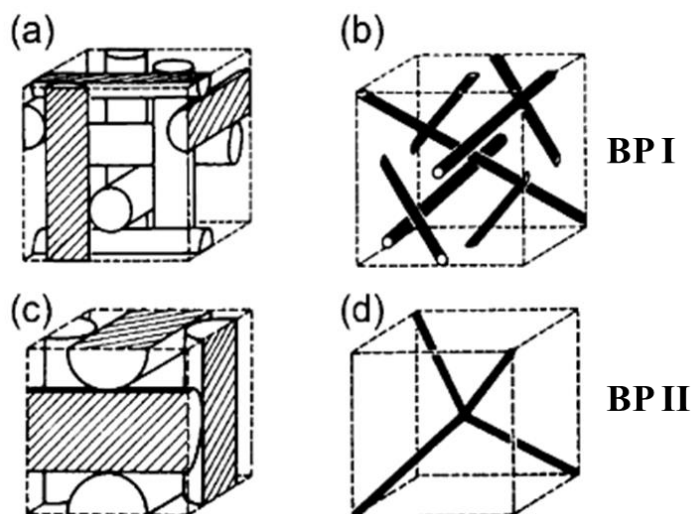


Figure 4.5- Representation of the three-dimensional cubic arrays of BP I (a; body-centered cubic) and BP II (c; simple cubic) mesophases and the defect lines (black lines; b and d) that result. (Copyright 2008 Springer-Verlag, reprinted with permission)²⁸

The number of materials that adopt a stable blue phase over a temperature range greater than ~ 20 °C is rather minimal with only a handful of examples in literature mainly due to the frustrated assembly of the mesophase.^{20,25-27,29} In addition, none of these examples include lyotropic LCs or polymeric materials with all of the mesogens reported being small molecule, thermotropic LC materials. The rod-like and stable, single-handed helical nature of specific polycarbodiimides causes them to assemble into a variety of LC mesophases including simple nematic, smectic, and cholesteric phases in concentrated solutions.^{30,31} The relatively low degradation temperatures of most polycarbodiimides typically results in the absence of thermotropic mesophases with a few exceptions.

Previously in Chapter 3, we discussed an interesting polycarbodiimide, PNOC; **Poly-14**, which undergoes reversible temperature and solvent induced chiroptical switching resulting from conformational reorganization of the naphthyl pendant groups and alterations

to the helical pitch of the polymer backbone.^{32,33} This reorganization has been hypothesized to potentially cause large-scale self-assembly differences between state A and B. First, we studied the LC behavior of this polymer (*S*-PNOC polymerized with **Cat-2S**) in concentrated solutions as a function of solvent and temperature. The solvents chosen for these LC studies include benzene (state B), CHCl₃ (2:1 state B: state A), THF (1:2 state B: state A), and toluene (state A) to provide a wide breadth of conformational populations.

In 15 w% solutions of benzene, CHCl₃, and THF, **Poly-14** adopts unique mesophases at 25 °C, identified by POM, including chiral nematic (N*), isotropic (or possibly BP III), and chiral nematic (N*), respectively (Figure 4.6). The black, isotropic nature of **Poly-14** in CHCl₃ does not appear featureless, typical of complete isotropy, but with a slight wave texture observed possibly attributed to an amorphous mesophase such as BP III. In benzene and THF, however, the clear spherulite, polygonal textures, most commonly called focal conic domains (FCD), of the cholesteric phases are visible via POM (all images at 100x magnification). Upon heating to 40 °C, the spherulite textures in the benzene and THF solutions fade away and a distinct color change to blue is observed. In CHCl₃ at 40 °C, the once black, isotropic mesophase now displays vibrant blue color, as in benzene and THF, believed to be a new, lyotropic BP I mesophase.

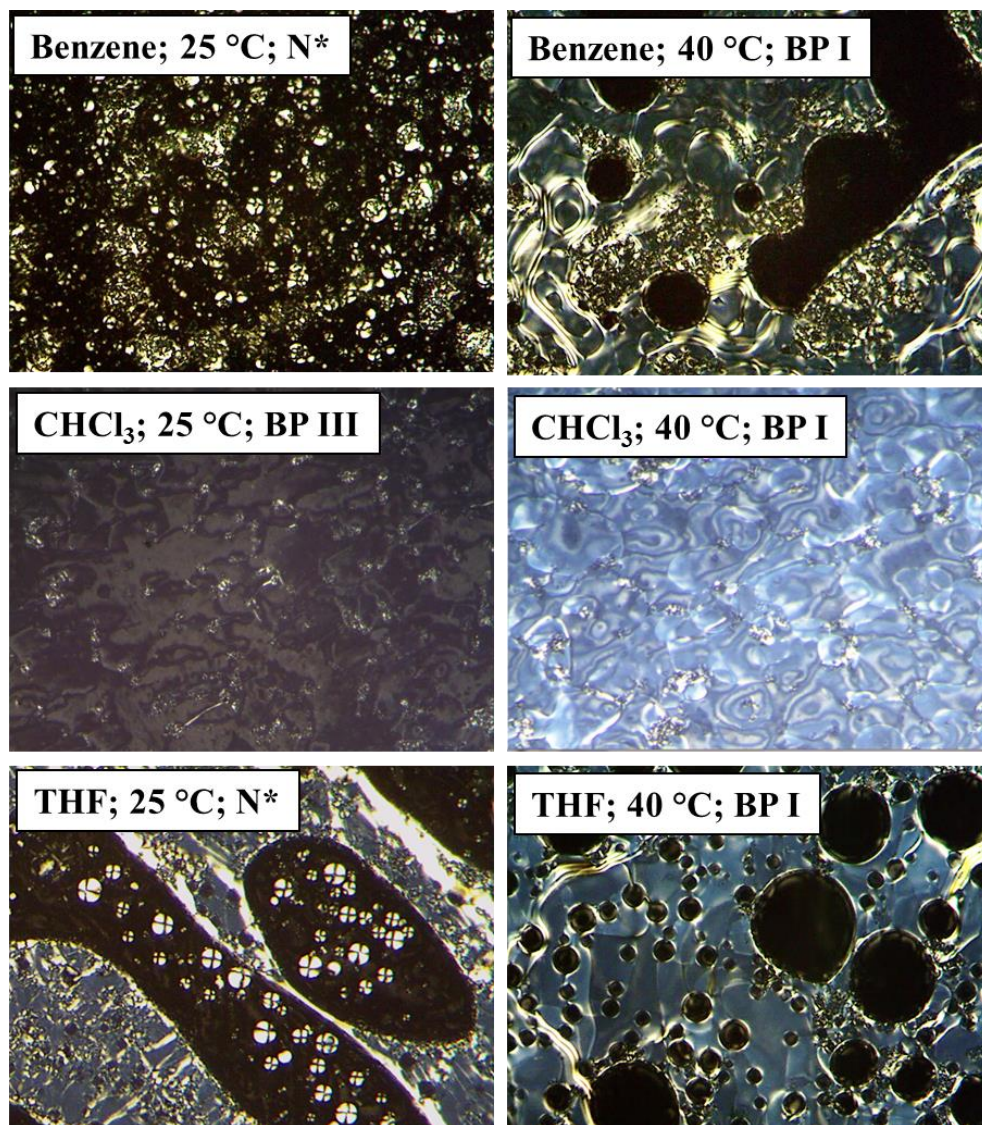


Figure 4.6- POM images of 15 w% solutions of **Poly-14** (100x magnification) in benzene, CHCl₃, and THF at 25 and 40 °C displaying the clear mesophase transition to the lyotropic BP I mesophase at higher temperatures.

The lyotropic mesophases of **Poly-14** form at vastly different rates depending on the solvent employed. In CHCl₃, the mesophase formation took less than an hour to form whereas the mesophases took ~12 hours to form in THF and benzene. Leaving the 15 w%

solution in CHCl_3 for the 12 hours caused the solution to completely gel forming bright rainbow colored gel possibly due to solvent evaporation. This is unlikely, however, since the solution was sealed in a vial and wrapped with Parafilm to prevent significant evaporation. Additionally, THF shows comparable volatility to CHCl_3 but the same gelation was not observed. Another viable explanation is that the polymer fully crystallizes from the concentrated CHCl_3 solution causing the LC solution to solidify. In 15 w% solutions of toluene, no mesophase was observed for **Poly-14** at 25 and 40 °C. The mesophase transition, in all cases, was completely reversible with the BP I transition at higher temperatures through 3 heating and cooling cycles.

If this mesophase is indeed a variation of the blue phase, casting the concentrated polymer solutions should lock the structure into place resulting in specific photonic behaviors. Under cross-polarizers, reflected colors can be observed with vivid blue, orange, and green hues observed throughout the films cast from benzene, CHCl_3 , and THF LC solutions, respectively (Figure 4.7). To the naked eye, these films also reflect vibrant colors but not always the same as observed using POM. Upon solvent evaporation the benzene-cast film exhibited the same blue color observed under POM whereas the CHCl_3 and THF cast films appear green-blue and yellow-orange, respectively. To confirm or refute these observations pertaining to photonic band-gaps of the locked in blue-phase, thin-film XRD and Bragg reflection spectroscopy are necessary to both identify the specific packing parameters and photonic band-gap wavelengths for each film, respectively.

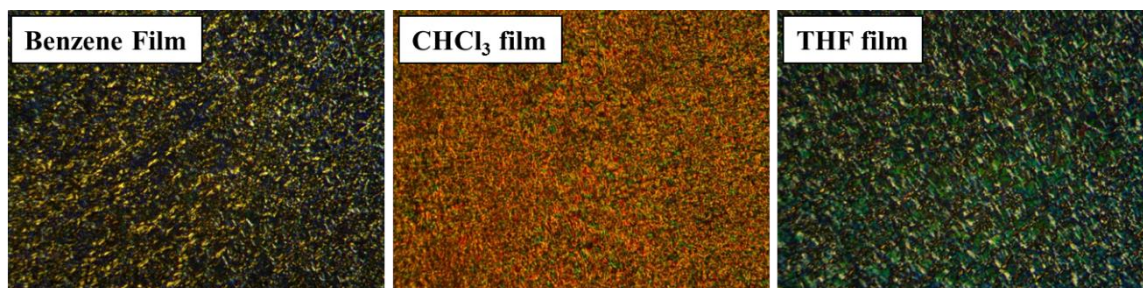


Figure 4.7- POM images (100x magnification) of thin-films cast from 15 w% LC solutions of **Poly-14** in benzene, CHCl_3 , and THF.

The full transition to the hypothesized lyotropic BP I mesophase at 40 °C requires ~90 seconds to form in all solvents studied. Upon placing the LC solution, on a glass slide with cover slip, onto the preheated microscope stage, there is a slight incubation period of ~5 s before any transition begins. By $t = 30$ s, the transition becomes apparent with the light blue color becoming more and more visible and, at $t = 90$ s, the BP I mesophase formation appeared complete without any significant changes at $t > 90$ s. At 50 °C, the rate of formation increases with full conversion to the BP I mesophase in ~30 s. Temperatures greater than 50°C were not studied due to the relatively low boiling points of all three solvents. For the time-resolved POM images of **Poly-14** in 15 w% solutions benzene, CHCl_3 , and THF, see the experimental section.

To confirm these mesophase transitions and study the effect of concentration, **Poly-14** was also dissolved in the same four solvents at $c = 25$ w% and imaged using POM. In the 25 w% benzene solution at 25 °C, again **Poly-14** adopts the cholesteric mesophase but with the different, oily-streak textures (Figure 4.8; 40x magnification) rather than the spherulite textures observed in 15 w% solutions. This oily-streak defect textures are most typically

observed in lamellar LCs and chiral smectic LCs which are both subsets of cholesteric LCs. To determine the specific packing parameters of these LCs, XRD is necessary. Additionally, the 25 w% solution displays a consistent mesophase throughout the entire sample unlike the 15 w% solution which showed large portions of isotropy (i.e., disorder) intermittent with the cholesteric phase. Heating the cholesteric LC to 40 °C again initiates the $N^* \rightarrow$ BP I transition as evident by the vibrant blue color that forms. In 25 w% solutions in THF, the LC behavior mimics that of the 25 w% solutions in benzene with the same oily-streak textures at 25 °C and the distinct BP I mesophase transition at 40 °C. These mesophase transitions were much faster than the 15 w% LC mesophase transition with full conversion to the BP I phase in ~20 s at 40 °C (see experimental section).

In 25 w% CHCl_3 solutions at 25 °C, **Poly-14** displays mixed polygonal and lamellar textures characteristic of the cholesteric mesophase (Figure 4.8; 100x magnification); in contrast to the largely isotropic mesophase observed in 15 w% solutions. Heating the cholesteric LC to 40 °C again results in the distinct $N^* \rightarrow$ BP I mesophase transition displaying very similar LC textures to the benzene and THF LC solutions at 40 °C. The mesophase transition in CHCl_3 was slightly slower than when dissolved in benzene and THF with complete conversion to the BP I mesophase in ~40 s rather than 20 s. The POM image of the 25 w% CHCl_3 LC solution at 25 and 40 °C are displayed with higher magnifications (100x) to better view the finer features of the mesophase textures. At 40 °C, we can visualize certain portions resembling layered packing which may be evidence of the different layers in the cubic packing attributed to the BP I or II mesophase. Again, this

hypothesis must be confirmed with various XRD techniques as well as reflection spectroscopy which show distinct diffraction patterns and reflections associated with BP I and II.

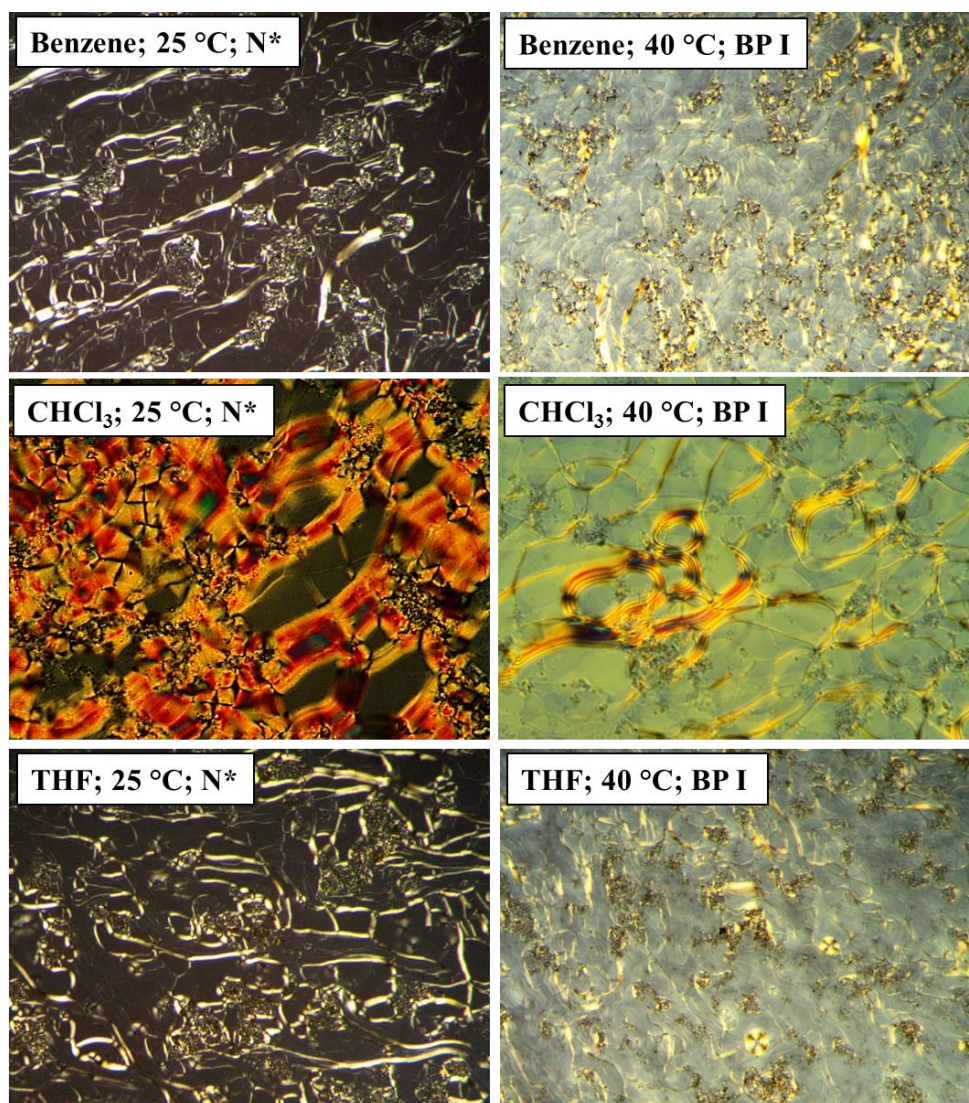


Figure 4.8- POM images of 25 w% LC solutions of **Poly-14** dissolved in benzene (40x), CHCl₃ (100x), and THF (40x) at 25 and 40 °C showing the proposed N*→BP I mesophase transition.

The 25 w% solution of **Poly-14** in toluene, however, displays a highly colored mesophase with several different hues present including red, orange, pink, and green in different portions of the LC at 25 °C. The specific mesophase associated with these images remains a mystery. The POM images (shown in Figure 4.9) seem to lack truly discernable features such as the typical fingerprint, polygonal, or oil-streak textures observed previously for the cholesteric mesophases in benzene, CHCl₃, and THF. The higher boiling point of toluene also allows for the screening of a wider temperature range to observe the effect of temperature on the mesophase structure. Interestingly, the mesophase textures do not seem to change greatly but the colors change significantly. The initial POM of the toluene LC solution at 25 °C shows mixed green and red reflections which convert converts to pink and orange upon heating to 50 °C. The color changes further upon heating to 80 °C with mixtures of yellow, pink and, green visible by POM. Upon cooling back to 25 °C, the color does not return to the original green color. Instead the LC remains mainly yellow in color with streaks of pink and orange scattered throughout. Color change in cholesteric LCs is most typically attributed to the change in helical pitch of the cholesteric packing. This also may be the case for **Poly-14** in toluene but additional evidence is required to confirm this hypothesis.

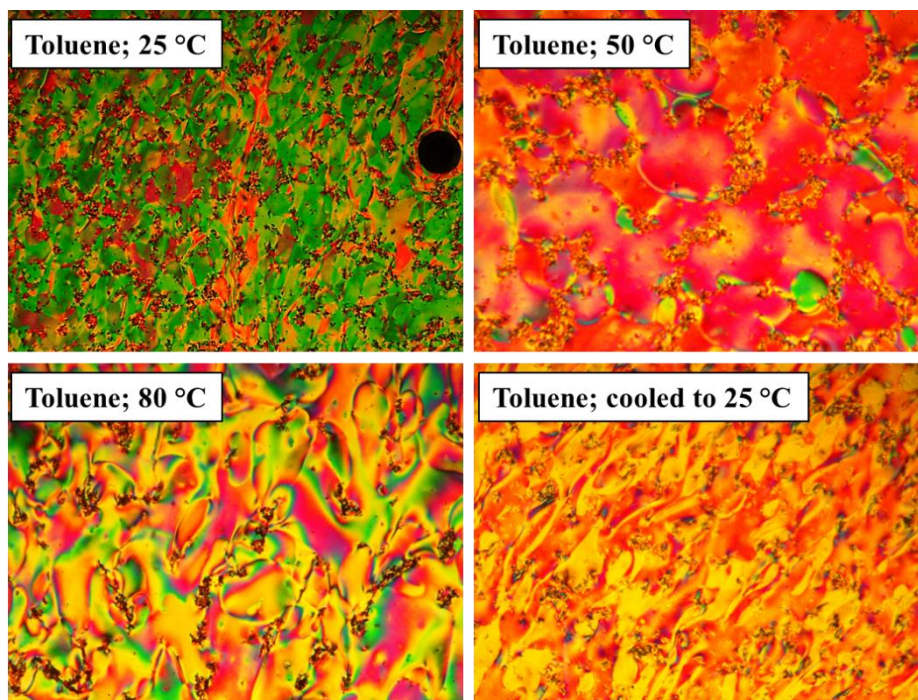


Figure 4.9- POM images (40x magnification) of 25 w% toluene solutions of **Poly-14** at 25, 50, and 80 °C as well as the image after cooling back to 25 °C.

The POM images of the thin-films of **Poly-14** cast from 25 w% LC solutions in benzene, CHCl_3 , THF, and toluene can be found in Figure 4.10. The films from 25 w% solutions in benzene, CHCl_3 , and THF are very similar to the films cast from the 15 w% LC solutions with the analogous reflected colors in all three cases. The film cast from the concentrated toluene solution, however appears substantially different than the others with a much smoother surfaces and broader features. Additionally, the film cast from toluene shows no reflected colors to the naked eye suggesting that morphology does not contain any specific photonic band-gap. This was somewhat surprising considering the vibrant colors observed in concentrated toluene solutions. Under cross polarizers, the film exhibited mixtures of colors throughout including yellow, green, and orange.

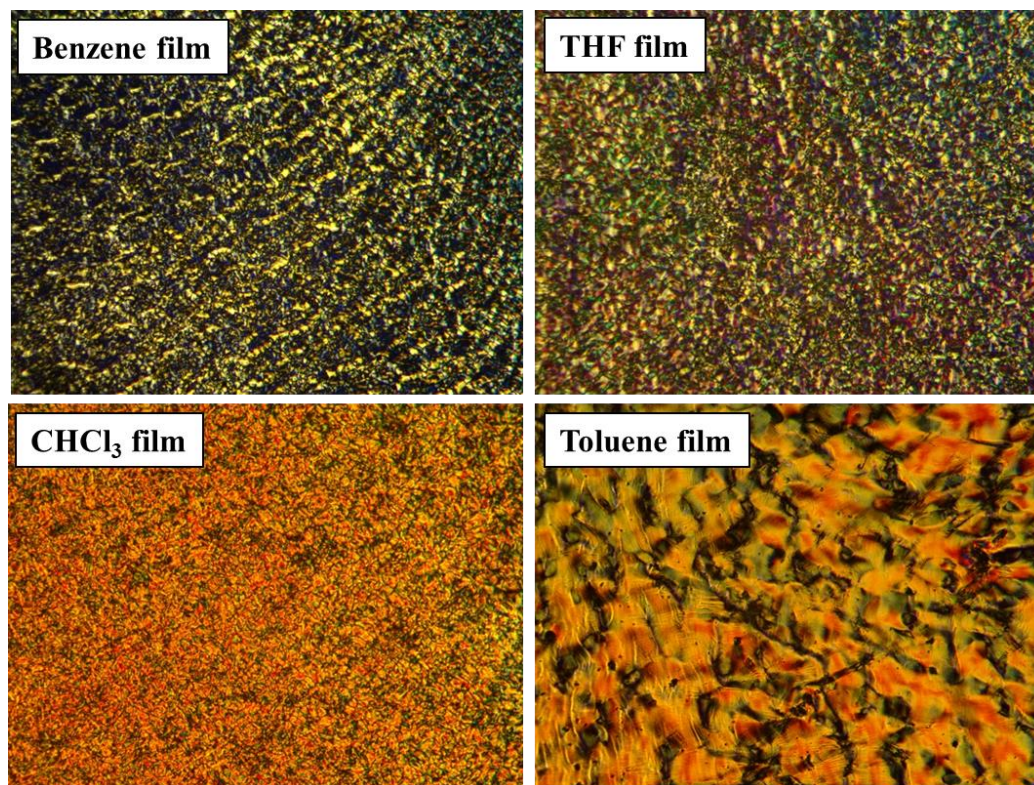


Figure 4.10- POM images (100x magnification) of **Poly-14** thin-films cast from 25 w% LC solutions in benzene, CHCl_3 , THF, and toluene.

4.3 Comparison of LC Behaviors Exhibited by PNOC and PPOC-

The dynamic, tunable LC behaviors of **Poly-14** are enticing and could open up substantial opportunities for potential applications. It is still unclear, however, whether this property is consequence of the dynamic temperature and solvent induced conformational switching observed for **Poly-14**. The distinct differences in LC mesophase and textures as a function of temperature and solvent does suggest that this switching may play a role but there are certain outliers. No thermal chiroptical switching occurs in benzene but we do observe a distinct $\text{N}^* \rightarrow \text{BP I}$ mesophase transition as we increase the temperature to 40 °C from room temperature. Additionally, the mesophases observed for **Poly-14** dissolved in THF and

benzene appear very similar despite the conformational populations of benzene and CHCl_3 being closer in proportion. As a control experiment, a new polymer, poly(*N*-phenyl-*N'*-octadecylcarbodiimide); PPOC; **Poly-41**, was synthesized using **Cat-2S**. **Poly-41** has a very similar structure to **Poly-14** but shows no chiroptical/conformation switching as a function of solvent or temperature. To compare, the LC behaviors of **Poly-41** were studied in concentrated 25 w% solutions of benzene, CHCl_3 , THF, and toluene to see if the same dynamic LC behavior persists.

In all solvents, **Poly-41** appears to adopt the same mesophase at 25 w % with a single, distinct texture observed by POM in all cases (Figure 4.11). With **Poly-41**, we observe the distinct blue-gray/yellow colors at 25 and 40 °C in all solvents but this mesophase displays significantly different textures from that of the proposed lyotropic BP I of **Poly-14**. This specific texture resembles previously reported platelet-like structure of BP II mesophases^{26,27} but this must be confirmed using the techniques aforementioned. In toluene, the blue color and platelet-like texture persists even at 80 °C but with small, circular portions of isotropy forming suggesting that the mesophase is beginning to breakdown. If this is indeed evidence of a new, lyotropic BP II, it would not only be the first reported lyotropic BP II but also the most stable BP II mesophase ever observed. Furthermore, the fact that **Poly-41** displays identical mesophases in all solvents and temperatures studied suggests that the dynamic behaviors of **Poly-14** are indeed influenced by the conformational switching experienced by **Poly-14** induced by different solvents.

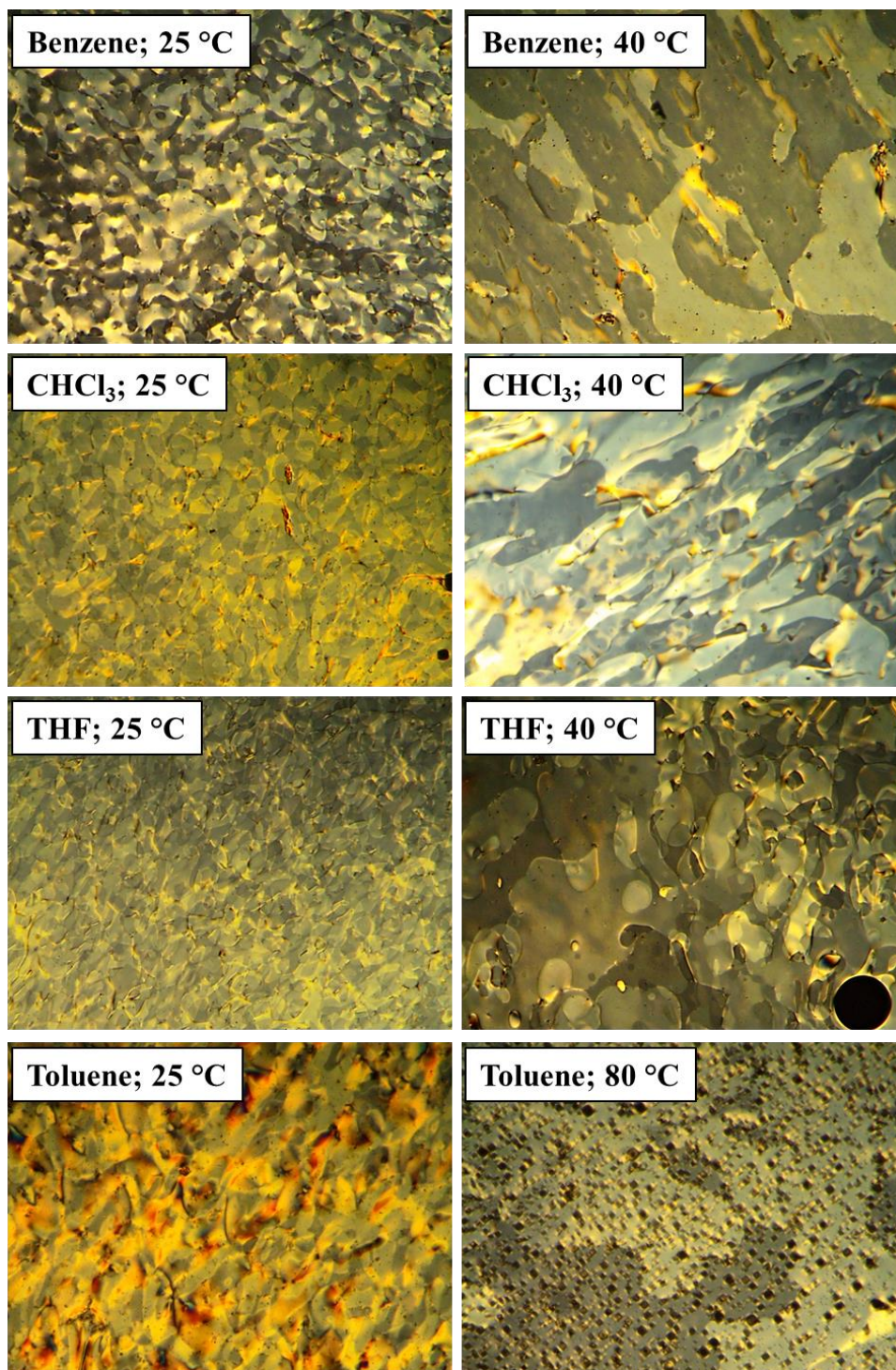


Figure 4.11- POM images (40x magnification) of 25 w% **Poly-41** LC solutions in benzene, CHCl₃, THF, and toluene at 25 and 40 °C.

Casting each of the **Poly-41** LC solutions forms highly-aligned polymer films as evident by POM (Figure 4.12). Surprisingly, all of the films did not exhibit any colors to the naked eye suggesting that the periodic lamellar-like structures are not on the correct length scale to exhibit photonic band-gaps. Also, under cross-polarizers, the only film that exhibited brilliant colors was that cast from LC CHCl_3 solution despite the mesophase being largely identical in all solvents. These aligned films, however, do display similar morphologies to that of previously reported blue phases providing further evidence for the proposed mesophase.²⁸ These films appear to be very similar in all cases, unlike **Poly-14**, providing further evidence that the dynamic mesophase formation and photonic behaviors are consequence the conformational switching phenomenon.

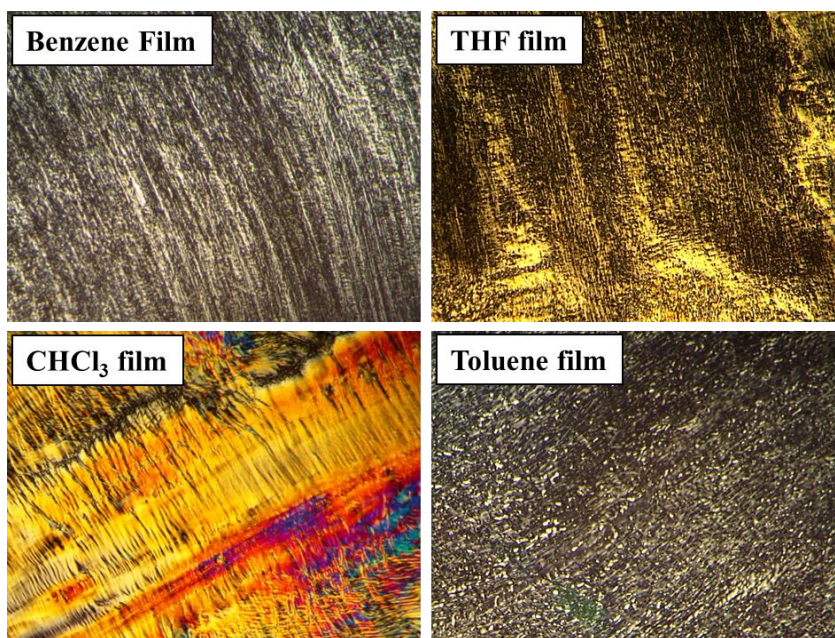


Figure 4.12- POM images (40x magnification) of **Poly-41** thin-films cast from 25 w% LC solutions in benzene, CHCl_3 , THF, and toluene.

4.4 Tunable Surface Morphology of PNOC-

To better visualize the specific structural changes associated with the conformational switching, the DFT optimized, 7mer models used for VCD calculations were extended to 35 repeat units and the methyl pendant groups, which were used for simplicity, were supplanted by a fully extended octadecyl chain (Figure 4.13). The octadecyl chains were not theoretically optimized and are only meant to act as visual aids to better represent the actual polymer structure. In reality, the octadecyl chains would not be fully extended as shown. The polymer backbone, however, is believed to be a good representation of the actual conformation for each state. Interestingly, the helical pitch contraction exhibited upon switching to state B (model B) also induces a somewhat twisted conformation with a right-handed helical tertiary structure formed in conjunction with the right-handed helical rotation of the repeating units. This twisting is believed to relieve some of the added steric strain caused from the helical contraction. In turn, this twisting also causes the overall end-to-end distance of individual 35mer polymer chains to decrease significantly with an overall contraction of 75.6 Å to 69.3 Å switching from model A to B, respectively. In order to see whether this conformational switching causes significant alterations to the self-assembly of **Poly-14**, AFM was employed to image the morphologies of each state in the thin-film.

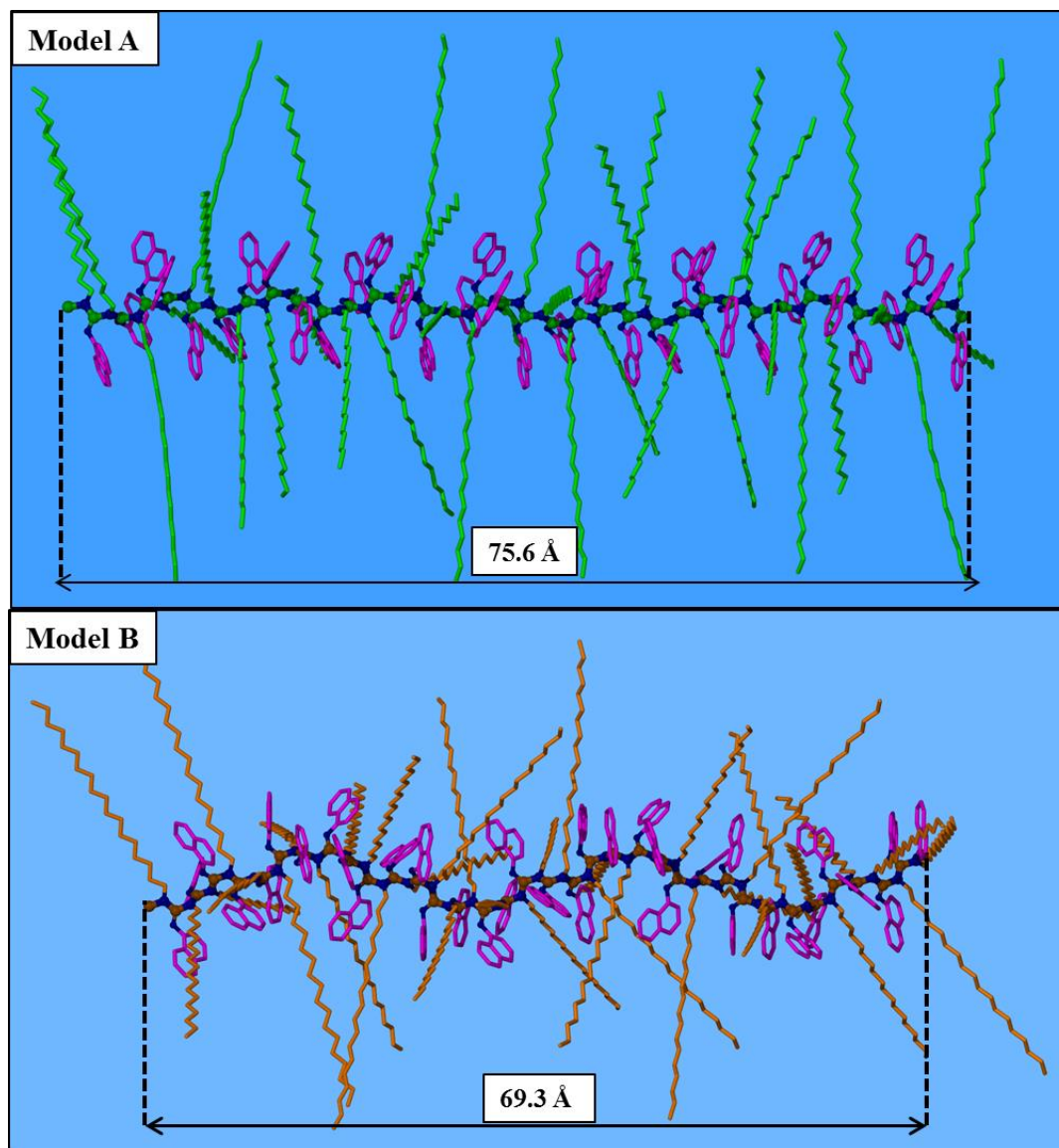


Figure 4.13- Extended 35mer models of **Poly-14** with added octadecyl pendant groups used to better visualize the subtle conformational changes associated with switching from state A to B.

To prepare thin-films of state A and B, **Poly-14** was dissolved ($c = 5.0$ mg/mL) in toluene (state A) and benzene (state B) and spin-coated onto highly-polished silicon wafers. The necessity for spin-coating and the use of extremely flat silicon substrates proved to be

imperative in the acquisition of AFM images with the necessary resolution to observe the subtle differences in the polymer films. The spin-coating procedure provides a uniform coating of the polymer across the entire substrate whereas drop-coating causes large variations in film thickness depending on the solvent evaporation. The films were then allowed to anneal in saturated solvent atmospheres to allow the thin-films to reorganize to their thermodynamically stable morphologies. This solvent annealing process also proved to be necessary to observe specific morphological features, in particular with the toluene-cast films.

The AFM micrograph of **Poly-14** spin-coated from toluene reveals helical bundles of polymer chains throughout the thin-film (Figure 4.14). These bundles should not be confused for single, helical polymer chains due to their larger overall dimensions. The relatively small size of the bundles and the low resolution of the AFM images, however, make it somewhat difficult to measure the dimensions of these aggregates with a high degree of accuracy. Therefore, the measuring of helical pitch, width, and length should be considered qualitative estimates. Nonetheless, these measurements were attempted on the most individualized aggregates like that shown in the zoomed AFM micrograph in Figure 4.14d. The width of a single **Poly-14** chain with fully extended octadecyl chains was calculated to be ~ 4.5 nm which is substantially smaller than the average measured width of the observed helical bundles (ca. 71 ± 9 nm). The pitch of these helical nanofibers was also measured using these AFM images with an average pitch of 51 ± 5 nm. The calculated average length (ca. 327 ± 56 nm) was the most challenging to measure due to difficulties in determining the start and end of each nanofiber and was measured using a very small sample size (sample size = 10). The

AFM phase map shown in Figure 4.14b displays only one phase, as expected, due to the homogeneity of the sample. Now, to see if this morphology persists for state B, the same sample preparation was employed except with benzene as the solvent and annealing vapor.

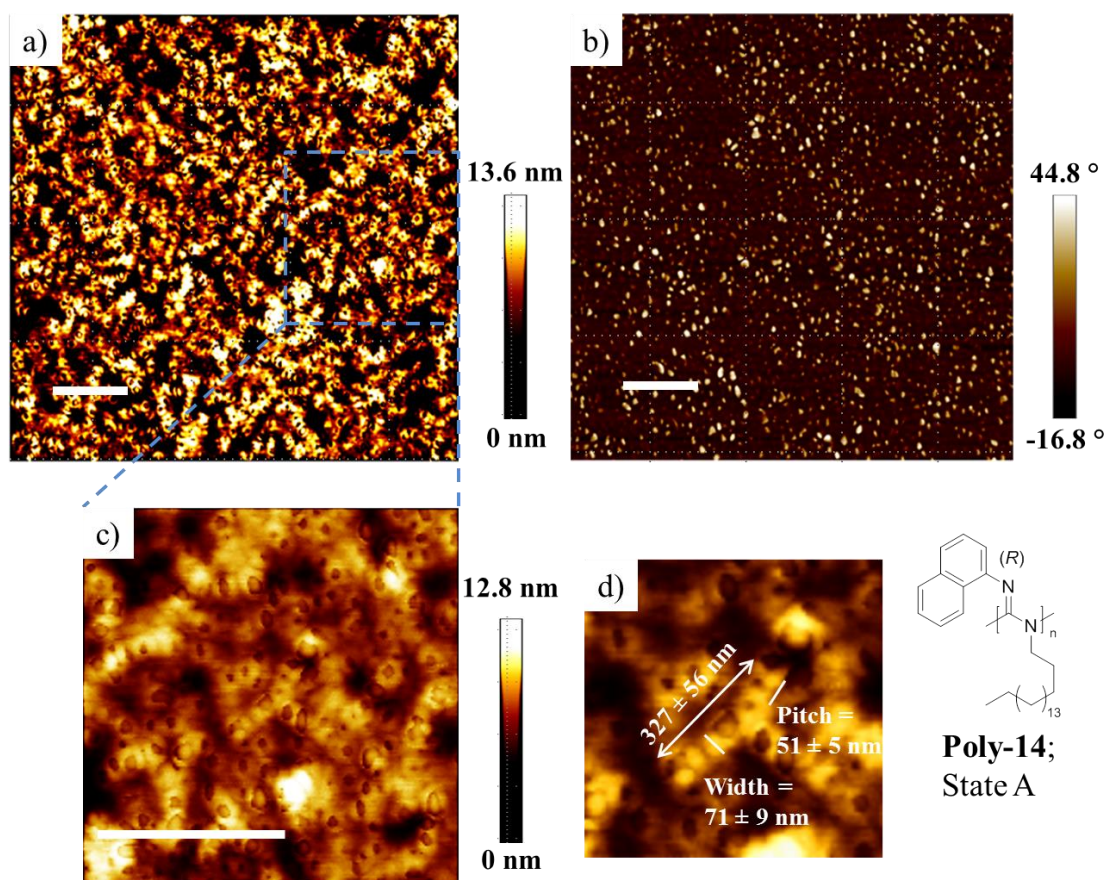


Figure 4.14- Height (a) and phase (b) AFM micrographs (scan size = 3 x 3 μm) of **Poly-14** thin-films spin-coated from toluene and annealed in toluene vapor for 48 hours. Also shown are two zoomed height images (c, scan size = 1 x 1 μm; d, scan size = 500 x 500 nm) used to measure the dimensions of the helical bundles (all white scale bars = 500 nm).

Poly-14 was spin-coated from benzene ($c = 5.0$ mg/mL) to observe if there is a change in morphology when the polymer adopts state B rather than state A. AFM was again employed to image the specific surface morphology of state B revealing nanofibular morphology (Figure 4.15) with much smaller dimensions than that of state A. Additionally, no helical bundles were observed when spin-coated from and annealed in benzene. The relative dimensions of these nanofibers cannot be measured, however, due to their significantly smaller size and lack of resolution. The cause of this is hypothesized to be correlated directly with the specific structure of each conformation. In state A, the helix is substantially more expanded allowing for interdigitation/crystallization of the octadecyl pendant groups from adjacent polymer chains to occur. This, in turn, causes the formation of large helical bundles consisting of several polymer chains aggregated together. Two proposed interdigitation pathways for state A are depicted in the dimer (a) and trimer (b) bundle models shown in Figure 4.16. The same level of interdigitation cannot occur in state B due to the tighter helical conformation and twisted tertiary structure preventing significant crystallization to occur. This results in the presence of much smaller aggregates as evident by AFM.

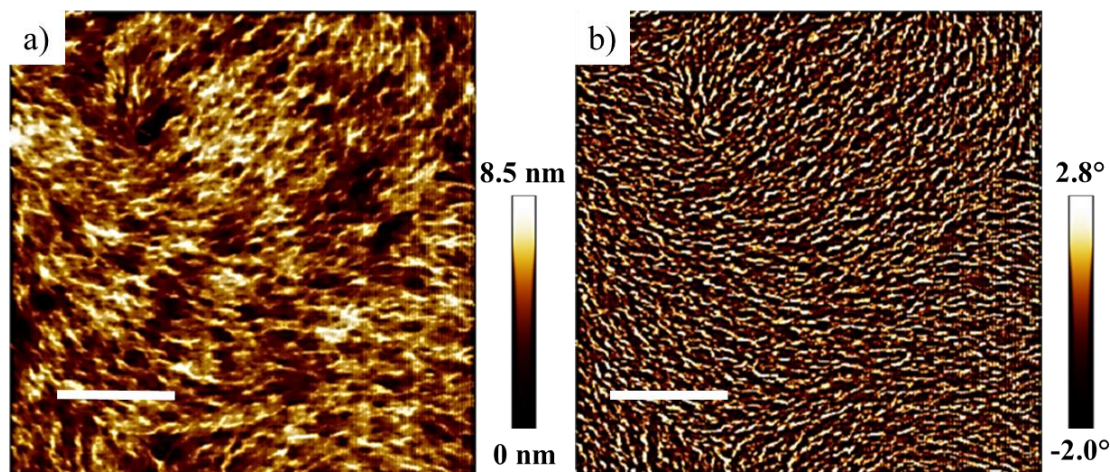


Figure 4.15- Height (a) and phase (b) AFM micrographs (scan size = $2 \times 2 \mu\text{m}$; white scale bar = 500 nm) of **Poly-14** spin-coated from benzene ($c = 5.0 \text{ mg/mL}$) and annealed under benzene vapor for 48 hours prior to imaging.

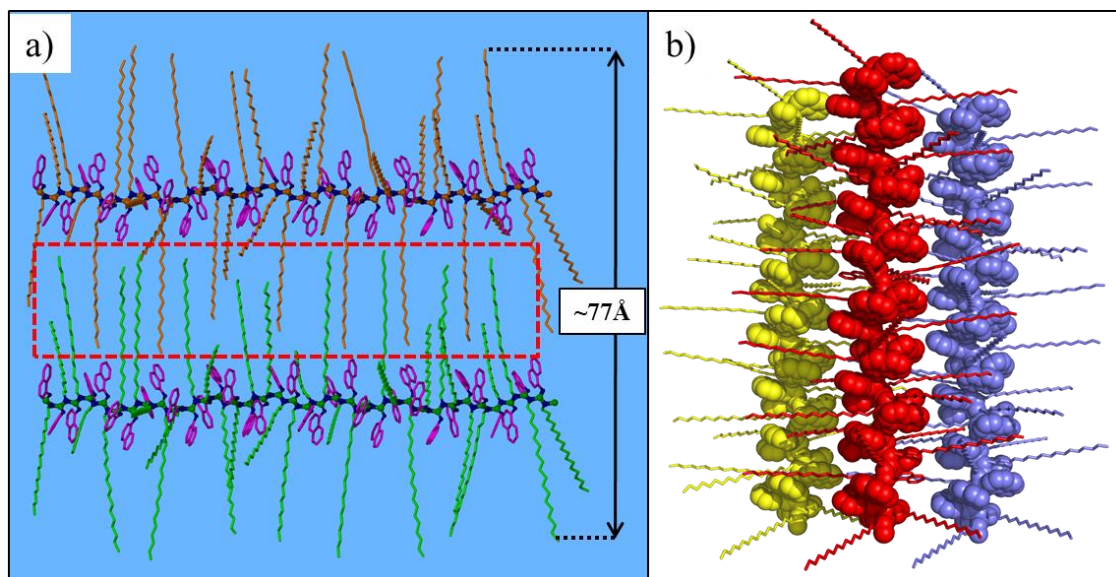


Figure 4.16- Two proposed interdigitation pathways of state A which, in turn, cause the formation of the large, helical aggregates observed by AFM.

To confirm or refute the hypothesis that the distinct surface morphologies observed for **Poly-14** spin-coated from toluene and benzene are a result of the bistability of the polymer, thin-films of the PPOC control polymer, **Poly-41**, were prepared via the same protocol as **Poly-14** and imaged using AFM (Figure 4.17). This analysis revealed that **Poly-41** cast from and annealed in benzene and toluene adopts the same surface morphology, unlike **Poly-14**. The morphologies of **Poly-41** cast from both solvents mimic that of **Poly-14** spin-coated from benzene with small, nanofibular aggregates present rather than larger helical bundles. This suggests that the conformation of **Poly-41** is most likely very similar to **Poly-14** adopting state B causing the aggregation of several polymer chains to be less favorable. Again, like the AFM of **Poly-14** cast from benzene, the dimensions could not be accurately measured due to the lack of resolution in the AFM images.

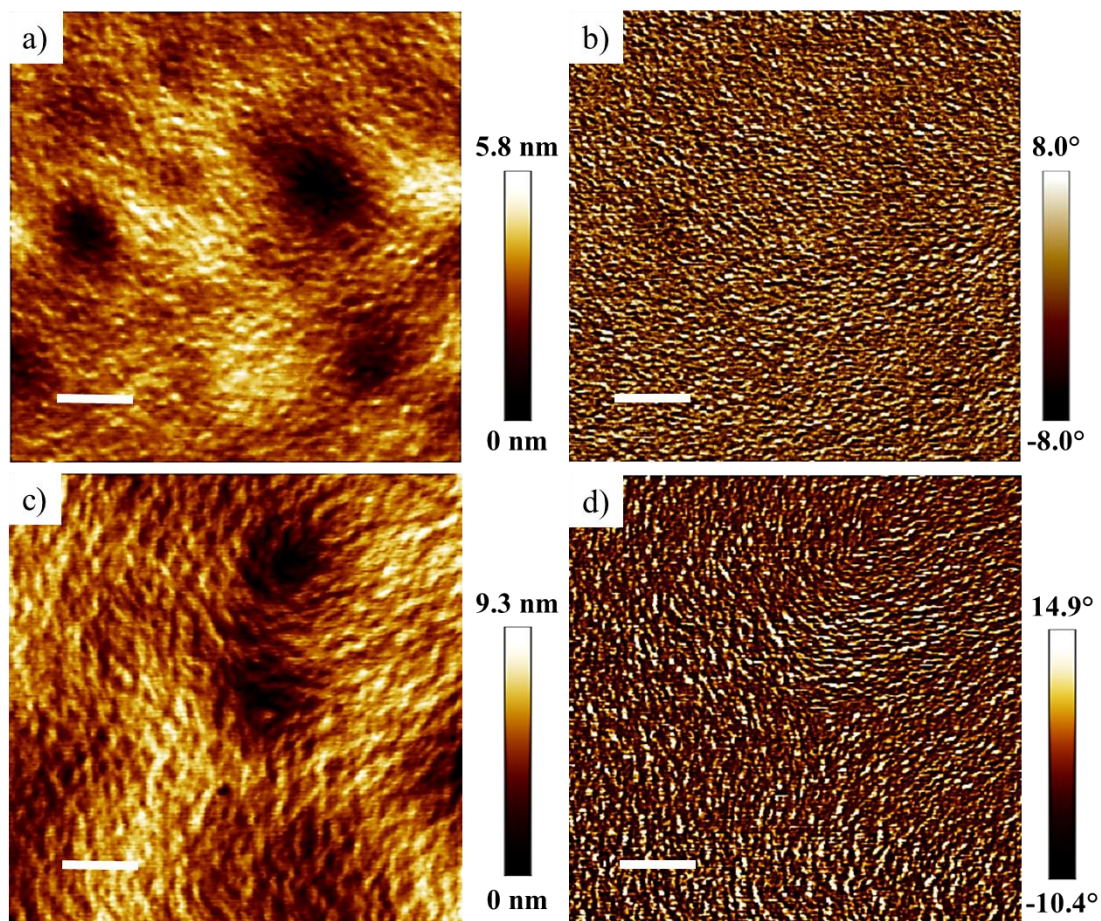


Figure 4.17- Height (a,c) and phase (b,d) AFM micrographs (scan size = 3 x 3 μm ; white scale bar = 500 nm) of **Poly-41** spin-coated from and annealed in toluene (a,b) and benzene (c,d) showing nanofibular morphologies similar to **Poly-14** cast from benzene in both cases.

4.5 Unique Droplet Movement Induced by Surface Reorganization of Thin PNOC and PPOC Films-

A couple of recent articles focusing on a new method for measuring the level of chiral discrimination between chiral surfaces and chiral probing liquids sparked our interest in attempting similar experiments with chiral polycarbodiimides. These articles outlined the measurement of contact angles for small drops of chiral liquids with specific handedness (*R*

or *S*) onto chiral surfaces of specific configuration (*R* or *S*) showing distinct differences depending on the chirality pairing (i.e. *R-R*, *S-S*, *R-S*, and *S-R*).^{34,35} Unfortunately, only minute contact angle differences (within error) were observed for the (*R*)- or (*S*)-propanediol probing liquid dropped on chiral surfaces of polycarbodiimides with (**Poly-1**; PPEMC) and without (**Poly-13**; PPHC) chiral pendant groups (see experimental section for results).

For **Poly-14**, we had hoped to display the ability to selectively tune the chiral discrimination depending on the solvent used for sample preparation. However, a completely different and unexpected phenomenon was observed when dropping propanediol onto the thin-films spin-coated from and annealed in toluene. When spin-coated from and annealed in benzene (state B), the drop of propanediol on the **Poly-14** surface reached a stable contact angle of 64.5° within 1.2 seconds. Dropping the propanediol on the toluene-cast surface, however, caused specific surface reorganization as evident by the dynamic contact angle as a function of time. When initially dropped, the propanediol contact angle on the toluene-cast surface exhibits the same value as the benzene-cast film (ca. 68°) but begins to wet the surface relatively slowly (over the course of ~15 seconds) until reaching a value of 31°. At this point, the droplet began to spontaneously move across the flat, level surface (Figure 4.18) at a constant rate. Interestingly, the chirality of the PNOC surface and propanediol probing liquid played no role in the reorganization and droplet movement behaviors. This unique droplet movement, however, was proven to be highly dependent on processing with this behavior only observed, thus far, when spin-coated from toluene solutions with $c = 5.0$ mg/mL at 1000 rpm for 30 seconds and annealed for 48 hours under toluene atmosphere. Also, not all droplets placed on the surface moved but, in all cases observed, the droplets did

induced surface reorganization as evident by the slow decrease in contact angle to $\sim 35^\circ$ (see experimental section). This could be due to the presence of surface defects that pin the drop not allowing it to move across the surface.

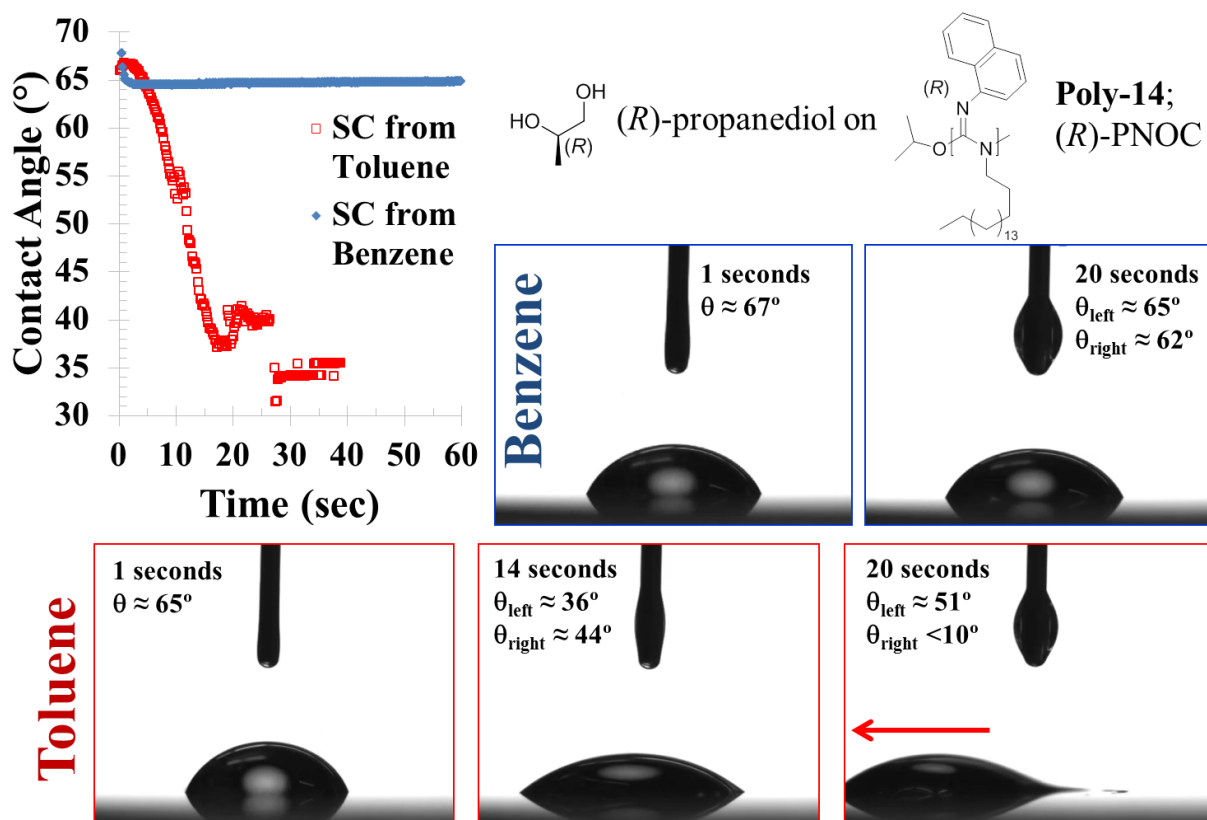


Figure 4.18- Contact angle measurements of propanediol dropped on (R)-PNOC (**Poly-14**) thin-films prepared by spin-coating **Poly-14** from toluene and benzene ($c = 5.0$ mg/mL) and annealed under solvent vapor for 48 hours. Also shown are the images of the drops at specific times showing the droplet movement after surface reorganization on the toluene-cast film.

There have been a number of reports on the movement of droplets caused by fabricated surface energy, wettability gradients of surfaces.³⁶⁻³⁸ This, however, does not

particularly apply to this case. Several hypothesized causes for this unique phenomenon have been proposed within our group but none have been definitively identified. We first hypothesized that upon dropping the propanediol liquid onto the toluene surface, the initial reorganization involves the breaking up of the helical bundles observed by AFM in Figure 4.14. Once the bundles are sufficiently separated, the expanded structure of state A allows for the propanediol molecules to penetrate the surrounding aliphatic corona of octadecyl pendant groups. Once the propanediol reaches the polymer backbone, the conformational switching to state B is induced causing the polymer backbone to contract and expel the solvent molecules from the alkyl sheath, which was the proposed cause for the large entropy gain observed by van't Hoff analysis of the switching process. This hypothesis would explain where the necessary energy comes from required to spontaneously move the droplet.

To test this hypothesis, the same procedure for sample preparation was carried out for the control polymer **Poly-41** to see if this behavior persists. On the thin-film spin-coated from and annealed in benzene, the droplet of propanediol again reaches a stable contact angle of $\sim 65^\circ$ within one second and remains constant. Dropping the propanediol on the toluene-cast film of **Poly-41**, however, again induced surface reorganization causing the droplet to move across the surface. This was attempted with both (*R*)- and (*S*)-PPOC with slightly different behavior observed depending on the chirality of the backbone. For (*R*)-PPOC, the droplet movement was substantially less prevalent (occurred in 2/8 drops tested) with the surface reorganization caused by both (*R*)- and (*S*)-propanediol resulting in a steady decrease in contact angle over the course of ~ 15 seconds to a plateau of 27° before remaining constant in most cases (see experimental section).

Dropping propanediol on (*S*)-PPOC surfaces (Figure 4.19), however, resulted in highly active surface reorganization with all droplets applied moving substantially. The rate of reorganization/ induced droplet movement occurred much more rapidly for (*S*)-PPOC (within ~4-7 second of dropping) than that observed for (*R*)-PNOC. These results somewhat refute the hypothesis proposed due to PPOC exhibiting no conformational switching as a function of solvent. This, however, does not necessarily mean that the proposed hypothesis is completely wrong. Propanediol is a poor solvent for these polymers, so if it were able to reach the backbone of PPOC, the helical contraction and solvent expulsion may still take place. The real question is why is the backbone of PPOC more accessible when spin-coated from and annealed in toluene compared to benzene despite the AFM micrographs displaying the same morphology? Additionally, why does the (*R*)-PPOC surface show limited activity in terms of droplet movement whereas (*S*)-PPOC surfaces are highly active? Both (*R*)- and (*S*)-PPOC exhibit very similar optical activity (albeit of opposite sign; ca. $[\alpha]_{435}^{25} = 295^\circ$ and -325° in toluene, respectively) and MWs (ca. $M_n = 26.1$ kDa; $M_w/M_n = 1.39$ and $M_n = 25.8$ kDa; $M_w/M_n = 1.36$, respectively). This suggests that the differences between the two samples of **Poly-41** thin-films were most likely a consequence of slight differences in sample preparation/ annealing.

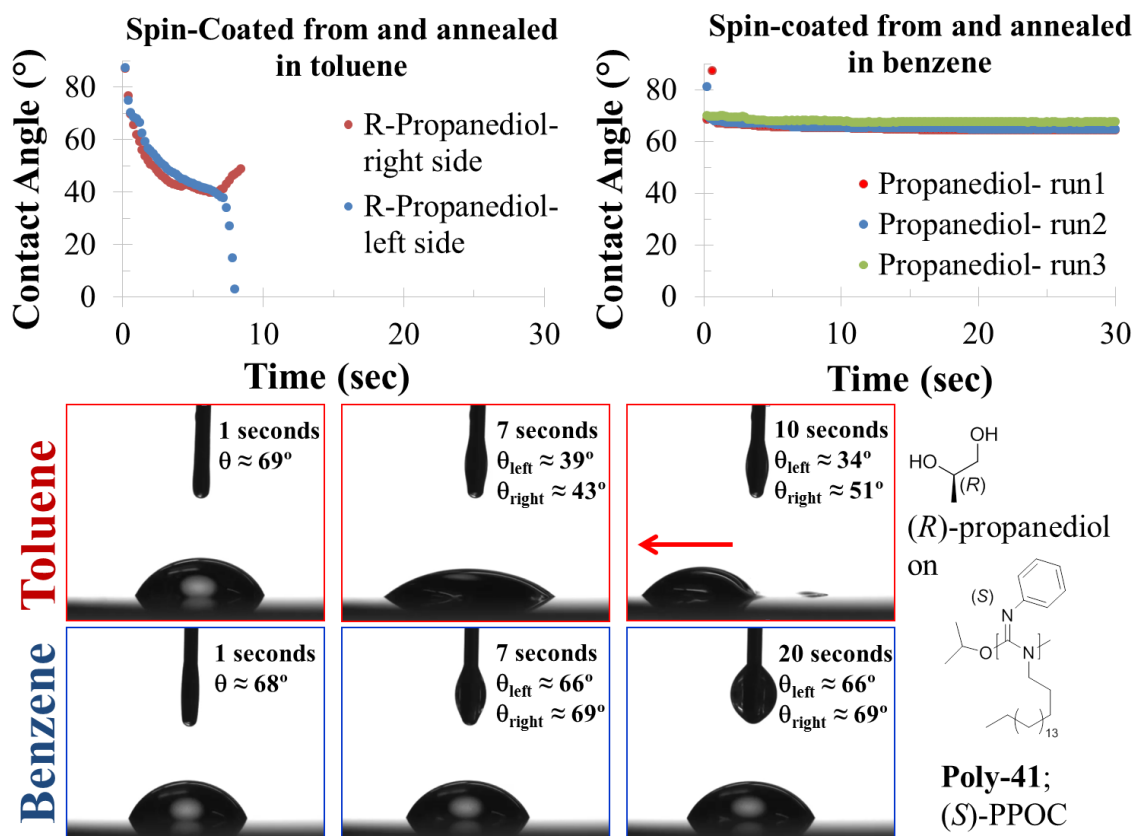


Figure 4.19- Contact angle measurements of propanediol dropped on (*S*)-PPOC (**Poly-41**) thin-films prepared by spin-coating from toluene and benzene ($c = 5.0 \text{ mg/mL}$) and annealed under solvent vapor for 48 hours. Also shown are the images of the drops at specific times showing the droplet movement after surface reorganization on the toluene-cast film.

The thin-film of (*S*)-PPOC spin-coated from and annealed in benzene exhibited the same behavior as (*R*)-PPOC reaching the stable propanediol contact angle of $\sim 65^\circ$ in ≤ 1.0 second and remaining constant. This result was highly reproducible with each of attempt resulting in the same behavior observed.

The droplet on the toluene-cast surfaces of PNOC and PPOC always deforms in some manner with different contact angles observed on the right and left sides of the drops.

Interestingly, in some cases, the droplet appears as if it were being pulled (like that shown in Figure 4.18) with the contact angle on the left side of the drop being larger than the right side. However, other attempts appear as if the drop is being pushed away (like that shown in Figure 4.19) with the right side appearing larger than the left as the droplet moves to the left. The latter was observed with the highest frequency and suggests that, upon surface reorganization, the polymer-liquid interactions become less favorable causing the surface to repel the propanediol droplet. Additionally, the direction of the droplet movement appears to occur somewhat randomly. At first, when looking at the trend for PNOC, it appeared as if the drops moved in the direction of the spin-coating but that was refuted when observing the directionality of the droplet movements on the PPOC surface (Figure 4.20). The deformation of the droplet is also clearly visible in Figure 4.20, in particular for **Poly-41** where the droplets all appear almost crescent-shaped with the higher contact angles on the opposite side of the movement direction.

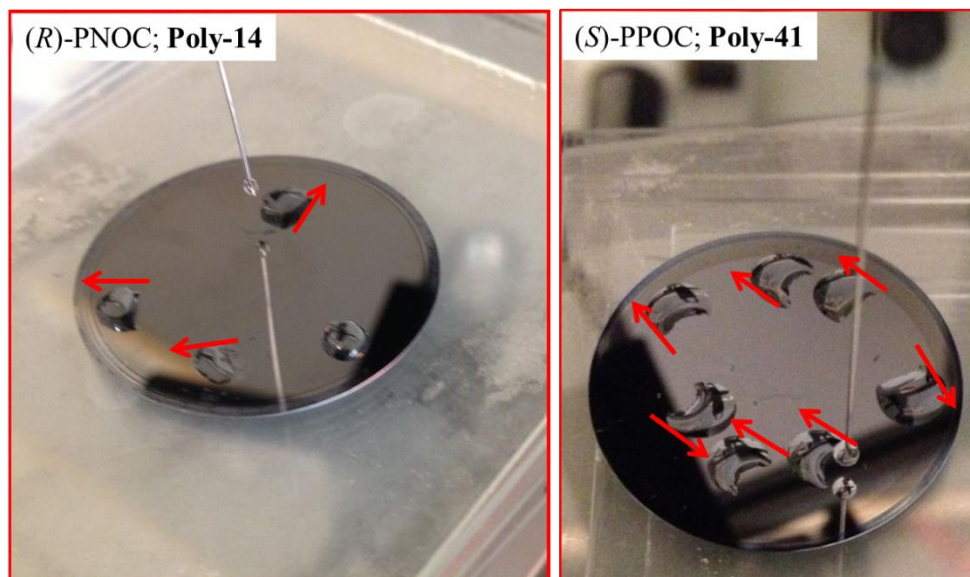


Figure 4.20- Picture of the moving propanediol droplets on **Poly-14** (left; *(R)*-PNOC) and **Poly-41** (right; *(S)*-PPOC) thin films prepared by spin-coating from and annealing in toluene.

Without the use of a goniometer, we attempted the same experiment on *(R)*-PNOC surfaces prepared from toluene but with ethylene glycol substituted for propanediol. Again, we observed similar droplet motion behaviors suggesting that this phenomenon is consequence of some interaction between the diol moiety and the polycarbodiimide backbone. These experiments need to be repeated with the goniometer to better visualize the changes and measure the contact angles. Dropping water onto *(R)*-PNOC surfaces, however, did not result in any specific reorganization behaviors but the contact angles of the water droplets on the thin-films spin-coated from and annealed in toluene did differ from benzene. The advancing (maximum) contact angles were very similar for both films ($\theta_{adv} = 114^\circ$ for toluene; $\theta_{adv} = 110^\circ$ for benzene) but the receding (minimum) contact angle for each film was substantially different ($\theta_{rec} = 73^\circ$ for toluene; $\theta_{rec} = 92^\circ$ for benzene). The differences in

receding contact angles is believed to be a result of the expanded helical structure of state A allowing for the aliphatic sheath to be more readily penetrated. Like the films cast from LC solutions, thin-film XRD is necessary to identify/ confirm the specific differences between the toluene and benzene cast films of **Poly-14**. Additionally, to image the minute changes associated with the observed surface reorganization, both AFM and thin-film XRD must be conducted on the film after exposure to propanediol. This will be attempted in future work.

4.6 Conclusions-

Since the discovery of the controlled Ti(IV) mediated polymerization of carbodiimides, research in this area has mainly focused on their synthesis and characterization with little emphasis on the application of these novel polymer systems. In our studies, a wide range of potentially fruitful behaviors have been discovered for polycarbodiimides including chiral sensing, chiroptical switching, and liquid crystallinity, to name a few. To add to this, both **Poly-14** and **Poly-41** have shown some intensely interesting properties that could further expand the potential applications of these polymers. **Poly-14** was shown to adopt unique, lyotropic LC mesophases as a function of solvent and temperature. One of these phases include a brand new, lyotropic “blue phase” which is adopted at higher temperatures (ca. 40 °C) in concentrated CHCl₃, benzene, and THF solutions (ca. 15 and 25 w%). In toluene, **Poly-14** adopts a still unidentified lyotropic mesophase that exhibit a wide range of brilliant colors including green, orange, purple, pink, yellow, and red and is stable up to ~90 °C. The films cast from these LC solutions also reflect

brilliant colors such as blue, green, and orange believed to be consequence of the locked-in photonic band-gap structure adopted in solution. The specific photonic structure must be identified and confirmed using Bragg reflection spectroscopy and XRD. **Poly-41** also adopted unique, lyotropic blue phases that were stable at a variety of temperature but no mesophase transitions were observed for this polymer.

Additionally, the conformational bistability results in hierarchical alterations to the thin-film morphology of **Poly-14**. When spin-coated from and annealed in toluene ($c = 5.0$ mg/mL), **Poly-14** displays larger helical bundles by AFM believed to be a result of increased octadecyl interdigitation of the expanded helical conformation of state A. The PNOC thin-film spin-coated from and annealed in benzene (state B) reveals much smaller nanofibular morphologies due to the contracted, twisted structure of the polymer backbone deterring significant aggregation/ crystallization. These thin-films also displayed dynamic surface reorganization behaviors when exposed to propanediol depending on the solvent employed in spin-coating/ annealing. When dropping propanediol (or ethylene glycol) on the toluene-cast surface, a highly unique behavior was observed where the propanediol first reorganizes the surface in a specific manner which then causes the liquid-polymer interactions to be less favorable. These unfavorable interactions cause the droplet of propanediol to spontaneously move across the flat, level surface without any other external stimuli. This is one of the only examples of fully-synthetic polymer films providing spontaneous mechanical actuations as a function of solvent-polymer interactions. These new findings expand the potential uses for these polymers (with further research) to include tunable photonic Bragg reflectors and molecular muscles.

4.7 Experimental Section-

Materials- The synthesis and characterization of **Cat-2R**,³⁹ **Cat-2S**,³⁹ **Mono-14**,⁴⁰ **Mono-41**,⁴¹ **Poly-14**,⁴⁰ and **Poly-41**⁴¹ have been previously reported. The toluene solvent employed in the polymerizations of **Mono-14** and **Mono-41** and the synthesis of **Cat-2R** and **Cat-2S** was vacuum distilled over CaH₂ into an oven-dried Schlenk flask equipped with 3Å molecular sieves and stored in the MBraun UNILAB™ glove box prior to use. All other solvents were used as received. The highly-polished silicon wafers used as the solid support for polymer thin-films were purchased (Wafer World) and used as received. The (*R*)- and (*S*)-propanediol probing liquid was purchased (Sigma Aldrich) and used as received.

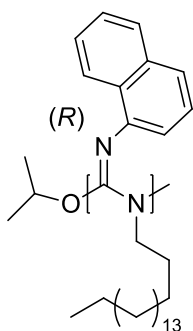
Equipment- Optical microscopy images were collected using a Meiji Techno ML9000 series OM through cross-polarizers and captured with an AmScope FMA050 fixed microscope digital camera. TMAFM was employed to investigate the thin-film morphologies of **Poly-14** and **Poly-41** copolymers using a Nanoscope IV-Multimode Veeco instrument equipped with an E-type vertical engage scanner. Dynamic contact angle measurements were conducted on a Dataphysics OCA15 optical goniometer. Static measurements were made on 4 μL droplets of probing liquid dropped onto sample spin-coated substrates. Advancing and receding measurements were made from videos of experiments. For dynamic measurements, 3 μL of probing liquid was added at 0.5 μL/sec through a 29 or 33 gauge, blunt-tipped needle to a 4 μL droplet of probing liquid already placed on the substrate, followed by removing 5 μL of liquid from the droplet. Specific optical rotations of chiral polymers were measured using a JASCO P-1010 polarimeter (435 nm, *l* = 10.0 cm) at room temperature in dilute solution (CHCl₃, *c* = 2.00 mg/mL). GPC analyses of MW for copolymers and homopolymers relative

to polystyrene standards were conducted on a Shimadzu Prominence Modular HPLC/GPC system equipped with refractive index (RI) detector. A two-column system was employed with both Agilent Mixed-E and Mixed-C column working in tandem.

Synthesis of Polycarbodiimides-

The synthesis procedure and characterization of **Poly-14** and **Poly-41** have been previously reported. Additionally, the polymerization of **Mono-14** and **Mono-41** follow the same procedure for the polymerization of carbodiimides outlined in previous chapters. The specific amounts of solvent, monomer, and catalyst, percent yield, MW via GPC, and specific optical rotations for the particular polymer samples used in this chapter are listed in the following section.

(R)-PNOC (Poly-14)-

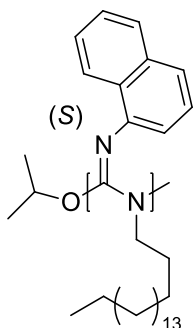


Following the procedure for the Ti(IV) mediated polymerization of carbodiimides outlined in Chapter 2 and 3: 2.02 g (4.79 mmol; 202 eq.) of **Mono-14**, 10.7 mg (23.8 μmol ; 1.0 eq.) of **Cat-2R**, ~0.4 mL of dry toluene. One alteration of the procedure reported includes

the addition of 1.0 v% DBU into the MeOH precipitating solvent to aid in the extraction of residual titanium.

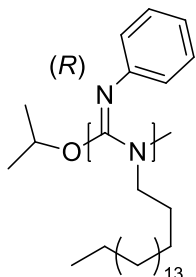
Yield: 1.57 g of white, spongy solid, 78%. Specific OR ($c = 2.0$ mg/mL, $l = 10.0$ cm, $\lambda = 435$ nm, 25 °C) $[\alpha] = +822^\circ$ in toluene; $[\alpha] = -444^\circ$ in benzene. GPC (Shimadzu GPC): $M_n = 10.4$ kDa; $M_w = 12.6$ kDa; M_w/M_n (PDI) = 1.21.

(*S*)-PNOC (**Poly-14**)-



Following the procedure for the Ti(IV) mediated polymerization of carbodiimides outlined in Chapter 2 and 3: 1.98 g (4.72 mmol; 201 eq.) of **Mono-14**, 10.6 mg (23.5 μ mol; 1.0 eq.) of **Cat-2S**, ~0.4 mL of dry toluene. One alteration of the procedure reported includes the addition of 1.0 v% DBU into the MeOH precipitating solvent to aid in the extraction of residual titanium.

Yield: 1.56 g of white, spongy solid, 79%. Specific OR ($c = 2.0$ mg/mL, $l = 10.0$ cm, $\lambda = 435$ nm, 25 °C) $[\alpha] = -794^\circ$ in toluene; $[\alpha] = +458^\circ$ in benzene. GPC (Shimadzu GPC): $M_n = 9.4$ kDa; $M_w = 11.1$ kDa; M_w/M_n (PDI) = 1.18.

(R)-PPOC (Poly-41)-

Following the procedure for the Ti(IV) mediated polymerization of carbodiimides outlined in Chapter 2 and 3: 1.24 g (3.34 mmol; 203 eq.) of **Mono-41**, 7.4 mg (16.4 μmol ; 1.0 eq.) of **Cat-2R**, ~0.8 mL of dry toluene. One alteration of the procedure reported includes the addition of 1.0 v% DBU into the MeOH precipitating solvent to aid in the extraction of residual titanium.

Yield: 1.16 g of white, spongy solid, 94%. Specific OR ($c = 2.0 \text{ mg/mL}$, $l = 10.0 \text{ cm}$, $\lambda = 435 \text{ nm}$, $25 \text{ }^\circ\text{C}$) $[\alpha] = +294^\circ$ in toluene; $[\alpha] = +296^\circ$ in benzene. GPC (Shimadzu GPC): $M_n = 26.1 \text{ kDa}$; $M_w = 36.3 \text{ kDa}$; M_w/M_n (PDI) = 1.39.

(S)-PPOC (Poly-41)-

Following the procedure for the Ti(IV) mediated polymerization of carbodiimides outlined in Chapter 2 and 3: 1.26 g (3.40 mmol; 191 eq.) of **Mono-41**, 8.0 mg (16.4 μmol ; 1.0 eq.) of **Cat-2S**, ~0.8 mL of dry toluene. One alteration of the procedure reported includes the addition of 1.0 v% DBU into the MeOH precipitating solvent to aid in the extraction of residual titanium.

Yield: 1.19 g of white, spongy solid, 95%. Specific OR ($c = 2.0 \text{ mg/mL}$, $l = 10.0 \text{ cm}$, $\lambda = 435 \text{ nm}$, $25 \text{ }^\circ\text{C}$) $[\alpha] = -325^\circ$ in toluene; $[\alpha] = -318^\circ$ in benzene. GPC (Shimadzu GPC): $M_n = 25.8 \text{ kDa}$; $M_w = 35.1 \text{ kDa}$; M_w/M_n (PDI) = 1.36.

Preparation of Polymer LC Solutions and Samples for Imaging-

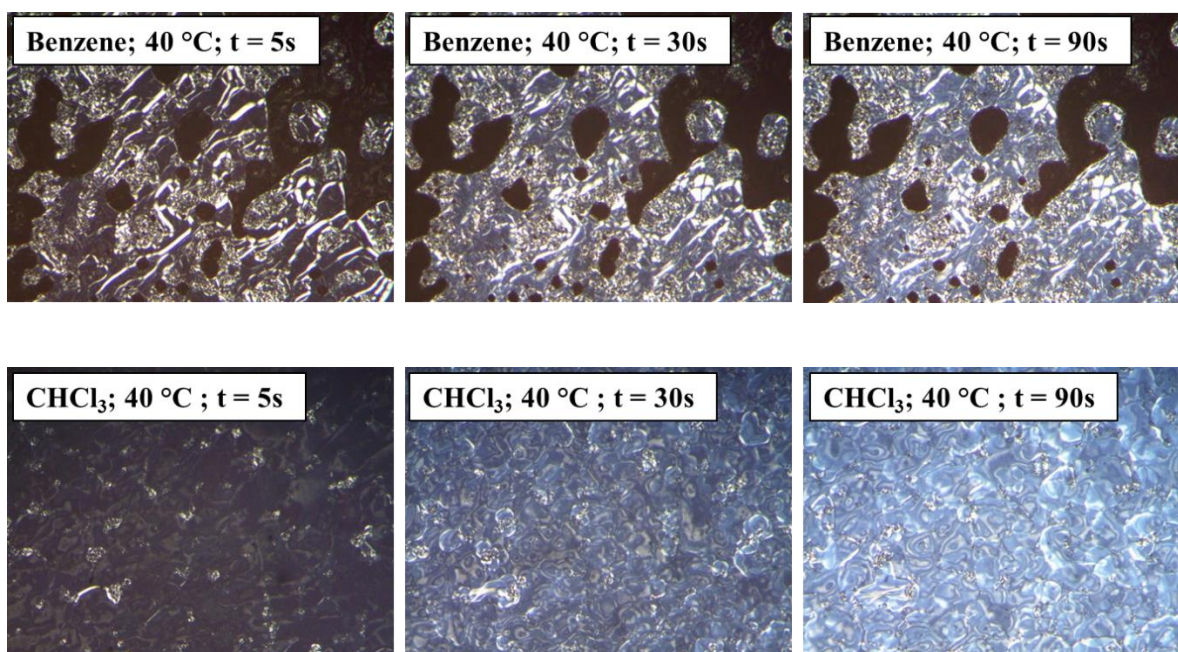
A small amount (50 – 100 mg) of the corresponding polymer (**Poly-14** or **Poly-41**) was measured in a small, shell vial and the necessary amount of solvent (benzene, CHCl_3 , THF, toluene) to achieve a final concentration of 15 or 25 w%. The vial was then sealed and wrapped heavily with Parafilm to avoid significant solvent evaporation. The 15 w% solutions in benzene, THF, and toluene were allowed to incubate at room temperature for 12 hours to allow the LC mesophase to form. However, the LC mesophase formed in ~1 hour for the 15

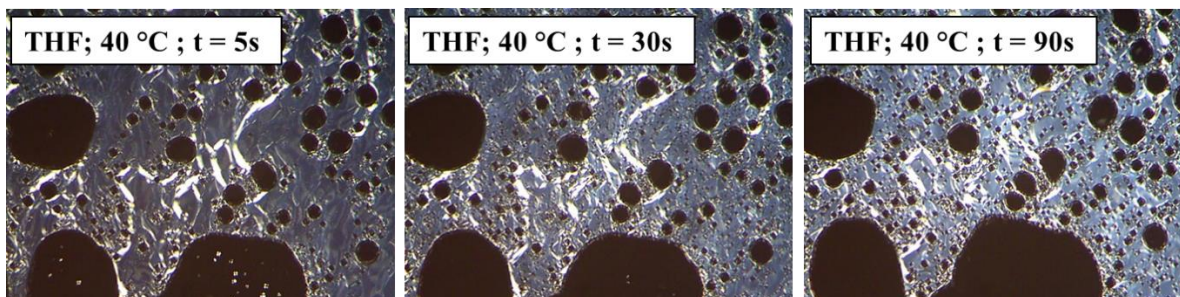
w% solution in CHCl_3 and all 25 w% solutions. A drop of the solution was placed on a glass slide and covered with a cover slip and all images were captured under cross-polarizers towards the center of the sandwiched solution. The cover slip was removed and the solvent was allowed to evaporate in order to image the LC thin-films shown in the discussion.

Time-Resolved Variable-Temperature POM-

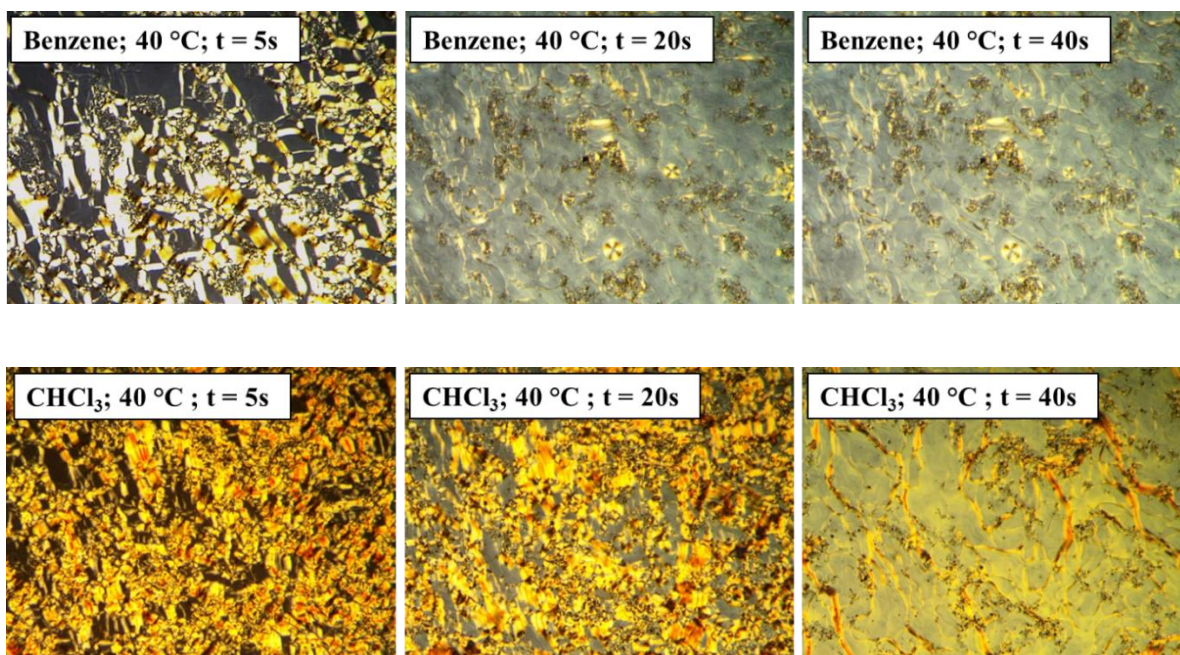
The variable-temperature POM imaging was carried out by preheating the microscope stage to the corresponding temperature and placing the LC slides on the heat. The images below were collected after specific time-intervals (measured via stop-watch) on the preheated stage at the specified temperature shown. In each case, it took specific amounts of time for the mesophase transition to occur. All images were captured at 40x magnification.

15 w% LC solutions-





25 w% LC solutions-



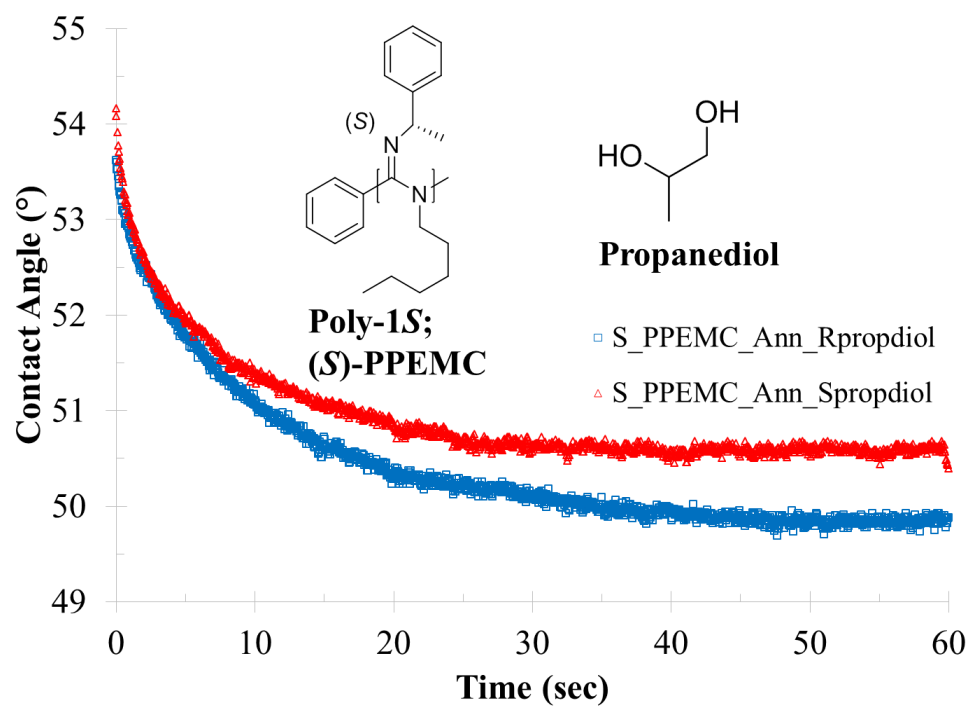
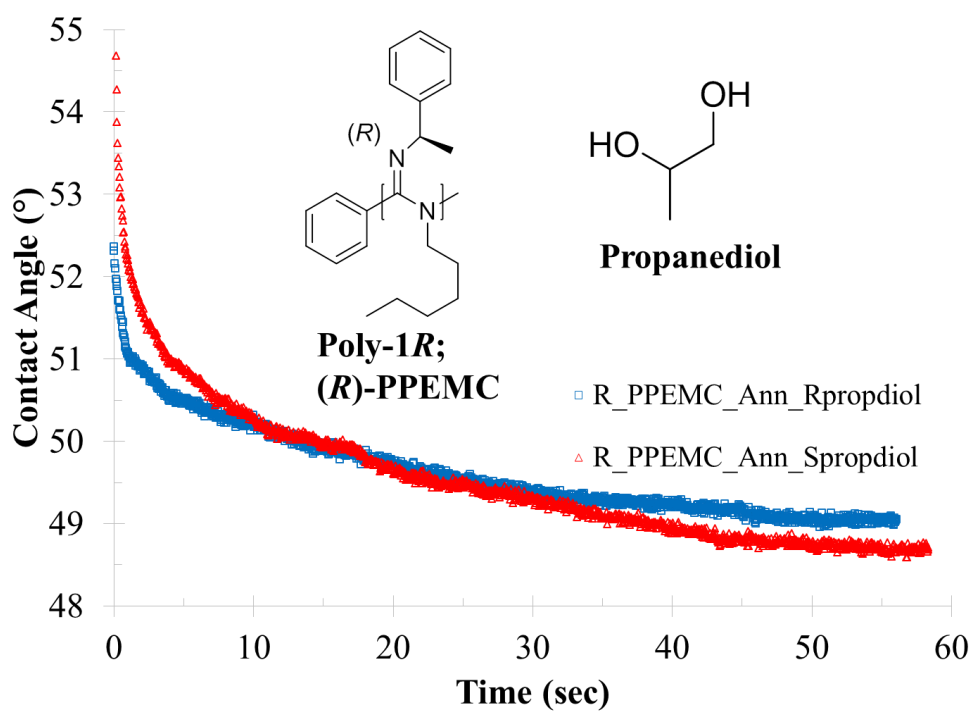
TMAFM Imaging and Contact Angle Measurements of **Poly-14** and **Poly-41**-

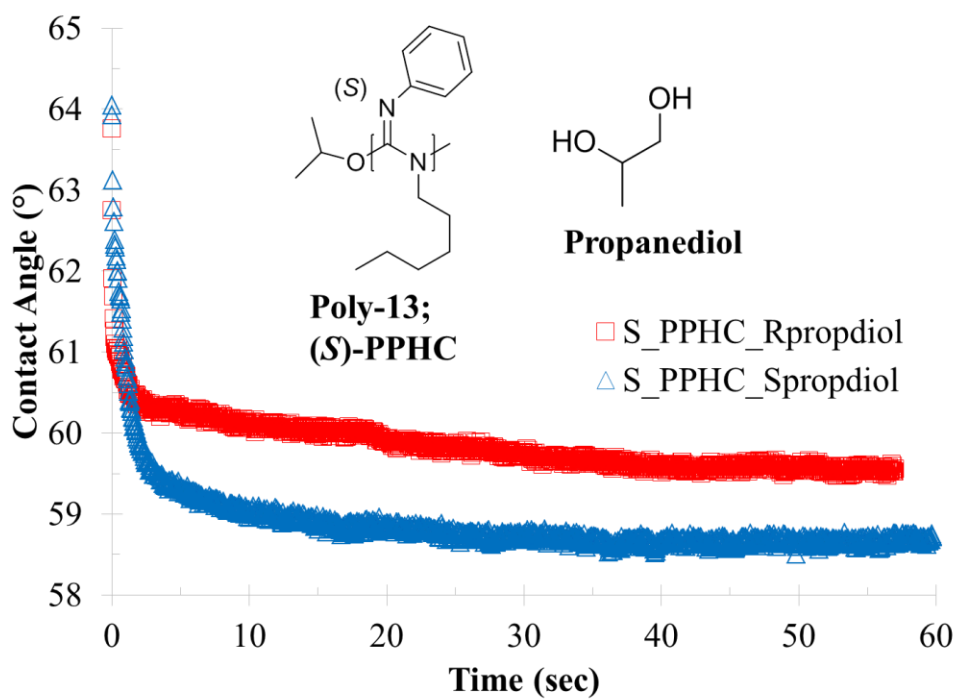
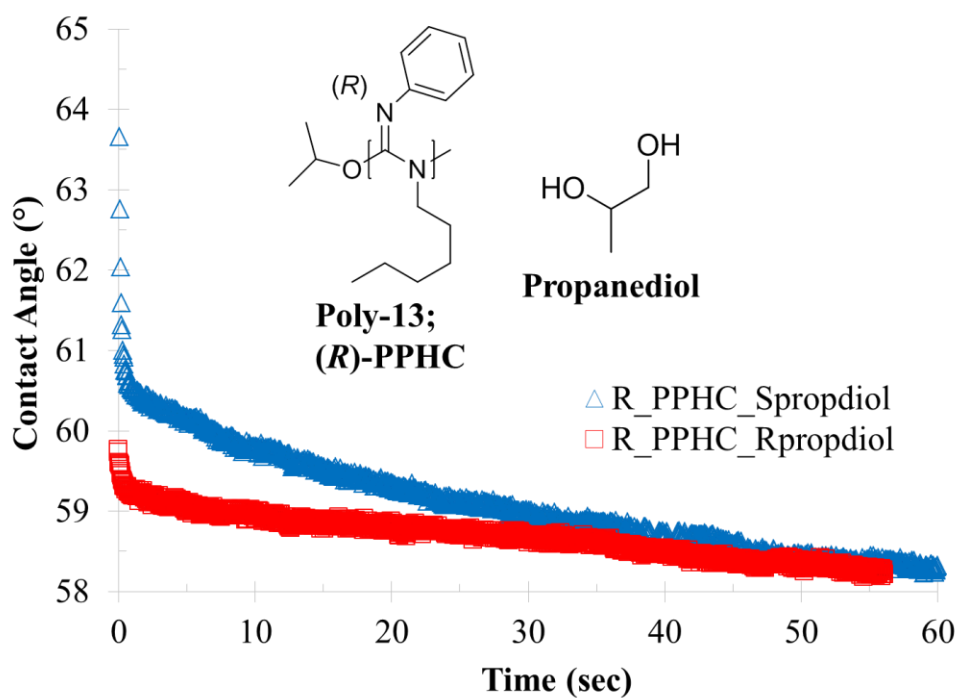
Thin-films of both polymers were prepared via the same procedure with two different solvents employed. The polymers were dissolved in either toluene or benzene ($c = 5.0$ mg/mL) and the solutions were passed through a $0.45 \mu\text{m}$ PTFE syringe filter onto a highly polished silicon wafer (Wafer World). The filtered solution was then spin-coated at 1000 rpm for 30 seconds to provide a uniform distribution of the polymer throughout the entire

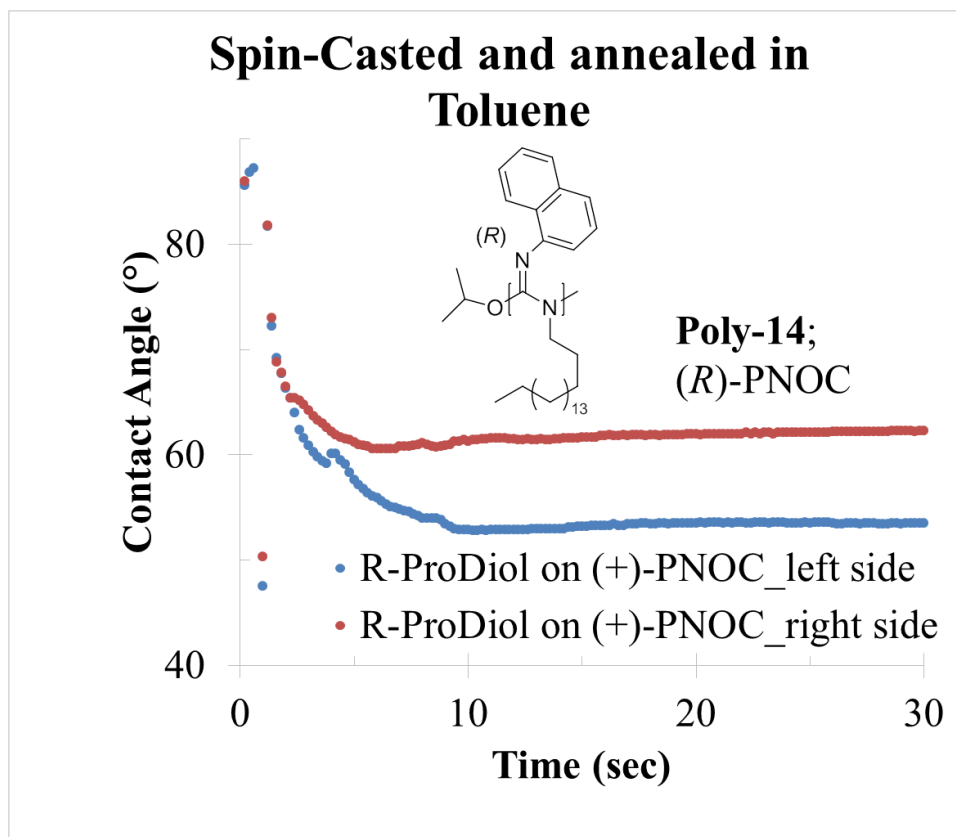
substrate. The thin-films were then placed in the corresponding saturated solvent chamber and allowed to anneal under the solvent vapor for 48 hours. Prior to AFM imaging/ contact angle measurements, the films were dried and stored under vacuum in a desiccator. All images were recorded with resonant frequencies of 320 kHz and lateral scan frequencies of 0.996 Hz using silicon TESP, V-shaped cantilever probes with a nominal spring constant of 42 N/m. Scan areas ranged from 500 x 500 nm to 5 x 5 μm .

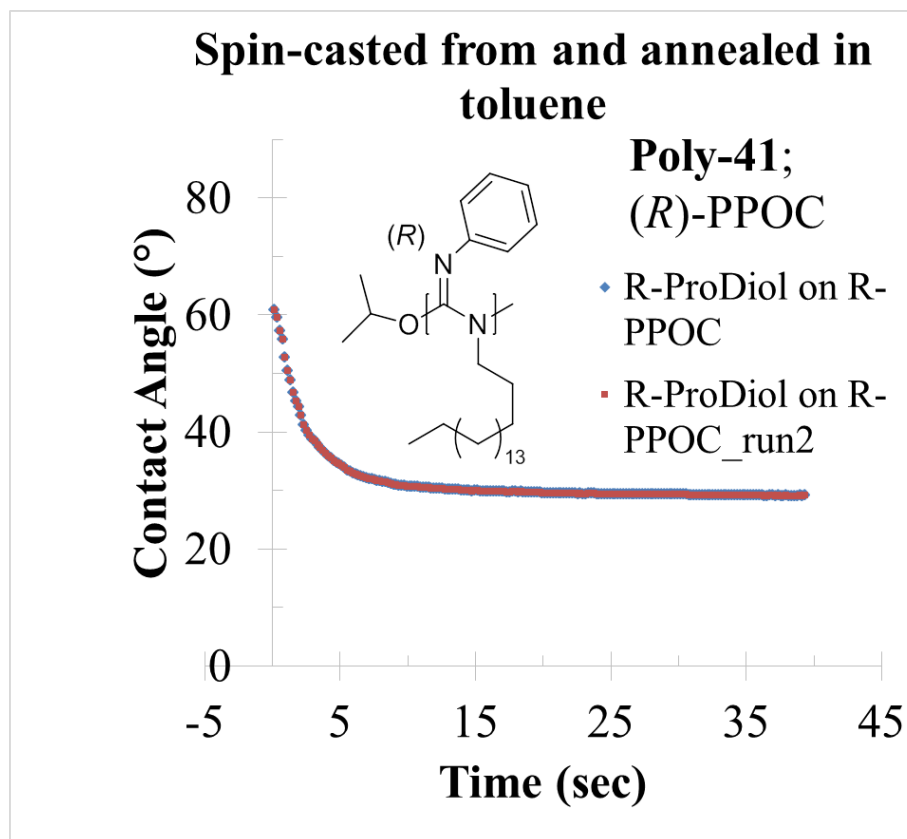
Attempted Chiral Wetting Experiments-

The initial goal of measuring the contact angles of (*R*)- and (*S*)-propanediol on (*R*)- and (*S*)-chiral polycarbodiimide surfaces in order to see whether different contact angles result from different chiral pairing (*R-R*, *R-S*, *S-R*, or *S-S*). Unfortunately, only minute contact angle differences were observed (see below) for (*R*)- and (*S*)-PPEMC (**Poly-1R** and **S**) polymerized with achiral initiators. The same was true for PPHC (**Poly-13**) with no chiral centers but polymerized with **Cat-2R** or **Cat-2S** forming a polymer backbone with an excess single-handed helical sense. In all cases, however, some sort of surface reorganization was observed as evident by the dynamic contact angle as a function of time. Also displayed are the time-dependant contact angle plots of propanediol dropped on toluene-cast surfaces of (*R*)-PNOC (**Poly-14**) and (*R*)-PPOC (**Poly-41**) that didn't display the induced droplet movement.









4.8 References-

- (1) Michler, G. H. *Electron Microscopy of Polymers*; Springer: Heidelberg, Germany, 2008.
- (2) Goodhew, P. J.; Humphreys, F. J.; Beanland, R. *Electron Microscopy and Analysis*; 3rd ed.; Taylor & Francis: London, England, 2000.
- (3) Schonherr, H.; Vancso, G. J. *Scanning Force Microscopy of Polymers*; Springer: Heidelberg, Germany, 2010.
- (4) Khulbe, K. C.; Feng, C. Y.; Matsuura, T. *Synthetic Polymeric Membranes: Characterization by Atomic Force Microscopy*; Springer: Heidelberg, Germany, 2008.
- (5) Zhong, Q.; Inniss, D.; Kjoller, K.; Elings, V. B. *Surf. Sci.* **1993**, 290, L688-L692.
- (6) Eaton, P.; West, P. *Atomic Force Microscopy*; Oxford University Press: New York, USA, 2010.

- (7) Barron, A. R. Physical Methods in Chemistry and Nanoscience, OpenStax-CNX Web site. <http://cnx.org/content/col10699/1.14/>, June 26, 2012
- (8) Edrington, A. C.; Urbas, A. M.; DeRege, P.; Chen, C. X.; Swager, T. M.; Hadjichristidis, N.; Xenidou, M.; Fetters, L. J.; Joannopoulos, J. D.; Fink, Y.; Thomas, E. L. *Adv. Mater.* **2001**, *13*, 421-425.
- (9) Maxein, G.; Keller, H.; Novak, B. M.; Zentel, R. *Adv. Mater.* **1998**, *10*, 341-345.
- (10) Ge, J.; Yin, Y. *Angew. Chem., Int. Ed.* **2011**, *50*, 1492-1522.
- (11) Akahane, Y.; Asano, T.; Song, B.-S.; Noda, S. *Nature* **2003**, *425*, 944-947.
- (12) Finkelmann, H.; Kim, S. T.; Munoz, A.; Palffy-Muhoray, P.; Taheri, B. *Adv. Mater.* **2001**, *13*, 1069-1072.
- (13) Krauss, T. F. *Nat. Mater.* **2003**, *2*, 777-778.
- (14) Birner, A.; Wehrspohn, R. B.; Gosele, U. M.; Busch, K. *Adv. Mater.* **2001**, *13*, 377-388.
- (15) Campbell, M.; Sharp, D. N.; Harrison, M. T.; Denning, R. G.; Turberfield, A. J. *Nature* **2000**, *404*, 53-56.
- (16) Fudouzi, H.; Xia, Y. *Langmuir* **2003**, *19*, 9653-9660.
- (17) Kang, Y.; Walish, J. J.; Gorishnyy, T.; Thomas, E. L. *Nat. Mater.* **2007**, *6*, 957-960.
- (18) Li, Y.; Wang, M.; White, T. J.; Bunning, T. J.; Li, Q. *Angew. Chem., Int. Ed.* **2013**, *52*, 8925-8929.
- (19) Kosa, T.; Sukhomlinova, L.; Su, L.; Taheri, B.; White, T. J.; Bunning, T. J. *Nature* **2012**, *485*, 347-349.
- (20) Lin, T.-H.; Li, Y.; Wang, C.-T.; Jau, H.-C.; Chen, C.-W.; Li, C.-C.; Bisoyi, H. K.; Bunning, T. J.; Li, Q. *Adv. Mater.* **2013**, *25*, 5050-5054.
- (21) Zhai, L.; Nolte, A. J.; Cohen, R. E.; Rubner, M. F. *Macromolecules* **2004**, *37*, 6113-6123.
- (22) Hwang, J.; Song, M. H.; Park, B.; Nishimura, S.; Toyooka, T.; Wu, J. W.; Takanishi, Y.; Ishikawa, K.; Takezoe, H. *Nat. Mater.* **2005**, *4*, 383-387.

- (23) Pavlichenko, I.; Exner, A. T.; Guehl, M.; Lugli, P.; Scarpa, G.; Lotsch, B. V. *J. Phys. Chem. C* **2012**, *116*, 298-305.
- (24) Wang, H.; Chen, Q.-W.; Yu, Y.-F.; Cheng, K.; Sun, Y.-B. *J. Phys. Chem. C* **2011**, *115*, 11427-11434.
- (25) Coles, H. J.; Pivnenko, M. N. *Nature* **2005**, *436*, 997-1000.
- (26) Coles, H.; Morris, S. *Nat. Photonics* **2010**, *4*, 676-685.
- (27) Hur, S.-T.; Lee, B. R.; Gim, M.-J.; Park, K.-W.; Song, M. H.; Choi, S.-W. *Adv. Mater.* **2013**, *25*, 3002-3006.
- (28) Kikuchi, H. In *Liquid Crystalline Functional Assemblies and Their Supramolecular Structures*; Kato, T., Ed.; Springer Berlin Heidelberg: 2008; Vol. 128, p 99-117.
- (29) Kikuchi, H.; Yokota, M.; Hisakado, Y.; Yang, H.; Kajiyama, T. *Nature Materials* **2002**, *1*, 64-68.
- (30) Kim, J.; Novak, B. M.; Waddon, A. J. *Macromolecules* **2004**, *37*, 1660-1662.
- (31) Kim, J.; Novak, B. M.; Waddon, A. J. *Macromolecules* **2004**, *37*, 8286-8292.
- (32) Merten, C.; Reuther, J. F.; DeSousa, J. D.; Novak, B. M. *Phys. Chem. Chem. Phys.* **2014**, *16*, 11456-11460.
- (33) Reuther, J. F.; Novak, B. M. *J. Am. Chem. Soc.* **2013**, *135*, 19292-19303.
- (34) Rapp, M.; Ducker, W. A. *J. Am. Chem. Soc.* **2010**, *132*, 18051-18053.
- (35) Shundo, A.; Hori, K.; Ikeda, T.; Kimizuka, N.; Tanaka, K. *J. Am. Chem. Soc.* **2013**, *135*, 10282-10285.
- (36) Chaudhury, M. K.; Whitesides, G. M. *Science* **1992**, *256*, 1539-1541.
- (37) Subramanian, R. S.; Moumen, N.; McLaughlin, J. B. *Langmuir* **2005**, *21*, 11844-11849.
- (38) John, K.; Bar, M.; Thiele, U. *European Physical Journal E* **2005**, *18*, 183-199.
- (39) Tian, G.; Lu, Y.; Novak, B. M. *J. Am. Chem. Soc.* **2004**, *126*, 4082-4083.

- (40) Kennemur, J. G.; Clark, J. B.; Tian, G.; Novak, B. M. *Macromolecules* **2010**, *43*, 1867-1873.
- (41) Tang, H.-Z.; Garland, E. R.; Novak, B. M.; He, J.; Polavarapu, P. L.; Sun, F. C.; Sheiko, S. S. *Macromolecules* **2007**, *40*, 3575-3580.

CHAPTER 5: Controlled “Living” Polymerization of Carbodiimides using Versatile Nickel(II) Initiators

5.1 Introduction to Living Polymerizations-

Polymeric macromolecules of discrete size and corresponding molecular weights can only be found in nature. Examples include RNA, DNA, proteins, and enzymes. A method for synthesizing discrete macromolecules was first described by Paul Flory in 1940.¹ The proposed ionic chain growth polymerization was not successfully demonstrated until 1956 when Szwarc successfully polymerized styrene and butadiene via anionic polymerization techniques under inert conditions in the absence of impurities.² The polymers synthesized displayed abnormally narrow MW distributions, i.e., monodisperse, due to the minimization of various chain transfer and terminating reactions that typically occur in polymer syntheses. He, at this time, coined the name “living polymerizations” and demonstrated that the polymerization occurred in a very efficient, controlled manner with all of the monomer being consumed in the reaction. Truly “monodisperse” polymer systems, however, can only be found in nature but the synthetic polymers synthesized by controlled “living” techniques have closed the gap significantly with very narrow MW distributions ($M_w/M_n \leq 1.02$) which are typically referred to as monodisperse. The addition of monomer following the consumption of all monomer present resulted in the continued growth of the polymer chains suggesting that the polymer chains retain their active end group throughout the polymerization reaction. Addition of a dissimilar monomer, in this case butadiene, to the styrene polymerization following the consumption of all monomer led to the formation of a

block copolymer with very well-defined structures providing further evidence that this polymerization occurs absent of chain transfer and terminating reactions.

For a polymerization to be considered “living,” it must satisfy the majority if not all of several criteria which were specifically designed to demonstrate the absence of chain transfer and termination. It should be noted that not all polymerizations that are considered “living”, however, satisfy all of the criteria giving way to several specific classes of “living” polymerizations designated by the extent of “living” character.

1. The monomer, in its entirety, should be consumed throughout the polymerization reaction and addition of a second aliquot of the same monomer will continue the growth of all or nearly all of the polymer chains. This requirement can be characterized using gel permeation chromatography (GPC) where only a single, narrow signal, associated with a single MW distribution is observed.
2. Addition of a second, dissimilar monomer upon consumption of the first monomer will result in the formation of a block copolymer. Again, the resulting copolymer should display only one, narrow peak associated with a single MW distribution in the GPC chromatogram.
3. The plot of number average molecular weight (M_n) vs. percent conversion should yield a linear relationship only if chain transfer side reactions are absent. This is the most common experiment for demonstrating absence of chain transfer and is typically required for any novel polymerization to be considered “living.”

4. The plot of M_n vs. $[\text{Monomer}]/[\text{Initiator/Catalyst}]$ should also be linear displaying the ability to tailor polymer MWs in a highly controlled manner upon altering the monomer/initiator ratio.
5. A kinetic study of the polymerization should indicate that the concentration of reactive end groups remains constant throughout the reaction supporting the absence of chain terminating side reactions. This is most commonly demonstrated by showing a linear relationship in the plot of $\ln([\text{M}]_0/[\text{M}])$ vs. time where $[\text{M}]_0$ is the initial monomer concentration and $[\text{M}]$ is the monomer concentration at different time intervals. This experiment is also typically required before any polymerization can be considered “living.”
6. Addition of a specific reagent towards the end of the polymerization reaction should result in an end functionalized polymer. For example, adding a specific amount of a functional electrophile to an anionic polymerization will effectively end cap all propagating species covalently attaching the functionality to the terminus of the polymer chains.^{3,4}
7. The rate of initiation must be rapid relative to the rate of propagation. This essentially results in the number of active chain ends staying constant allowing for all polymer chains to propagate at the same rate. The polydispersity index (PDI; M_w/M_n) should be very close to 1.0 (All polymer chains are of the same MW) with the general accepted limit of $\text{PDI} \leq 1.5$. It is, however, possible for some “living” polymerization reactions to yield a system that does not reach these requirements, most notably

reversible equilibrium polymerizations such as that of the polymerization of polycarbodiimides with organotitanium(IV) initiators.⁵

Due to limitations associated with confirming each criterion, it is imperative to probe and confirm several of the above criteria to definitively demonstrate “living” character in any novel polymerization technique. When studying equilibrium polymerizations, like that of the Ti(IV) mediated polymerization of carbodiimides, some of these specific criteria will not always be satisfied like that of a true “living” ionic polymerizations due to the reversible nature of initiation. The necessity of low polydispersity can be tempered somewhat due to this reversibility giving rise to the general accepted limit of $M_n/M_w \leq 1.5$. These factors must be considered herein when discussing the “living” character of a new equilibrium polymerization.

Today, the number of polymerizations with “living” characteristics has grown tremendously and the development of novel “living” polymerization techniques continues to be one of the most exhaustively studied areas of polymer chemistry. Of these new techniques, “living” radical polymerizations is the most frequently studied due to the wide availability of olefin monomers and the development of several reliable methods. These techniques offer the ability to polymerize new types of monomers and form a wide array of complex yet well-defined nano-architectures that are otherwise unobtainable via conventional radical mediated polymerizations. Some examples of these widely studied techniques include **atom transfer radical polymerizations (ATRP)**,⁶⁻⁸ **reversible addition-fragmentation chain-transfer (RAFT) polymerizations**,⁹⁻¹¹ **nitroxide mediated polymerizations (NMP)**,^{12,13} and **iodine transfer polymerization (ITP)**.^{14,15}

Traditional cross-coupling polymerizations such as Sonogashira,¹⁶ Suzuki,¹⁷ Heck,¹⁸ and Negishi¹⁹ polymerizations occur via step-growth mechanisms offering little control over MW and copolymer composition. Several new “living” transition metal mediated polymerization techniques, however, have emerged such as ring opening metathesis polymerizations (ROMP),^{20,21} acyclic diene metathesis (ADMET) polymerizations, titanium(IV) mediated polymerizations of isocyanates/carbodiimides,^{5,22,23} and nickel(II) mediated polymerizations of isocyanides^{24,25} offering exciting new opportunities to synthesize novel polymer architectures with a variety of interesting properties. Of these transition metal mediated polymerization techniques, the “living” chain-growth Kumada cross-coupling polycondensation of arylenes (i.e., phenylenes,^{26,27} pyrrole,²⁶ thiophenes,²⁶⁻²⁸ fluorenes,²⁹ selenophenes³⁰) with nickel(II) catalysts has possibly been the most intensively studied due to the formation of highly regioregular, conjugated materials with controlled MWs and copolymer composition for their applications in organic field-effect transistors (OFETs) for solar cells.^{31,32} Though the theoretical maximum of efficiency for these devices becomes closer to a reality, the synthesis of novel, conjugated copolymers remains an exhaustively studied area of polymer chemistry.³³

5.2 End Functionalization of Macromolecules Using Functional Initiators-

Living polymerization techniques also offer the ability to incorporate specific functionalities to the end of polymer chains. This has been demonstrated using several different “living” polymerization techniques including ATRP, RAFT, NMP, and Kumada chain-growth polycondensation. The incorporation of these functional end-groups unlocks a

plethora of new opportunities in the design and construction of complex yet well-defined architectures such as block copolymers, graft copolymers, polymer functionalized surfaces, inorganic/organic hybrid materials, star polymers, polymer-bioconjugates and hyperbranched/dendritic polymer systems (*vide infra*). The most common technique employed to form end functional materials is the use of functional initiators (or chain transfer agent for RAFT polymerizations) that, following the polymerization reaction, are appended covalently to the terminus of the polymer chain. Some generalized examples of these types of initiators can be found in Figure 5.1.

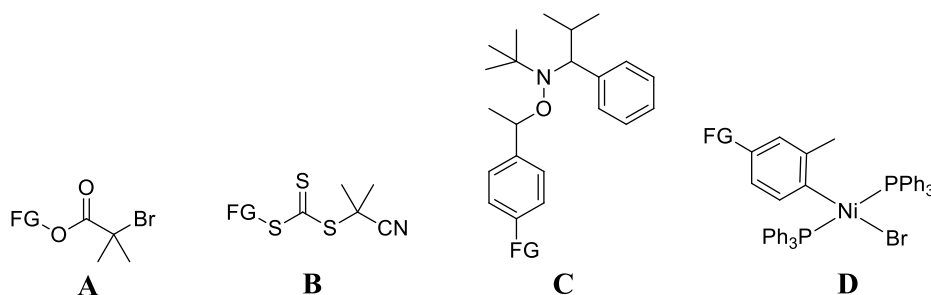


Figure 5.1- Examples of functional initiators (or chain transfer agent for RAFT) used in ATRP (**A**),⁶ RAFT polymerizations (**B**),⁹ NMP (**C**),^{13,34} and Kumada polycondensation (**D**)³⁵ where FG is a generic functional group.

The first three initiators shown (A-C) are used in “living” controlled-radical polymerizations of vinyl monomers such as styrene, methacrylates, acrylates, etc. In ATRP, the initiating radical is generated reversibly upon bromine atom transfer from an alkyl bromide initiator to a copper(I) source, most typically CuCl or CuBr, oxidizing the copper halide and generating a free alkyl radical. This free-radical then initiates the polymerization

and propagation ensues resulting in a polymer chain with the functionality of the initiator appended to the end terminus of the polymer chain. Using tri- and tetra functional initiators, Matyjaszewski et al. reported the synthesis of well-defined star polymers incorporating conventional systems like polystyrene, poly(*n*-butyl acrylate), and poly(methyl methacrylate) with controlled molecular weights.³⁶ Kreutzer et al. took the synthesis one step further forming highly-branched, amphiphilic star block copolymers from dendritically functionalized initiators (Figure 5.2).³⁷ The large number of hydroxyl functional groups in the Boltorn H40 dendrimer (HPB) was reacted with α -bromoisobutyryl bromide (step 1) resulting in a multi-functional ATRP initiator with several active polymerization sites per dendron. The copolymerization was then performed employing the hydrophobic *t*-butyl methacrylate and hydrophilic (octaethylene glycol) methacrylate as the two monomers incorporated. AFM of the copolymer cast from dilute solution confirms the formation of highly-branched, multi-arm star copolymers with 4 to 36 polymer arms per initiator.

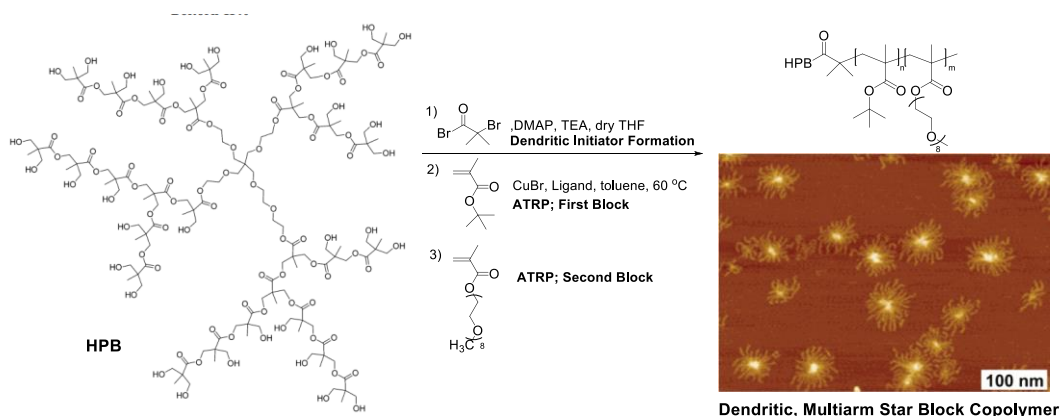
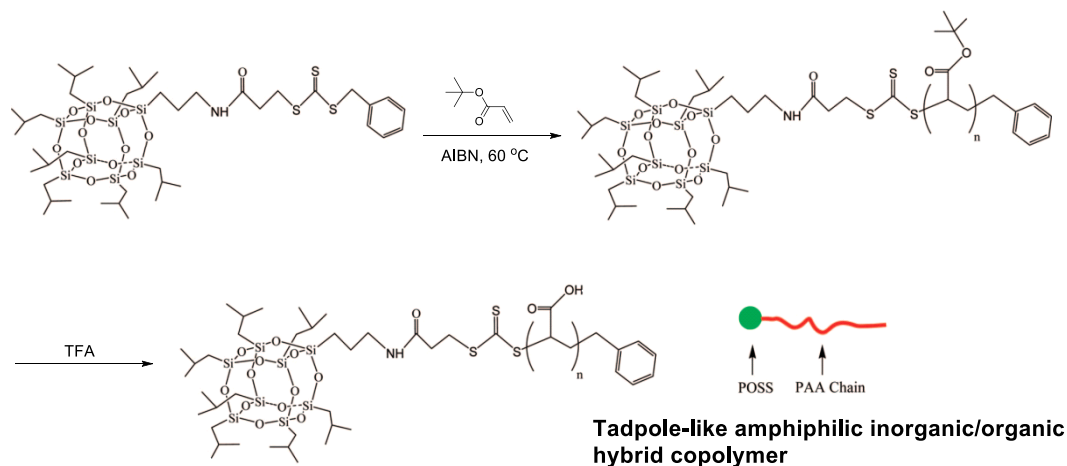


Figure 5.2- Synthesis of dendritic, multi-arm star copolymer and AFM image of resulting amphiphilic star polymer. (Copyright 2006 American Chemical Society, reprinted with permission)³⁷

RAFT polymerizations efficiently utilize reversible chain transfer reactions with specific dithioester, dithiocarbamate, xanthate, or trithioester (shown in Figure 5.1) additives to control the rate of propagation/ number of active chain ends. This chain transfer agent reversibly appends to the active chain end “deactivating” propagation until homolytic cleavage of the moiety regenerates the active radical on the polymer terminus. Upon consumption of monomer, the chain transfer agent reattaches to the polymer terminus allowing for the possibility of end functionalization. Using polyhedral oligomeric silsesquioxane (POSS) functionalized RAFT agents, Zhang et al. designed novel, tadpole-like hybrid inorganic/organic polymer upon polymerization of *t*-butyl acrylate and hydrolysis of the *t*-butyl ester forming T₈-isobutyl POSS terminated poly(acrylic acid) (PAA; Scheme 5.1).³⁸ The amphiphilic character of the polymer triggers specific micellular aggregation in water solutions as evident by TEM of casted polymer film and Cryo-TEM of vitrified solutions (Figure 5.3). The micelle assembles with the hydrophobic POSS end groups forming the inner core of the micelle and the hydrophilic PAA chains making up the outer corona of the micelle. Additionally, the repeating carboxylic acid functionality of the PAA backbone results in alterations to the hydrodynamic radius (R_h) of the micelles as a function of pH due to the extended chain conformation of the deprotonated PAA backbone compared to the protonated backbone at low pH.



Scheme 5.1- Synthesis of amphiphilic, tadpole-shaped POSS-PAA hybrid polymer using T₈-isobutyl POSS functionalized RAFT agents.

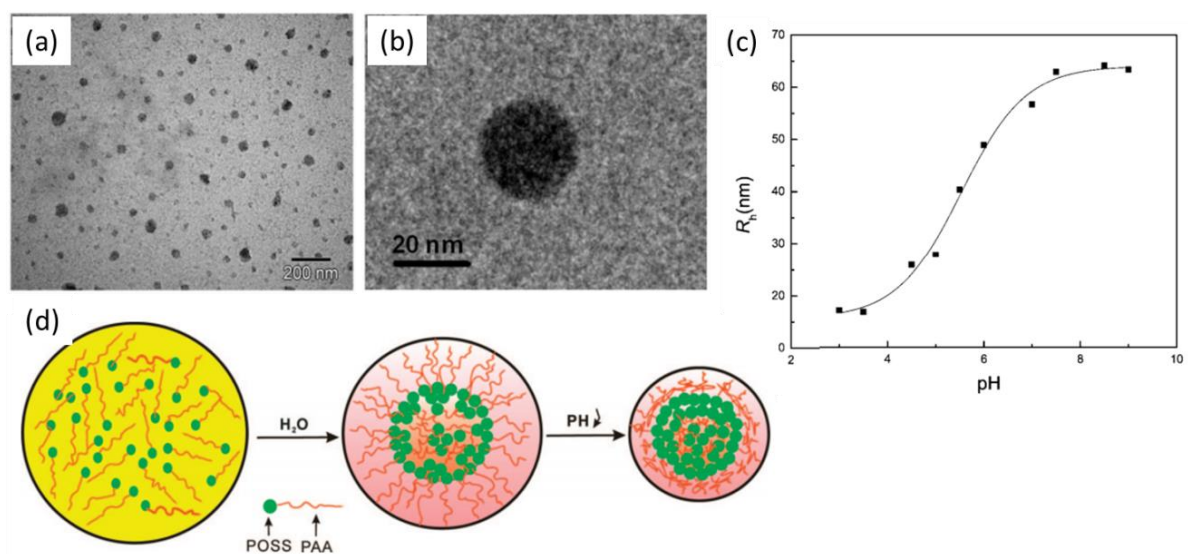


Figure 5.3- TEM image cast from water (a); Cryo-TEM image in water (b) of POSS-PAA micelle at pH = 8.5 and plot of hydrodynamic radius vs. pH (c) showing a decrease in radius at low pH due to the collapsed protonated PAA polymer chains(d). (Copyright 2008 American Chemical Society, reprinted with permission)³⁸

Using bulky alkoxyamine initiators (as in Figure 5.1), NMP employs the stable, persistent free-radical generated on the nitroxide moiety to provide the necessary reversible initiation/termination characteristic of “living” free-radical polymerizations. As in RAFT polymerizations, upon consumption of all monomer, the nitroxide radical reattaches to the terminus of the polymer chain. Hawker et al. applied this useful technique in the pioneering study focusing on embedding active NMP and ATRP initiators into molded photopolymer surfaces with nanometer size features.³⁹ This was accomplished by covalently attaching methacrylate moieties to known ATRP and NMP initiators and blending them in different concentrations (10-20 wt%) with *N*-vinyl pyrrolidinone and two crosslinking agents (Figure 5.4). This blend was then spin-coated onto highly polished silicon wafers, pressed with commercially available patterned stamps at fixed pressures (ca. 60 psi), and UV cured using 365 nm light for 1 minute. The stamp mold was then peeled leaving the patterned, initiator-embedded photopolymer film. The wafer was then submerged in a solution of monomer and catalyst (for ATRP) under inert N₂ atmosphere and subject to the necessary polymerization conditions. The resulting grafted polymer film was washed repeatedly with appropriate solvents to remove any free polymer chains from the surface and the film-thickness change was monitored before and after the surface polymerization using AFM and ellipsometry. Both techniques provided definitive evidence of surface polymerizations with visible increases in the nano-pillar diameters observed in AFM (Figure 5.5) and confirmed by ellipsometry/ contact angle. Tuning nanometer size features is an exhaustively studied technique due to the vast amounts of potential applications in molecular-scale electronics, magnetic storage, optoelectronics, and biotechnology. These findings offer a new, exciting

approach to designing sub-100 nm scale architectures with well-defined structures which were otherwise unobtainable via more conventional, bottom-up soft lithographic techniques.

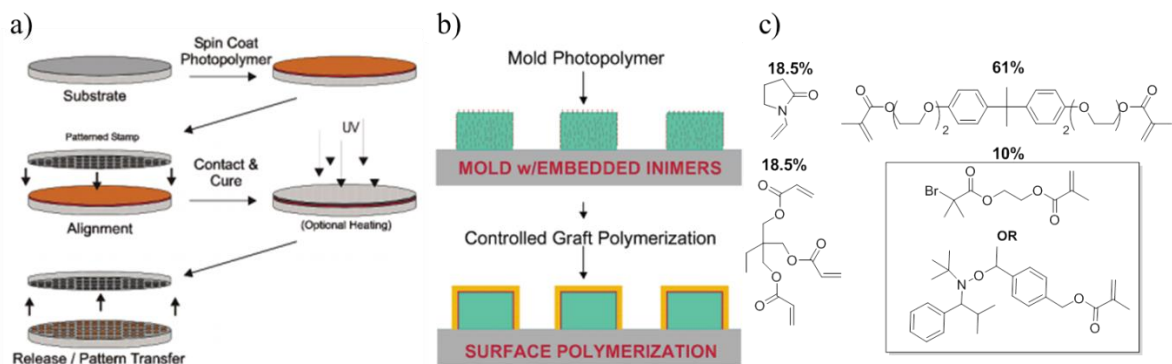


Figure 5.4- Synthesis of patterned photopolymer film (a), schematic of proposed surface polymerization (b), and photopolymer composition with 10 wt% ATRP or NMP initiator methacrylate moiety (c). (Copyright 2003 American Chemical Society, reprinted with permission)³⁹

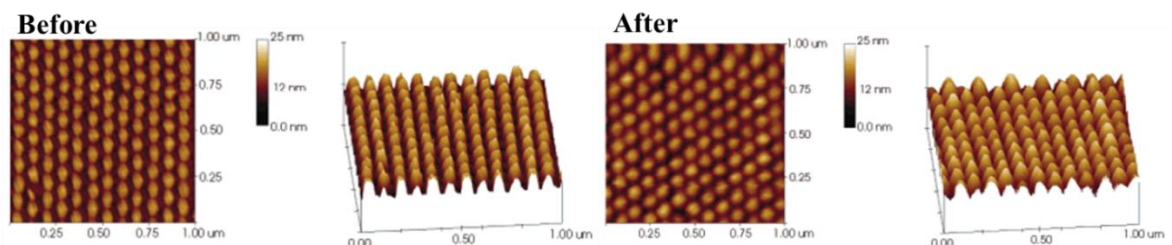


Figure 5.5- AFM images of patterned photopolymer film before (left) and after (right) surface graft polymerization showing an increase in diameter of the nano-pillar arrays from 60 nm to 75 nm. (Copyright 2003 American Chemical Society, reprinted with permission)³⁹

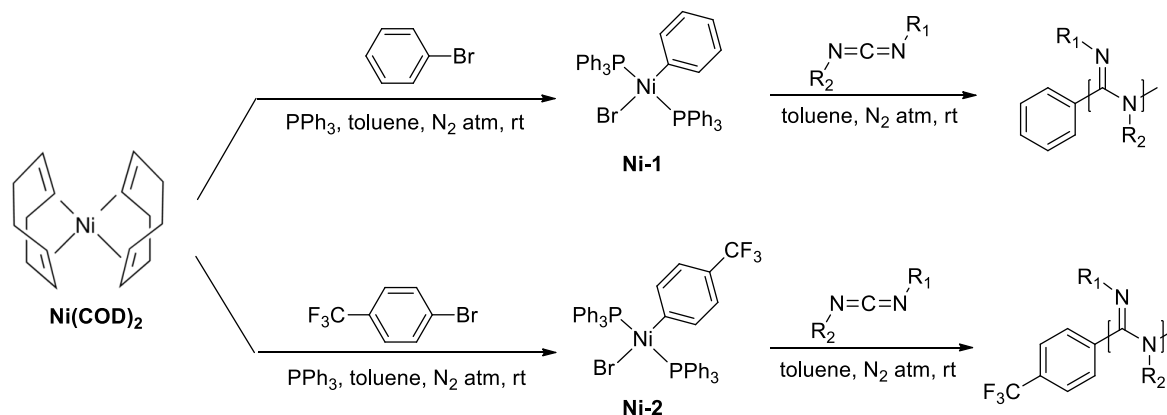
The end functionalization of polythiophenes has also been demonstrated by Koeckelberghs et al. using air-stable, functional bis(triphenylphosphino)aryl nickel(II)

bromide catalysts (see Figure 5.1) with various functional groups appended to the 4-position of η^1 -aryl ligand. The polymerization is initiated upon transmetallation of the magnesium bromide moiety in the thiophene based Grignard agent monomer with the active Ni(II) catalyst followed by reductive elimination appending the aryl ligand to the thiophene monomer. Sequential oxidative addition of the nickel complex into the second thiophene-bromide bond reforming the aryl Ni(II) bromide complex but with the thiophene η^1 -coordinated to the Ni(II) center. This process repeats propagating the polymer in a “living” fashion with the functional aryl ligand covalently attached to the terminus of the conjugated polythiophenes chain. Kiriya et al. extended the applicability of this technique by forming the active bis(triphenylphosphine)aryl Ni(II) bromide complex on aryl bromide functionalized surfaces⁴⁰ and silica nanoparticles⁴¹ for the controlled growth of P3HT conjugated materials from macroinitiator sites.

Polycarbodiimides are typically synthesized with titanium(IV) complexes. However, the air sensitivity and difficult synthesis of the titanium(IV) complexes used to polymerize carbodiimides provides significant challenges for the formation of functional initiators to end group functionalize polycarbodiimides and offers little opportunities for the copolymerization of carbodiimides with different classes of monomers. For these reasons, alternative, air stable nickel(II) complexes, like the ones used for the polymerization/ end group functionalization of polythiophenes, were hypothesized to be viable catalyst systems for the polymerization of carbodiimides due to the possibility of the negatively-charged, η^1 aryl ligand acting as the necessary initiator ligand similar to that of the titanium(IV) systems.

5.3 Controlled “Living” Ni(II) Mediated Polymerization of Carbodiimides-

Oxidative addition of bis(1,5-cyclooctadiene) nickel(0) with aryl bromides in the presence of triphenylphosphine yields square planar, trans-substituted bis(triphenylphosphino)aryl nickel(II) bromide complexes. Both bis(triphenylphosphino)phenyl nickel(II) bromide (**Ni-1**) and bis(triphenylphosphino)(4-trifluoromethylphenyl) nickel(II) bromide (**Ni-2**) were synthesized as a proof of concept for subsequent polymerizations of carbodiimide monomers (Scheme 5.2). Upon formation, both catalysts are air and moisture stable in the solid state providing substantially easier synthesis procedures than their titanium(IV) counterparts. However, these complexes, in the absence of monomer, quickly decompose via disproportionation (ca. 30 min) in solution to form colloidal Ni(0), Ni(I)Br, free PPh₃, and the corresponding, coupled bi-aryl species making the solution characterization of both **Ni-1** and **Ni-2** somewhat limited.³⁵ In order to characterize each complex by NMR, the compounds had to be dissolved in dry, deuterated CDCl₃ and immediately transferred to the instrument. ¹H NMR, ³¹P NMR, and ¹⁹F NMR (for **Ni-2** only) were successfully performed without significant decomposition but the longer times necessary for ¹³C NMR analysis allowed for significant decomposition making it very difficult to obtain suitable spectra.



Scheme 5.2- Synthesis of nickel (II) initiators **Ni-1** and **Ni-2** and applied polymerizations of various carbodiimide monomers forming high MW liquid crystalline macromolecules.

The initial polymerization using **Ni-1** as an initiator was successfully accomplished on the ^{15}N -labeled ^{15}N -hexyl-*N*-phenylcarbodiimide (**Mono-18**) (ca. $[\text{Mono-18}]/[\text{Ni-1}] = 48$). Previously, in Chapter 2, we discussed the determination of regioregularity in polycarbodiimide systems polymerized by titanium(IV) initiators using ^{15}N NMR.^{42,43} The resulting polymers were shown to be completely regioregular when incorporating two sterically inequivalent pendant groups, i.e. the phenyl and hexyl side groups, with the more sterically bulky group located on the C=N imine nitrogen in all cases studied. **Mono-18** was synthesized using the same protocol as previously reported and was polymerized to determine if the same regioisomer is formed upon polymerization with these new nickel(II) complexes. The resulting poly(^{15}N -hexyl-*N*-phenylcarbodiimide) (**Poly-18(Ni)**) was isolated with an 85% yield and was then characterized by ^1H NMR and ^{15}N NMR (Figure 5.6). The ^{15}N NMR spectra shows a single peak at 14.8 ppm confirming that the polymer is indeed regioregular with the hexyl pendant group only being incorporated onto the backbone amine

nitrogen. The phenyl end-group of the polymer is also clearly visible in the ^1H NMR spectra 7.71 and 7.54 ppm suggesting that the negatively charged, η^1 aryl ligand is transferred to the first carbodiimide monomer unit to initiate the polymerization. This makes these nickel(II) catalysts an attractive alternative to form end-group functionalized, liquid crystalline polycarbodiimides. As expected, the methylene unit directly attached to the polymer backbone from the hexyl side group is split into two chemical shifts due to the chirality of the helical backbone causing the protons to be diastereotopic.

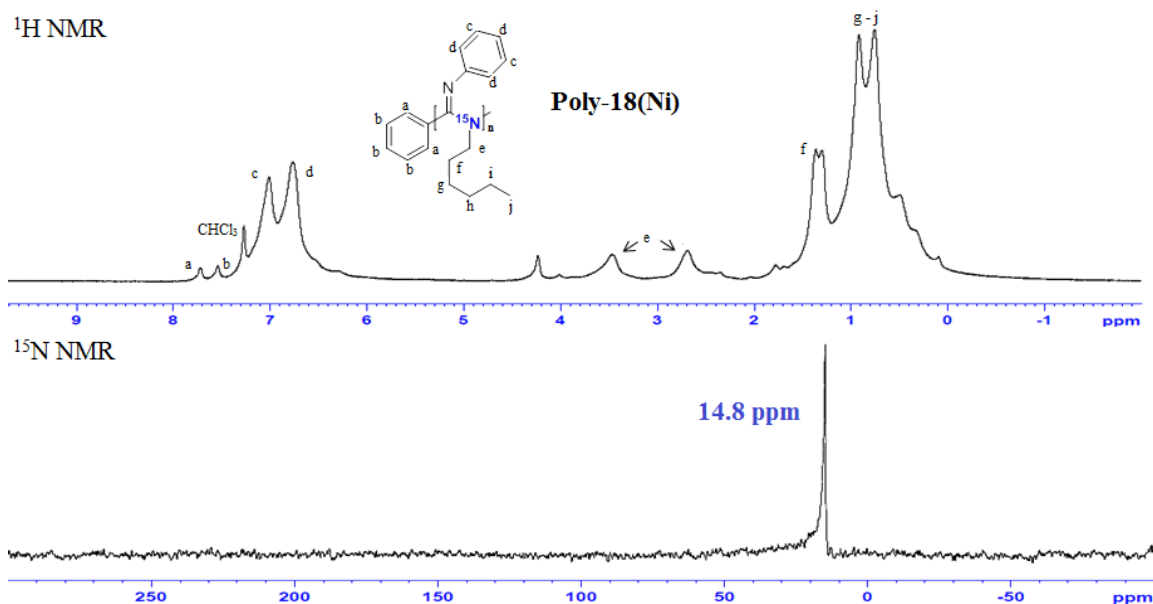


Figure 5.6- ^1H NMR and ^{15}N NMR spectra of ^{15}N -labeled **Poly-18(Ni)** clearly showing the phenyl end group and the formation of a single regioisomer upon polymerization with **Ni-1**.

Using the relative integration of end group peaks with respect to the diastereotopic methylene protons from the hexyl chain, the molecular weight was calculated to be $M_n =$

4400 Da which matches closely to GPC results (ca. $M_n = 5000$ Da; PDI = 3.30). Polycarbodiimides have been reported to display a high affinity to the polystyrene substrate in the GPC columns causing abnormally large PDI values and skewed molecular weights.⁵ One way to combat this problem is to add a small amount (~ 0.5 M) of an amine additive (*N,N*-dimethylethylenediamine in this case) to the mobile phase of the instrument to decrease the affinity of the polymer to the solid substrate. This method is helpful but does not completely remove the affinity of the polymer which is the reason for the slightly higher M_n value and unreliably large PDI observed.

For most applications of chiral, helical macromolecules, it is necessary to isolate predominantly single-handed helices upon polymerization. One way to bias the helicity of the polymer backbone is to employ chiral monomers resulting in optically active polymers with an excess single-handed screw sense. The chiral *N*-(*R*)-1-phenethyl-*N'*-methylcarbodiimide (**Mono-1R**; (*R*)-PEMC) and *N*-(*S*)-1-phenethyl-*N'*-methylcarbodiimide (**Mono-1S**; (*S*)-PEMC) were synthesized according to literature procedures.⁴⁴ The enantiomers of the monomers were polymerized using one of the two nickel initiators (i.e. **Ni-1** for **Mono-1R** and **Ni-2** for **Mono-1S**) and the kinetics of these polymerizations was monitored. The resulting polymers showed oppositely signed specific optical rotation values (ca. $[\alpha]_{435}^{25} = +51.2^\circ$ and $[\alpha]_{435}^{25} = -49.4^\circ$ respectively) suggesting that the opposite handed helices are formed when the opposite enantiomer of monomer is utilized. In order to determine the exact handedness of the resulting helices, vibrational circular dichroism (VCD) analysis was performed experimentally (Figure 5.7) and compared to previously reported,

DFT calculated VCD spectra of similar polycarbodiimides.^{45,46} The resulting VCD spectra of **Poly-1R** and **Poly-1S** shows a perfect mirror image spectra further substantiating the formation of opposite handed helices. The most important, diagnostic stretch in the spectra is the strong bisignate at 1649 and 1629 cm^{-1} corresponding to the C=N imine stretching mode of the polymer. When compared to the previously reported, theoretical spectra, we can assign the helical handedness of the polymers to left-handed (*M*-helix) for **Poly-1S** and right-handed (*P*-helix) for **Poly-1R**.

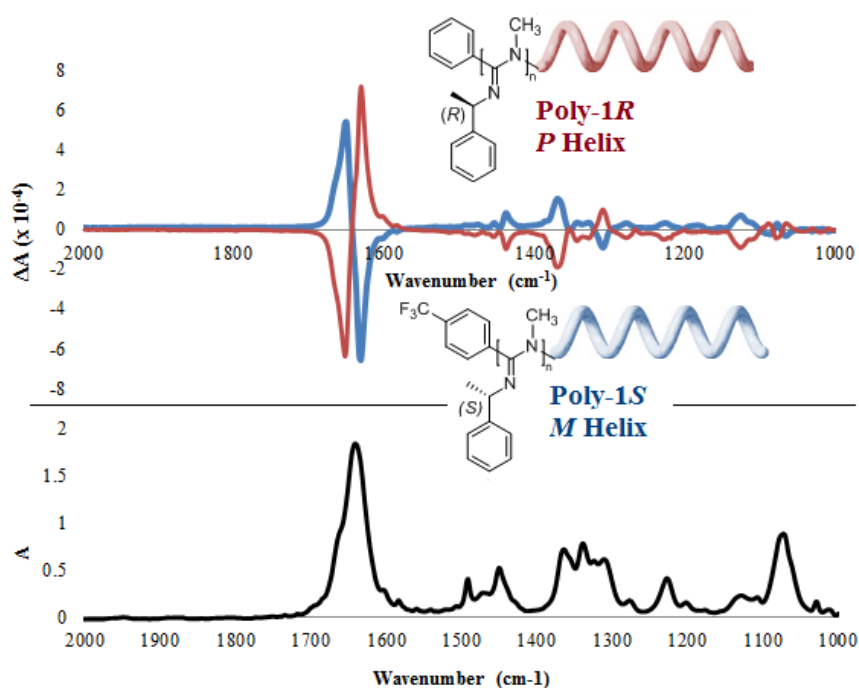


Figure 5.7- VCD (top) and IR (bottom) spectra of **Poly-1R** (red) and **Poly-1S** (blue) in CDCl_3 ($c = 25.0 \text{ mg/mL}$) showing the formation of opposite handed helices through mirror-image VCD spectra.

In order to classify this polymerization as “living,” we must show the absence of chain transfer and termination reactions. To determine this, the kinetics of the polymerization of **Mono-1** with **Ni-1** and **Ni-2** were monitored by GC/MS and GPC. Both polymerizations proceed very rapidly with ~90% of the monomers being consumed within the first 90 min. of both reactions. This new polymerization is significantly faster than the Ti(IV) mediated polymerizations which typically reach ~90% conversion in ~7 hours when employing analogous monomers. To confirm or refute the presence of chain termination reactions, the reaction progress, i.e., the consumption of **Mono-1** during the polymerization reaction, was monitored by GC/MS as a function of time. A linear plot was constructed when plotting $\ln([M]_0/[M])$ vs. time confirming the absence of termination reactions (Figure 5.7a). Despite the difficulties determining MW by GPC for most polycarbodiimides, a linear relationship was observed in the plot of percent conversion vs. M_n substantiating the absence of chain transfer reactions during the polymerization process when employing either **Cat-1** or **Cat-2** (Figure 5.8b). The PDI values of the resulting polymers were still somewhat inflated (ca. $M_n/M_w = 2.7 - 3.3$) which is uncommon for living polymerizations but, due to the aforementioned adhesion of polycarbodiimides to the GPC stationary phase, this is not unexpected.

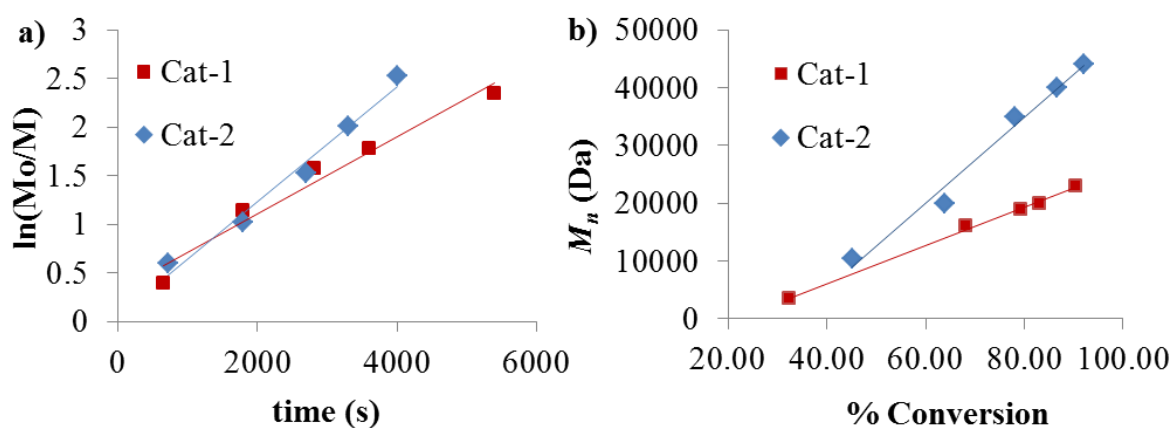


Figure 5.8- The polymerization kinetics of **Mono-1** with **Ni-1** and **Ni-2** shown in two plots: (a) time vs. $\ln([M_0]/[M])$ and (b) percent conversion vs. M_n . The linear relationship in both plots provides further evidence of “living” character. (a) **Ni-1**: $R^2 = 0.978$; **Ni-2**: $R^2 = 0.961$; (b) **Ni-1**: $R^2 = 0.998$; **Ni-2**: $R^2 = 0.980$

Though the end groups are clearly visible in the ^1H NMR spectra of the polymers, additional evidence is necessary to determine the extent of end functionalization. MALDI-TOF mass spectrometry is one of the most accurate method available for end group identification in polymer systems so **Poly-1R** was subject to this analysis to confirm the presence of the phenyl end groups on the terminus of the polymer chains. Additionally, we can use this method to unambiguously determine the functional group appended to the opposite terminus of the polymer. The polymerizations are quenched in 1.0 % (v/v) DBU solution in methanol so the conventional hypothesis has been that the negatively charged amidinate ligand on the terminus of the polymer abstracts a proton from the methanol molecule upon work up. Examination of the MALDI-TOF MS of **Poly-1R** (Figure 5.9) confirms this hypothesis showing nearly exact masses (± 1.0 Da) corresponding to the

polymer chains of different molecular weight with a phenyl group and hydrogen appended to the termini. Typically, MALDI-TOF MS is performed with a small amount of some metal salt mixed with sample and matrix to provide the necessary ionization source for detection. This is due to the use of a soft N₂ laser source used to ablate the matrix and sample rather than strong lasers used to fragment the sample in most conventional MS techniques. In the case of polycarbodiimides, however, no salt is added due to protonation of the basic, nitrogen-rich backbone providing the necessary ionization source. The overall MW and polydispersity cannot be accurately determined using MALDI-TOF MS at this time due to difficulties observing MWs over ~5000 Da. The low resolution and trailing amplitude of the m/z peaks (rather than the typical Gaussian distribution seen in MALDI-TOF MS of conventional polymer systems) suggests that only small portions of low MW polymer chains ablated with the matrix and reached the detector. Further optimization in sample preparation may be necessary to be able to observe the entire range of MWs.

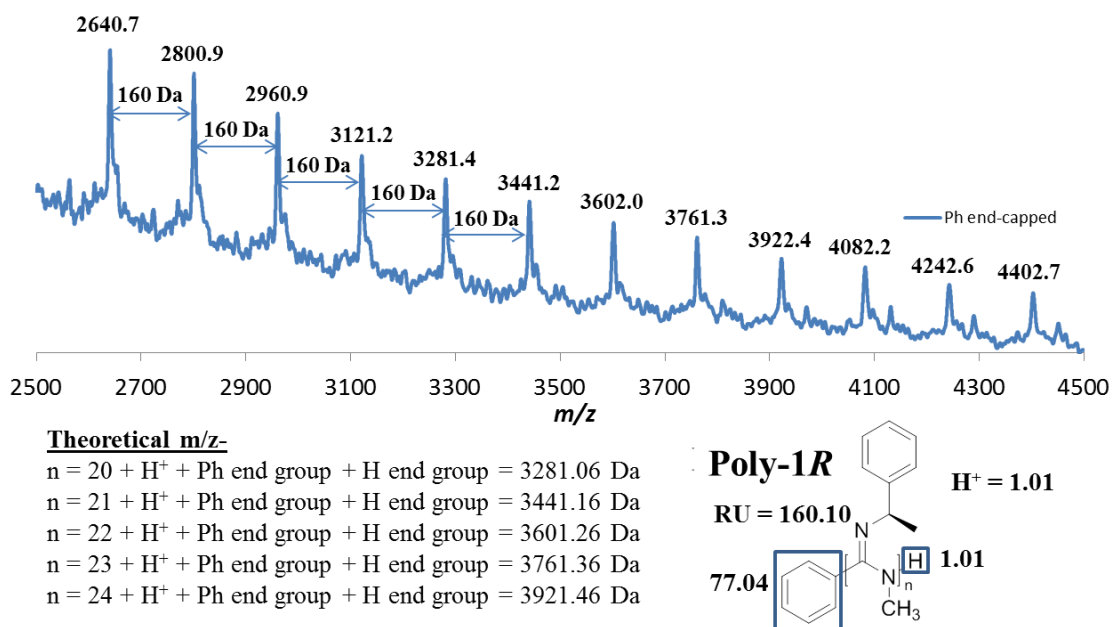


Figure 5.9- MALDI-TOF mass spec of **Poly-1R** showing a high degree of phenyl end group incorporation via polymerizations initiated by **Cat-1**. The second end group was also confirmed to be a hydrogen due to abstraction of a proton from methanol solvent molecule upon work up.

The trifluoromethyl group at the 4-position of the η^1 aryl ligand on **Ni-2** provides an alternate opportunity to monitor the molecular weight using ^{19}F NMR. This is possible by incorporating a chemically distinct fluorine atom on one of the pendant groups of the polymer to provide a handle for end group analysis by the relative integration of the two chemical shifts. ^{19}F NMR provides enhanced signal separation and amplified signal to noise to allow for accurate measurements of M_n to compare with traditional GPC analysis. The fluorinated *N*-4-fluorophenyl-*N'*-doceylcarbodiimide (**Mono-42**) was polymerized with **Ni-2** at a wide range of monomer to catalyst ratios to form poly(*N*-4-fluorophenyl-*N'*-doceylcarbodiimide) (**Poly-42**) with a variety of molecular weights. The ^{19}F NMR spectra

(Figure 5.10) indeed displays two peaks with the three fluorine atoms from the 4-trifluoromethylphenyl end group visible at -63 ppm and the fluorine atom from the 4-fluorophenyl pendant group showing up at -121 ppm. The relative integration of each peak provides an accurate, semi-quantitative determination of the average number of repeat units (n) which then can be converted to M_n .

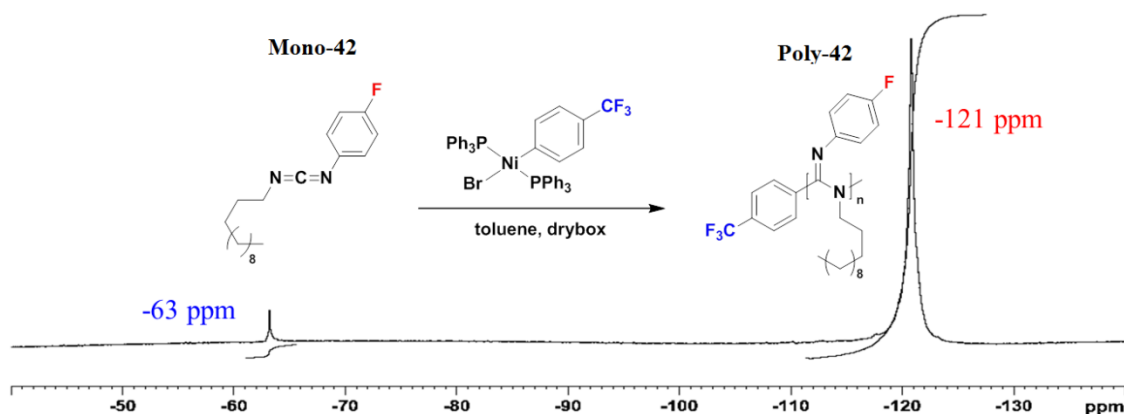


Figure 5.10- ¹⁹F NMR of **Poly-42** polymerized using **Ni-2** (ca. $[\text{Mono-42}]/[\text{Ni-2}] = 73$) allowing for quantification of the average number of repeat units by relative integration of the chemical shift of the end group versus the chemical shift of the pendant group.

The plot of M_n vs. $[\text{Mono-42}]/[\text{Ni-2}]$ was constructed using the M_n values measured using ¹⁹F NMR and GPC to determine the level of MW control for this polymerization (Figure 5.11). The M_n values given by ¹⁹F NMR analysis provide a nice, linear fit suggesting that the polymerization occurs in a highly controlled manner further supporting the living character of the polymerization. Additionally, the linear trendline seems to approach the

origin indicating that close to all of the Ni(II) catalysts are active in the initiation process. The MW data determined by GPC for the same polymers, however, provided largely erratic results. This was attempted on two different GPC instruments to ensure the validity of the results. Strangely, the MW data provided by each instrument varied significantly from each other and the calculated M_n values determined by ^{19}F NMR. The cause of this is still unknown and is under further investigation. For all tabulated M_n (^{19}F NMR and GPC), M_w (GPC), and PDI (GPC) values see the experimental section.

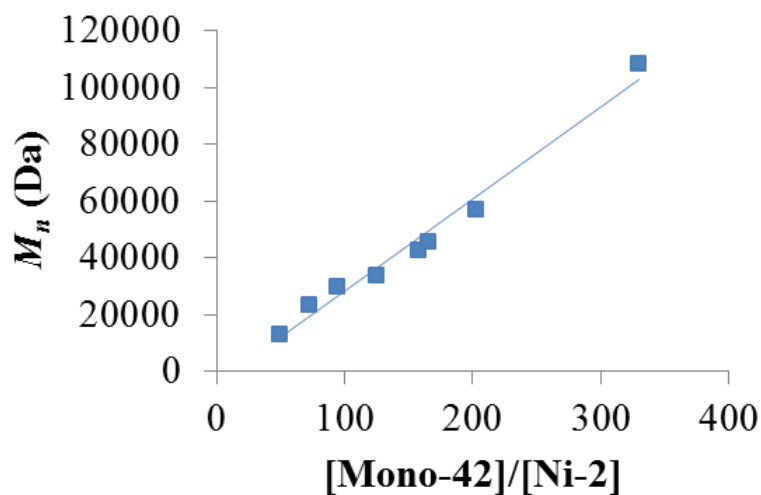
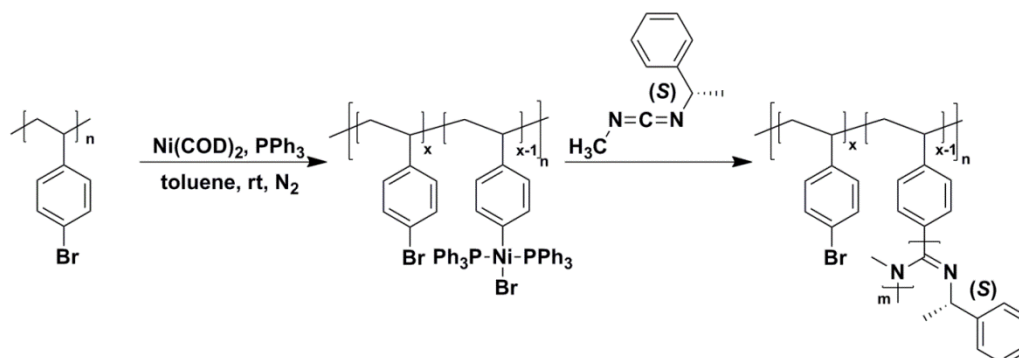


Figure 5.11- Plot of M_n vs. $[\text{Mono-42}]/[\text{Ni-2}]$ portraying the high degree of control over MW simply by altering the monomer-to-catalyst ratio. The M_n values were calculated using the relative intergration between the ^{19}F chemical shifts of the end group with respect to the pendant group chemical shifts.

5.4 Grafting PPEMC from Poly(4-Bromostyrene)-

In addition to forming end-functionalized, helical polycarbodiimides, this novel polymerization technique offers the ability to generate the active initiation site *in situ* in the presence of any aryl bromide offering the opportunity to functionalize a variety of candidates such as surfaces, nanoparticles, or single-polymer chains with rigid-rod, mesogenic polycarbodiimides. This route also may provide the potential to mechanically reinforce the typically soft, brittle nature of polycarbodiimides to broaden the range of potential applications for these interesting materials. To demonstrate this, poly(4-bromostyrene) (PBrS) was reacted with Ni(COD)₂ and PPh₃ to form the active bis(triphenylphosphino)aryl Ni(II) bromide complex appended to the random coil polymer backbone (Scheme 5.3). A similar procedure was employed by Kiriya et al. to graft poly(3-hexylthiophene) (P3HT) to partially crosslinked PBrS surfaces.³⁷ The complex formation was apparent upon addition of the Ni(COD)₂ as evident by the distinct clear to orange color change as well as the appearance of ³¹P NMR chemical shift at ca. 22.3 ppm (Figure 5.12). Comparing the ¹H NMR spectra of the parent PBrS and the nickel(II) activated macroinitiator also provides evidence of initiator formation with clear upfield shifts in the aromatic chemical shifts from 7.44 and 6.65 ppm to 5.67 ppm. The chiral (*S*)-PEMC (**Mono-1S**) monomer was then added to the mixture to form novel, helical-*graft*-random coil copolymers. The target was to functionalize ~22 % of the aryl bromide repeat units in PBrS with rod-like (*S*)-PPEMC (**Poly-1S**) chains to study the effect of incorporating main-chain liquid crystalline grafts to conventional random-coil polymer systems.



Scheme 5.3- Synthesis of (*S*)-PPEMC-*g*-PBrS rod-coil graft copolymer by forming the active Ni(II) macroinitiator appended to ~22 % ($x = 0.78$; $n = 48$) of the aryl bromide pendant groups of PBrS.

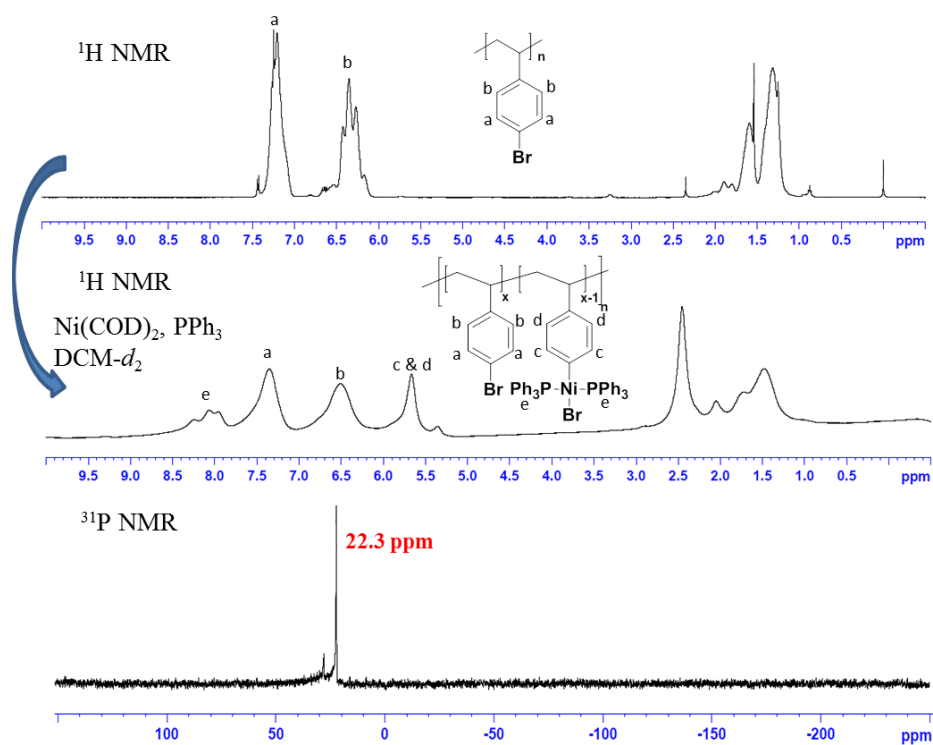


Figure 5.12- ^1H NMR of PBrS (top); Ni(II) activated PBrS macroinitiator (middle), and ^{31}P NMR of macroinitiator complex (bottom).

The grafting of (*S*)-PPEMC (**Poly-1S**) from PBrS was monitored and confirmed by ^1H NMR and GPC. Similar to the homo-polymerization of **Poly-1S** with **Ni-1**, the polymerization reaction was complete after ~ 90 min as evident by the complete disappearance of the $\text{N}=\text{C}=\text{N}$ stretching mode and the appearance of the $\text{C}=\text{N}$ imine stretching mode in the IR spectra. The formation of the covalently bound (*S*)-PPEMC-*g*-PBrS was confirmed by GPC (Figure 5.13) with a distinct increase in molecular weight and retention time from the parent PBrS sample ($M_n = 8800$ Da; PDI = 1.08; $t = 14.7$ min) to the graft copolymer ($M_n = 49600$ Da; PDI = 2.34; $t = 11.7$ min). Assuming that all available $\text{Ni}(0)$ reagent oxidatively adds to the polymer chain, which was confirmed by ^{31}P NMR, the polymer chains should grow from $\sim 22\%$ of the aryl bromide pendants. Correlating this to the observed MW increase in GPC suggests that each PPEMC graft is, on average, 56 repeat units long (ca. $M_n(\text{PPEMC}) = 8900$ Da). Thermogravimetric analysis (TGA) of the graft copolymer shows a two-step degradation with the first onset of mass loss at 174 °C corresponding to the decomposition of the (*S*)-PPEMC grafts followed by the decomposition of the PBrS main chain at 385 °C (Figure 5.14). The relative mass loss of each segment matches very closely with the observed MW increase in GPC with $\sim 81\%$ of the mass loss observed attributed to the PPEMC chains and $\sim 19\%$ mass loss associated with PBrS parent polymer chain. Differential scanning calorimetry (DSC) of the graft copolymer displays one thermal transition associated with T_g of PBrS at 125 °C. The graft copolymerization shows no effect on T_g , surprisingly, and no thermal transitions are typically observed for the PPEMC chains despite the crystallinity of the PPEMC homopolymers. This is believed to be due to the polymers low degradation temperature causing the polymer to thermally unzip

before any melting transition is observed. The DSC and TGA data can be found in the supporting information.

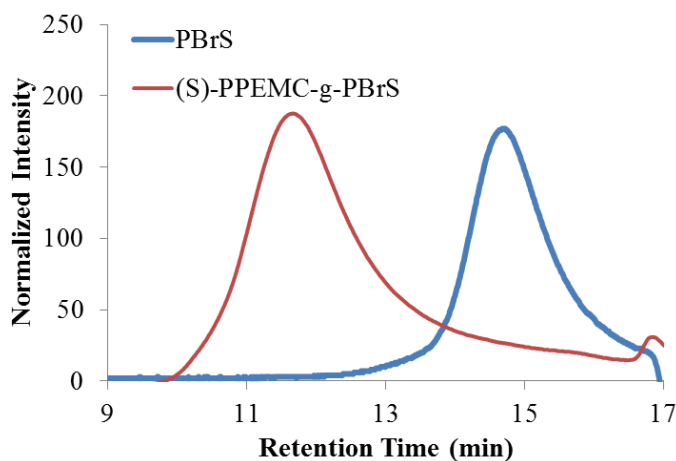


Figure 5.13- GPC chromatogram of parent PBrS (blue) and (S)-PPEMC-g-PBrS (red) showing distinct shift in retention time indicative of significant increases of MW upon graft copolymerization.

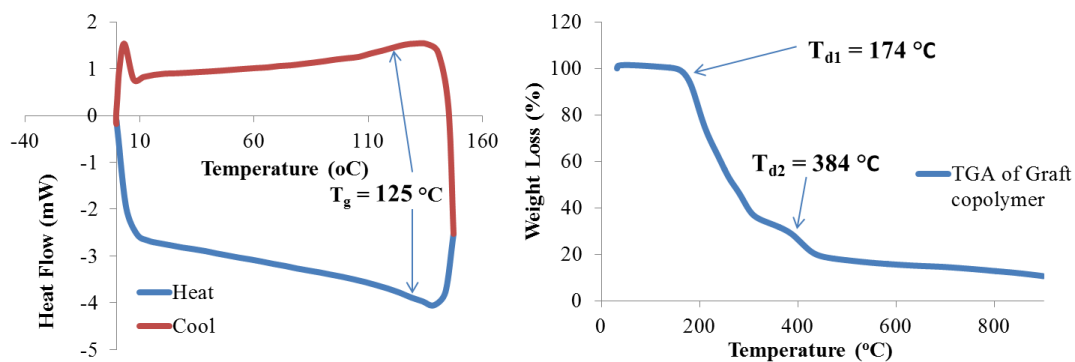


Figure 5.14- DSC (left) and TGA (right) thermograms of (S)-PPEMC-g-PBrS.

Incorporating mesogenic units into main chain random-coil polymers often results in the evolution of interesting aggregation behavior and thin film morphologies.^{47,48} The thin film morphology of (*S*)-PPEMC-*g*-PBrS was investigated by spin-coating dilute solutions of the polymer (ca. 5.0 mg/mL) onto highly-polished silicon wafers and annealing the thin films in a saturated CHCl₃ vapor for 24 hrs. The lyotropic liquid crystalline properties of (*S*)-PPEMC in CHCl₃ solutions is one the main reasons for the use of CHCl₃ to study the thin film morphology of the graft copolymer.⁴⁴ The thin films were then imaged using tapping-mode atomic force microscopy (TMAFM) revealing nanofibular aggregation behavior of the graft copolymers (Figure 5.15). The relative diameter of a single, fully extended graft copolymer chain (from one PPEMC chain end to another) was estimated to be ~17 nm in diameter using the experimental mass per length (M_L) and persistence length (P) values determined for (*R*)-PPEMC by Nieh et al.⁴⁹ Statistical analysis of the nanofibrul aggregates provides an average diameter of 171 ± 28 nm corresponding to, on average, ~10 polymer chains aligned from one fiber wall to another. To unambiguously determine the level of arrangement and spacing between polymer chains, a series of these copolymers must be synthesized and investigated by TMAFM and thin-film SA-XRD in future work. It is clear, however, that this new controlled “living” polymerization technique offers vast new opportunities in the incorporation of chiral, helical, rigid-rod polycarbodiimides into a variety of systems.

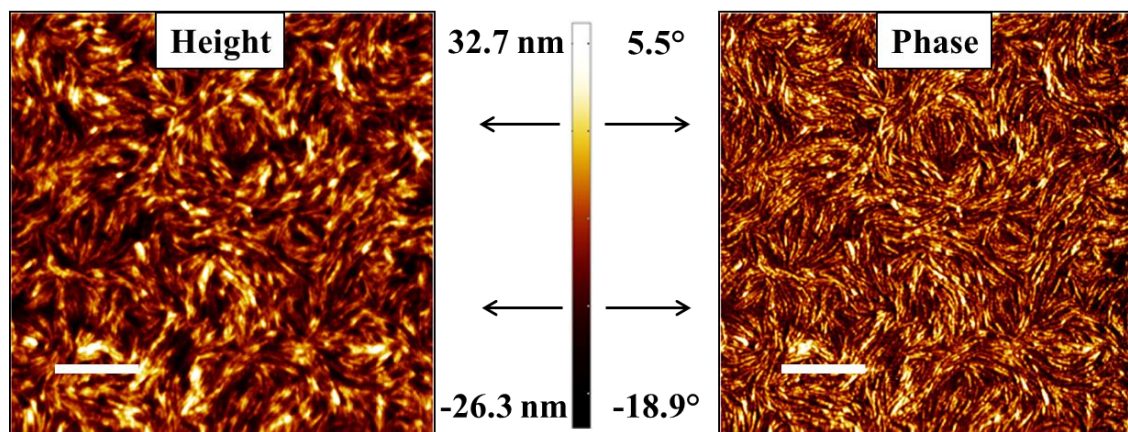


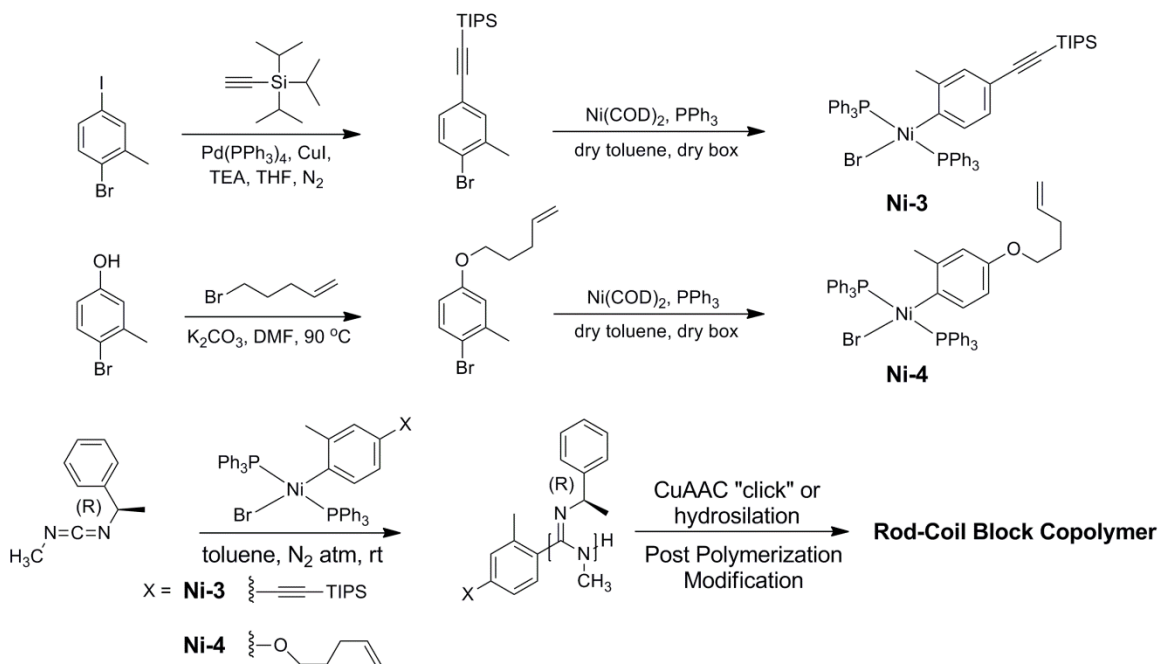
Figure 5.15- Height and Phase TMAFM micrographs of (*S*)-PPEMC-*g*-PBrS spin coat from CHCl₃ and annealed in saturated CHCl₃ vapor for 24 hrs (Scan Size = 15 x 15 μm; Scale Bar = 3 μm).

5.5 End-Functionalization of PPEMC with Functional Ni(II) Initiators-

The ability to polymerize carbodiimides with Ni(II) complexes allows for the facile synthesis and purification of initiators with latent reactive groups appended to the 4-position of the η¹-aryl ligand. Upon polymerization of carbodiimide monomers, the functional aryl ligand from the initiator is covalently bound to the terminus of polymer chains allowing for the application post-polymerization modification reactions. To demonstrate this, two functional bis(triphenylphosphino)aryl nickel(II) bromide initiators were synthesized via the same protocol used for **Ni-1** and **Ni-2**. The corresponding functional groups chosen were triisopropylsilyl (TIPS) protected alkyne (**Ni-3**) and aliphatic alkene moieties (**Ni-4**) to provide a large range of possible reactions with high efficiency and mild conditions for potential post-polymerization modifications. Adding the methyl group at the 2-position of the

aryl ligand has been shown to drastically increase the stability of the complex in solution according to previous reports.³⁵ For this reason, **Ni-3** and **Ni-4** were designed with this feature to aid in the ability to fully characterize the complexes. Using these end-functionalized polymers, a series of well-defined rod-coil block copolymers with chiral, helical polycarbodiimide segments were synthesized using copper-mediated azide-alkyne [3+2] cycloaddition (CuAAC) “click” or hydrosilation post-polymerization reactions

The corresponding TIPS-alkyne functionalized aryl bromide was synthesized via Sonogashira cross-coupling and then reacted with bis(1,5-cyclooctadiene) nickel(0) in the presence of triphenylphosphine forming the trans-substituted nickel(II) complex **Ni-3**. The alkene functionalized aryl bromide was synthesized in a single step via S_N2 nucleophilic substitution of 5-bromopent-1-ene with 3-methyl-4-bromophenol. Oxidative addition of the aryl-bromide bond with Ni(COD)₂ yields **Ni-4** with an aliphatic alkene moiety attached via ether linkage at the 4-position of the aryl ligand.



Scheme 5.4- Synthesis of protected alkyne and alkene functionalized bis(triphenylphosphino)aryl nickel(II) bromide initiators and subsequent polymerization of **Mono-1R** forming end-functionalized polycarbodiimides.

The added stability of these two initiators allows for full characterization by ^{13}C NMR, ^1H NMR, and ^{31}P NMR. Some decomposition was still observed for **Ni-4** after ~ 3 hours in solution but the **Ni-3** complex seemed to be stable in solution for > 24 hours. The appearance of the single peak at 21.0 ppm in the ^{31}P NMR of **Ni-3** and **Ni-4** confirms the formation of the desired trans-substituted nickel(II) complex and is comparable to previously reported chemical shifts of similar complexes.³⁵ Substantial peak broadening in the ^1H NMR of the initiators is observed most likely due to large relaxation times but the intact functionalities attached to the aryl ligand can be confirmed. In the ^1H NMR spectrum of **Ni-3**, the alkyne functionalized aryl ligand can be identified with the TIPS protons clearly

visible at 1.15 ppm and the aryl methyl group present at 2.13 ppm. The ^1H NMR spectra of **Ni-4** also shows chemical shifts corresponding to the intact functionality appended to the η^1 -aryl ligand with the vinyl protons present at 6.01, 5.73, and 4.99 ppm. Additionally, the aliphatic spacer (proceeding away from the ether oxygen) and *o*-methyl substituent are also visible at 3.49, 1.63, 2.08, and 2.37 ppm, respectively. The ^1H NMR and ^{31}P NMR of **Ni-3** and **Ni-4** can be found in Figure 5.16 and 5.17, respectively. The subsequent polymerization of the chiral **Mono-1** results in the specifically end-functionalized, excess single-handed helical polycarbodiimides to couple with end functionalized, random-coil polymers via post polymerization modification.

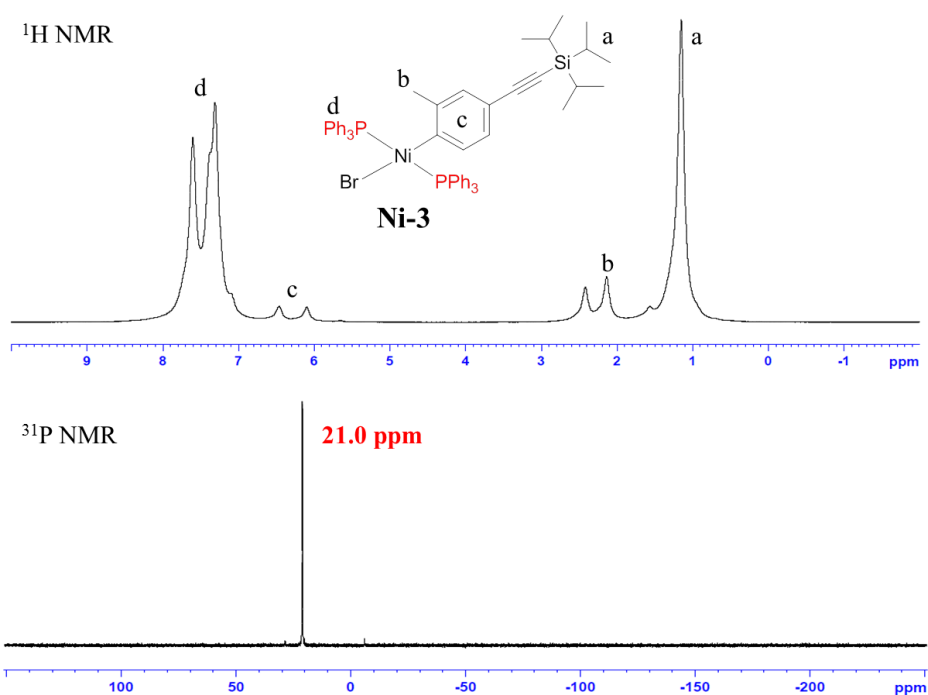


Figure 5.16- ^1H NMR and ^{31}P NMR spectra of **Ni-3**.

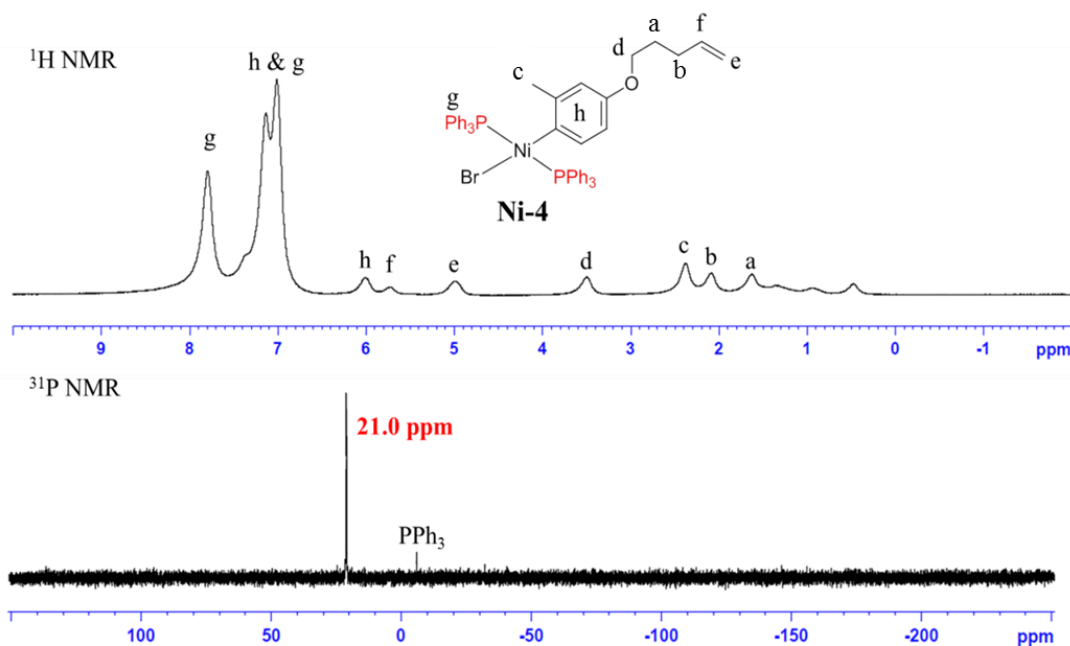


Figure 5.17- ^1H NMR and ^{31}P NMR spectra of Ni-4.

The resulting polymerization of **Mono-1R** with **Ni-3** is very fast and efficient providing near quantitative yields (~96%) within about 90 minutes giving this initiator comparable activity to that of **Ni-1** and **Ni-2** discussed previously. The ^1H NMR of the protected alkyne terminated (*R*)-PPEMC (**Poly-43**) clearly shows specific chemical shifts attributed to the aryl end group with peaks at ca. 1.09 ppm and 2.05 ppm corresponding to the TIPS protons and the *o*-methyl substituent, respectively (Figure 5.18). Additionally, the aryl protons are slightly visible at 7.52 ppm, although overlapped with the pendant aryl protons. The *o*-methyl group provides a handle for determining molecular weight by end group analysis using its relative integration with respect to the pendant methine proton at 5.62 ppm. The opposite terminus of the polymer was previously shown to become protonated

upon precipitation in MeOH during work-up as evident of MALDI-TOF MS of (*R*)-PPEMC polymerized from **Ni-1** discussed earlier. The proton associated with this end group is also visible at 3.96 ppm in the ^1H NMR of **Poly-43**. To confirm this, the polymer was redissolved in THF- d_8 and 2 drops of D_2O were added to the NMR tube causing the peak to disappear in the spectra. This suggests that these protons are exchangeable providing further evidence that these peaks correlate with the terminal N-H. The deprotection of the TIPS protecting group with tetrabutylammonium fluoride (TBAF) can also be monitored by ^1H NMR with the complete disappearance of the TIPS chemical shift after ~ 2 hours reacting at $0\text{ }^\circ\text{C}$. The ^1H NMR spectrum of the deprotected alkyne terminated **Poly-44** can also be found in Figure 5.15 showing no other changes in the characteristic pendant and end group chemical shifts.

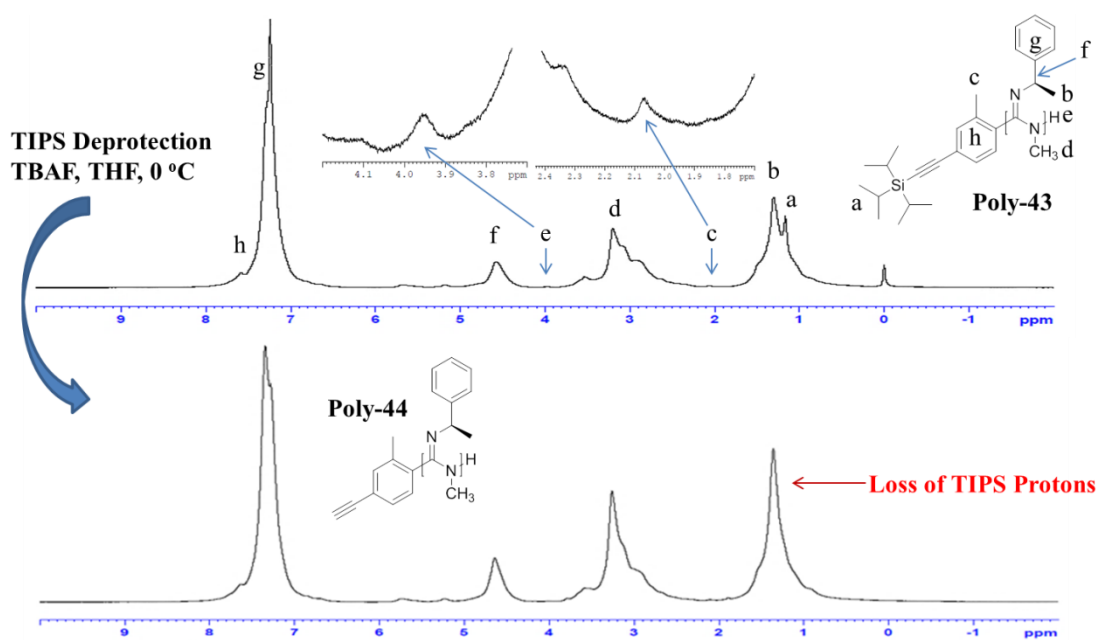


Figure 5.18- ^1H NMR spectra of the protected alkyne terminated **Poly-43** and deprotected **Poly-44** showing the clear loss of the TIPS protons upon reaction with TBAF.

To provide further evidence of these assignments, ^{13}C DEPTQ135 (a specific ^{13}C NMR experiment that displays distinct phases for methines/ methyls (down) compared to methylenes/ quaternary (up) carbons; Figure 5.19) was applied along with 2D $^1\text{H}/^{13}\text{C}$ HSQC to identify pendant and end group ^{13}C chemical shifts and correlate them with the ^1H NMR chemical shifts. The pendant group ^{13}C chemical shifts can easily be identified with distinct assignments for each shown in Figure 5.19. The chemical shift at 26.4 ppm correlates strongly with the ^1H NMR shifts at 1.23 ppm which corresponds to the benzylic-methyl group on the chiral center in the repeating unit. The backbone N- CH_3 proton and the methine proton chemical shift at 3.46 and 4.51 ppm match up nicely with the ^{13}C peak at 34.6 and 57.2 ppm, respectively. Finally, the aromatic carbons show up in three peaks in the ^{13}C NMR spectra at 126.4, 128.2, 148.2 ppm.

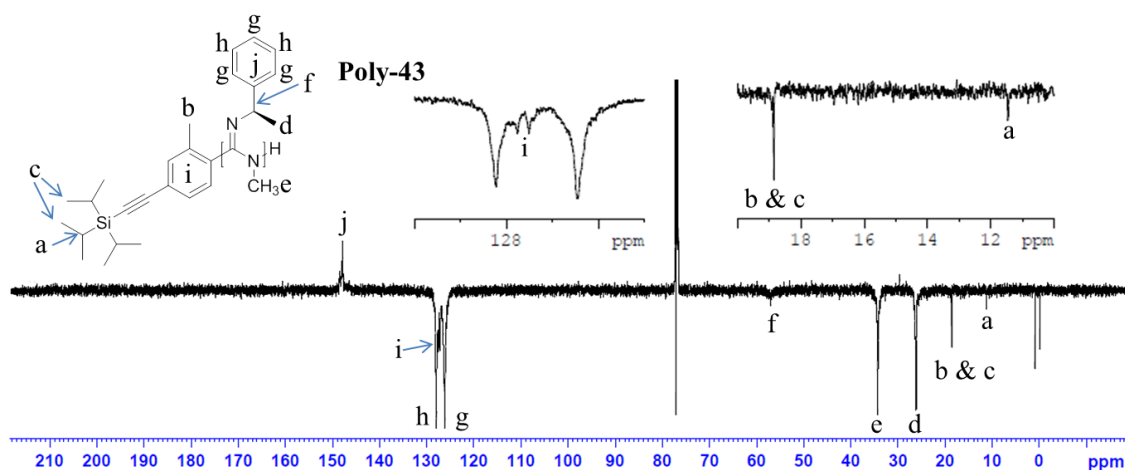


Figure 5.19- ^{13}C DEPTQ135 NMR spectra of **Poly-43** with peak assignments.

The TIPS-protons on the end-group at 1.09 ppm correlate strongly with the ^{13}C chemical shift at 11.4 ppm and the *o*-methyl substituent protons at 2.05 ppm match up with the phase down (methyls/methines) ^{13}C chemical shifts at 18.8 ppm. Additionally, the TIPS-protons at 1.09 ppm correlate in the HSQC with the peak at 18.8 ppm in the ^{13}C NMR suggesting that this chemical shift may correspond to other carbons besides the *o*-methyl substituent. This leads to the assignment shown in Figure 5.19 of both the methyl groups on the TIPS protecting group and the aromatic *o*-methyl substituent corresponding to this ^{13}C chemical shift. This would also explain the increased amplitude of this chemical shift when compared to the rest of the end group peaks. The aromatic end-groups are also clearly visible in between the ^{13}C chemical shifts of the pendant aromatic carbons at 127.5 and 127.8 ppm. The $^1\text{H}/^{13}\text{C}$ HSQC spectra for **Poly-43** can be found in the experimental section

Other chemical shifts in the ^1H NMR spectra of **Poly-43** at 3.46, 3.67, 5.18, and 5.71 ppm are also present but their specific origin is somewhat puzzling. The presences of the additional chemical shifts at 5.18 and 5.71 ppm, which are present in all samples of PPEMC, were found to be correlated to the methine carbon by $^1\text{H}/^{13}\text{C}$ HSQC. The other mystery chemical shifts present downfield from the N-CH_3 protons at 3.67 and 3.46 ppm were found to couple with the backbone methyl carbon. The cause for this unique peak splitting unknown but is believed to be associated with different environments of these protons in solution.

To accurately confirm the presence of the intact functionality appended to the terminus of the polymer, MALDI-TOF MS was applied to quantitatively measure the masses of specific polymer chains of different MWs. Again, only low MW polymer chains ablate

and reach the detector with an upper threshold of ~4500 Da for **Poly-43** (Figure 5.20). The theoretical m/z values of PPEMC with 11-15 repeat units (ca. 160.10 Da) were calculated with the protected alkyne functional aryl group (ca. 271.19 Da) and hydrogen (ca. 1.01 Da) as the two termini. In addition, the ionization source necessary for detection was found to be protonation of the basic polymer backbone, similar to previous examples. The corresponding mass loss to the removal of the TIPS protecting group (ca. 156.24 Da) was observed in the MALDI-TOF MS of **Poly-44** confirming the full deprotection of the TIPS protecting group within 2 hours of reacting (Figure 5.21). An additional distribution is also visible in the MALDI-TOF MS of **Poly-43** and **Poly-44** most likely a result of either different functionalization of one/both of the termini or presence of another ionization source (possibly some metal salt or different counter-ion). The exact source of this remains unknown but the relative intensity of these distributions is small (ca. 14%) with respect to the predominant mass distribution so it is not expected to be a large concern.

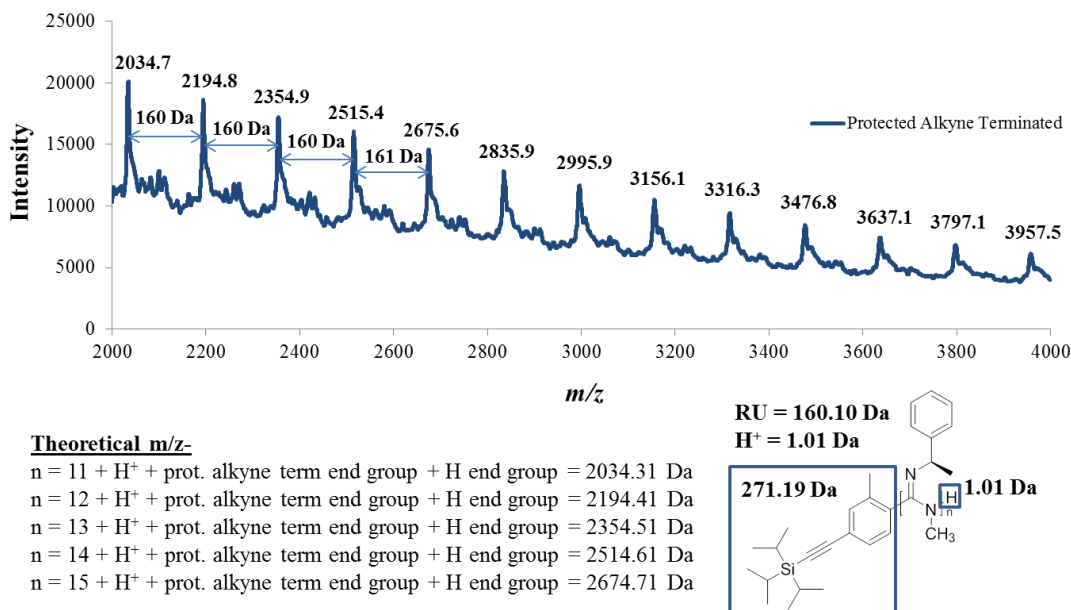


Figure 5.20- MALDI-TOF MS of TIPS protected alkyne end-functionalized **Poly-43** showing the major mass distribution corresponding to the desired two end groups plus H⁺.

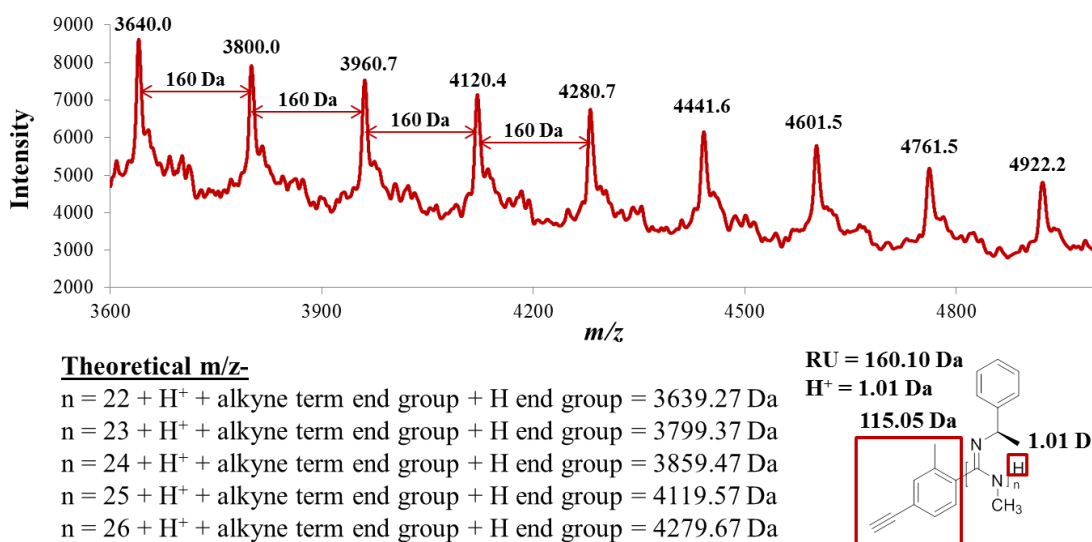


Figure 5.21- MALDI-TOF MS of deprotected alkyne end-functionalized **Poly-44** after deprotection with TBAF showing the major mass distribution corresponding to the desired two end groups plus H⁺.

Similar to **Ni-3**, the polymerization of **Mono-1R** with **Ni-4** is fast and efficient with complete disappearance of the N=C=N stretching mode in the IR spectra and formation of C=N imine stretch within 90 minutes. The isolated yield of the resulting alkene end-functional polymer (**Poly-45**) is also very high (>90%) similar to the previous polymerizations with Ni(II). The ^1H NMR spectrum of **Poly-45** displays distinct chemical shifts associated with the alkene functionalized aryl end group (Figure 5.22). The aliphatic spacer (in order of proximity to oxygen) and *o*-methyl substituent appear at 4.01, 1.96, 2.05, and 2.29 ppm, respectively. The proton appended to the opposite terminus of the polymer chain also appears at 4.01 ppm overlapping with the methylene protons directly adjacent to the ether oxygen resulting in the increased intensity when compared to **Poly-43** or **Poly-44**. The vinyl protons are also visible in the ^1H NMR spectrum at 5.05, 5.12, and 5.89 ppm overlapping with the two small chemical shifts at 5.18 and 5.71 ppm.

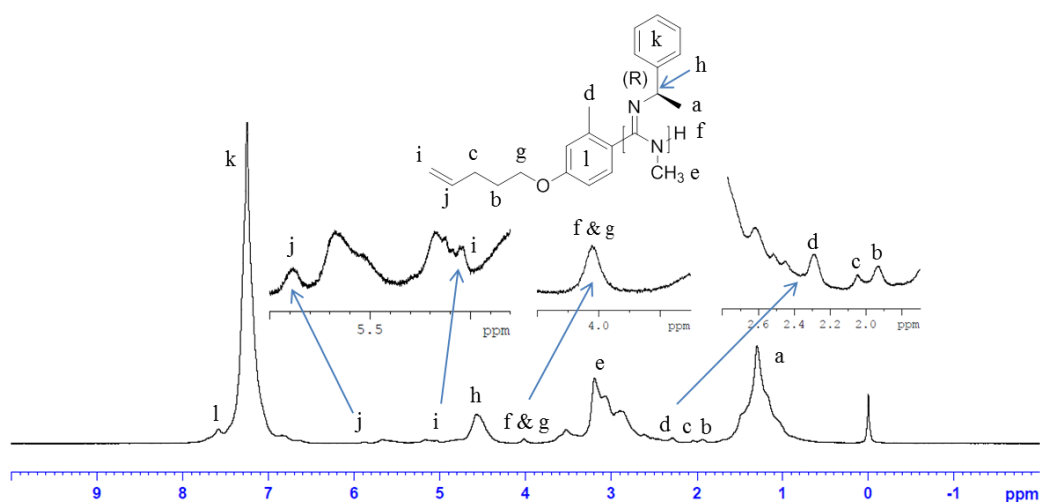


Figure 5.22- ^1H NMR spectrum of alkene end-functionalized **Poly-45** with peak assignments.

All chemical shifts associated with the end and pendant group carbons can be identified in the ^{13}C DEPTQ135 NMR spectra of **Poly-45** (Figure 5.23). The pendant group carbons appear at the same shifts described previously for **Poly-43**. Similar to the *o*-methyl end-group protons, the ^{13}C chemical shifts appears farther downfield compared to **Poly-43** at 23.6 ppm. The alkyl spacer methylene carbons are visible at 87.7, 29.8, and 30.3 ppm (in order of proximity to oxygen) and all show the correct positive phase (methylene/ quaternary carbons). Most importantly, the vinyl carbons can be confirmed intact with distinct chemical shifts at 115.5 and 137.8 ppm corresponding to the terminal and internal vinyl carbons, respectively. The end-group aromatic ^{13}C chemical shifts are located in the same position as **Poly-43** at 127.5 and 127.8 ppm between the pendant group aromatic chemical shifts. The 2D-HSQC experiment was somewhat inconclusive for most of the end group peaks showing very little peak correlation between the expected ^{13}C and ^1H chemical shifts (see experimental section).

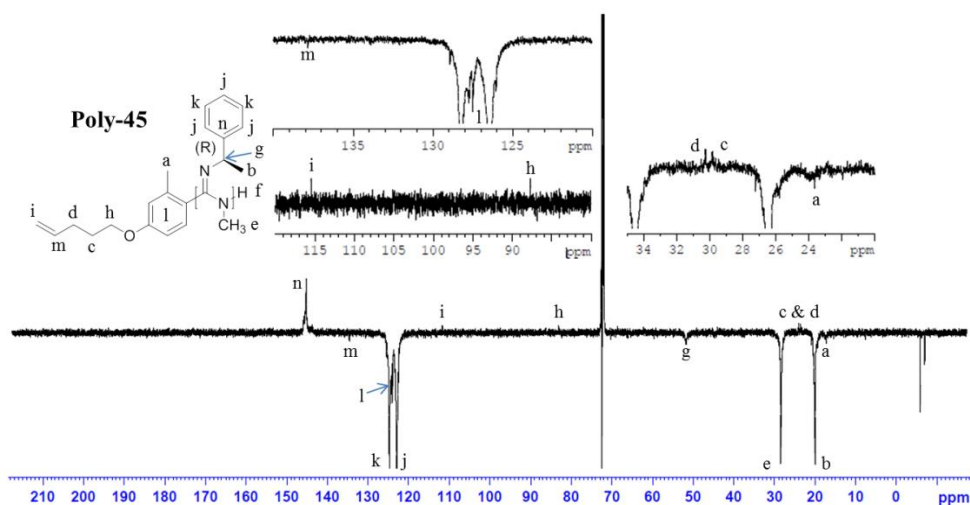
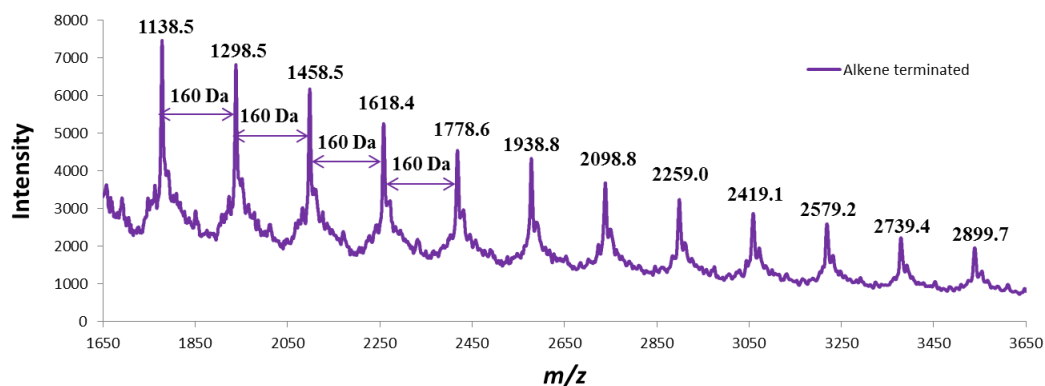


Figure 5.23- ^{13}C DEPTQ135 NMR spectra of **Poly-45** with peak assignments.

Like before, MALDI-TOF MS was employed to confirm the presence of the intact functionality appended to the terminus of **Poly-45** (Figure 5.24). Only one mass distribution is present in the MS supporting the presence of only one specific end group per terminus/ one ionization source. The upper threshold of observed m/z was surprisingly lower than previous examples with no masses observed above ~3000 Da. The theoretical m/z values of various polymer chains with 10 - 14 repeat units (ca. 160.10 Da) were calculated with the alkene functional aryl group (ca. 175.11 Da) and proton (ca. 1.01 Da) appended to the terminus and protonation of the nitrogen-rich backbone as the ionization source. The experimental m/z show a high level of agreement with the theoretical values within ± 1.0 Da confirming the presence of the latent functional alkene moiety appended to the end of **Poly-45**. Now that we have confirmed the presence of these functional end groups, we can now employ various post-polymerization techniques, such as hydrosilation or CuAAC, to synthesize various rod-coil block copolymers.



Theoretical m/z-

$n = 10 + \text{H}^+ + \text{alkene term end group} + \text{H end group} = 1778.13 \text{ Da}$
 $n = 11 + \text{H}^+ + \text{alkene term end group} + \text{H end group} = 1938.23 \text{ Da}$
 $n = 12 + \text{H}^+ + \text{alkene term end group} + \text{H end group} = 2098.33 \text{ Da}$
 $n = 13 + \text{H}^+ + \text{alkene term end group} + \text{H end group} = 2258.43 \text{ Da}$
 $n = 14 + \text{H}^+ + \text{alkene term end group} + \text{H end group} = 2418.53 \text{ Da}$

RU = 160.10 Da

H⁺ = 1.01 Da

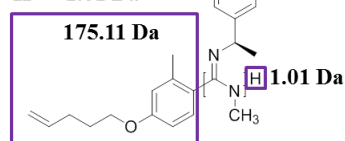


Figure 5.24- MALDI-TOF MS of **Poly-45** showing the clear mass distribution corresponding to the alkene end functionalized PPEMC.

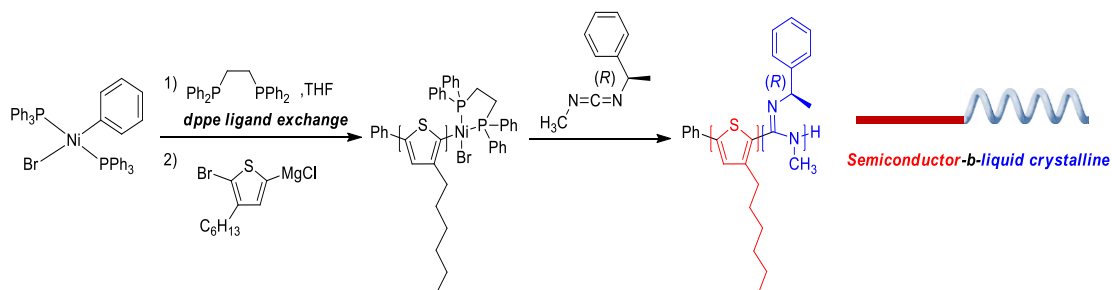
5.6 Attempted Copolymerization of Polycarbodiimides with Poly(3-hexylthiophene)

Using Nickel(II) Complexes-

The polymerization of arylenes using similar aryl Ni(II) bromide complexes offers the possibility of copolymerizing these monomers with carbodiimides forming a new class of conjugated-*block*-main chain liquid crystalline rod-rod block copolymers. This should, in theory, be simple to achieve since both monomers are readily polymerized in a living fashion using similar nickel(II) species. The main difference between these nickel systems is the use of the chelating ligand bis(diphenylphosphino)ethane (dppe) or bis(diphenylphosphino)propane (dppp) for the polymerization of arylenes rather than triphenylphosphine.²⁷ This provides enhanced stability of the active propagating species and

results in conjugated polymers with superior MW control and regioselectivity. The formation of regioregular conjugated materials is of the utmost importance in that it drastically affects its performance of these polymers in OFET devices for solar cells.³¹

As a proof of concept, 2,5-dibromo-3-hexylthiophene (DBHT) was copolymerized with the chiral **Mono-1R** via this method in order to determine the effect of incorporating rigid-rod, helical polycarbodiimides into the conjugated poly(3-hexylthiophene) (P3HT) (Scheme 5.5). The initiator **Ni-1** was first reacted with dppe for ~2 hours to exchange the more labile triphenylphosphine ligand. This exchange is quantitative and can be easily monitored by ³¹P NMR spectroscopy according to previous reports.³⁵ The active monomer also has to be generated *in situ* by reacting DBHT with *t*-butyl magnesium chloride forming the Grignard thiophene monomer seen in Scheme 5.5. This monomer was then added directly into the stirring catalyst solution initiating the polymerization. The clear change of color from beige to deep red confirms the formation of the extended conjugated P3HT. Upon consumption of thiophene monomer, **Mono-1R** was added to the reaction mixture in order to continue the propagation by P3HT transfer to the electrophilic carbodiimide. The reaction was then allowed to stir overnight and precipitated in from 1.0% (v/v) DBU in methanol the following day yielding purple fibrous polymer sample. To further purify, the polymer was continuously washed with hexanes and methanol, each for 12 hrs, using soxlet extraction to remove any low MW homopolymer chains from the sample.



Scheme 5.5- Proposed synthesis of P3HT-*b*-(*R*)-PPEMC using dpe ligated **Ni-1** via one-pot tandem Kumada polycondensation/controlled “living” nickel(II) mediated polymerization of carbodiimides.

The resulting polymer displayed specific chemical shifts in the ^1H NMR spectrum corresponding to both the P3HT and (*R*)-PPEMC segments (Figure 5.25). The aromatic pendant groups appended to the PPEMC block show up at their normal spot at 7.23 ppm. The phenyl end group, surprisingly, appears at the same chemical shift seen for the end functionalized PPEMC homopolymers (ca. 7.52 ppm) even though it should be appended to the terminus of the P3HT block. The single aromatic proton associated with the P3HT block is clearly visible at 6.91 ppm with no other significant peaks in the vicinity suggesting that the P3HT block is largely regioregular. This is an extremely important feature for the development of new organic semiconductors since the overall performance of these materials is largely dependent on the regioregularity. Additional chemical shifts associated with the hexyl chain of the P3HT block are also clearly visible at 2.54, 1.64, 1.28 and 0.842 ppm. The calculated ratio of mole% of PPEMC incorporated for the ^1H NMR displayed is 71%. Several different ratios of carbodiimide to thiophene were employed in order to synthesize a variety of block copolymers with different copolymer compositions.

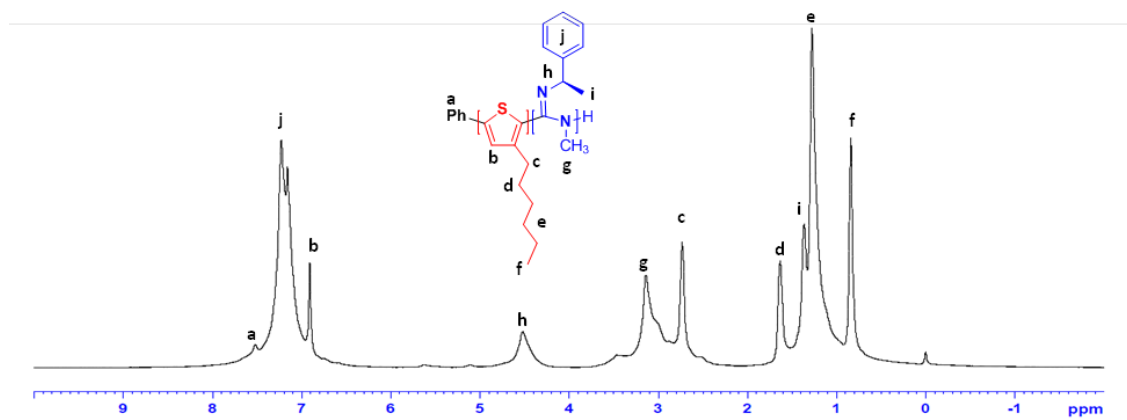


Figure 5.25- ^1H NMR spectrum of P3HT-*b*-(*R*)-PPEMC.

It is clear that both polymers formed but whether or not the polymers are covalently bound (forming a block copolymer) remains to be seen. To confirm or refute this, GPC must be employed in hopes to observe a single, narrow peak in the chromatogram corresponding to a single, monodisperse MW distribution for the polymer chains in the system. Several attempts of this polymerization were carried out at different monomer: initiator ratios and thiophene: carbodiimide ratios to synthesize a series of polymers with various MWs and copolymer compositions. The GPC chromatograms of these resulting polymers all showed multimodal distributions with 2 or even 3 peaks present in all samples (Figure 5.26). This suggests that the polymeric “ligand transfer” from the propagating polythiophene chains did not occur and the carbodiimide monomers may have been initiated by residual free Ni(II) initiator leftover in solution. This also suggests that the active Ni(II) propagating center appended to the P3HT chain decomposes prior to addition of carbodiimide monomer. These results were quite disappointing but this copolymerization is still believed to be possible to achieve. Future work should include the use of various chelating ligands to increase the

stability of the propagating species and to allow for the successful block copolymerization to occur.

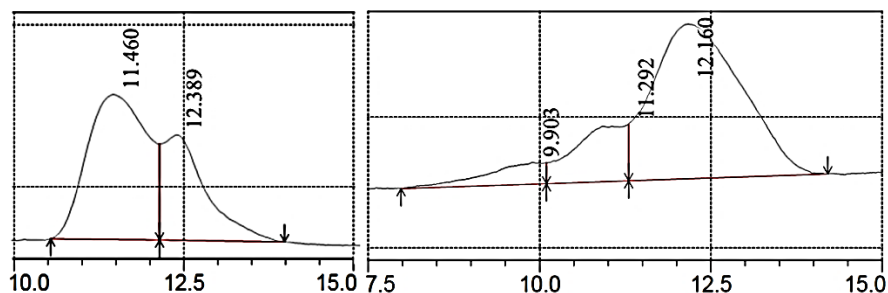


Figure 5.26- Examples of GPC chromatograms for two attempted copolymerizations of P3HT and (*R*)-PPEMC showing the multimodal distributions corresponding to multiple MW distributions.

5.7 Conclusions-

The polymerization of carbodiimide monomers with bis(triphenylphosphino)aryl nickel(II) bromide initiators was discovered to occur in a controlled “living” fashion. One of the main advantages of these nickel(II) initiators compared to their titanium(IV) counterparts is their high air/moisture stability in the solid state making them much simpler to synthesize and purify. The polymerization is initiated upon aryl ligand transfer to the center carbodiimide carbon forming the active Ni(II) amidinate complex. Additional carbodiimide monomer units then insert themselves into the nickel-nitrogen bond forming a new amidinate complex and propagation ensues. Linear relationships of percent conversion vs. M_n , $\ln([M]_0/[M])$ vs. time, and monomer: initiator ratio vs. M_n provide substantial evidence that the polymerization occurs via “living” chain-growth mechanism. The presence of the

transferred aryl end group at the terminus of the polymer chain was characterized by MALDI-TOF MS and ^{19}F NMR spectroscopy providing further evidence for the proposed mechanism of polymerization.

The *in situ* formation of the active Ni(II) initiator appended to the random coil polymer PBrS was also demonstrated by reacting ~22% of the available aryl bromide pendants with Ni(COD) $_2$ and triphenylphosphine. The chiral **Mono-1S** was then “grafted from” the PBrS macroinitiator chain forming a novel class of helical-*g*-coil copolymers with mesogenic, rigid rod polycarbodiimide segments covalently bound to the PBrS chains. This graft copolymer adopts nanofibular morphology as evident by TMAFM believed to be caused to the aggregation of the mesogenic PPEMC segments into large, fiber-like aggregates with an average diameter of 171 ± 28 nm.

Finally, two functional Ni(II) initiators were synthesized and employed to specifically end-functionalize polycarbodiimides with latent reactivity. TIPS-protected alkyne functional Ni(II) initiator (**Ni-3**) and alkene functional initiator (**Ni-4**) were synthesized via the same protocol used for **Ni-1** and **Ni-2**. The resulting polymerization of **Mono-1** using these initiators was fast and efficient with full conversion occurring in ~90 minutes and near quantitative isolated yields. The intact functional end-groups of these polymers were identified by ^1H and ^{13}C 1D NMR experiments, 2D- $^1\text{H}/^{13}\text{C}$ HSQC NMR and MALDI-TOF MS. These reactive end groups can now be employed in the formation of novel rod-coil block copolymers which will be discussed in Chapter 6. This novel polymerization technique offers exciting new opportunities in the facile incorporation of helical, rigid-rod

polycarbodiimides into a variety of systems such as block copolymers, graft copolymers, star polymers, hybrid inorganic/organic materials, etc.

5.8 Experimental Section-

Materials- All solvents, reagents, and reactants used for the synthesis of monomers were purchased from Sigma Aldrich and used as received. The bis(cyclooctadiene) Ni(0) (Alfa Aesar, 99%), triphenylphosphine (Sigma Aldrich, 99%), bromobenzene (Alfa Aesar, 99%), and 4-trifluoromethylbromobenzene (Alfa Aesar, 98%) used in the synthesis of **Ni-1** and **Ni-2** were also used as received. The aryl bromides used for the synthesis of **Ni-3** and **Ni-4** were synthesized via procedures outlined below and used following purification. The toluene used in the synthesis of catalysts and polymers was vacuum distilled over CaH₂ into an oven dried Schlenk flask equipped with 3Å molecular sieves and stored in an N₂ atmosphere MBraun UNILAB™ glove box prior to use. The 4-bromostyrene was distilled into an oven-dried Schlenk flask equipped with 3Å molecular sieves prior to RAFT polymerization. The RAFT agent 2-cyano-2-propyldodecyltrithiocarbonate (Sigma-Aldrich) and AIBN (Sigma-Aldrich) were used as received.

Equipment- All NMR spectra (including ¹H, ¹³C, ¹⁵N, ¹⁹F, and ³¹P) were recorded on a Bruker AVANCE III™ 500 MHz NMR spectrometer. All FTIR spectra were collected on Thermo Scientific Nicolet 380 ATR-FTIR spectrometer. Specific optical rotations of chiral polymers were measured using a JASCO P-1010 polarimeter (435 nm, *l* = 10.0 cm) at room temperature in dilute solution (CHCl₃, *c* = 2.00 mg/mL). Vibrational circular dichroism

(VCD) spectra were collected using a BioTools ChiralIR-2XTM VCD spectrometer equipped in deuterated chloroform ($c = 25.0 \text{ mg/mL}$, $l = 50.0 \text{ }\mu\text{m}$). Matrix-assisted laser desorption/ionization time-of-flight (MALDI-TOF) mass spectrometry of polymers was carried out using a Shimadzu Axima Confidence MALDI-TOF mass spec using dithranol (Sigma Aldrich) as a matrix, CHCl_3 as a solvent, and no salt added. The progress of the polymerizations were monitored via GC/MS on an Agilent 6890-5973 GC-MS workstation equipped with a Hewlett-Packard fused silica capillary column cross-linked with 5% phenylmethyl siloxane. All GC/MS analyses were conducted via the same method: injector and detector temperature, $250 \text{ }^\circ\text{C}$; initial temperature, $70 \text{ }^\circ\text{C}$; temperature ramp, $10 \text{ }^\circ\text{C}/\text{min}$; final temperature, $280 \text{ }^\circ\text{C}$. TMAFM was employed to investigate the thin-film morphology of the graft copolymer using a Nanoscope IV-Multimode Veeco instrument equipped with an E-type vertical engage scanner.

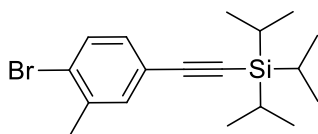
Characterization- All NMR spectra were recorded in either CDCl_3 (Sigma Aldrich) or toluene- d_8 (Sigma Aldrich). ^1H NMR spectra were referenced internally to tetramethylsilane (TMS) set to 0 ppm; ^{15}N NMR spectra were referenced externally to ^{15}N -benzamide set to 0 ppm; ^{19}F NMR spectra were referenced externally to trichlorofluoromethane (CFCl_3) set to 0 ppm; ^{31}P NMR spectra were referenced externally to 85% phosphoric acid (H_3PO_4) set to 0 ppm. The procedure for MALDI-TOF analysis of polymers is as follows: each polymer solution ($20 \text{ }\mu\text{L}$; 5.0 mg/mL) was mixed with the dithranol solution ($200 \text{ }\mu\text{L}$; 15.0 mg/mL) in a clean Eppendorf tube. Proteomass ACTH Fragment 18-39 (exact mass = 2464.1989 Da), Proteomass Insulin Chain B oxidized (exact mass = 3493.6513 Da), and Proteomass Insulin (exact mass = 5729.6087 Da) were purchased from Sigma Aldrich and used to calibrate

externally for all MALDI-TOF mass spec collected. All MALDI-TOF MS reported for samples and calibrants were analyzed in linear mode. Thin-films for TMAFM were prepared by passing dilute polymer solutions (5.0 mg/mL; CHCl₃) through 0.45 μm PTFE syringe filters, spin-casting on silicon wafer (Wafer World) at 1000 rpm for 30 seconds and annealed in CHCl₃ vapor for 24 hrs. The images were recorded at room temperature using silicon cantilever probes with a nominal spring constant of 42 N/m and resonance frequency of 320 kHz. The images reported herein were acquired at 0.996 Hz scan frequency in 5, 10, and 15 μm scan areas.

Synthesis/ Characterization of Small Molecule Precursors-

The synthesis and characterization of all small molecule precursors is outlined in the section below. All J-coupling values are reported in hertz and the FTIR labels are as follows: s= strong intensity, m= moderate intensity, and w= weak intensity. ¹H NMR peak splitting labels are as follows: s= singlet, d= doublet, t= triplet, q= quartet, p = pentet, m= multiplet (greater than pentet), dd= doublet of doublets, td= triplet of doublets, etc.

((4-bromo-3-methylphenyl)ethynyl)triisopropylsilane-

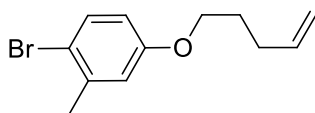


An oven-dried, 3-neck round bottom flask was equipped with a stir bar and evacuated/backfilled with N₂ three times followed by a continuous purge of N₂ throughout the reaction. To the purged flask, 1.568 g of 5-iodo-2-bromotoluene (5.28 mmol, 1.0 eq.),

0.9589 g of TIPS-acetylene (5.26 mmol, 1.0 eq.), and 2.56 mL of triethylamine (TEA, 18.5 mmol, 3.5 eq.) were added with ~20 mL of toluene. Following dissolution of the other reagents, 0.0503 g of copper(I) iodide (CuI, 0.264 mmol, 0.05 eq.) and 0.1255 g of tetrakis(triphenylphosphino) Pd(0) (Pd(PPh₃)₄, 0.109 mmol, 0.025 eq.) were added to the mixture and the reaction was allowed to stir for 24 hours at room temperature. The crude mixture was then washed with 1M HCl (1x 50 mL), sat. NH₄Cl solution (1 x 50 mL), 1M NaOH solution (1 x 50 mL), and Brine solution (1 x 50 mL). The solution was then dried over anhydrous sodium sulfate and further purified via column chromatography (hexanes as mobile phase). The product was collected as clear oil and dried under high vacuum.

Yield: 1.7513 g (4.98 mmol) of clear oil, 95%. ¹H NMR (500 MHz, CDCl₃): δ (ppm) 7.45 (Ar-H, d, *J*_{H-H} = 8.0 Hz, 1H), 7.33 (Ar-H, s, 1H), 7.14 (Ar-H, *J*_{H-H} = 7.5 Hz, d, 1H), 2.37 (Ar-CH₃, s, 3H), 1.12 (TIPS-H, s, 21H). ¹³C NMR (125 MHz, DMSO-*d*₆): δ (ppm) 137.9, 134.1, 132.2, 130.7, 125.1, 122.7, 106.1, 91.4, 22.1, 18.7, 11.3.

1-bromo-2-methyl-4-(pent-4-en-1-yloxy)benzene-

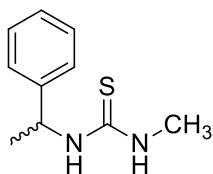


A 250 mL round bottom flask was charged with 0.485 g of 4-bromo-3-methylphenol (2.60 mmol, 1.0 eq.), 0.441 of 5-bromopent-1-ene (2.97 mmol, 1.2 eq.), 1.250 g of potassium carbonate (K₂CO₃, 9.04 mmol, 3.5 eq.), and 25 mL of DMF. The reaction mixture was heated to 85-90 °C and allowed to stir for 16 hours. Upon cooling to room temperature, 100 mL of

D.I. water was added to the mixture and the product was extracted with diethyl ether (4 x 40 mL). The ether extracts were combined, washed with 1M NaOH (2 x 20 mL) and Brine solution (1 x 100 mL), and dried over anhydrous sodium sulfate. The solution was decanted into a clean flask and the solvent was removed under vacuum to afford pure product as a clear liquid.

Yield: 0.4085 g (1.61 mmol) of clear oil, 62%. ^1H NMR (500 MHz, CDCl_3): δ (ppm) 7.51 (Ar-H, d, $J_{\text{H-H}} = 8.5$ Hz, 1H), 6.82 (Ar-H, s, 1H), 6.58 (Ar-H, $J_{\text{H-H}} = 9.0$ Hz, $J_{\text{H-H}} = 3.0$ Hz, dd, 1H), 5.90 (internal vinyl-H, $J_{\text{H-H}} = 6.5$ Hz, m, 1H), 5.21-5.15 (terminal vinyl-H, overlapped m, 2H), 3.67 (O- CH_2 , $J_{\text{H-H}} = 6.5$ Hz, t, 2H), 2.38 (Ar- CH_3 , s, 3H), 2.25 (O- $\text{CH}_2\text{-CH}_2\text{-CH}_2$ -, $J_{\text{H-H}} = 6.5$ Hz, q, 2H), 1.70 (O- $\text{CH}_2\text{-CH}_2\text{-CH}_2$ -, $J_{\text{H-H}} = 7.0$ Hz, p, 2H). ^{13}C NMR (125 MHz, $\text{DMSO-}d_6$): δ (ppm) 138.6, 137.6, 132.8, 128.0, 127.9, 127.7, 117.2, 115.0, 113.4, 66.8, 30.0, 28.3, 22.7.

N-1-phenethyl-*N*'-methylthiourea-

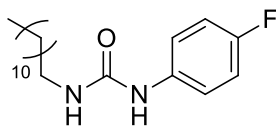


The synthesis and characterization of this thiourea has been previously reported.⁵ To a 250 mL round bottom flask, 5.99 mL (81.9 mmol; 1.0 eq) of methyl isothiocyanate, 10.5 mL (82.1 mmol; 1.2 eq.) of (*R*) or (*S*)-1-phenethylamine, and ~100 mL of CHCl_3 were added along with a stir bar. The reaction mixture was allowed to stir at room temperature for 24 hrs. The solvent was then removed under reduced pressure to afford a viscous liquid. The product

was then precipitated upon vigorous stirring with ~200 mL of hexanes for 24 hrs. The product was then isolated by filtration as a white solid and dried under high vacuum.

Yield: 10.8 g (55.6 mmol) of white solid, 69%. ^1H NMR (500 MHz, $\text{DMSO-}d_6$): δ (ppm) 7.38-7.28 (Ar-H, overlapped m, 5H), 6.51 (N-H, broad s, 1H), 5.88 (N-H, broad s, 2H), 5.02 (benzylic methine-H, broad s, 1H), 2.94 (N- CH_3 , $J_{\text{H-H}} = 4.5$ Hz, d, 3H), 1.53 (benzyl- CH_3 , $J_{\text{H-H}} = 7.0$ Hz, d, 3H). ^{13}C NMR (125 MHz, $\text{DMSO-}d_6$): δ (ppm) 181.9, 142.2, 129.1, 127.9, 125.9, 53.8, 31.5, 23.4.

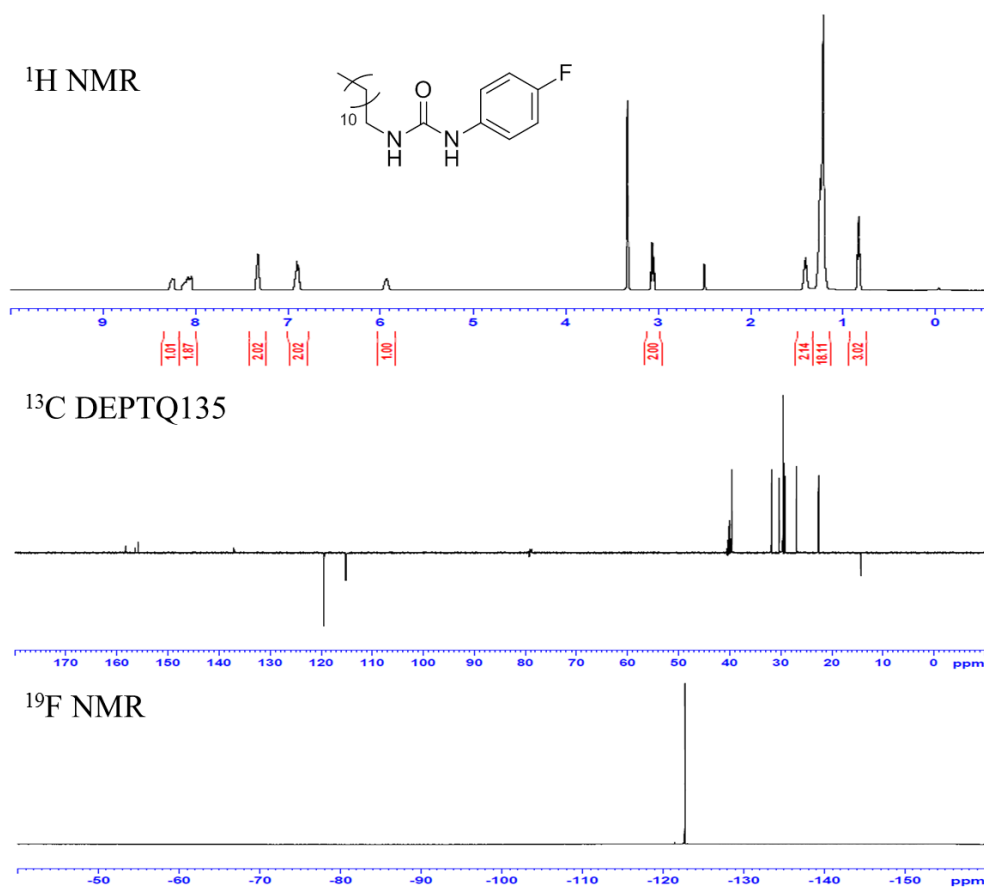
N-4-fluorophenyl-*N'*-dodecylurea-



To a 250 mL round bottom flask, 0.820 mL (3.40 mmol; 1.0 eq) of dodecyl isocyanate, 0.390 mL (4.12 mmol; 1.2 eq.) of 4-fluoroaniline, and ~50 mL of CHCl_3 were added along with a stir bar. The reaction mixture was heated to reflux and allowed to stir for 15 hrs. Upon cooling to room temperature, the solvent was removed via rotatory evaporation and the product was recrystallized from ethanol. The pure product was filtered and collected as a white crystalline solid and dried under high vacuum.

Yield: 1.023 g (3.17 mmol) of white solid, 93%. ATR-FTIR (cm^{-1}): 3335 (N-H str, m), 2954 (Ar-H str, w), 2916 (alkyl-H, s), 2847 (alkyl-H str, s), 1630 (C=O str, s), 1567 (C=C aryl, s). ^1H NMR (500 MHz, $\text{DMSO-}d_6$): δ (ppm) 8.11 (N-H, s, 1H), 7.32 (Ar-H, $J_{\text{H-H}} = 5.0$ Hz, d, 2H), 6.91 (Ar-H, $J_{\text{H-H}} = 5.0$ Hz, d, 2H), 5.93 (N-H, s, 1H), 3.06 (N- CH_2 -

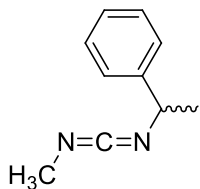
CH₂-(CH₂)₉-CH₃, $J_{1H-1H} = 6.5$ Hz, q, 2H), 1.41 (N-CH₂-CH₂-(CH₂)₉-CH₃, $J_{1H-1H} = 6.5$ Hz, t, 2H), 1.21 (N-CH₂-CH₂-(CH₂)₉-CH₃, s, 18H), 0.828 (N-CH₂-CH₂-(CH₂)₉-CH₃, $J_{1H-1H} = 6.0$ Hz, t, 2H). ¹³C NMR (125 MHz, DMSO-*d*₆): δ (ppm) 158.3, 155.8, 137.1, 119.5, 115.3, 115.1, 39.6, 31.8, 30.3, 29.6, 29.5, 29.3, 29.2, 26.9, 22.6, 14.3. ¹⁹F NMR (500 MHz, DMSO-*d*₆): δ (ppm) -122.7. HRMS-ESI: $M_{\text{theoretical}} = 345.23130$, $M_{\text{sample}} = 345.23140$, $\Delta M = 0.10$ mmass units (-0.45 ppm), C₁₉H₃₁N₂FO, (M+Na)⁺.



Synthesis of Carbodiimide Monomers-

The general procedure for all carbodiimide monomers is as follows: An oven dried 500 mL round bottom flask was purged with N₂ for 30 min. and cooled to 0 °C in an ice bath. Dibromotriphenylphosphorane (PPh₃Br₂, 1.2 eq.) was then added to the purged flask along with ~10 mL of dry dichloromethane (DCM). Triethylamine (TEA, 2.5 eq.) was then added slowly to the cool solution and the resulting vapors were allowed to dissipate prior to addition of the urea/thiourea (1.0 eq.). The reaction mixture was then allowed to stir at 0 °C, monitored by the appearance of N=C=N stretch at 2100-2200 cm⁻¹ in the IR spectrum. Upon completion, typically ~1 - 4 hours, the reaction was quenched with ~250 mL of hexanes and the resulting precipitate was filtered. The filtrate was then concentrated by rotatory evaporation and the quenching process was repeated twice more to remove the majority of byproducts (triphenylphosphine oxide/sulfide and triethylammonium bromide). The remaining purification varied from monomer to monomer. The synthesis and characterization of **Mono-18** can be found in the experimental section of Chapter 2.

N-1-phenethyl-*N'*-methylcarbodiimide (**Mono-1**)-

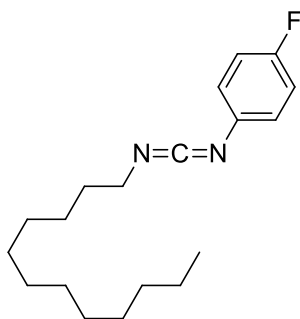


Following the outlined procedure above: 8.87 g (45.6 mmol; 1.0 eq.) of *N*-1-phenethyl-*N'*-methylthiourea, 19.4 g (45.9 mmol; 1.0 eq.) of dibromotriphenylphosphorane

(PPh_3Br_2), 16.0 mL (115 mmol; 2.5 eq.) of triethylamine, and ~35 mL of DCM. The product was further purified via vacuum distillation (~250 mBar) at 55 °C and collected as a clear oil. The synthesis and characterization of this monomer has been previously reported.⁵

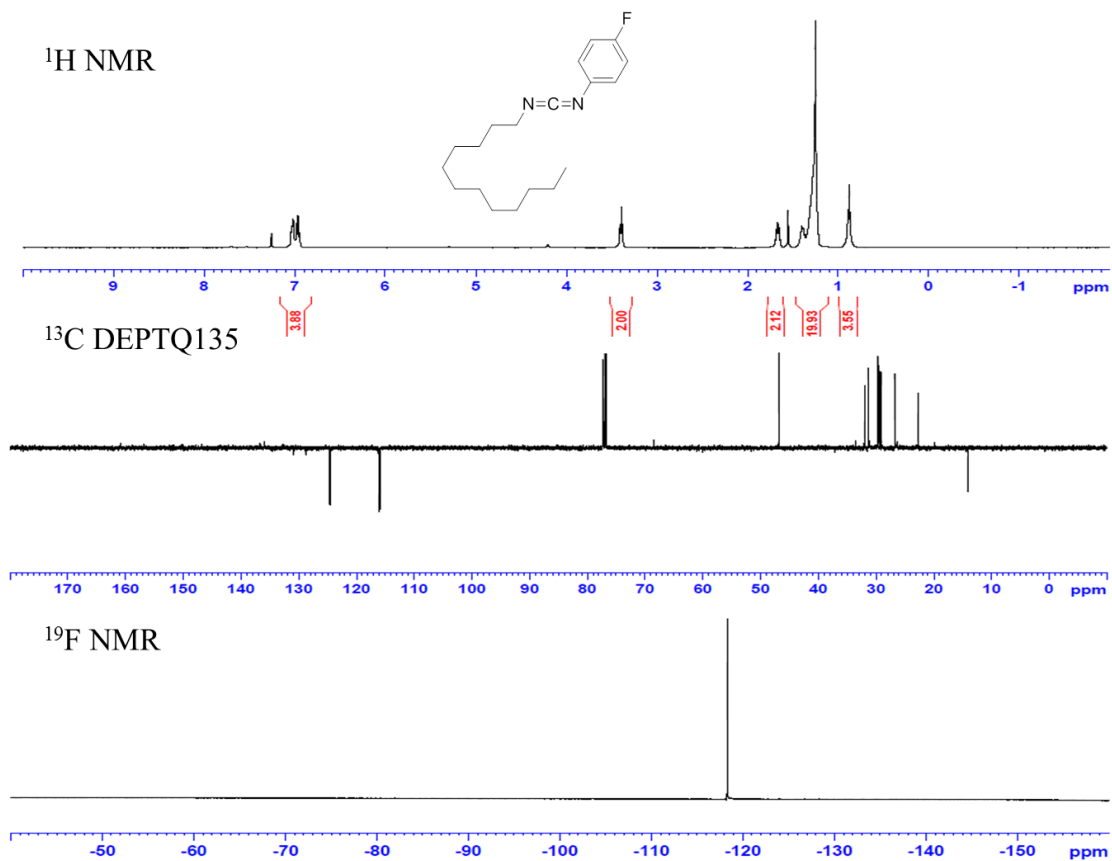
Yield: 3.06 g (19.1 mmol) of clear oil, 42%. ATR-FTIR (cm^{-1}): 3055 (Ar-H, m), 2908 (alkyl-H, s), 2124 (N=C=N, s), 1492 (C=C aryl, s). ^1H NMR (500 MHz, CDCl_3): δ (ppm) 7.37-7.25 (Ar-H, overlapped m, 5H), 4.60 (benzylic methine-H, $J_{\text{H-H}} = 6.5$ Hz, q, 2H), 2.94 (N- CH_3 , s, 3H), 1.55 (benzyl- CH_3 , $J_{\text{H-H}} = 7.0$ Hz, d, 3H). ^{13}C NMR (125 MHz, CDCl_3): δ (ppm) 144.0, 128.5, 127.3, 125.8, 56.6, 32.8, 25.0.

N-4-fluorophenyl-*N'*-dodecylcarbodiimide (**Mono-42**)-



Following the outlined procedure above: 0.976 g (3.03 mmol; 1.0 eq.) of *N*-4-fluorophenyl-*N'*-dodecylurea, 1.623 g (3.84 mmol; 1.2 eq.) of dibromotriphenylphosphorane (PPh_3Br_2), 1.11 mL (8.01 mmol; 2.5 eq.) of triethylamine, and ~15 mL of DCM. The product was further purified via column chromatography (DCM as mobile phase), collected as a clear oil, and dried under high vacuum.

Yield: 0.789 g (2.60 mmol) of clear oil, 86%. ATR-FTIR (cm^{-1}): 2922 (alkyl-H, s), 2852 (alkyl-H, s), 2125 (N=C=N, s), 1508 (C=C aryl, s). ^1H NMR (500 MHz, CDCl_3): δ (ppm) 7.02 (Ar-H, overlapped m, 2H), 6.93 (Ar-H, $J_{1\text{H}-1\text{H}} = 8.5$ Hz, overlapped t, 2H), 3.39 (N-**CH**₂-CH₂-, $J_{1\text{H}-1\text{H}} = 7.0$ Hz, t, 2H), 1.67 (N-CH₂-**CH**₂-, $J_{1\text{H}-1\text{H}} = 7.5$ Hz, p, 2H), 1.39 (N-CH₂-CH₂-**CH**₂-(CH₂)₈-CH₃, overlapped m, 2H), 1.25 (N-CH₂-CH₂-CH₂-(**CH**₂)₈-CH₃, overlapped s, 16H), 0.878 (N-CH₂-CH₂-CH₂-(**CH**₂)₈-CH₃, $J_{1\text{H}-1\text{H}} = 6.5$ Hz, t, 16H). ^{13}C NMR (125 MHz, CDCl_3): δ (ppm) 160.8, 136.0, 130.9, 124.6, 124.5, 116.1, 115.9, 46.9, 32.2, 31.9, 31.4, 31.2, 29.6, 29.5, 29.4, 29.1, 26.8, 26.4, 14.1. ^{19}F NMR (500 MHz, CDCl_3): δ (ppm) -118.3. HRMS-ESI: $M_{\text{theoretical}} = 305.23880$, $M_{\text{sample}} = 305.23910$, $\Delta M = -0.30$ mmass units (-1.02 ppm), $\text{C}_{19}\text{H}_{29}\text{N}_2\text{F}$, ($\text{M}+\text{H}$)⁺.

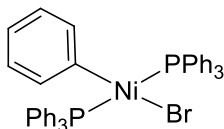


Synthesis/ Characterization of Ni(II) Initiators-

All initiators were synthesized following the same procedure outlined below. The synthesis and characterization of **Ni-1** has been previously reported in literature^{50,51} but via a different method than that reported herein. In an N₂ atmosphere glove box, an oven dried vial was charged with triphenylphosphine (PPh₃; 3.0 eq.), the corresponding aryl bromide (1.5 eq.) and ~3 mL of dry toluene. For **Ni-2**, catalytic amount of benzonitrile (PhCN; 0.1 eq.) was added to the mixture to aid in the oxidative addition of the aryl bromide onto the metal center as explained by Hartwig et al.⁵² To the stirring solution, the bis(1,5-cyclooctadiene)

nickel(0) ($\text{Ni}(\text{COD})_2$) was added with an additional 0.5 mL of dry toluene and the mixture was allowed to stir at room temperature for 30 min for **Ni-1** and **2**; 2 hours for **Ni-3** and **4**. The reaction vial was then removed from the glove box and ~15 mL of hexanes was added to the mixture precipitating the product. The suspension was allowed to stir for 2 hours; the solid was filtered, and washed with 100 mL of hexanes, 100 mL of methanol, and 50 mL of isopropanol. The pure products were then collected as yellow-orange solids and dried under high vacuum.

Bis(triphenylphosphino)phenyl Nickel(II) Bromide (Ni-1)-



Following the outlined procedure for the synthesis of nickel initiators: 1.054 g (6.71 mmol; 1.5 eq.) of bromobenzene, 3.469 g (13.2 mmol; 3.0 eq.) of triphenylphosphine, 1.267 g (4.56 mmol; 1.0 eq.) of bis(1,5-cyclooctadiene) nickel(0) ($\text{Ni}(\text{COD})_2$), and ~3 mL of dry toluene. The synthesis and characterization of **Cat-1** has been reported previously but via a different method.^{50,51} The NMR and FTIR data was reported below for comparison to literature values confirming the formation of the desired product.

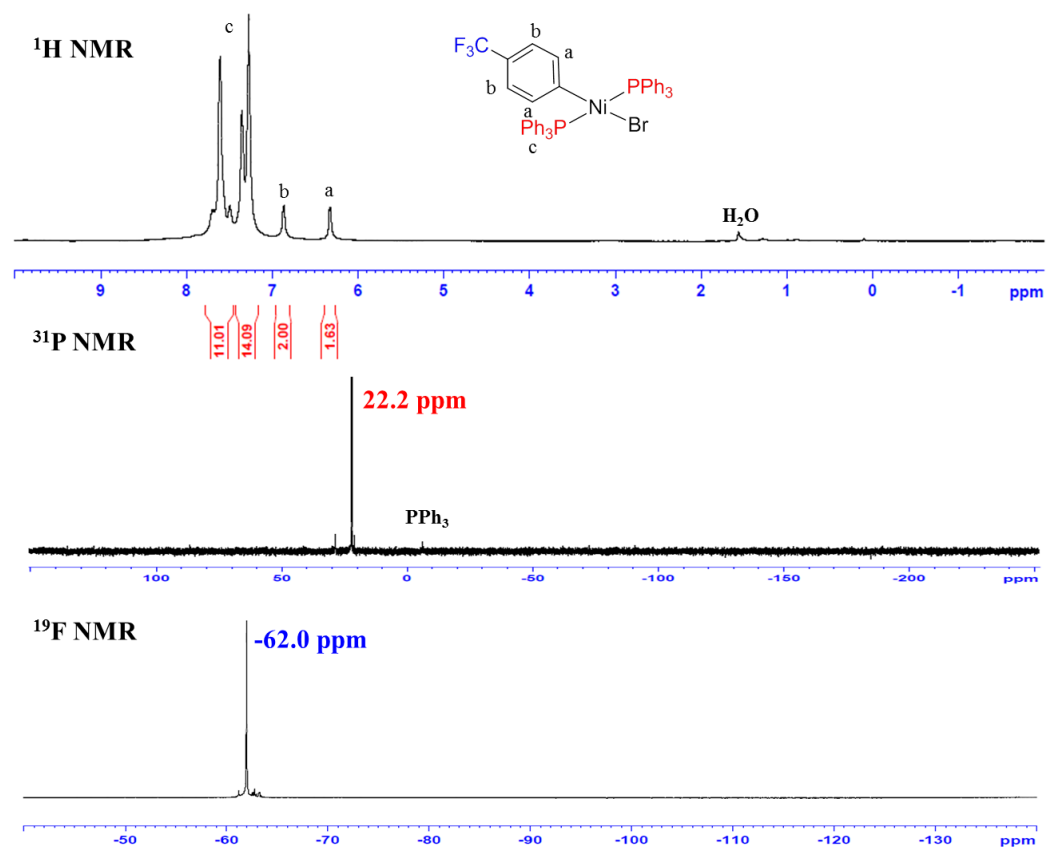
Yield: 2.530 g (3.42 mmol) of orange-yellow solid, 75%. ATR-FTIR (cm^{-1}): 3048 (Ar-H, w), 1558 (C=C aryl, m). ^1H NMR (500 MHz, CDCl_3): δ (ppm) 7.59 (P-Ph-H, broad s, 15H), 7.32-7.26 (P-Ph-H, overlapped broad d, 15H), 6.74 (Ni-Ph-H, broad s, 2H), 6.20-6.17 (Ni-Ph-H, broad d, 3H). ^{31}P NMR (202 MHz, CDCl_3): δ (ppm) 21.4 (Ni- PPh_3 , s).

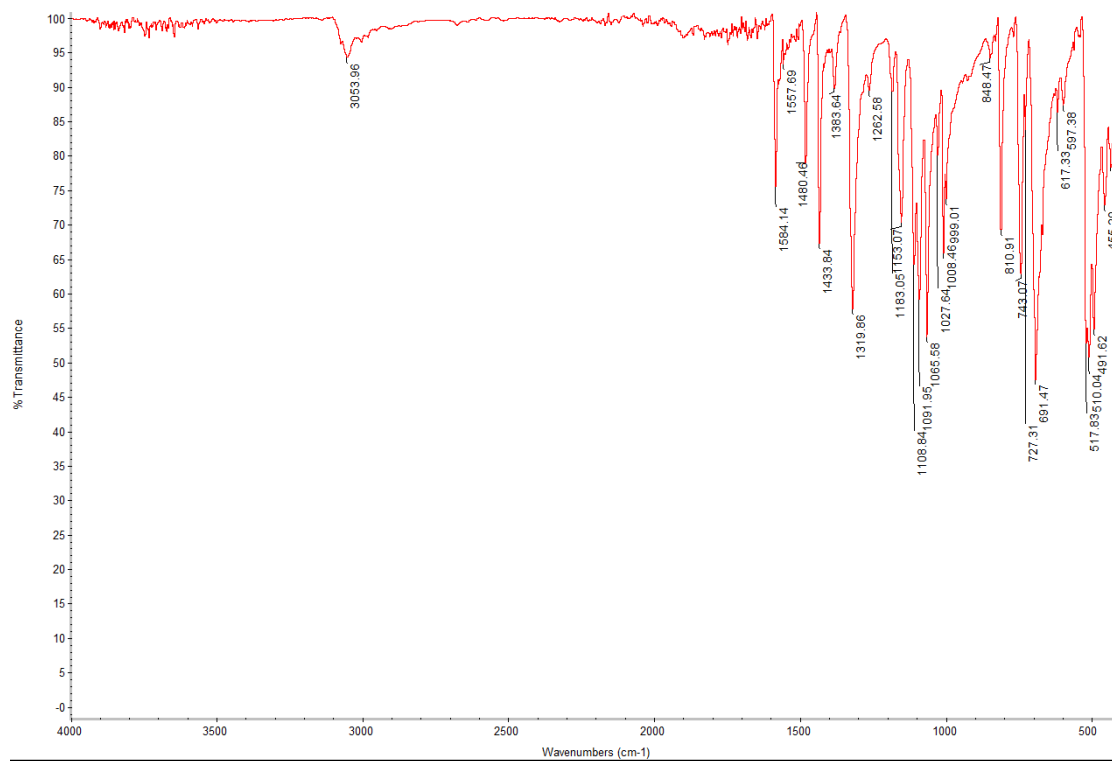
Bis(triphenylphosphino)(4-trifluoromethylphenyl) Nickel(II) Bromide (Ni-2)-



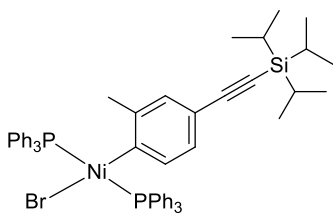
Following the outlined procedure for the synthesis of nickel initiators: 0.350 g (1.56 mmol; 1.5 eq.) of 4-bromobenzotrifluoride, 0.823 g (3.13 mmol; 3.0 eq.) of triphenylphosphine, 0.291 g (1.06 mmol; 1.0 eq.) of bis(1,5-cyclooctadiene) nickel(0) (Ni(COD)₂), and ~3 mL of dry toluene.

Yield: 2.530 g (3.42 mmol) of yellow solid, 75%. ATR-FTIR (cm⁻¹): 3054 (Ar-H, w), 1584 (C=C_{aryl}, m), 1319 (C-F, s). ¹H NMR (500 MHz, CDCl₃): δ (ppm) 7.70-7.49 (P-Ph-H, broad m, 15H), 7.35-7.27 (P-Ph-H, overlapped s, 15H), 6.87 (Ni-Ph-H, *J*_{H-H} = 7.0 Hz, d, 2H), 6.33 (Ni-Ph-H, *J*_{H-H} = 6.5 Hz, d, 2H). ³¹P NMR (202 MHz, CDCl₃): δ (ppm) 22.2 (Ni-PPh₃, s). ¹⁹F NMR (500 MHz, CDCl₃): δ (ppm) -62.0 (Ph-CF₃, s).



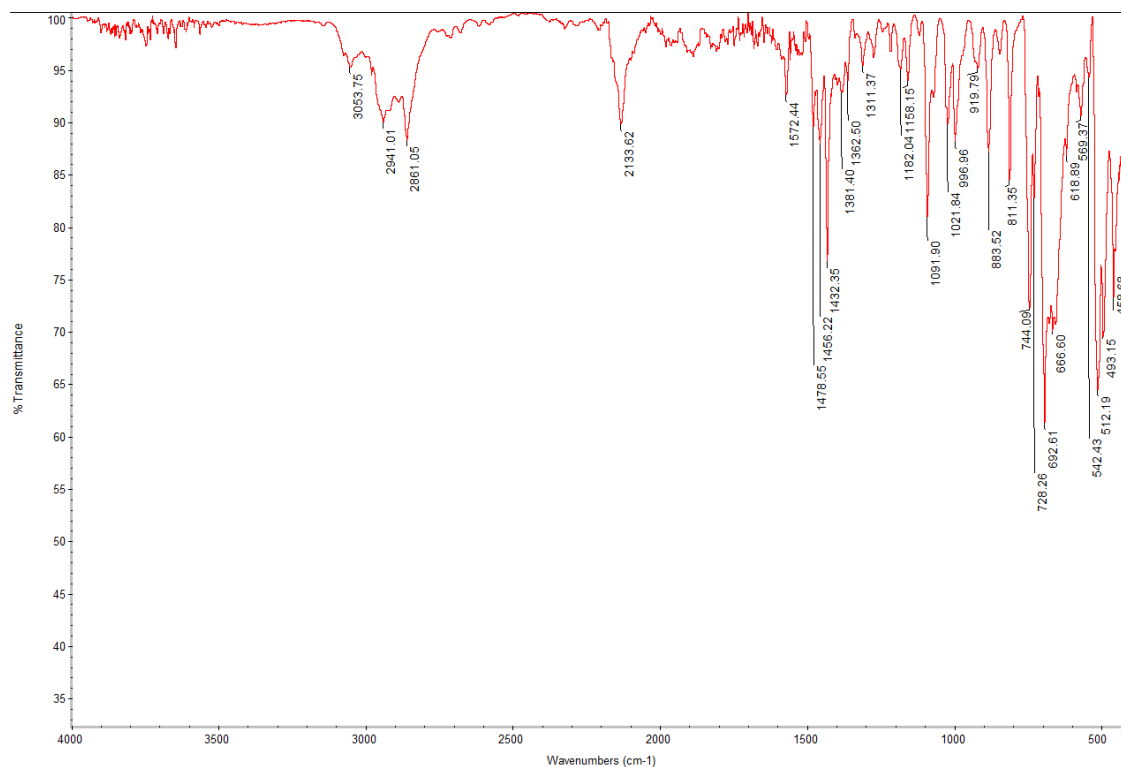


Bis(triphenylphosphino)(4-triisopropylsilylethynyl-2-methylphenyl) Nickel(II) Bromide (Ni-3)-

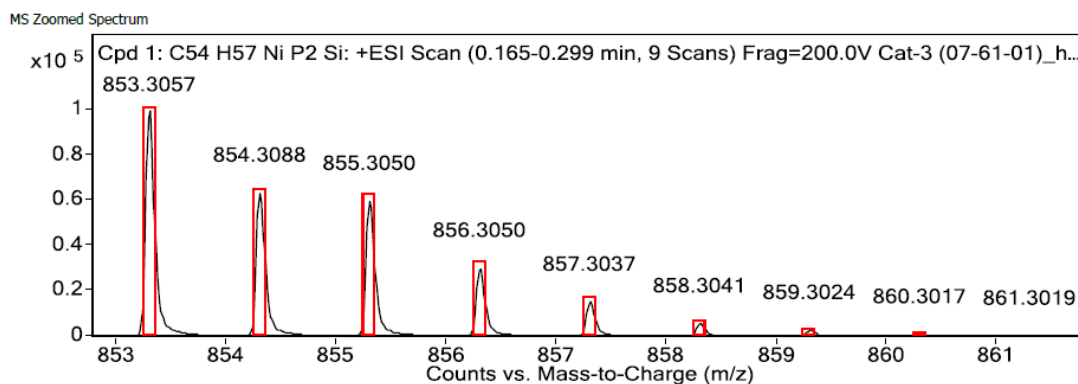


Following the outlined procedure for the synthesis of nickel initiators: 0.579 g (1.65 mmol; 1.5 eq.) of ((4-bromo-3-methylphenyl)ethynyl)triisopropylsilane, 1.54 g (5.85 mmol; 3.0 eq.) of triphenylphosphine, 0.424 g (1.54 mmol; 1.0 eq.) of bis(1,5-cyclooctadiene) nickel(0) (Ni(COD)₂), and ~3 mL of dry toluene.

Yield: 0.824 g (0.815 mmol) of orange solid, 57%. ATR-FTIR (cm^{-1}): 3054 (Ar-H, w), 2941 (alkyl-H, m), 2861 (alkyl-H, m), 2134 ($-\text{C}\equiv\text{C}-$, m), 1572 ($\text{C}=\text{C}_{\text{aryl}}$, w). ^1H NMR (500 MHz, CDCl_3): δ (ppm) 7.61-7.31 (P-Ph-H, broad m, 30H), 6.46 (Ni-Ph-H, broad s, 2H), 6.10 (Ni-Ph-H, broad s, 2H), 2.14 (Ar- CH_3 , broad s, 3H), 1.15 (TIPS-H, broad s, 20H). ^{13}C NMR (125 MHz, CDCl_3): δ (ppm) 143.3, 134.7, 129.7, 126.2, 117.2, 109.0, 86.8, 25.7, 18.7, 11.4. ^{31}P NMR (202 MHz, CDCl_3): δ (ppm) 21.0 (Ni- PPh_3 , s). HRMS-ESI: $M_{\text{theoretical}} = 853.30570$, $M_{\text{sample}} = 853.30530$, $\Delta M = -0.40$ mmass units (-0.49 ppm), $\text{C}_{54}\text{H}_{57}\text{NiP}_2\text{Si}$, ($\text{M}-\text{Br}$) $^+$



Ni-3

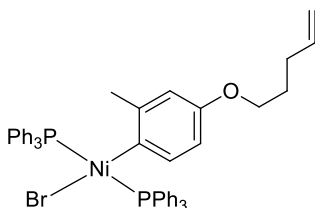


MS Spectrum Peak List

Obs. m/z	Calc. m/z	Charge	Abund	Formula	Ion/Isotope	Tgt Mass Error (ppm)
853.30570	853.30530	1	100826.92	C ₅₄ H ₅₇ NiP ₂ Si	M+	-0.49
854.30880	854.30840	1	63688.94	C ₅₄ H ₅₇ NiP ₂ Si	M+	-0.47
855.30500	855.30430	1	60057.8	C ₅₄ H ₅₇ NiP ₂ Si	M+	-0.81
856.30500	856.30510	1	30402.43	C ₅₄ H ₅₇ NiP ₂ Si	M+	0.19
857.30370	857.30370	1	15443.26	C ₅₄ H ₅₇ NiP ₂ Si	M+	0.06
858.30410	858.30420	1	5874.14	C ₅₄ H ₅₇ NiP ₂ Si	M+	0.04
859.30240	859.30200	1	2964.92	C ₅₄ H ₅₇ NiP ₂ Si	M+	-0.53
860.30170	860.30260	1	1107.34	C ₅₄ H ₅₇ NiP ₂ Si	M+	1.1
861.30190	861.30370	1	419.02	C ₅₄ H ₅₇ NiP ₂ Si	M+	2.08

--- End Of Report ---

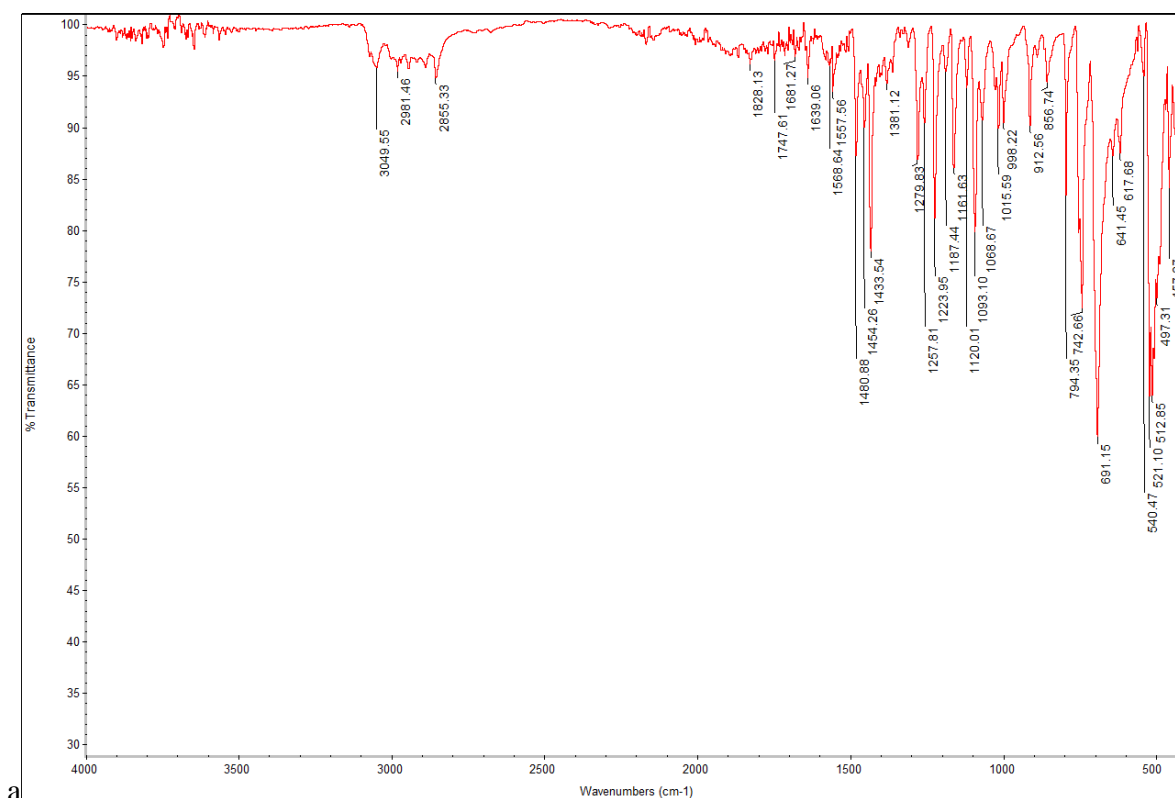
Bis(triphenylphosphino)(2-methyl-4-(pent-4-en-1-yloxy)phenyl) Nickel(II) Bromide (Ni-4)-



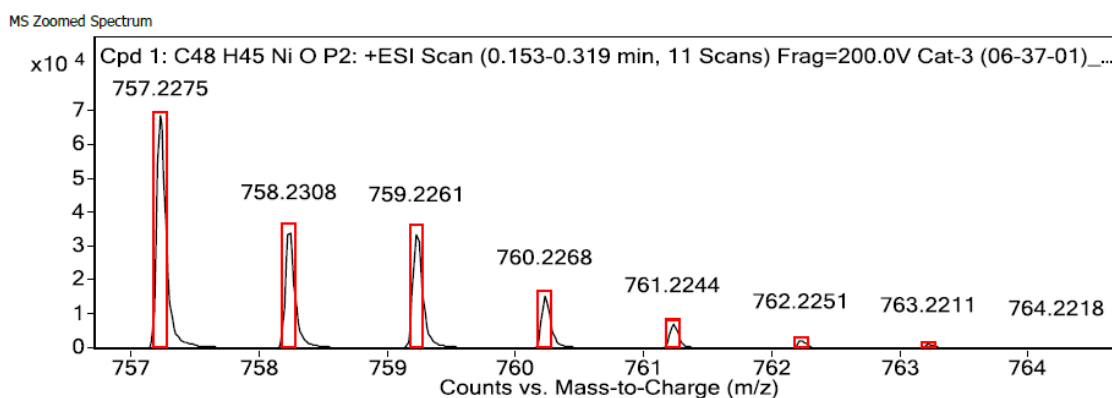
Following the outlined procedure above: 0.424 g (1.67 mmol; 1.5 eq.) of aryl bromide, 1.36 g (5.18 mmol; 3.0 eq.) of triphenylphosphine, 0.403 g (1.46 mmol; 1.0 eq.) of bis(1,5-cyclooctadiene) nickel(0) (Ni(COD)₂), and ~3 mL of dry toluene.

Yield: 0.777 g (3.42 mmol) of yellow solid, 64%. ATR-FTIR (cm⁻¹): 3049 (Ar-H, m), 2981 (vinyl-H, w) 2940 (alkyl-H, w), 2855 (alkyl-H, w), 1639 (-C=C-, w), 1480 (C=C_{aryl}, m). ¹H NMR (500 MHz, CDCl₃): δ (ppm) 7.80 (P-Ph-H, broad m, 10H), 7.14 (P-Ph-H, broad

m, 20H), 6.01 (Ni-Ph-H, broad s, 2H), 5.73 (internal vinyl-H, broad s, 1H), 4.98 (terminal vinyl-H, broad s, 2H), 3.50 (O-CH₂-, broad s, 2H), 2.37 (Ar-CH₃, broad s, 3H), 1.62 (O-CH₂-CH₂-CH₂-, broad s, 2H), 1.34 (O-CH₂-CH₂-CH₂-, broad s, 2H). ¹³C NMR (125 MHz, CDCl₃): δ (ppm) 135.0, 132.6, 129.3, 127.9, 127.7, 127.5, 114.7, 111.1, 66.8, 30.3, 28.6. ³¹P NMR (202 MHz, CDCl₃): δ (ppm) 21.0 (Ni-PPh₃, s). HRMS-ESI: M_{theoretical} = 757.22940, M_{sample} = 757.22750, ΔM = 1.90 mmass units (2.51 ppm), C₄₈H₄₅NiP₂O, (M-Br)⁺



Ni-4



MS Spectrum Peak List

Obs. m/z	Calc. m/z	Charge	Abund	Formula	Ion/Isotope	Tgt Mass Error (ppm)
437.20180	479932.38					
757.22750	757.22940	1	69711.24	C ₄₈ H ₄₅ NiOP ₂	M+	2.51
758.23080	758.23270	1	34875.43	C ₄₈ H ₄₅ NiOP ₂	M+	2.52
759.22610	759.22780	1	34228.64	C ₄₈ H ₄₅ NiOP ₂	M+	2.25
760.22680	760.22910	1	15568.09	C ₄₈ H ₄₅ NiOP ₂	M+	3.04
761.22440	761.22740	1	7393.87	C ₄₈ H ₄₅ NiOP ₂	M+	3.97
762.22510	762.22830	1	2556.18	C ₄₈ H ₄₅ NiOP ₂	M+	4.32
763.22110	763.22540	1	1487.25	C ₄₈ H ₄₅ NiOP ₂	M+	5.69
764.22180	764.22670	1	504.39	C ₄₈ H ₄₅ NiOP ₂	M+	6.45
765.22530	765.22940	1	197.4	C ₄₈ H ₄₅ NiOP ₂	M+	5.36

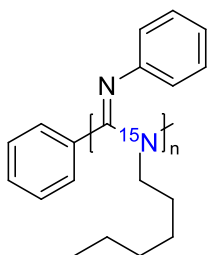
--- End Of Report ---

Synthesis/characterization of Polymers-

In an inert N₂ atmosphere glove box, an oven-dried vial was charged with the corresponding amount of monomer along with 2-5 mL of dry toluene. The initiator was then added directly into the stirring mixture and allowed to stir for 12 hrs. The reaction vial was then removed from the glove box and the product was precipitated from 100 mL of 1.0% (v/v) 1,8-diazabicyclo[2.5.0]undec-7-ene (DBU) solution in methanol. The DBU is added to the precipitating solvent in order to aid in the extraction of the residual nickel in the system. If the color associated with residual catalyst persists after the first precipitation, the polymer was redissolved in the minimal amount of CHCl₃ and precipitated again. For all cases studied, this is a sufficient method to remove the vast majority nickel from the system. The

pure polymer was then isolated by filtration as a white solid, washed with 100 mL of methanol, and dried under high vacuum. The specific amounts of reagents, yields, ^1H NMR, FTIR, MW, etc. for all synthesized polymer can be found below.

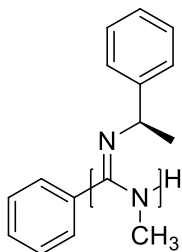
Poly(N-phenyl- ^{15}N -hexylcarbodiimide) (Poly-18 from Ni-1)-



Following the outlined procedure for the polymerization of carbodiimides from the experimental section of the main text: 0.293 g (1.45 mmol; 48 eq.) of *N*-phenyl- ^{15}N -hexylcarbodiimide (**Mono-18**), 22.1 mg (29.9 μmol ; 1.0 eq.) of bis(triphenylphosphino)phenyl nickel(II) bromide (**Ni-1**), and ~1.5 mL of dry toluene. The IR and NMR data for **Poly-18** polymerized from Ti(IV) initiators can be found in Chapter 2.

Yield: 0.250 g of white solid; 85%. ATR-FTIR (cm^{-1}): 3059 (Ar-H, w), 3018 (Ar-H, w), 2954 (alkyl-H, s), 2858 (alkyl-H, m), 1626 (C=N, s), 1589 (C=C aryl, m). ^1H NMR (500 MHz, CDCl_3): δ (ppm) 7.71 (end group Ph-H, broad s), 7.54 (end group Ph-H, broad s), 7.26 (pendant Ph-H, overlapped broad s, 2H), 7.00 (pendant Ph-H, overlapped broad s, 3H), 3.46 and 2.61 (N- CH_2 -, diastereotopic methylene, two broad s, 2H), 1.34-0.45 (N- CH_2 - $(\text{CH}_2)_4$ - CH_3 , overlapped m, 9H). ^{15}N NMR (50 MHz, CDCl_3): δ (ppm) 14.8. GPC (Viscotek GPC): $M_n = 5000$ Da, PDI = 3.30.

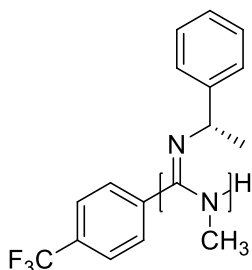
Poly(N-(R)-1-phenethyl-N'-methylcarbodiimide) (Poly-1R from Ni-1)-



Following the outlined procedure for the polymerization of carbodiimides from the experimental section of the main text: 0.425 g (2.65 mmol; 200 eq.) of *N-(R)-1-phenethyl-N'-methylcarbodiimide* (**Mono-1R**), 9.8 mg (13.2 μmol ; 1.0 eq.) of bis(triphenylphosphino)phenyl nickel(II) bromide (**Ni-1**), and ~2.0 mL of dry toluene. The IR and NMR data for **Poly-1** has been previously reported but were reported below for comparison to previous polymers formed with Ti(IV) initiators.⁵

Yield: 0.417 g of white solid; 98%. ATR-FTIR (cm^{-1}): 3024 (Ar-H, w), 2964 (alkyl-H, w), 1627 (C=N, s), 1557 (C=C aryl, w). ^1H NMR (500 MHz, CDCl_3): δ (ppm) 7.53 (end group Ph-H, broad s), 7.23 (pendant Ph-H, overlapped broad s, 5H), 5.12 (benzyl-CH, broad s, 1H), 3.14 (N-CH₃, broad s, 3H), 1.24 (benzyl-CH₃, broad s, 3H). Specific OR ($c = 2.0$ mg/mL, $l = 10.0$ cm, 435 nm, 25 °C) $[\alpha] = +51.2^\circ$. TGA (T_{decomp}): 174 °C.

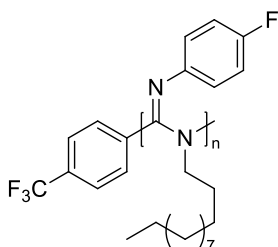
Poly(N-(S)-1-phenethyl-N'-methylcarbodiimide) (Poly-1S from Ni-2)-



Following the outlined procedure for the polymerization of carbodiimides from the experimental section of the main text: 0.390 g (2.43 mmol; 200 eq.) of *N*-(*S*)-1-phenethyl-*N'*-methylcarbodiimide (**Mono-1S**), 9.8 mg (12.1 μmol ; 1.0 eq.) of bis(triphenylphosphino)(4-trifluoromethylphenyl) nickel(II) bromide (**Ni-2**), and \sim 2.0 mL of dry toluene. The IR and NMR data for **Poly-1** has been previously reported but were reported below for comparison to previous polymers formed with Ti(IV) initiators.⁵

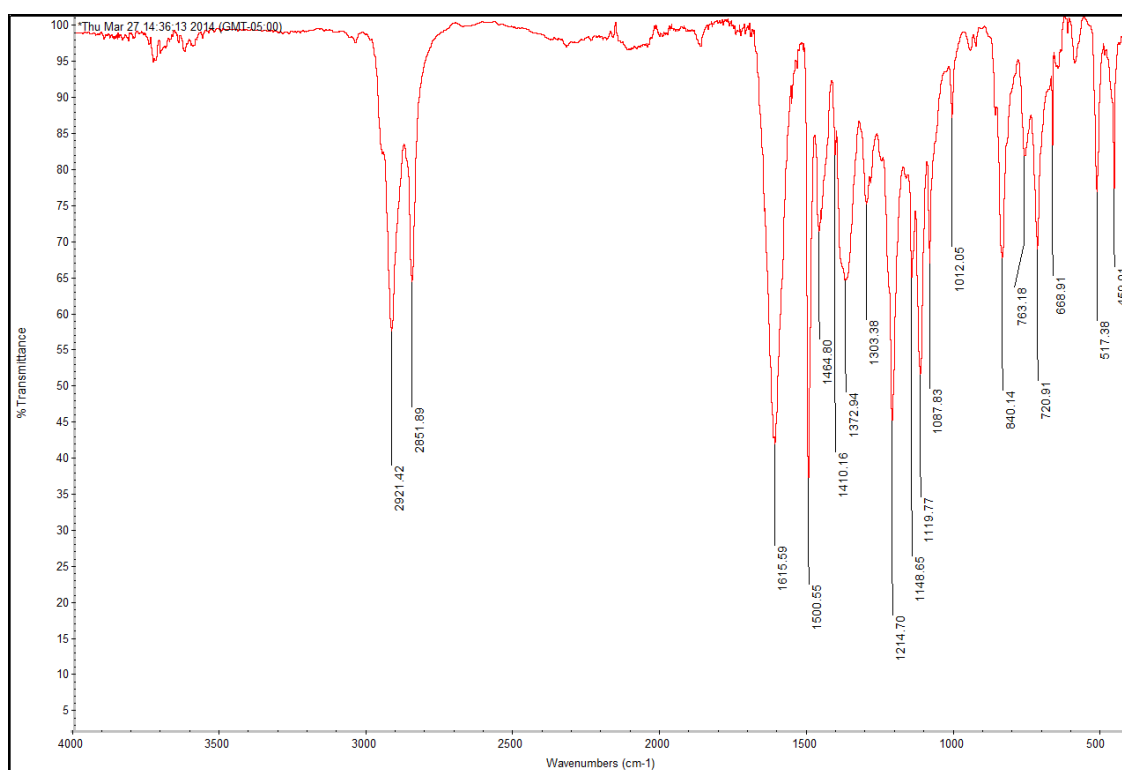
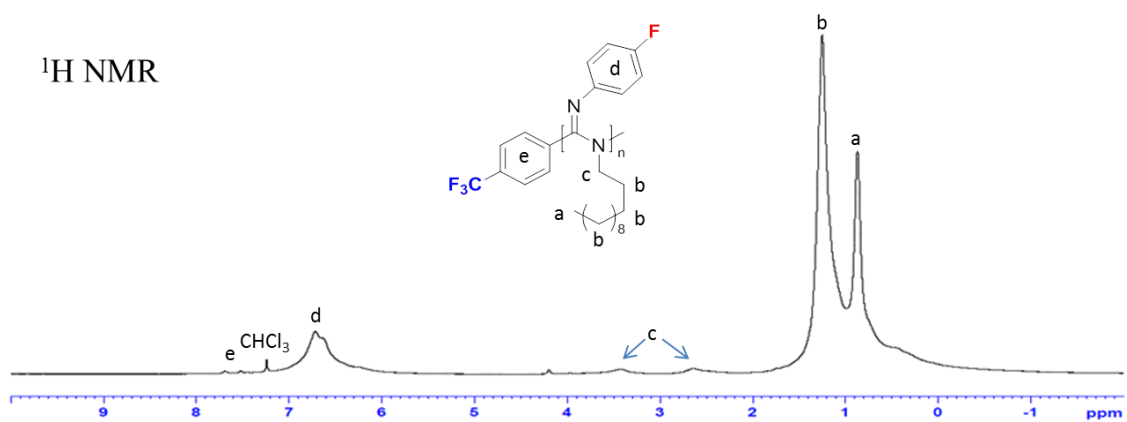
Yield: 0.374 g of white solid; 96%. ATR-FTIR (cm^{-1}): 3024 (Ar-H, w), 2964 (alkyl-H, w), 1627 (C=N, s), 1557 (C=C aryl, w). ^1H NMR (500 MHz, CDCl_3): δ (ppm) 7.53 (end group Ph-H, broad s), 7.23 (pendant Ph-H, overlapped broad s, 5H), 5.12 (benzyl-CH, broad s, 1H), 3.14 (N-CH₃, broad s, 3H), 1.24 (benzyl-CH₃, broad s, 3H). ^{19}F NMR (500 MHz, CDCl_3): δ (ppm) -63. Specific OR ($c = 2.0 \text{ mg/mL}$, $l = 10.0 \text{ cm}$, $\lambda = 435 \text{ nm}$, $25 \text{ }^\circ\text{C}$) $[\alpha] = -49.4^\circ$. TGA (T_{decomp}): $174 \text{ }^\circ\text{C}$.

Poly(N-4-fluorophenyl-N'-dodecylcarbodiimide) (Poly-42)-

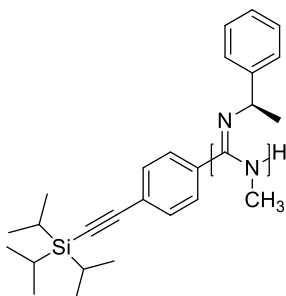


This polymerization was performed at a variety of monomer: initiator ratios to provide a wide breadth of MWs to be analyzed by ^{19}F NMR. The amounts shown below reflect the polymerization at $[\text{Mono-42}]/[\text{Ni-2}] = 125$. Following the outlined procedure for the polymerization of carbodiimides from the experimental section of the main text: 0.406 g (1.33 mmol; 125 eq.) of *N*-4-fluorophenyl-*N'*-dodecylcarbodiimide (**Mono-42**), 8.6 mg (10.6 μmol ; 1.0 eq.) of bis(triphenylphosphino)(4-trifluoromethylphenyl) nickel(II) bromide (**Ni-2**), and ~ 0.5 mL of dry toluene.

Yield: 0.356 g of white solid, 88%. ATR-FTIR (cm^{-1}): 2921 (alkyl-H, s), 2851 (alkyl-H, s), 1615 (C=N, s), 1501 (C=C aryl, s). ^1H NMR (500 MHz, CDCl_3): δ (ppm) 7.70 (end group Ph-H, broad s), 7.53 (end group Ph-H, broad s), 6.73-6.65 (pendant Ph-H, overlapped broad s, 4H), 3.43 and 2.64 (N-**CH**₂-, diastereotopic methylene, two broad s, 2H), 1.34-0.882 (N-CH₂-(**CH**₂)₁₀-**CH**₃, overlapped m, 22H). ^{19}F NMR (500 MHz, CDCl_3): δ (ppm) -63, -122.

$^1\text{H NMR}$ 

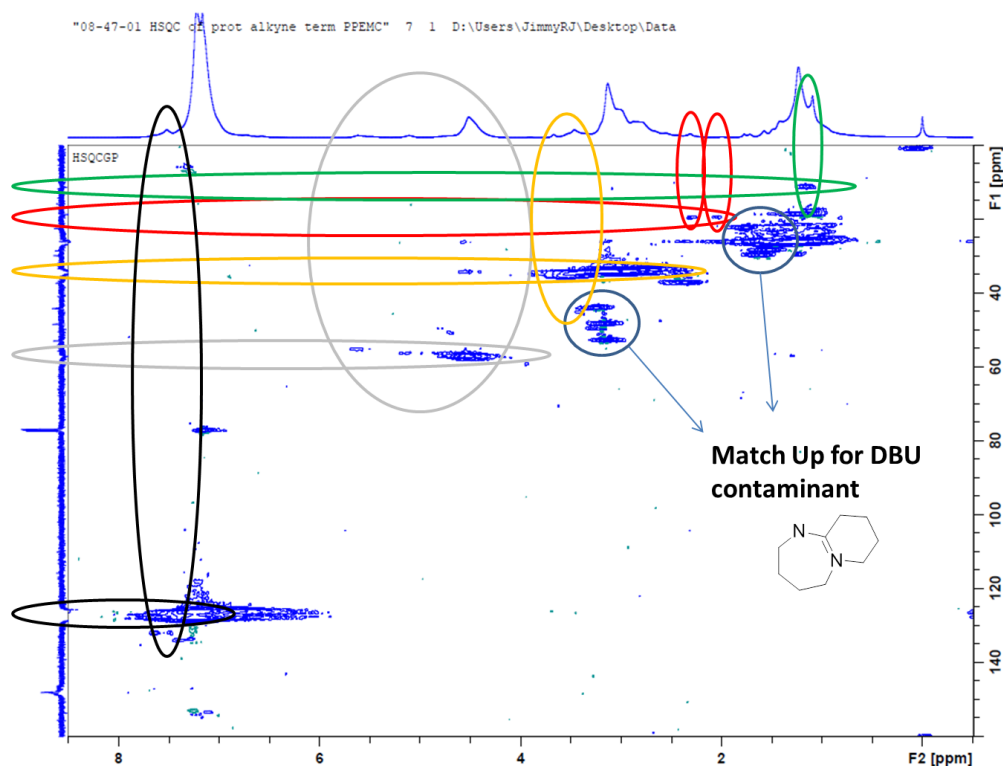
*Alkyne terminated Poly(*N*-(*R*)-1-phenethyl-*N'*-methylcarbodiimide) (Poly-43 from Ni-3)-*



Several different batches of **Poly-43** were synthesized with a variety of monomer-to-initiator ratios. The following amounts reflect a specific batch that provided the most monodisperse results in the GPC. Following the outlined procedure for the polymerization of carbodiimides from the experimental section of the main text: 1.17 g (7.31 mmol; 103 eq.) of *N*-(*R*)-1-phenethyl-*N'*-methylcarbodiimide (**Mono-1R**), 66.6 mg (71.3 μ mol; 1.0 eq.) of bis(triphenylphosphino)(4-triisopropylsilylethynyl-2-methylphenyl) nickel(II) bromide (**Ni-3**), and ~2.0 mL of dry toluene. The IR spectra displayed the exact same spectra as other PPEMC samples prepared with other initiators but NMR spectra for **Poly-43** display distinct chemical shifts associated with the new, functional end-group.

Yield: 1.13 g of white solid; 97%. ATR-FTIR (cm^{-1}): 3024 (Ar-H, w), 2964 (alkyl-H, w), 1627 (C=N, s), 1557 (C=C aryl, w). ^1H NMR (500 MHz, CDCl_3): δ (ppm) 7.52 (end group Ph-H, broad s), 7.23 (pendant Ph-H, overlapped broad s, 5H), 5.61, 5.12, 4.51 (benzyl-**CH**, broad m, 1H), 3.90 (end-group N-H, broad s), 3.67, 3.46, 3.14 (N-**CH**₃, broad m, 3H), 1.98 (end-group Ar-**CH**₃, broad s), 1.24 (benzyl-**CH**₃, broad s, 3H), 1.09 (end-group TIPS-**H**, s). ^{13}C NMR (125 MHz, CDCl_3): δ (ppm) 148.2, 147.0, 128.2, 127.8, 127.5, 126.4, 57.2,

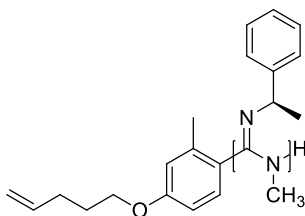
34.6, 24.0, 18.8, 11.5. Specific OR ($c = 2.0 \text{ mg/mL}$, $l = 10.0 \text{ cm}$, $\lambda = 435 \text{ nm}$, $25 \text{ }^\circ\text{C}$) $[\alpha] = +48.7^\circ$. TGA (T_{decomp}): $174 \text{ }^\circ\text{C}$. GPC (Shimadzu GPC): $M_n = 13.7 \text{ kDa Da}$, PDI = 1.26.



Deprotection of TIPS-protecting group with TBAF (Poly-44)-

The protected alkyne terminated PPEMC (1.0 eq, **Poly-43**) was dissolved in ~25 mL of THF in a 100 mL R.B. flask and cooled to $0 \text{ }^\circ\text{C}$ in an ice bath. The corresponding amount of TBAF solution in THF (3.0 eq.) was then injected into the cold, stirring solution and the reaction was allowed to stir for 3 hours. Upon completion, the product was precipitated in MeOH and collected by filtration with quantitative conversions confirmed by both ^1H NMR and MALDI-TOF MS.

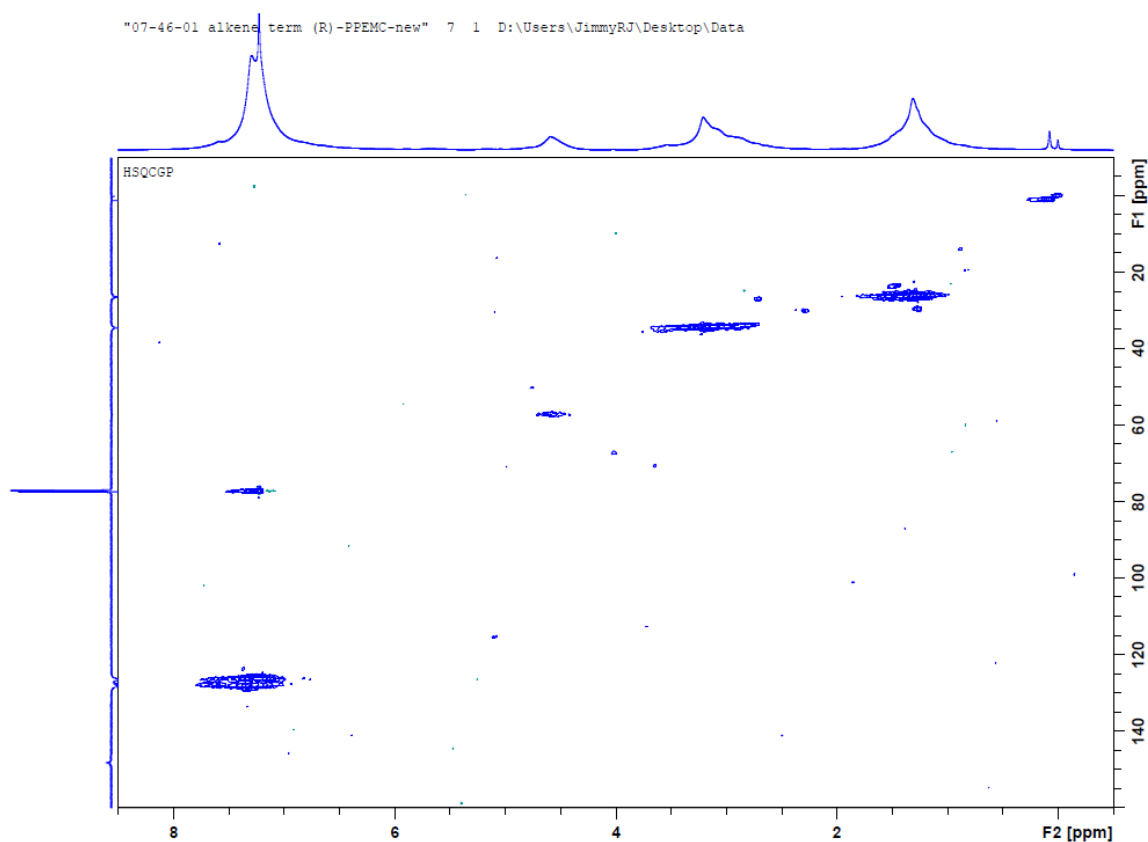
Alkene terminated Poly(*N*-(*R*)-1-phenethyl-*N'*-methylcarbodiimide) (**Poly-45** from **Ni-4**)-



Several different batches of **Poly-45** were synthesized with a variety of monomer-to-initiator ratios. The following amounts reflect a specific batch that provided the most monodisperse results in the GPC. Following the outlined procedure for the polymerization of carbodiimides from the experimental section of the main text: 1.21 g (7.57 mmol; 97 eq.) of *N*-(*R*)-1-phenethyl-*N'*-methylcarbodiimide (**Mono-1R**), 65.1 mg (77.7 μ mol; 1.0 eq.) of bis(triphenylphosphino)(2-methyl-4-(pent-4-en-1-yloxy)phenyl) nickel(II) bromide (**Ni-4**), and ~2.0 mL of dry toluene. The IR spectra displayed the exact same spectra as other PPEMC samples prepared with other initiators but NMR spectra for **Poly-45** display distinct chemical shifts associated with the new, functional end-group.

Yield: 1.15 g of white solid; 95%. ATR-FTIR (cm^{-1}): 3024 (Ar-H, w), 2964 (alkyl-H, w), 1627 (C=N, s), 1557 (C=C aryl, w). ^1H NMR (500 MHz, CDCl_3): δ (ppm) 7.59 (end group Ph-H, broad s), 7.23 (pendant Ph-H, overlapped broad s, 5H), 5.88 (end-group internal vinyl-H, broad s), 5.12, 5.05, (end-group terminal vinyl-H, broad m), 5.61, 5.12, 4.51 (benzyl-CH, broad m, 1H), 4.02 (end-group N-H and -O-CH₂-, overlapped s), 3.67, 3.46, 3.14 (N-CH₃, broad m, 3H), 2.36 (end-group Ar-CH₃, broad s), 2.05 (-O-CH₂-CH₂-CH₂-, broad s), 1.94 (-O-CH₂-CH₂-CH₂-, broad s), 1.24 (benzyl-CH₃, broad s, 3H), 1.09 (end-

group TIPS-H, s). ^{13}C NMR (125 MHz, CDCl_3): δ (ppm) 148.2, 146.7, 137.8, 128.2, 127.8, 127.5, 126.4, 115.5, 87.7, 57.2, 34.6, 30.3, 29.8, 26.4, 23.6. Specific OR ($c = 2.0$ mg/mL, $l = 10.0$ cm, $\lambda = 435$ nm, 25 °C) $[\alpha] = +47.2^\circ$. TGA (T_{decomp}): 174 °C. GPC (Shimadzu GPC): $M_n = 11.6$ kDa Da, PDI = 1.53.



Molecular Weight Determination-

Molecular weights of the synthesized polymers were measured by Gel Permeation Chromatography (GPC) analysis on a Viscotek VE 3580 system (GPC1) equipped with ViscoGEL™ columns (GMHHR-M), connected to a refractive index (RI) detectors. GPC solvent/sample module (GPCmax) was used with HPLC grade chloroform as the eluent and

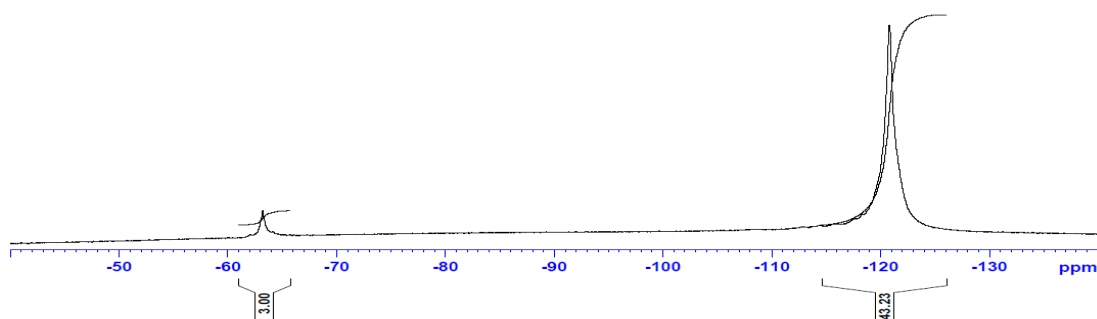
calibration was based on polystyrene standards. Running conditions for SEC analysis were: flow rate = 1.0 mL/min, injector volume = 100 μ L, detector temperature = 30 $^{\circ}$ C, column temperature = 35 $^{\circ}$ C. All the polymers samples were dissolved in chloroform and the solutions were filtered through PTFE filters (0.45 μ m) prior to injection. For comparison, the MWs of several polymer systems were also run on a Shimadzu Prominence Modular HPLC/GPC system (GPC2) connected to a refractive index (RI) detector relative to a polystyrene standard. A two-column system was employed consisting of an Agilent Mixed-E and Mixed-C column. The polymer samples were dissolved in HPLC grade chloroform (ca. 1.8 mg/mL) with 0.5% (v/v) *N,N*-dimethylethylenediamine added to the sample. The samples were passed through 0.45 μ m PTFE filter prior to injection. The flow rate for all samples was 1.0 mL/min and the injection volume was 50 μ L.

Polymerization Kinetics-

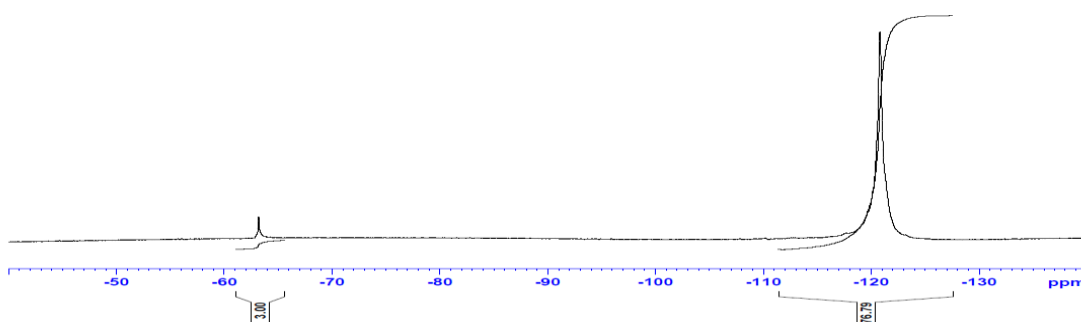
Both initiators were studied using the following conditions: In an inert N_2 atmosphere glove box, the PEMC monomer (**Mono-1**; 3.77 mmol) and the internal standard 1,4-dimethoxybenzene (DMB; 0.938 mmol) were added to an oven dried vial along with 4.0 mL of dry toluene. The corresponding initiator (18.8 μ mol; 200:1 Mono:Cat ratio) was then added to the stirring mixture along with 1.0 mL of dry toluene. The progress of the polymerization was monitored by taking aliquots (~0.2 mL) of the polymerization reaction at different time intervals and then quenching into 5 mL of MeOH. The concentration of monomer was monitored relative to DMB internal standard by GC-MS in order to measure percent conversion and $\ln([M]_0/[M])$. The polymer precipitate was filtered, washed with 50

mL methanol, and dried under high vacuum. The polymer was then redissolved in 1.0 M *N,N*-dimethylethylenediamine CHCl_3 solution and the molecular weight was determined by SEC. The *N,N*-dimethylethylenediamine additive is added to the injection solution in order to reduce the affinity of polycarbodiimides with the SEC stationary phase.

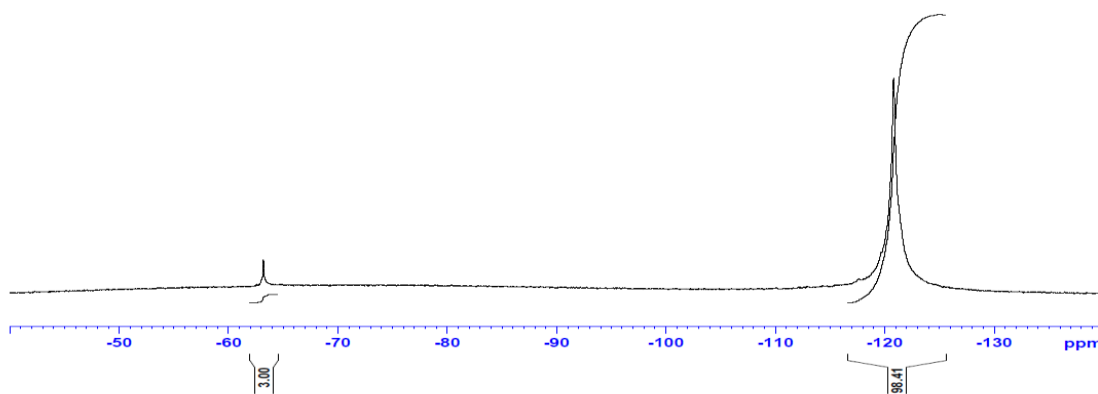
^{19}F NMR Traces of Poly-42 for M_n vs. $[\text{Mono-42}]/[\text{Ni-2}]$ -



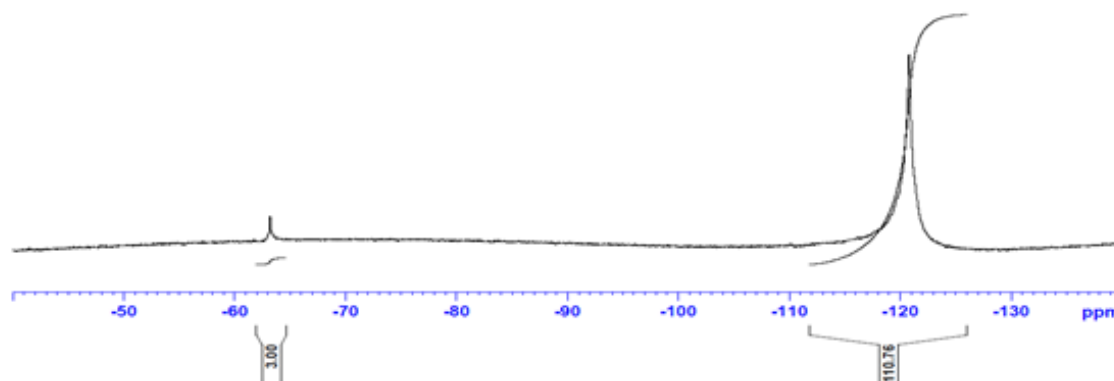
^{19}F NMR of **Poly-42** polymerized with the monomer:initiator ratio of $[\text{Mono-42}]/[\text{Ni-2}] = 50$.



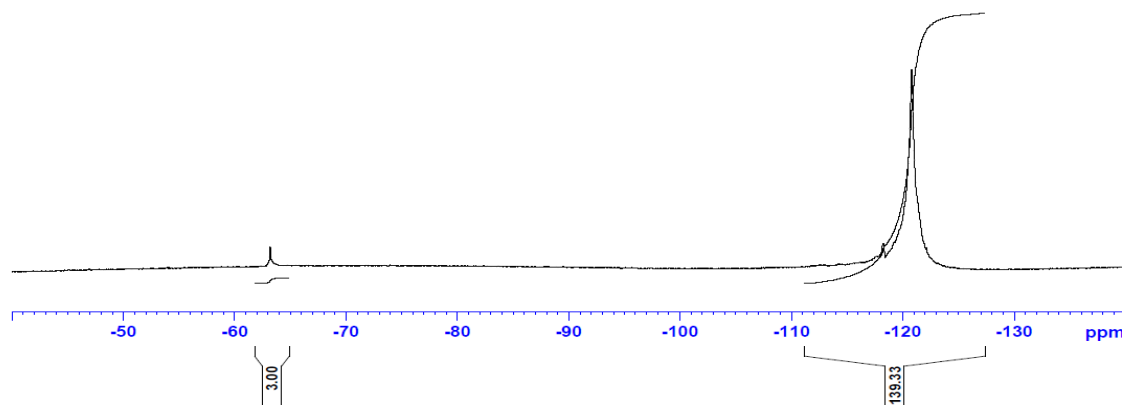
^{19}F NMR of **Poly-42** polymerized with the monomer:initiator ratio of $[\text{Mono-42}]/[\text{Ni-2}] = 73$.



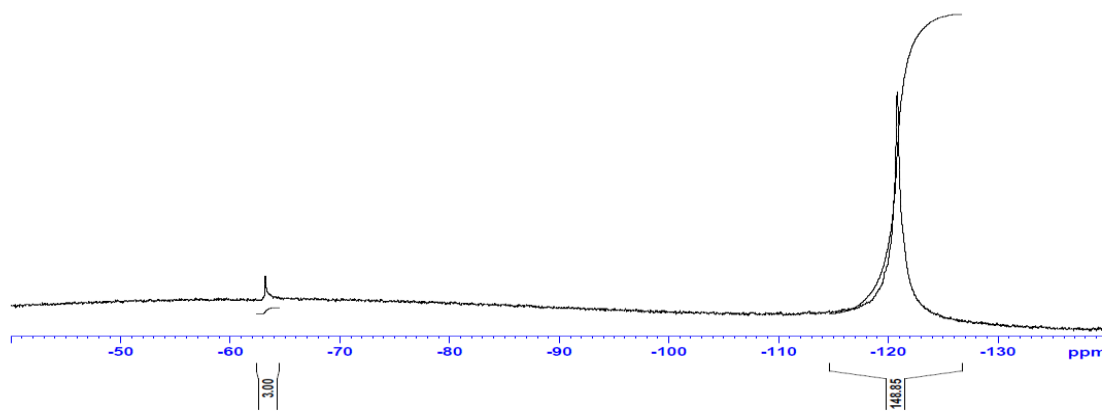
^{19}F NMR of **Poly-42** polymerized with the monomer:initiator ratio of $[\text{Mono-42}]/[\text{Ni-2}] = 94$.



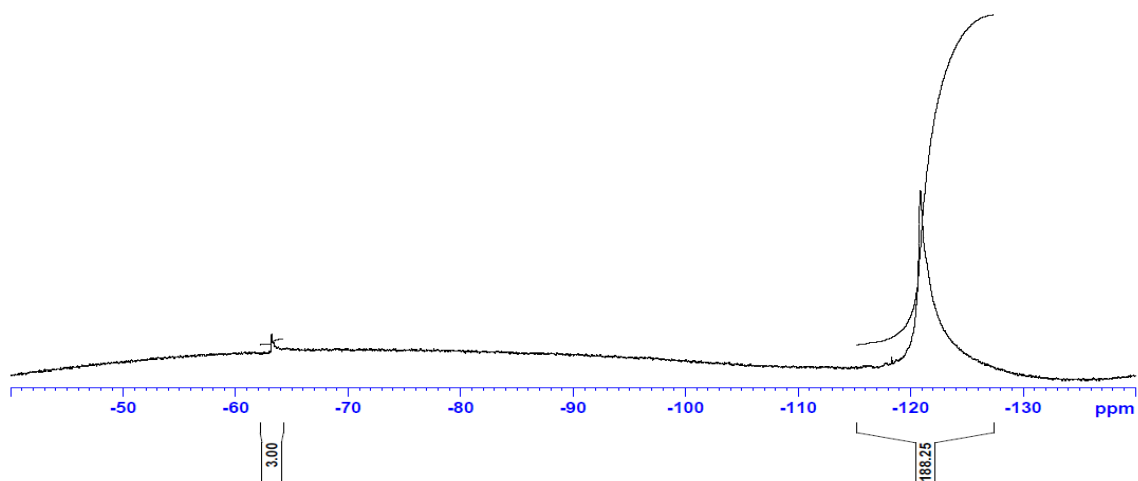
^{19}F NMR of **Poly-42** polymerized with the monomer:initiator ratio of $[\text{Mono-42}]/[\text{Ni-2}] = 125$.



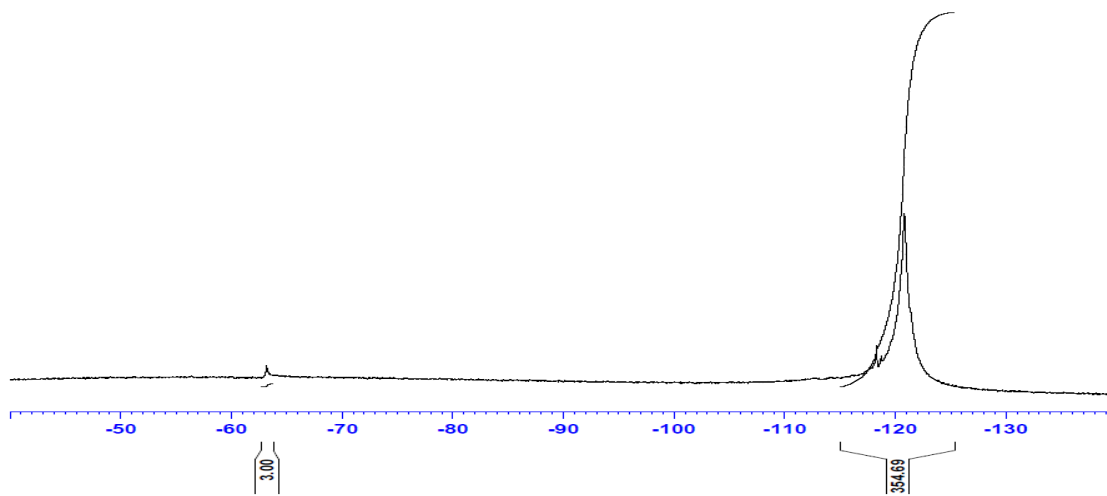
^{19}F NMR of **Poly-42** polymerized with the monomer:initiator ratio of $[\text{Mono-42}]/[\text{Ni-2}] = 158$.



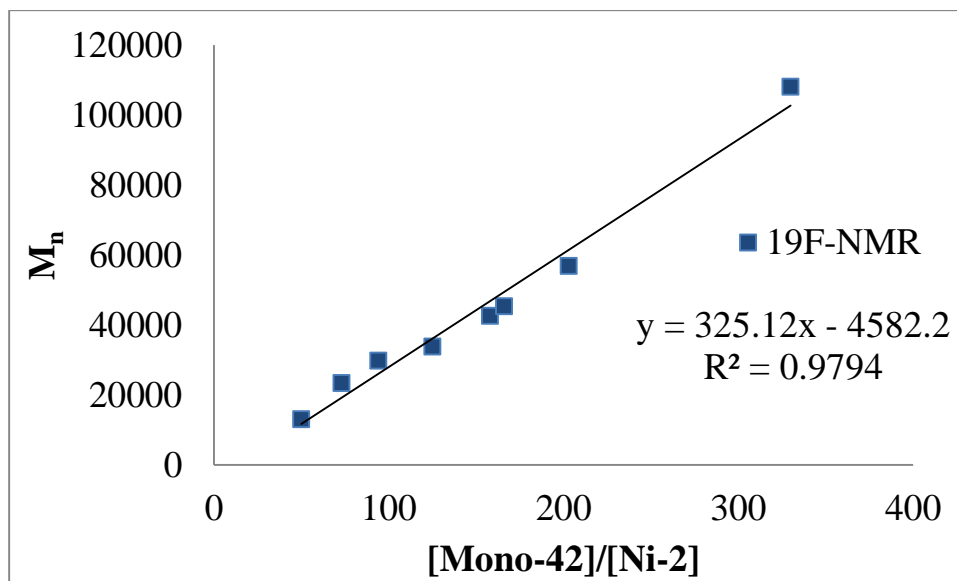
^{19}F NMR of **Poly-42** polymerized with the monomer:initiator ratio of $[\text{Mono-42}]/[\text{Ni-2}] = 166$.



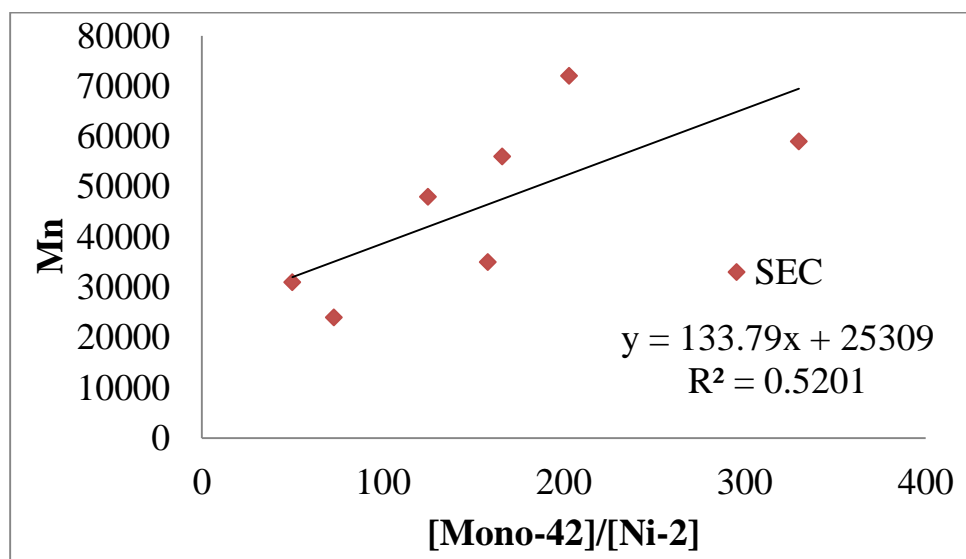
^{19}F NMR of **Poly-42** polymerized with the monomer:initiator ratio of $[\text{Mono-42}]/[\text{Ni-2}] = 203$.

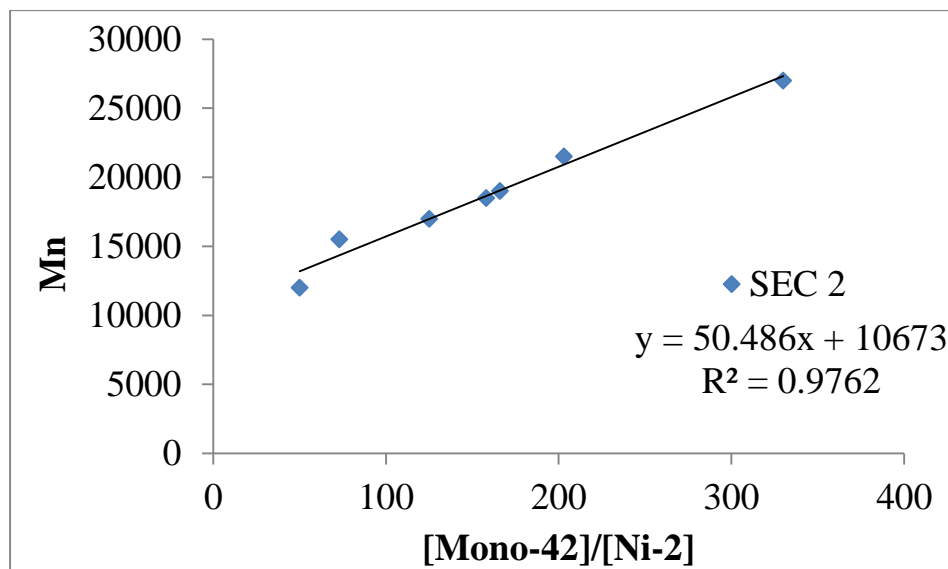


^{19}F NMR of **Poly-42** polymerized with the monomer:initiator ratio of $[\text{Mono-42}]/[\text{Ni-2}] = 330$.



GPC Results for different MW Poly-42 Samples-



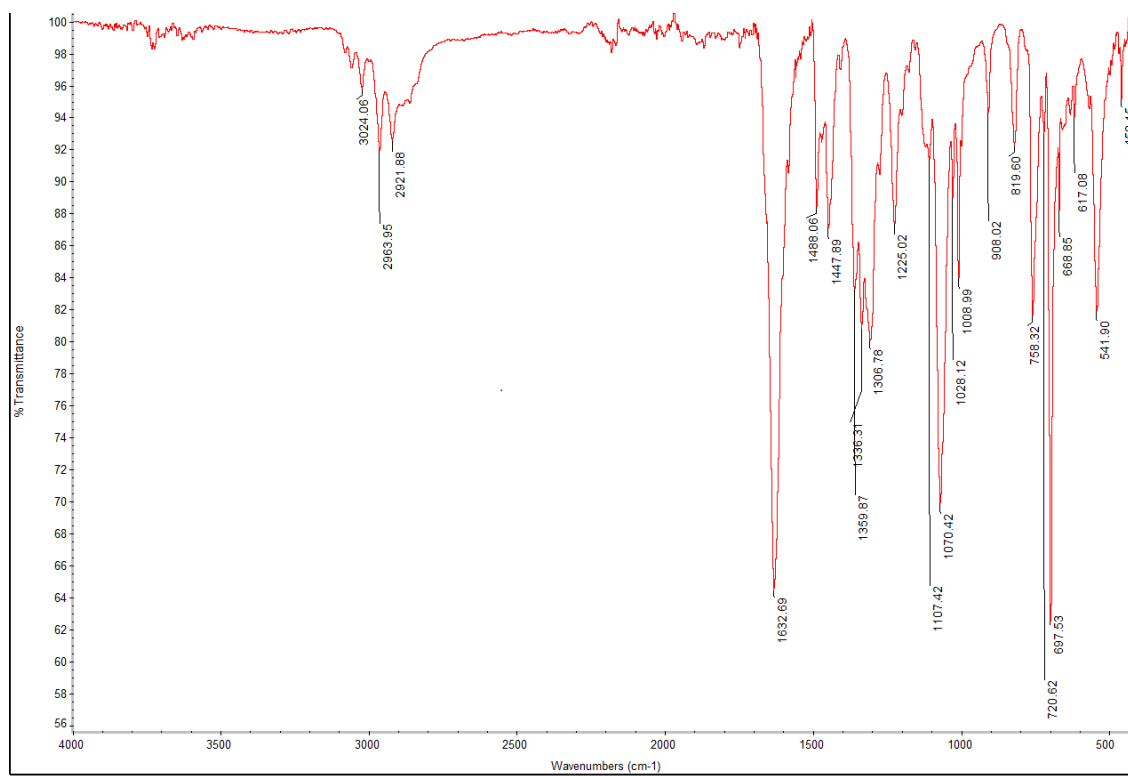
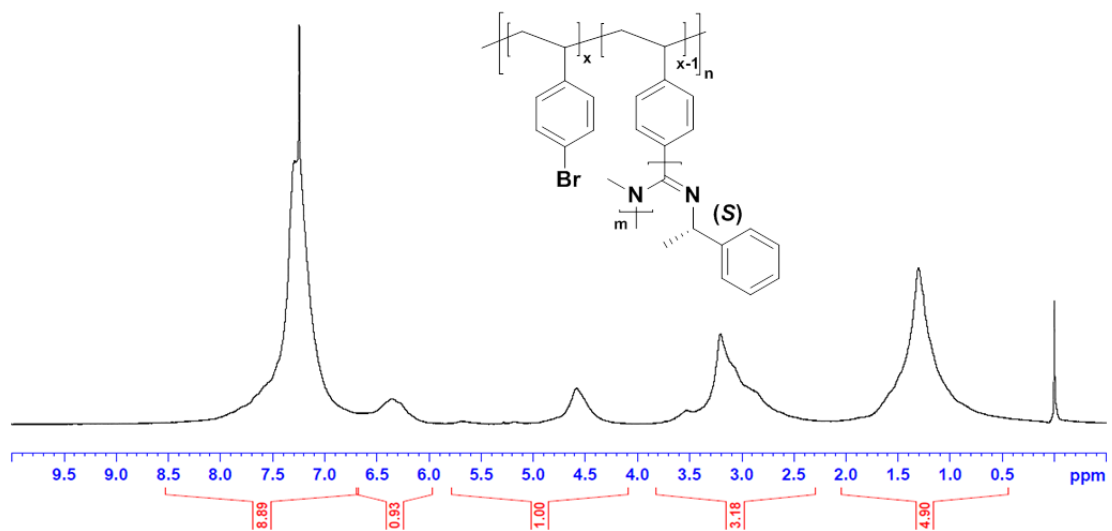


$[\text{Mono-42}]/[\text{Ni-2}]$	n (^{19}F NMR)	M_n (^{19}F NMR)	M_n (GPC 1)	PDI (GPC 1)	M_n (GPC 2)	PDI (GPC 2)
50	43	13.1 kDa	31.0 kDa	2.52	12.0 kDa	2.40
73	77	23.4 kDa	24.2 kDa	2.33	15.5 kDa	2.53
94	98	29.8 kDa	35.8 kDa	2.65	16.3 kDa	3.02
125	111	33.8 kDa	48.0 kDa	2.66	17.4 kDa	3.24
158	140	42.6 kDa	35.3 kDa	2.26	18.5 kDa	2.38
166	149	45.4 kDa	56.4 kDa	2.87	19.6 kDa	3.15
203	187	56.9 kDa	72.0 kDa	2.49	21.5 kDa	2.86
330	355	108 kDa	59.7 kDa	2.28	27.8 kDa	2.69

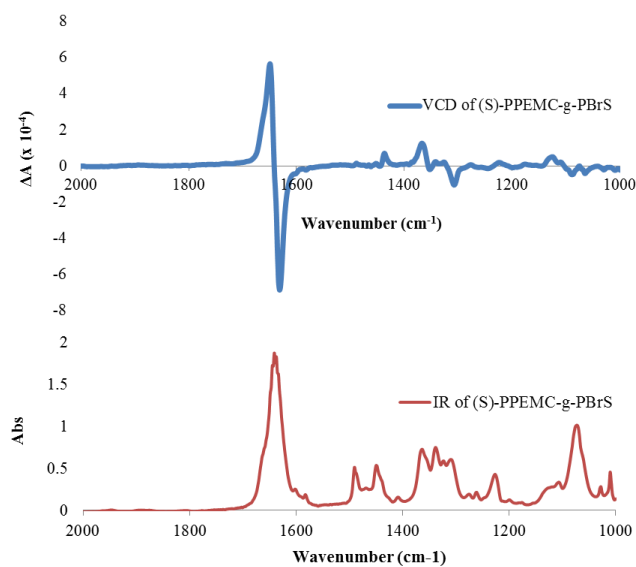
Synthesis/ Characterization of PBrS and grafted (R)-PPEMC-g-PBrS-

The poly(4-bromostyrene) ($M_n = 8800$, PDI = 1.08) was synthesized using previously reported RAFT polymerization of 4-bromostyrene in the presence of 2-cyano-2-propyldodecyltrithiocarbonate (RAFT agent) and AIBN as an initiator.⁵³ In an N₂ atmosphere glove box, an oven dried vial was charged with poly(4-bromostyrene) (0.408 g; 2.23 mmol of repeat units), triphenylphosphine (0.530 g; 2.02 mmol) and 5.0 mL of dry toluene. The Ni(COD)₂ (0.136 g; 0.493 mmol) was then added to the stirring solution and the reaction was allowed to proceed for ~1 hour monitoring the formation of the active initiation site by ³¹P NMR. The (S)-PEMC monomer (1.04 g; 6.49 mmol) was then added to the solution and the graft copolymerization was allowed to react for an additional 8 hrs. Upon completion, the copolymer product was precipitated in MeOH/ 1.0 v% DBU, collected by filtration as an beige solid, and dried under high vacuum overnight.

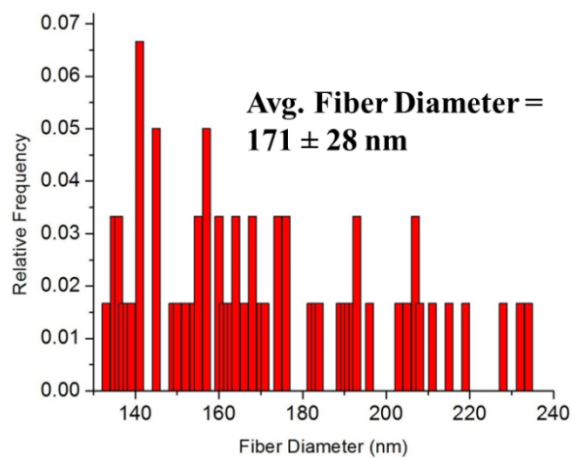
Yield: 1.291 g of off-white solid; 92% conversion. ATR-FTIR (cm⁻¹): 3024 (Ar-H, w), 2963 (alkyl-H, m), 2922 (alkyl-H,w), 1632 (C=N, s). ¹H NMR (500 MHz, CDCl₃): δ (ppm) 7.29 (PPEMC pendant Ph-H and PBrS Ar-H, overlapped broad s, 5H), 6.36 (PBrS Ar-H, broad s, 1H) 5.12 (benzyl-CH, broad s, 1H), 3.14 (N-CH₃, broad s, 3H), 1.24 (benzyl-CH₃ and PBrS backbone alkyl-H, broad s, 5H). SEC (Shimadzu Prominence): $M_n = 49600$ Da, $M_w = 116000$ Da, PDI = 2.34. Specific OR (c = 2.0 mg/mL, λ = 435 nm, 25 °C) [α] = -49.4°. TGA (T_{decomp}): 174 °C and 384 °C. DSC (T_g): 125 °C



VCD (top) and IR (bottom) of (S)-PPEMC-g-PBrS-



Statistical Analysis of Fiber Diameter using AFM micrograph of (S)-PPEMC-g-PBrS-



Attempted One Pot, Ni(II) Mediated Copolymerization of 3-Hexylthiophene and (R)-PEMC-

In an inert N₂ atmosphere glove box, an oven dried vial was charged with 2,5-dibromo-3-hexylthiophene and 2.0 mL of dry THF. Equimolar amounts of 1.0 M *tert*-butyl

magnesium chloride in THF were added to the stirring solution and allowed to react for 1.5 hours generating the active 2-bromo-3-hexyl-5-magnesioclorthiophene monomer. In a separate vial, stoichiometric amounts of 1,2-bis(diphenylphosphino)ethane (dppe) and **Ni-1** were dissolved in ~2 mL of THF and stirred for 1.5 hours at room temperature to allow for dppe ligand exchange to occur. The monomer solution was then added directly to the catalyst solution and the reaction mixture was allowed to stir for 2 hours. The (*R*)-PEMC (**Mono-1**) monomer was then sequentially added to the stirring mixture and allowed to react for an additional 4 hrs. Upon completion, the reaction vial was removed from the glove box and the polymer was precipitated from 1.0% (v/v) DBU solution in methanol. The crude polymer was isolated by filtration and further purified via soxlet extraction in methanol and hexanes overnight. Upon completion, the pure polymer was collected and dried under high vacuum.

5.9 References-

- (1) Flory, P. J. *J. Am. Chem. Soc.* **1940**, *62*, 1561-1565.
- (2) Szwarc, M. *Nature* **1956**, *178*, 1168-1169.
- (3) Anderson, B. C.; Andrews, G. D.; Arthur, P., Jr.; Jacobson, H. W.; Melby, L. R.; Playtis, A. J.; Sharkey, W. H. *Macromolecules* **1981**, *14*, 1599-1601.
- (4) Istratov, V.; Kautz, H.; Kim, Y.-K.; Schubert, R.; Frey, H. *Tetrahedron* **2003**, *59*, 4017-4024.
- (5) Goodwin, A.; Novak, B. M. *Macromolecules* **1994**, *27*, 5520-5522.
- (6) Matyjaszewski, K.; Tsarevsky, N. V. *Nat. Chem.* **2009**, *1*, 276-288.
- (7) Matyjaszewski, K.; Xia, J. *Chem. Rev.* **2001**, *101*, 2921-2990.
- (8) Wang, J.-S.; Matyjaszewski, K. *J. Am. Chem. Soc.* **1995**, *117*, 5614-5615.

- (9) Chiefari, J.; Chong, Y. K.; Ercole, F.; Krstina, J.; Jeffery, J.; Le, T. P. T.; Mayadunne, R. T. A.; Meijs, G. F.; Moad, C. L.; Moad, G.; Rizzardo, E.; Thang, S. H. *Macromolecules* **1998**, *31*, 5559-5562.
- (10) Chong, Y. K.; Krstina, J.; Le, T. P. T.; Moad, G.; Postma, A.; Rizzardo, E.; Thang, S. H. *Macromolecules* **2003**, *36*, 2256-2272.
- (11) Perrier, S.; Takolpuckdee, P. *J. Polym. Sci., Part A: Polym. Chem.* **2005**, *43*, 5347-5393.
- (12) Benoit, D.; Chaplinski, V.; Braslau, R.; Hawker, C. J. *J. Am. Chem. Soc.* **1999**, *121*, 3904-3920.
- (13) Hawker, C. J.; Bosman, A. W.; Harth, E. *Chem. Rev.* **2001**, *101*, 3661-3688.
- (14) Cunningham, M. F. *Prog. Polym. Sci.* **2008**, *33*, 365-398.
- (15) David, G.; Boyer, C.; Tonnar, J.; Ameduri, B.; Lacroix-Desmazes, P.; Boutevin, B. *Chem. Rev.* **2006**, *106*, 3936-3962.
- (16) Bunz, U. H. F. *Macromol. Rapid Comm.* **2009**, *30*, 772-805.
- (17) Rehahn, M.; Schlüter, A.-D.; Wegner, G.; Feast, W. J. *Polymer* **1989**, *30*, 1060-1062.
- (18) Heitz, W.; Bruegging, W.; Freund, L.; Gailberger, M.; Greiner, A.; Jung, H.; Kampschulte, U.; Niessner, N.; Osan, F.; et, a. *Makromol. Chem.* **1988**, *189*, 119-127.
- (19) Chen, T.-A.; Wu, X.; Rieke, R. D. *J. Am. Chem. Soc.* **1995**, *117*, 233-244.
- (20) Bielawski, C. W.; Grubbs, R. H. *Prog. Polym. Sci.* **2007**, *32*, 1-29.
- (21) Lynn, D. M.; Kanaoka, S.; Grubbs, R. H. *J. Am. Chem. Soc.* **1996**, *118*, 784-790.
- (22) Kennemur, J. G.; Novak, B. M. *Polymer* **2011**, *52*, 1693-1710.
- (23) Patten, T. E.; Novak, B. M. *Macromolecules* **1993**, *26*, 436-439.
- (24) Nolte, R. J. M.; Van, B. A. J. M.; Drenth, W. *J. Am. Chem. Soc.* **1974**, *96*, 5932-5933.
- (25) Schwartz, E.; Koepf, M.; Kitto, H. J.; Nolte, R. J. M.; Rowan, A. E. *Polym. Chem.* **2011**, *2*, 33-47.

- (26) Kim, Y.-J.; Sato, R.; Maruyama, T.; Osakada, K.; Yamamoto, T. *J. Chem. Soc., Dalton Trans.* **1994**, 0, 943-948.
- (27) Lanni, E. L.; Locke, J. R.; Gleave, C. M.; McNeil, A. J. *Macromolecules* **2011**, *44*, 5136-5145.
- (28) Tkachov, R.; Senkovskyy, V.; Komber, H.; Sommer, J.-U.; Kiriy, A. *J. Am. Chem. Soc.* **2010**, *132*, 7803-7810.
- (29) Traina, C. A.; Bakus Ii, R. C.; Bazan, G. C. *J. Am. Chem. Soc.* **2011**, *133*, 12600-12607.
- (30) Palermo, E. F.; McNeil, A. J. *Macromolecules* **2012**, *45*, 5948-5955.
- (31) Sheina, E. E.; Liu, J.; Iovu, M. C.; Laird, D. W.; McCullough, R. D. *Macromolecules* **2004**, *37*, 3526-3528.
- (32) Yokoyama, A.; Miyakoshi, R.; Yokozawa, T. *Macromolecules* **2004**, *37*, 1169-1171.
- (33) Ameri, T.; Dennler, G.; Lungenschmied, C.; Brabec, C. J. *Energy Environ. Sci.* **2009**, *2*, 347-363.
- (34) O'Reilly, R. K.; Joralemon, M. J.; Hawker, C. J.; Wooley, K. L. *J. Polym. Sci., Part A: Polym. Chem.* **2006**, *44*, 5203-5217.
- (35) Smeets, A.; Van den Bergh, K.; De Winter, J.; Gerbaux, P.; Verbiest, T.; Koeckelberghs, G. *Macromolecules* **2009**, *42*, 7638-7641.
- (36) Matyjaszewski, K.; Miller, P. J.; Pyun, J.; Kickelbick, G.; Diamanti, S. *Macromolecules* **1999**, *32*, 6526-6535.
- (37) Kreutzer, G.; Ternat, C.; Nguyen, T. Q.; Plummer, C. J. G.; Mnson, J.-A. E.; Castelletto, V.; Hamley, I. W.; Sun, F.; Sheiko, S. S.; Herrmann, A.; Ouali, L.; Sommer, H.; Fieber, W.; Velazco, M. I.; Klok, H.-A. *Macromolecules* **2006**, *39*, 4507-4516.
- (38) Zhang, W.; Fang, B.; Walther, A.; Mueller, A. H. E. *Macromolecules* **2009**, *42*, 2563-2569.
- (39) von Werne, T. A.; Germack, D. S.; Hagberg, E. C.; Sheares, V. V.; Hawker, C. J.; Carter, K. R. *J. Am. Chem. Soc.* **2003**, *125*, 3831-3838.

- (40) Khanduyeva, N.; Senkovskyy, V.; Beryozkina, T.; Bocharova, V.; Simon, F.; Nitschke, M.; Stamm, M.; Groetzschel, R.; Kiriya, A. *Macromolecules* **2008**, *41*, 7383-7389.
- (41) Senkovskyy, V.; Tkachov, R.; Beryozkina, T.; Komber, H.; Oertel, U.; Horecha, M.; Bocharova, V.; Stamm, M.; Gevorgyan, S. A.; Krebs, F. C.; Kiriya, A. *J. Am. Chem. Soc.* **2009**, *131*, 16445-16453.
- (42) DeSousa, J. D.; Novak, B. M. *ACS Macro Lett.* **2012**, *1*, 672-675.
- (43) Reuther, J. F.; DeSousa, J. D.; Novak, B. M. *Macromolecules* **2012**, *45*, 7719-7728.
- (44) Kim, J.; Novak, B. M.; Waddon, A. J. *Macromolecules* **2004**, *37*, 8286-8292.
- (45) Tang, H.-Z.; Novak, B. M.; He, J.; Polavarapu, P. L. *Angew. Chem., Int. Ed.* **2005**, *44*, 7298-7301.
- (46) Tang, H.-Z.; Garland, E. R.; Novak, B. M.; He, J.; Polavarapu, P. L.; Sun, F. C.; Sheiko, S. S. *Macromolecules* **2007**, *40*, 3575-3580.
- (47) Fischer, H.; Poser, S. *Acta Polymerica* **1996**, *47*, 413-428.
- (48) Poser, S.; Fischer, H.; Arnold, M. *Progress in Polymer Science* **1998**, *23*, 1337-1379.
- (49) Nieh, M.-P.; Goodwin, A. A.; Stewart, J. R.; Novak, B. M.; Hoagland, D. A. *Macromolecules* **1998**, *31*, 3151-3154.
- (50) Hidai, M.; Kashiwagi, T.; Ikeuchi, T.; Uchida, Y. *J. Organometal. Chem.* **1971**, *30*, 279-282.
- (51) Otsuka, S.; Nakamura, A.; Yoshida, T.; Naruto, M.; Ataka, K. *J. Am. Chem. Soc.* **1973**, *95*, 3180-3188.
- (52) Ge, S.; Hartwig, J. F. *J. Am. Chem. Soc.* **2011**, *133*, 16330-16333.
- (53) De Brouwer, H.; Schellekens, M. A. J.; Klumperman, B.; Monteiro, M. J.; German, A. L. *J. Polym. Sci., Part A: Polym. Chem.* **2000**, *38*, 3596-3603.

CHAPTER 6: Synthesis and Self-Assembly of Novel Rod-Coil Block Copolymers with Chiral Polycarbodiimide Segments

6.1 Background on Rod-Coil Block Copolymers-

The tunable self-assembly and microphase separation of conventional coil-coil block copolymer have been studied and modelled extensively.^{1,2} The ability to covalently bind polymers of varying composition and structure allows for the combination of polymer properties many times with synergistic effects and expanded function. The self-assembly of these macromolecules is governed by a variety of non-covalent forces such as hydrophobic/hydrophilic interactions, electrostatic interactions, hydrogen bonding, and microphase separation. The synthesis of rigid rod-*b*-random coil block copolymers, however, has recently attracted significant attention due to their unique capabilities to form stable supramolecular structures with a wide array of unique self-assembly behaviors observed in solution and the solid state.³⁻⁶ The rod-like macromolecules typically consist of polymeric/oligomeric helical and/or π -conjugated segments offering significant potential in organic electronics, biological mimics, drug-delivery, and high-performance composites.

The anisotropic nature of rigid-rod blocks characteristically results in lyotropic/thermotropic liquid crystallinity with nematic or highly-ordered, layered smectic mesophases adopted in solution and/or the melt.^{7,8} Therefore, the assembly behaviors of rod-coil block copolymers (RCPs) in solution and the solid state follow vastly different behaviors from that of coil-coil block copolymers (CCPs) arising from a combination of microphase

immiscibility of the two blocks and the self-organization behaviors of the rigid-rod block. Several different supramolecular assemblies can be fabricated depending on the structure and characteristics of the RCP including spherical micelles,⁹⁻¹³ non-spherical micelles,^{14,15} vesicles,^{10,12,16} helices,^{17,18} worm-like micelles,^{10,16} ribbons,^{19,20} microcapsules,^{21,22} tubules,²³ and nanofibrils.²⁴⁻²⁶

As previously mentioned, the incorporation of oligomeric/polymeric π -conjugated blocks into RCPs offers the potential to form well-defined shapes and geometries due to their unique self-assembly behaviors. A variety of structurally diverse systems have been incorporated into RCPs including oligophenylene,¹⁰ oligo(*p*-vinylene phenylene),¹⁹ oligo(*p*-benzamide),^{15,20} polyfluorene,^{27,28} polythiophene,²⁶ and poly(phenyl quinolone) (PPQ).^{21,22,29} Highlighting some interesting examples, Jenekhe et al. ignited the interest in this field publishing several articles detailing the self-assembly behaviors of PS-*b*-PPQ/ PPQ-*b*-PS-*b*-PPQ diblock and triblock RCPs. These novel materials assemble into large microcapsules with variable shape (spherical, cylindrical, vesicular, or lamellar) and size (typical diameters of 0.5 to 10 μm) depending on the mixed TFA:DCM and TFA:Toluene solvent ratios and solution drying rates. The basic heterocyclic nitrogen in the phenyl quinolone repeating unit allows for its good solubility of the PPQ block in TFA whereas PS is completely insoluble, hence the self-assembly. These capsules were shown to effectively encapsulate C₆₀ and C₇₀ fullerenes and were imaged by a variety of microscopy techniques including polarizing optical microscopy (POM), fluorescence microscopy, and scanning electron microscopy (SEM) (Figure 6.1). Slow evaporation of the solvent causes ordering of the C₇₀ encapsulated

microcapsules results in microporous polymer films with controlled pore size (ca. 3.4 ± 0.2 μm) and center-to-center hole periodicity (ca. 4.4 ± 0.2 μm).

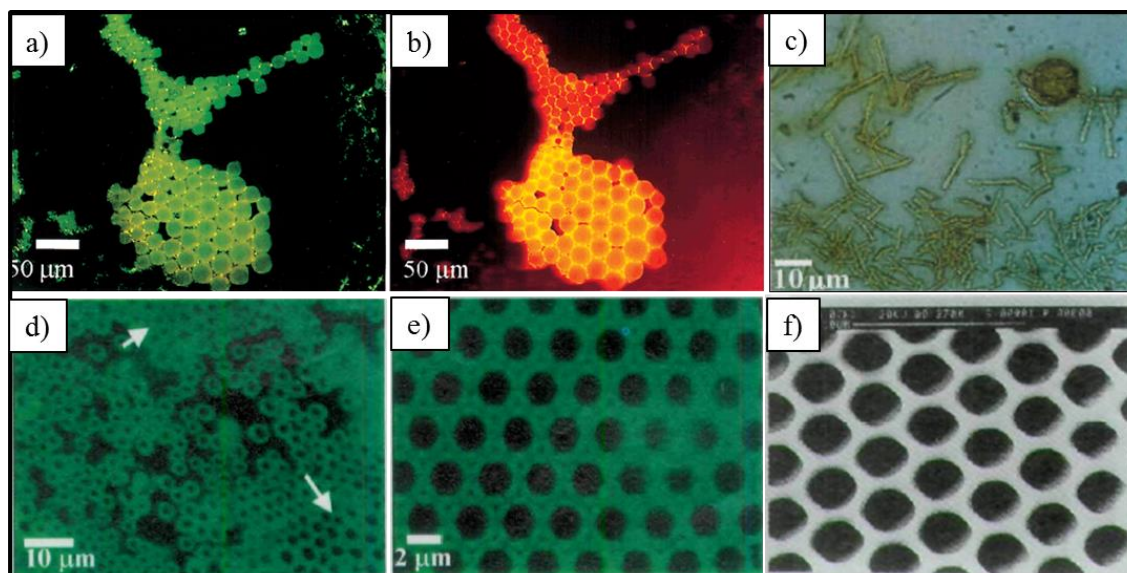


Figure 6.1- Polarizing optical micrographs (a and c) and fluorescence micrographs (b and d) of different PS-*b*-PPQ supramolecular assemblies including spheres (a,b), cylinders (c), and vesicles (d) used for the encapsulation of C₆₀ and C₇₀ fullerenes.^{21,22} Also shown are the fluorescence (e) and SEM (f) micrographs of the highly ordered, microporous thin-film resulting from the slow evaporation of the solvent.²⁹ (Copyright 1997 and 1998 AAAS, reprinted with permission)

More recently, in 2012, Park et al. synthesized a series of RCPs consisting of P3HT-*b*-PEG via CuAAC “click” reaction of alkyne terminated, rigid-rod P3HT and azide terminated, random-coil poly(ethylene glycol) (PEG).²⁶ In selective solvents for the hydrophilic PEG block such as methanol and water, these RCPs adopt interesting nanofibular aggregates with the rod-like P3HT relegated to the core of the nanofiber. Depending on the MW of the PEG blocks, the relative lengths of the nanofibers can be tuned with larger MW

PEG blocks resulting in short nanofibers with smaller aggregation numbers. Blending homopolymers of P3HT with P3HT-*b*-PEG causes very interesting aggregation behavior with the amphiphilic RCP effectively encapsulating all of the hydrophobic P3HT homopolymer within bundled and highly branched nanofibers (Figure 6.2). The proposed structure of these types of bundles consists of the RCPs either surrounding the bundled P3HT homopolymer nanofibers in parallel (in the bundled nanofiber structures; Figure 6.2c) or wrapping around the homopolymer nanofiber perpendicular to the length (in the branched structures; Figure 6.2d).

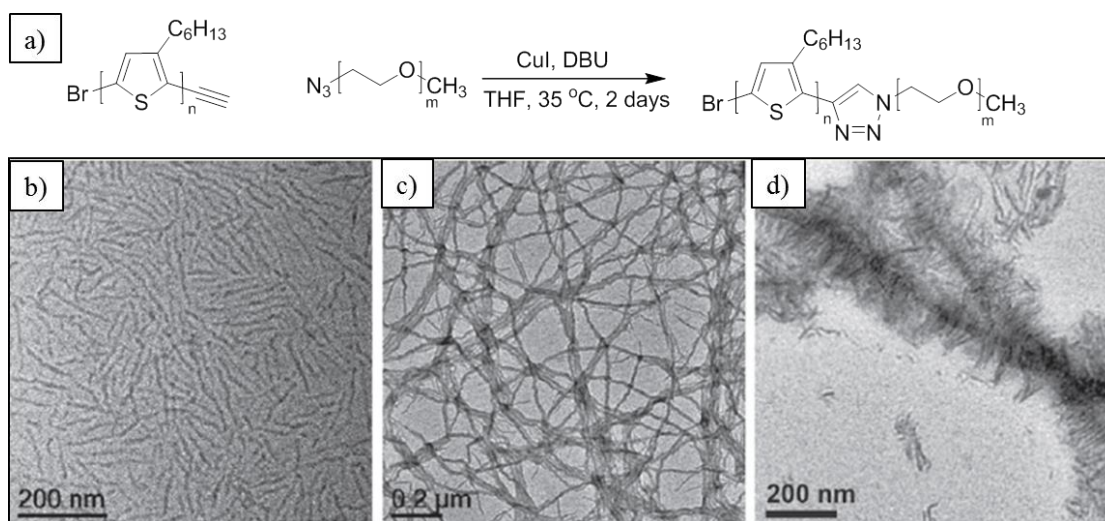


Figure 6.2- CuAAC “click” reaction of alkyne terminated P3HT and azide terminated PEG forming a novel, π -conjugated RCP (a). Also shown are TEM images of resulting nanofiber aggregates (b) of copolymer cast from water, bundled nanofibers (c) of RCP and P3HT homopolymer blends cast from methanol, and highly branched superstructures of 480:1 molar ratio RCP: P3HT homopolymer cast from water/ methanol mixtures. (Copyright 2012 American Chemical Society, reprinted with permission)²⁶

The incorporation of rigid-rod, helical macromolecules into RCPs have also recently attracted significant interest from researchers again due to their highly unique, supramolecular assemblies adopted in solution and the solid state. Polypeptides are the most typical helical, rigid-rod block incorporated into RCPs including such systems as poly(γ -benzyl-L-glutamate) (PBLG),^{8,17,18,24,25} poly(L-lysine),^{14,16} poly(L-glutamic acid),⁹ and poly(γ -diethyleneglycol-L-glutamate).²³ Synthetic helical polymers have been slow to make the transition into RCPs with the exception of the incorporation poly(*n*-hexyl isocyanate) (PHIC) into a variety of random-coil systems such as PS³⁰ and PEG.^{7,12,13,31} The PHIC-*b*-PS was one of the first helical-*b*-random coil copolymers reported, in 1995 by Thomas et al., and was synthesized by sequential anionic polymerizations.³⁰ This polymer adopts very unique “zig-zag” thin film morphologies cast from toluene as evident by TEM. The most studied rod-block, by far, for this class of RCP is poly(γ -benzyl-L-glutamate) (PBLG) due to its simple synthesis and biologically benign nature. In two recent communications, Lin et al. reported the directed self-assembly of PBLG-*b*-PEG and blends of PBLG-*b*-PEG and high MW PBLG in THF-H₂O mixtures.^{17,18} The PBLG-*b*-PEG block copolymers adopt simple, spherical micelles (Figure 6.3a) in THF/DMF-water solutions but, when blended with high MW PBLG homopolymer (ca. $M_n = 520$ kDa), the homopolymers are encapsulated in large supramolecular helical/ring aggregates at ratios of 100:15 RCP: PBLG homopolymer and 25 v% water content (Figure 6.3b and c). AFM analysis of the supramolecular helical aggregates reveals an average diameter of 140 nm with a helical pitch of 80 nm.

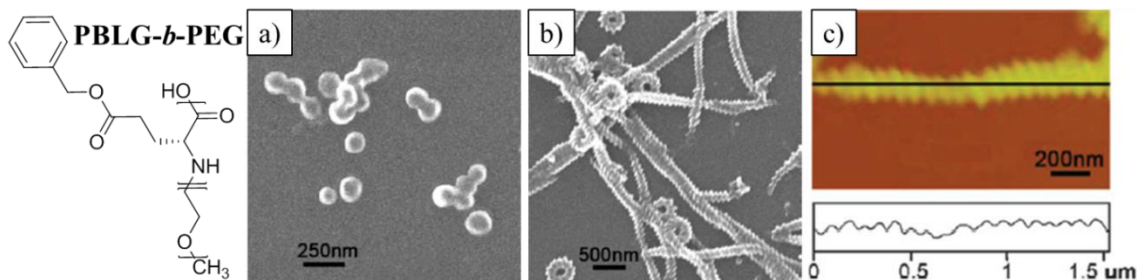


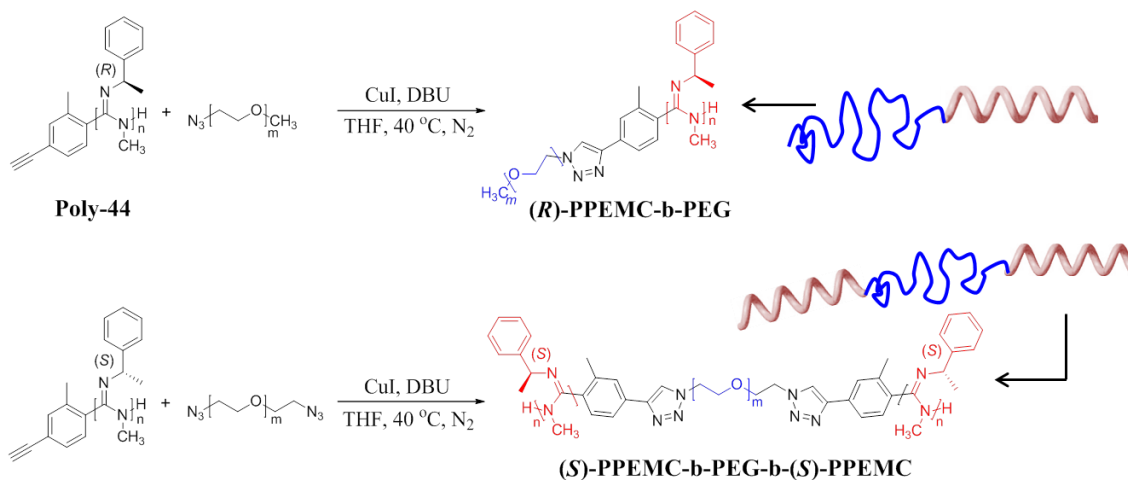
Figure 6.3- Structure of PBLG-*b*-PEG; TEM (a and b) and height AFM (c) micrographs of spherical micelles (a) adopted by PBLG-*b*-PEG in THF/DMF-water solutions and helical ribbon/ ring aggregates (b and c) of RCP blended with high MW PBLG homopolymer. Also shown, with the AFM image, is the height step-function across the length of the helical aggregate showing the relative periodicity of the helical rotation, i.e., the helical pitch. (Copyright 2006 Royal Society of Chemistry, reprinted with permission)¹⁷

The previous chapter outlined the new, controlled “living” polymerization of carbodiimides with bis(triphenylphosphino)aryl nickel(II) bromide complexes. This polymerization technique allowed for the facile synthesis, when compared to their Ti(IV) counterparts, of alkyne and alkene functional nickel initiators (**Ni-3** and **Ni-4**, respectively) which were then used to synthesize polycarbodiimides with these latent reactive groups on the end of polymer chains. Taking advantage of efficient/ quantitative reactions such as copper-catalyzed alkyne-azide cycloaddition (CuAAC) “click” chemistry or hydrosilation provides a simple, new route to the formation of a novel class of helical-*b*-random coil RCPs with chiral, rigid-rod polycarbodiimide segments.

6.2 Synthesis of Amphiphilic PPEMC-*b*-PEG RCPs-

Using post-polymerization modifications of the functional alkyne end-groups in **Poly-44**, a series of amphiphilic RCPs was synthesized via CuAAC “click” reaction of the alkyne

moiety with commercially available, mono- and bis-azide terminated PEG (Scheme 6.1). The conversion of this reaction can be monitored by the disappearance of the azide stretching mode at 2107 cm^{-1} in the FTIR spectrum. Accurately controlling the stoichiometry of the two polymers proved to be challenging due to difficulties in determining the MW of polycarbodiimides using GPC. ^1H NMR integration of the *o*-methyl substituent on the end group relative to the methine hydrogen on the pendant group of the polymer provided accurate estimations of M_n for subsequent “click” post-polymerization modifications.



Scheme 6.1- Synthesis of amphiphilic (*R*)-PPEMC-*b*-PEG and (*S*)-PPEMC-*b*-PEG-*b*-(*S*)-PPEMC di- and tri- RCPs (*n* denotes number of polycarbodiimide repeat units and *m* denotes number of PEG repeat units) via CuAAC “click” reaction of functional end-groups.

Confirmation of the successful reaction, however, can be accomplished by GPC as evident by a single MW distribution (one peak) in the chromatogram and decreased retention time (increased MW). Two different methods of detection are available for this particular GPC instrument including both refractive index (RI) and UV-Vis absorbance detection. To

test different additives for decreasing the affinity of polycarbodiimides with the stationary phase, DBU was substituted for the *N,N*-dimethylethylenediamine used previously. The DBU additive was found to work even better at decreasing the adhesion of the polycarbodiimide chains to the PS stationary phase as evident by the lower PDI values observed. The GPC chromatogram of the **Poly-44** sample used for initial “click” reactions revealed a $M_n = 66.8$ kDa and PDI = 2.15 corresponding to $n = 417$ repeat unit long PPEMC₄₁₇ (using the RI detector). This value was significantly larger than the M_n value calculated from ¹H NMR (ca. $M_n = 43.9$ kDa). Again, we observe very large PDI values due to the aforementioned adhesion of polycarbodiimides on the polystyrene stationary phase.

After the attempted “click” reaction with 10 kDa and 20 kDa average MW (ca. $m = 225$ and 455, respectively) PEG- monoazide (PEG₂₂₅; PEG₄₅₅), the GPC chromatogram provided by the RI detector displays two peaks corresponding to two different MW distributions. The chromatogram from the UV-Vis detector displays only one peak, however, in both cases, suggesting that one of the peaks correlates with residual PEG homopolymer (see experimental section). This is due to the absence of any UV-Vis absorbance for PEG homopolymer at the wavelength of detection (254 nm). Using this detector, we can confirm that the other species present is the block copolymer due to the shift to lower retention time, i.e., higher MW, upon “click” reaction. The calculated MW for PPEMC₄₁₇-*b*-PEG₂₂₅ and PPEMC₄₁₇-*b*-PEG₄₅₅ via GPC shows $M_n = 100$ kDa and PDI = 2.13; $M_n = 125$ kDa and PDI = 1.98, respectively. These MW values are somewhat larger than the calculated values via ¹H NMR which could possibly be due to errors in the calculated M_n values from ¹H NMR due to the small S/N of the end group chemical shifts relative to the pendant groups. This would

also explain the presence of residual PEG after the reaction is complete. For this reason, lower MW PPEMC samples were synthesized to allow for more accurate calculations of M_n using ^1H NMR.

Two new samples of **Poly-44** were used in subsequent “click” coupling with PEG-mono- and bis-azide denoted (*S*)-PPEMC₁₄₆ ($n = 146$, $M_n = 23.4$ kDa by ^1H NMR; $M_n = 27.8$ kDa, PDI = 2.70 by GPC) and (*R*)-PPEMC₂₀₂ ($n = 202$, $M_n = 32.3$ kDa by ^1H NMR; $M_n = 36.3$ kDa, PDI = 2.01 by GPC). The (*R*)-PPEMC₂₀₂ was coupled with both PEG₂₂₅ and PEG₄₅₅ monoazides forming the two new block copolymers (*R*)-PPEMC₂₀₂-*b*-PEG₂₂₅ (**CoPoly-1**) and (*R*)-PPEMC₂₀₂-*b*-PEG₄₅₅ (**CoPoly-2**) with varying hydrophilicity. The GPC of the material following both “click” reactions shows a single MW distribution and a decrease in retention time using the chromatogram provided by the RI detector confirming the successful coupling of both blocks. The calculated M_n from GPC increases to 48.3 kDa and 53.8 kDa upon click reaction with PEG₂₂₅ and PEG₄₅₅, respectively. The “click” reaction of (*S*)-PPEMC₁₄₆ with PEG₄₅₅ bisazide was also confirmed by GPC forming (*S*)-PPEMC₁₄₆-*b*-PEG₄₅₅-*b*-(*S*)-PPEMC₁₄₆ triblock copolymer (**CoPoly-3**) with an increase in M_n to 65.4 kDa (PDI = 1.37) corresponding closely to the attachment of two PPEMC chains to the single PEG-bisazide. Additionally, in all cases, the PDI decreases upon “click” reaction due to the decrease in the relative amount of polycarbodiimide resulting in the decreased adhesion to the stationary phase. For all scans of GPC chromatograms and used for MW determination, see the experimental section. The tabulated MW data is summarized in Table 6.1.

Table 6.1- Summarized MW data for **Poly-44** and resulting copolymers synthesized via successful alkyne-azide “click” coupling of end groups.

^a Calculated using relative integration of *o*-methyl substituent on aryl end-group to the methine pendant group hydrogen. Block Copolymers M_n were determined from calculated M_n of **Poly-44** added with the M_n of each PEG block and the relative ratios were confirmed by ¹H NMR (*vide infra*).

^b Mole-fraction of polycarbodiimide block calculated with n from ¹H NMR.

<i>Polymer</i>	n^a (¹ H-NMR)	m (¹ H-NMR)	M_n^a (¹ H-NMR; kDa)	M_n (GPC; kDa)	<i>PDI</i> (GPC)	f_{rod}^b
PP EMC ₂₀₂	202	-	32.3	36.3	2.01	1.0
CoPoly-1	202	225	42.3	48.3	1.77	0.47
CoPoly-2	202	455	52.3	53.8	1.70	0.31
PP EMC ₁₄₆	146	-	23.4	27.8	2.70	1.0
CoPoly-3	146	455	66.8	65.4	1.37	0.39

The incorporation of the PEG blocks is apparent in the ¹H NMR spectra of the copolymers by the intense chemical shift at 3.57 ppm corresponding to the equivalent methylene protons on the PEG backbone (Figure 6.4). The *o*-methyl substituent and N-H end-groups are still visible, albeit very small in intensity, at 2.07 and 3.84 ppm, respectively. Also, the new peak associated with the methylene attached to the triazole is believed to be present at 3.20 ppm (shifted from 2.23 ppm in the ¹H NMR spectra of the azide terminated PEG) providing further evidence of successful “click” reaction. The relative integration of the PEG protons (4 per repeat unit) compared to the polycarbodiimide methine proton should provide a good estimate for the proportions of each block in the system. The calculated MWs of each homopolymer added together match closely with the expected proportions of each block in **CoPoly-1** and **CoPoly-2** with a relative integration of methine: PEG backbone protons equal to 1: 3.98 (~1:1 moles of PPEMC:PEG) and 1: 5.95 (~1:1.5 moles of PPEMC:PEG), respectively. The PEG protons in **CoPoly-5** appear in much greater intensity

(ca. 1: 25.1 methine: PEG protons or ~1:6 moles of PPEMC:PEG) with respect to the PPEMC protons and do not match up with the expected proportions from GPC. This suggests that there is excess PEG homopolymer present in the sample (despite the absence of such in GPC).

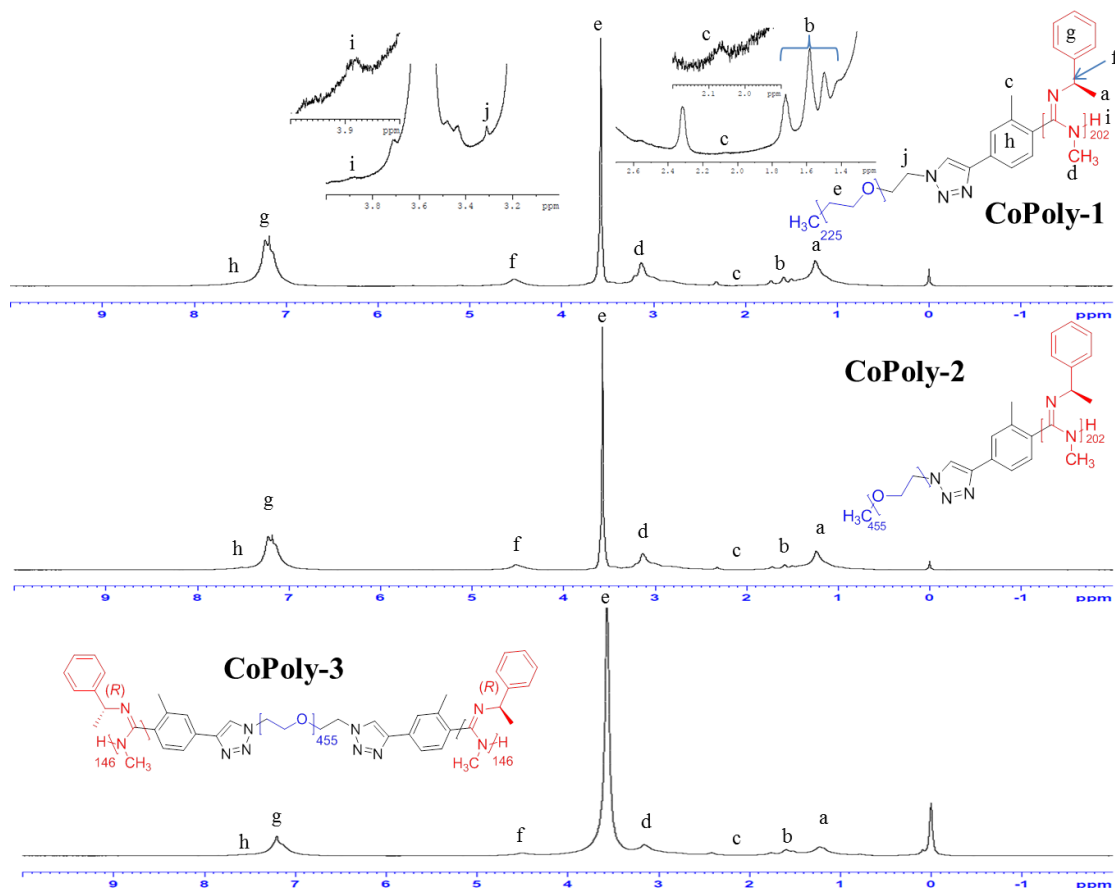


Figure 6.4- ^1H NMR spectra of **CoPoly-1, 2, and 3** with zoomed regions of **CoPoly-1**.

Interestingly, new, small peaks appear in the ^1H NMR spectra of all RCPs at 2.32, 1.73, 1.58, and 1.50 ppm (labeled b). These are peaks present at in the ^1H NMR of some

samples of PPEMC which leads us to believe these may be due to some impurities present in the sample. These chemical shifts are somewhat puzzling and led to the application of $^{13}\text{CDEPTQ135}$ NMR and 2D NMR techniques such as $^1\text{H}/^{13}\text{C}$ -HSQC to further elucidate the end-group protons from these mystery peaks for **CoPoly-2**. Comparing to literature ^1H and ^{13}C NMR chemical shifts of possible contaminants revealed that these peaks in the ^1H NMR are a result of residual DBU present in the system. Using $^1\text{H}/^{13}\text{C}$ -HSQC, the protons were correlated with several chemical shifts in the ^{13}C NMR spectra at 53.1, 49.6, 48.5, 37.4, and 28.6 ppm so these peaks can be ignored for the analysis of the block copolymers. The chemical shift at 3.20 ppm in the ^1H NMR spectra correlates with the methylene ^{13}C NMR chemical shift at 45.3 ppm which matches with the expected values for the methylene protons adjacent to the triazole unit. Additionally, the end-group aromatic protons with a chemical shift at 7.51 were found to be associated with overlapping ^{13}C chemical shifts at 127.7 and 127.5. The $^{13}\text{CDEPTQ135}$ NMR spectra and HSQC for **CoPoly-2** can be found in the experimental section.

Though PPEMC characteristically shows no thermal transitions via DSC prior to degrading at ca. 174 °C, the semi-crystalline nature of PEG typically results in a specific melting endotherms and crystallization exotherms in DSC. The same is true for **CoPoly-1**, **2**, and **3** with all three showing strong melting transitions upon heating to 60 – 62 °C and strong crystallization endotherms at 34 – 36 °C upon cooling in the DSC (Figure 6.5). The mass normalized energies associated with the melting transitions are largely identical for all copolymers with values of 83.5, 84.0, and 83.6 J/g for **CoPoly-1**, **2**, and **3**, respectively. These thermal transitions are believed to be the melting and crystallization of the PEG blocks

and will be important to consider when discussing the thin-film morphology which will be discussed herein.

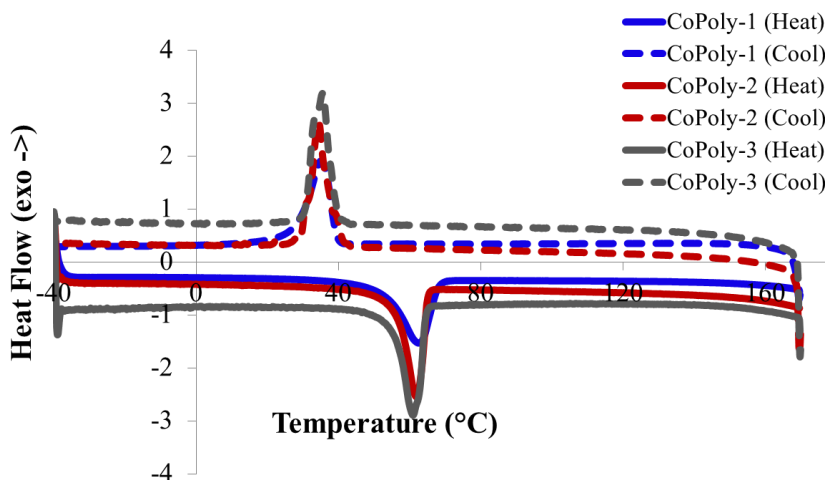


Figure 6.5- DSC thermograms of **CoPoly-1, 2, and 3.**

6.3 Surface Morphologies of PPEMC-*b*-PEG RCPs-

Each of the copolymers adopt unique, thin-film morphologies depending on the solvent used and annealing conditions. Without annealing or with only solvent annealing, the thin-films displayed very little order in the phase segregation of each block prompting the need for thermal annealing (see experimental section for TMAFM examples of unannealed films). The copolymers were spin-coated from THF solutions (ca. 5.0 mg/mL) onto highly-polished silicon wafers to provide a uniform application of the polymer across the entire surface. Both spin-coating and the use of the very flat silicon wafers are imperative in the collection of nicely-resolve images due to the necessity of uniformity in the surface.

Additionally, the added uniformity of spin-coating provides nearly identical thin-film characteristics throughout the entire surface. The films were then annealed at 65 °C (right above the observed melting temperature for all block copolymers) to allow for the films to order and reach their thermodynamically favored morphology.

CoPoly-1 and **CoPoly-2** display ordered nanofibular morphologies with varying phase separated domain sizes as observed by AFM (Figure 6.6). The domains of the chemically distinct blocks can be differentiated in the image by the different colors in the AFM phase image. These different colors correspond to the specific response from the AFM cantilever depending on the structural and mechanical properties of the material (i.e., the phase; see Section 4.1 for more details). Comparing the image for **CoPoly-1** and **CoPoly-2**, we observe a large increase in the lightly-colored yellow phase that is believed to be consequence of the increase in MW of the PEG block. For this reason, the yellow colored phase can be assigned to the hydrophilic PEG block and the dark-brown colored phase to the PPEMC block. To verify whether this morphology is indeed evidence of block copolymer formation, a 50:50 w% blend of PPEMC₁₄₆ and PEG₄₅₅ homopolymers was spin-coated from THF (final $c = 5.0$ mg/mL) and annealed at 65 °C to mimic the thin-film preparation of **CoPoly-1** and **2**. This film, like the RCPs, was imaged via AFM revealing completely different phase separation behaviors. The surface appeared to be composed of a single phase due to the higher surface energy polymer surface migrating during the annealing process (see experimental section).

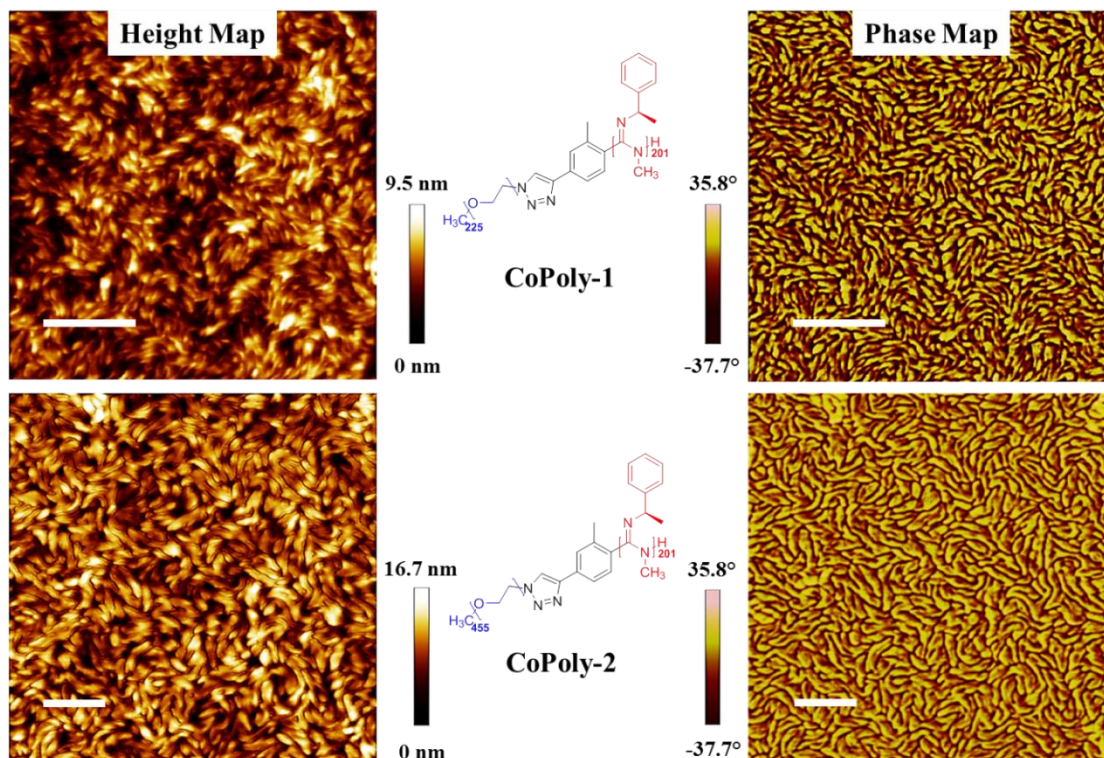


Figure 6.6- Height (left) and phase (right) AFM micrographs of **CoPoly-1** (scan size = 2 x 2 μm) and **CoPoly-2** (scan size = 3 x 3 μm) showing ordered nanofibular morphologies with distinct phase separation (white scale bar = 500 nm).

To compare the relative dimensions of each phase separated domain in the AFM micrographs of **CoPoly-1** and **2**, we must first estimate the approximate chain lengths for each block. For the rigid PPEMC block with 202 repeating units, the extended chain length is calculated to be 30 nm using the experimentally determined mass-per-length (M_L) value calculated using various light scattering experiments by Nieh et al.³² This is a good estimate for the MW range of this particular sample due to lack of conformational degrees of freedom resulting in large persistence length (P) characteristic of rigid-rod polymers (ca. $P = 42 \pm 8$ nm also determined by Nieh et al.).

For the high MW random-coil PEG chains, however, massive amounts of potential conformations in solution and the solid state are possible due to rotation about the sp^3 hybridized backbone. This makes the determination of the overall chain length somewhat more difficult and depends heavily on the solvent, temperature, MW, etc. The fully extended chain length of 10 kDa and 20 kDa PEG is about 56 nm and 114 nm, respectively, when using C-C bond length = 0.154 nm, C-O bond length = 0.143 nm, and C-C-O bond angle = 108° .¹³ The probability of the polymer chain being fully extended in solution or in the solid state is very low, however, so a more accurate model is necessary. In good solvents for PEG such as THF, the unperturbed root-mean-squared average end-to-end distance ($\langle r^2 \rangle^{1/2}$) can be estimated as a function of MW and viscosity using the Flory-Fox relationship as explained by Güner et al.³³ Using the calculated values in this article, we estimate the unperturbed chain-length of PEG₂₂₅ and PEG₄₅₅ to be 19 and 38 nm, respectively (Figure 6.7).

The use of AFM allows for the accurate, quantitative measurements of nanometer size features like that observed for **CoPoly-1** and **2**. Using the step function in the AFM software, one can easily differentiate the start and end of each phase separated domain (shown in the dotted line representation in Figure 6.7). The average diameter of the dark-brown PPEMC phase was measured experimentally for **CoPoly-1** and **2** to be 24 ± 5 and 24 ± 4 nm, respectively, matching closely with the calculated extended end-to-end distance of the PPEMC₂₀₂ chains. Additionally, the identical average diameter is expected since the same sample of PPEMC was used in the synthesis of both block copolymers. The yellow-colored PEG phase, however, nearly doubled in diameter when comparing the AFM of **CoPoly-1** and

2 (ca. 35 ± 9 and 61 ± 15 nm, respectively) as expected due to the doubling of MW of the respective PEG chains. The average diameters are larger than the calculated $\langle r^2 \rangle^{1/2}$ values for the PEG chains and larger standard deviation values are observed for the PEG phase diameter as measured by AFM. This is believed to be due to the presence of both mono- (lower bound diameter) and bi-layers (upper bound diameter) of the PEG chains throughout the thin-film (see cartoon representation in Figure 6.7).

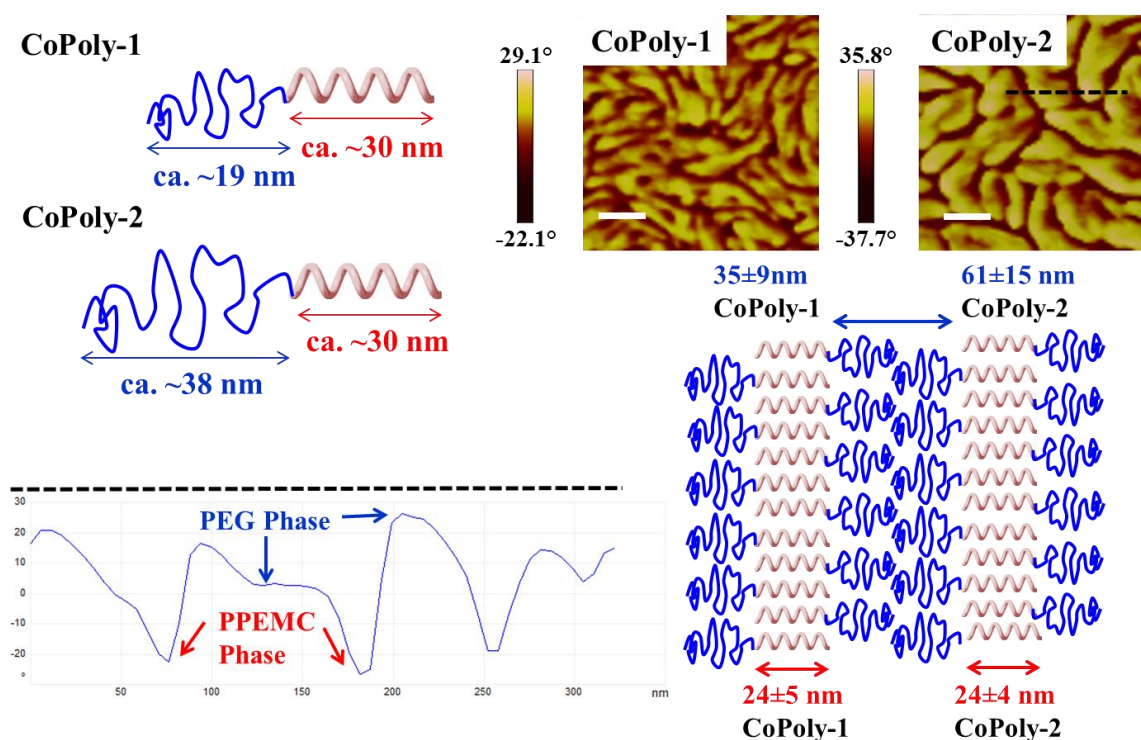


Figure 6.7- Cartoon Representations of CoPoly-1 and 2 with estimated chain dimensions are shown with the zoomed AFM phase image (scan size = 500 nm; white scale bar = 100 nm) and phase step function across the dotted-black line showing the distinct phases. Statistical analysis of the diameter for each phase results in the predicted morphology depicted above.

The thin-film morphology of **CoPoly-3** was vastly different than **CoPoly-1** and **2** with well-ordered macroporosity throughout the entire surface. Again, this film was prepared via spin-coating THF solution (ca. 5.0 mg/mL) onto silicon wafers and annealing at 65 °C for 24 hours. Without thermal annealing, no porosity was observed but somewhat similar phase segregation behaviors were confirmed (see experimental section). Upon thermal annealing, large craters with an average diameter of 832 ± 194 nm and depth of 82 ± 6 nm developed with largely the same phase throughout the entire film (Figure 6.8b). The development of these large craters suggests that there is a large amount of free-volume built into the polymer film upon spin-coating from THF. The diameters of these craters also are much larger than the dimensions of each block (ca. 22 nm for each PPEMC₁₄₆ block and again 38 nm for the unperturbed $\langle r^2 \rangle^{1/2}$ value of PEG₄₅₅) so simple phase separation can be ruled out as the real cause of this morphology. To see if this porosity persists in SEM, the copolymer was dissolved in THF, precipitated into hexanes, dried under vacuum, and annealed at 65 °C to mimic the sample preparation of the thin-films for AFM. The SEM micrograph of the bulk, annealed material also displayed similar macroporosity in regions of the bulk sample further corroborating the morphology viewed in AFM. The SEM of **CoPoly-1** and **2** subject to the same preparation procedure showed no porosity (see experimental section) suggesting that this property is specific to **CoPoly-3**.

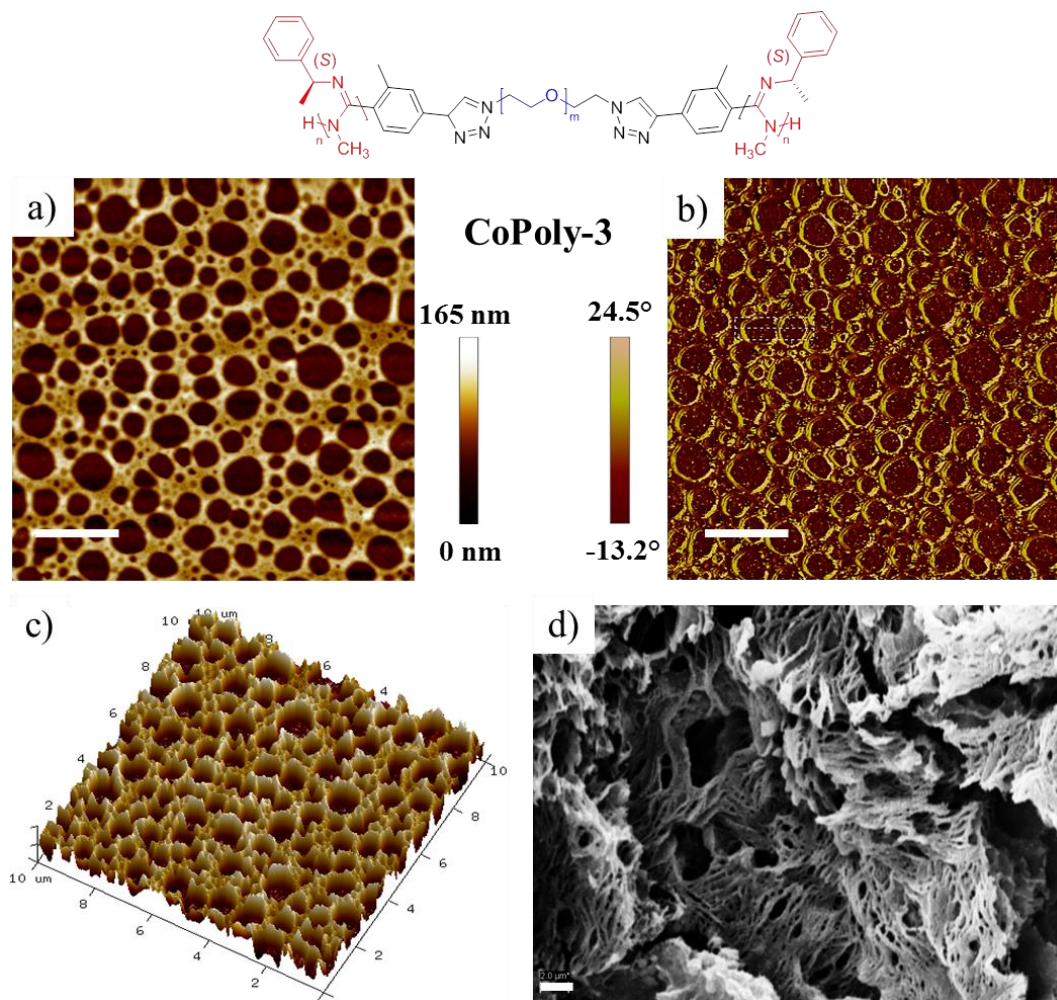


Figure 6.8- Height (2D in a and 3D in c) and phase (b) AFM micrograph (scan size = 10 x 10 μm) of **CoPoly-3** spin-coated from THF solution ($c = 5.0 \text{ mg/mL}$) and annealed at 65 $^{\circ}\text{C}$ displaying the macroporous morphology. The porous morphology is also observed in the SEM micrograph bulk polymer precipitated from THF and annealed at 65 $^{\circ}\text{C}$ (All white scale bars = 2.0 μm).

The origin of this is believed to be associated with specific aggregation behaviors of the **CoPoly-3** in THF solutions. This aggregation behavior was first noticed in the polarizing optical microscope (POM) images of **CoPoly-3** in concentrated THF solutions (ca. 30 and 40 wt%) where we observed large spherical aggregates believed to be microcapsule assemblies

(Figure 6.9). These same aggregates were not observed for **CoPoly-1** and **2** in concentrated THF solutions as evident by the black POM image suggesting the solution is completely isotropic (no order). Upon solvent evaporation, we propose that these microcapsule aggregates order themselves into a thin-film and are frozen into place when all the solvent is removed. The large diameters of these aggregates suggest that they possess a hollow interior which would explain the large amount of free-volume associated with the thin-film. Upon increasing the temperature to 65 °C, above the observed melting temperature (T_m) of **CoPoly-3**, the surrounding walls of the capsule (consisting of the copolymer ordered with the PPEMC chains on the interior of the bilayer) melted, filling the free-volume of the hollow interior, forming the sub-micron diameter craters observed in the AFM.

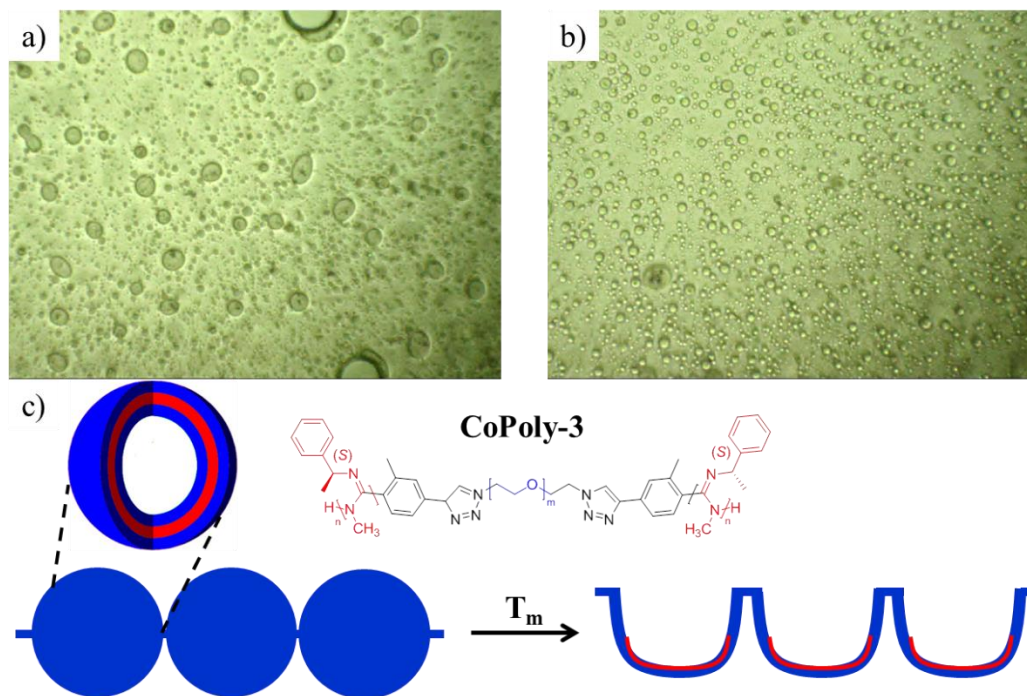


Figure 6.9- POM images of **CoPoly-3** in concentrated 30 wt% (a) and 40 wt% (b) THF solutions showing the large microcapsule aggregates (40x magnification). Also depicted (c) is the hypothesized ordering of the vesicles upon solvent evaporation and melting of the aggregates forming the large, sub-micron diameter craters observed in AFM.

In concentrated toluene solutions (ca. 30 wt%), these copolymers displayed liquid crystalline order adopting the chiral nematic (or cholesteric; N^*) mesophase as evident by the characteristic spherulite textures in the POM images. This LC order, however, was not persistent throughout the solution with large regions of isotropy evident for all copolymers under cross-polarizers (Figure 6.10).

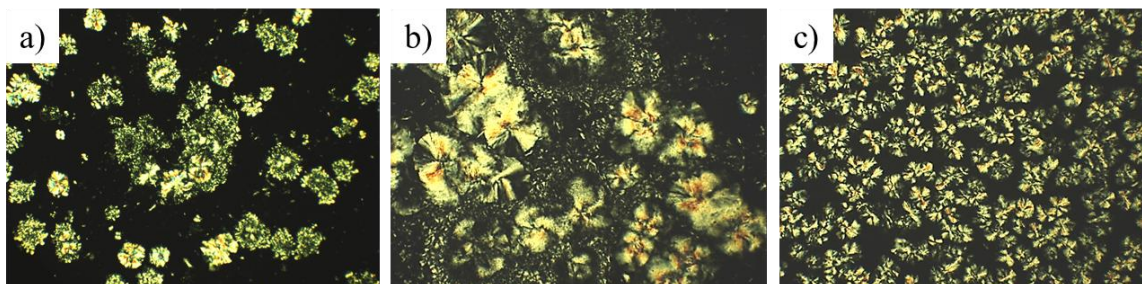


Figure 6.10- POM images (40x magnification) of **CoPoly-1** (a), **2** (b), and **3** (c) in concentrated toluene solutions (ca. 30 wt%) displaying the ordered, chiral nematic mesophase in portions of the solution.

The thin-film morphologies of the copolymers spin-coated from toluene ($c = 5.0$ mg/mL) and annealed at 65 °C display similar helical bundles believed to be aggregates of multiple RCP chains. These bundles are similar to that observed for (*R*)-PNOC spin-coated from and annealed in toluene (discussed in Chapter 4). The AFM phase images of each copolymer showed largely one phase (dark-brown) throughout the image correlating to the PPEMC blocks. Since toluene is a poor solvent for PEG, this is not surprising and is believed to be due to the suppression of the PEG blocks underneath the surface of the thin-film. The dimensions of these bundles were somewhat difficult to measure due to lower resolution in the resulting AFM images. Nonetheless, measurements were attempted to determine the average diameter of the clearer, individualized helical bundles in each image but these values are believed to be relatively rough estimates. All images showed around the same diameter for helical bundles with average values for **CoPoly-1**, **2**, and **3** equal to 35 ± 6 , 42 ± 9 , 41 ± 7 nm, respectively. The helical pitch of these bundles could not be measured, however, due to the low resolution of the image. In an attempt to individualize the helical bundles for more accurate measurements, more dilute solutions of toluene ($c = 1.0$ mg/mL) were spin-coated

onto the silicon wafers and imaged again using AFM. Unfortunately, no helical bundles were observed when spin-coated from these more dilute solutions suggesting that the bundling behavior only takes place at specific concentrations. The AFM height images for **CoPoly-1**, **2**, and **3** can be found in Figure 6.11.

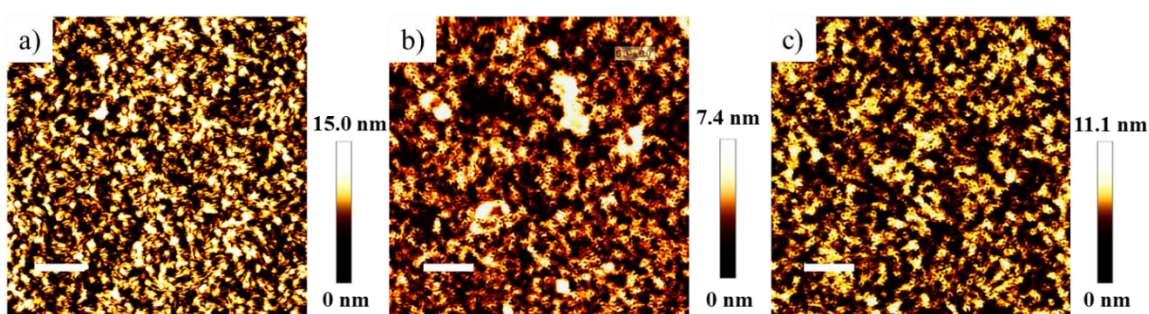


Figure 6.11- AFM height image of **CoPoly-1** (a), **2** (b), and **3** (c) spin-coated from toluene and annealed at 65 °C for 24 hour (scan size = 3 x 3 μm ; white scale bar = 500 nm).

Another very common method for characterizing surface composition/ properties is measuring the contact angle of specific liquids dropped on the thin-film surface. For the PPEMC-PEG copolymers, the contact angle of water droplets were measured on thin-films prepared following the same protocol used for AFM samples. Reported are both the advancing (maximum) contact angle (θ_{adv}) and receding (minimum) contact angle (θ_{rec}) to accurately reflect the surface composition. **CoPoly-1** and **2** spin-coat from THF and annealed at 65 °C have very similar water contact angles (both advancing and receding) to that of PPEMC homopolymer due to the tightly-packed morphology not allowing any surface reorganization to occur. The same was true for these copolymers spin-coated from toluene which is not unexpected since the surface composition by AFM seemed to be predominantly

polycarbodiimide. Interestingly, **CoPoly-3** showed much smaller advancing contact angles (ca. $\theta_{adv} = 39.7^\circ$) and the droplet irreversibly wetted the film suggesting that the surface composition is mainly PEG. This was also expected for the proposed morphology since the PEG blocks are the surrounding shell of the vesicle so, upon melting, the surface composition in and around the large craters is comprised of mostly PEG. **CoPoly-3** spin-coated from toluene and annealed in toluene vapor showed the largest hysteresis suggesting that the helical bundles are not as tightly bound for the triblock copolymer which allows for penetration of the water droplet and the surface migration of the PEG blocks (i.e., surface reorganization). The results of this analysis are shown in Table 6.2.

Table 6.2- Advancing and receding water contact angles of PPEMC-PEG block copolymer thin-films prepared via the same protocol used for AFM sample preparation

^a Did not recede due to the irreversible wetting of the water drop on the surface.

	<i>CoPoly-1</i> <i>from THF</i>	<i>CoPoly-1</i> <i>from Tol.</i>	<i>CoPoly-2</i> <i>from THF</i>	<i>CoPoly-2</i> <i>from Tol.</i>	<i>CoPoly-3</i> <i>from THF</i>	<i>CoPoly-3</i> <i>from Tol.</i>
θ_{adv}	96.3±0.8°	95.0±0.6°	98.9±1.4°	92.9±0.3°	39.7±0.8°	93.7±0.3°
θ_{rec}	62.1±1.3°	55.2±0.6°	62.8±1.4°	61.6±0.6°	N/A ^a	42.2±1.7°

6.4 Self-Assembly of PPEMC-PEG Copolymers Cast from THF/H₂O-

The amphiphilic character of these novel RCPs stems from the hydrophilic properties of the PEG coil-blocks and hydrophobic properties of the PPEMC rod-block. PEG polymers have good solubility in water and polar organic solvents such as methanol and ethanol whereas polycarbodiimides show no solubility. For this reason, these polymers should adopt specific self-assembly behaviors in selective polar solvents. One of the most popular and well-known methods for measuring particle size of aggregates in solution is dynamic light

scattering (DLS). In this technique, the scattering of light by particles in solution causes localized changes in refractive index and, in turn variations in intensity (I) which are evaluated using the second order normalized autocorrelation function $g_2(\tau)$ expressed in (1).

$$(1) \quad g_2(\tau) = \frac{G_2(\tau)}{\langle I \rangle^2}$$

In this equation, the term $\langle I \rangle^2$ is the average intensity, τ is the correlation time, and $G_2(\tau)$ is the temporal correlation function. This function is then related to a first order correlation function (2) where q refers to the scattering vector, D is the translational diffusion coefficient, and τ is the correlation time.

$$(2) \quad g_1(\tau) = -\exp(-q^2 D \tau)$$

The diffusion coefficient can then be applied to the Stokes-Einstein equation (3) to measure the hydrodynamic radius (R_h) of particles in solution where k_B is Boltzmann's constant, T is the absolute temperature, η is the viscosity of the solvent and again D is the diffusion coefficient.

$$(3) \quad R_h = \frac{k_B T}{6\pi\eta D}$$

This technique was first applied to **CoPoly-1**, **2**, and **3** dissolved in THF-H₂O mixtures to see whether large aggregates exist in solution. Two solvent combinations (all measurements were conducted at $c = 0.5$ mg/mL) were chosen including H₂O/ 10 v% THF and THF/ 10 v% H₂O to probe the effect of water content on R_h (Figure 6.12). The DLS plots for all copolymers display the same trend with larger aggregates present with only 10 v% of

H₂O in the THF solution. In the H₂O/ 10 v% THF solutions, aggregates were observed with radii of $R_h = 73.7 \pm 15.4$ nm, 121 ± 23.1 nm, and 111 ± 25.1 nm for **CoPoly-1**, **2**, and **3**, respectively. The R_h values for **CoPoly-1** and **2** closely reflected the calculated dimensions of the copolymer (ca. 49 nm and 78 nm, respectively) suggesting that the aggregates, with a diameter about twice the size of the individual chains, are most likely micellular in nature. In THF/ 10 v% H₂O, much larger aggregates were shown by DLS with the average hydrodynamic radii of **CoPoly-1**, **2**, and **3** equal to $R_h = 205 \pm 44.4$, 192 ± 70.2 , and 184 ± 44.7 nm, respectively. The structures of these aggregates are harder to determine by DLS since the diameters are significantly larger than the end-to-end chain dimensions of the copolymers so, to reveal the self-assembly behavior, AFM was employed. As a control, PPEMC₂₀₂ and PEG₄₅₅ homopolymers were dissolved in THF/ 10 v% H₂O (the maximum amount of water allowed before PPEMC precipitates from solution) and DLS was again performed (for plots see experimental section). The DLS of PPEMC displayed a single size distribution of 29.6 ± 9.7 nm which is substantially smaller than the aggregates observed for the RCPs and correlates with the calculated end-to-end distance of the PPEMC. Unexpectedly, the PEG₄₅₅ homopolymer actually displayed large aggregates by DLS with a size distribution of $R_h = 304 \pm 43.8$ nm in THF/ 10 v% H₂O which is strange considering PEG typically has very good solubility in THF and H₂O. These aggregates, however, have vastly different sizes than the copolymers providing further evidence of successful block copolymer formation.

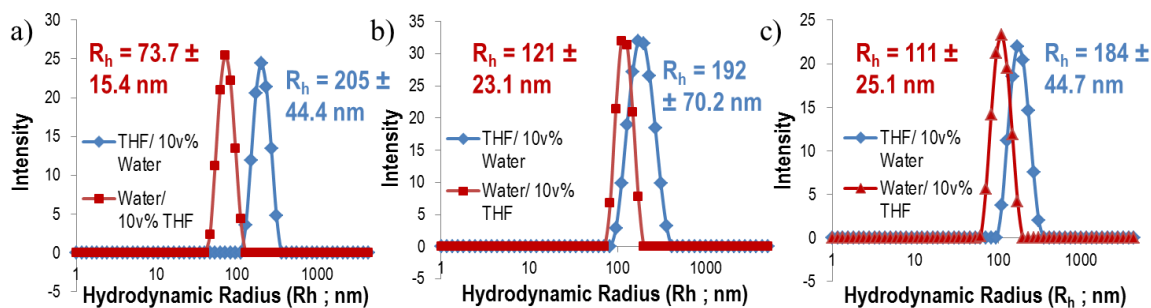


Figure 6.12- DLS plots of hydrodynamic radius (R_h) vs. scattering intensity for **CoPoly-1** (a), **2** (b), and **3** (c) in THF/ 10 v% water (blue line) and Water/ 10 v% THF (red line) showing the change in aggregation size and behavior as a function of water content ($c = 0.5$ mg/mL).

To image the specific, nanometer-scale aggregates of these copolymers, we utilized AFM to provide accurate, high-resolution images for the quantitative characterization of these assemblies. Solutions with the same solvent combinations and concentrations ($c = 0.5$ mg/mL) were spin-coated onto silicon wafers to quickly evaporate the solvent without significant alterations to the supramolecular structures. **CoPoly-1** was first spin-coated from dilute H₂O/ 10 v% THF solutions to image the smaller aggregate observed by DLS. The small amount of THF is necessary to dissolve the copolymer which is then injected into the appropriate amount of water so the final concentration equals 0.5 mg/mL (same preparation as the DLS solutions). The resulting AFM micrograph (Figure 6.13) displayed a large number of spherical micelle aggregates with an average diameter of 96.2 ± 16.0 nm by statistical analysis (sample size = 65 micelles). This diameter matches closely with the calculated end-to-end chain dimensions (ca. 49 nm) multiplied by two alluding to the micellular structure. The diameter provided by DLS (ca. 167 ± 27.2 nm) is larger than that observed in AFM but this is a typical observation in DLS due to the inclusion of the

surrounding solvation sphere in the calculated R_h value as explained by Mecartney et al.³⁴ The hypothesized structure of the micelle is also depicted in Figure 6.13d with the hydrophobic PPEMC chains making up the core of the micelle and the hydrophilic PEG chains consisting of the solvent exposed corona of the micelle.

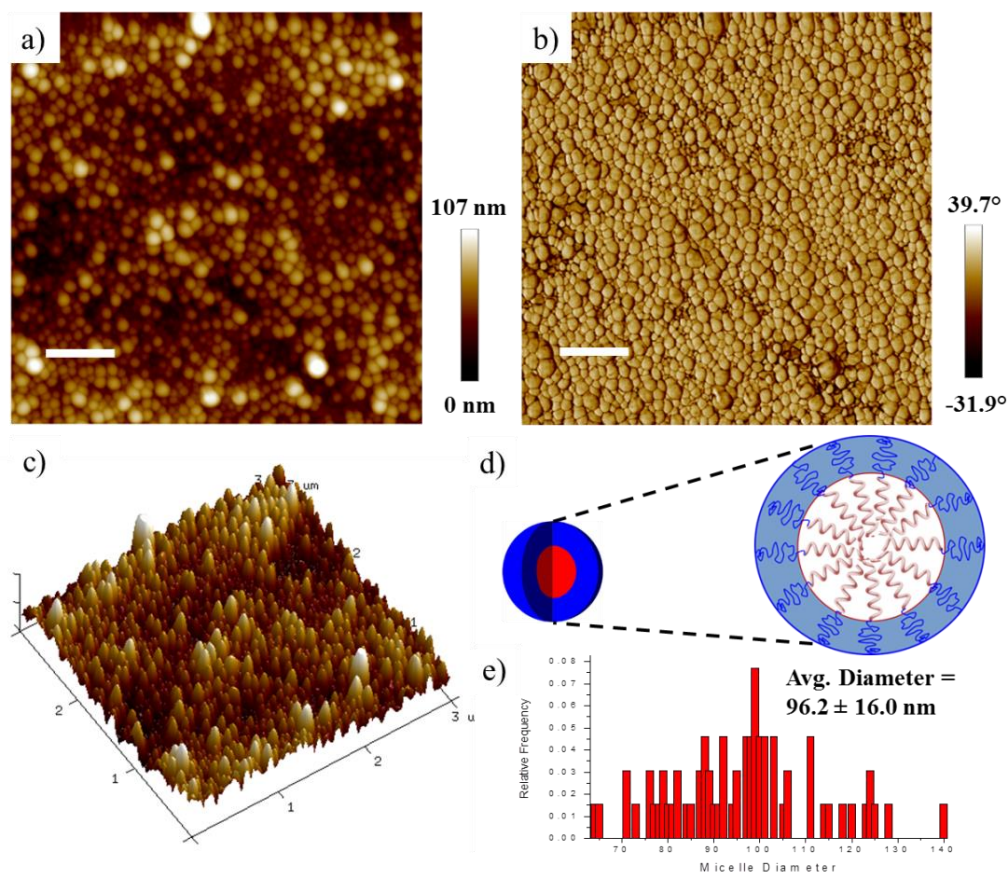


Figure 6.13- 2D Height (a) and phase (b) AFM micrographs (scan size = 3 x 3 μm , scale bar = 500 nm) and 3D height plot (c) of **CoPoly-1** spin-coated from $\text{H}_2\text{O}/10\text{ v\% THF}$ displaying micellar aggregation behaviors with the structure depicted (d). Statistical analysis of the AFM image (e) provides average diameter of the micelles and the standard deviation.

The same procedure was repeated to image the larger aggregates by switching the solvent mixtures to THF/ 10 v% water. The resulting AFM image (Figure 6.14) indeed showed much larger spherical aggregates with an average diameter of 294 ± 22 nm by statistical analysis (sample size = 58 aggregates). Again, the hydrodynamic diameter (D_h) calculated by DLS (ca. 410 ± 88.8 nm) was significantly larger than the observed average diameter in the AFM image, most likely due to the aforementioned inclusion of the solvation sphere in the R_h calculation. Interestingly, the AFM phase map of the spherical aggregates showed positive phases around the edges and negative phases in the center portions. This phenomenon is believed to be a consequence of their hollow nature suggesting that these copolymers adopt vesicle supramolecular assemblies. The diameter of the positive phase in the vesicle aggregates should give us a good approximation of the diameter of the bilayer-like aggregation of the copolymer chains around the shell of the aggregate (depicted in Figure 6.14d). The average measured diameter of the bilayer by statistical analysis is 76.0 ± 8.0 nm which closely reflects the calculated diameter of the assembly depicted (ca. 68 nm).

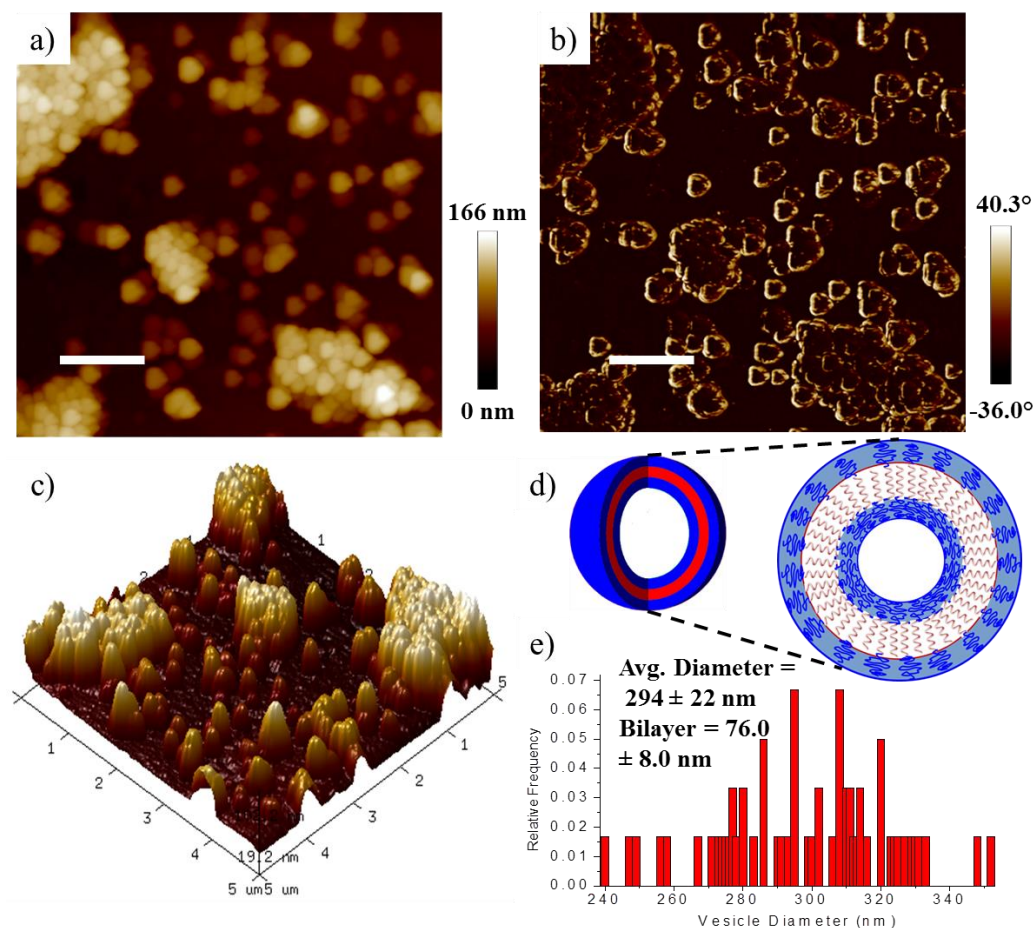


Figure 6.14- 2D Height (a) and phase (b) AFM micrographs (scan size = 5 x 5 μm , scale bar = 1 μm) and 3D height plot (c) of **CoPoly-1** spin-coated from THF/ 10 v% H_2O displaying vesicle aggregation behaviors with the structure depicted (d). Statistical analysis of the AFM image (e) provides average diameter of the vesicles; the bilayer and their standard deviations.

The same aggregation behavior was observed by DLS of **CoPoly-2** with smaller aggregates present in $\text{H}_2\text{O}/ 10 \text{ v\% THF}$ solutions (ca. $D_h = 241 \pm 46.2 \text{ nm}$) than in $\text{THF}/ 10 \text{ v\% H}_2\text{O}$ solutions (ca. $D_h = 384 \pm 140 \text{ nm}$). To see if the same assembly behavior persists for **CoPoly-2**, AFM was again utilized to specifically image the polymer nanoparticles spin-cast from each solution. When cast from $\text{H}_2\text{O}/ 10 \text{ v\% THF}$ solution, the AFM micrograph

displayed larger spherical aggregates with respect to **CoPoly-1** with a single phase throughout suggesting that the assemblies are again micellular in nature. The average diameters of the micelles by AFM statistical analysis (sample size = 90) is 148 ± 25 nm. The diameters of each micelle were again measured using the step function (Figure 6.15d) of individual micelles in the AFM height image. This value compares closely with the calculated chain length of the copolymer multiplied by two (ca. 136 nm) providing further evidence that this copolymer assembles into micelles which are frozen into place when cast from the majority water solutions. As evident by all AFM images thus far, these spherical aggregates have a propensity to aggregate and gather together upon solvent evaporation which further supports the mechanism of formation for the porous morphology seen in the thin-film of **CoPoly-3**.

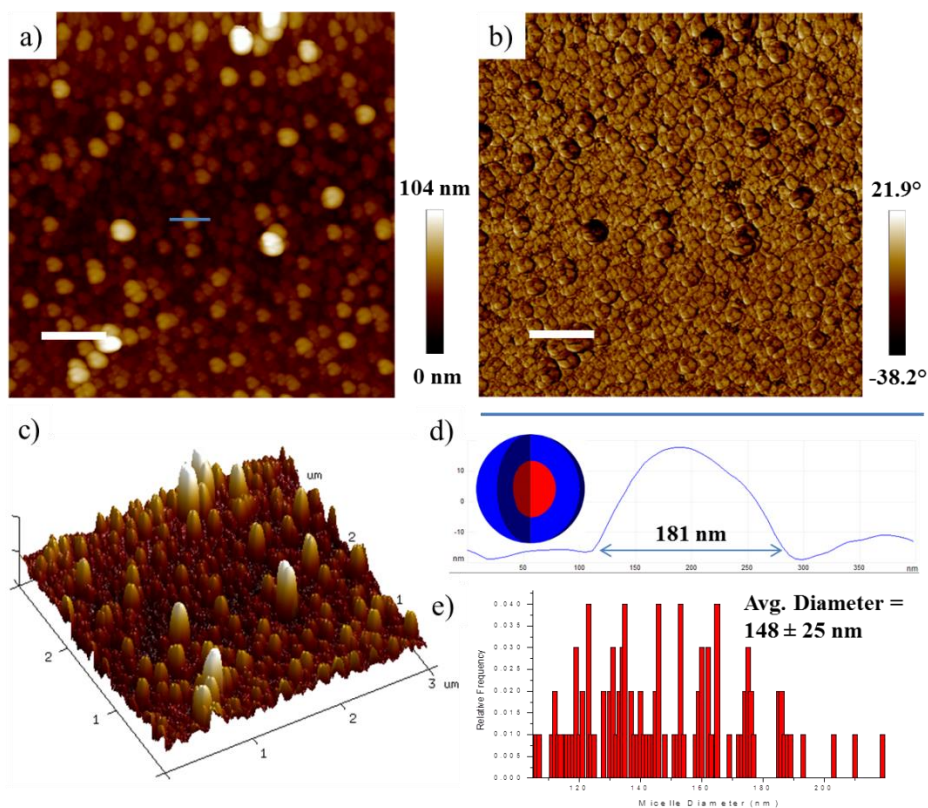


Figure 6.15- 2D Height (a) and phase (b) AFM micrographs (scan size = 3 x 3 μm , scale bar = 500 nm) and 3D height plot (c) of **CoPoly-2** spin-coated from H_2O / 10 v% THF displaying micelle aggregation. The height step function shown in (d) was used for statistical analysis (e) providing an average diameter of the micelles and their standard deviations.

The AFM of the **CoPoly-2** spin-coated from THF/ 10 v% H_2O ($c = 0.5 \text{ mg/mL}$) again displayed large spherical vesicle assemblies with positive phase around the edge of the aggregates and negative AFM phase in the center regions. Statistical analysis of the vesicle aggregates by AFM revealed an average diameter of $289 \pm 19 \text{ nm}$ (sample size = 60) which is actually smaller than that of the vesicles formed by **CoPoly-1**. The measured average diameter of the bilayer, however, increased from **CoPoly-1** to **CoPoly-2** to $82.5 \pm 8.0 \text{ nm}$. The theoretical bilayer thickness using the calculated end-to-end distance of **CoPoly-3** and

the hypothesized structure reveals a larger expected value of ca. 106 nm. This is hypothesized to be a result of the PEG chains adopting a slightly more collapsed conformation due to the added water in the system. The dark-brown phase in the portions of the AFM phase image of **CoPoly-1** and **2** spin-coated from THF/ 10 v% H₂O is simply the hard, flat silicon substrate which is visible due to the low concentrations employed for spin-coating.

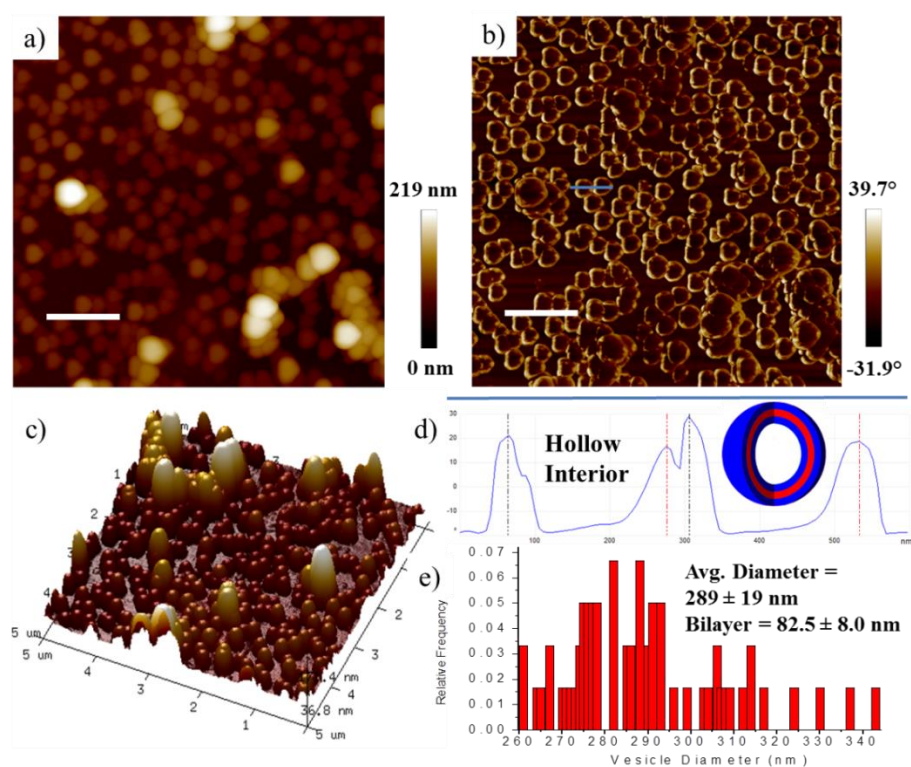


Figure 6.16- 2D Height (a) and phase (b) AFM micrographs (scan size = 5 x 5 μm, scale bar = 1 μm) and 3D height plot (c) of **CoPoly-2** spin-coated from THF/ 10 v% H₂O displaying vesicles aggregation behaviors. The phase step function (d) shows the phase difference associated with the edge and the hollow interior of the vesicle. Statistical analysis of the AFM image (e) provides average diameter of the vesicles; the bilayer and their standard deviations.

Interestingly, the diameter of the aggregates in H₂O/ 10 v% THF solutions of **CoPoly-3** were much larger than **CoPoly-1** (ca. $D_h = 222 \pm 50.2$ nm) at this solvent combination despite having similar hypothesized micelle diameter. One can envision the only possible way for the triblock **CoPoly-3** to assemble into micelles would be for the PEG block to fold in half so both of the PPEMC blocks can occupy the micelle core. This should essentially cut the diameter of the PEG block in half theoretically reducing the size of the micelle. Spin-coating the solution of **CoPoly-3** reveals micelle assemblies by AFM but again with much larger diameters than expected. Statistical analysis of the image provides an average micelle diameter 149 ± 17 nm which is also the largest average of the three copolymers (Figure 6.17). This is hypothesized to be due to encapsulation of some copolymers within the micelle structures causing the diameter to increase. The true cause of this phenomenon, however, is under further investigation.

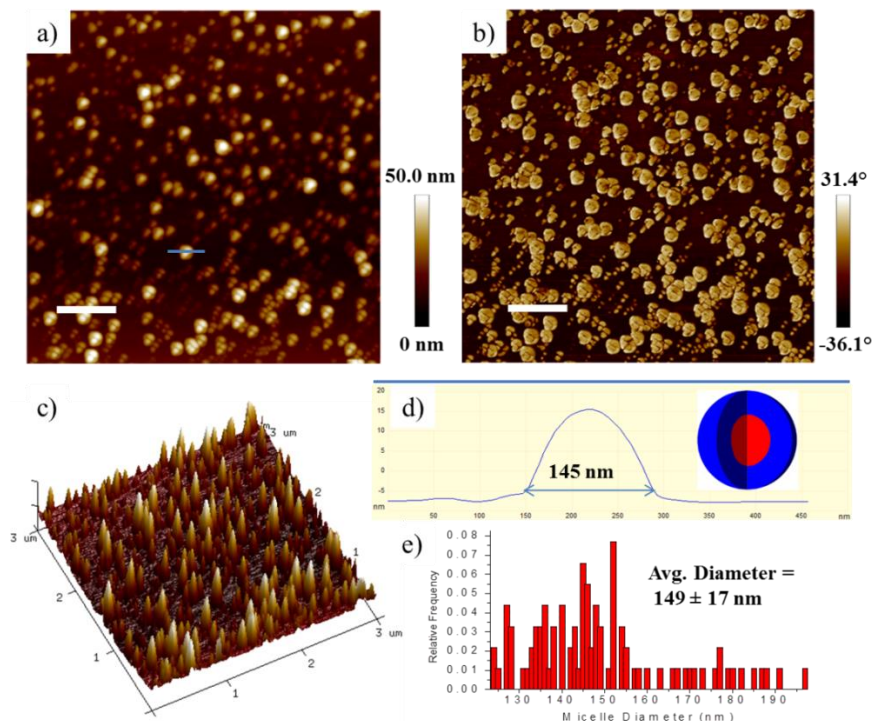


Figure 6.17- 2D Height (a) and phase (b) AFM micrographs (scan size = 3 x 3 μm , scale bar = 500 nm) and 3D height plot (c) of **CoPoly-3** spin-coated from H_2O / 10 v% THF displaying micelle aggregation. The height step function shown in (d) was used for statistical analysis (e) providing an average diameter of the micelles and their standard deviations.

Though the disparity between the DLS and AFM diameters is believed to be largely due to the aforementioned inclusion of the solvation sphere in the R_h calculation, it is difficult to definitively say that the aggregates in solution are the same as the aggregates observed upon casting the solution. For this, cryo-TEM of the vitrified solution is needed to correlate with AFM and DLS but this analysis is expensive and time-intensive. Nonetheless, we had the opportunity to test this technique on a single sample to see if the aggregates in solution mimic those observed in AFM. For this, the solution of **CoPoly-3** in H_2O / 10 v% THF ($c = 0.5 \text{ mg/mL}$) was vitrified in liquid N_2 and imaged using TEM (Figure 6.18). These

images displayed mixtures of both micelles and vesicles which could be the origin of the larger average D_h and standard deviation values observed in DLS for **CoPoly-3**. The “Image J” visualization showing in Figure 6.18 is similar to the phase map in AFM showing the difference in relative electron density as a function of the image area. The dark gray portion shown in one TEM image (Figure 6.18c) is the carbon mesh used as the support for the frozen solution. The micelles observed in the cryo-TEM images displayed very similar diameters to the micelles in the AFM micrograph suggesting that the casting of the aggregates does largely preserve the integrity of the assemblies observed in solution. However, further imaging of the different copolymers and solvent combinations using cryo-TEM is still required to definitively confirm this hypothesis.

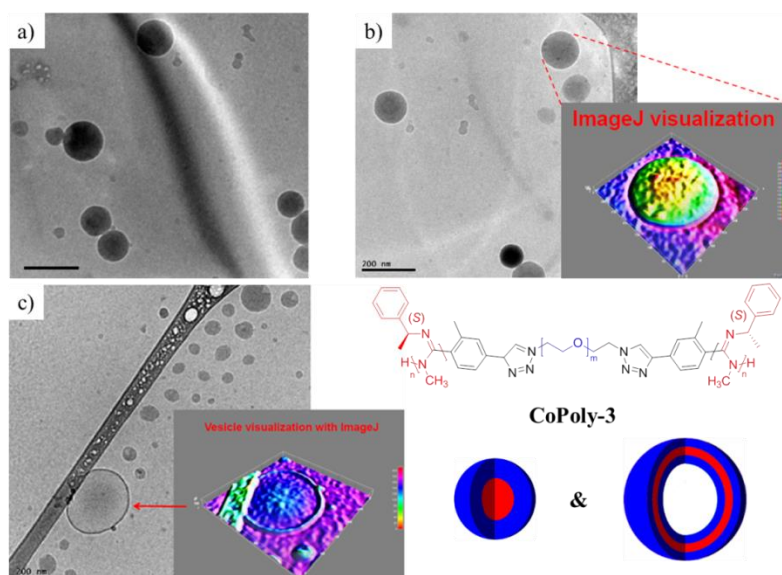


Figure 6.18- Cryo-TEM images of **CoPoly-3** vitrified in H₂O/ 10 v% THF solutions ($c = 0.5$ mg/mL) and embedded in a carbon grid showing the presence of both micelles (a-c) and vesicles (c) in solution (black scale bars = 200 nm).

Finally, **CoPoly-3** was spin-coated from THF/ 10 v% H₂O and AFM was performed to image the larger aggregates observed in DLS with $D_h = 368 \pm 89.4$ nm. AFM of **CoPoly-3** spin-coat from this solvent combination again revealed large vesicle aggregates with an average diameter of 299 ± 19 nm (sample size = 60) and a bilayer thickness of 105 ± 9.5 nm. The significantly larger bilayer diameter suggests that bilayer composition the triblock copolymer is different than **CoPoly-1** and **2** most likely adopting the bilayer structure depicted in Figure 6.19e. This structure consists of two rows of block copolymers aggregating with PPEMC blocks occupying the core of the vesicle walls. The calculated diameter of the structure shown using the chain dimensions calculated for PPEMC₁₄₆ (ca. 22 nm) and half of unperturbed $\langle r^2 \rangle^{1/2}$ value for PEG₄₅₅ (ca. 19 nm) is 82 nm which is a closer estimate to the average bilayer diameter observed in AFM.

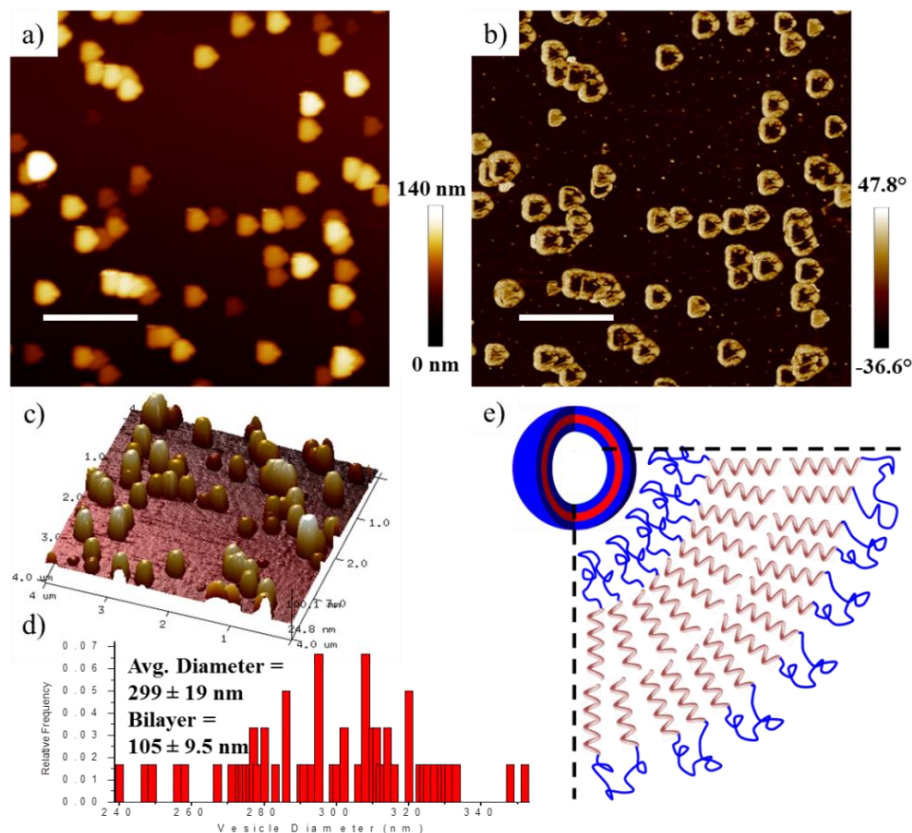


Figure 6.19- 2D Height (a) and phase (b) AFM micrographs (scan size = $4 \times 4 \mu\text{m}$, scale bar = $1 \mu\text{m}$) and 3D Height plot (c) of **CoPoly-3** spin-coated from THF/ 10 v% H_2O displaying vesicles aggregation behaviors. Statistical analysis of the AFM image (d) provides average diameter of the vesicles; the bilayer and their standard deviations with larger than expected diameter values associated with the bilayer leading to the hypothesized structure shown (e).

6.5 Self-Assembly of PPEMC-PEG Copolymers Cast from THF/MeOH-

All of the synthesized PPEMC-PEG copolymers adopted rather conventional aggregation behaviors such as spherical micelles and vesicles when the copolymer was cast from THF/ H_2O solutions. It is still unclear, however, whether changing the selective solvent from H_2O to polar organic solvents such as methanol (MeOH) will affect the supramolecular self-assembly behaviors of these novel RCPs. DLS was performed on **CoPoly-1**, **2**, and **3** in

similar solvent combinations as before but substituting MeOH for H₂O (i.e., THF/ 10 v% MeOH and MeOH/ 10 v% THF; Figure 6.20). Intriguingly, the copolymers showed vastly different aggregation behavior in these MeOH/THF solvent combinations when compared to the simple aggregation behavior observed in H₂O/THF mixtures. Again, the aggregation behavior for all copolymers seemed to follow a trend by DLS and displayed two size distributions for all copolymers in each solvent combination.

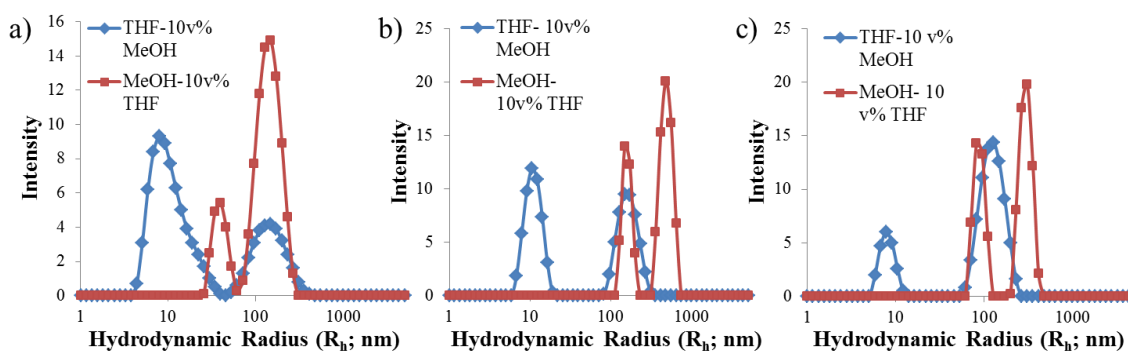


Figure 6.20- DLS plots of **CoPoly-1** (a), **2** (b), and **3** (c) in THF/ 10 v% MeOH (blue) and MeOH/ 10 v% THF (red) showing the change in aggregation behavior as a function of solvent ($c = 0.5$ mg/mL).

In THF/ 10 v% MeOH, **CoPoly-1** displayed one small size distribution with an average $D_h = 22.3 \pm 11.5$ nm and one less populated, large size distribution with $D_h = 304 \pm 126$ nm. Switching the solvent concentrations to MeOH/ 10 v% THF caused the large aggregates (ca. $D_h = 291 \pm 84.4$ nm) to become much more populated and a new, less populated distribution with $D_h = 78.9 \pm 14.7$ nm to appear. Similar behavior is observed for **CoPoly-2** dissolved in these solvent combinations with two size distributions in THF/ 10 v% MeOH with $D_h = 22.1 \pm 5.0$ nm and $D_h = 331 \pm 90.4$ nm. In MeOH/ 10v% THF, the smaller

size distribution disappeared and a new, large aggregation distribution appeared with the largest diameter observed thus far (ca. $D_h = 974 \pm 162$ nm). **CoPoly-3**, again, followed the same trend with smaller size distributions observed in THF/ 10 v% MeOH with $D_h = 16.3 \pm 3.0$ nm and $D_h = 255 \pm 74.5$ nm. In MeOH/ 10 v% THF, both size distributions observed disappear and two new, aggregate sizes are observed with $D_h = 177 \pm 24.3$ nm and $D_h = 596 \pm 92.8$ nm. The smaller size distributions observed in all three copolymers dissolved in THF/ 10 v% MeOH are somewhat puzzling due to the size being significantly smaller than the calculated chain dimensions of each copolymer. This distribution is believed to be free, solubilized copolymer and the disparity in size observed is most likely due to the inaccuracies of DLS in the measurement of particle size for bimodal systems such as these.³⁴ For this reason, the distributions observed for the aggregates may be skewed in some way so should be considered rough estimates only. Again, to image these specific aggregates, AFM was utilized.

CoPoly-1 was first spin-coated from THF/ 10 v% MeOH solutions ($c = 0.5$ mg/mL) despite the predominant size distribution in DLS being small in size suggesting the copolymers are largely solubilized. A very different behavior was observed in AFM, however, with oblong, maggot-like micelle aggregates dispersed throughout. Several different spots on the substrate were imaged confirming the presence of these assemblies throughout the majority of the sample (see experimental for additional images). These aggregates have an average width of 109 ± 13 nm by statistical analysis (sample size = 60) of the AFM height image which mirrors closely with the diameters of the spherical micelles observed for **CoPoly-1** spin-coat from H₂O/ 10 v% THF. The length of these aggregates,

however, was found to be more than double the width with an average length of 247 ± 42 nm. This is a very intriguing aggregation behavior and prompted the necessity for additional AFM analysis.

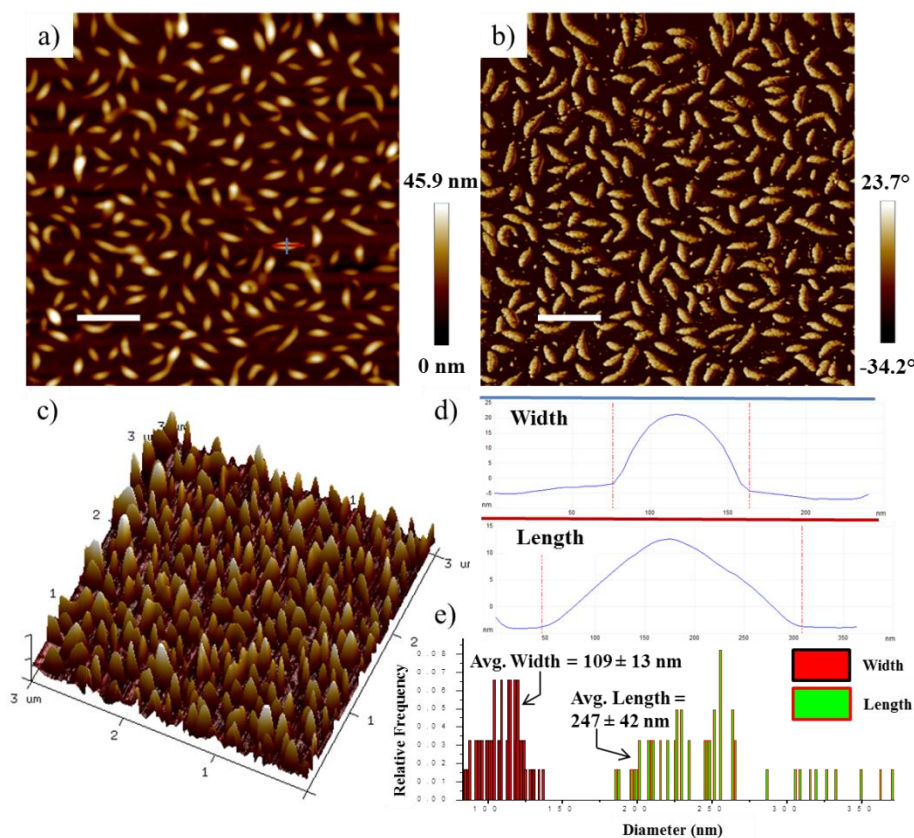


Figure 6.21- 2D Height (a) and phase (b) AFM micrograph (scan size = $3 \times 3 \mu\text{m}$; white scale bar = 500 nm) and 3D height plot (c) of **CoPoly-1** spin-coated from THF/ 10 v% MeOH displaying maggot-like micelle aggregation behaviors. The height step function shown in (d) was used for statistical analysis (e) providing an average width and length of the micelles and their standard deviations.

When spin-coated from MeOH/ 10 v% THF, **CoPoly-1** showed a range of aggregation behaviors with much smaller, spherical assemblies present with intermittent

large, worm-like micelles (Figure 6.22). Interestingly, the phase images of the majority of spherical assemblies look similar to the large vesicle aggregates observed previously when spin-coated from THF/ 10 v% H₂O (with light-colored phase around edge and dark phase in the center) except with diameters similar to the micellular assemblies (ca. 87 ± 19 nm by statistical analysis; sample size = 60). These aggregates are slightly larger in average diameter than the smaller, less populated size distribution observed in DLS (ca. $D_h = 78.9 \pm 14.7$ nm). The large, worm-like micelles appear as if they are formed from the linear clustering of spherical micelles. The formation of the worm-like micelles with higher frequency may depend highly on the time left in solution, so more in depth, time-resolved analysis may be necessary. The longest worm-like micelle (shown in the zoomed in Figure 6.22c and d) displayed a fully-extended length greater than $2.09 \mu\text{m}$ with a range of widths from 42 – 130 nm depending on the spot measured.

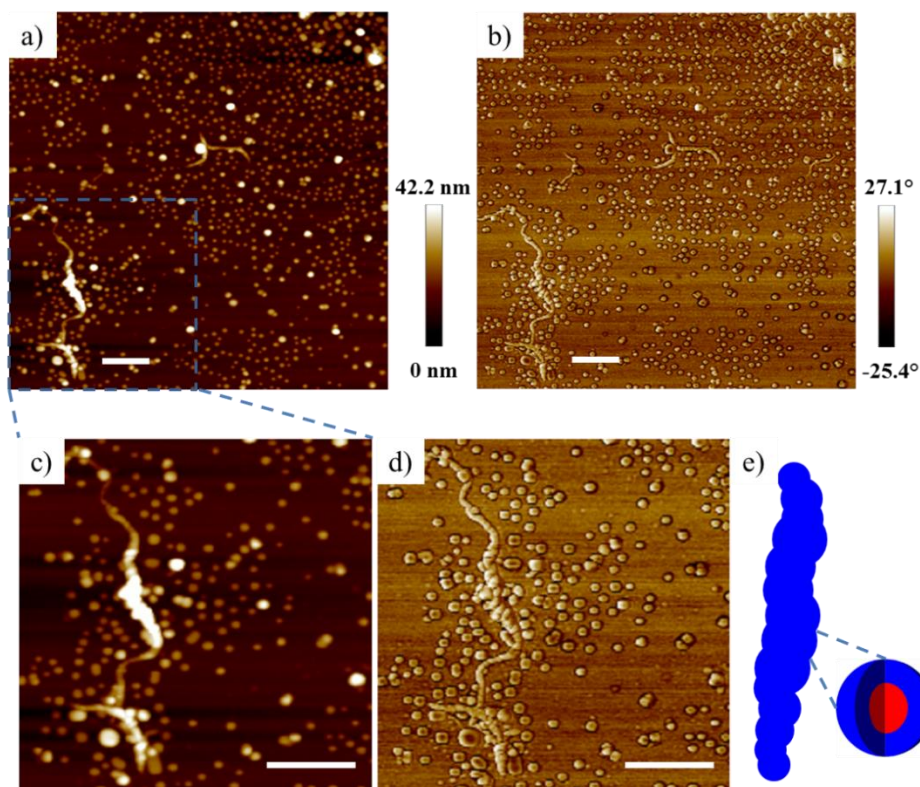


Figure 6.22- 2D Height (a,c) and phase (b,d) AFM micrographs (scan size = 4 x 4 μm for a/b; scan size = 2 x 2 μm for c/d; white scale bars = 500 nm) of **CoPoly-1** spin-coated from MeOH/ 10 v% THF showing mixtures of spherical and worm-like micelle assemblies (depicted in e).

To observe if this new aggregation behavior persists with **CoPoly-2**, this copolymer was again spin-coated first from THF/ 10 v% MeOH ($c = 0.5 \text{ mg/mL}$) and AFM was performed. The resulting AFM micrograph displayed spherical micelle-size aggregates dispersed throughout the substrate (Figure 6.23). The average diameter of these aggregates by statistical analysis (sample size = 60) was found to be $138 \pm 11 \text{ nm}$ matching closely to the observed micelle diameter of **CoPoly-2** spin-coat from dilute $\text{H}_2\text{O}/ 10 \text{ v\% THF}$ solutions (ca. $148 \pm 25 \text{ nm}$). Strangely, like the micelles observed in Figure 6.22, the AFM phase map

across the diameter of the micelle shows a dark, negative phase in the center of the micelle and the light, positive phase around the edge of the micelles. This phase change was previously attributed to the hollow nature of the much larger, vesicle assemblies observed when spin-coating all three copolymer from THF/ 10 v% H₂O. This phenomenon is believed to be due to the presence of the stiffer PPEMC chains in the center of the micelle causing the slight phase change observed in these images.

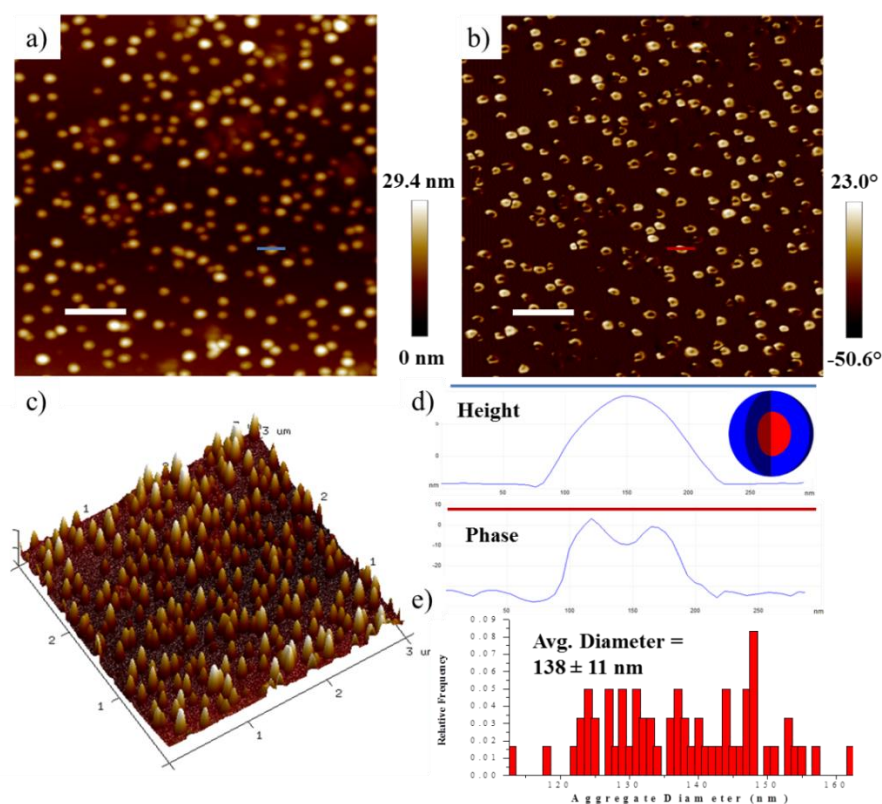


Figure 6.23- 2D Height (a) and phase (b) AFM micrograph (scan size = 3 x 3 μm; white scale bar = 500 nm) and 3D height plot (c) of **CoPoly-2** spin-coated from THF/ 10 v% MeOH displaying spherical micelle aggregation behaviors. The height step function shown in (d) was used for statistical analysis (e) providing an average diameters of the micelles and their standard deviations.

In dilute MeOH/ 10 v% THF solutions, **CoPoly-2** displayed two distinct size distributions by DLS with diameters of $D_h = 317 \pm 41$ and 974 ± 162 nm. The latter is the largest size distribution observed for all RCPs and solvent combinations attempted thus far. The AFM micrograph of **CoPoly-2** spin-coated from these MeOH / 10 v% THF solutions revealed large, worm-like micelles similar to the assemblies observed for **CoPoly-1** spin-coat from MeOH/ 10 v% THF except with much higher frequency. The measured, average widths of these worm-like micelles is 130 ± 20 nm by statistical analysis (sample size = 65) which closely reflects the diameter of the micelles observed previously for **CoPoly-2** spin-coat from THF/ 10 v% MeOH. This provides further evidence of the proposed linear bundling of spherical micelles in MeOH (depicted in Figure 6.24d) forming the worm-like structures observed. A closer look at the AFM height step function across the length of the worm (Figure 6.24e) also alluded to this hypothesis due to the apparent undulation of the worms with width of these undulations according closely to the diameter of the micelles observed for **CoPoly-2** in THF/MeOH solutions. The length of the worm-like micelles varied greatly ranging from extended lengths of 275 nm to 2.48 μm and with an average length of 842 ± 508 nm by statistical analysis (sample size = 35). Neither the width nor length was highly correlated with the observed diameters in DLS but this is not completely unexpected due to the aforementioned difficulties in estimating sizes of bimodal systems.³⁴ The exact cause for the self-association of the spherical micelles is not fully understood but the self-assemblies of these systems are obviously very interesting.

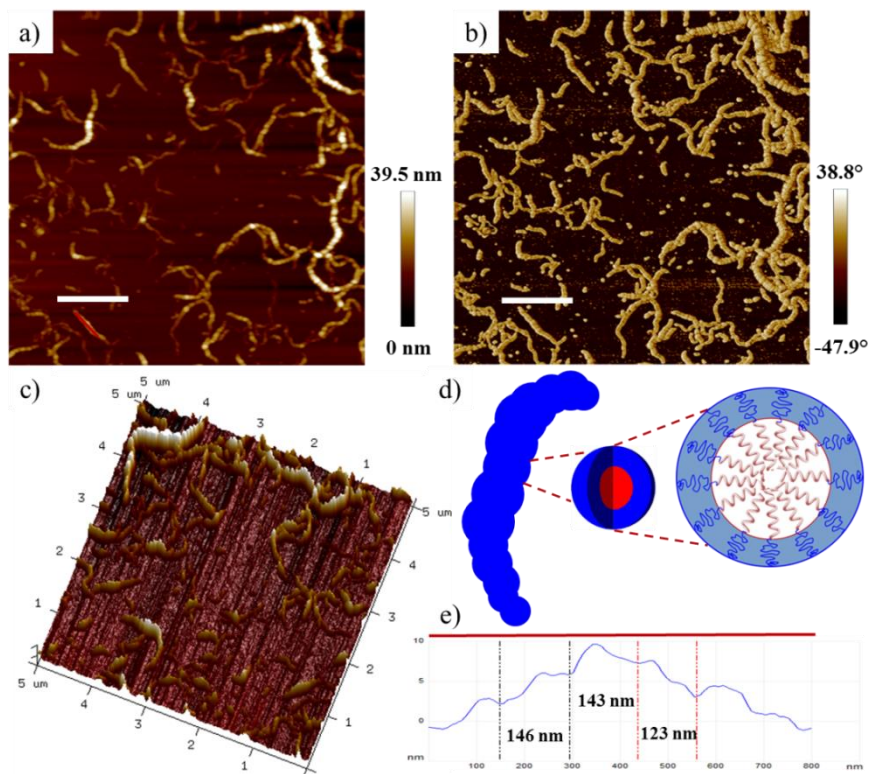


Figure 6.24- 2D Height (a) and phase (b) AFM micrograph (scan size = 5 x 5 μm ; white scale bar = 1.0 μm) and 3D height plot (c) of **CoPoly-2** spin-coated from MeOH/ 10 v% THF displaying worm-like micelle aggregation behaviors. The formation of these assemblies is believed to be consequence of the bundling of spherical micelles (depicted in d) as evident by the undulation displayed in the height step function across the length of the worm (e).

The AFM micrograph of **CoPoly-3** spin-coated from THF/ 10 v% MeOH reveals the presence of both spherical and short, worm-like micelle assemblies (Figure 6.24). Again, the worm-like micelles displayed the repetitive undulation across the length of the worms (shown in the zoomed AFM and step function in Figure 6.25d and e, respectively) implying that these worm-like micelles are fashioned upon accumulation of spherical micelles. The free spherical micelles displayed small diameters of 69 ± 10 nm by statistical analysis of the AFM height image (sample size = 45) which was substantially smaller than the observed

diameters of the micelles observed upon casting **CoPoly-3** from H₂O/ 10 v% THF. This is believed to be due to the PEG chains adopting a more collapsed geometry in MeOH compared to water causing the micelle to shrink. The average width of the worm-like micelles by statistical analysis (ca. 86 ± 13 nm) was slightly larger and correlated closely with the calculated micelle diameter using the chain dimensions calculated previously (ca. 82 nm). The average length of the worm-like micelles visible in the AFM micrograph (ca. 275 ± 84 nm) was similar to that of the maggot-like micelles formed when casted **CoPoly-1** from THF/ 10 v% MeOH solutions.

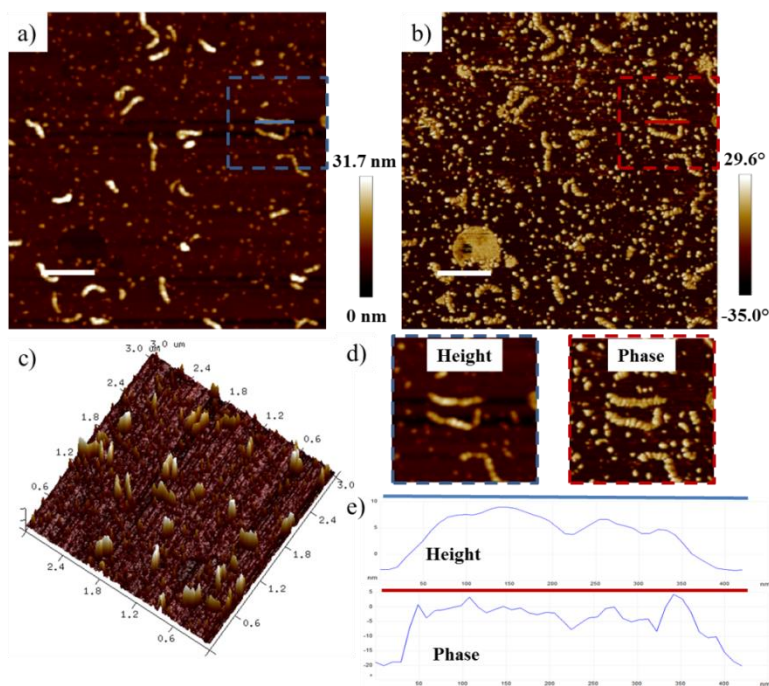


Figure 6.25- 2D Height (a) and phase (b) AFM micrograph (scan size = 3 x 3 μm ; white scale bar = 500 nm) and 3D height plot (c) of **CoPoly-3** spin-coated from THF/ 10 v% MeOH displaying both spherical and worm-like micelle aggregation behaviors. The step function in (e) shows the height and phase across the worm-like aggregate shown in the zoomed AFM image (d).

In nearly all of the AFM images displaying the aggregation behaviors of these RCPs, it seems apparent that the assemblies of polymer chains formed also have the tendency to group together upon casting the dilute solution. This is most likely due to more favorable intramolecular interactions between the adjacent PEG shells compared to the silicon substrate. This was especially apparent when spin-coating **CoPoly-3** from dilute MeOH/ 10 v% THF solutions (Figure 6.26). Towards the center of the sample, more individualized worm-like micelles can be viewed via AFM but, even in these less concentrated spots, it is clear that the assemblies preferred to self-associate as evident by the large amount of free space in the image (Figure 6.26a and c). Moving to the edge of the substrate, the slightly more concentrated area when spin-coating, we identified large clusters of these worm-like micelles that bundle and form interconnected networks (Figure 6.26b and d). Due to the more intriguing assemblies occurring in MeOH/THF solutions, these solutions were also employed for RCP-homopolymer blended systems to observe the effect of adding rod-like homopolymers on the self-assembly behaviors.

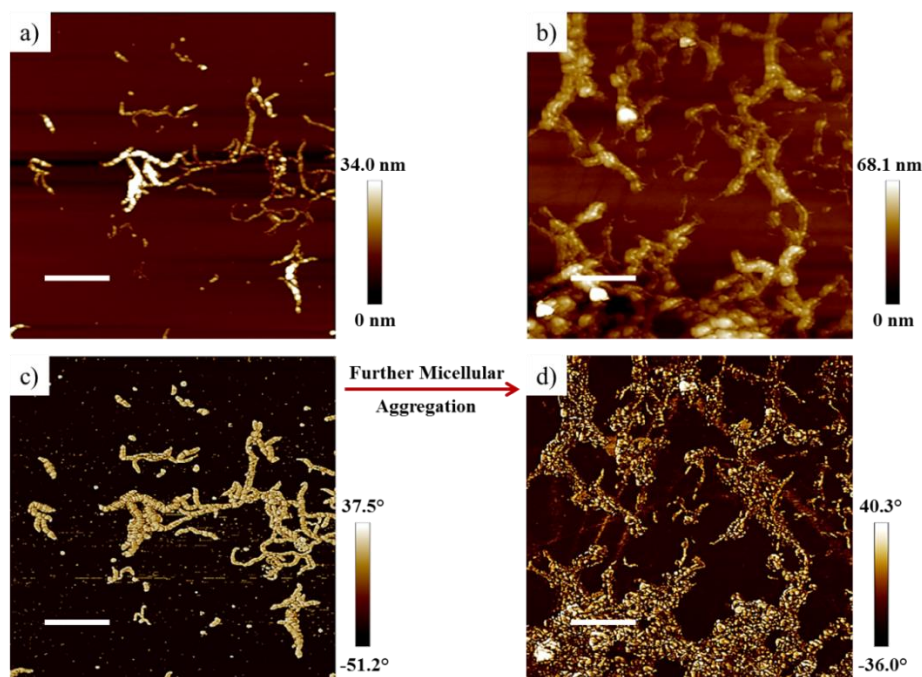


Figure 6.26- 2D Height (a,b) and phase (c,d) AFM micrograph (scan size = 5 x 5 μm ; white scale bar = 1.0 μm) of **CoPoly-3** spin-coat from MeOH/ 10 v% THF showing the presence of worm-like micelles (a,c) that, in more concentrated areas, aggregate together forming large bundled networks of worm-like micelles (b,d).

6.6 Self-Assembly of PPEMC-PEG Copolymer/ PPEMC Homopolymer Blends-

Some of the more enticing aggregation phenomena have been achieved by blending hydrophobic, rigid-rod homopolymer with amphiphilic RCPs in selective solvents effectively encapsulating all hydrophobic homopolymer within complex macromolecular architectures such as helices,^{17,18} bundle nanofibers,²⁶ and branched nanofibers.²⁶ This blending process was attempted using our newly synthesized RCPs with high MW, chiral (*R*)-PPEMC₇₇₄ homopolymer blended ($n = 774$; $M_n = 124$ kDa; PDI = 1.60 by GPC; synthesized using **Ni-2** initiator). Only a very small amount of homopolymer (ca. 15 wt%) was able to be blended with all three copolymers in THF solutions with 10 v% H₂O. Any more water content/

homopolymer added caused the polymer to precipitate fully from solution. Casting these blended THF/H₂O solutions reveals simple micelle/ vesicle aggregation behaviors by SEM (Figure 6.27) which can only encapsulate small amounts of the high MW homopolymer causing the majority to crash from solution. For this reason, the blended systems were investigated herein with THF/MeOH solvent combinations.

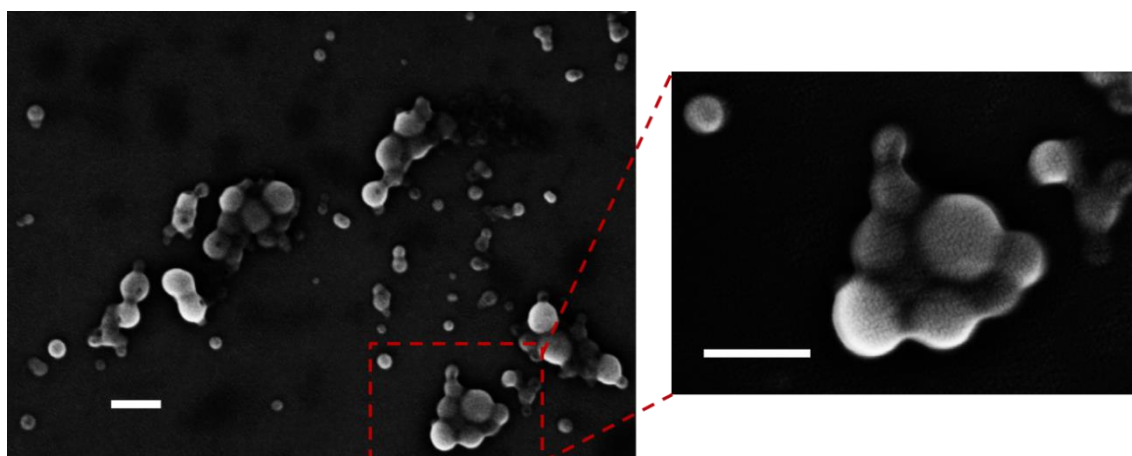


Figure 6.27- SEM micrograph of **CoPoly-1** spin-coated from dilute THF/ 10 v% H₂O solutions ($c = 0.5$ mg/mL) with 15 wt% PPEMC₇₇₄ homopolymer blended showing micelle/ vesicle assemblies with the homopolymer chains encapsulated within (scale bar = 400 nm).

To see if new self-assembly behaviors can be accomplished by blending specific amounts of high MW PPEMC₇₇₄, we converted to THF/MeOH solutions first spin-coating dilute solutions ($c = 0.5$ mg/mL final concentration for all samples) of **CoPoly-1** mixed with 25 wt% of homopolymer in THF/ 25 v% MeOH. These solutions were mixed with agitation for 15 minutes when first prepared then left unperturbed for 15 hours to allow the assemblies to form. AFM was then employed to image the specific aggregates formed revealing

branched, tangled nanofiber assemblies (Figure 6.28). These nanofibers are distinct from the worm-like micelles observed upon spin-coating the RCPs from THF/MeOH in that they do not possess the same undulation believed to be consequence of the linear bundling of spherical micelles. The nanofibers, however, were very long and cylindrical which are intertwined throughout a continuous fibrous network. Additionally, a few small, doughnut-like assemblies were visualized in the AFM images (seen clearly at the bottom of Figure 6.28c and d) which are believed to be looped nanofibers.

The average lengths of the nanofibers are difficult to measure due to the branching and the interconnected nature of the nanofiber network making it somewhat hard to determine where each nanofiber starts and ends. The average widths, however, were measured to be 148 ± 30 nm by statistical analysis (sample size = 60) which takes into account the RCP around the walls of the nanofiber aggregates and the high MW homopolymer encapsulated in the core (depicted in Figure 6.28e). Taking into account the calculated dimensions of **CoPoly-1** (ca. 49 nm), the estimated residual width occupied by the high MW homopolymer is 50 nm. The calculated extended chain length of PPEMC₇₇₄ using the same method aforementioned provides a very large extended length of 115 nm which is larger than the experimentally determined persistence length of 42 nm. This suggests that the extended chain length may not be a very accurate model to the actual chain dimensions of the polymer. Nonetheless, due to the significantly larger chain lengths, it is hypothesized that the homopolymer chains are aligned parallel to the length of the nanofiber.

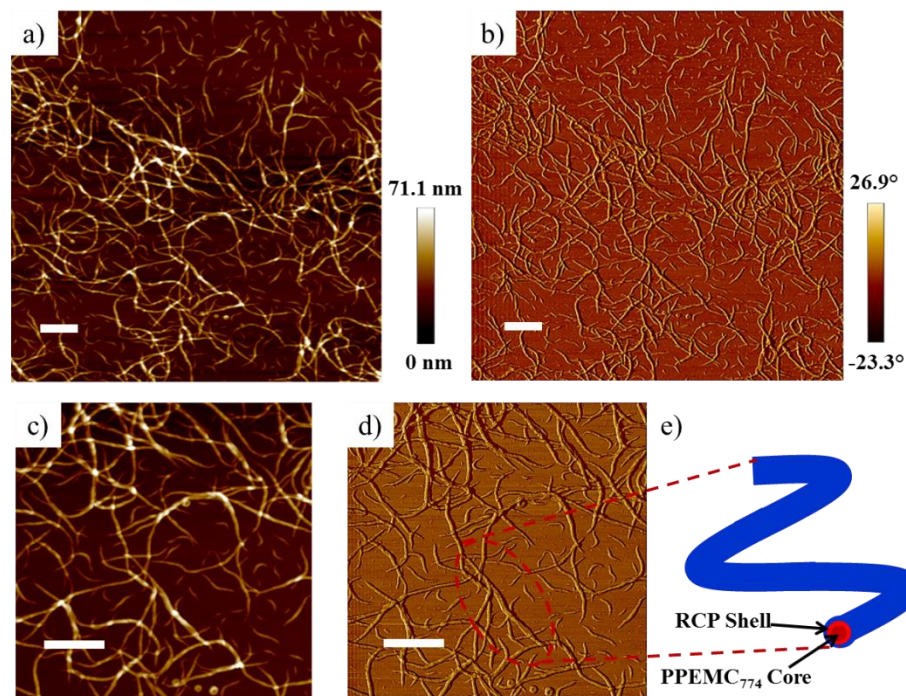


Figure 6.28- 2D Height (a,c) and phase (b,d) AFM micrograph (scan size = 10 x 10 μm (a,b); scan-size = 5 x 5 μm (c,d); white scale bar = 1.0 μm) of **CoPoly-1** blended with 25 wt% high MW PPEMC₇₇₄ and spin-coated from THF/ 25 v% MeOH displaying long, interconnected nanofibers with the hypothesized structure depicted in (e).

To see if this interesting self-assembly behavior persists for **CoPoly-2** when blended with 25 wt% PPEMC₇₇₄, this blend was spin-coated from THF/ 25 v% MeOH, like **CoPoly-1**, and imaged using AFM. Again, we observed long, interconnected nanofibers with the high, MW PPEMC homopolymer encapsulated within (Figure 6.29). The average width of the nanofibers increased, with respect to **CoPoly-1**, to 167 ± 30 nm by statistical analysis (sample size = 60). This is a somewhat smaller width than expected increase due to the PEG chains doubling in relative size from **CoPoly-1** to **CoPoly-2**. The cause of this may be due to a smaller amount of PPEMC homopolymer encapsulated in individual nanofibers. This hypothesis is also supported by the increased frequency of the nanofibers allowing for the

more even dispersion of the homopolymer throughout the intertwined, fibrous network. The proposed structure of these nanofibers is depicted in Figure 6.29d showing the parallel arrangement of the high MW PPEMC₇₇₄ within the core of the nanofiber. In this assembly, the RCP shell of the nanofibers makes up ~136 nm using the calculated dimensions of **CoPoly-2** leaving 31 nm for the encapsulated homopolymer. The long, rigid-rod conformation of the PPEMC₇₇₄ backbone is believed to be the cause for this enticing self-assembly behavior.

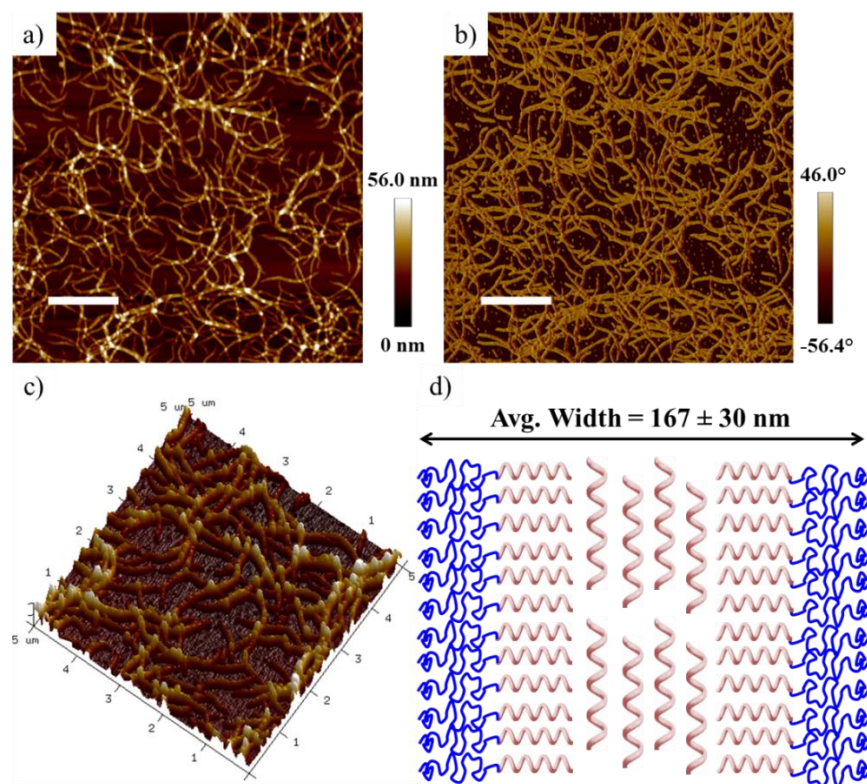


Figure 6.29- 2D Height (a) and phase (b) AFM micrograph (scan size = 10 x 10 μm ; white scale bar = 2.0 μm); 3D height Plot (c; scan size = 5 x 5 μm) of **CoPoly-2** blended with 25 wt% high MW PPEMC₇₇₄ and spin-coated from THF/ 25 v% MeOH displaying long, interconnected nanofibers with the hypothesized structure depicted in (d).

Concurrent with the trend, spin-coating **CoPoly-3** blended with 25 wt% PPEMC₇₇₄ from THF/ 25 v% MeOH solutions results in long, nanofiber aggregates as observed by AFM (Figure 6.30). These assemblies, however, do not appear as interconnected as previously with **CoPoly-1** and **2**. Additionally, the average width of the nanofiber assemblies was measured to be 166 ± 32 nm by AFM statistical analysis (sample size = 60) matching closely with the widths observed for **CoPoly-2** despite the dimensions of the RCP shell mimicking **CoPoly-1**. This is believed to be due to the lesser frequency of nanofibers compared to both **CoPoly-1** and **CoPoly-2** suggesting that a larger number of high MW, PPEMC homopolymer is encapsulated in the fibrous assemblies. This also implies that **CoPoly-3** is able to encapsulate the largest amount of homopolymer per nanofiber aggregate. Along with the nanofibers, several spherical aggregates are also present believed to be mixtures of micelles and small vesicles sparsely scattered throughout the image. In the center of the phase micrograph appears a large positive phase defect which is somewhat puzzling. The origin of this is still unknown and may be just be an artifact caused by an altered response from the tip or simply a surface defect from the silicon substrate.

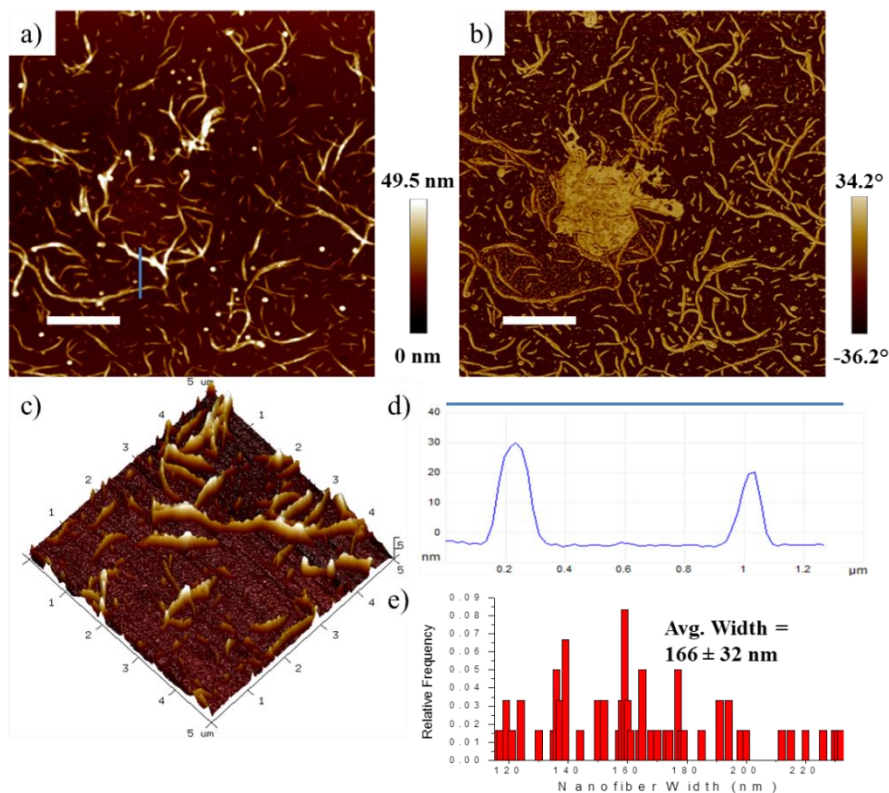


Figure 6.30- 2D Height (a) and phase (b) AFM micrograph (scan size = 10 x 10 μm ; white scale bar = 2.0 μm); 3D height Plot (c; scan size = 5 x 5 μm) of **CoPoly-3** blended with 25 wt% high MW PPEMC₇₇₄ and spin-coated from THF/ 25 v% MeOH. The height step function shown in (d) was used for statistical analysis (e) providing an average width of the nanofibers and their standard deviations.

Increasing the relative amount of homopolymer to 50 wt% in the blend with **CoPoly-1** still resulted in similar nanofiber self-assembly behaviors by the AFM when spin-coated from THF/ 25 v% MeOH (Figure 6.31). The width of the nanofiber aggregates increased to 166 ± 25 nm when increasing the homopolymer content to 50 wt% from 25 wt% homopolymer. Removing the calculated dimensions of the RCP shell (ca. 98 nm), the PPEMC₇₇₄ core increases in diameter from 49 to 68 nm upon increasing the homopolymer content from 25 wt% to 50 wt%. This correlates to a 39% increase of the core diameter

which is similar to the expected 50% increase by weight. Furthermore, the small, doughnut-like aggregates believed to be looped nanofibers are again visible in the AFM micrographs. These blending capabilities now offer the ability to fine tune the nanofiber width by altering the relative content of the high MW homopolymer.

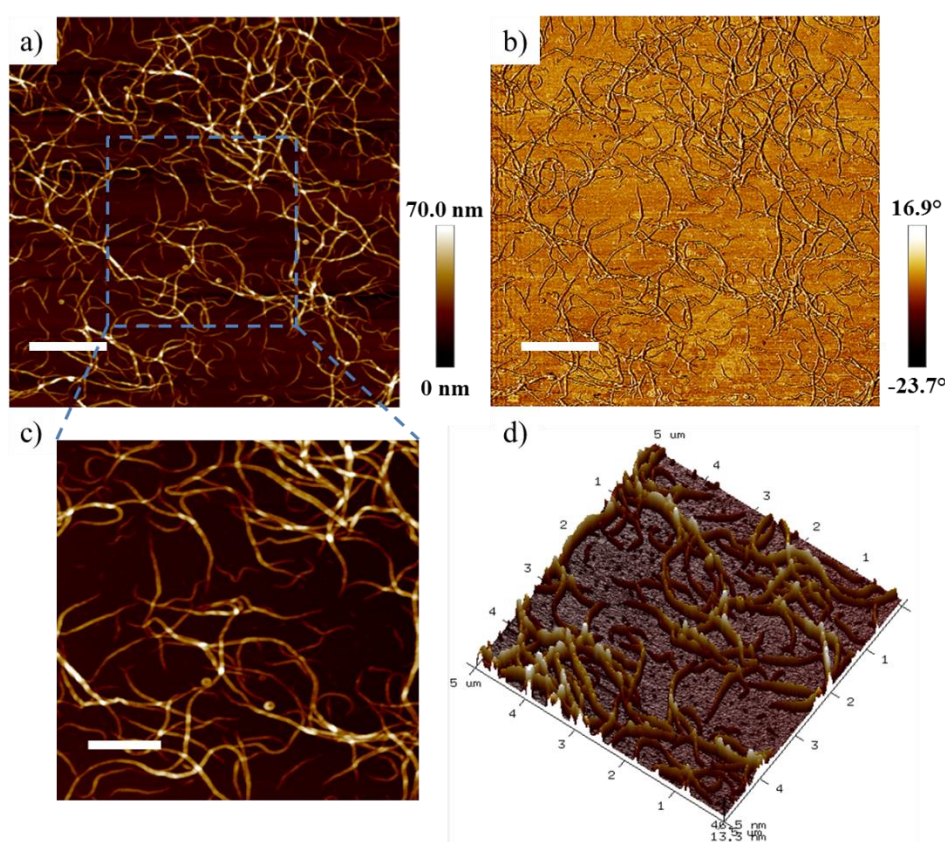


Figure 6.31- 2D Height (a) and phase (b) AFM micrograph (scan size = 10 x 10 μm ; white scale bar = 2.0 μm); Zoomed 2D height micrograph (scan size = 5 x 5 μm ; white scale bar = 1.0 μm); 3D Height Plot (d; scan size = 5 x 5 μm) of **CoPoly-1** blended with 50 wt% high MW PPEMC₇₇₄ and spin-coated from THF/ 25 v% MeOH displaying long, interconnected nanofibers and small, looped nanofibers.

Thus far, for all of the RCP-homopolymer blended systems, we have observed long, interwoven nanofiber self-assembly behaviors by AFM. These nanofibers largely remain individualized, however, lying on top of one another without significant bundling and/or coiling between multiple nanofibers. The AFM micrographs of **CoPoly-2** blended with 50 wt% PPEMC₇₇₄ (Figure 6.32) spin-coated from THF/ 25 v% MeOH again displayed the long, interconnected, nanofibrous network, but with large amounts of branching and coiling points clearly visualized in the zoomed AFM regions. Several different bundling behaviors were observed in these images including the parallel and perpendicular bundling as well as the helically twisted bundling of these nanofiber assemblies (all can be seen clearly in Figure 6.32e). These bundles branched off from one another, as well, with several different connecting points along a single nanofiber assembly. This assembly behavior is believed to be necessary to effectively encapsulate the larger amounts of PPEMC₇₇₄ homopolymer present in the sample. Also clearly displayed in the AFM micrographs, most notably in Figure 6.32c and d, are the doughnut-like, looped nanofibers intermittent with the extended nanofiber aggregates. Strangely, the average diameter of the nanofibers did not increase significantly with a measured average of 171 ± 33 nm (sample size = 45) closely mimicking the diameters measured when spin-coating **CoPoly-2** blended with 25 wt% homopolymer (ca. 167 ± 30 nm). This could simply be consequence of the specific scan area displaying a less concentrated portion of nanofibers when compared to those observed in Figure 6.29. The individualized nanofibers not in the continuous network typically display smaller diameters possibly causing the average to be skewed lower than expected.

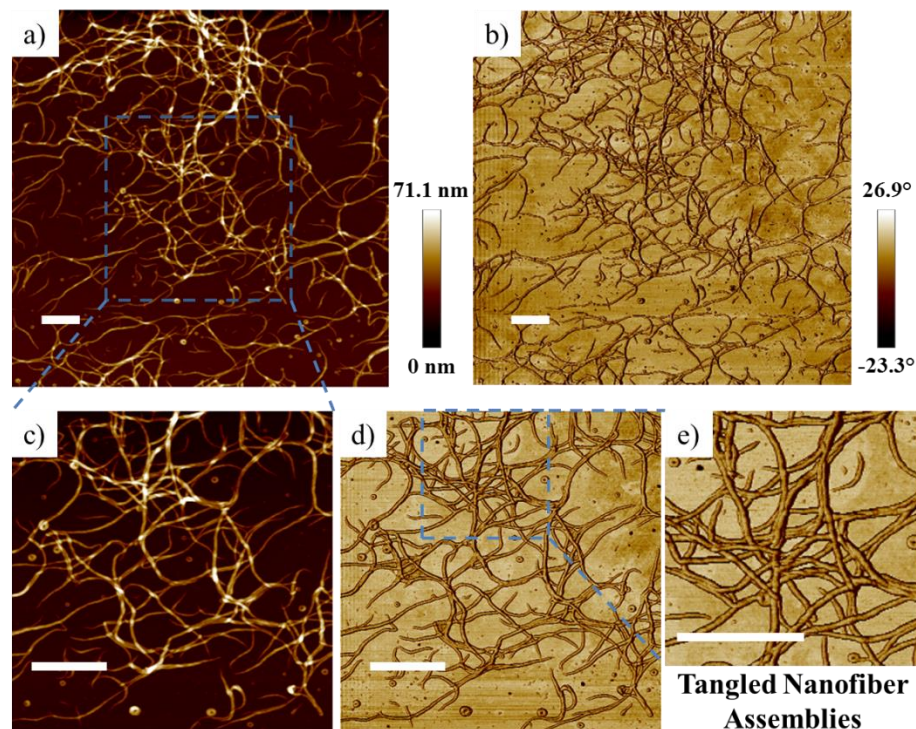


Figure 6.32- 2D Height (a,c) and phase (b,d,e) AFM micrograph (scan size = 10 x 10 μm (a,b); scan size = 5 x 5 μm (c,d); scan size = 2 x 2 μm (e); white scale bar = 1.0 μm) of **CoPoly-2** blended with 50 wt% high MW PPEMC₇₇₄ and spin-coated from THF/ 25 v% MeOH displaying long, interconnected nanofibers with specific parallel, perpendicular, and helically twisted bundling visualized (e).

Finally, the same AFM sample preparation procedure was carried out for **CoPoly-3** blended with 50 wt% PPEMC₇₇₄ homopolymer to see if the aggregation behavior continues with the trend. Again, we saw bundled nanofibers assemblies by AFM (Figure 6.33) with mainly parallel aggregation of multiple nanofibers in a single bundle. The nanofibers within the bundles also clearly split off from one another and form bundles with other nanofibers creating several branching points throughout a continuous, nanofibrous network (highlighted by the blue circles in Figure 6.33d). Unlike **CoPoly-2** blended with 50 wt% homopolymer,

no helically twisted or perpendicular bundles were observed via AFM. The measured average diameter of these nanofibers is 168 ± 46 nm which is close to the average width of the nanofibers formed from spin-coating **CoPoly-3** blended with only 25 wt% homopolymer. This is not unexpected, however, due to the much higher frequency and larger average length of the nanofibers aggregates formed with 50 wt% PPEMC₇₇₄ blended compared to the 25 wt% homopolymer blend. Moreover, the substantially larger standard deviation reflects the large disparity in width due to the presence of single and bundled nanofiber aggregates.

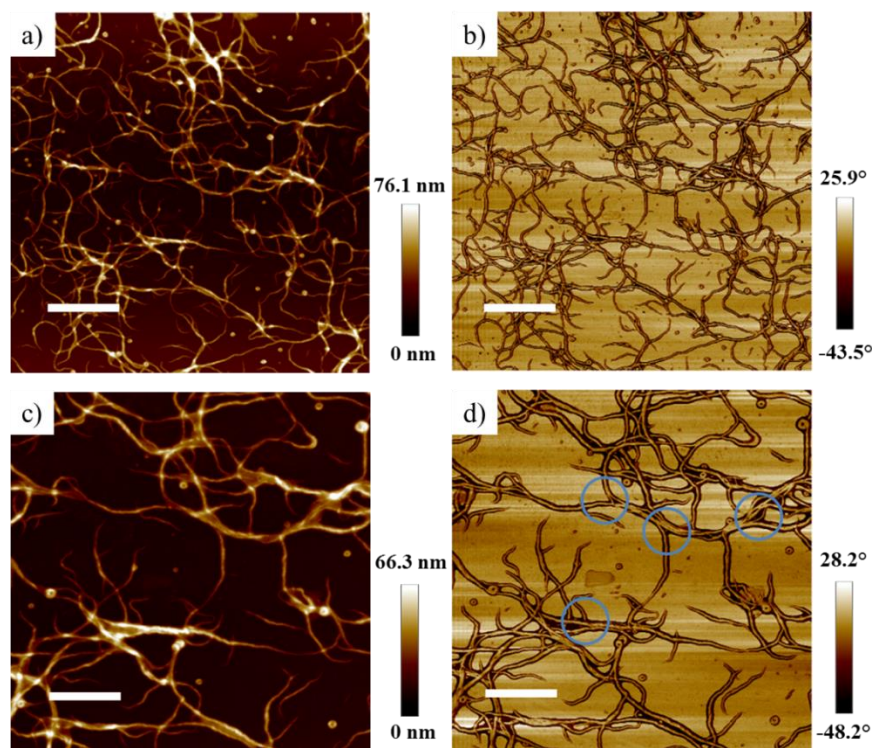
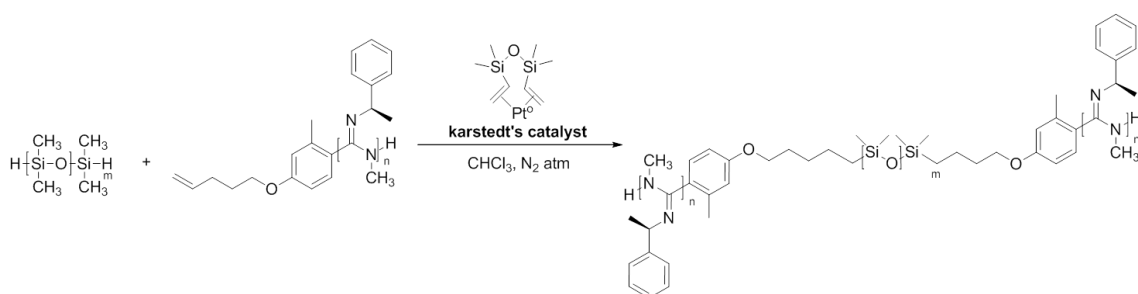


Figure 6.33- 2D Height (a,c) and phase (b,d) AFM micrograph (scan size = 10 x 10 μm (a,b), white scale bar = 2.0 μm ; scan size = 5 x 5 μm (c,d), white scale bar = 1.0 μm) of **CoPoly-2** blended with 50 wt% high MW PPEMC₇₇₄ and spin-coated from THF/ 25 v% MeOH displaying long, parallel bundled nanofiber with several branching points (circled in d) interconnecting the nanofiber network.

6.7 Attempted Synthesis of PPEMC-*b*-PDMS-*b*-PPEMC via Hydrosilation-

We can now also take advantage of several different high yielding reactions such as Heck coupling, thiol-ene click coupling, and, in this case, hydrosilation to functionalize the alkene moiety at the terminus of **Poly-45** via post-polymerization modification. Hydrosilation reactions are platinum/ ruthenium catalyzed coupling of Si-H silane bonds with C=C vinyl bonds forming new Si-C and C-H bonds. These reactions are typically very high yielding and are employed extensively in cross-linking and chain extending reactions for poly(dimethylsiloxane) (PDMS) coatings. Commercially-available, monodisperse bis(silane) terminated PDMS ($M_n = 17.2$ kDa) was purchased and employed to couple with the alkene end-functionalized **Poly-45** via hydrosilation of end-groups forming new PPEMC-*b*-PDMS-*b*-PPEMC triblock RCPs. This was first attempted using Kardstedt's catalyst, a divinyl platinum(0) complex widely used in hydrosilation chemistry (Scheme 6.2).



Scheme 6.2- Hydrosilation reaction of **Poly-45** with bis(silane) terminated PDMS forming a new class of RCP with highly flexible PDMS and highly rigid polycarbodiimide segments.

This reaction was attempted several times at room temperature and 50 °C in CHCl_3 but with little success. In all cases, the proton chemical shifts at 5.05, 5.12, and 5.89 ppm

associated with the vinyl end-group persisted even after allowing the two polymers to react at 50 °C for 6 days (Figure 6.34). Strangely, however, the peaks corresponding to the aliphatic spacer at 1.96 and 2.05 ppm shift upfield significantly after the reaction to 1.31 and 1.49 ppm and a new peak appears at 0.85 ppm suggesting that the reaction did indeed take place. The *o*-methyl substituent and ether methylene end-group protons remain unchanged throughout the reaction, as expected. The presence of the large singlet 0.08 ppm corresponds to the pendant group protons of PDMS but it is still unclear the level at which the two polymers are covalently attached. To confirm or refute this, GPC is necessary to see if there is an increase in MW upon hydrosilation.

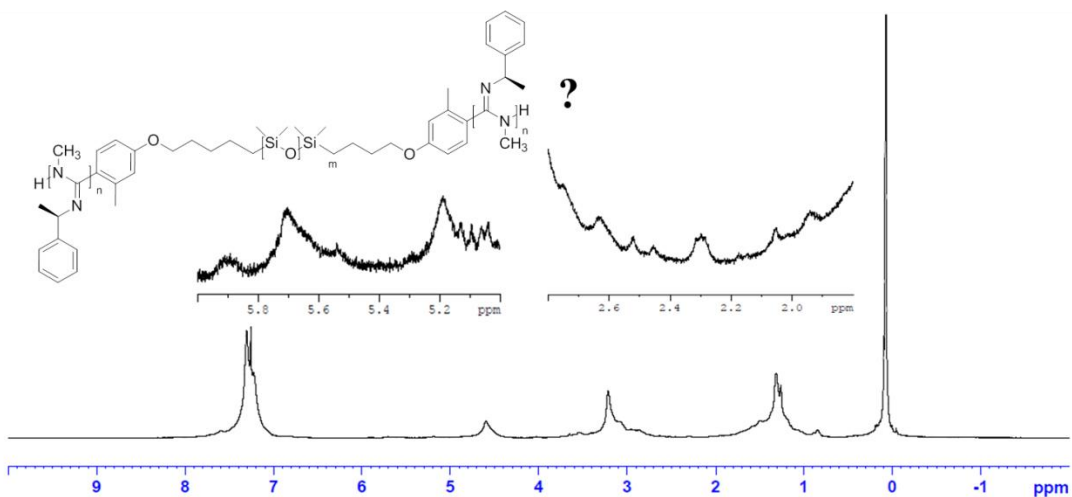


Figure 6.34- ^1H NMR spectrum of attempted hydrosilation reaction between **Poly-45** and bis(silane) terminated PDMS carried out at 50 °C for 6 days showing distinct chemical shifts associated with both polymers.

The resulting GPC chromatogram before and after the attempted hydrosilation reaction appear unchanged with a single MW distribution eluting at 16.7 - 16.8 min for both

suggesting that the block copolymer formation was not successful (see experimental section). The GPC for the parent **Poly-45** before hydrosilation provides a $M_n = 13.1$ kDa and PDI = 2.46 which does not increase significantly (within error) after reacting for 6 hours at 50 °C (ca. $M_n = 16.3$ kDa; PDI = 2.30). The PDMS homopolymer exhibits very low refractive index (1.40 – 1.42) and does not typically show up in GPC chromatograms detected by RI which is why we only observe one peak after attempted hydrosilation corresponding to **Poly-45** homopolymer. The reason for this failure is hypothesized to be caused by the favorable coordination of the platinum(0) complex to the nitrogen-rich backbone of **Poly-45** compared to the divinyl ligand. This, in turn, prevents the necessary oxidative addition into the Si-H silane bond and reductive elimination across the vinyl group. Also, another possibility is the incorporation of the divinyl ligand as the double bond source to couple with the Si-H of the PDMS end-groups. This would essentially result in a simple chain extension of the PDMS polymer chains with the polycarbodiimide end-groups remaining intact.

To possibly break up this coordination, the reaction was again attempted at 80 °C rather than 50 °C and allowed to react for 3 days with the vinyl protons being monitored by ^1H NMR. Again, no decrease in intensity for the vinyl end-group protons was observed via ^1H NMR. The GPC chromatogram of **Poly-45** before hydrosilation (ca. $M_n = 33.9$ kDa; PDI = 1.43) is actually significantly larger than post-hydrosilation (ca. 9.2 kDa; PDI = 1.37). This suggests that substantial degradation to the PPEMC polymer chains occurs at this elevated temperature in the presence of the platinum catalyst (see experimental section).

Finally, this reaction was attempted with another different, very common hydrosilation catalyst, Speier's catalyst, which is hexachloroplatinic acid (H_2PtCl_6) in

isopropanol. This reaction was carried out at room temperature to prevent any significant degradation to occur. Unfortunately, no progress was observed by ^1H NMR with the chemical shifts associated with the vinyl end-groups persisting even after reacting for 6 days. Additionally, the GPC chromatogram before and after the reaction display nearly identical retention times (ca. 11.51 and 11.47 minutes, respectively) and calculated MWs (ca. $M_n = 72.9$ kDa and $M_n = 80.9$ kDa, respectively) suggesting that the reaction failed once again (see experimental section). One possible way to combat these issues would be to try different metal centers other than platinum such as ruthenium and rhodium complexes which have also been shown to readily perform hydrosilation reactions. Also the use of larger, more bulky ligands appended to the metal center may aid in preventing significant coordination to the polycarbodiimide backbone. These should be attempted in future work.

6.8 Conclusions-

A series of novel, amphiphilic rod-coil block copolymers was synthesized via CuAAC “click” reaction between the chiral, alkyne end-functionalized PPEMC (**Poly-44**) and azide end-functionalized PEG. Both PPEMC-*b*-PEG and PPEMC-*b*-PEG-*b*-PPEMC helical-*b*-random coil di- and tri-block copolymers were synthesized via this method and their self-assembly behaviors were studied by DLS, AFM, SEM, and TEM. In the thin-film, both PPEMC₂₀₂-*b*-PEG₂₂₅ (**CoPoly-1**) and PPEMC₂₀₂-*b*-PEG₄₅₅ (**CoPoly-2**) adopted nanofibular morphologies when cast from THF ($c = 5.0$ mg/mL) and annealed at 65 °C for 24 hours. The PPEMC₁₄₆-*b*-PEG₄₅₅-*b*-PPEMC₁₄₆ triblock copolymer (**CoPoly-3**), however, adopted macroporous morphologies in the thin-film and in the bulk as evident by AFM and

SEM. Due to their amphiphilic nature; these polymers adopted a variety of unique aggregation behaviors in selective solvents for the hydrophilic PEG blocks such as MeOH and H₂O. In dilute THF/ H₂O solvent mixtures, these copolymers assembled into conventional micelle and vesicle aggregates depending on the ratio of solvents with the chiral PPEMC chains occupying the core of the micelle or interior of the vesicle walls. Substituting MeOH for H₂O resulted in different aggregation behaviors with large worm-like and maggot-like micelles adopted for all three copolymers. Blending high MW PPEMC₇₇₄ homopolymer with the block copolymers in dilute MeOH/THF solutions caused these polymers to form long, interconnected nanofibrul networks with all of the hydrophobic PPEMC homopolymer chains effectively encapsulated inside.

Also another RCP synthesis was attempted via hydrosilation between the alkene end-functionalized **Poly-45** and bis(silane) terminated PDMS. This reaction was unsuccessful after several attempts at different temperature and reaction times. Additionally, two different platinum catalysts were employed for this reaction but with no success. Future work should include attempting this reaction with bulkier rhodium or ruthenium catalysts to see if this would result in the successful coupling of the silane end-group of the PDMS with the vinyl end-group of **Poly-45**.

6.9 Experimental Section-

Materials- The materials, synthesis procedure, and characterization of end-functionalized **Poly-44** and **Poly-45** are outlined in Chapter 5. The solvents employed in CuAAC “click” reaction and hydrosilation reactions were used as received. The tetrakis(triphenylphosphine)

palladium(0) ($\text{Pd}(\text{PPh}_3)_4$; Sigma Aldrich), copper(I) iodide (CuI ; Sigma Aldrich), and triethylamine (TEA; Sigma Aldrich) used in “click” reactions were used as received. The monoazide terminated PEG₂₂₅; PEG₄₅₅ and bisazide terminated, telechelic PEG₄₅₅ were purchased from Sigma Aldrich and used as received. The monodisperse, di-silane terminated PDMS and Kardstedt’s were purchased from Gelest and used for hydrosilation reactions as received. All deuterated solvents used for NMR (including CDCl_3 , $\text{THF-}d_8$, and D_2O) were purchased from Sigma Aldrich and used as received.

Equipment- All NMR spectra (including ^1H , ^{13}C) were recorded on a Bruker AVANCE III™ 500 MHz NMR spectrometer. ^1H NMR spectra were referenced to TMS internal standard set at 0.00 ppm. All FTIR spectra were collected on Thermo Scientific Nicolet 380 ATR-FTIR spectrometer. Specific optical rotations of chiral polymers were measured using a JASCO P-1010 polarimeter (435 nm, $l = 10.0$ cm) at room temperature in dilute solution (CHCl_3 , $c = 2.00$ mg/mL). DSC was performed for **CoPoly-1**, **2**, and **3** on a TA Instruments Q2000 Automated DSC with a 10 °C/min ramp rate from -40 °C to 165 °C. GPC analyses of MW for copolymers and homopolymers relative to polystyrene standards were conducted on a Shimadzu Prominence Modular HPLC/GPC system equipped with both refractive index (RI) and UV-Vis detectors ($\lambda = 254$ nm). A two-column system was employed with both Agilent Mixed-E and Mixed-C column working in tandem. TMAFM was employed to investigate the thin-film morphologies and self-assembly behaviors of the coupled block copolymers using a Nanoscope IV-Multimode Veeco instrument equipped with an E-type vertical engage scanner. Optical microscopy images were collected using a Meiji Techno ML9000 series OM through cross-polarizers and captured with an AmScope FMA050 fixed microscope digital

camera. SEM images were captured using a Zeiss-LEO Model 1530 variable pressure field effect SEM. Cryo-TEM was accomplished using JEOL 2100 Transmission Electron Microscope equipped with a cryogenic module to keep sample vitrified at -196 °C during sample acquisition. DLS measurements were conducted on Malvern Zetasizer particle sizer Nano ZS model equipped with He-Ne laser source (633 nm; Max 4 mW).

Synthesis of PPEMC-PEG Block Copolymers via CuAAC “click” reaction-

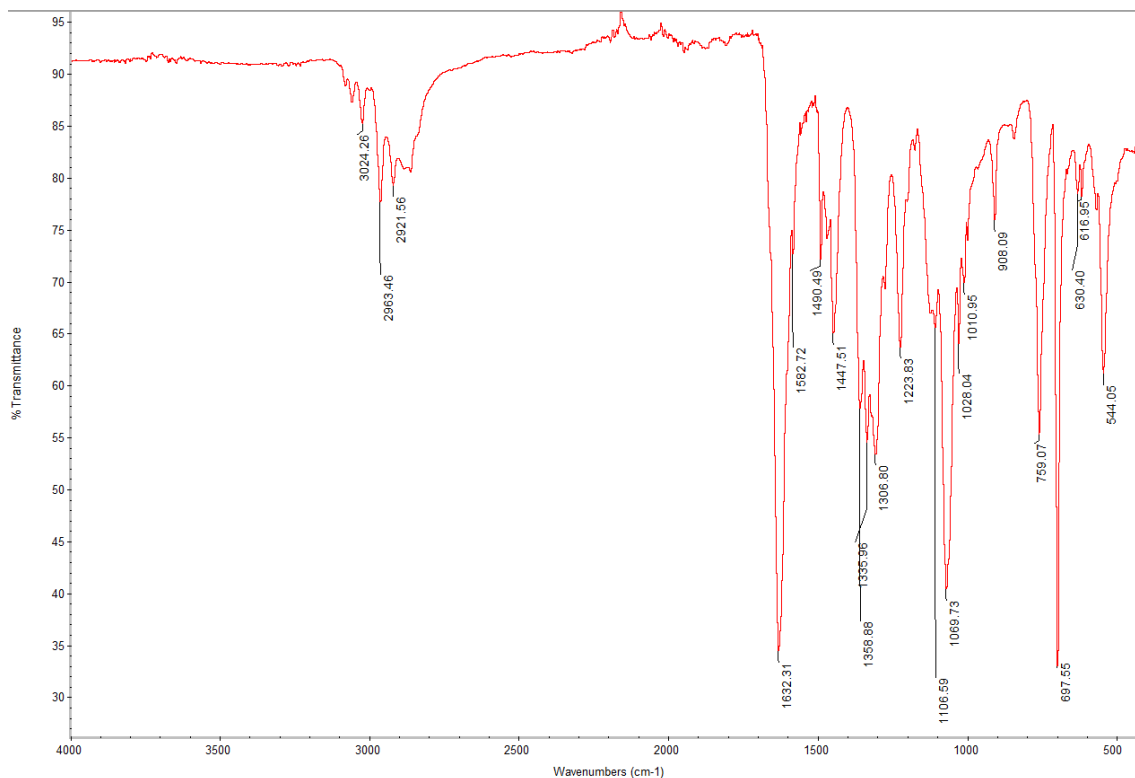
The procedure outlined was employed for the synthesis of all copolymers (**CoPoly-1**, **2**, and **3**). A 100 mL oven-dried, three-neck R.B. flask equipped with a small stir bar was evacuated and purged with N₂ three times prior to addition of any reagents. Each of the individual, end-functionalized polymers (1.0 eq. for PEG monoazides and bisazides; 1.0 eq. of PPEMC for **CoPoly-1** and **2**, 2.0 eq. of PPEMC for **CoPoly-3**) were dissolved in ~5.0 mL of THF and added to the purged flask under a constant N₂ flow. The DBU (4.0 eq.) was then added to the stirring mixture followed by CuI (0.2 - 0.5 eq. with respect to the end groups) and the stirring reaction mixture was heated to 40 °C in a preheated oil bath for 24 hours. Upon cooling to room temperature, the solution was concentrated slightly and precipitated from either MeOH or hexanes with 1.0 v% DBU. **CoPoly-1** and **CoPoly-2** precipitated nicely from MeOH and were isolated upon filtration with 78% and 60% yields, respectively. The lower yields are believed to be due to some of the copolymer staying in solution due to their partial solubility in MeOH. For this reason, the polymer product could not be washed with additional MeOH resulting in residual DBU observed in ¹H NMR. **CoPoly-3** displayed complete solubility in MeOH when a single drop was added hence the necessity to precipitate the copolymer from hexanes. This caused the isolated yield to reach the near quantitative

amounts characteristic of “click” reactions (ca. 92%) but the color associated with residual copper persisted even after 2 precipitations. The specific amounts used, NMR, TGA, and IR data for all successfully synthesized copolymers is outlined below

PPEMC₂₀₂-b-PEG₂₂₅ (CoPoly-1)

Following the outlined procedure for the CuAAC “click” reaction: 0.111 g (~11.1 μmol ; 1.0 eq.) of PEG₂₂₅-monoazide, 0.345 g (~10.7 μmol ; 1.0 eq.) of PPEMC₂₀₂, 0.100 mL (0.673 mmol) of DBU, and 1.4 mg (6.73 μmol) of CuI.

Yield: 0.354 g (8.36 μmol) of fibrous, white solid, 78%. ATR-FTIR (cm^{-1}): 3024 (Ar-H, w), 2963 (alkyl-H, m), 2921 (alkyl-H, m), 1632 (C=N, s), 1582 (C=C_{aryl}, m), 1107 (C-O, m). ¹H NMR (500 MHz, CDCl₃): δ (ppm) 7.54 (end-group Ar-H, broad s), 7.30 (pendant Ar-H, 5H), 5.70, 5.18, 4.59 (pendant methine-H, broad m, 1H), 3.65 (-O-CH₂-, s, 3.98H), 3.21 (triazole-CH₂-, small s), 3.13 - 2.86 (N-CH₃, broad m), 2.04 (end-group Ar-CH₃, s), 1.31 (pendant benzylic-CH₃, broad s). DSC (Three Heating-cooling cycles -40 °C – 165 °C) T_m = 62.2 °C; T_c = 35.2 °C.

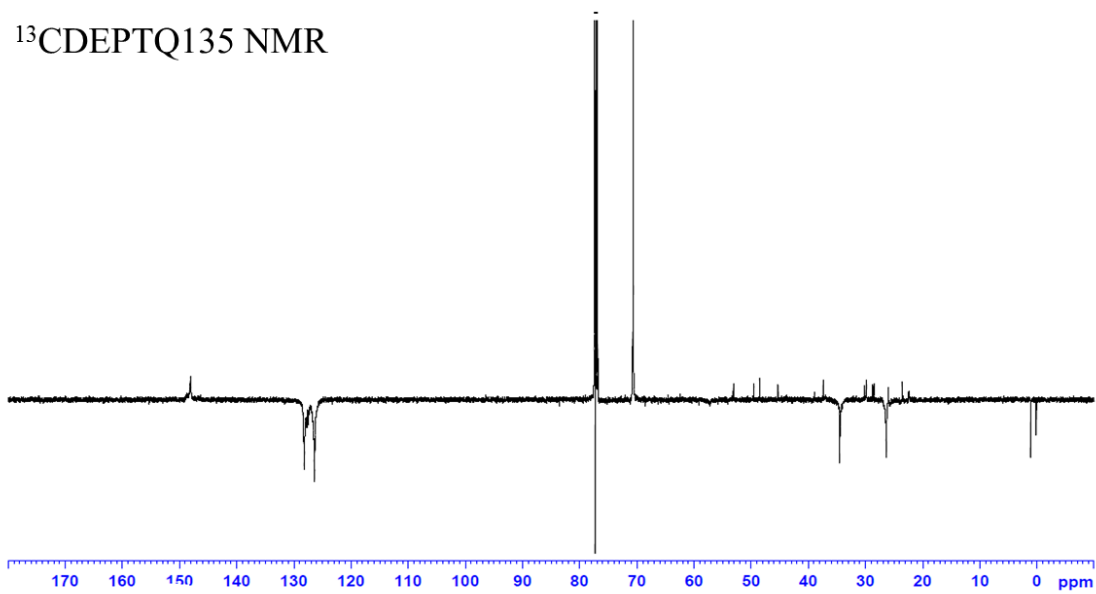
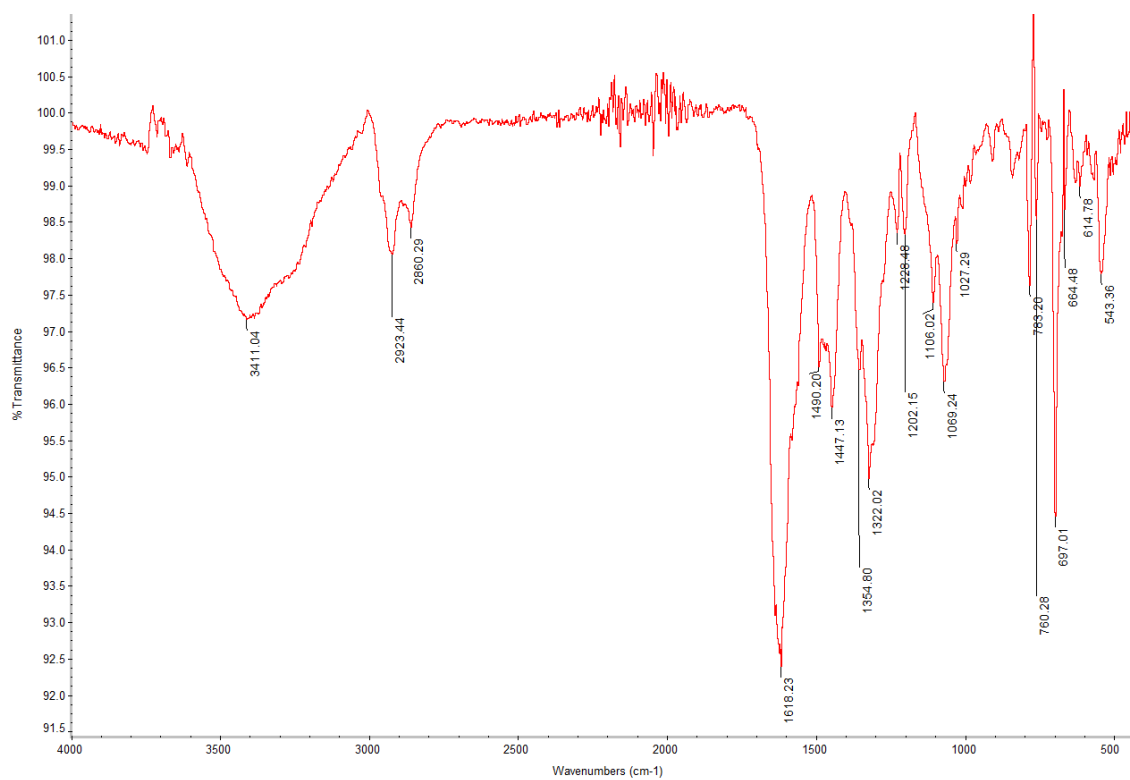


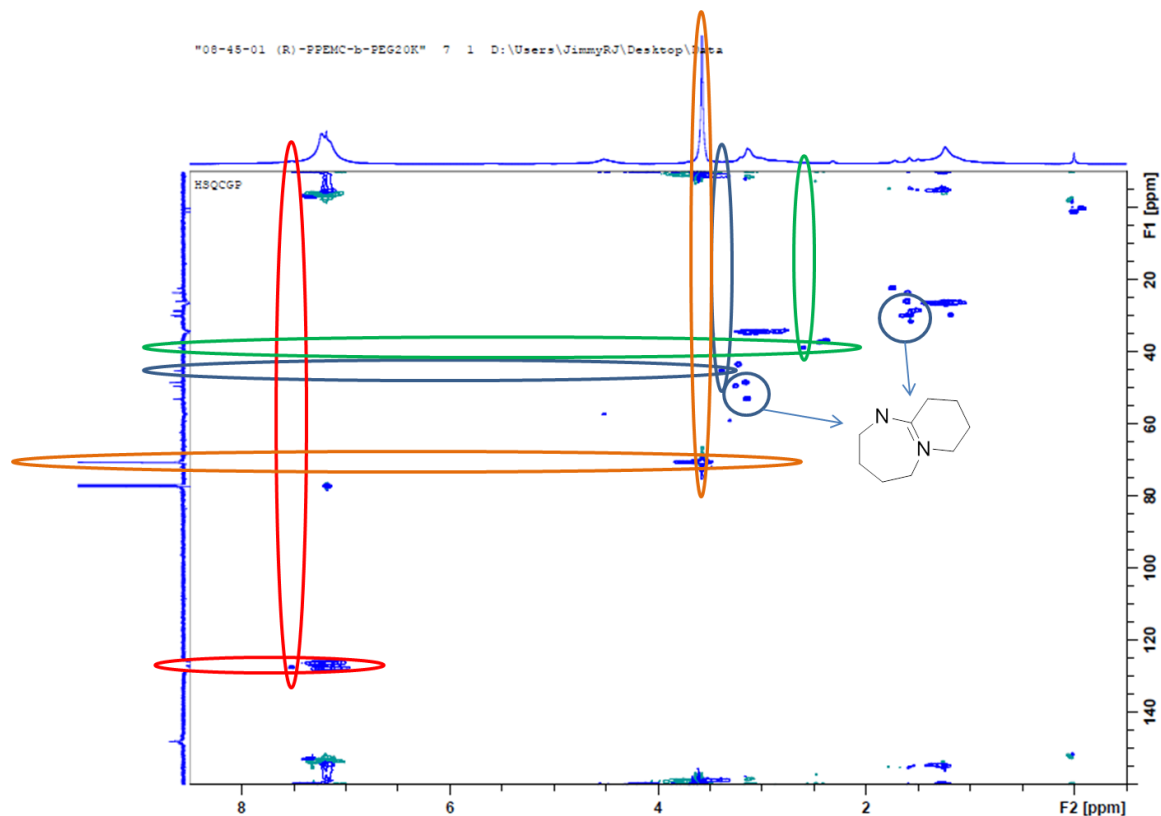
PPEMC₂₀₂-b-PEG₄₅₅ (CoPoly-2)-

Following the outlined procedure for the CuAAC “click” reaction: 0.150 g (~7.52 μmol ; 1.0 eq.) of PEG₄₅₅-monoazide, 0.231 g (~7.45 μmol ; 1.0 eq.) of PPEMC₂₀₂, 0.050 mL (0.336 mmol) of DBU, and 1.2 mg (6.30 μmol) of CuI.

Yield: 0.232 g (4.43 μmol) of fibrous, white solid, 60%. ATR-FTIR (cm^{-1}): 2923 (alkyl-H, m), 2860 (alkyl-H, m), 1618 (C=N, s), 1582 (C=C_{aryl}, m), 1106 (C-O, m). ¹H NMR (500 MHz, CDCl₃): δ (ppm) 7.52 (end-group Ar-H, broad s), 7.30 (pendant Ar-H, 5H), 5.62, 5.11, 4.78 (pendant methine-H, broad m, 1H), 3.58 (-O-CH₂-, s, 5.95H), 3.20 (triazole-CH₂-, small s), 3.14 - 2.88 (N-CH₃, broad m), 2.07 (end-group Ar-CH₃, s), 1.24 (pendant benzylic-CH₃, broad s). ¹³C NMR (125 MHz, CDCl₃): δ (ppm) 148.7, 148.2, 128.2, 127.7, 127.5,

126.4, 70.7, 45.3, 34.5, 26.4, 23.6. DSC (Three Heating-cooling cycles -40 °C – 165 °C) T_m
= 61.7 °C; T_c = 34.7 °C.



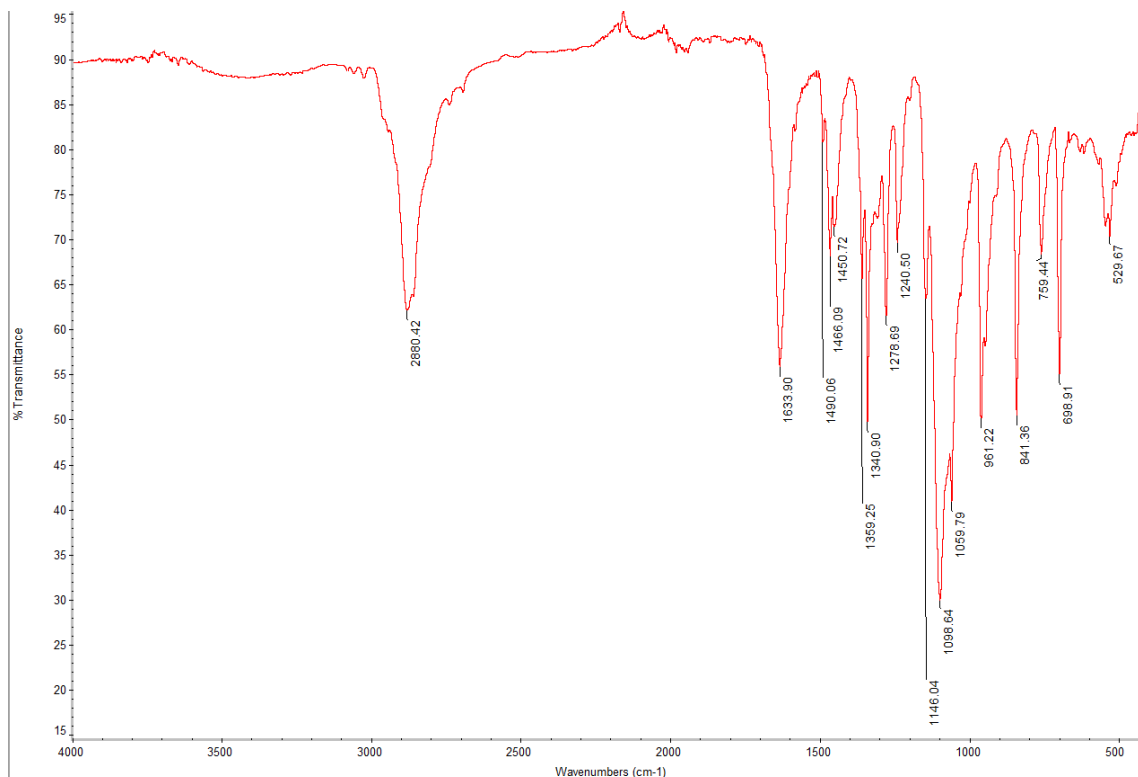


PPEMC₁₄₆-b-PEG₄₅₅-b-PPEMC₁₄₆ (CoPoly-3)-

Following the outlined procedure for the CuAAC “click” reaction: 0.50 g (~25.0 μmol ; 1.0 eq.) of PEG₄₅₅-bisazide, 0.584 g (~49.8 μmol ; 1.0 eq.) of PPEMC₁₄₆, 0.020 mL (0.141 mmol) of DBU, and 3.1 mg (16.3 μmol) of CuI.

Yield: 1.01 g (47.3 μmol) of fluffy, white powder, 92%. ATR-FTIR (cm^{-1}): 2880 (alkyl-H, m), 1634 (C=N, s), 1490 (C=C_{aryl}, s), 1146 (C-O, m). ¹H NMR (500 MHz, CDCl₃): δ (ppm) 7.52 (end-group Ar-H, broad s), 7.20 (pendant Ar-H, 5H), 5.72, 5.18, 4.51 (pendant methine-H, broad m, 1H), 3.57 (-O-CH₂-, s, 3.98H), 3.16 - 2.86 (N-CH₃, broad m), 1.23

(pendant benzylic-**CH₃**, broad s). DSC (Three Heating-cooling cycles -40 °C – 165 °C) $T_m = 59.8$ °C; $T_c = 35.6$ °C.



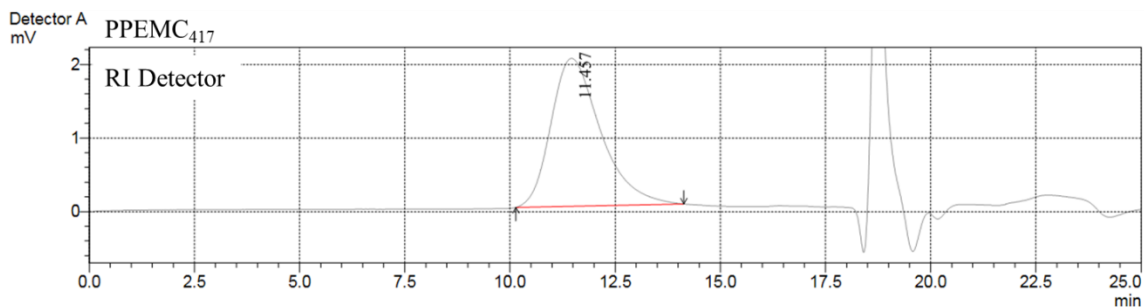
TMAFM imaging of Copolymers-

The self-assembly behaviors of all PPEMC copolymers synthesized depend greatly on the specific sample preparation procedures employed. Drop-coating dilute polymer solutions often resulted in large deviations in height throughout the film making the collection of high-resolution images very challenging. For this reason, all TMAFM samples reported were prepared by passing dilute copolymer solutions through 0.45 μm PTFE syringe filters and spin-coating onto silicon wafers (Wafer World) at 1000 rpm for 30 seconds to allow for the uniform distribution of the polymer film across the entire silicon substrate. For

successful imaging of thin-film morphologies of **CoPoly-1**, **2**, and **3**, each of the polymers were spin-coat from THF or toluene solutions ($c = 5.0 \text{ mg/mL}$) and annealed in an oven at $65 \text{ }^\circ\text{C}$ for 24 hour under air. Specific aggregation behaviors in mixed-solvent systems were prepared by first dissolving the copolymers in THF stock solutions (5.0 mg/mL) and injecting specific amounts (typically $100 \text{ }\mu\text{L}$) into corresponding solvent mixtures of THF/ H_2O or THF/MeOH so that the final solvent combinations are those outlined in the discussion (final $c = 0.5 \text{ mg/mL}$). Each solution was then spin-coat onto silicon wafers as before and dried/stored under vacuum in a desiccator prior to imaging. All images were recorded with resonant frequencies of 320 kHz and lateral scan frequencies of 0.996 Hz using silicon TESP, V-shaped cantilever probes with a nominal spring constant of 42 N/m . Scan areas ranged from $500 \times 500 \text{ nm}$ to $15 \times 15 \text{ }\mu\text{m}$.

GPC Traces of Attempted and Successful PPEMC-PEG “Click” Reactions-

Below are the GPC traces and calculated MW data for all unsuccessful and successful “click” reactions outlined in Section 6.2. The first two copolymers display multimodal chromatograms provided by RI detector suggesting that there is residual homopolymer is present in the system. The chromatogram from the UV-Vis detector of these polymers displays one peak associated with the copolymer formed due to the lack of absorbance of PEG homopolymers in the spectral range of the detector (254 nm).



Peak#:1 (Detector A Ch1)

[Peak Information]

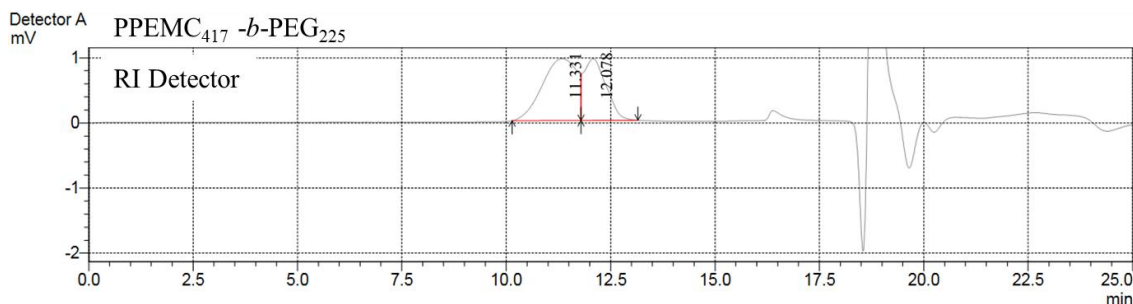
	Time(min)	Molecular Weight	Height
Start	10.142	1467431	57
Top	11.457	129614	2011
End	14.133	5339	104

Area : 164863

Area% : 100.0000

[Average Molecular Weight]

Number Average Molecular Weight(Mn)	66784
Weight Average Molecular Weight(Mw)	143615
Z Average Molecular Weight(Mz)	264844
Z+1 Average Molecular Weight(Mz1)	428151
Mw/Mn	2.15045
Mv/Mn	0.00000
Mz/Mw	1.84413



Peak#:1 (Detector A Ch1)

[Peak Information]

	Time(min)	Molecular Weight	Height
Start	10.142	1467431	34
Top	11.331	158464	952
End	11.792	77982	38

Area : 54582

Area% : 60.8910

[Average Molecular Weight]

Number Average Molecular Weight(Mn)	164215
Weight Average Molecular Weight(Mw)	228174
Z Average Molecular Weight(Mz)	341612
Z+1 Average Molecular Weight(Mz1)	500456
Mw/Mn	1.38948
Mv/Mn	0.00000
Mz/Mw	1.49715

Peak#:2 (Detector A Ch1)

[Peak Information]

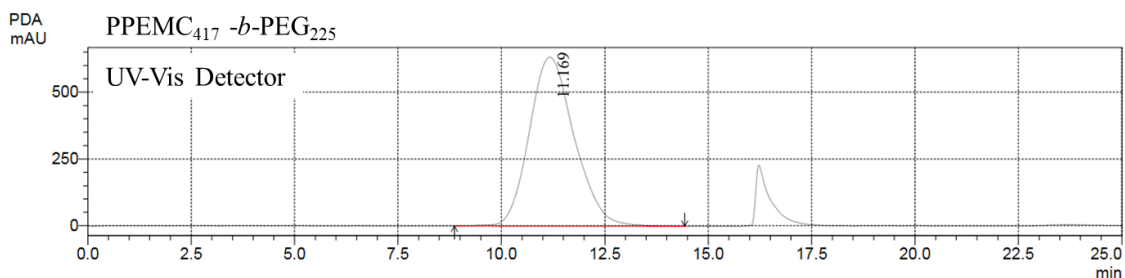
	Time(min)	Molecular Weight	Height
Start	11.792	77982	38
Top	12.078	52052	950
End	13.158	14028	42

Area : 35057

Area% : 39.1090

[Average Molecular Weight]

Number Average Molecular Weight(Mn)	44393
Weight Average Molecular Weight(Mw)	48939
Z Average Molecular Weight(Mz)	53119
Z+1 Average Molecular Weight(Mz1)	56768
Mw/Mn	1.10242
Mv/Mn	0.00000
Mz/Mw	1.08541



Peak#:1 (PDA Ch1)

[Peak Information]

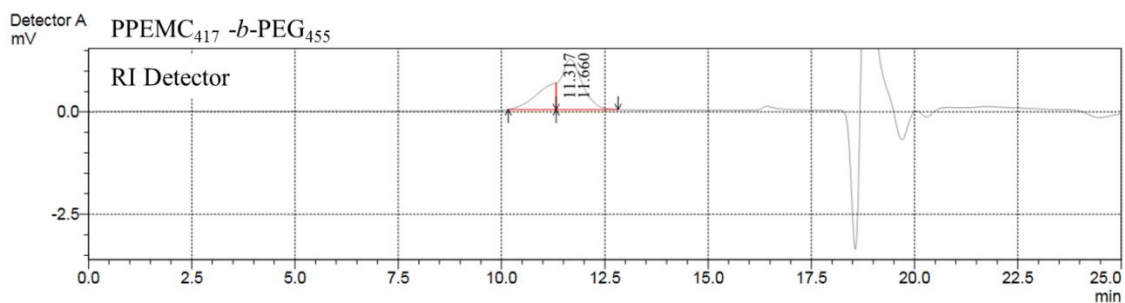
	Time(min)	Molecular Weight	Height
Start	8.864	23286231	-1178
Top	11.169	160307	632758
End	14.432	3572	-1896

Area : 47986000

Area% : 100.0000

[Average Molecular Weight]

Number Average Molecular Weight(Mn)	100153
Weight Average Molecular Weight(Mw)	213800
Z Average Molecular Weight(Mz)	818064
Z+1 Average Molecular Weight(Mz1)	5426482
Mw/Mn	2.13474
Mv/Mn	0.00000
Mz/Mw	3.82631



Peak#:1 (Detector A Ch1)

[Peak Information]

	Time(min)	Molecular Weight	Height
Start	10.158	1416098	58
Top	11.317	162210	649
End	11.325	160025	58

Area : 21338

Area% : 32.7488

[Average Molecular Weight]

Number Average Molecular Weight(Mn)	265691
Weight Average Molecular Weight(Mw)	324005
Z Average Molecular Weight(Mz)	420485
Z+1 Average Molecular Weight(Mz1)	553879
Mw/Mn	1.21948
Mv/Mn	0.00000
Mz/Mw	1.29777

Peak#:2 (Detector A Ch1)

[Peak Information]

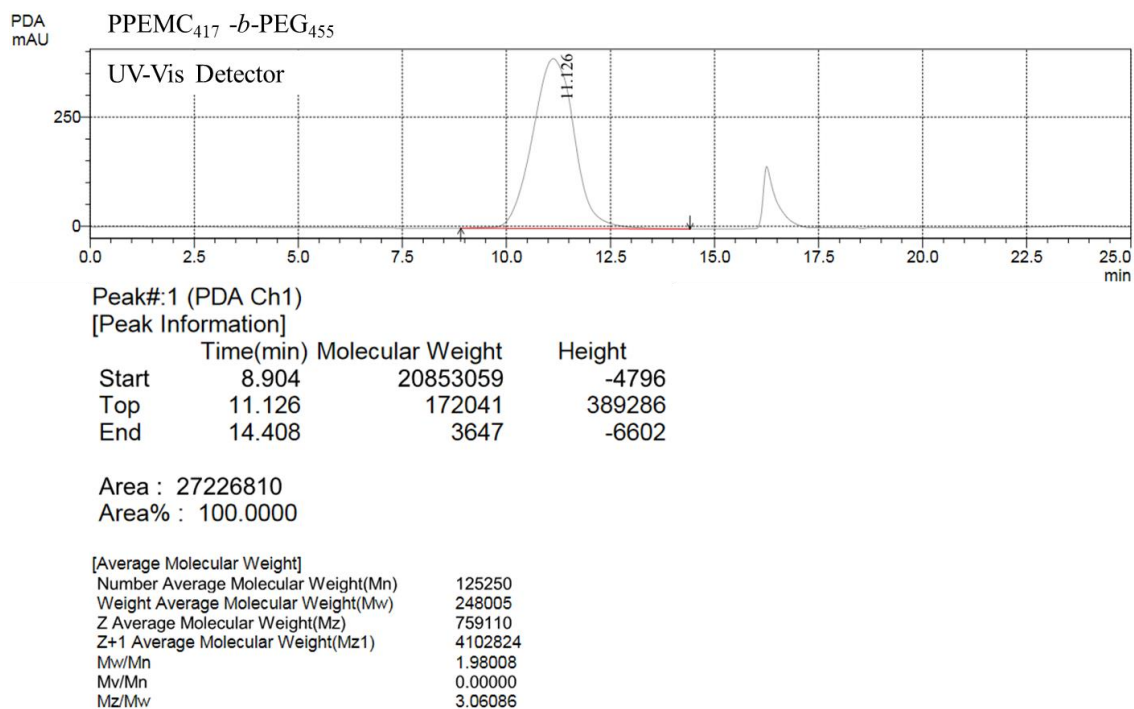
	Time(min)	Molecular Weight	Height
Start	11.325	160025	58
Top	11.660	94704	1232
End	12.825	20363	58

Area : 43819

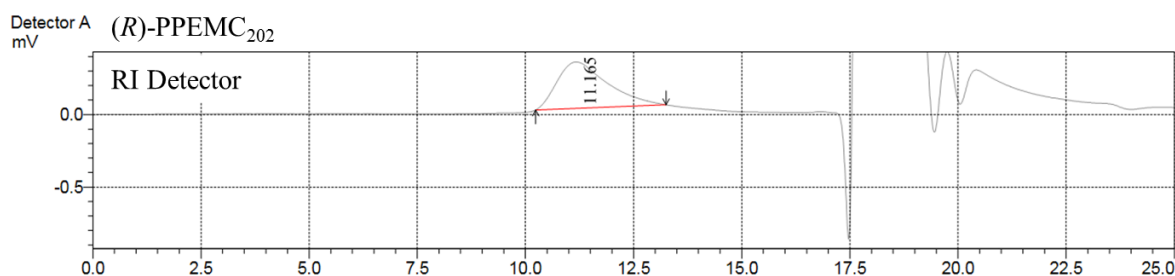
Area% : 67.2512

[Average Molecular Weight]

Number Average Molecular Weight(Mn)	80269
Weight Average Molecular Weight(Mw)	91134
Z Average Molecular Weight(Mz)	101137
Z+1 Average Molecular Weight(Mz1)	109954
Mw/Mn	1.13536
Mv/Mn	0.00000
Mz/Mw	1.10976



GPC Traces for PPEMC parent polymers (PPEMC₂₀₂ and PPEMC₁₄₆) and products from successful “click” reactions (**CoPoly-1**, **2** and **3**) are displayed below. The narrow, monomodal MW distribution and decrease in retention time provides substantial evidence for successful block copolymer formation



Peak#:1 (Detector A Ch1)

[Peak Information]

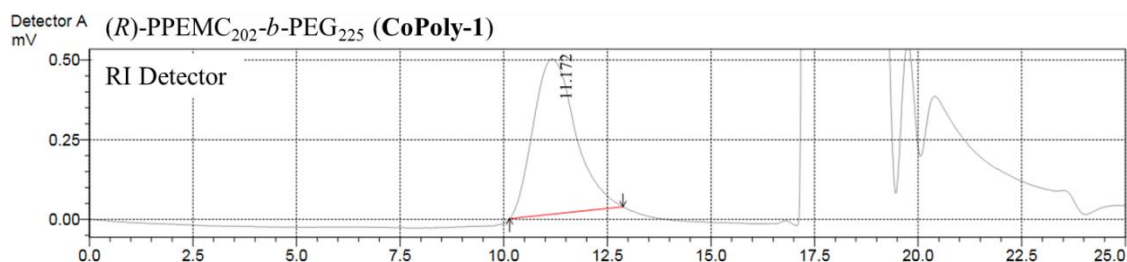
	Time(min)	Molecular Weight	Height
Start	10.233	463631	32
Top	11.165	72825	320
End	13.250	5609	67

Area : 25809

Area% : 100.0000

[Average Molecular Weight]

Number Average Molecular Weight(Mn)	36291
Weight Average Molecular Weight(Mw)	73003
Z Average Molecular Weight(Mz)	125791
Z+1 Average Molecular Weight(Mz1)	180797
Mw/Mn	2.01159
Mv/Mn	0.00000
Mz/Mw	1.72310



Peak#:1 (Detector A Ch1)

[Peak Information]

	Time(min)	Molecular Weight	Height
Start	10.142	575075	3
Top	11.172	71957	487
End	12.875	8019	40

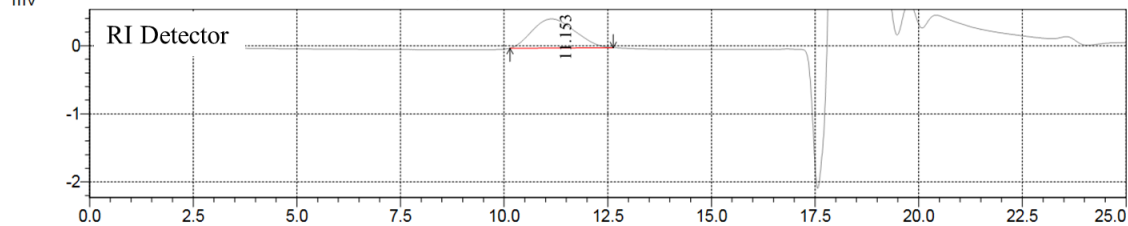
Area : 34542

Area% : 100.0000

[Average Molecular Weight]

Number Average Molecular Weight(Mn)	48276
Weight Average Molecular Weight(Mw)	85530
Z Average Molecular Weight(Mz)	141932
Z+1 Average Molecular Weight(Mz1)	208165
Mw/Mn	1.77170
Mv/Mn	0.00000
Mz/Mw	1.65944

Detector A (R)-PPEMC₂₀₂-b-PEG₄₅₅ (CoPoly-2)
mV



Peak#:1 (Detector A Ch1)

[Peak Information]

	Time(min)	Molecular Weight	Height
Start	10.142	575075	-36
Top	11.153	74325	426
End	12.633	10266	-27

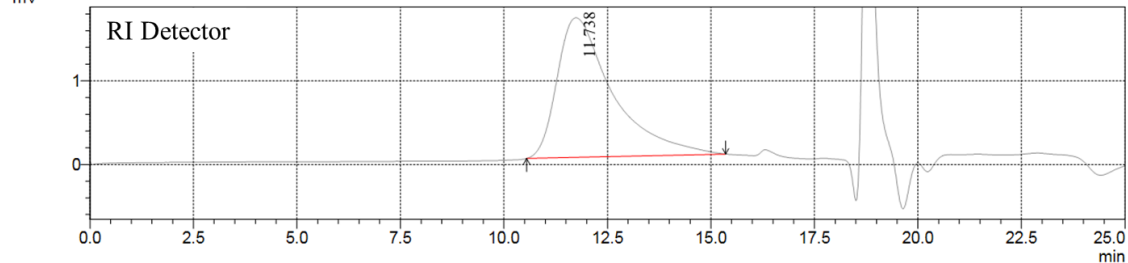
Area : 30341

Area% : 100.0000

[Average Molecular Weight]

Number Average Molecular Weight(Mn)	53759
Weight Average Molecular Weight(Mw)	91243
Z Average Molecular Weight(Mz)	150281
Z+1 Average Molecular Weight(Mz1)	218731
Mw/Mn	1.69728
Mv/Mn	0.00000
Mz/Mw	1.64704

Detector A (S)-PPEMC₁₄₆
mV



Peak#:1 (Detector A Ch1)

[Peak Information]

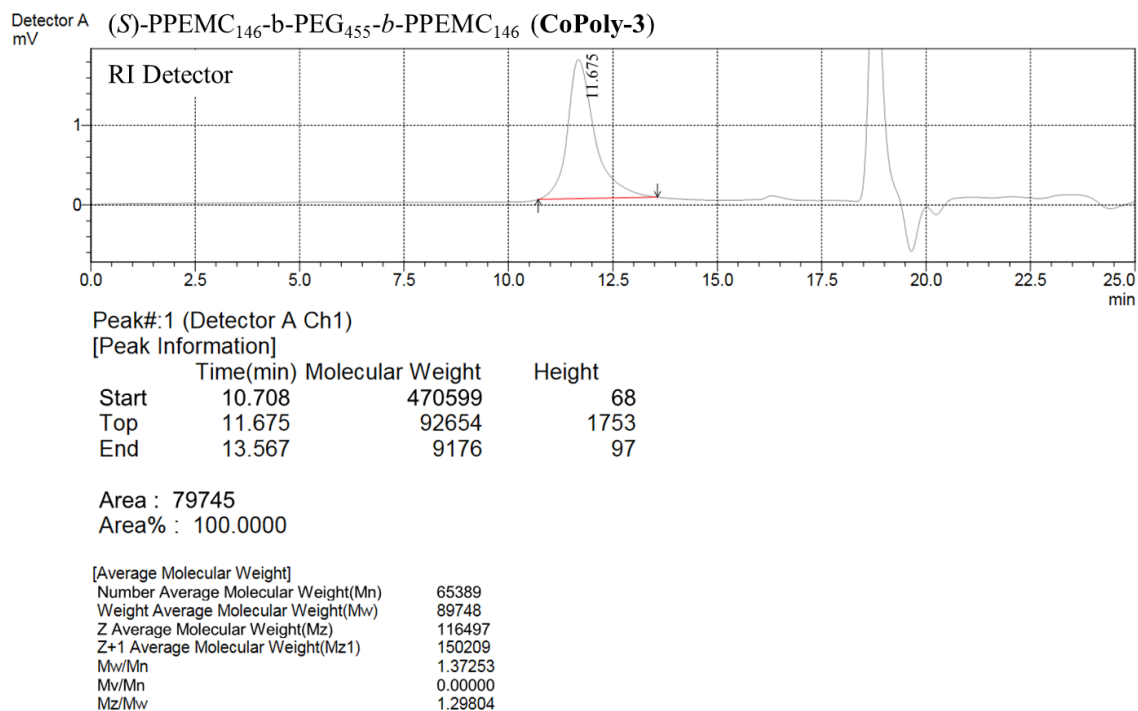
	Time(min)	Molecular Weight	Height
Start	10.550	637101	71
Top	11.738	84373	1670
End	15.358	1859	124

Area : 155915

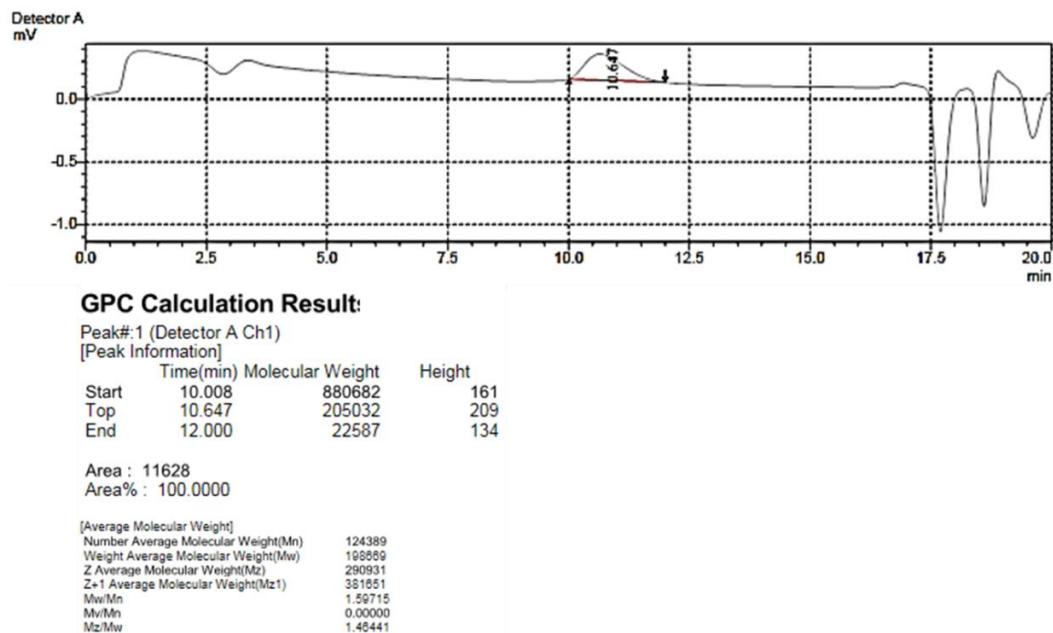
Area% : 100.0000

[Average Molecular Weight]

Number Average Molecular Weight(Mn)	27761
Weight Average Molecular Weight(Mw)	75128
Z Average Molecular Weight(Mz)	134180
Z+1 Average Molecular Weight(Mz1)	196739
Mw/Mn	2.70624
Mv/Mn	0.00000
Mz/Mw	1.78601

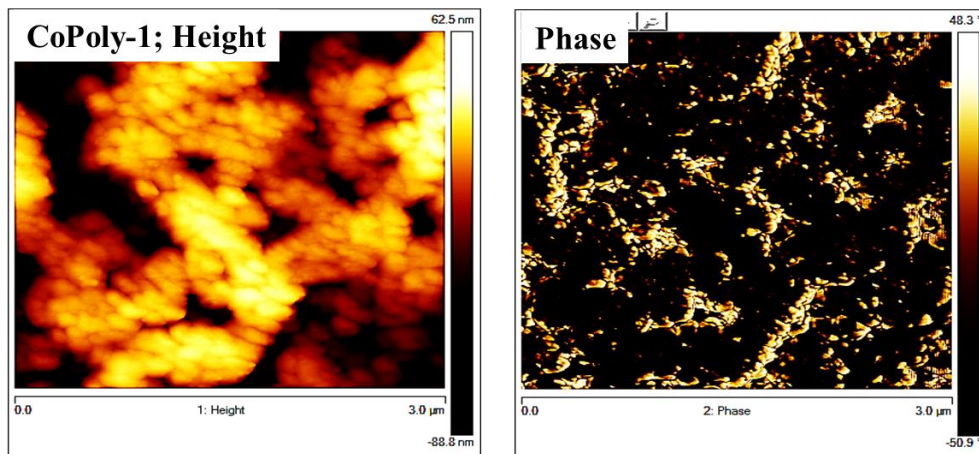


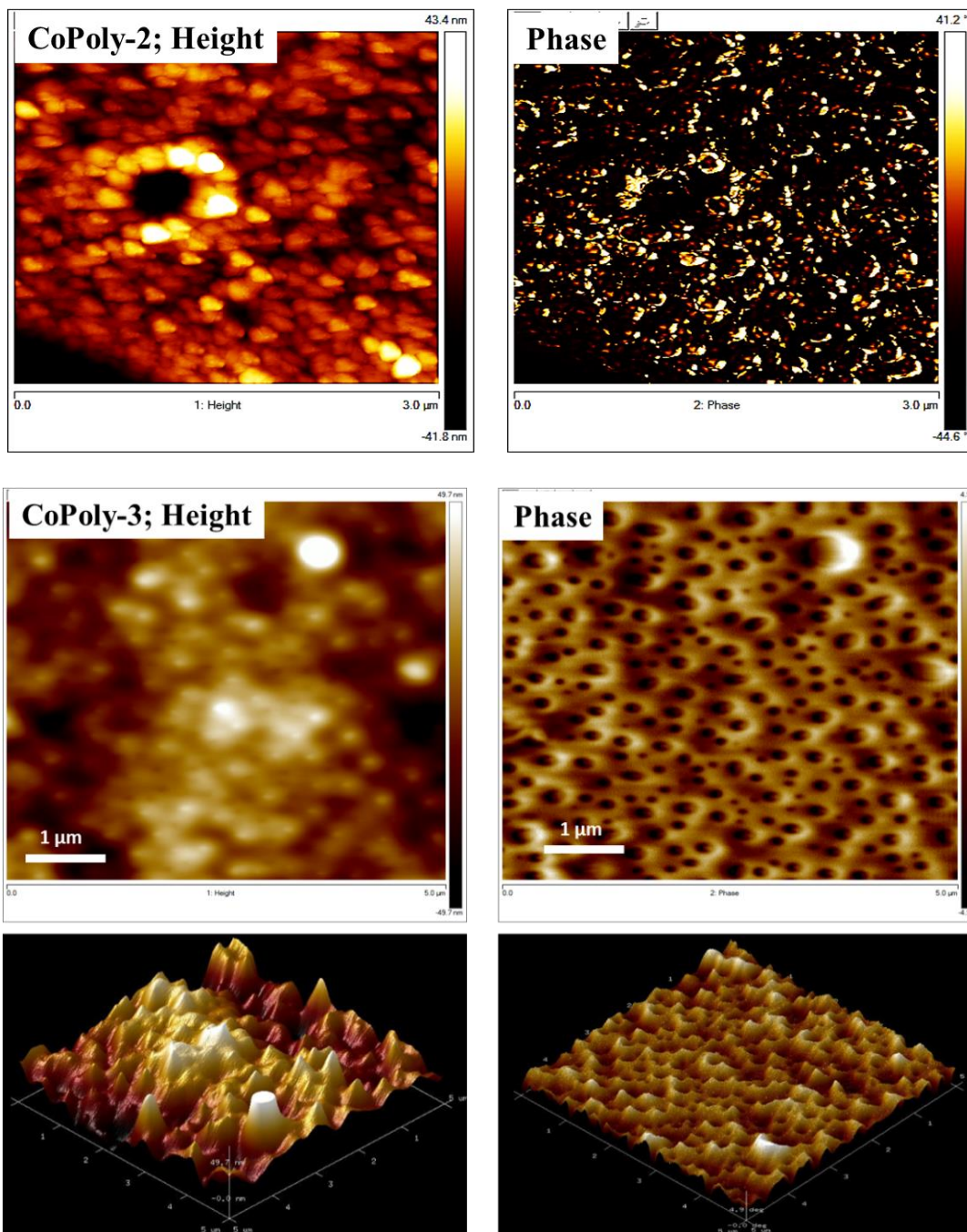
The GPC trace for the PPEMC₇₇₄ homopolymer that was used to study the self-assembly of the PPEMC-PEG RCs blended with high MW PPEMC homopolymer is shown below.

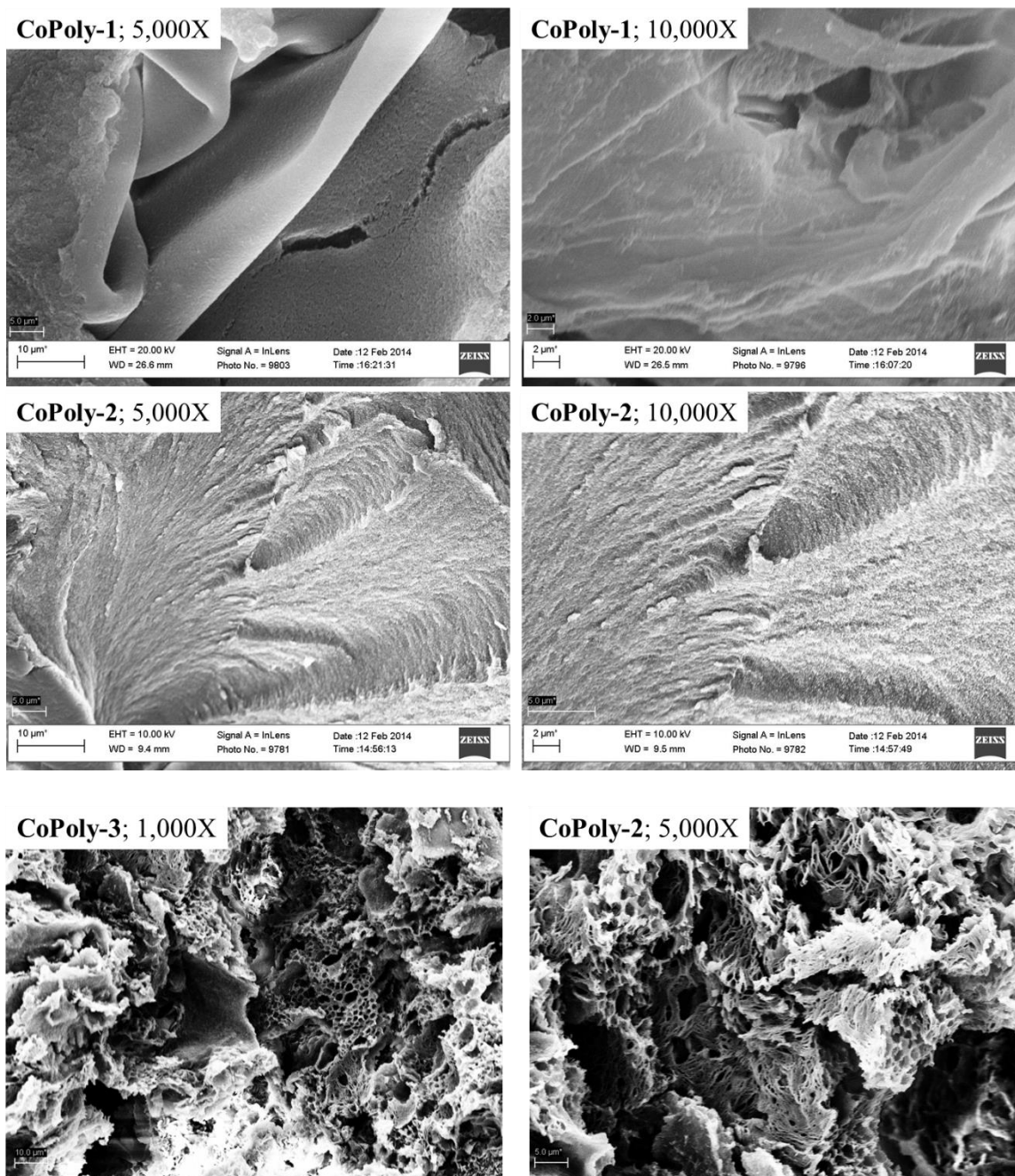


AFM Images of Unannealed Films of CoPoly-1, 2, and 3-

Shown are examples of AFM micrographs of the PPEMC-PEG copolymers spin-coated from THF ($c = 5.0$ mg/mL) prior to annealing at 65 °C. **CoPoly-1** and **2** display very little order and the films were very easily deformed by the AFM tip. **CoPoly-3** displayed interesting morphologies similar to the annealed films corroborating the proposed mechanism of formation.



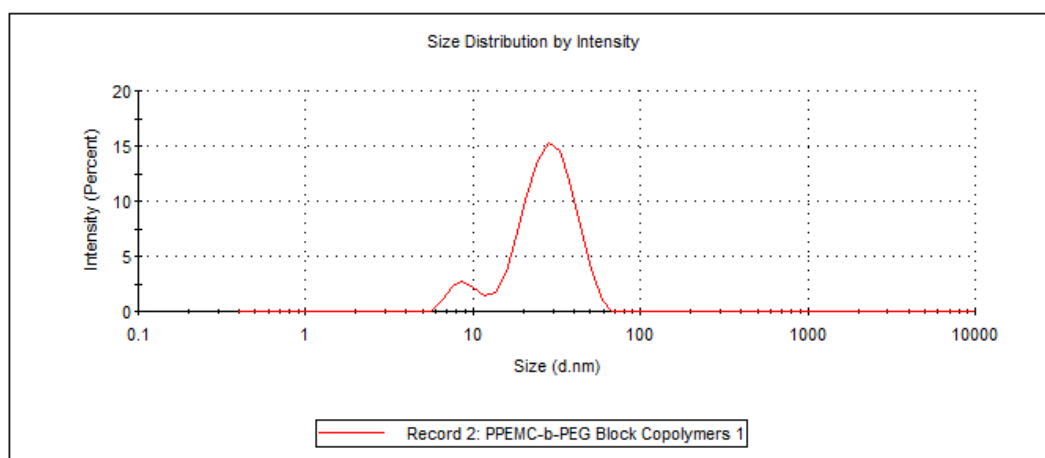


SEM Micrographs of CoPoly-1, CoPoly-2, and Additional CoPoly-3-

DLS of PPEMC₂₀₂ and PEG₄₅₅ Control Homopolymers in THF/ 10 v% H₂O-

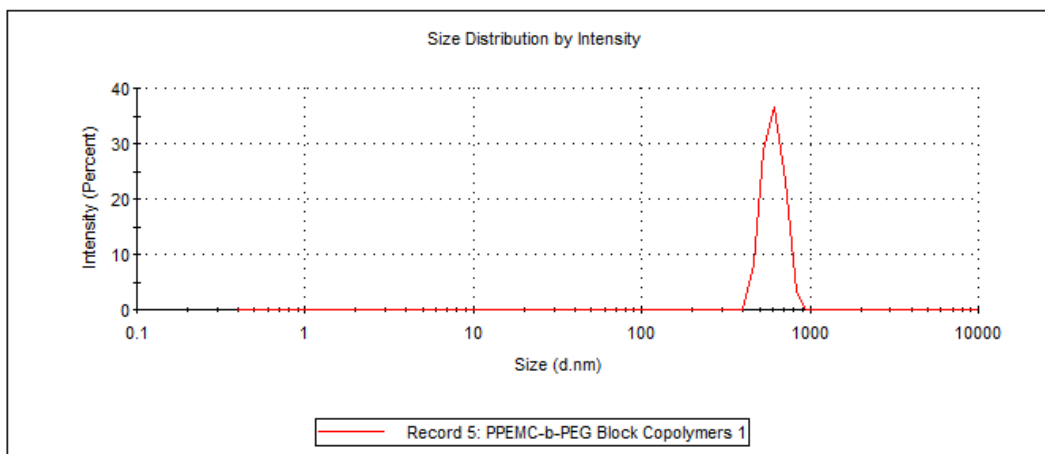
PPEMC₂₀₂

	Size (d.nm):	% Intensity:	St Dev (d.nm):
Z-Average (d.nm): 24.87	Peak 1: 29.63	90.6	9.774
Pdl: 0.292	Peak 2: 8.942	9.4	1.609
Intercept: 0.698	Peak 3: 0.000	0.0	0.000
Result quality : Good			



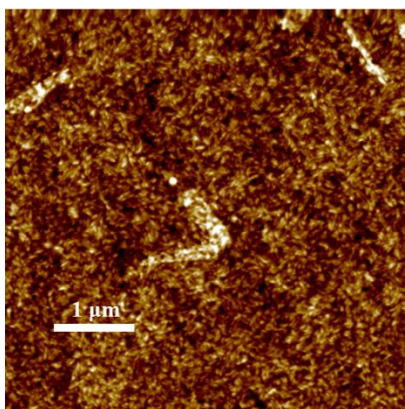
PEG₄₅₅

	Size (d.nm):	% Intensity:	St Dev (d.nm):
Z-Average (d.nm): 559.5	Peak 1: 607.3	100.0	87.47
Pdl: 0.115	Peak 2: 0.000	0.0	0.000
Intercept: 0.947	Peak 3: 0.000	0.0	0.000
Result quality : Good			



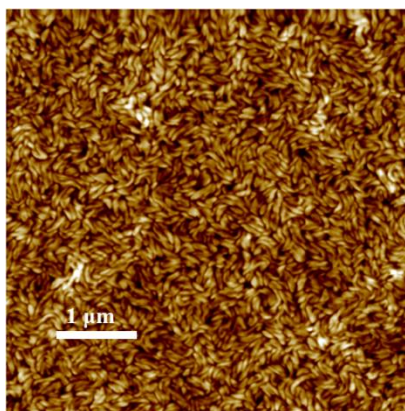
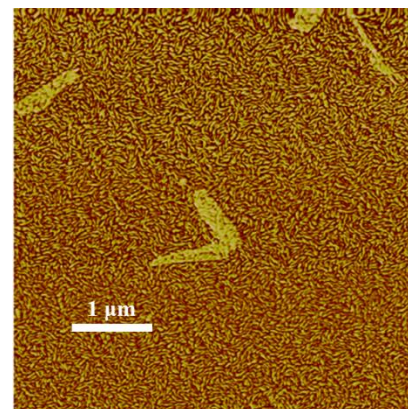
Additional AFM Images of Self-Assembly Behaviors-

Shown are additional AFM images of the surface morphologies prepared from spin-coating from THF ($c = 5.0 \text{ mg/mL}$) and annealing the thin-films at $65 \text{ }^\circ\text{C}$ for 24 hours. Also shown are the AFM micrographs of the 50:50 w% blend of PPEMC₁₄₆ and PEG₄₅₅ homopolymers in the thin-film prepared via the same protocol as the copolymers. Finally, additional AFM images of the aggregates formed in selective solvents can be found below. All of which were used in the statistical measurements of aggregate dimensions.



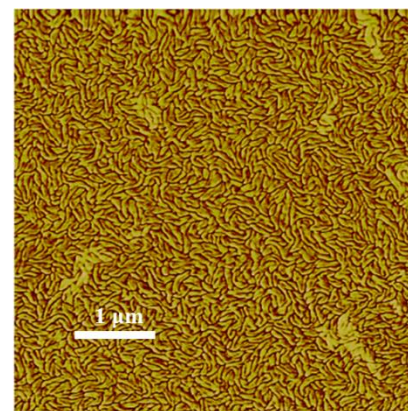
**Thin-films cast
from THF and
annealed at 65 °C**

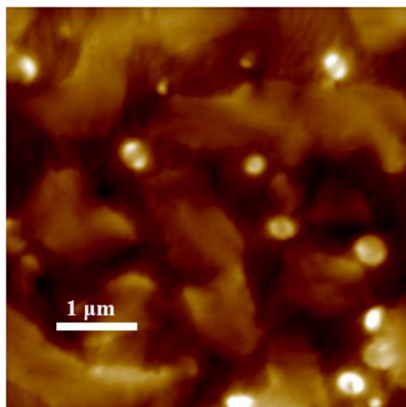
**CoPoly-1
5 x 5 μm**



**Thin-films cast
from THF and
annealed at 65 °C**

**CoPoly-2
5 x 5 μm**

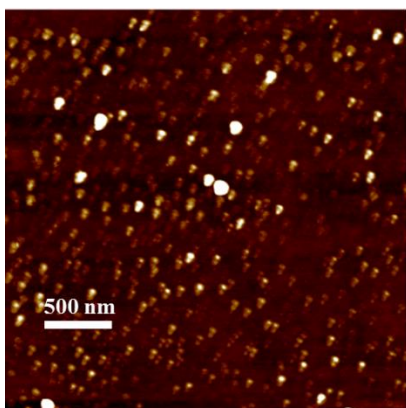
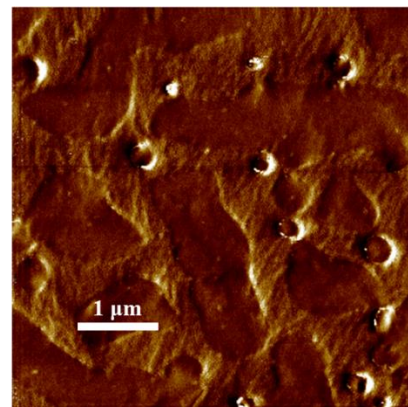




Thin-films cast
from THF and
annealed at 65 °C

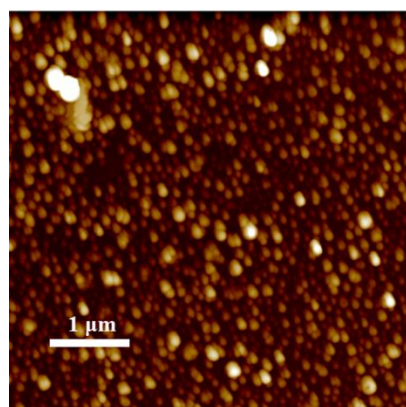
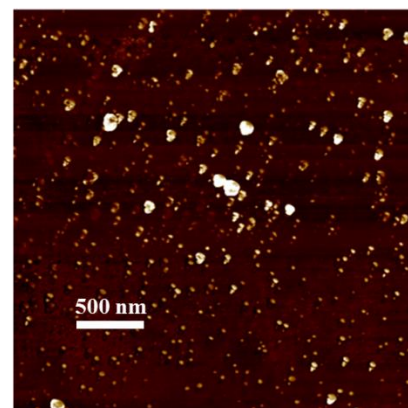
50:50 by weight blend
of PPEMC₁₄₆ and
PEG₄₅₅ homopolymers

5 x 5 μm



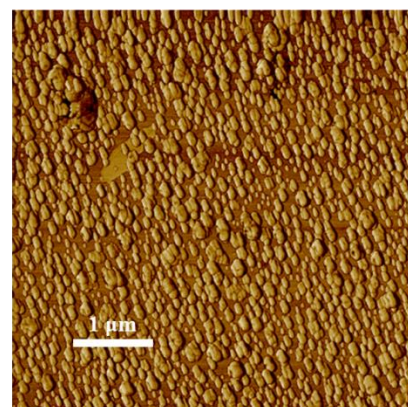
Micelle Aggregates
cast from H₂O/ 10 v%
THF

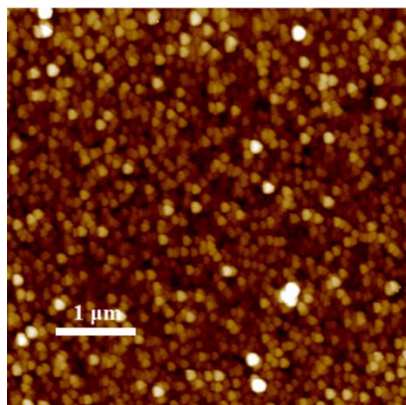
CoPoly-1
3 x 3 μm



Micelle Aggregates
cast from H₂O/ 10 v%
THF

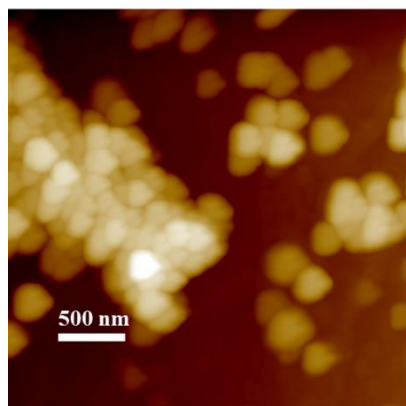
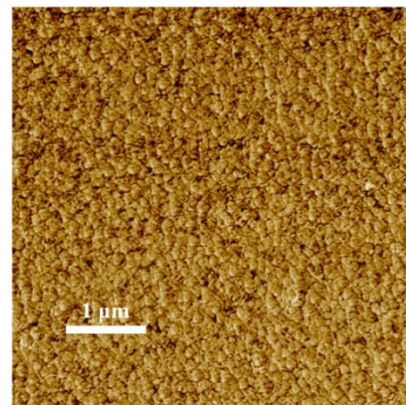
CoPoly-2
5 x 5 μm





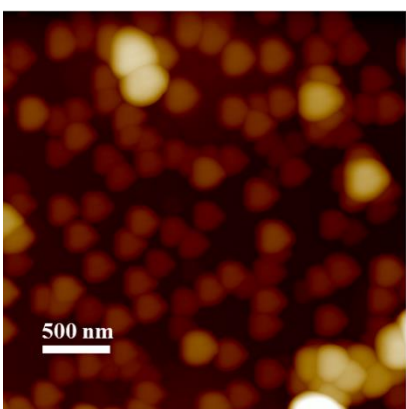
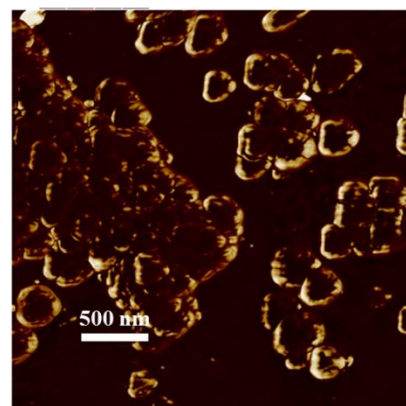
Micelle Aggregates
cast from H₂O/ 10 v%
THF

CoPoly-3
5 x 5 μm



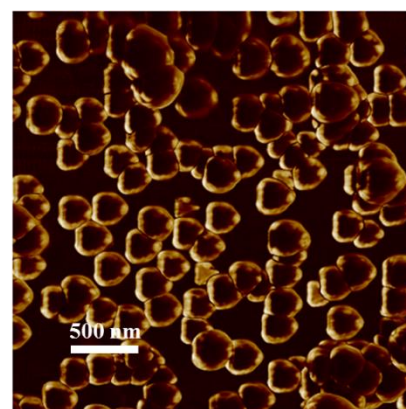
Vesicle Aggregates cast
from THF/ 10 v% H₂O

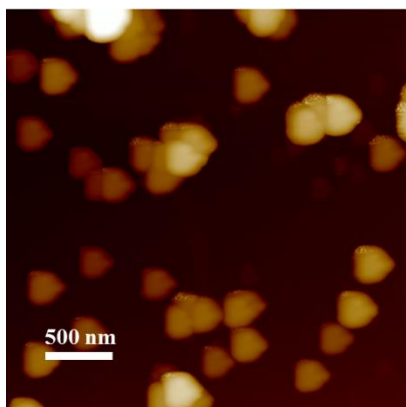
CoPoly-1
3 x 3 μm



Vesicle Aggregates cast
from THF/ 10 v% H₂O

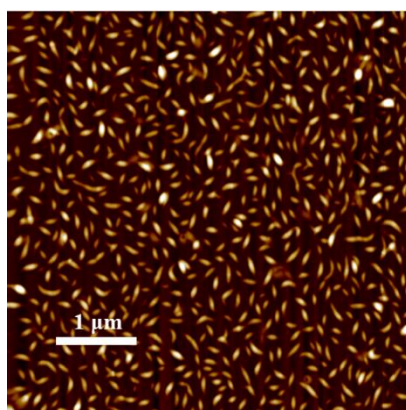
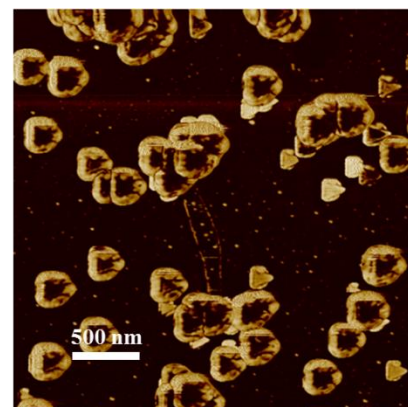
CoPoly-2
3 x 3 μm





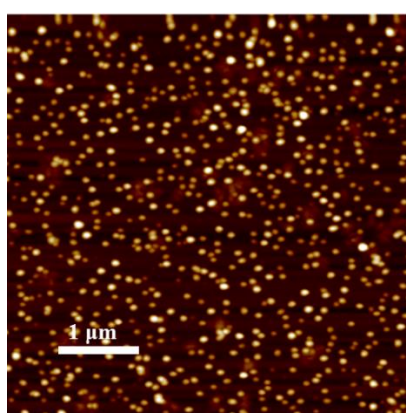
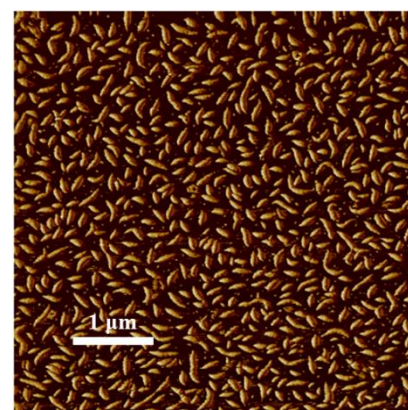
Vesicle Aggregates cast from THF/ 10 v% H₂O

**CoPoly-3
3 x 3 μ m**



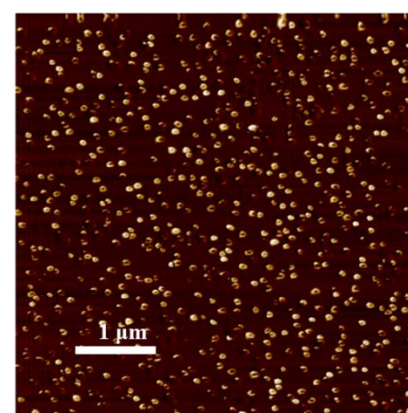
Maggot-like Micelle Aggregates cast from THF/ 10 v% MeOH

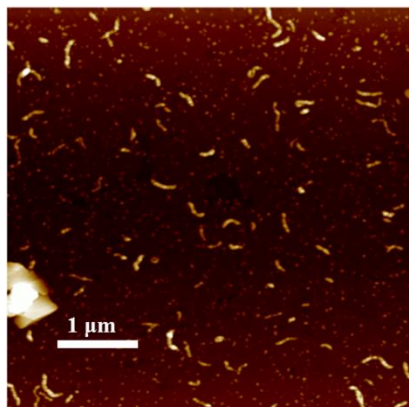
**CoPoly-1
5 x 5 μ m**



Spherical Micelle Aggregates cast from THF/ 10 v% MeOH

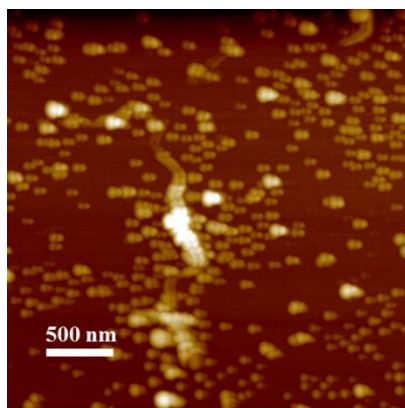
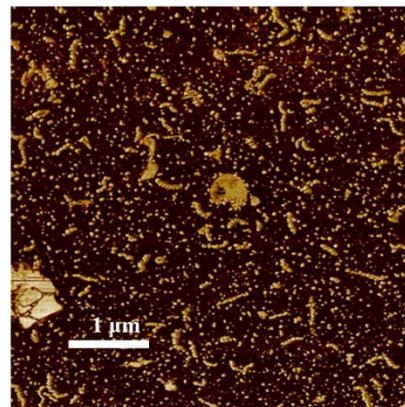
**CoPoly-2
5 x 5 μ m**





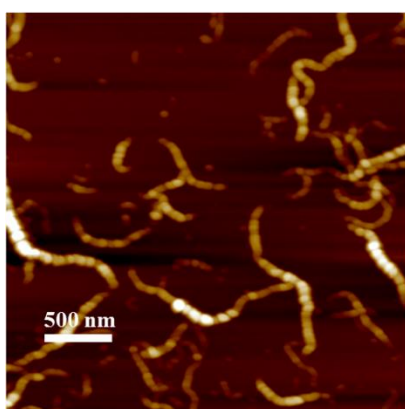
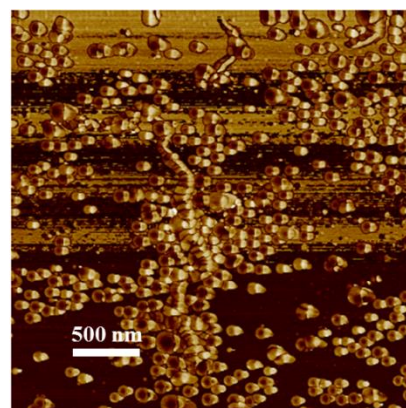
**Spherical and worm-like
Micelle
Aggregates cast from
THF/ 10 v% MeOH**

**CoPoly-3
5 x 5 μm**



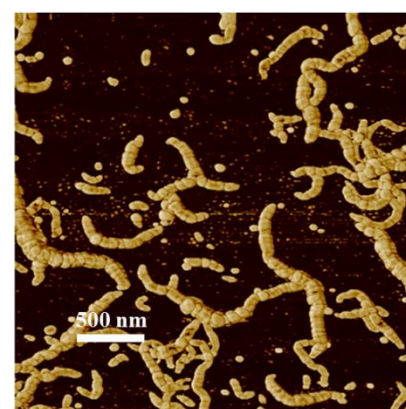
**Spherical and worm-like
Micelle
Aggregates cast from
MeOH/ 10 v% THF**

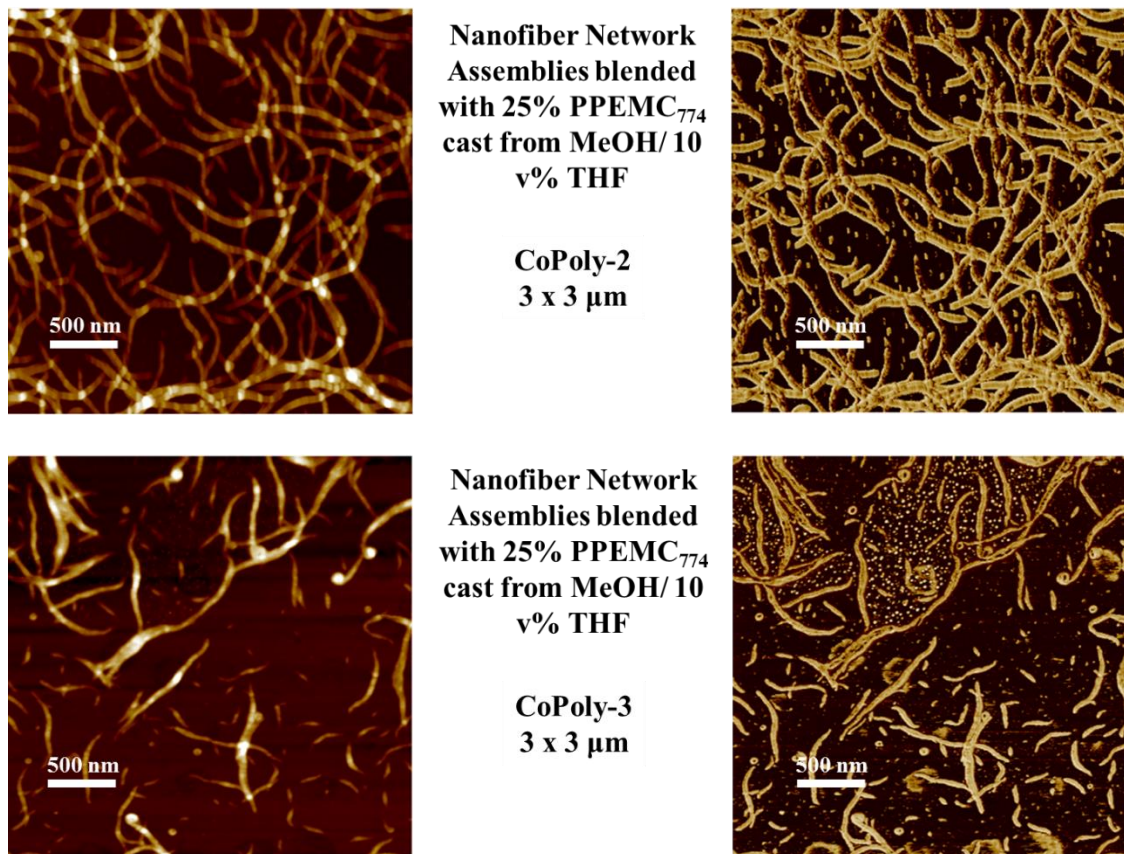
**CoPoly-1
3 x 3 μm**



**Worm-like Micelle
Aggregates cast from
MeOH/ 10 v% THF**

**CoPoly-2
3 x 3 μm**



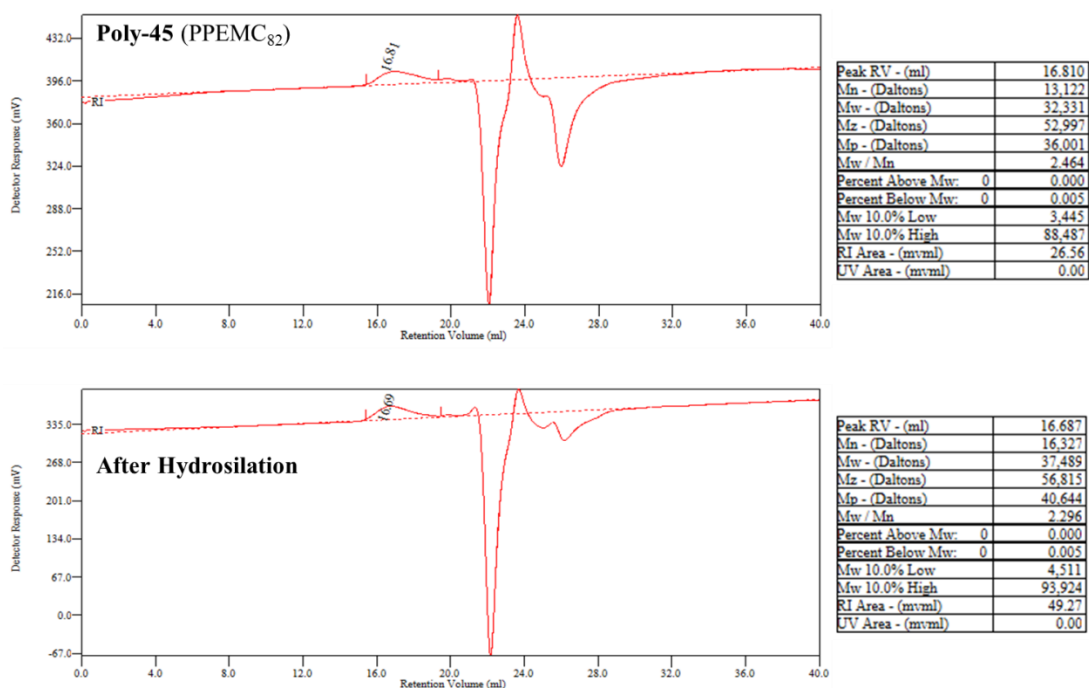


Attempted Synthesis of PPEMC-*b*-PDMS-*b*-PPEMC Triblock Copolymer-

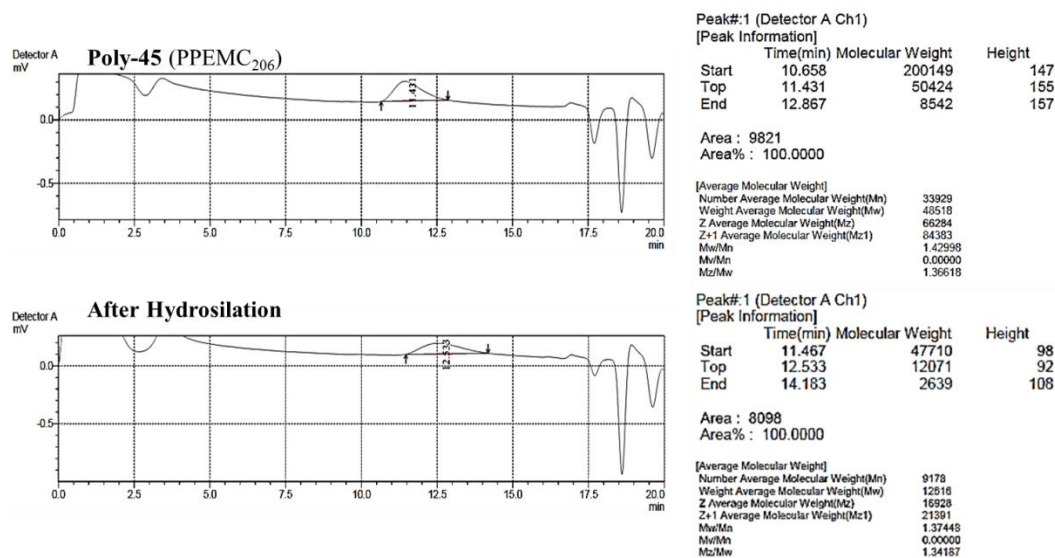
The following procedure was employed at different temperatures (ca. 25, 50, 80 °C) in either CHCl₃ (for 25 and 50 °C) or toluene (80 °C). Additionally, two different platinum catalysts were attempted to mediate the hydrosilation reaction between bis(silane) terminated PDMS and the alkene end-functionalized **Poly-45**. The commercially-available, monodisperse bis(silane) terminated PDMS (1.0 eq.) was added to a oven-dried, three-neck R.B. flask under constant N₂ purge along with ~10 mL of the corresponding solvent. The particular sample of **Poly-45** (2.0 eq.) was then added to the stirring mixture with an additional 10 mL of solvent. Finally, either two drops of the either the Karstedt's catalyst

solution (2.1-2.4% Pt in xylenes; purchased from Gelest) or one drop of the H_2PtCl_6 in IPA (1.0 M; Speier's catalyst) was added to the mixture and then the mixture was allowed to stir for specific amounts of time at different temperature. In all attempts the reaction progress was monitored by ^1H NMR spectroscopy. Three different samples of **Poly-45** of different MWs were used in subsequent attempts. The lower MW PPEMC₈₂ used in the for the 50 °C reaction was one of the samples used for MALDI-TOF MS analysis to verify the intact functionality at the terminus of the polymer. In all cases, no intensity decrease in the ^1H NMR chemical shifts associated with the alkene end-group protons suggesting that the reaction was not progressing. GPC analysis (shown below) displayed either no MW increase or a decrease in MW post hydrosilylation.

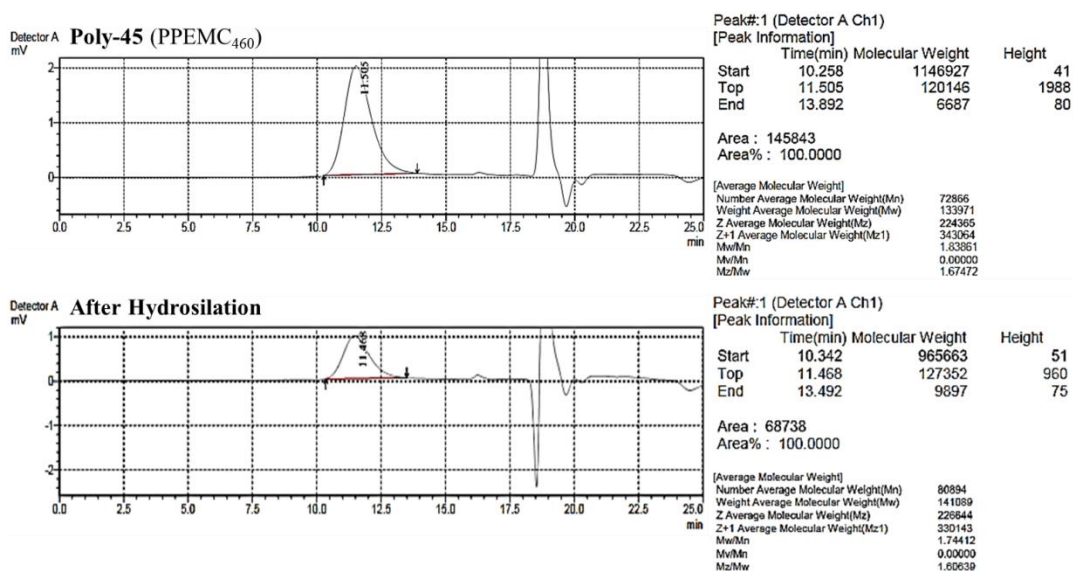
Hydrosilylation at 50 °C with Karstedt's Catalyst-



Hydrosilation at 80 °C with Karstedt's Catalyst-



Hydrosilation at Room Temperature with Speier's Catalyst-



6.10 References

- (1) Bates, F. S.; Fredrickson, G. H. *Phys. Today* **1999**, 52, 32-38.

- (2) Stupp, S. I.; LeBonheur, V.; Walker, K.; Li, L. S.; Huggins, K. E.; Keser, M.; Amstutz, A. *Science* **1997**, *276*, 384-389.
- (3) Klok, H.-A.; Lecommandoux, S. *Adv. Mater.* **2001**, *13*, 1217-1229.
- (4) Lee, M.; Cho, B.-K.; Zin, W.-C. *Chem. Rev.* **2001**, *101*, 3869-3892.
- (5) Lee, M.; Yoo, Y.-S. *J. Mater. Chem.* **2002**, *12*, 2161-2168.
- (6) Zhang, J.; Chen, X.-F.; Wei, H.-B.; Wan, X.-H. *Chem. Soc. Rev.* **2013**, *42*, 9127-9154.
- (7) Wu, J.; Pearce, E. M.; Kwei, T. K. *Macromolecules* **2001**, *34*, 1828-1836.
- (8) Floudas, G.; Papadopoulos, P.; Klok, H. A.; Vandermeulen, G. W. M.; Rodriguez-Hernandez, J. *Macromolecules* **2003**, *36*, 3673-3683.
- (9) Rao, J.; Luo, Z.; Ge, Z.; Liu, H.; Liu, S. *Biomacromolecules* **2007**, *8*, 3871-3878.
- (10) Kim, B.-S.; Hong, D.-J.; Bae, J.; Lee, M. *J. Am. Chem. Soc.* **2005**, *127*, 16333-16337.
- (11) Loos, K.; Boeker, A.; Zettl, H.; Zhang, M.; Krausch, G.; Mueller, A. H. E. *Macromolecules* **2005**, *38*, 873-879.
- (12) Rahman, M. S.; Changez, M.; Yoo, J.-W.; Lee, C. H.; Samal, S.; Lee, J.-S. *Macromolecules* **2008**, *41*, 7029-7032.
- (13) Wu, J.; Pearce, E. M.; Kwei, T. K.; Lefebvre, A. A.; Balsara, N. P. *Macromolecules* **2002**, *35*, 1791-1796.
- (14) Yang, Z.; Yuan, J.; Cheng, S. *Eur. Polym. J.* **2005**, *41*, 267-274.
- (15) Schleuss, T. W.; Abbel, R.; Gross, M.; Schollmeyer, D.; Frey, H.; Maskos, M.; Berger, R.; Kilbinger, A. F. M. *Angew. Chem., Int. Ed.* **2006**, *45*, 2969-2975.
- (16) Huang, C.-J.; Chang, F.-C. *Macromolecules* **2008**, *41*, 7041-7052.
- (17) Cai, C.; Lin, J.; Chen, T.; Wang, X.-S.; Lin, S. *Chem. Commun.* **2009**, 2709-2711.
- (18) Cai, C.; Li, Y.; Lin, J.; Wang, L.; Lin, S.; Wang, X.-S.; Jiang, T. *Angew. Chem., Int. Ed.* **2013**, *52*, 7732-7736.

- (19) Wang, H.; Wang, H. H.; Urban, V. S.; Littrell, K. C.; Thiyagarajan, P.; Yu, L. *J. Am. Chem. Soc.* **2000**, *122*, 6855-6861.
- (20) Koenig, H. M.; Gorelik, T.; Kolb, U.; Kilbinger, A. F. M. *J. Am. Chem. Soc.* **2007**, *129*, 704-708.
- (21) Chen, X. L.; Jenekhe, S. A. *Macromolecules* **2000**, *33*, 4610-4612.
- (22) Jenekhe, S. A.; Chen, X. L. *Science* **1998**, *279*, 1903-1907.
- (23) Shen, J.; Chen, C.; Fu, W.; Shi, L.; Li, Z. *Langmuir* **2013**, *29*, 6271-6278.
- (24) Ibarboure, E.; Papon, E.; Rodriguez-Hernandez, J. *Polymer* **2007**, *48*, 3717-3725.
- (25) Ibarboure, E.; Rodriguez-Hernandez, J. *Eur. Polym. J.* **2010**, *46*, 891-899.
- (26) Kamps, A. C.; Fryd, M.; Park, S.-J. *ACS Nano* **2012**, *6*, 2844-2852.
- (27) Chiu, Y.-C.; Chen, Y.; Kuo, C.-C.; Tung, S.-H.; Kakuchi, T.; Chen, W.-C. *ACS Appl. Mater. Interfaces* **2012**, *4*, 3387-3395.
- (28) Lu, S.; Liu, T.; Ke, L.; Ma, D.-G.; Chua, S.-J.; Huang, W. *Macromolecules* **2005**, *38*, 8494-8502.
- (29) Jenekhe, S. A.; Chen, X. L. *Science* **1999**, *283*, 372-375.
- (30) Chen, J. T.; Thomas, E. L.; Ober, C. K.; Hwang, S. S. *Macromolecules* **1995**, *28*, 1688-1697.
- (31) Liu, X.; Deng, J.; Wu, Y.; Zhang, L. *Polymer* **2012**, *53*, 5717-5722.
- (32) Nieh, M.-P.; Goodwin, A. A.; Stewart, J. R.; Novak, B. M.; Hoagland, D. A. *Macromolecules* **1998**, *31*, 3151-3154.
- (33) Dinç, C. Ö.; Kibarer, G.; Güner, A. *Journal of Applied Polymer Science* **2010**, *117*, 1100-1119.
- (34) Hoo, C. M.; Starostin, N.; West, P.; Mecartney, M. L. *J. Nanopart. Res.* **2008**, *10*, 89-96.